NONRADIAL OSCILLATIONS OF STARS

Second Edition

Wasaburo Unno/Yoji Osaki/Hiroyasu Ando
Hideyuki Saio/Hiromoto Shibahashi

UNIVERSITY OF TOKYO PRESS

ISBN 4-13-066103-5
ISBN 0-86008-439-6
Printed in Japan

Contents

Preface

With increasing accuracy and higher time resolution, recent observations have revealed that nonradial oscillations and related phenomena are inherent to most of the stars that are the main constituent of the universe. There are two theoretical aspects of nonradial oscillations of stars. In one sense, stars are musical instruments that are able to oscillate with variation in wave length or in frequency. The modes of oscillation differ from one star to another and change in a delicate way as a star evolves. It is, however, the stars themselves which power and control the oscillations. The second aspect, therefore, is the sense in which stars function as heat engines to drive their own oscillations.

Our research group in the Department of Astronomy, University of Tokyo, has been engaged in developing the theory of the above two aspects and in interpreting observations. We wrote the first edition of *Nonradial Oscillations of Stars* in 1979, summarizing the fundamental concepts of nonradial oscillations and reviewing studies up to that time. Nearly a decade has passed, and much progress has been made since then in this field, so it seemed a good time to consider the publication of a new, fully revised edition. In particular, a new field of research called "helio- and astero-seismology" has been opened up, in which the internal structures of the sun and stars can be probed using their oscillations.

Hideyuki Saio has joined us in the new edition, which has been revised to incorporate recent progress in this field; our intention is that this monograph will remain useful not only to specialists but also to nonspecialists as a textbook. It covers nonradial oscillations of stars from the basics to the most recent developments. Special emphasis is placed on the linear adiabatic and non-adiabatic theory of nonradial oscillations of stars. However, the recent extension of the theory to general relativity and the nonlinear problems are considered outside the scope of the present monograph and they are not treated here. Three of seven chapters are completely new, and the others have been revised in order to update their contents. The newly added chapters are Chapter IV, Nonadiabatic Oscillations; Chapter VI, Nonradial Oscillations in Rotating Stars; and Chapter VII, Helio- and Asteroseismology. Major authorial and editorial responsibility for the various chapters of the new edition is as follows: Chapter I, Introduction: Unno and Osaki; Chapter II, Observational Aspects of Nonradial Oscillations: Osaki, Ando, Saio,

Shibahashi; Chapter III, Basic Equations and Adiabatic Oscillations: Shibahashi, Unno, Osaki, Saio; Chapter IV, Nonadiabatic Oscillations: Saio; Chapter V, Excitation and Damping of Oscillations: Ando, Unno, Saio, Shibahashi; Chapter VI, Nonradial Pulsations in Rotating Stars: Saio, Ando, Shibahashi; Chapter VII. Helio- and Asteroseismology, Shibahashi. A list of symbols, reference list, and subject index are included at the end of the volume. References include the section numbers where the works are referred to. We hope that this volume will contribute to future progress in the study of nonradial oscillations.

We thank Mr. M. Inoue of the University of Tokyo Press for various editorial arrangements, Mrs. K. Sakurai for her help in preparing the manuscript, and Messrs. M. Hirose and T. Sekii for preparing some figures. The publication of this book was supported in part by the Grant-in Aid for Publication of Scientific Research Result from the Ministry of Education, Science and Culture of Japan.

17 February 1989

Wasaburo Unno
Yoji Osaki

Chapter I

INTRODUCTION

1. What are Nonradial Oscillations ?

Every one of the stars, including our sun, is a self-gravitating gaseous sphere that radiates an enormous amount of energy to its outer space. Energy radiated from the surface of a star is generated in the deep interior by thermonuclear reactions. A star, born out of an interstellar cloud, spends most of its life in the hydrogen-burning main-sequence stage. As a star consumes its nuclear fuel, it evolves by changing its internal structure. A star is by no means a quiet object, but it is in a sense a kind of heat engine exhibiting various activities. Some stars blow out stellar winds from their surfaces with speeds ranging up to a few thousand kilometers per second, while some others are pulsating variables. A pulsating variable is a star that changes its brightness periodically by changing its volume just as a human body breathes rhythmically.

This monograph deals with one such stellar activity: nonradial oscillations (or nonradial pulsations), the general type of stellar eigen-oscillations. There exist two kinds of stellar oscillations: radial and nonradial. The radial oscillation (or radial pulsation) is a simple type of oscillation in which a star oscillates around its equilibrium figure, by expanding and contracting, while keeping its spherical shape. Nonradial oscillations are a more general type in which a star oscillates in such a way as to deviate from its spherical shape. The radial oscillation may be regarded as one of the special cases of nonradial oscillations with the spherical harmonic index $l = 0$. (See Section 4 for the definition of the spherical harmonic index.)

The theory of stellar pulsation was originally developed in order to explain the pulsations of classical variable stars such as the Cepheids and RR Lyrae stars. These variables are thought to be radial pulsators. However, in recent years, pulsations and oscillation-related phenomena have also been discovered in many stars that were regarded as

non-pulsating stars before. They include our sun itself, white dwarfs, Ap stars, and early-type O and B stars with slow and rapid rotation. The most important characteristics of oscillations in these stars are that they are thought to be nonradial and are usually multi-periodic with several modes of oscillations involved. In fact, the sun is oscillating in thousands of nonradial eigenmodes. By using these oscillations, one can probe the internal structure of the sun, just as one probes the interior of the earth by using the data of seismic waves. This new field of research is thus called "helioseismology." As will be discussed in the last chapter, helioseismology is very successful in studying the internal structure of the sun. The same method may in principle apply to stellar oscillations, and it is in this case called "asteroseismology". Asteroseismology is at the present moment still in its infancy, but it has the potential to develop into a major field of stellar physics.

Every one of the stars differs from all others in its mass and in its evolutionary stage. From the standpoint of the theory of nonradial oscillation, stars are like musical instruments that are able to oscillate in modes which differ from one star to another and change in delicate ways as a star evolves. Let us study stars as musical instruments.

2. Stellar Stability and Oscillations

Three types of stability are fundamental for the equilibrium configuration of stars: dynamical stability, vibrational stability, and thermal stability. For an arbitrary small contraction of a star as a whole, the increment of the pressure gradient exceeds that of the gravitational force, and then the equilibrium structure is restored. This is the state of dynamical stability, in which stars should spend almost all their lives. The dynamical instability, however, can be present locally inside a star. In fact, convection in stars is the manifestation of a dynamical instability against nonradial perturbations. Since the treatment of convection is much the same as that of nonradial oscillations as far as the linear theory is concerned, some consideration will also be given to convection in this monograph.

Thermal stability is sometimes called secular stability, although the definitions may differ slightly. The reason is that the thermal time scale is much longer than the dynamical time scale in most stars. For instance, the characteristic solar thermal energy divided by the solar luminosity is about 3×10^7 years, while the characteristic solar dynamical time scale (the free-fall time) is only about a half-hour. The ratio is quite large even in supergiant stars. Hydrostatic equilibrium can, therefore, be assumed in the study of thermal stability. Ordinarily, an excess input of

thermal energy causes a perfect gas star to expand as the virial theorem implies, and the temperature is normally decreased by the hydrostatic adjustment. This is the state of thermal stability. Thermal instability is found typically at the commencement of helium burning (or carbon burning, etc.) in the degenerate helium core (carbon core, etc.). The result is known as the helium flash (carbon detonation, etc.). Also, a nondegenerate helium-burning shell can provide thermal instability (thermal flicker). The reason is that the hydrostatic adjustment to a temperature excess in a thin shell affects the pressure distribution within a star by only a small amount. In general, however, the thermal instability is not related to nonradial oscillations, because the hydrostatic equilibrium restricts the pressure and density perturbations to spherical symmetry in the absence of strong magnetic field or rotation. Although a nonradial thermal instability may be possible with the gradient in mean molecular weight, no important example of such a case has been found. Only brief mention of thermal instability will be made hereinafter.

A dynamically stable system undergoes oscillation if perturbation is applied to it. Inversely, a system is said to be dynamically stable if it oscillates under the influence of any arbitrary perturbation. An oscillation of a system may or may not grow in time. If it grows, it is said to be overstable or vibrationally (or pulsationally) unstable. In order for an oscillatory stable system to maintain a regular periodic oscillation, external force must be applied periodically. This is a forced oscillation such as is found in the tidal oscillation of an ocean. On the other hand, free oscillations will continue for at least some time once a perturbation has been applied initially. The physical properties of nonradial free oscillations of stars are the main subject of this monograph.

Stars are like musical instruments which have various modes of oscillation and tones. As will be shown later, the normal modes in a spherically symmetric stars are characterized by the eigenfunctions that are proportional to the spherical harmonics: $Y_l^m(\theta,\phi)$ ($l = 0, 1, 2, \ldots$; $m = 0, \pm1, \ldots, \pm l$). In particular, the radial modes are special cases of $l=0$. The $l=1$ and 2 harmonics are called the dipole and the quadrupole oscillations, respectively. The eigenfrequencies depend on l but are degenerate by $(2l+1)$-folds in m. The normal modes belonging to the harmonic index l are further distinguished by the number of nodes, n, in the radial component of displacement from the center to the surface of a star. The n-values are 0 for the fundamental mode, 1 for the first overtone mode, 2 for the second overtone mode, etc. The normal modes are classified by the radial quantum number n and the angular quantum number l. When "Zeeman splitting" is introduced by rotation

or by magnetic field, the azimuthal quantum number m has to be added.

In what follows, we call the quantum number l the harmonic degree, the quantum number m the azimuthal order, and the quantum number n the radial order.

Cepheid variables are known as pulsating stars. Most of them are pulsating in the fundamental or the first overtone radial modes (n=0, 1; l=0), but a few seem to be oscillating in the second overtone mode (n=2; l=0). Nonradial oscillations are less prominent observationally, because a portion of the star is in the opposite phase in brightness and in velocity to the adjacent portion of the same star. Their astrophysical importance, however, is by no means less than that of radial pulsation, as will be demonstrated in detail in later chapters. The pulsation of white dwarf variables and the solar five-minute oscillation are well-known examples of nonradial oscillations. Perhaps, as theory and observation make rapid progress in the near future, it will become more difficult to find a star without nonradial oscillations than to find a star with nonradial oscillations. The reason is that nonradial oscillations are indeed rich in the variety of physical properties. A star is then likely to have some nonradial modes which are favorably excited either in the core or in the envelope, depending on the structure of the star.

The richness of nonradial oscillations compared with radial pulsation is partly due to the degree of freedom in the horizontal wave number represented by the harmonic degree l. There is also the physical reason that not only pressure but also gravity can act as the restoring force causing nonradial oscillations. Since the change in the gravitational force is inward in the compressed phase, or outward in the expanded phase, gravity cannot be the restoring force for the radial pulsation. On the other hand, as we can see by throwing a stone into a pond, gravity can act through buoyancy as the restoring force for nonradial oscillations. Thus, while the radial oscillation has only the spectrum of the pressure mode (p-mode) or the acoustic (wave) mode, the nonradial oscillation shows the spectrum of the gravity (wave) mode (g-mode) as well. The behaviors of the p- and the g-mode oscillations as determined by the internal structure of stars are among the main interests in this monograph and will be discussed in detail in later chapters.

Since the p- and the g-mode spectra show the ∞^2 normal modes corresponding to different values of n and l, nonradial eigenfrequencies can be found almost everywhere in the frequency space. However, they are not necessarily self-excited. In order for an oscillation to be overstable, some excitation mechanism is needed. According to thermodynamics, such an excitation mechanism has to provide an entropy increase or a heat input during the high temperature phase in an

oscillation cycle. The positive temperature dependence of the opacity and the high temperature sensitivity of the nuclear energy generation are known to provide the excitation mechanisms called the κ-mechanism and the ε-mechanism, respectively. There are also other mechanisms, operating particularly on nonradial oscillations, which will be discussed in Chapter V. By those mechanisms, some oscillation modes are selected among all the p- and g-mode spectra and maintained in a finite amplitude at which some nonlinear energy dissipations should work against the overstability. But a higher temperature normally implies a larger radiation loss, leading to the damping of oscillations. The stability is the result of the competition between the excitation and damping mechanisms. In order for a mode to be excited, some excitation mechanism must be operative in the region where the amplitude of eigenfunctions is large. Numerical computations with an electronic computer are usually required to find an overstable mode for a given stellar model.

The role of the convection zone in oscillatory stability is rather complicated. The turbulent viscosity should be effective for damping. However, there are also efficient excitation mechanisms associated with the superadiabaticity in the convection zone. Convection-pulsation coupling will be discussed in Section 30. The semiconvection zone surrounding the hydrogen-depleted convective core of a massive star is another place of special interest in examining overstability. The semiconvection zone is supposed to be superadiabatic but dynamically stable because of the gradient of the mean molecular weight. These properties are favorable for the trapping and excitation of some g-mode oscillations. A similar situation may be expected in the rapidly rotating cores of early type stars. In this case, convection will be stabilized by rotation, resulting in an overstable oscillation. This problem will be discussed in Chapter VI.

Stars have been thought in the past to be less susceptible to nonradial oscillations than to radial oscillations because of the increased dissipation of the oscillation energy by the lateral radiative heat exchange. However, recent investigations show that much variety in the geometrical and physical properties of nonradial oscillation should give some nonradial oscillations a better chance to get excited. The excitation mechanisms are also numerous for nonradial oscillations. The purpose of this monograph is to show that variability is rather common among stars although the observational detection may not be definitive in some cases.

3. Historical Background and Recent Development

The early history of studies on stellar pulsation was concisely described by Rosseland (1949) in the introductory chapter of his famous textbook, *The Pulsation Theory of Variable Stars*. It is interesting to see that the theory of nonradial pulsation developed by Lord Kelvin (1863) preceded the theory of radial pulsation developed by Ritter (1879). However, the Cepheids have been the chief concern of pulsation theory, which was founded by Eddington as summarized in *The Internal Constitution of the Stars* (1926). In spite of the remarkable progress in the development of the theory of radial pulsation, the theoretical study of nonradial pulsation remained largely within academic circles until recently. But the work of Pekeris and Cowling should be mentioned. Pekeris (1938) obtained the exact analytic solution for adiabatic nonradial oscillations in the homogeneous compressible model. Cowling (1941) extended the study to the polytrope model. For a description of these and other studies, readers can refer to the comprehensive article by Ledoux and Walraven (1958).

The development of the study of nonradial pulsation may be regarded to have started from the work of Ledoux (1951). He suggested that nonradial oscillations could explain the double periodicity and the large temporal variations in the broadening of spectral lines observed in β Canis Majoris (a prototype of β Cephei type variable stars). Osaki (1971) examined Ledoux's theory by calculating line profiles for a star undergoing nonradial oscillations and compared the result with observations available at that time. He also suggested (Osaki, 1974) a possible mechanism for the origin and maintenance of β Cephei pulsation based on nonradial oscillation. However, the very question of whether pulsation modes of β Cephei stars are radial or nonradial still remains unsettled. There is an argument that the main pulsation of β Cephei stars is radial (Smith, 1980a, b). Even so, some β Cephei stars show multi-period beating, and this indicates that nonradial oscillations must be involved as well in those β Cephei stars.

The discovery of the solar five-minute oscillation by Leighton, Noyes, and Simon (1962) was also epoch-making. A number of interesting theories had been proposed to explain this phenomenon (see Stein and Leibacher, 1974). Some fifteen years later, Deubner (1975) succeeded in resolving observed oscillations into discrete modes in the so-called diagnostic diagram (see Section 11). A comparison between his observation and theoretical eigenfrequencies of nonradial modes calculated by Ando and Osaki (1975) has established that the solar

five-minute oscillations are global nonradial p-modes of the sun with high spherical harmonic degree l ($l = 200 - 1000$). Since the late 1970s, observations using integrated sunlight over the whole disk, both in radial velocity variation and in total irradiance variation, by several groups (Birmingham/Tenerife, Crimea, Nice, Stanford, and SMM satellite) have revealed the existence of other p-mode oscillations with low degree l ($l = 0 - 5$). Furthermore, p-mode oscillations with intermediate degree l ($l = 1 - 200$) have also been detected. In addition, full two-dimensional analyses of oscillation data over the solar disk have been performed (Brown, 1985; Libbrecht, 1989) yielding eigenfrequency spectra with information on individual modal numbers of n, l, and m. The sun must be regarded as one of pulsating stars, pulsating in many p-modes with $l = 0 - 1000$. The most important and unique aspect of solar oscillations is the possibility of a seismological approach, by which one can probe the solar deep interior by using oscillations. A more detailed description of the development of helioseismology will be given in Chapter VII.

Since the late 1960s and early 1970s, pulsations and oscillation-related phenomena have been observed in many stars that were regarded as non-pulsating stars before. They include white dwarfs, Ap stars, and early type O and B stars. It is now believed that nonradial oscillations are responsible for variability observed in these stars in most cases. Observational aspects of nonradial oscillations in these stars will be presented in detail in the next chapter.

Along with these observational developments, much progress has been made in the theoretical side of nonradial oscillations in the sun and stars. Since the middle of the 1970s, full equations of linear adiabatic and linear non-adiabatic nonradial oscillation have been solved numerically for realistic stellar models with the help of electronic computers, and the variations in nature of nonradial oscillation modes along an evolutionary sequence of a star have been discussed (e.g., Osaki, 1975; Saio and Cox, 1980). The basic method of these calculations is now well established and it will be described in detail in later chapters. The eigenvalue problem of nonradial oscillations is not described by that of the standard Strum-Liouville type, as is the case for the radial oscillation, and this brings about various peculiarities of nonradial oscillations. The introductions of the so-called propagation diagram and phase diagram and of the concept of "wave trapping" (Scuflaire, 1974; Unno, 1975a; Osaki, 1975; Shibahashi and Osaki, 1976a) have greatly improved our understanding of nonradial oscillations in stars.

Some curious behavior of nonradial eigenmodes (i.e., the "mode bumping" phenomenon) along the evolutionary sequence of a 10 $M_\odot$

star was first noticed by Osaki (1975) and was interpreted as a coupling of oscillations of different nature in the core and the envelope (Aizenman, Smeyers, and Weigert, 1977). Modal analysis by the WKBJ-type asymptotic method has been made to clarify the nature of nonradial oscillations (Shibahashi, 1979; Wolff, 1979), and such a method yielded a convenient analytic formula for eigenfrequencies of higher order nonradial modes (Tassoul, 1980). As for the theoretical investigation of some particular stars, excitation mechanisms of nonradial oscillations in white dwarf variable stars were explored, and it has been confirmed that the white dwarf stars are indeed unstable against nonradial g-modes due to the κ-mechanism of the hydrogen and helium ionization zones (Dziembowski and Koester, 1981; Dolez and Vauclair, 1981; and Winget, Van Horn, Tassoul, Hansen, Fontaine, and Carroll, 1982a). In the field of helioseismology, some ingenious inversion methods were devised (Gough, 1984a; Shibahashi, 1988) that could yield the information of the solar interior directly from the observed oscillation frequency spectrum. Theoretical investigations of nonradial oscillations in rotating stars have also been made, yielding some interesting results (Berthomieu, Gonczi, Graff, Provost, and Rocca, 1978; Lee and Saio, 1986, 1987a).

A number of theoretical problems remain to be studied. Among them are nonlinear problems, including the mixing of matter due to finite amplitude oscillations, oscillations in the presence of a strong magnetic field or rotation, and energy and momentum transport by waves. Both theory and observation are still in progress, but further developments can be expected in the near future.

4. *Basic Properties of Nonradial Oscillations*

We consider a spherically symmetric star as an unperturbed state upon which small perturbations of oscillation are superimposed. The effects of rotation or of magnetic field will be neglected or regarded as small perturbations in most cases. In this section, we explain the basic properties of nonradial oscillations and introduce the symbols related to them; these symbols will be used in the expanded presentation in later chapters.

Assuming that the unperturbed state is in time-independent equilibrium, we take the perturbations of the physical variables to be proportional to $Y_l^m(\theta,\phi)e^{i\sigma t}$, where $Y_l^m(\theta,\phi)$ denotes the spherical harmonics, θ the colatitude and ϕ the azimuth angle in the spherical polar coordinate, σ the angular frequency, and t the time. The function $Y_l^m(\theta,\phi)$ is expressed explicitly by

$$Y_l^m(\theta,\phi) = N_l^m P_l^{|m|}(\cos\theta)e^{im\phi}, \tag{4.1}$$

where $P_l^{|m|}(x)$ denotes the associated Legendre polynomial of degree l and order m, and $l\,(=0, 1, 2, \ldots)$ and $m\,(=-l, -l+1, \ldots, 0, \ldots, l-1, l)$ are integers, and N_l^m is the normalization constant, which will be given in Chapter III. As will be shown explicitly in Chapter III, all the coefficients in the linearized basic equations are functions of the radial distance r from the center of a star. In other words, the radial component ξ_r of a small displacement is governed by the following equation:

$$\mathcal{L}[\xi_r] = 0, \tag{4.2}$$

where $\mathcal{L}[\xi_r]$ is a linear operator in which the scalar functions appearing as the coefficients are independent of t, θ, and ϕ. Thus, we can express ξ_r of an arbitrary displacement by

$$\xi_r = \sum_{n,l,m} \xi_{r,nl}(r)Y_l^m(\theta,\phi)\exp(i\sigma_{nl}t), \tag{4.3}$$

where n is an integer ordering the radial eigenfunctions. In a simple stellar model, n corresponds to the number of nodes satisfying

$$\xi_{r,nl}(r_i) = 0 \qquad (i = 1, 2, \ldots, n) \tag{4.4}$$

except when $r = 0$. As will be discussed in detail in Chapter III, one-to-one correspondence between the number of nodes and the ordinal number n ceases to exist in complicated stellar models, but we can still assign an ordinal number to each eigenmode. Since each mode does not interact with the other modes differing in n, l, or m in the linear theory, we can study each mode separately, dropping the summation in equation (4.3). This procedure is called the normal mode analysis. The symbol σ denotes the (angular) frequency of oscillation in general, but it will often be used to represent an eigenfrequency.

When we express eigenfunctions of nonradial oscillations, we use complex forms like equation (4.3) throughout this book because of the mathematical convenience. It should be understood that we take the real part of complex expressions if we need real physical quantities. For instance, the expression of real physical displacement is

$$\begin{aligned}\xi_r = & N_l^m P_l^{|m|}(\cos\theta)[\mathrm{Re}(\xi_{r,nl}(r))\cos(\sigma_R t+m\phi) \\ & -\mathrm{Im}(\xi_{r,nl}(r))\sin(\sigma_R t+m\phi)]\exp(-\sigma_I t) \\ = & |\xi_{r,nl}(r)|\, N_l^m P_l^{|m|}(\cos\theta)\cos(\sigma_R t+m\phi+\delta_n^{(l)})\exp(-\sigma_I t)\end{aligned} \tag{4.5}$$

where Re and Im indicate the real and imaginary parts of complex numbers, σ_R and σ_I are the real and imaginary parts of eigenfrequency σ, and $\delta_n^{(l)}$ is the argument of complex variable $\xi_{r,nl}(r)$. In what follows, subscripts n and l are sometimes omitted, if there is no confusion.

For a given spherical equilibrium model (hence for the boundary conditions as well), the eigenfrequency σ, which is complex in the nonadiabatic oscillation, is a function of n and l. Both the radial eigenfunction and the eigenfrequency σ of a normal mode are independent of m and show the $(2l+1)$-fold degeneracy. The harmonic degree l represents the number of border lines by which the stellar surface is divided to oscillate in the opposite phase, and the azimuthal order m is the number of roots of $\cos(m\phi) = 0$ in the region $0 \leq \phi < \pi$. The radial modes correspond to the case of $l = 0$. The normal modes belonging to a given l for a spherical star without rotation may be written either in the form of equation (4.1) or in the form

$$Y_l^m(\theta,\phi) \propto P_l^m(\cos\theta) \begin{cases} \cos(m\phi) \\ \sin(m\phi), \end{cases} \qquad (4.6)$$

where $m = 0, 1, 2, \ldots, l$ is a natural number from zero up to l. The former representation with $\cos(\sigma t + m\phi)$ expresses a normal mode as a wave traveling around the equator (the equator of the symmetry axis of oscillation) with phase velocity $(\partial\phi/\partial t)_{phase} = -\sigma/m$; a mode with positive m represents a wave traveling in one direction while a mode with negative m does that in its opposite direction. The latter representation of equation (4.6) with $\cos(m\phi)\cos(\sigma t)$, on the other hand, expresses a mode as a standing wave in longitude. The two expressions are equivalent insofar as the unperturbed state is spherically symmetric because one can form, for instance, a standing wave of the form $\cos(m\phi)\cos(\sigma t)$ by superposing two traveling wave modes of positive and negative m.

Figure 4.1 illustrates what patterns of several nonradial oscillation modes look like over the stellar surface. At any given instant of time, the pattern of an individual mode is one of alternating regions of opposite signs (e.g., approaching or receding flows, or higher or lower temperatures). Modes with $m=0$, such as an $l=3$ and $m=0$ mode, are called zonal modes, and all the nodal lines of the spherical harmonics are lines of latitude, while modes with $m=l$ are called sectoral modes and all the nodal lines are lines of longitude. Modes other than the above two are called tesseral modes, and their nodal lines are lines of both latitude and longitude.

The degeneracy in m arises from the rotational symmetry of the equilibrium structure around an arbitrary axis. Therefore, if a slow

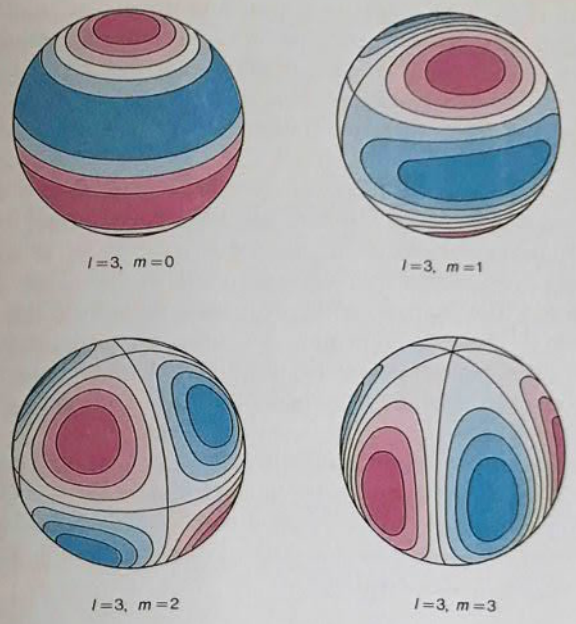

Fig. 4.1 Modal patterns of nonradial oscillations for four normal modes of degree $l = 3$ and order $m = 0$, 1, 2 and 3. Figure shows four modes viewed from an inclination $i = 60°$. The regions shown in blue are expanding while regions in red are contracting. The border lines dividing blue regions and red regions are nodal lines on which there are no motions. There are three nodal lines in the case of $l = 3$ mode irrespective of its m-value, while the m-value represents the number of nodal lines in longitude. When we can directly resolve the stellar image like in the case of the sun, these modal patterns are observable as Doppler shifts of spectral lines at each point of the surface. In the real sun, thousands of such eigenmodes are superimposed.

rotation or a weak magnetic field is introduced, the degeneracy is resolved much as in the Zeeman effect of the spectral lines. The perturbation theory (see Section 19) gives, for a star of uniform angular frequency Ω of rotation (in the rotating frame),

$$\sigma = \sigma_0 - m\Omega C_{nl}, \qquad (4.7)$$

where σ_0 denotes σ of the nonrotating case and the constant C_{nl} depends on the equilibrium structure and the mode considered. Thus the degeneracy is lifted by slow rotation, giving $(2l+1)$ separate eigenfrequencies with equal spacing just like Zeeman levels of atomic spectra. In this case, eigenfunctions of normal modes are only described by those

of equation (4.1), that is, those of traveling wave type, and those of standing waves of equation (4.6) are no longer normal modes. With rapid rotation (or strong magnetic field), a normal mode cannot be expressed by a single term in equation (4.3) but is expressed as the sum of an infinite number of terms if the expansion in Y_l^m is still used (Section 34).

In stars the dynamical time scale is much shorter than the thermal time scale (by a factor of 10^{10} for the sun), the exact amount depending on the stellar structure and on the local position in a star under consideration. Therefore, we can adequately study the adiabatic oscillations as a first approximation, neglecting the nonadiabatic effects and viscosity. The eigenfunctions and the eigenfrequencies thus obtained are not much different from the nonadiabatic values in most cases, although the difference is essential in the consideration of the overstability problem.

The general properties of adiabatic radial and nonradial oscillations have been discussed extensively by Ledoux and Walraven (1958), by Ledoux (1974), and by Cox (1976, 1980). The peculiarity of the nonradial oscillations compared with the radial oscillations is that the adiabatic oscillation described by

$$\mathcal{L}_{ad}[\xi_r] = 0 \tag{4.8}$$

together with the boundary conditions does not form an eigenvalue problem of the Sturm-Liouville type. Equation (4.8) becomes bilinear in σ^2 and σ^{-2} and tends to be the Sturm-Liouville type only for $\sigma^2 \to \infty$ or $\sigma^2 \to 0$. This property corresponds physically to the existence of two kinds of restoring forces, pressure and gravity.

As will be discussed extensively in Chapter III, the local vibrational property is characterized by two characteristic frequencies. One of them is the frequency corresponding to a reciprocal of the time scale of one horizontal wave length divided by the local sound speed. This frequency will be called the Lamb frequency and denoted by L_l, given by

$$L_l^2 = (k_h c)^2 = \frac{l(l+1)c^2}{r^2}, \tag{4.9}$$

where c denotes the velocity of sound,

$$c^2 = \Gamma_1 p_0/\rho_0, \qquad \Gamma_1 = (d\ln p/d\ln\rho)_{ad}, \tag{4.10}$$

p_0 and ρ_0 are the pressure and the density of the unperturbed state, and Γ_1 is the adiabatic exponent. Here $k_h = [l(l+1)]^{1/2}/r \simeq l/r$ stands for horizontal wave number and is related to horizontal wavelength λ_h by $k_h = 2\pi/\lambda_h$. A sound wave travels a wavelength $\lambda_h = 2\pi r/l$ horizontally in a

period $2\pi/L_l$. The other characteristic frequency is the Brunt-Väisälä frequency (denoted by N) with which a bubble of gas may oscillate vertically around its equilibrium position under gravity. The Brunt-Väisälä frequency is given by

$$N^2 = g\left(\frac{1}{\Gamma_1}\frac{d\ln p_0}{dr} - \frac{d\ln\rho_0}{dr}\right), \tag{4.11}$$

where $g(=GM_r/r^2)$ is the local gravitational acceleration, G is the gravitational constant, and M_r is the stellar mass contained inside the spherical volume of radius r. A small parcel of gas oscillates vertically with positive or negative buoyancy under local pressure balance with its surrounding gas with the angular frequency N.

For high-frequency oscillations ($\sigma^2 > L_l^2, N^2$), the relative Eulerian pressure perturbation p'/p_0 dominates the relative radial displacement ξ_r/H_p where H_p denotes the pressure scale height. Thus, the restoring force is due mainly to the excess pressure, and the oscillation shows locally the characteristics of the acoustic wave. For low-frequency oscillations ($\sigma^2 < L_l^2, N^2$), p'/p_0 is less than ξ_r/H_p, the restoring force is due mainly to buoyancy, and the oscillation shows the characteristics of

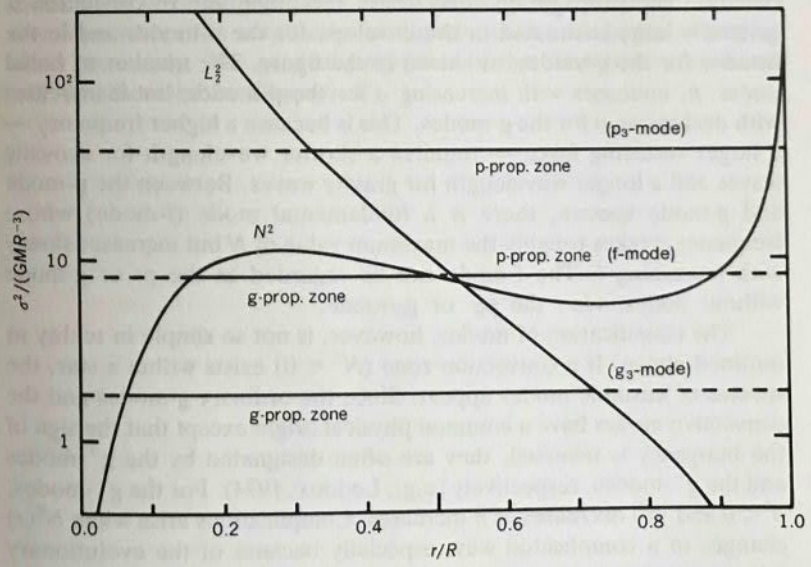

Fig. 4.2 Variations of N^2 and L_2^2 (normalized by GM/R^3) with respect to r/R for a polytrope (with the polytropic index 3) model. Three horizontal lines show the wave propagation zones (thin full lines) for the p_3-mode, the f-mode, and g_3-mode of spherical harmonic degree $l = 2$.

the gravity wave. In the other regions ($L_l^2>\sigma^2>N^2$ or $L_l^2<\sigma^2<N^2$), the eigenfunction does not show spatial oscillation but decreases exponentially with the distance from the wave propagation region. The temporal oscillation in such a region is called the evanescent wave. Two propagation regions separated by an evanescent zone are generally coupled with a "tunnel effect" as in the wave mechanics of thermonuclear reactions. The two propagation regions can behave almost independently if the potential wall (the evanescent zone) is thick and high.

Figure 4.2 shows the propagation diagram given essentially by Scuflaire (1974) for a polytrope (index 3) model. The value of N^2 is zero at the center ($r=0$), has a maximum and a minimum in the envelope, and then increases very rapidly toward the surface, $r=R$. On the other hand, the value of L_l^2 is infinite at $r=0$ and decreases monotonically toward the surface. The L_l^2-curve must be shifted vertically for different values of l proportionally to a factor of $l(l+1)$. Only the L_2^2-curve is shown in Fig. 4.2. These behaviors of N^2 and L_l^2 determine the general properties of oscillations. The p-mode spectra occupy the high frequency domain, while the g-mode spectra occupy the low frequency domain. The propagation zone where the amplitude of oscillation is generally large is situated in the envelope for the p-modes and in the interior for the g-modes, as shown in the figure. The number of radial nodes, n, increases with increasing σ for the p-modes, but it increases with decreasing σ for the g-modes. This is because a higher frequency — a larger restoring force — requires a shorter wavelength for acoustic waves and a longer wavelength for gravity waves. Between the p-mode and g-mode spectra, there is a fundamental mode (f-mode) whose frequency σ takes roughly the maximum value of N but increases slowly with increasing l. The f-mode can be regarded as the p- or g-mode without nodes, *viz.*, the p_0- or g_0-mode.

The classification of modes, however, is not so simple in reality as outlined above. If a convection zone ($N^2<0$) exists within a star, the spectra of unstable modes appear. Since the ordinary g-modes and the convective modes have a common physical origin except that the sign of the buoyancy is reversed, they are often designated by the g^+-modes and the g^--modes, respectively (e.g., Ledoux, 1974). For the g^--modes, $\sigma^2<0$ and $|\sigma^2|$ decreases as n increases. Complications arise when $N^2(r)$ changes in a complicated way, especially because of the evolutionary inhomogeneity in the mean molecular weight distribution. Even in the zero-age main-sequence star of one solar mass, $N^2(r)$ increases from zero at the center to a maximum and decreases in the envelope, becomes negative in the convection zone, then increases rapidly,

fluctuates in the photosphere-chromosphere-corona transitions, and decreases slowly in the corona (see Figs. 15.8 and 15.10 below). The value of L_l^2 decreases monotonically from infinity at the center to the temperature minimum in the chromosphere, then increases rapidly toward the corona and decreases slowly. A single mode having an intermediate frequency has characteristics of acoustic, gravity, and evanescent waves in different regions within a star. Then, for some stars with high central condensation, the one-to-one correspondence does not exist between the modes and the number of nodes n. Even in such a case, however, the mode number can be identified in an unambiguous way by distinguishing the nodes in the p-propagation region (or simply the P-region) from the nodes in the G-region, as we shall argue in detail in Chapter III (Section 17). The p- and g-characteristics can be distinguished conveniently in the phase diagram to be discussed later (see also Eckart, 1960).

We will adopt the simple nomenclature p, f, g mainly in Chapters I and II, and discussions of mode classification in complicated stellar models will be deferred to Chapter III.

In order for a particular mode to be excited, some excitation mechanism must be present in the main trapping zone or in the outer envelope where the amplitudes of eigenfunctions are large, as emphasized previously. The general properties of the excitation mechanisms will be discussed in Chapter V.

Chapter II

OBSERVATIONAL ASPECTS OF NONRADIAL OSCILLATIONS

5. General Remarks

Let us now turn to the observational side of nonradial oscillations. It has been well established that variable stars such as Cepheids, RR Lyrae, and Mira variables are pulsating stars and that their pulsations are explained in terms of simple *radial, spherically symmetric pulsations* — that is, their variations in light and radial velocity are caused by alternate expansion and contraction of a star as a whole. On the other hand, for *nonradial oscillations* in which the stellar form periodically deviates from the spherical shape, observational evidence for their existence was rather meager. In fact, before 1970, the pulsation of β Cephei stars was the only case in which nonradial oscillation was suspected as a possible cause of stellar variability. However, the situation has since changed drastically: new observations and new interpretations have been accumulated for various stars and for various phenomena—for example, the discovery of many variable white dwarfs and an interpretation of the solar five-minute oscillation in terms of the nonradial p-mode oscillations of the sun.

We summarize in Table 5.1 various observational phenomena for which nonradial oscillations have been either claimed or suggested. The meaning of individual terms in Table 5.1 will become clear later as details of various phenomena and of individual stars are discussed. Also shown in Fig. 5.1 is the location of the relevant stars together with some other stars on the Hertzsprung-Russel (HR) diagram. Although all of the evidence for nonradial oscillations in these stars is not firmly established, the variety of phenomena and the widespread incidence of nonradial oscillations in stars over the HR diagram are remarkable.

In the following two sections, we will discuss how nonradial oscillation manifests itself observationally and how it can be distinguished from simple radial pulsation. Data on the pertinent observations of individual stars will be given in subsequent sections. That is,

Table 5.1 Observational phenomena for which nonradial oscillations are either claimed or suspected.

Kind of star	Period	Phenomena (evidence for nonradial oscillations)	Oscillation modes
Early-type O-B Variables			
β Cephei variables	3~6 hr	light & radial velocity variations (multiperiodicity)	l =2~4 f- or p-modes
53 Per variables	0.5~2 days	line profile variation	low l g-modes
ζ Oph variables	several hours	line profile variation	low l g-modes l=5~8 p- and g-modes (or r-modes?)
A type variables			
Ap stars	5~15 min	light variation (multiperiodicity)	low l high overtone p-modes
δ Sct stars	1~2 hr	light variation & line profile variation	low l p-modes
White Dwarf Variables			
variable DA white dwarfs	100~1,000 s	radial velocity- and intensity variations [diagnostic (k_h, σ)-diagram]	l =0~1,000 p-modes low l g-modes
variable DB white dwarfs	100~1,000 s	light variation (multiperiodicity & length of periods)	low l g-modes
variable DO stars	400~1,600 s		
the sun	5~10 min	radial velocity- and intensity variations [diagnostic (k_h, σ)-diagram]	l =0~1,000 p-modes low l g-modes
	1~3 hr		
late-type dwarfs	5~10 min	light variation (sun-like oscillation, power spectra)	low l p-modes
early- and intermediate-type supergiants	several to several tens days	semi-regular light & radial velocity variations	low l p- and g-modes

Fig. 5.1 Location of the stars given in Table 5.1 for which nonradial oscillations are suspected to be involved and other related stars.

observations of early-type O,B variables, rapidly oscillating Ap stars, and white dwarf variables will be presented in Sections 8, 9, and 10, respectively, while solar oscillations will be discussed in Section 11.

Except for those stars mentioned above, observational evidence for the existence of nonradial oscillations is still meager. This does not necessarily mean that nonradial oscillations are not present in most of other stars. Instead, it is quite possible that nonradial oscillations are quite prevalent and that they form underlying causes for various activities. In particular, nonradial oscillations with high spherical harmonic degree l, such as observed in the sun as the five minute oscillations, could never be directly identified as such in distant stars.

Although not discussed in a separate section, the existence of nonradial oscillations is claimed or suspected in several stars other than mentioned above. The first case to be mentioned concerns the semiregular variability of the supergiant star α Cygni that was extensively studied by Lucy (1976). By analyzing large numbers of radial velocity observations of α Cyg (spectral type A2Ia), he showed that the variability might be due to the simultaneous excitation of as many as sixteen discrete pulsation modes. He has suggested that most of

them are nonradial modes because of the length of periods and because these modes tend to occur in close pairs, implying rotational splitting of nonradial modes. He has further suggested that the "macroturbulence" required for large line-broadening can be explained by superposition of numerous nonradial modes. The semiregular variability in radial velocity and the large macroturbulence velocities observed in many early- and intermediate-type supergiants (Abt, 1957; Rosendhal, 1970) may also be explained by the same mechanism.

It has been suspected that nonradial oscillations are involved in light variations in pulsating variables of δ Scuti type (Shobbrook and Stobie, 1974), but Walker, Yang, and Fahlman (1987) have recently discovered, in four rapidly rotating δ Scuti variables, line-profile variations of traveling signature which are characteristic of ζ Ophiuchi variables (high degree l nonradially pulsating stars).

There exist a small group of hot extreme helium stars (or extreme hydrogen-deficient stars), and low-amplitude light variations have been reported in several members of them. Jeffery, Skillen, Hill, Kilkenney, Malaney, and Morrison (1985) and Lynas-Gray, Kilkenny, Skillen, and Jeffery (1987) have recently claimed that variations in the two member stars BD–9°4395 and HD160641 are due to nonradial g-mode pulsations because of length of periods and because of no detectable colour change.

6. Observational Evidence for Nonradial Oscillations

6.1 Resolved Stellar Images

If the stellar image is resolved to a finite disk and if we observe directly a stellar pulsation such that one part of the stellar surface is expanding while the other part is contracting as illustrated schematically in Fig. 6.1, then we can evidently claim the existence of nonradial oscillation in preference to radial pulsation. This is impossible for most of the distant stars. But it should be possible in the case of the sun, if the sun undergoes nonradial oscillation. In fact, the five-minute oscillation seen over the solar surface is now considered a superposition of thousands of nonradial eigenmodes.

Except for the sun, the resolution of the stellar image into a disk is difficult, and there are only a few situations in which the image resolution plays an essential role in inferring nonradial oscillation. One of the possibilities is to use an interferometer to resolve the stellar image into a disk for nearby giants and supergiants. One observation with a speckle interferometer has shown that the interferometric image of α Ori, a star with the largest angular diameter in the sky, has barely visible

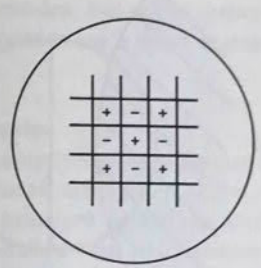

Fig. 6.1 Higher-harmonic nonradial oscillation with a tesseral pattern.

fine structures (Lynds, Worden, and Harvey, 1976). The most likely interpretation for this is that the fine structures seen by the interferometer may be a manifestation of the giant convective cells which are presumed to exist in the atmosphere of later-type supergiants like α Ori (Schwarzschild, 1975). However, at present, the origin of the structures on the surface of α Ori is not certain observationally, and it may be premature to discuss them further.

Another possibility is to project the stellar visible disk over the wavelength position of spectral lines in rapidly rotating stars. The surface of a rapidly rotating star can be projected through Doppler shifts onto a spectral line profile, and one-to-one correspondence between a position across the disk and a wavelength position of a rotationally broadened profile is made. Any feature over the visible disk will then manifest itself in line profiles. This mapping is called "Doppler Imaging" and it will be discussed in detail in Sections 7 and 8. Still another possibility is using the eclipse of a close binary in which one of the components is a pulsating star, as discussed below.

6.2 Phase Shift of Pulsation During Eclipse

Let us suppose that a nonradially pulsating star is a component of an eclipsing binary. If the nonradial oscillation is of low-degree harmonics (small l), the visible hemisphere of the pulsating star may be divided into two parts whose oscillations are roughly 180° out of phase with each other. When the eclipse occurs and the occulting star gradually cuts off the disk of the pulsating star (as illustrated schematically in Fig. 6.2), the phase of the pulsation will be shifted accordingly. This kind of phenomenon has, in fact, been observed in the old nova DQ Her (Warner, Peters, Hubbard, and Nather, 1972) and in the nova-like binary UX UMa (Nather and Robinson, 1974). It was once used as evidence for traveling wave-type nonradial oscillations with $l = 2$ and

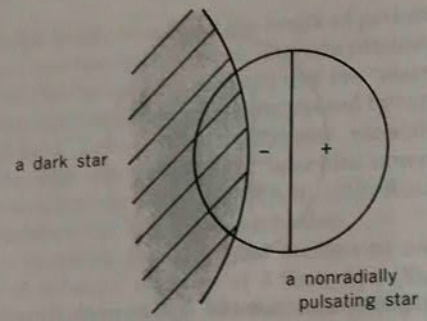

Fig. 6.2 Eclipse of a nonradially pulsating star by a companion.

$m=-2$ or $+2$ (Nather and Robinson, 1974).

However, this kind of phenomenon of phase shift during eclipse can be equally well explained by other traveling features around the equator of a star, and interpretation based on nonradial oscillations is by no means unique. In fact, observed phase shifts during eclipses in DQ Her and UX UMa can be better reproduced by the oblique rotator model. The oblique rotator model was developed to explain periodic variability in Ap stars and the pulsars; in this model a rotating star has a magnetic field and its magnetic axis is oblique to the rotation axis. As the star rotates, its magnetic pole is directed to observers once every rotation period. In the cases of DQ Her and UX UMa, it is thought that material is accreted on the magnetic pole of a rotating white dwarf and that the radiating beam from the magnetic polar regions irradiates the accretion disk, producing traveling features in accretion disks (Petterson, 1980).

The cases of DQ Her and UX UMa were therefore not good examples, but there is still the possibility of observing phase shifts during eclipse due to nonradial oscillations, and it is interesting to find pulsating stars in eclipsing binary systems.

6.3 Length of Period in Pulsating Variable Stars

In the case of radial pulsations, the period of the fundamental mode is longer than those of the higher harmonics. In the case of nonradial oscillations, the f-mode and the p-modes have periods similar to those of the corresponding radial modes, but in general the g-modes have periods much longer than those of radial pulsations. Suppose that there exists a group of pulsating variable stars whose periods turn out to be much longer than that expected theoretically for the radial fundamental mode. It is then possible for pulsations of these variables to be explained

in terms of nonradial g-modes, but not in terms of the radial pulsations. In fact, white dwarf variables are a good example of this case. (Section 10)

6.4 Amplitude Modulation

In some variable stars, amplitudes of pulsation in the light curve and/or in the radial velocity curve are known to be modulated with periods much longer than the principal periods as illustrated schematically in Fig. 6.3. This is the so-called beat phenomenon; the simplest explanation for it may be the simultaneous excitation of two oscillations with nearly equal periods. In the case of radial pulsations it is difficult for two oscillations with nearly equal periods to occur. But in the case of nonradial oscillations, the existence of nearly equal periods can be easily explained in terms of the rotational splitting of eigenfrequencies of nonradial modes with the same quantum numbers n and l but differing in m, i.e., the lifting of the degeneracy of nonradial modes in the presence of rotation. In fact, the beat phenomenon has been used to infer nonradial oscillations for β Cephei stars and white dwarf variables.

Amplitude modulation also occurs in the case of nonradial oscillations if the symmetry axis of a nonradial mode is oblique to the rotation axis of a star. This possibility was first suggested by Kurtz (1982) to explain amplitude modulation observed in rapidly oscillating Ap stars. This model was called the "oblique pulsator model," in that the pulsation is a nonradial zonal mode with $m=0$ with low degree l, whose symmetry axis is coincident to the stellar magnetic axis that is in turn inclined to the rotation axis. As the star rotates, the symmetry axis of pulsation (and the magnetic axis) is then periodically exposed to observers, producing modulation in amplitude of pulsation. More details on this phenomenon will be discussed in Section 9.

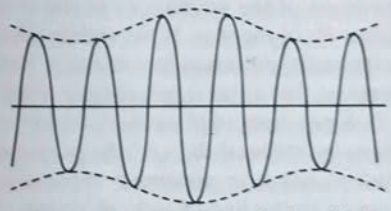

Fig. 6.3 Beat phenomenon in which the amplitude of oscillations is modulated with a long period.

6.5 Characteristic Variations in Line Profiles

In nonradial oscillations different parts of the surface of a star move in different ways, and this kind of motion (the macroscopic velocity field)

must naturally affect spectral line profiles. As will be shown in the next section, the nonradial oscillation coupled with the stellar rotational velocity field gives rise to significant variations in line profiles. The characteristic line profile variations observed in O and B variable stars (or line-profile variable O and B stars) can be explained successfully by nonradial oscillation.

6.6 Baade's Pulsation Test

Baade (1926) first proposed an empirical method by which the radial pulsation hypothesis for an intrinsic variable star can be tested observationally. Wesselink (1946, 1947) formulated it in a more practical form, and this method is called the Baade-Wesselink method. We can distinguish nonradial oscillations from radial pulsations using Baade's pulsation test. The principle of this test is as follows: the luminosity variation in a *radially pulsating* star may be written as

$$L(t) = S(t)B(t) = 4\pi R^2(t)\sigma_{rad}T_{eff}^4(t), \qquad (6.1)$$

where $S(t)$ and $B(t)$ stand for the instantaneous surface area of a star projected on the celestial plane and its instantaneous surface brightness, respectively, σ_{rad} denotes the Stefan-Boltzmann constant, and $R(t)$ and $T_{eff}(t)$ are the instantaneous radius and effective temperature, respectively, of the star. The observed luminosity variation is therefore the result of two effects: a change in the surface area (or radius) and a change in the surface brightness (or temperature). It is possible to separate the two effects because the temperature variation may be estimated from the color variation. We may then calculate the relative variation of the radius $R(t)/R_0$ from equation (6.1). On the other hand, the radial velocity curve provides the absolute variation in radius $R(t)-R_0$. If the pulsation theory is correct, these two plots agree in phase, and a comparison of the amplitudes of the two curves yields an estimate of the radius R_0 of the star. If the radius thus obtained gives a reasonable value, the radial pulsation hypothesis is justified for the star.

Let us now suppose that a star is pulsating nonradially—say, with a p-mode of $l = 2$. Since nonradial oscillation looks like a volume-conserving pulsation, the stellar disk (i.e., the projected area of the star against the celestial plane) is in maximum expansion at the phase of maximum compression in the line-of-sight direction. Thus the relation between the line-of-sight motion (responsible for the radial velocity curve) and the subtended area of the star (responsible for the light curve) for the nonradial oscillation of $l = 2$ is just opposite to that in the case of radial pulsation.

If we applied Baade's pulsation test to a nonradially pulsating star,

we would get a negative value for the radius in the case of $l = 2$ or an unrealistically large radius in the case of $l = 1$. Walker (1954a, b) applied this pulsation test to two β Cephei stars, BW Vul and 16 Lac, and obtained results which failed to confirm the *radial* pulsation hypothesis. In the case of BW Vul, the entire light variation was explained by the temperature variation, and in the case of 16 Lac a radius of minus 50 $R_\odot$ was obtained. These two results led Walker to conclude: "The observations, if they mean anything, might be taken as strengthening the supposition that these two stars undergo some sort of nonradial pulsation."

Dziembowski (1977b) has given analytical expressions for light variations and radial velocity variations in the case when a star undergoes nonradial oscillations. Balona and Stobie (1979a, b, 1980) have discussed the application of the Baade-Wesselink method to nonradial oscillations. Recent progress on this matter was summarized by Stamford and Watson (1981).

6.7 Dynamical Phenomena in the Stellar Atmosphere

Nonradial oscillations with higher spherical harmonics may not give rise to light variations, but they may manifest themselves as surface velocity fields. It may then be possible that nonradial oscillations are underlying causes of certain kinds of dynamical phenomena, such as macro- and micro-turbulences, the heating of stellar chromospheres and coronae, and the stellar wind. However, further theoretical discussions and observations are needed to reveal these phenomena.

7. Line-Profile Variations by Nonradial Oscillation

When a star undergoes nonradial oscillation, different parts of the stellar surface move in different phases and this kind of motion produces a certain characteristic variation of line profile when combined with stellar rotation (i.e., the macroscopic velocity field). In the past decade or so, a new class of variable stars called "line-profile variable stars" have been discovered owing to the development of high precision spectroscopy with the use of solid-state detectors such as CCDs and Reticons (see Section 8). These stars manifest their variability most conspicuously in spectral line profiles, with little accompanying change in brightness or radial velocity (line centroid). It is now thought that line-profile variations in these stars are caused by nonradial oscillations (or nonradial pulsations, often abreviated as NRP).

Historically, Ledoux (1951) was the first to suggest that nonradial oscillations may be responsible for variability of some class of pulsating

stars, in his case, the β Cephei variable stars. He has shown that the nonradial mode with spherical harmonic indices $l = 2$ and $m = 2$ combined with stellar rotational velocity field may produce the right kind of line width variation observed in β CMa, a prototype of β Cephei stars. Ledoux's model of line-profile variation by nonradial oscillation was appreciated by Christy (1967) for the explanation of line doubling observed in some of these stars. Osaki (1971) then calculated line-profile variations for stars undergoing nonradial oscillations in the presence of rotation and compared with variations of observed line profiles in β Cephei stars. Theoretical line profile variations due to nonradial oscillations have further been examined by Stamford and Watson (1976, 1977), Smith (1977), Kubiak (1978), Balona (1986a, b, 1987), and Kambe and Osaki (1988). Observations of line-profile variable stars will in general be discussed in the next section, but Smith (1977), Vogt and Penrod (1983), and Baade (1984) have shown that observed variations in line-profiles in these stars can be matched by model profiles produced by NRP velocity fields.

In general, low degree nonradial modes such as $l = 1$, 2, and 3 can produce variations in line width and line asymmetry. Smith (1977) has shown that line-profile variation in slowly rotating B-type variables called 53 Per stars can be explained by low l NRP modes. It was thought before that high degree NRP modes (i.e., $l > 4$) could not produce appreciable line-profile variations because they tend to cancel themselves over the visible disk, and further that line-profile variations due to NRP could be difficult to detect in rapidly rotating stars because the pulsational velocity may be hidden by much larger rotational velocity. However, these arguments were found to be somewhat prejudiced, and it turned out that rapid rotation rather helps to increase the visibility of intermediate l NRP modes (i.e., $l = 4 \sim 8$), as it resolves the stellar visible disk through rotational Doppler shift. In fact, the existence of a nonradial mode as high as $l = 16$ was claimed by Smith (1985) in a rapid rotator, Spica (α Vir). This effect is called "Doppler imaging" (Vogt and Penrod, 1983), as it projects a two-dimensional stellar disk into one-dimensional velocity (or wavelength) space. In what follows, we present general characteristics of line profile variations due to nonradial modes of low and intermediate l ($l = 2 \sim 8$).

7.1 Formulation of Line-Profile Modeling

Nonradial oscillations can produce line-profile variations mainly in two ways: by the Doppler shift of surface elements and by local surface brightness variation. Variations in surface area and in surface normal due to nonradial oscillation may also produce some variations of line

profile, but their effects are probably minor compared with the two effects mentioned above. Most of the work so far done is on velocity effects of oscillation, and studies on the local brightness variation are rather limited [see, however, e.g., Balona (1987)]. In this monograph, we study only effects of velocity variation of oscillation on line profile.

We describe here the standard procedure of line profile modeling by nonradial pulsations, which was first described by Osaki (1971) and refined by Smith (1977). In this procedure, we first choose a certain stellar absorption line for which we wish to model, and then calculate its intrinsic profile for a given effective temperature T_{eff} and surface gravity g appropriate to the star of interest by using the standard stellar atmosphere computer code. We then choose a particular nonradial mode. As outlined in Section 4, there are three kinds of NRP modes: p-modes, g-modes, and f-modes. We have so far restricted ourselves to the case of non-rotating stars. However, there may exist in the presence of rotation another class of modes called Rossby modes or r-modes (Papaloizou and Pringle, 1978; see also Section 19). We shall consider line profile variations due to r-modes as well in this section.

Nonradial p-modes and g-modes are described by the spheroidal modes, while r-modes are described by toroidal modes (see Section 13). In the case of spheroidal modes, pulsation velocity fields are written in the spherical polar coordinates (r,θ,ϕ) as

$$\boldsymbol{V}_{sph} = A\left(1,\ k\frac{\partial}{\partial\theta},\ k\frac{1}{\sin\theta}\frac{\partial}{\partial\phi}\right)Y_l^m(\theta,\phi)e^{i\sigma t}, \tag{7.1}$$

while in the case of toroidal modes, they are written as

$$\boldsymbol{V}_{tor} = A\left(0,\ \frac{1}{\sin\theta}\frac{\partial}{\partial\phi},\ -\frac{\partial}{\partial\theta}\right)Y_l^m(\theta,\phi)e^{i\sigma t}. \tag{7.2}$$

Here σ denotes the angular frequency of oscillation, and $Y_l^m(\theta,\phi)$ is the spherical harmonic function given by

$$Y_l^m(\theta,\phi) = P_l^{|m|}(\cos\theta)e^{im\phi}. \tag{7.3}$$

The quantity k, appearing only in the case of the spheroidal mode of equation (7.1), is the ratio of the horizontal to radial velocity amplitudes. It is not a free parameter, but it is related to the frequency of oscillations such that [see equation (14.13) and Ledoux, 1951]

$$k = \frac{GM/R^3}{\sigma^2} = \frac{1}{\omega^2} = \left(\frac{Q}{0.116}\right)^2, \tag{7.4}$$

where G is the gravitational constant, M and R are the mass and radius of the star of our interest, ω is the dimensionless frequency defined by

this equation, $Q\ [=\Pi(\bar{\rho}/\bar{\rho}_\odot)^{1/2}]$ is the pulsation constant, and Π is the pulsation period in days. Generally speaking, the k value is smaller than one for p-modes, and it can be larger than one for g-modes. We here adopt 0.15 and 1.2 as the standard values of k for p-modes and g-modes, respectively.

The normalization of the spherical harmonic function Y_l^m adopted in this section is that the maximum value of the largest component of the vector is unity so that A stands for the velocity amplitude of NRP mode. Thus, for a p-mode in which the radial velocity component dominates the horizontal one, A represents the radial velocity amplitude, while for a g-mode with the dominant horizontal component, A represents the horizontal velocity amplitude and the radial one is given by A/k. It may be noted that the normalization of the spherical harmonic function in this sub-section is different from that discussed in other parts of this monograph.

In the above discussion, we have assumed that p-modes and g-modes are described by spheroidal modes while r-modes are described by toroidal modes. However, this is correct only for a non-rotating star. In a rotating star, an eigenfunction of a *single* nonradial mode is described neither by a single spheroidal component with a given l and m nor by a single toroidal component; it is in general given by a sum of spheroidal and toroidal components with a given m (m remains a quantum number even in a rotating star). Its velocity vector is written in spherical polar coordinates as (see Section 34)

$$V = \sum_{l\geq|m|} \left(AS_l,\ AS_lk\frac{\partial}{\partial\theta}+AT_l\ \frac{1}{\sin\theta}\ \frac{\partial}{\partial\phi},\right.$$

$$\left. AS_lk\frac{1}{\sin\theta}\ \frac{\partial}{\partial\phi}-AT_l\frac{\partial}{\partial\theta}\right)Y_l^m(\theta,\phi)e^{i\sigma t}, \qquad (7.5)$$

where AS_l and AT_l are velocity amplitudes of spheroidal and toroidal components, respectively. Equation (7.5) is the general expression for the velocity vector of NRP mode, but profile calculations have so far been restricted to a single spheroidal or toroidal mode and calculations based on the general eigenfunction of rotating stars remain to be performed.

We usually assume that the symmetry axis of oscillation is aligned to the rotation axis. The cases in which these two axes are inclined are not discussed here, but Baade and Weiss (1987) examined line-profile variations in such a case. The general discussion of the oblique pulsator model may be found in Section 9. To calculate theoretical line profiles, we need to specify first the equatorial rotational velocity V_e and the

inclination i of the axis of rotation to the line of sight. We then divide the stellar visible disk into many surface elements, as many as 20,000 depending on the mode of interest, and calculate the velocity of each element due to combined effect of rotation and oscillation. The line profiles are constructed by adding the intrinsic profile of each element with due account of Doppler shift corresponding to the line of sight velocity and of a weight appropriate to the limb darkening law. In the above prescription, we have neglected variations in surface area and in brightness due to oscillation. Thus, profile variations are assumed to be generated solely by Doppler effects of oscillations. However, the brightness variation due to oscillation over the visible surface can be as important as the velocity variation, particularly for nonradial p-modes. The brightness and surface area variations due to oscillation remain to be investigated thoroughly.

We summarize parameters necessary to construct a single line-profile due to a single NRP mode: (1) equatorial rotational velocity V_e, (2) inclination i, (3) NRP mode specified by l and m and either spheroidal or toroidal, (4) its velocity amplitude A, (5) the ratio of the horizontal to vertical velocity amplitude k in the case of spheroidal mode, and (6) the phase of oscillation ϕ_p. We sometimes include (7) the effect of broadening due to the macroturbulent velocity. If a single coherent oscillation is involved, all parameters must remain constant all the time except the oscillation phase ϕ_p, which should increase linearly with time. Observed profiles usually exhibit migratory signatures across the profile, and they are best reproduced by nonradial oscillation modes with $m \neq 0$, which represent waves traveling around the equator with the phase velocity:

$$(\partial\phi/\partial t)_{phase} = -\sigma/m. \qquad (7.6)$$

Thus, modes with negative m (i.e., $m < 0$) represent waves propagating in the same direction to rotation*, and they are called *prograde modes*; those with $m > 0$ are waves traveling in the opposite direction to rotation and called *retrograde modes*, while the mode with $m = 0$ represents a standing oscillation.

It should be noted here that the frequency of oscillation of non-axisymmetric NRP mode with $m \neq 0$ and its sense of "prograde" or "retrograde" depend on the coordinate system observed, that is, either from the inertial system or from the co-rotating system of the star. The frequency σ_c of oscillation in the co-rotating frame of reference to the

* Note that the relation between the sign of m and the direction of propagation of traveling waves used here is opposite to that used in the first edition because of the different convention for the sign of σ in equations (7.1) and (7.2).

star is related to that of the inertial frame σ in such a way that

$$\sigma = \sigma_c - m\Omega, \tag{7.7}$$

where Ω denotes the angular velocity of rotation of the star and the term Ω in equation (7.7) represents the well-known Doppler effect of waves in the moving system. In what follows we show some sample calculations of line profile variations due to NRP modes.

7.2 Profile Variations Due to Low l Modes

Main characteristics of profile variations due to low l modes are variations in line width and line skewness. A typical example is shown in Fig.7.1 for a case of a prograde p-mode with $l = 2$ and $m = -2$ and amplitude $A/V_e = 0.4$, $k = 0.15$, and $i = 90°$.

The corresponding radial velocity curve and variation in line half-width are illustrated in Figs.7.2(a) and 7.2(b), respectively. Here the radial velocity of a spectral line is defined by the position of the deepest point in the profile, and it is not the centroid of the line. The

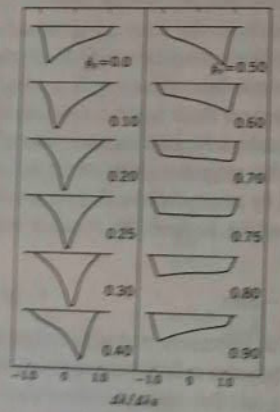

Fig. 7.1 Variation in line profile with phase ϕ_p for $A/V_e = 0.4$, $k = 0.15$ and $i = 90°$. The abscissa is $\Delta\lambda/\Delta\lambda_R$ (or $V/V_e \sin i$), where $\Delta\lambda_R$ denotes the rotational width of the spectral line and $\Delta\lambda$ denotes the wavelength measured from the line-center and the ordinate uses an arbitrary scale (after Osaki, 1971).

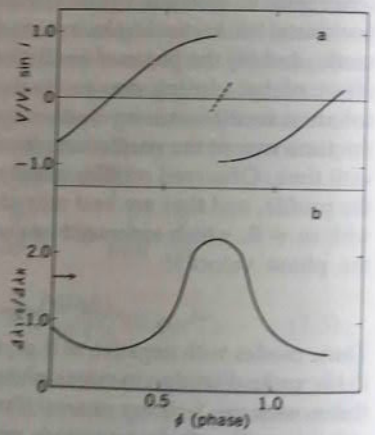

Fig. 7.2 (a) Radial velocity curve, and (b) variation in line half-width ($\Delta\lambda_{1/2}$) for the same parameters as in Fig. 7.1. It is noted that the radial velocity in this figure is defined by the deepest point in profile and it is not that of the line centroid. The arrow in the lower figure indicates the half-width for pure rotation (after Osaki, 1971).

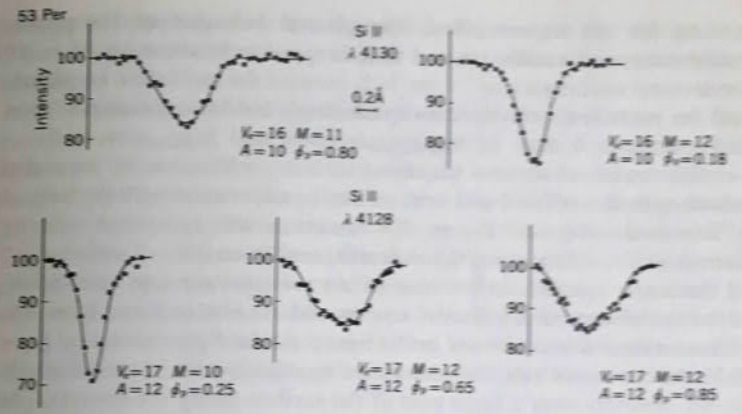

Fig. 7.3 Observations of a line in 53 Per (B5 V) matched with nonradial pulsation profile models (after Smith, 1977).

phase ϕ_p is chosen in such a way that $\phi_p = 0.25$ and $\phi_p = 0.75$ correspond, respectively, to the maximum expansion and the maximum contraction at the disk center of the star (the phase convention used by Osaki, 1971). Therefore, if the adiabatic pulsation is assumed, they are the phases of the minimum and the maximum of the light curve, respectively. As seen in Fig.7.1, the variation in line profile looks as if a kind of wave were sweeping over the rotationally broadened profile once per cycle: a weak component first appearing on the violet edge of the profile moves toward the center, increasing in intensity; it reaches the maximum intensity and the narrowest width at $\phi_p = 0.25$ when the radial velocity passes the γ-velocity on the ascending branch of the radial velocity curve. (Here the γ-velocity signifies the average radial velocity over one cycle of pulsation and represents the radial velocity of space motion of the star.) It then moves toward the red edge, decreasing in intensity and increasing in half-width. At $\phi_p = 0.75$, the line becomes the broadest, and it takes a dish-shaped profile. Lines are symmetric at $\phi_p = 0.25$ and $\phi_p = 0.75$, but they are very asymmetric near $\phi_p = 0.0$ and $\phi_p = 0.50$ with an extensive wing on the red side or on the violet side. When the red component finally disappears, a new violet component appears, and a new cycle starts to repeat. These characteristics simulate very well observed profiles of line profile variable stars called 53 Persei stars. Figure 7.3 shows five profiles, observed during three nights for its representative member 53 Per (B5V) itself and computed simulation by Smith (1977). The computed solution is shown by a solid line which fits remarkably well with observation.

As for the aspect effect, the general behavior of line-profile variations remains similar over a wide range of inclinations $i = 45 \sim 90°$ for sectoral modes such as $l = |m| = 2$, because the oscillation amplitude and the rotational velocity show qualitatively similar dependence upon the colatitude θ, that is, $V_{\text{oscillation}} \propto \sin^l\theta$ and $V_{\text{rotation}} \propto \sin\theta$.

The cause of curious variations in line profiles due to nonradial traveling modes of $l = 2$ and $m = -2$ can be understood with the help of a schematic diagram. Figure 7.4 illustrates the combined velocity vectors due to rotation and the nonradial oscillation of $l = 2$ and $m = -2$ at the star's equator. In the case of a traveling-wave-type oscillation, different phases of oscillation correspond to observations from the different directions indicated in the figure. As the figure shows, at $\phi_p = 0.25$ the combined velocity vectors are mostly directed perpendicularly to the observer over a large part of the surface facing the observer. In this condition a very sharp line is observed. At $\phi_p = 0.75$, on the other hand, the combined velocity vectors on the left half of the visible disk are mostly directed toward the observer while on the right half of the disk they are directed away from the observer. This condition gives a very broad line and sometimes a line doubling for an appropriate combination of the rotation velocity V_e and the oscillation velocity amplitude A.

A wave traveling in the opposite direction to the rotation with $m = 2$ gives rise to the same variation in line profiles as that of $m = -2$, but the sign of the radial velocity is interchanged. In other words, for a

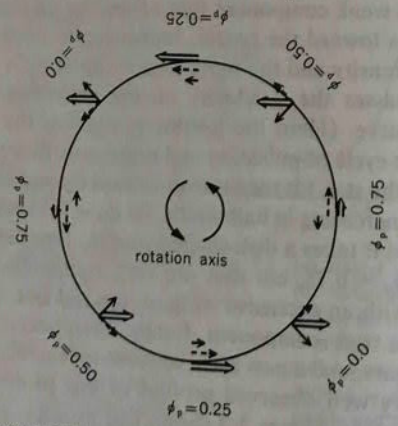

Fig. 7.4 Velocity vector at the equator for a rotating nonradially pulsating star with a prograde wave of $l = 2$ and $m = -2$. Three kinds of arrows show the rotational velocity vector (⇢),the nonradial oscillation velocity vector (→), and the combined velocity vector (⇒).

retrograde traveling wave the sharpest lines occur on the descending branch of the velocity curve, and lines become diffuse on its ascending branch.

The mode with l=2 and m=−1 is also an oscillation of the traveling-wave type, but it is antisymmetric with respect to the equatorial plane so that the radial velocity over the northern hemisphere is just opposite to that of the southern hemisphere. In this mode the amplitude of oscillation becomes largest at the colatitude $\theta = 45°$. Line profiles for this mode were calculated in a case of $i = 45°$ by Osaki (1971). The general behavior of line-profile variations in this case is surprisingly similar to that of the $m = -2$ mode. However, unlike the $m = -2$ sectoral mode, the results are rather sensitive to the inclination i. This general characteristic applies for tesseral modes other than the sectoral ones.

7.3 Profile Variations Due to Intermediate and High l Modes

As discussed in the introduction to this section, it was thought earlier that intermediate and high l (say, $l > 4$) nonradial modes could not be observed in stars because of the cancellation effects over the visible disk. But it turned out that intermediate l nonradial modes (i.e., $l = 4\sim 8$) can well be observed in rapidly rotating stars, as rapid rotation rather helps to resolve the stellar disk through rotational Doppler shift. Vogt and Penrod (1983) were the first to realize this, and they have demonstrated that so-called traveling bumps (quasi-absorption/emission bumps traveling across rotationally broadened line-profiles) observed in ζ Oph can be explained by a nonradial mode of $l = 8$ and $m = -8$.

Figure 7.5(a) exhibits an example of line profiles produced by a nonradial spheroidal mode of $l = 8$ and $m = -8$ with $k = 0.15$. Three absorption bumps (actually four bumps, if a weak bump near the line wing is counted) at a time are seen, and they are traveling across a rotationally broadened profile from blue to red. Figure 7.6 illustrates how bumps are formed in the line profiles of a rapidly rotating nonradially oscillating star. In this figure, the lightest shaded zones represent material moving toward the observer; darkest ones, that moving away from the observer. There is a one-to-one correspondence between position across the disk (or, more exactly, strip parallel to the projected rotation axis) and wavelength in a rotationally broadened profile. The mapping between spatial position over the stellar disk and position in a rotationally broadened line profile is called *Doppler imaging*, as it images a two-dimensional stellar disk into one-dimensional wavelength position of line profile. The arrows beneath the star represent the direction in which a local absorption line is shifted by

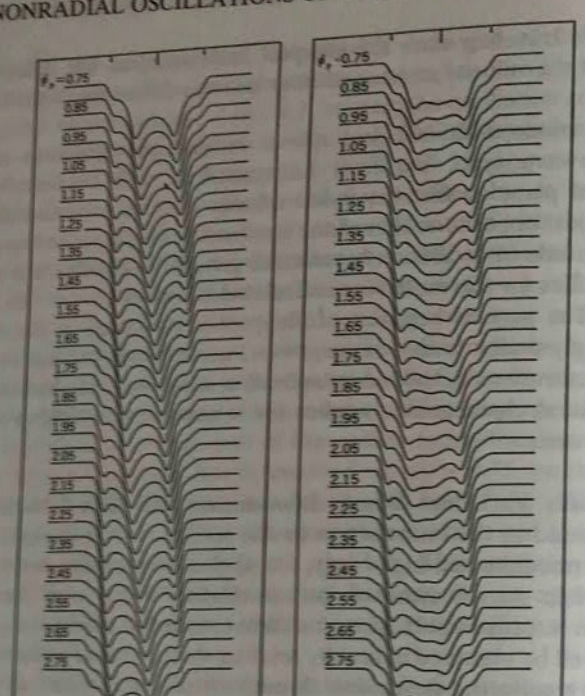

Fig. 7.5 (a) Line profiles for a sectoral spheroidal mode of $l = 8$, $m = -8$, $k = 0.15$, $i = 90°$, and $A/V_e = 0.1$, which corresponds to a p-mode. (b) the same as (a) but for a mode with $k = 1.2$, which corresponds to a g-mode (after Kambe and Osaki, 1988). The abscissa is $\Delta\lambda/\Delta\lambda_R$ ($=V/V_e \sin i$) and the ordinate uses an arbitrary scale.

the addition of the nonradial oscillation; material approaching us (light shaded zones) produces a blueward shift, while material moving away (darkest zones) produces a redward shift. The pronounced dips (bumps) in the line profiles occur when the absorption from a redshifted lobe to the left and a blueshifted lobe to the right combine to produce local absorption within the line profile.

Line-profile variations due to nonradial oscillations have been examined for rapidly rotating stars in a wide range of parameters by Kambe and Osaki (1988). Some of their results are summarized below. As is discussed above, the so-called traveling bumps observed in B-type variable stars are usually interpreted in terms of spheroidal sectoral

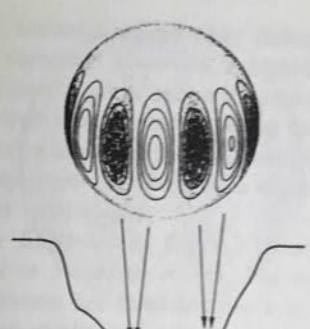

Fig. 7.6 Velocity map of a nonradial oscillation mode with $l = 8$ and $m = -8$ in a rotating star and resultant line profile shown below. The width of the line profile has been scaled to match the diameter of the star. The darkest regions correspond to material moving away from the observer, while the lightest regions moving toward the observer (after Vogt and Penrod, 1983).

modes, and an example of such a mode is presented in Fig.7.5(a). In line profile calculations, there exists a parameter defined by k in equation (7.1), which measures the ratio of the horizontal velocity amplitude to the vertical one at the stellar surface. In the standard line profile calculations, this k value is usually chosen to be less than, say, 0.15. On the other hand, the k-value is related to the oscillation frequency by equation (7.4). Thus, the assumption of small k is appropriate only for high frequency p-modes.

In order to see characteristics of line-profile variation for a mode with large k, we show in Fig.7.5(b) line profiles for the same sectoral spheroidal mode with $l = 8$ and $m = -8$ but $k = 1.2$, which corresponds to a g-mode. We see that a strong bump appearing near the blue wing propagates toward the line center, but it becomes obscure as it approaches the line center. It reappears in the red wing later. Since k is large, profile variation is caused mainly by the horizontal component of the NRP velocity vector. The horizontal velocity component significantly contributes to the profile variation only near the disk limb. The oscillation of a sectoral mode with intermediate or large l is confined in the equatorial belt so that bumps appear only near line wings, as the ϕ component of oscillation velocity vector is dominant for the sectoral spheroidal mode.

Let us now consider line profiles produced by toroidal modes. Motions produced by toroidal modes are essentially a two-dimensional eddy confined on the spherical surface, and their velocity vectors are transverse. Since transverse velocity fields can produce no Doppler shift

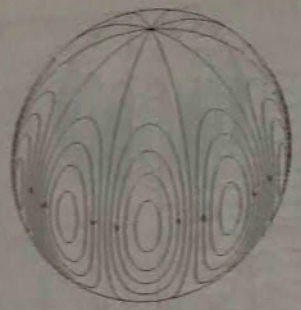

Fig. 7.7 Illustration of stream lines of flow produced by a toroidal mode with $l = 5$ and $m = -5$ which is viewed from a direction $i = 60°$

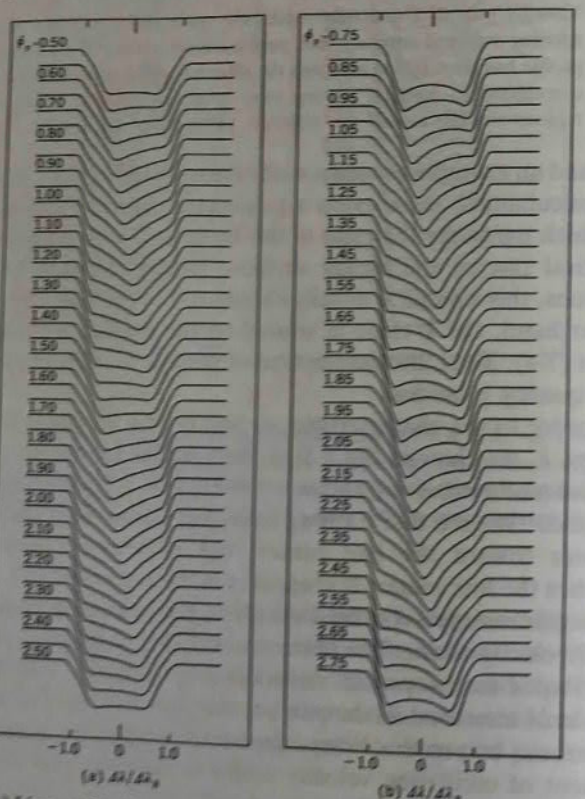

Fig. 7.8 (a) Line profiles for a sectoral toroidal mode of $l = 5$, $m = -5$, and $A/V_e = 0.1$ viewed from an intermediate inclination $i = 60°$. (b) For comparison, we show profiles of the corresponding spheroidal mode with $l = 5$, $m = -5$, $k = 0.15$, and $A/V_e = 0.1$ viewed from the same inclination $i = 60°$ (after Kambe and Osaki, 1988).

near the disk center, toroidal modes were thought not to be of much help for line-profile variation observed in variable B stars. However, Osaki (1986b) has found that a sectoral toroidal mode (or sectoral r-mode) can equally well reproduce "traveling bumps" observed in line profile variable B stars when seen from an intermediate inclination $i \sim 60°$, and thus the uniqueness of NRP mode identification based on line profile modeling was questioned.

To see this, we illustrate in Fig.7.7 stream lines of a sectoral toroidal mode with $l = 5$ and $m = -5$. We see that the regions of large-amplitude oscillation are confined more or less in the equatorial belt and the dominant oscillation velocity is its θ-component near the equator. Therefore, if observed from nearly the equator-on direction (i.e., $i \sim 90°$), oscillation velocity vectors due to this kind of mode can produce no Doppler shifts and thus the resulting line profiles are essentially rotationally broadened profiles, as expected. However, if we see the same oscillation velocity fields from a somewhat inclined direction (say the inclination i is about $60°$), we can see a significant line of sight component for the oscillatory transverse fields of the equatorial belt.

Figure 7.8(a) exhibits line profiles produced by the sectoral toroidal mode with $l = 5$ and $m = -5$ seen from $i = 60°$. We see from Fig.7.8(a) that the sectoral toroidal modes can produce "traveling bumps." For comparison, we exhibit line profiles of corresponding spheroidal mode in Fig.7.8(b). As seen in Fig.7.8, profiles produced by these two modes are very similar, and these modes are indistinguishable from the profiles alone. However, line profiles produced by sectoral toroidal modes are rather sensitive to inclination. As noted above, the same sectoral toroidal mode merely produces rotationally broadened profile if seen from the equator-on direction of $i = 90°$.

Kambe and Osaki (1988) have found that the case of sectoral toroidal modes is by no means unique but that there exists another example of toroidal modes, that can produce "traveling bumps." That is a tesseral toroidal mode with $|m| = l-1$, which can produce traveling bumps for a fairly large range of inclination. Figure 7.9(a) exhibits line profiles for a tesseral toroidal mode with $l = 6$, and $m = -5$. Traveling bumps are seen clearly. Figure 7.9(b) shows corresponding profiles for a sectoral spheroidal mode of $l = 5$, and $m = -5$. We see that very similar profiles are again produced by these two modes. It is furthermore found that traveling bumps in this case are seen for a fairly wide range of inclination with $i = 60° \sim 90°$.

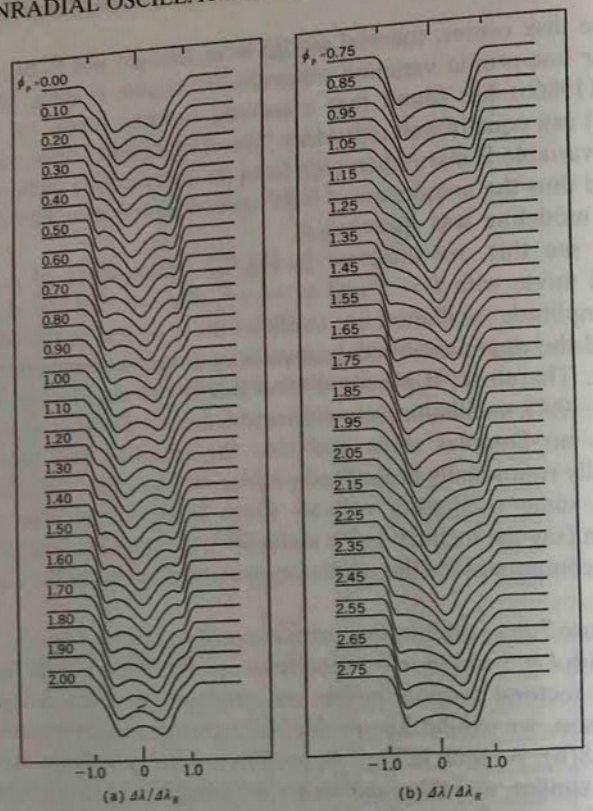

Fig. 7.9 (a) Line profiles for a tesseral toroidal mode of $l = 6, m = -5, i = 90°$, and $A/V_e = 0.1$. (b) For comparison, we show profiles of the sectoral spheroidal mode with $l = 5, m = -5, k = 0.15, i = 90°$, and $A/V_e = 0.1$ (after Kambe and Osaki, 1988).

8. Early Type O, B Variables

Only a decade ago, β Cephei stars were only the known pulsating variables among early type stars. However, recent observations with high precision spectroscopy and photometry have revealed that pulsations and related variations are quite ubiquitous among early type stars (see Smith, 1986; Waelkens and Rufener, 1985). These variables ranges from spectral type O4 (Baade, 1986a) to B8 (McNamara, 1985) and also from luminosity class V to class I. They surround the β Cephei variables on the HR diagram.

Light variations of O, B variables are generally not large (usually

amplitude $\Delta m_v \leq 0.1$ mag). It is, however, noted that the majority of these stars shows the spectroscopic variations in which absorption line width and asymmetry vary with time and in some cases several quasi-emission/absorption bumps travel across an absorption line. In particular, those stars which exhibit characteristic variations in line profile are called "line profile variable stars," and their variations are now believed to be caused by nonradial pulsations (NRP) in rotating stars. In fact, there is some good evidence for such beliefs. The time scale ($0.5 \sim 2$ days) of variations in these stars is too long for radial pulsations. The beat phenomena appearing in some cases cannot be explained by radial pulsations.

There have been many suggestions for classification of variable O, B stars. For example, Cox (1987) suggested dividing these stars into three groups: one that shows at least one radial mode (Smith, 1980c) and two that display only nonradial modes, which are divided in turn into two subgroups: slow rotators and rapid rotators. Smith (1980a, 1981) defined the first group as β Cephei stars, and called the other two groups 53 Persei variables and ζ Ophiuchi variables, respectively. However, the mode identification of these stars (radial or nonradial) is still controversial. So, in this monograph, we call O, B variables that show relatively large light- and radial velocity variations with timescales of several hours the β Cephei (or β Canis Majoris) variables. The other variables show mainly variations in line-profiles. We call the slow rotators ($V_e \sin i < 170$ km s^{-1}) among them 53 Persei variables, and call the rapid rotators ζ Ophiuchi variables. In what follows, we present the general features of these variables [see also a recent review by Baade (1986b)].

8.1 β Cephei Variables

The β Cephei stars are a small group of pulsating variables of early spectral type. Table 8.1 lists the β Cephei stars (Underhill, 1966, 1982; LeContel, Sareyan, and Valtier, 1981). Pulsation periods of β Cephei stars range from about 3.5 to 6 hours. The amplitudes of light variation are rather small, and the typical amplitudes in visual light are $\Delta m_v = 0.01 \sim 0.08$ mag. The largest amplitude is shown by BW Vul, for which $\Delta m_v = 0.24$ mag. The radial velocity variations are also small: their typical range is $2K = 10 \sim 50$ km s^{-1} where $2K$ is the full amplitude in the radial velocity curve. BW Vul is again exceptional in that $2K = 150$ km s^{-1}. There is no appreciable phase lag of the light curve to the radial velocity curve, in the sense that the maximum light occurs at the phase of "maximum compression" when the radial velocity crosses the γ-velocity on the descending branch of the velocity curve. In this sense,

Table 8.1 Representative β Cephei variables.

HD number	Name	Sp. type	Period	Light Amplitude Δm_v(mag)	Velocity Amplitude (km s^{-1})	$V_e \sin i$ (km s^{-1})	NRP	Beat Periods (days)
886	γ Peg	B2IV	3^h38^m	0.015	7	3		
16582	δ Cet	B2IV	3 52	0.025	13	13		
19374	53 Ari	B1.5V	3 40	0.07	5	18		
21803	KP Per	B2IV	4 48	0.1	16–25	–		
29248	ν Eri	B2III	4 10	0.05–0.18	27–71	25	Yes	7.0
44743	β CMa	B1II–III	6 02	0.03	6–18	36	Yes	49.1
46328	ξ^1 CMa	B0.5IV	5 02	0.01–0.045	36	27		
50707	15 CMa	B1IV	4 26	0.01	7	49	Yes	
111123	β Cru	B0.5III	5 40	0.04	14	38	Yes	
116658	α Vir	B1III–IV	4 10	0.014–0.029	16	159	Yes	
118716	ε Cen	B1III	4 05	0.01	–	159		
122451	β Cen	B1III	3 46	0.0–0.04	14	139	Yes	
126341	τ^1 Lup	B2IV	4 16	0.03	11	30		
129056	α Lup	B1.5III	6 14	0.03	14–20	24		
136298	δ Lup	B1.5IV	3 58	0.03	–	221		
147165	σ Sco	B2III	5 55	0.08	80–120	53	Yes	8.0
157056	θ Oph	B2IV	3 22	0.06	5–20	35	Yes	6.0
158926	λ Sco	B2IV	5 08	0.023	17	163		
160578	κ Sco	B1.5III	4 48	0.009	6	131		7.37
165174	V986 Oph	B0III	6 56	0.03	–	434		
199140	BW Vul	B2III	4 49	0.19–0.26	150	26	Yes	
205021	β Cep	B1IV	4 34	0.02–0.05	18–46	28		
214993	12 Lac	B2III	4 38	0.03–0.11	20–55	53	Yes	8.9
216916	16 Lac	B2IV	4 04	0.06–0.11	20–40	23	Yes	17.16

the β Cephei variables are simple pulsating variables. The β Cephei stars were, as pointed out by McNamara and Hansen (1961), once considered to be slow rotators, but Shobbrook and his co-workers (Shobbrook, Herbison-Evans, Johnston, and Lomb, 1969; Shobbrook and Lomb, 1972; Shobbrook, 1972) discovered a few rapidly rotating β Cephei stars (larger than 100 km s^{-1}): rotational velocity is not an indicator of β Cephei stars at all.

Concerning the pulsation mode of β Cephei stars, Smith (1980a, 1981) has argued that the main pulsation of β Cephei variables is radial, and he has proposed that the β Cephei stars must be defined as those early type variables whose main pulsation is radial (Smith, 1980b). It should be noted that some β Cephei stars show multi-period beating, which indicates that nonradial pulsations must be involved as well (see Section 6.6).

Although there are uncertainties in absolute luminosities and masses of β Cephei stars, observations indicate that the pulsation

constant or Q-value of β Cephei pulsations ranges from 0.025 to 0.04 days, which means either the radial fundamental mode or the first harmonic mode, if the stars are radial pulsators.

The β Cephei stars are to be confined to a narrow region in the observational HR diagram; their spectral types are restricted to between B0.5 and B2 and between luminosity classes III and IV. This instability strip of β Cephei stars was believed to lie about 1 magnitude above the zero-age main-sequence (ZAMS), being nearly parallel to it. The existence of the instability strip of β Cephei stars is very important to assign the excitation mechanism of pulsation because it will give an observational clue to the seat from which the pulsation is driven. In fact, Schmalberger (1960) and Lesh and Aizenman (1973) pointed out that this instability strip almost coincides with the so-called S-bend stage of stellar evolution in which the evolutionary path of a massive star with $M = 10 \sim 15 M_\odot$ crosses the instability strip three times: core hydrogen burning, overall contraction, and shell hydrogen burning. In this respect, it should be noted that in the galactic open clusters NGC 3293 (Balona and Engelbrecht, 1983) and NGC 6231 (Balona and Shobbrook, 1983; Balona and Engelbrecht, 1985a), several β Cephei stars are identified. However, the variables in the young cluster NGC 6231 are still on the ZAMS. The present observations now establish that the β Cephei stars are normal main-sequence stars in the core hydrogen burning stage. It is now interpreted that amplitude of pulsation of β Cephei stars has its peak at the center of the classical instability strip stated above and decreases towards both directions of luminosity.

Amplitudes and periods of β Cephei variables are rather stable among O, B variable stars. But Shobbrook (1979) has shown from Fourier analysis that some of the β Cephei variables seem to give different frequency spectra from decade to decade, or even from year to year. Amplitude changes in α Vir and 16 Lac are also an intriguing matter. α Vir was once found to be a β Cephei star before 1970, but its amplitude decreased almost to zero between 1968 and 1972 and remained there since then (Lomb, 1978). α Vir has recently been found to show line-profile variations due to the nonradial pulsations (Walker, Moyes, Yang, and Fahlman, 1981; Smith, 1985). The eclipsing variable 16 Lac also has amplitudes decayed by half for all three pulsation modes between 1965 and 1977 (Jarzebowski, Jerzykiewicz, LeContel, and Musielok, 1979).

8.2 53 Persei Variables

The 53 Persei stars are nonradial pulsators with slow rotational velocity ($V_e \sin i \leq 170$ km s^{-1}). This class of variables was first recognized by

Smith and Karp (1976) and Smith (1977, 1980b). The 53 Persei stars surround the β Cephei variables on the HR diagram, extending from late O stars (10 Lac) to mid-B stars (53 Per), and from the main-sequence (υ Ori) to the supergiants (ρ Leo). The slow variables in mid-B stars photometrically discovered by Waelkens and Rufener (1985) would be 53 Persei variables. In fact, Waelkens (1987) confirmed line profile variations for HD 74195 and HD 74560 in this sample. In addition to these variables, the other kinds of variable B stars previously recognized might also be included in 53 Persei variables such as Maia variables (Struve, 1955; McNamara, 1987) and the ultrashort B star variables (Jakate, 1979). Table 8.2 lists representative 53 Persei variables.

The 53 Persei variables exhibit both light and line-profile variations, but line-profile variations are crucial for distinguishing this class from others. The 53 Persei stars have periods usually of 0.5 to 2 days, too long for radial modes. Therefore, their line-profile variations are interpreted in terms of nonradial pulsations. In fact, with the assumption of sectoral nonradial modes ($m = \pm l$), Smith (1977), as illustrated in Fig. 7.3, performed mode typing (assignment of l and m) in 53 Per, the prototype variable. For the majority of these slowly rotating pulsators, modes are considered to be prograde with low degree l spherical harmonics. However, there are some problems in our understanding of the variations of these stars. Apparent mode switching occurs in many of them within months or even days, which is far sooner than expected theoretically. The amplitude for a certain mode changes

Table 8.2 Representative 53 Persei variables.

HD number	Name	Sp. type	Period[1)]	Light Amplitude Δm_v(mag)	Velocity Amplitude[2)] (km s^{-1})	$V_e \sin i$ (km s^{-1})
3360	ζ Cas	B2IV	21^h30^m	–	4	18
24760	ε Per	B0.5V	3 51	0.008	35–40	153
27396	53 Per	B4IV	45 00	0.01–0.04	10–12	19
35039	22 Ori	B2IV–V	14 06	–	5–7	14
36512	υ Ori	B0V	11 30	–	5	20
51309	ι CMa	B3II	–	–	–	29
74195	o Vel	B3IV	66 43	0.012–0.02	–	40
74560		B3IV	37 13	0.015–0.02	–	22
91316	ρ Leo	B1Ib	–	–	–	61
160762	ι Her	B3IV	9 54	–	4–6	11
214680	10 Lac	09V	4 54	–	4–10	31

Note: 1) Main period in the case of multiple perodicity.
2) Amplitude estimated by NRP modeling.

even within a day. Balona (1985) pointed out that periods obtained photometrically in many of the 53 Persei stars rarely correspond to those determined by modeling of the line profile variations with nonradial pulsations.

Finally, in some of the 53 Persei variables such as 22 Ori and υ Ori (Balona and Engelbrecht, 1985b) and ι Her (LeContel, Ducatel, Sareyan, Morel, Chapellier, and Endiqnoux, 1987), short periods of 0.12 to 0.14 days with smaller amplitude are also discovered.

8.3 ζ Ophiuchi Variables

ζ Ophiuchi stars are nonradial pulsators with rapid rotation ($V_e \sin i \geq 170$ km s^{-1}), named after the prototype line profile variable ζ Oph (Walker, Yang, and Fahlman, 1979). They, like the 53 Persei variables, surround β Cephei variables on the HR diagram. Table 8.3 (*cf.* Percy, 1986) indicates that ζ Ophiuchi stars include both B emission (Be) stars and B normal (Bn) stars. In late B stars, both light and line-profile variations are fairly small.

Owing to the rapid rotation of this class of variables, detectability of nonradial modes as high as $l = |m| = 16$ have been suggested (Smith, 1985). In fact, Vogt and Penrod (1983) have demonstrated for the first time that the observed moving "bumps" in the line profiles in ζ Oph can be interpreted in terms of nonradial sectoral mode with $l = |m| = 8$ according to the "Doppler imaging" discussed in Section 7 for a rapid rotator (see Fig. 8.1).

Many of the modes in ζ Ophiuchi stars appear to be retrograde (except for ζ Oph) when seen from a rotating frame. In this respect, Be

Table 8.3 Representative ζ Ophiuchi variables.

HD number	Name	Sp. type	Period	Light Amplitude Δm_v(mag)	Velocity Amplitude (km s^{-1})	$V_e \sin i$ (km s^{-1})
5394	γ Cas	B0IVe	2^h47^m	–	–	300
33328	λ Eri	B2IVe	16 48	0.03	2–6	336
37490	ω Ori	B3IIIe	45 50	0.05	–	194
120324	μ Cen	B2IV–Ve	12 14	0.015	15	175
149757	ζ Oph	O9.5Ve	3 18	0.02	20–24	379
157246	γ Ara	B1Ib	20 53	–	–	281
157042	ι Ara	B2IIIe	12 22	0.05	–	369
180968	2 Vul	B0.5IVe	14 38	0.06	–	332
191610	28 Cyg	B3Ve	16 48	0.06–0.10	–	310
205637	ε Cap	B3Ve	18 27	0.03	–	293
217050	EW Lac	B4IIIe	17 17	0.06	–	350
217675	o And	B6IIIe	37 41	0.05	–	330

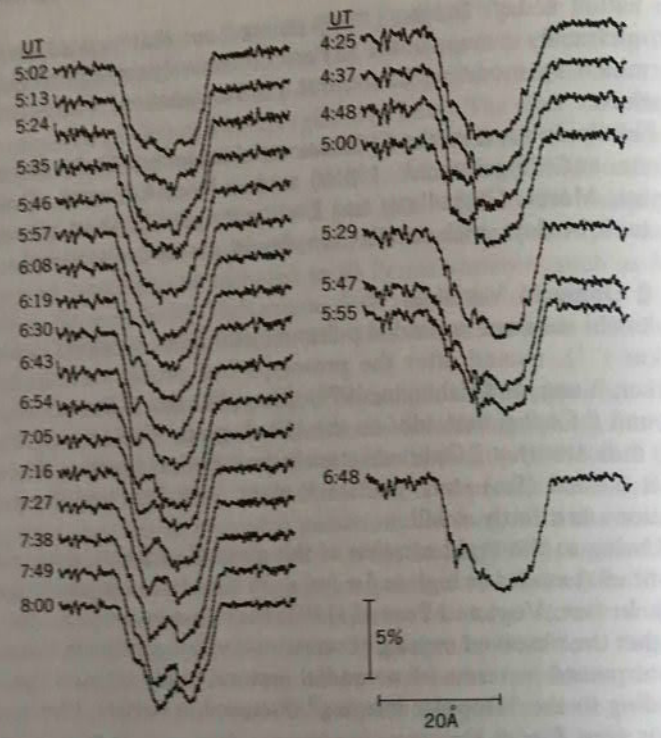

Fig. 8.1 Line profile variation of the He I λ6678 line of ζ Oph (after Vogt and Penrod, 1983).

star μ Cen (Baade, 1984) is quite unique that a series of bumps in the line profile apparently move from red to blue wing even in the inertial frame (*cf.* Kambe and Osaki, 1988).

Observationally Penrod (1987) has suggested that a Be star has an $l = 2$ mode in addition to high l sectoral modes, while a Bn star has only high l modes (with the exception of ζ Oph). This difference seems to be important, since it may indicate that nonradial pulsation (particularly low l, say $l = 2$ mode) and rapid rotation are essential ingredients which allow a B star to become a Be star. Radial motion of nonradial pulsation (particularly $l = 2$ modes) may puff up its matter from the surface of a B star. Another possibility is that nonradial nonaxisymmetric ($m \neq 0$) modes can redistribute angular momentum over the stellar envelope, and the nonradial (prograde) modes can occasionally accelerate the equatorial surface velocity to lead to mass loss, whose mechanism will be discussed in subsection 36.2. These effects are considered to be possible additional forces for the episodic mass loss of Be stars to the

centrifugal force of rotation. It should be noted that there are some Be stars with $V_e \sin i < 170$ km s^{-1} (e.g., 28 CMa, $V_e \sin i = 120$ km s^{-1}) which show line-profile variations. This is interpreted in terms of low inclination, and we consider that Be stars exhibiting line-profile variations are all included in this type of variable.

In many ζ Ophiuchi variables (e.g., μ Cen, γ Ara, ε Per), an intriguing observational fact is that the superperiod $m \times \Pi$ is apparently constant for all modes with different values of $l = -m$. This constant is the time needed for the pulsation pattern to revolve completely about the rotation axis. The constant value is different for different stars. The existence of the superperiod would be considered an important clue to the excitation mechanism of nonradial pulsations in these stars. However, it is also possible that the intrinsic pattern speed seen from the rotating frame is much smaller, say by one order of magnitude, than the stellar rotational speed, and so the wave pattern speeds in the inertial (observer's) frame for all modes seem to be constant within the range of observational error.

There remain unsolved problems: the apparent unequal spacing between adjacent crests of the sectoral modes, the occasional masking of a crest that results in either an amplitude change or even a disappearance, and rapid mode switching; some of these problems are also seen in 53 Persei variables. Balona and Engelbrecht (1986) have proposed the possibility that some of the line-profile variations are due to star spots. To attain complete comprehension of these variations, a number of both observational and theoretical works will be needed.

8.4 Line-Profile Modeling and Related Problems

The historical development and the actual procedure in line profile modeling by nonradial pulsations have been described in detail in Section 7. Line profile modeling by NRPs for "line profile variable stars" among O, B stars has been used for mode identification of NRPs in these stars. However, the uniqueness of the solutions obtained hereby is often questioned. The physical parameters (say, degree l, amplitude, etc.) for modeling are chosen by trial and error until the difference between theoretical and observational profiles is well within the limits of observational error.

Recently Balona (1986a, b, 1987) proposed an objective method for determining mode parameters in line-profile variations. A time series of the first two or three moments of a certain line profile is composed, and the mode parameters are derived from the profile's Fourier analysis. By this technique, Balona (1986a) has suggested that the mode switching often seen in 53 Per might be accounted for by the

scarcity of its data. However, it is noted that the variations in the first two or three moments of the line profile decrease with spherical harmonic degree l, and thus this method is not effective for high l values.

Gies and Kullavanijaya (1988) also developed another objective method of analyzing line-profile variations, and applied it to line profile data of ε Per for five nights, in which the time evolution of a line profile is displayed as the deviation from the averaged line profile as a function of wavelength position. They have calculated power spectra at each point across the line profile in order to search for periodic variability. From this calculation, four prominent peaks have been found in the power spectra of ε Per. In this procedure, there are neither artificial assumptions nor preferences to degree l, which is superior to Balona's method. Gies and Kullavanijaya (1988) diagrammed the phase of the complex power spectrum as a function of position across the line profile, and derived the order of nonradial pulsation modes $m = -3, -4, -5$, and -6, assuming that these variations are due to nonradial pulsations.

We want to mention the so-called "k-problem." The parameter k is defined as the ratio of horizontal to vertical velocities. As discussed in Section 7.1, the parameter k is physically related to the intrinsic pulsation period [equation (7.4)], such that k is smaller for shorter-period NRPs (e.g., p-mode). In O, B variables except for β Cephei stars, g-modes are expected owing to their long periodicity in the co-rotating frame. By definition, k values should be large for g-modes ($k \geq 1$) whereas line profile fitting usually suggests that this value is of order 0.15 or smaller. This is the "k-problem." One possible explanation, already presented in Section 7.3, was proposed by Osaki (1986b): that the sectoral toroidal modes seen from intermediate inclination ($\sim 60°$) show traveling bumps similar to those due to the sectoral spheroidal mode. Kambe and Osaki (1988) have further shown that the tesseral toroidal mode (e.g., $l = 6$, $m = -5$) gives a similar traveling bumps to those of sectoral spheroidal mode for a fairly large range of inclination. In these discussions, a single spherical harmonics (being the solution only for nonrotating stars) is used for line profile fitting. However, in rotating stars like O, B variables, line profiles should be expressed by a sum of spheroidal and toroidal components as in equation (7.5). Therefore, the k-problem remains to be studied.

The most fundamental problem of O, B variables concerns the excitation mechanism of pulsations. So far, no definite destabilizing mechanism has been found, although almost all possible mechanisms known in stars have probably been proposed: (1) κ-mechanism, (2) ε-mechanism, (3) overstable convection, (4) shear instabilities in a differentially rotating star, and (5) tidally forced oscillation and nonlinear coupling between modes. The problem of excitation mechanisms of pulsations in O, B variables will be discussed in Section 35.

9. *Rapidly Oscillating Ap Stars*

The rapidly oscillating Ap stars are cool Ap stars which pulsate with short periods in the range of 4-15 min and small amplitudes: $\Delta m_v < 10$ mmag (1 mmag = 0.001 mag), generally much less; most are less than 1 mmag. They were first found in 1978 by Kurtz, and so far twelve have been counted. The name of this class of stars evidently comes from the shortness of their periods, which are much shorter than the dynamical timescale, $2\pi/(GM/R^3)^{1/2}$, of these stars that is of the order of ≈ 2 hr.

In Table 9.1 we list all of the known members of this class of star. They are cool, magnetic Ap stars with SrCrEu line strength peculiarities. Some are well-known oblique magnetic rotators, and it is a reasonable presumption that they all are. Although uncertainty remains about their position in the HR diagram because of their spectral peculiarities, they lie in or near to the lower portion of the Cepheid instability strip, where the δ Scuti stars are located. However, it has not yet been established whether the rapidly oscillating Ap stars are limited in the instability strip. Also, whether or not all of the cool, magnetic, SrCrEu-type Ap stars show rapid oscillations has not yet been established. Indeed, there are some Ap stars whose characteristics are almost the same as those of the rapidly oscillating Ap stars except for the appearance of oscillations. Detailed description of eleven of these stars and references to the literature on them is available in Kurtz's (1986a,b) review, and information on the twelfth, HD 166473, can be found in Kurtz and Martinez (1987). Other reviews on these stars are also available in Weiss (1986), Shibahashi (1987), and Kurtz (1988). The oscillations were first found by means of high-speed photometry, but they have also been detected as the Doppler shift of spectroscopic lines (Matthews, Wehlau, Walker, and Yang, 1988b; Libbrecht, 1988a).

Figure 9.1 shows a typical example of luminosity variation of the rapidly oscillating Ap stars. The power spectrum of this star is shown in Fig. 9.2. One of the most conspicuous characteristics of the rapidly oscillating Ap stars is that the pulsation amplitudes are modulated with the rotation period of the star in the sense that the amplitudes are correlated with the phase of the magnetic strength which varies with the rotation. As shown in Fig. 9.1, it is evident that the pulsation amplitude varies.

Figure 9.3 indicates the variation in the pulsation amplitude of HD

Table 9.1 Rapidly oscillating Ap stars.

HD	Sp.Type	H_s(G)	Freq.(mHz)	Amp.(mmag)	Refs.
6532	Ap SrCrEu		2.39612	1.01	(1)
			2.40210	0.37	
			2.40761	0.55	
24712	A5p	+300 to +1200	2.7208	2.13	(2)(3)(4)
			2.6528	2.07	
			2.6875	2.07	
			2.7556	2.07	
			2.6200	2.07	
			2.7936	2.07	
60435	Ap Sr(Eu)		1.10077	2	(5)
			1.30371	6	
			1.35210		
			1.38088		
			1.40749		
			1.43364		
			2.75	15	
			4.17307		
83368	Ap SrCrEu	−700 to +700	1.423950	2.14	(4)
			1.432069	1.75	
			1.428011	0.38	
			2.856019	0.45	
			2.847906	0.20	
			2.864139	0.18	
101065	Controversial	−2200	1.372865	5.40	(6)(7)(8)
			1.315079	0.67	
			2.7459	0.26	
128898	Ap SrEuCr	−300(variable)	2.442041	1.91	(9)
			2.4395	0.38	
134214	F0 SrEu		2.9496	3.23	(10)(11)
137949	Fp SrCrEu	+1400 to +1800	2.0148	1.39	(4)
166473	Ap SrEuCr		1.891944	0.49	(12)
			1.823890	0.27	
			1.928169	0.25	
201601	F0p	+500 to −800	1.339	0.86	(13)
203932	Ap SrEu		2.804789	0.66	(14)
217522	Ap SiCr		1.21510	2.	(15)

References to Table 7.1

(1) Kurtz and Kreidl (1985)
(2) Kurtz and Seeman (1983)
(3) Kurtz, Schneider, and Weiss (1985)
(4) Kurtz (1982)
(5) Matthews, Kurtz, and Wehlau (1986a)
(6) Kurtz (1981)
(7) Kurtz (1980)
(8) Kurtz and Wegner (1979)
(9) Kurtz and Balona (1984)
(10) Kreidl (1985)
(11) Kreidl and Kurtz (1986)
(12) Kurtz and Martinez (1987)
(13) Kurtz (1983a)
(14) Kurtz (1984)
(15) Kurtz (1983b)

83368 with the rotational phase, where the zero of the rotational phase is the phase at which the observed magnetic field strength is zero. We can see that the pulsation amplitude is almost sinusoidally varying with the rotation phase and that it becomes the largest at the magnetic maximum phase. Figure 9.4 is a schematic sketch of an extension of the part in problem of the power spectrum of Fig. 9.2; it shows that there is a triplet fine structure of which each of the side-components is separated from the central peak by the stellar rotational frequency.

In order to explain this character, Kurtz (1982) proposed the oblique pulsator model, in which the pulsation is interpreted as nonradial, axisymmetric ($m = 0$) oscillations with low degree l, whose symmetry axis is coincident with the stellar magnetic axis which is itself oblique to the stellar rotation axis. Figure 9.5 indicates the pattern of an

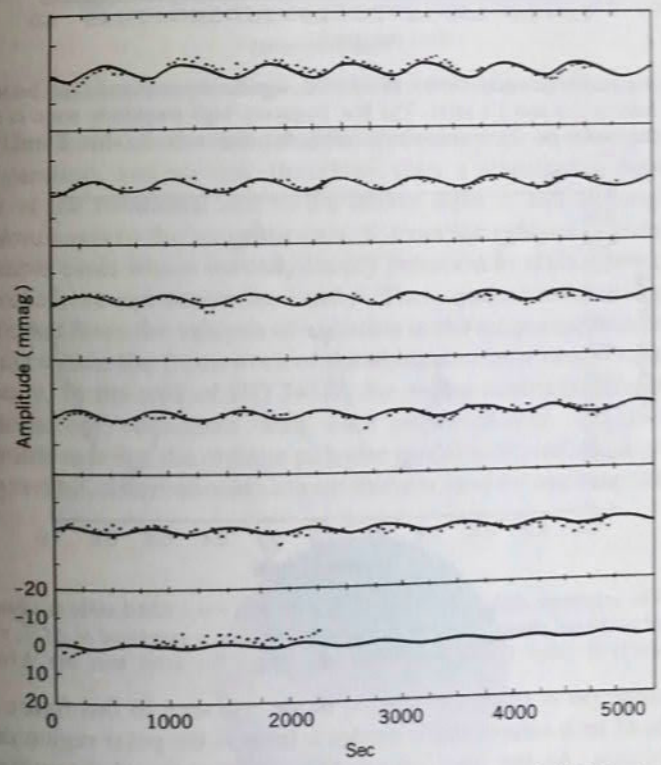

Fig. 9.1 The light curve of HD 83368 (dots). The abscissa is 5,000 s long and the ordinates 40 mmag high with tick marks at 10 mmag intervals. The continuous light curves have been folded into 5,000 s consecutive sections which should be read from left to right, top to bottom, just like lines of print (after Kurtz, 1982).

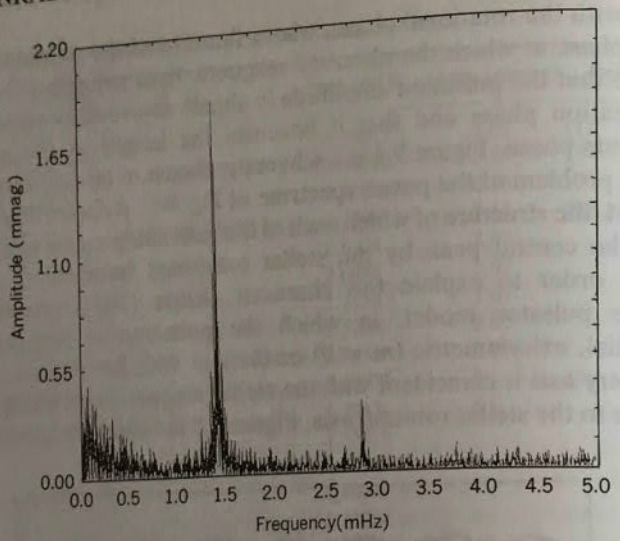

Fig. 9.2 An amplitude spectrum for HD 83368. Significant amplitude can be seen at both at 1.4 and 2.8 mHz. The low frequency high amplitude noise is due to fluctuation in sky transparency during the observations (after Kurtz, 1982).

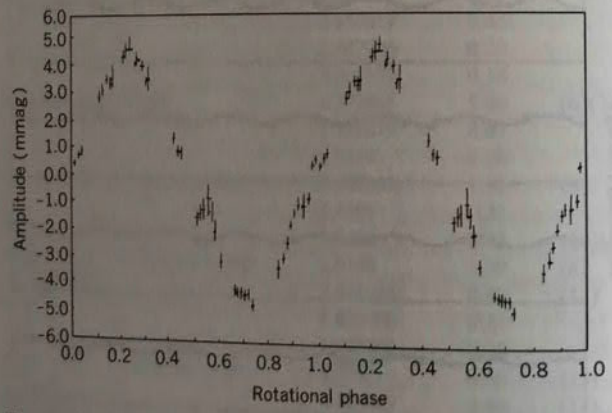

Fig. 9.3 The amplitude $A(t)$ of the dipole oscillation with $\nu = 1.42801$ mHz as a function of rotational phase, where the luminosity variation is expressed as $\Delta L/L = A(t) \sin(2\pi\nu t)$ (after Kurtz and Shibahashi, 1986). The error bars are $\pm 1\sigma$.

axisymmetric ($m = 0$) dipole ($l = 1$) mode. As seen in this figure, the amplitude of such axisymmetric modes is large at the polar region of the symmetry axis. As the star rotates, the aspect angle of the pulsation (and the magnetic axis) varies; hence the apparent pulsation amplitude varies synchronously with the magnetic strength which is also modulated with the rotation.

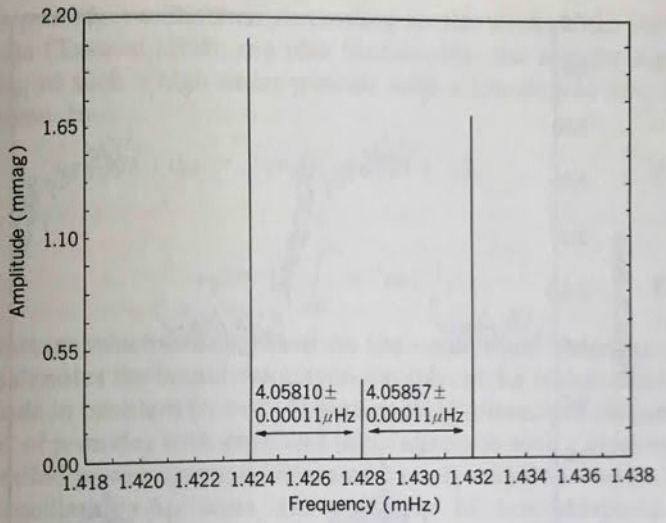

Fig. 9.4 A schematic amplitude spectrum for HD 83368 showing the frequency triplet.

The form of the modulation is dependent on the geometrical configuration, and we can, therefore, infer a relationship between the angle of the rotational axis to the line-of-sight, i, and the angle of the rotational axis to the magnetic axis, β, from the analysis of pulsation. In favorable cases where we can identify pulsation in at least two modes of different l, we can determine i and β. These quantities are independently inferred from the analysis of variation in the magnetic field strength of the star within the framework of the oblique rotator model for magnetic Ap stars. In the case of HD 24712, the angles determined by these two methods are consistent with each other (Kurtz, 1982). Another favorable case for the oblique pulsator model is HD 83368. Kurtz (1982) analyzed his observational data on this star, and by applying this model,

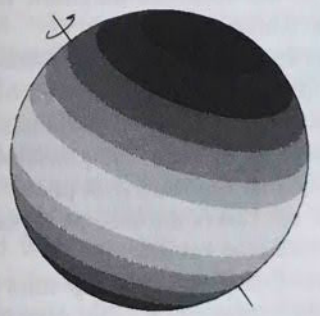

Fig. 9.5 The pattern of an axisymmetric ($m = 0$) dipole ($l = 1$) mode.

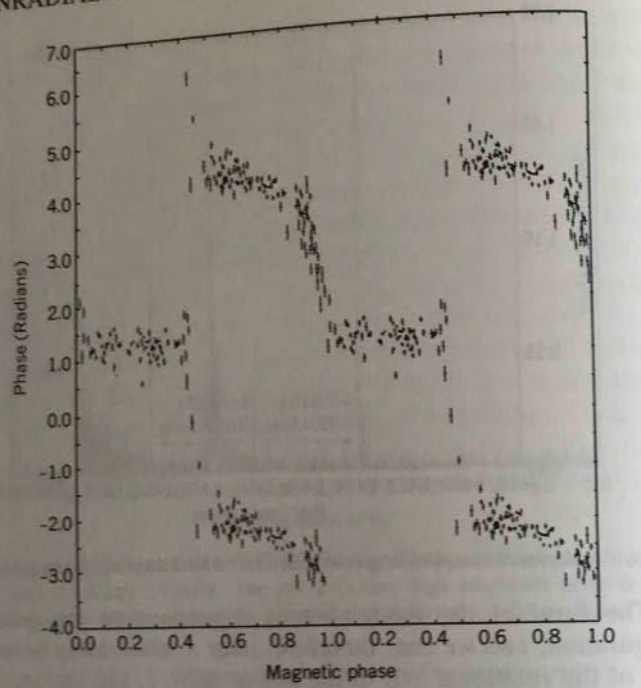

Fig. 9.6 The phase of the dipole oscillation with $\nu = 1.42801$ mHz as a function of magnetic phase (after Kurtz and Shibahashi, 1986). The error bars are $\pm 1\sigma$.

he deduced that $i = 86°$ and $\beta = 36°$. This led to the predictions that the rotational velocity, $V_e \sin i$, should be ≈ 32 km s^{-1} and that the polarity of the observed magnetic field of this star should reverse when the line-of-sight becomes parallel to the magnetic equator. Polarity-reversing of the magnetic field was later confirmed by Thompson (1983), and the rotational velocity was also measured later to be $V_e \sin i \approx 33 \pm 3$ km s^{-1} by Carney and Peterson (1985). The angles i and β provided by variation in the observed magnetic field are also confirmed to be consistent with Kurtz's prediction.

If the oscillation is due to a dipole ($l = 1$) axisymmetric mode whose symmetric axis is oblique to the rotational axis of the star, the phase of the oscillation is expected to jump by π radians at magnetic quadrature and remain constant in other phases. The phase of the pulsation mode in HD 83368 is plotted against the magnetic phase in Fig. 9.6 (Kurtz and Shibahashi, 1986). We see this is the case as expected. All of these facts support the oblique pulsator model.

The periods of rapid oscillations of Ap stars are much shorter than that of the radial fundamental mode. The very high frequencies of the oscillations of these Ap stars are then naturally interpreted as very high

overtone p-mode oscillations. According to the asymptotic theory of oscillations (Tassoul, 1980; see also Section 16), the angular eigenfrequency σ_{nl} of such a high order p-mode with a low degree l is, to first order, given by

$$\sigma_{nl} \approx 2\pi\nu_0(n + l/2 + \epsilon), \tag{9.1}$$

where

$$\nu_0 \equiv [2\int_0^R c^{-1}dr]^{-1}, \tag{9.2}$$

ϵ is a constant which is dependent on the equilibrium structure of the star, $c(r)$ denotes the sound velocity in the star, and n is the radial order of the mode in problem ($n \gg l$). Equation (9.1) means that frequencies, $\nu \equiv \sigma/2\pi$, of p-modes with even and odd l alternate with a separation of $\nu_0/2$. Detailed power spectrum analyses have revealed that some of the rapidly oscillating Ap stars are pulsating in several modes with uniformly spaced frequencies (Kurtz and Seeman, 1983). The observed frequency spacing (e.g., ≈ 33 μHz for HD 24712) is consistent with the theoretical values of $\nu_0/2$ for stellar models with $M \approx 2M_\odot$ in the main-sequence stage, which indicates that the observed oscillations are an alternation of even and odd degree p-modes (Shibahashi, 1984; Gabriel, Noels, Scuflaire, and Mathys, 1985; Shibahashi and Saio, 1985). The odd degree modes in HD 24712 are supposed to be $l = 1$ since they have triplet fine structure which is well interpreted by the oblique pulsator model of $l = 1$. As for the even degree modes appearing in the middle of $l = 1$ modes in the power spectrum, the degree is likely to be $l = 0$ or 2; otherwise the total amplitude of the variability integrated over the stellar disk is too small to be detected. By substituting the observed frequency spacing into $\nu_0/2$ in equation (9.1) and supposing $l = 1$ from the arguments given in the above, we estimate the radial order $n \approx 30$.

The appearance of such high order p-modes reminds us of solar five-minute oscillations, whose period range is also much shorter than that of the radial fundamental mode of the sun. There are, however, differences in the rapid oscillations in Ap stars and the solar oscillations. One of them is that the rapid oscillations in Ap stars are significantly influenced by strong magnetic fields of the stars so that their symmetric axis is coincident with the magnetic axis of the star. Another difference is that most of the rapidly oscillating Ap stars, except for HD 60435 (Matthews, Kurtz, and Wehlau, 1988a, c), seem to pulsate with only a single or a few eigenmodes among the dense frequency spectrum while the solar oscillations consist of many modes whose amplitudes are the same order of magnitude. The selective excitation of overtones may be a

consequence of the strong magnetic fields of Ap stars. The oscillations in Ap stars seem to be quite stable; hence by having a long time-span of observations we can determine eigenfrequencies with high accuracy (see Table 9.1). If many eigenfrequencies are determined for each of rapidly oscillating Ap stars, seismological approach will be useful to study the physics of Ap stars.

Dziembowski and Goode (1985, 1986) paid attention to the inequality of the amplitudes of the frequency components in a triplet fine structure in the power spectrum. If the pulsation were due to a purely axisymmetric ($m = 0$) mode with $l = 1$ whose symmetric axis is oblique to the rotational axis of the star, the rotational modulation of the amplitude would cause the triplet fine structure in the power spectrum to be symmetric with respect to the central component. As seen in Fig. 9.4, the observation shows this is not the case. Dziembowski and Goode (1985, 1986) formulated the oscillations of a rotating magnetic star as an eigenvalue problem by taking into account both the oblique magnetic field and the rotation, and showed that the relative amplitudes in a fine structure of the power spectrum is dependent on the rotation and the internal magnetic field strength of the star. This result leads to a possibility of using fine structure of the power spectrum as diagnosis of the internal magnetic field of Ap stars (see also Kurtz and Shibahashi, 1986). The detail of theoretical treatments of oscillations in a rotating magnetic star will be discussed in Section 19. The asteroseismological aspect will also be discussed in Section 43.

The classical pulsating variables in the lower portion of the Cepheid instability strip near the main sequence have been known as the δ Scuti variables, whose periods are in the range of 30 min $\sim$ 4.7 hr (typically $\approx$ 2 hr). The interesting thing is that not all the stars in this region of the instability strip are observed to vary and only about one third of the stars in this region are δ Scuti variables. All the Ap stars had been included among the apparently non-pulsating stars. Variability in Ap stars was searched for, but until the first discovery of the rapidly oscillating Ap stars (Kurtz, 1978) explicit evidence for pulsation in Ap stars had not been discovered. Therefore, chemical peculiarity and pulsation had been empirically regarded as mutually exclusive. The discovery of the rapidly oscillating Ap stars has thus raised many questions: What is the relationship between these stars and the δ Scuti stars? What is the relationship between the pulsation and the anomalous chemical abundances? Why do these stars pulsate in such high overtones? Why are the pulsations aligned with the magnetic axis? What is the excitation mechanism of the rapid oscillations? Most of these questions have not yet been answered. The answers to these questions

should provide us useful concepts for understanding the physics of Ap stars.

10. Variable Degenerate Stars

There are at least three distinct groups of variable degenerate (single) stars. These are, in the order of increasing luminosity, DAV stars [= ZZ Ceti stars; i.e., variable DA (hydrogen envelope) white dwarfs], DBV stars [variable DB (helium envelope) white dwarfs], and DOV stars [= PG1159 stars; variable hot pre-white dwarf stars] including a variable planetary nebula nucleus. The periods of their light variations, ranging from $\sim$ 100 s to $\sim$ 2,000 s, are consistent with the periods of the nonradial g-mode oscillations with low spherical degrees. Amplitudes of their luminosity variations are less than $\sim$ 0.3 mag, and in most cases they show complex beat phenomena due to multiple modes simultaneously excited. Accurate high speed photometry over a long time span is necessary to delineate such complex light variations to obtain accurate periods. Because of this difficulty, only approximate periodicities have been obtained for many degenerate variables. If accurate periods are obtained on a long time base line, this data set may reveal period change due to the change of the stellar structure that accompanies the cooling evolution of these stars, which may give an independent check of the microphysics for the dense degenerate matter.

Cataclysmic variables are different from the above variables. They are made of degenerate stars and the accretion disks around them in interacting close binary systems. They also show small amplitude luminosity variations with periods from $\sim$ 10 s to $\sim$ 1,200 s. In the following subsections, we discuss the characteristics of the luminosity variation for each group.

10.1 Variable DA White Dwarfs (ZZ Ceti Variables)

At the time of writing, twenty variable DA white dwarfs (DAV stars or ZZ Ceti stars) are known. The observed properties of the twenty known DAV stars are listed in Table 10.1. They are listed in the order of increasing main periods. It is apparent that they form a narrow instability strip of 11,000 K $\leq T_{eff} \leq$ 13,000 K, which corresponds to the color region of $-0.41 \leq G - R \leq -0.29$ (Greenstein, 1982, 1984), where $(G - R)$ color of white dwarfs is correlated with their effective temperature more accurately than the $(B - V)$ or $(b - y)$ color is. All the DA white dwarfs in the instability strip seem to show luminosity variations (Greenstein, 1982; Fontaine, McGraw, Dearborn, Gustafson, and Lacombe, 1982; Fontaine, Bergeron, Lacombe, Lamontagne,

and Talon, 1985a). Figure 10.1 shows two-color diagram of the variable and nonvariable white dwarfs (Greenstein, 1982). The DAV stars are located in the color region where the hydrogen Balmer absorption is maximum at the stellar surface. This suggests that the cause of the light variations of the DAV stars is related to the hydrogen partial ionization zone (see Section 28). There is no clear correlation between the main period and the effective temperature of the DAV stars (Winget and Fontaine, 1982).

The luminosity variations are believed to be caused by temperature variations due to nonradial g-mode oscillations (Robinson, Kepler, and Nather, 1982; Kepler, 1984b). The variations are, in most cases, multiperiodic with periods in the range of 100 − 1,200 s. In some cases, a few periods coexist in a small period range and the amplitude of the light variation shows a complex beat phenomenon. These closely spaced periods may be produced by the rotational "*m*-splitting" (see Sections 4 and 19). Inspecting Table 10.1, we notice that the periods of the DAV stars are divided roughly into short period and long period groups. This is seen more clearly in Fig. 10.2, where the peak-to-peak amplitudes are plotted against the periods of the DAV stars. The peak-to-peak amplitudes of the DAV stars in the long period group are systematically larger than those in the short period group. The cause of this grouping is not clear, although it may be related to the mode trapping caused by compositionally stratified envelopes of the DA white dwarfs (Winget, Van Horn, and Hansen, 1981).

Pulsational properties of the DAV stars may be largely classified into three groups. One is the group of small amplitude variables such as R548 and G226-29, whose pulsations are mainly governed by one or two periods accompanied by a few closely spaced periods. Second is the group of the intermediate amplitude variables such as GD154 and BPM31594, whose light curves are relatively regular and are explained by one period with its harmonics. Probably, the main period consists of two or three very closely spaced components. The third group is the large amplitude group such as HL Tau-76, G29-38, and G38-29, whose light curves are complex; several periods as well as their harmonics are excited simultaneously. In what follows, we describe the observed characteristics of the light curves for a representative star of each group.

The variability of the DA white dwarf R548 (ZZ Ceti) was first discovered by Lasker and Hesser (1971). They found that R548 had a main period of 213 s and a secondary period of 274 s. Osaki and Hansen (1973) and Brickhill (1975) demonstrated that these periods are consistent with the periods of nonradial g_1- and g_2-modes for $l = 2$. Later, Robinson, Nather, and McGraw (1976) demonstrated that the

Table 10.1 The variable DA white dwarfs (ZZ Ceti variables).

Name	V (mag)	$B-V$ (mag)	$b-y$ (mag)	$G-R$ (mag)	$U-V$ (mag)	T_{eff} (K)	Amp (mag)	Periods[a] (s)	Refs.[b]
G226-29	12.14		.069	−0.36	0.31	12,300	0.02	109	(1)
L19-2	13.75	0.25				12,300:	0.04	193,114	(2)
G238-53	15.51			−0.30	0.61		0.01	206	(3)
R548	14.10	0.20	.029	−0.37	0.50	12,500	0.02	213,274	(4)
G185-32	13.00	0.17	.091	−0.33	0.42	12,000	0.02	215,141	(5)
G117-B15A	15.52	0.20	.029	−0.41	0.37	12,900	0.06	215,304,271	(6)
GD385	15.13	0.19	.053	−0.39	0.38	11,800	0.05	256	(7)
GD66	15.6	0.22		−0.31		10,800	0.08	272,301,813	(8)
G207-9	14.64	0.17	.071				0.06	318,557,292	(9)
GD99	14.55	0.19	.064	−0.36	0.39	12,000	0.13	480:,590:,260:	(10)
BPM31594	15.03	0.21					0.21	617,403	(11)
HL Tau-76	14.97	0.20		−0.31	0.51	11,300	0.34	746,626,663	(12) (13)
PG 2303+243	15.5		.09	−0.31	0.37		0.11	795,901,623	(14)
BPM30551	15.26	0.29					0.18	823	(15)
R808	14.36	0.17	.090	−0.34	0.41	11,900	0.15	830,513	(10)
G255-2	16.04			−0.34	0.46		0.28	830,685	(16)
G191-16	15.98	0.03:	.070	−0.31:	0.44:	12,400:	0.28	883,588	(5)
G38-29	15.63	0.16	.060	−0.34	0.54	11,200	0.21	926,1020	(17)
G29-38	13.10	0.20	.054	−0.37	0.46	11,700	0.28	933,820,671	(17)
GD154	15.33	0.18		−0.29	0.51	11,600	0.10	1186,780	(18)

a) Harmonics are not included.
b) References for the pulsation periods.

L19-2=MY Aps
R548=ZZ Ceti
G238-53=GR 538=LP66-262
BPM31594=VY Hor
R808=G180-23

(1) Kepler, Robinson, and Nather (1983)
(2) O'Donoghue and Warner (1987)
(3) Fontaine and Wesemael (1984)
(4) Stover, Hesser, Lasker, Nather, and Robinson (1980)
(5) McGraw et al. (1981)
(6) Kepler et al. (1982)
(7) Kepler (1984a)
(8) Fontaine et al. (1985b)
(9) Robinson and McGraw (1976)
(10) McGraw and Robinson (1976)
(11) O'Donoghue (1987)
(12) Page (1972)
(13) Fitch (1973)
(14) Vauclair, Chevreton, and Dolez (1987)
(15) McGraw (1977)
(16) Vauclair, Dolez, and Chevreton (1981)
(17) McGraw and Robinson (1975)
(18) Robinson, Stover, Nather, and McGraw (1978)

two periods in the light curves of R548, one at 213 s and one at 274 s, vary in amplitude and in phase, and that the amplitude and phase variations are strictly periodic, with periods of about 1.5 days. A portion of their light curve and the power spectra of the light curve of R548 for three consecutive nights are reproduced in Figs. 10.3 and 10.4, respectively. The periodic amplitude- and phase-modulations of each of

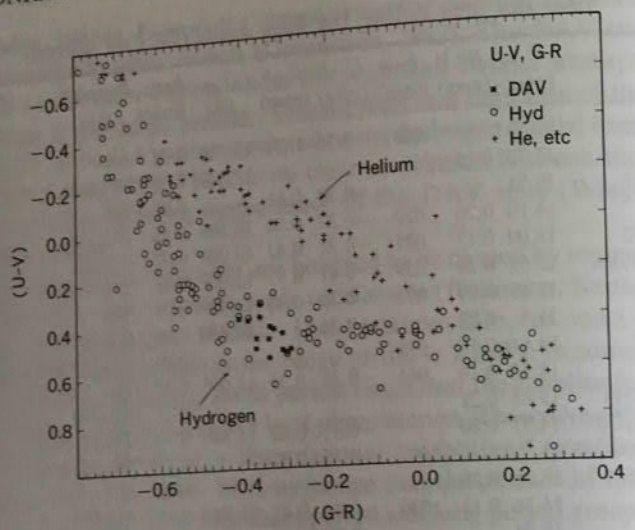

Fig. 10.1 Color-color diagram ($U - V$, $G - R$), for variable and nonvariable white dwarfs (from Greenstein, 1982). Plus signs are helium-atmosphere stars. Asterisks are DAV stars (ZZ Ceti stars) and open circles are nonvariable DA white dwarfs.

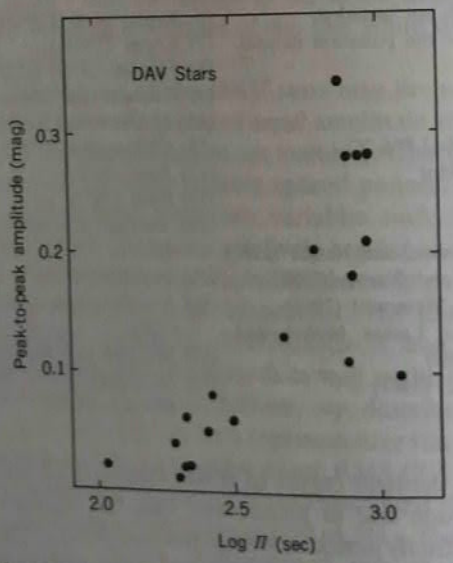

Fig. 10.2 Period-amplitude correlation for DAV stars. The vertical axis is peak-to-peak amplitude in magnitude and the horizontal axis is logarithm of period in second.

the two oscillations are explained by the beating of two very closely spaced pulsation frequencies; in other words, each of the oscillations actually consists of a pair of pulsation modes, and the individual pulsation modes are constant in both amplitude and phase. Combining all the data available, Stover et al. (1980) obtained the following four periods (and amplitudes in mag): 213.132605 s (0.007), 212.768427 s (0.0044), 274.250814 s (0.0049), and 274.774562 s (0.0034). The beat periods are 1.44122 days for the 213 s pair and 1.66528 days for the 274 s pair. With these periods, the observed light curves are almost completely reproduced.

The existence of closely spaced periods is naturally accounted for by the m-splitting of nonradial pulsations due to the stellar rotation (see Section 4). If the difference between the m-values of the two adjacent frequencies is one ($\Delta m = 1$), the rotation period is approximately equal to the beat period. Then, the rotation period of R548 is about 1.5 days. If we adopt a typical radius, 9×10^3 km, we obtain the equatorial rotational velocity of about 0.4 km s^{-1}.

Similarly very closely spaced periods have been obtained for GD385 (Kepler, 1984a), for which the beat period is 3.7 days, and for G226-29 (Kepler et al., 1983), for which the beat period is 0.72 days. Attempts to detect the period change due to the cooling evolution of the white dwarf have been made for some stars in the short-period group because they have relatively simple light variations. The cooling time is expected to be of the order of 10^9 yr. Only the upper limits of the period change have been obtained. Among them the smallest upper limit obtained so far for the DAV stars is $|d\Pi/dt| \leq 9.9 \times 10^{-15}$ for G117-B15A by Kepler, Winget, Robinson, and Nather (1988), which corresponds to the lower limit of the timescale of the period change of 7×10^8 yr. We expect that the cooling time of a DA white dwarf will actually be measured using the nonradial pulsations in the near future.

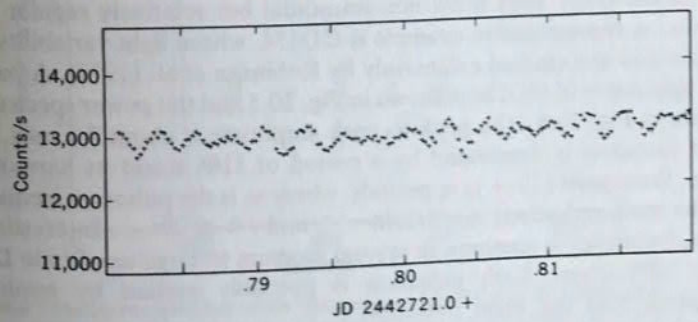

Fig. 10.3 A portion of the light curve of R548 after Robinson et al. (1976).

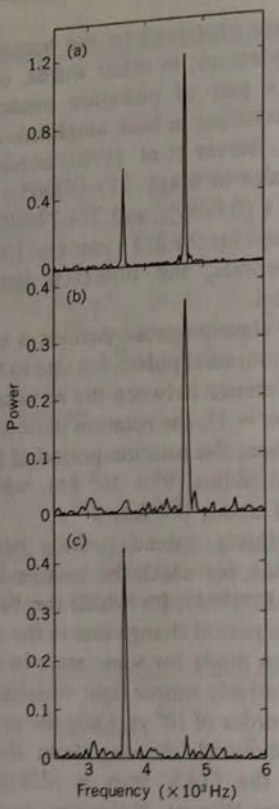

Fig. 10.4 Power spectra of the light curves of R548 for three consecutive nights, after Robinson et al. (1976).

Some DAV stars show non-sinusoidal but relatively regular light curves. A representative example is GD154, whose light variability was discovered and studied extensively by Robinson et al. (1978). A part of the light curve of GD154 is shown in Fig. 10.5 and the power spectrum is shown in Fig. 10.6. The peak-to-peak amplitude is about 0.1 mag. The light variation is dominated by a period of 1186 s and its harmonics. Also, there exist $(1/2 + j)\,\nu_0$ periods, where ν_0 is the pulsation frequency of the main pulsation; $\nu_0 = 1/1186\ \mathrm{s}^{-1}$, and $j = 1, 2, \ldots$. Interestingly, $1.5\nu_0$ frequency is common in several medium to large amplitude DAV and DBV stars. Such pulsation is probably excited by nonlinear coupling with the main pulsation.

Robinson et al. (1978) reported that for the first nine nights the

light curves and their power spectrum are similar to that shown in Fig. 10.5 and Fig. 10.6, respectively, but on the tenth night the amplitude of the main frequency decreased significantly and $1.5\nu_0$ pulsation dominated the light curve. There are two possible explanations for this phenomenon: beating and nonlinear mode switching. If the main pulsation with frequency ν_0 consists of two (or more) pulsations whose frequencies are so closely spaced (by the rotational m-splitting) that these are not resolved, the decrease in the amplitude of the main pulsation on the tenth night may be explained by the beating with a very long beat period. Another explanation is to assume that nonlinear coupling among the modes shifts the pulsation energy from ν_0 mode to

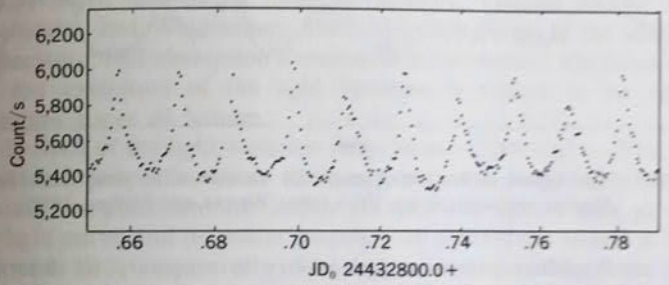

Fig. 10.5 The light curve of GD154 after Robinson et al. (1978).

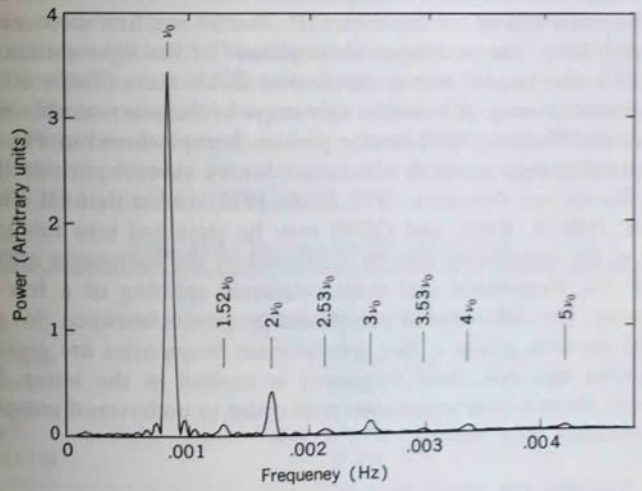

Fig. 10.6 The power spectrum of the light curve of GD154 after Robinson et al. (1978). The peak labeled ν_0 is the main frequency of the light curve ($\nu_0 = 1/1186\ \mathrm{s}^{-1}$). The peaks labeled $n\nu_0$ ($n = 2, 3, 4, 5$) are harmonics of the main frequency ν_0.

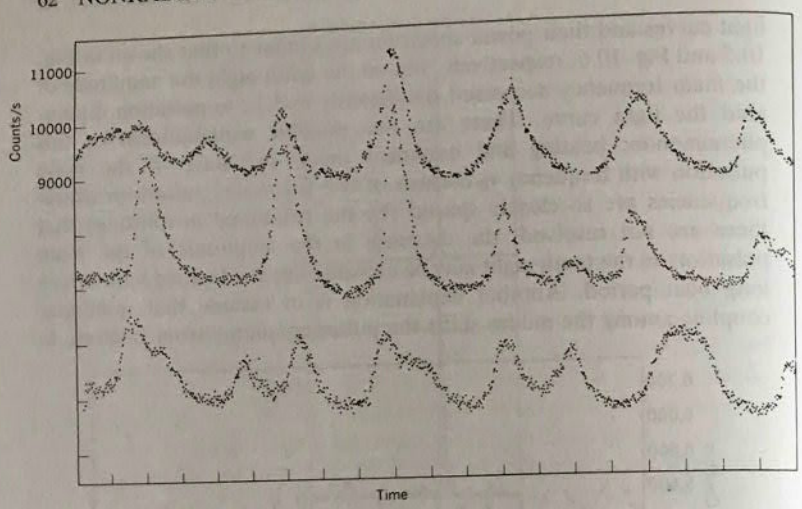

Fig. 10.7 Light curves of the largest amplitude variable white dwarf, HL Tau-76. Abscissa marks are every 200 s (after Warner and Nather, 1972).

$1.5\nu_0$ mode. More extensive photometry is necessary to determine which (or what other) mechanism is appropriate to explain the pulsational behavior observed in GD154.

The variability of a white dwarf HL Tau-76 was first discovered by Landolt (1968). The peak-to-peak amplitude of the light variations of this star is the largest among the known DAV stars (Table 10.1); it amounts to 0.34 mag. A beautiful light curve of this star was obtained by Warner and Nather (1972), and a portion is reproduced in Fig. 10.7. This complex light curve is accounted for by several periods (Page, 1972; Warner and Robinson, 1972; Fitch, 1973). Other than HL Tau-76, G29-38, G38-29, R808, and GD99 may be classified into this group. Many of the frequencies may be explained by the harmonics including $(0.5 + j)\nu_0$ frequencies and their rotational splitting of a few main pulsations. The difference in pulsational properties between this group and the previous group is that several main frequencies are excited in the former and one main frequency is excited in the latter. More extensive observations are necessary in order to understand completely such complex light curves.

10.2 Variable DB White Dwarfs

Although the light variation of the first DAV star HL Tau-76 was discovered accidentally (Landolt, 1968), the light variation of the first DBV, GD358, was discovered during a search for a variable DB (helium envelope) white dwarf itself. In the study of the excitation mechanism of the DAV stars, Winget, Van Horn, Tassoul, Hansen, Fontaine, and Carroll (1982a) predicted the existence of pulsating DB white dwarfs, whose pulsations are excited by the effect of the partial helium ionization zone. After an extensive search, Winget, Robinson, Nather, and Fontaine (1982b) actually found that a DB white dwarf, GD358, does pulsate. Since this discovery, four other DBV stars have been found. The known members of the DBV stars are listed in Table 10.2. The DBV stars are located in the temperature region of 23,000 K $\leq T_{eff} \leq$ 27,000 K (Liebert, Wesemael, Hansen, Fontaine, Shipman, Sion, Winget, and Green, 1986; *cf.* Koester, Vauclair, Dolez, Oke, Greenstein, and Weidemann, 1985). For this range of the effective temperature, HeI absorption is maximum at the surface, which indicates that the excitation of the light variation is related to the partial ionization zones of helium.

Periods of the light variation range from ~ 1000 s to ~ 100 s. The pulsational properties seem to change with the length of the main periods; i.e., pulsations are simpler for stars with shorter main periods. The light curve and its power spectrum for GD358 are shown in Figs. 10.8 and 10.9, respectively. The light curve shows apparent beat phenomenon indicating multiperiodic pulsations. Its power spectrum shows the existence of more than 28 modes between 952 s and 142 s, in contrast to the existence of only a few periods for the DAV stars and the DOV stars (see below). This difference may be caused by the difference in the composition stratifications between the DA and the DB white dwarfs. These pulsation frequencies are divided into several groups which contain several nearly equally spaced frequencies. The frequency distribution is probably a combination of a dense frequency spectrum of g-modes and rotational m-splitting.

Table 10.2 The variable DB white dwarfs.

Name	V (mag)	$B-V$ (mag)	$b-y$ (mag)	T_{eff} (K)	Amp. (mag)	Periods (s)	Refs.
PG1351+489				24,000	0.16	489,333	(1)
PG1456+103				23,000	0.11	657,793,425	(2)
PG1654+160				25,000	0.18	851−149	(3)
GD358	13.65	−0.11	−.049	27,000	0.30	952−142	(4)
PG1115+158				25,000	0.11	1000:−106:	(1)

(1) Winget Nather, and Hill (1987)
(2) Grauer, Bond, Green, and Liebert (1988)
(3) Winget, Robinson, Nather, and Balachandran (1984)
(4) Winget et al. (1983)

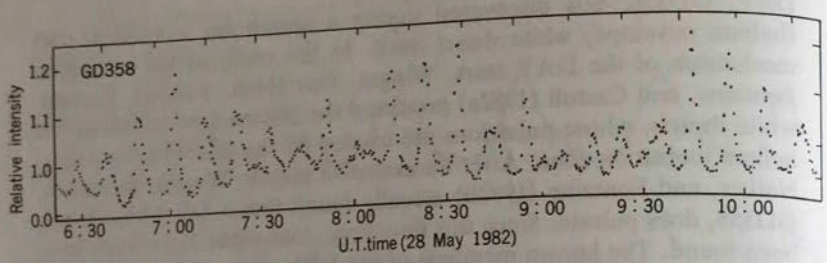

Fig. 10.8 The light curve of DBV star GD358, taken from Winget et al. (1982b).

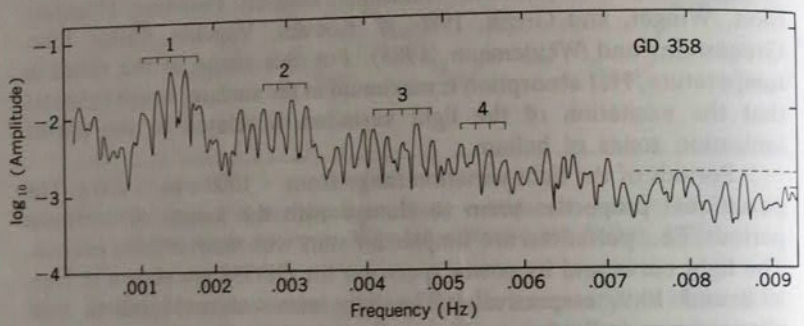

Fig. 10.9 The amplitude spectrum (the square root of the power spectrum) of the light curve of GD358 (from Winget et al., 1982b). Groups of periodicities that are evenly spaced in frequency are marked with the joined tick marks.

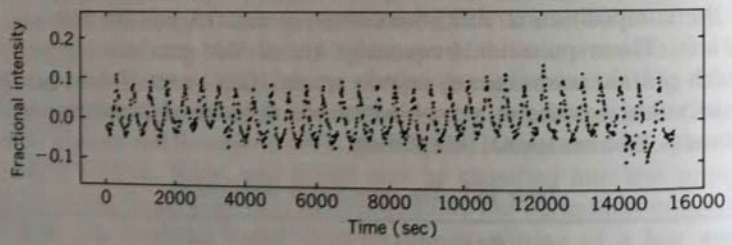

Fig. 10.10 The light curve of DBV star PG 1351+489 after Winget et al. (1987).

The light variation of the DBV star PG1351+489 discovered by Winget et al. (1987) gives another extremum of the degenerate variables. A part of the light curve is reproduced in Fig. 10.10. Like the light variation of the DAV star GD154 (Figs. 10.5 and 10.6), the light variation of PG1351+489 is extremely regular, and is dominated by a single period of 489 s ($\nu_0 = 2.04$ mHz) and its harmonics. The light variations are so regular that Winget et al. (1987) even obtained a mean

pulse shape by superposing many pulses. It is interesting to note that, as in some DAV stars, there are frequencies of $\nu \simeq (j + 1/2)\,\nu_0$ $(j = 1,2,\ldots)$ which are common to the large and intermediate amplitude nonradial pulsators of the degenerate variables. The 489 s period corresponds to a nonradial g-mode with $\sim$ 15th radial order if $l = 2$ is assumed. The frequency spectrum around such high radial order g-mode pulsations is densely populated. It is not known why a single frequency is selectively excited in PG1351+489 and so many frequencies are excited in GD358, PG1654+160, and PG1115+158.

10.3 Variable Hot Pre-White Dwarfs (PG1159 Variables)

The first DOV star, PG1159 − 035 (= GW Vir), was discovered by McGraw, Starrfield, Liebert, and Green (1979). At present, five DOV stars are known, including a planetary nebula nucleus, K1-16, whose luminosity variation was discovered by Grauer and Bond (1984). These stars are listed in Table 10.3. Their spectra are characterized by the presence of He II and C IV absorption lines and the absence of Balmer lines. The spectra indicate that these objects are in the pre-white dwarf stage with extremely high effective temperature (higher than $\sim$ 100,000 K) and high surface gravity (Wesemael, Green, and Liebert, 1985). Although the radii of these stars are uncertain, the observed periods are believed to be high radial order nonradial g-modes ($n > 40$ if $l = 2$ is assumed; Starrfield, Cox, Kidman, and Pesnell, 1984; Kawaler, Hansen, and Winget, 1985a). The pulsational properties are similar to those of the short period DAV stars. The light curve of the prototype star PG1159 − 035 is shown in Fig. 10.11, which is taken from Winget, Kepler, Robinson, Nather, and O'Donoghue (1985). Because of the high luminosity of these stars, the time scale of the period change due to the evolutionary change of the stellar structure is expected to be shorter than that for the DAV and DBV stars. Actually, Winget et al. (1985)

Table 10.3 The variable hot pre-white dwarfs (PG1159 variables).

Name	V (mag)	$B-V$ (mag)	$b-y$ (mag)	$G-R$ (mag)	$U-V$ (mag)	T_{eff} (K)	Amp. (mag)	Periods (s)	Refs.
PG2131+066	16.63	−0.36		−0.21	−0.79		0.10	386,413	(1)
PG0122+200	17.90			−0.73	−0.81		0.10	404,444	(2)
PG1707+427	16.69			−0.81	−0.84		0.13	450,333,493:	(1)
PG1159−035	14.84		−0.37	−0.71	−0.78		0.08	516,539,451	(3)
K1−16	15.04	−0.38				>80,000	0.04	1698	(4)

(1) Bond, Grauer, Green, and Liebert (1984)
(2) Bond and Grauer (1987)
(3) Winget et al. (1985)
(4) Grauer and Bond (1984)

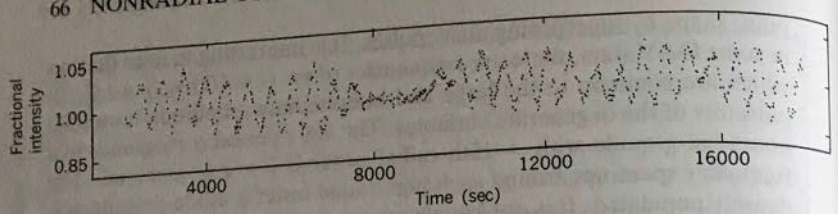

Fig. 10.11 The light curve of DOV star PG 1159−035 (GW Vir) after Winget et al. (1985).

obtained $d\Pi/dt = (1.2 \pm 0.1) \times 10^{-11}$, which corresponds to an evolutionary time scale of $(1.4 \pm 0.1) \times 10^6$ yr.

10.4 Cataclysmic Variables

Cataclysmic variables are eruptive variables which from time to time exhibit sudden luminosity increases in various scales. They are usually divided into three classes: (1) novae, (2) dwarf novae, and (3) nova-like variables. All the cataclysmic variables form close binary systems with periods ranging from $\sim$ 1 hr to $\sim$ 2 days, each of which consists of a white dwarf, an accretion disk, and a low mass star. Many short period light variations of cataclysmic variables are also reported. Recent reviews on the short period variations are found in Cordova and Mason (1982) and Warner (1986). The period range extends from $\sim$ 7 s to $\sim$ 1,200 s. These short period light variations are grouped into three types: (1) extremely stable pulsations observed for DQ Her (nova), (2) quite coherent oscillations seen in dwarf novae during outbursts, and (3) the quasi-periodic oscillations, also seen in dwarf novae outbursts. The stable pulsation of DQ Her is now believed to be caused by a radiating beam from the rotating white dwarf illuminating the surface of the accretion disk (Petterson, 1980). The rate of change of period, $d\Pi/dt = -8.1 \times 10^{-13}$ obtained by Balachandran, Robinson, and Kepler (1983), is explained as the spinning up of the white dwarf by accretion, which supports the above picture. The periods of the coherent and quasi-periodic oscillations of the dwarf novae change with the luminosity of the system. The period is shorter when the star is brighter. This change of the period makes it less convincing to explain the light variations by nonradial pulsations of the white dwarf itself. These pulsations are believed to be caused by the accretion disk (possibly nonradial pulsations in the accretion disk).

The absence of nonradial pulsations of the white dwarf itself in the cataclysmic variables is consistent with the fact that the effective temperature of white dwarfs in cataclysmic variables is higher than the blue edge of the DAV stars. The surface composition of the white dwarf

in the cataclysmic variables is, in many cases, hydrogen rich, because the mass donor has a hydrogen-rich envelope. There are a few exceptions, in which the donor has no hydrogen. In such a case the central accreting white dwarf must be a DB white dwarf. The effective temperature of the instability strip of the DBV stars is much higher than that of the DAV stars. It is possible that such exceptional helium cataclysmic variables show nonradial pulsations if the effective temperature of the white dwarf enters into the instability strip for the DBV stars. Wood, Winget, Nather, Hessman, Liebert, Kurtz, Wesemael, and Wegner (1987) recently found a candidate for such a phenomenon, a helium cataclysmic variable PG1346+082 which consists of two degenerate stars. This star shows, in some phase of the cataclysmic variations, 200 to 400 s light variations whose light curve is very reminiscent of the DBV stars. In such phase the effective temperature seems to be consistent with the DBV stars.

11. Oscillatory Motions of the Sun

11.1 Five-Minute Oscillation

In 1960, Leighton and his co-workers (Leighton, Noyes, and Simon, 1962) discovered that the solar surface was almost entirely covered with vertically oscillating elements. This oscillatory motion was called the "five-minute" oscillation, as its period was near five minutes. Since then, extensive observations of the five-minute oscillation have been made by various researchers. In the very early studies, the five-minute oscillation was thought to be excited locally by overshooting of convective elements (observed as "granules") into the stably stratified photosphere from below. However, as more and more observations were accumulated, it became clear that the five-minute oscillation was independent of granules. Instead, these oscillations have been identified as superposition of eigenmodes of the sun—that is, many of the nonradial p-modes of the sun are somehow excited and observed as five-minute oscillations. Furthermore, it was found that the sun is oscillating even in radial modes with periods near five minutes. It was also shown later that the brightness on the solar disk varies with the period near five minutes that is associated with the oscillatory motion. Stein and Leibacher (1974) reviewed early observations and theoretical models of the five-minute oscillations before the oscillations have been recognized as the eigenmodes of the sun.

In order to see how the five-minute oscillations look, we reproduce, in Fig. 11.1, a velocity and a brightness plot as functions of time and position on the solar disk which were obtained by Musman and Rust

(1970) and Nishikawa, Hamana, Mizugaki, and Hirayama (1986). Several features of the five-minute oscillation are apparent in the figure. Oscillations are almost always present to some degree. When large oscillations are observed, they begin and end with small amplitudes, and a maximum is reached only after some period. That is, they do not start abruptly as would be expected in the case of "excitation" by single overshooting granules. Rather, it appears that a steady oscillation is always present and that transient large-amplitude "wave trains," which last four to five cycles, are superposed. Although the typical horizontal scale for amplitude coherence is of the order of $5 \sim 10$ Mm, occasionally phase coherence occurs over a distance as long as 30 Mm.

There has been some confusion and contradiction concerning the horizontal scale of oscillating elements. Rather small horizontal scales (≈ 2 Mm) for oscillating elements were reported in early observations, but much larger scales (even to the solar diameter scale) were indicated in recent observations. This inconsistency is thought to be caused by a confusion of (small-scale) granulation velocity fields and oscillatory velocity fields. It is thus important to distinguish these two velocity

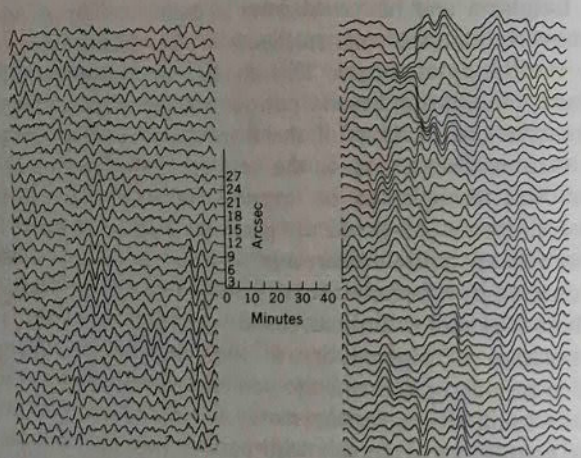

Fig. 11.1 (Left) Vertical velocity variation with time for points along a scan line on the solar surface separated by intervals of 3 arcsec (2.2 Mm) obtained by Musman and Rust (1970). The distance between the curves for adjacent points is equal to a velocity of 400 m s^{-1}. (Right) Intensity variation with time in the image compressed into one dimension (5450 Å, FWHM of 400 Å) obtained by Nishikawa et al. (1986). Each curve is separated by 2.26 arcsec and 0.08% in the intensity fluctuation. (The radius of the sun is 0.696×10^6 km, and the angular diameter of the sun viewed from the earth is 32 arcmin. Thus, 1 arcsec on the solar disk corresponds to 725 km; i.e., 1 arcsec = 0.725 Mm.)

fields clearly. For this purpose and for a comparison with theory, the most useful is the so-called diagnostic diagram in which observed powers are shown as a function of horizontal wavenumber k_h and angular frequency σ. The wave natures of oscillations are clearly seen from the location of powers in that diagram. The diagnostic (k_h, σ)-diagram has been discussed and used extensively in geophysics (see, e.g., Eckart, 1960), and it was first discussed in the context of waves in the solar atmosphere by Whitaker (1963). Before presenting power spectral observations, we give a brief explanation of the diagnostic diagram below.

Let us consider the wave propagation in a plane isothermal atmosphere under a constant gravitational field. The pressure p_0 and density ρ_0 of a static isothermal atmosphere are well known to vary with height z as

$$p_0,\ \rho_0 \propto \exp(-z/H_p), \tag{11.1}$$

where $H_p \equiv p_0/(\rho_0 g) = \mathcal{R}T_0/(\mu g) = \text{const.}$ is the scale height, g the gravitational acceleration, T_0 the temperature, μ the mean molecular weight, and $\mathcal{R}$ the gas constant, and the subscript 0 is used to signify undisturbed quantities. The linearized system of equations in hydrodynamics of adiabatic perturbations allows a simple solution of plane waves for velocity $\boldsymbol{v}$, the pressure variation p', and the density variation ρ' of the form

$$\boldsymbol{v},\ p',\ \rho' \propto \exp\left(\frac{z}{2H_p}\right) \exp[i(\sigma t + k_h x + k_z z)], \tag{11.2}$$

where x stands for the horizontal coordinates. The exponentially growing factor with height in equation (11.2) arises so as to conserve wave energy in vertical direction since the density ρ_0 in atmosphere decreases with height.

The angular frequency σ and the horizontal and vertical wavenumbers k_h and k_z must then satisfy a dispersion relation (see Eckart, 1960, p.107; Whitaker, 1963; *cf.* Chapter III, Section 15) which is given by

$$(\sigma^2 - \sigma_{ac}^2)\sigma^2 - (k_h^2 + k_z^2)c^2\sigma^2 + k_h^2 c^2 N^2 = 0, \tag{11.3}$$

where $c^2 = \gamma p_0/\rho_0 = \gamma \mathcal{R} T_0/\mu_0$, and γ and c are the ratio of the specific heats of gas and the sound velocity, respectively. The quantity σ_{ac} is the acoustic cut-off frequency and N is the Brunt-Väisälä frequency. They are given by

$$\sigma_{ac} = \frac{c}{2H_p} = \frac{\gamma g}{2c} \tag{11.4}$$

and

$$N = \frac{g}{c}\sqrt{\gamma - 1} \qquad (11.5)$$

for the isothermal atmosphere. The acoustic cut-off frequency is slightly greater than the Brunt-Väisälä frequency, and $\sigma_{ac} = 1.02\,N$ for $\gamma = 5/3$. Equation (11.3) may also be written as

$$c^2 k_z^2 = (\sigma^2 - \sigma_{ac}^2) + k_h^2 c^2 (N^2 - \sigma^2)/\sigma^2. \qquad (11.6)$$

If σ and k_h are given, the above equation determines k_z^2. If $k_z^2 > 0$, waves can propagate vertically. On the other hand, if $k_z^2 < 0$ no waves can propagate, and the energy density perturbation decreases exponentially with height (evanescent waves) if no wave flux is coming from above. This situation is most conveniently shown in the (k_h, σ)-diagram of Fig. 11.2. The diagnostic (k_h, σ)-diagram is divided into three regions: (1) $k_z^2 > 0$, denoted "P", where modified acoustic (pressure) waves can propagate, (2) $k_z^2 > 0$, denoted "G", where modified gravity waves can propagate, and (3) $k_z^2 < 0$, where waves are evanescent. The straight line with $\sigma = k_h c$ in the figure shows the "Lamb waves" first discovered by Lamb (1932); they represent vertically evanescent but horizontally propagating acoustic waves. The Lamb wave is closely related to the f-mode which separates the p-modes from the g-modes.

The solar atmosphere is by no means isothermal, and, strictly speaking, the wave nature cannot be discussed locally. However, the diagnostic diagram is still helpful in approximately representing the wave nature of the five-minute oscillations. The critical acoustic cut-off frequency σ_{ac} varies with the inverse square-root of temperature T_0.

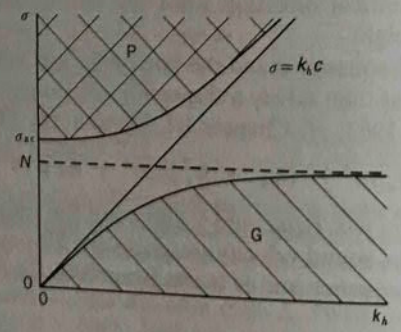

Fig. 11.2 Diagnostic diagram for the plane isothermal atmosphere. The quantity k_z^2 is positive in the hatched region (G) and in the cross-hatched region (P), while it is negative in the other regions.

Thus the heighest acoustic cut-off frequency (and also the highest Brunt-Väisälä frequency) occurs at the temperature minimum in the solar atmosphere where $\sigma_{ac} \approx 0.034\ \mathrm{s}^{-1}$, which corresponds to a critical period of oscillation of about 185 s.

Let us turn to observations of power spectra in the two-dimensional (k_h, σ)-diagram. Figure 11.3 illustrates one of such power spectra obtained in early periods, reproduced from the work of Frazier (1968). It is immediately apparent from the figure that there are two distinct regions of power: low wavenumber ($k_h \approx 1\ \mathrm{Mm}^{-1}$) oscillatory power with periods near five minutes, and high wavenumber ($k_h \approx 2 \sim 4\ \mathrm{Mm}^{-1}$), nonperiodic low frequency power which corresponds to the granulation. Thus the five-minute oscillation and the granulation are very clearly separated in the diagnostic (k_h, σ)-diagram. We can also see that the power of the five-minute oscillation falls on the region of evanescent waves in the diagnostic diagram for the upper photosphere. The horizontal scale in Frazier's observations was rather limited (i.e., the observational lower limit of wavenumber $k_h \approx 0.6\ \mathrm{Mm}^{-1}$) because of the small total area of observations, but recent observations with longer base lines and/or two-dimensional observations of solar disk yield

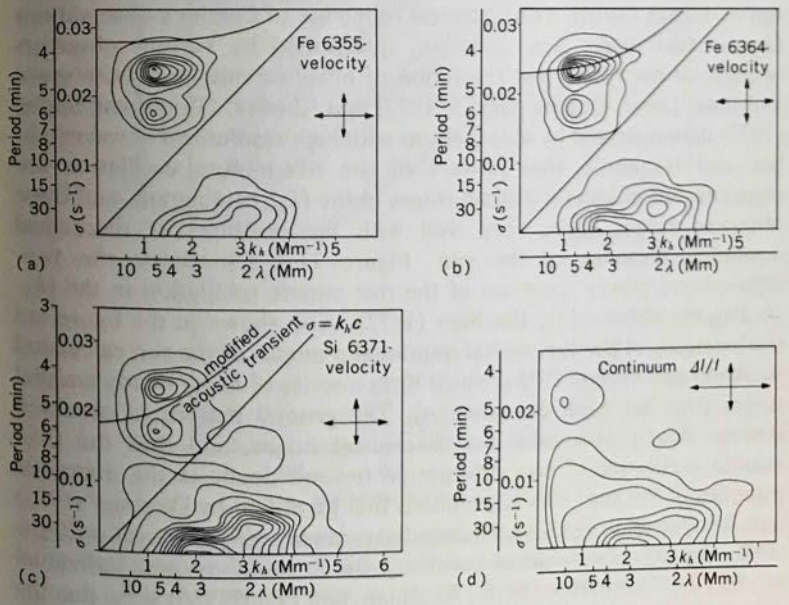

Fig. 11.3 Observed diagnostic diagrams after Frazier (1968). (a) Fe 6355, velocity; (b) Fe 6364, velocity; (c) Si II 6371, velocity; (d) continuum $\Delta I/I$.

results for power of the five-minute oscillation with much lower horizontal wavenumber (see Chapter VII).

The observational fact that the five-minute oscillations fall in the evanescent wave regions of the diagnostic diagram for the photosphere implies strongly that they are standing eigenmodes of the sun—in particular, acoustic eigenmodes trapped in the subphotospheric regions. That is because standing eigenmodes are trapped waves that are reflected at the two boundaries of the system. The fact that the observed oscillations are evanescent (and thus non-propagating as waves) in the photosphere means that the photosphere can act as a reflecting boundary for the five-minute oscillations. The word "evanescent" sometimes seemed misunderstood in the past, but it simply means that the energy of oscillations is contained largely in the subphotospheric regions and the energy density, ρv^2, decreases exponentially with height within the photosphere. It does not mean that the amplitude of velocity v itself decreases with height. Indeed, it is possible that v increases with height because density ρ decreases exponentially with height more rapidly than the energy density.

Two separate maxima at periods of 270 s and 350 s are seen in Fig.11.3, and this was interpreted as indicating two eigenmodes of the sun by Ulrich (1970). The statistical reliability of Frazier's observations for the two peaks was, however, questioned by various observers because of the rather low resolution of his observations in both space and time. Later, Deubner (1975, 1977) and Rhodes, Ulrich, and Simon (1977) demonstrated by observations with high resolutions in wavenumber and frequency that powers of the five-minute oscillation are concentrated in several distinct ridges in the (k_h, σ)-diagram, and these observed ridges agree very well with the positions of theoretical nonradial p-modes of the sun. Figure 11.4 reproduces the two-dimensional power spectrum of the five-minute oscillation in the (k_h, σ)-diagram obtained by Deubner (1977). Also shown in the figure are the locations of the theoretical nonradial p-modes of the sun calculated by Ando and Osaki (1975), which form a series of many nearly parallel ridges (one for each overtone, n). The general pattern of observed powers closely resembles the theoretical ridges, and thus the five-minute oscillation is now interpreted beyond doubt as the nonradial p-modes of the sun. The eigenmodes first identified by Deubner (1975) and Rhodes et al. (1977) are nonradial p-modes with degrees $l \approx 200 \sim 1000$. Recent observations resolving the oscillations into individual modes (e.g., Libbrecht, Popp, Kaufman, and Penn, 1986) show that the velocity amplitude of each of p-mode is of the order of 10 cm s^{-1}. These modes are, however, occasionally in phase with each other, and the

superposition of many modes with such minute amplitudes transiently leads a velocity field as large as 500 m s^{-1}. On the other hand, when most p-modes are not in phase, superposition of these modes turns to a very small amplitude velocity field. As a consequence, the oscillations apparently look like Fig. 11.1 in the case of observations with low resolution in space and time. It is seen in Fig. 11.4 that theoretical ridges tend to deviate above the observed ridges. There still remain small discrepancies between the observed frequencies and the theoretical

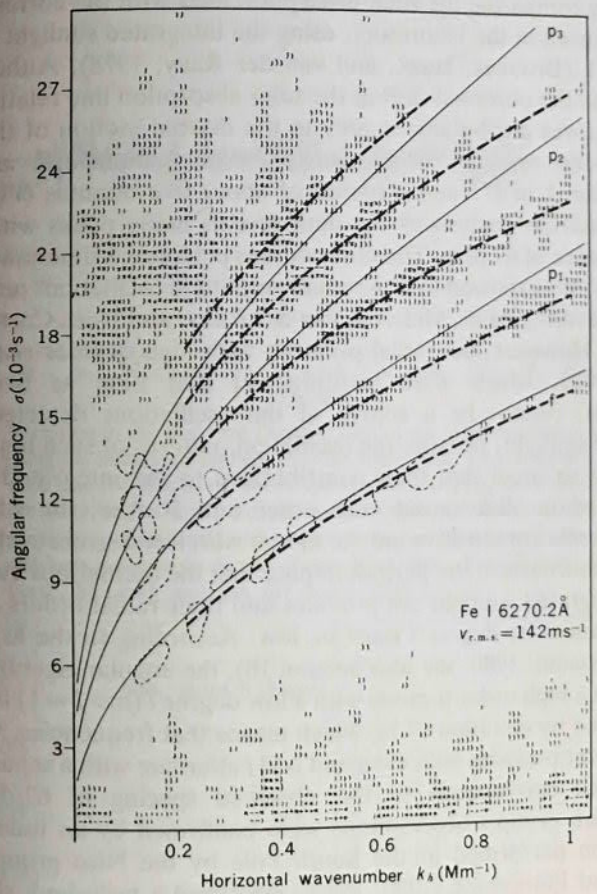

Fig. 11.4 (k_h, σ)-diagram of velocity fluctuations (Doppler shifts of the Fe I 6270.2 line) sampled at 105 s intervals over half the solar diameter (from Deubner, 1977). The diagram represents an average of the spectra obtained from four observing runs of 5 hr 50 min each. The heavy dashed lines outline the top of the ridges observed in the domain of the 300 s oscillations. The solid lines show theoretical eigenfrequencies of p-modes by Ando and Osaki (1975).

frequencies based on even the most up-to-date theoretical models of the sun. The discrepancies between theory and observation are thought to be caused by some uncertainties in the solar equilibrium model used in the theoretical calculations, and the observed oscillations are now used to observe the solar structure just as we examine the earth's interior using seismic waves (see Chapter VII).

In the late 1970's, Isaak and his colleagues in the Unversity of Birmingham were attempting to measure the gravitational redshift of the sun by comparing the solar absorption lines with the corresponding lines produced in the laboratory, using the integrated sunlight over the whole disk (Brookes, Isaak, and van der Raay, 1978). Although the variation in the observed shift of the solar absorption line relative to the laboratory was attributable mainly to the diurnal motion of the earth, there existed residuals which showed a fluctuation with amplitude smaller than 1 m s^{-1} and a period of about five minutes (Fig. 11.5). Power spectrum analysis of the data reveals many peaks with almost equal distance of 67 μHz. The observations performed simultaneously at two distant sites showed that the small amplitude oscillations are of solar origin (Claverie, Isaak, McLeod, van der Raay, and Roca Cortés, 1979, 1981a,b). However, nonradial p-modes with high degrees such as $l \approx 200 \sim 1000$, which were identified at that time as five-minute oscillations, cannot be a source of the oscillations detected in the integrated sunlight, because the oscillation patterns of such high degree modes are so small that their contributions to the integrated sunlight over the whole disk cancel each other out. Rather, the whole-disk measurements are sensitive only to modes with low degrees such as $l \approx 0 \sim 4$. The shortness of the periods implies that the oscillations discovered in the integrated sunlight are p-modes and their radial orders n should be large since the degree l must be low. According to the asymptotic theory (Tassoul, 1980; see also Section 16), the angular eigenfrequency σ_{nl} of such a high order p-mode with a low degree l ($n \gg l \approx 1$) is, to first order, given by equation (9.1), which means that frequencies, $\nu \equiv \sigma/2\pi$, of high order p-modes with even and odd l alternate with a separation of $\nu_0/2$, which corresponds to the observed spacing of 67μHz. The Birmingham group's observations were confirmed by an independent observation performed at the South Pole by the Nice group (Grec, Fossat, and Pomerantz, 1980, 1983), who used a technique similar to that of the Birmingham group. Observations from the South Pole are of great advantage in obtaining long strings of uninterrupted observational data, which are necessary to secure high resolution in the power spectrum. Indeed, Grec et al. (1980, 1983) succeeded in measuring the Doppler shift using integrated sunlight over the disk for 120 hr without

interruption. Their data yield higher resolutions in the power spectrum than those given by the first-order asymptotic formula (9.1), and individual p-modes with l and n have been resolved for each sequence of $l = 0$, 1, 2, and 3. The Birmingham group also performed observations from two distant sites (Tenerife and Hawaii) and combined these data to get high resolution in the power spectrum and also resolved peaks of individual p-modes (Claverie, Isaak, McLeod, van der Raay, Pallé, and

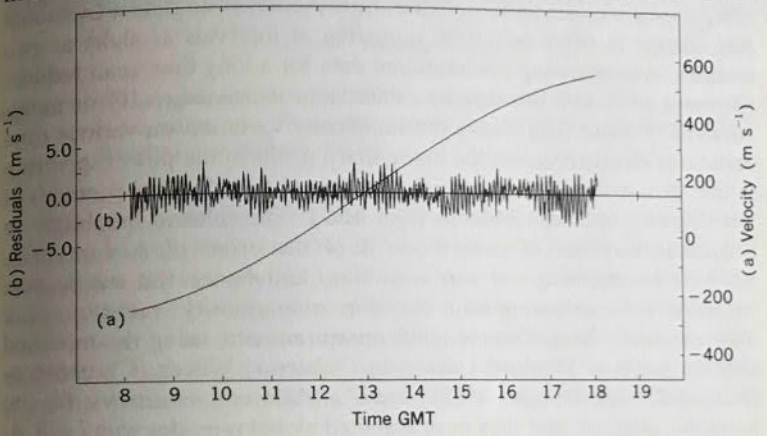

Fig. 11.5 Variation in the observed Doppler shift of the solar absorption line obtained using the integrated sunlight over the whole disk. The variation is attributable mainly to the diurnal motion of the earth as shown by the smoother curve and the scale on the right, but the residuals show a fluctuation with a period of about five minutes and with amplitude smaller than 1 m s^{-1}. The scale for the residuals is shown on the left. Taken from Pallé, Perez, Régulo, Roca Cortés, Isaak, McLeod, and van der Raay (1986a).

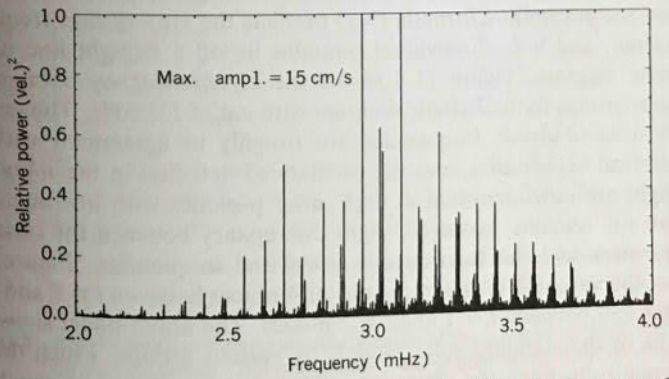

Fig. 11.6 Velocity power spectrum obtained by the Birmingham group after a three-month observation run from Tenerife and Hawaii. After Isaak (1986).

Roca Cortés, 1984). Figure 11.6 reproduces their power spectrum obtained after a three-month observation run. Their results are also confirmed by the measurements of the total irradiance variation of the sun from the Solar Maximum Mission (SMM) satellite (Woodard and Hudson, 1983a, b). The SMM satellite took the Active Cavity Radiometer Irradiance Monitor (ACRIM) on board to perform sensitive, broad-band measurements over the wavelength range carrying the bulk of the sun's radiation flux. ACRIM can detect fractional flux change as small as 0.01% occurring at intervals as short as two minutes. Accumulating observational data for a long time span reduces the noise level, and the signal-to-noise ratio increased to 10^6 or more. Analysis of these data shows the luminosity variation on various time scales and clearly presents the many sharp peaks in the power spectrum in the "five-minute" range, which correspond to individual p-modes of low degree l and high order n (Fig. 11.7). The relative amplitude in brightness variation of each mode is of the order of $\Delta I/I \sim 10^{-6}$. ACRIM is observing the sun as a star, and hence the sun is now regarded as a pulsating star showing a luminosity variation of a millimagnitude level. Doppler shift measurements, using the modified magnetograph at Stanford University (Scherrer, Wilcox, Christensen-Dalsgaard, and Gough, 1982), have a different sensitivity to the harmonic degree l, and they have detected global p-modes with $l = 3, 4$, and 5.

It is convenient to use the so-called Echelle diagram to plot the individual p-modes of low degree l, on which the string of frequency is divided into constant segments which are placed in a vertical row. As a result, eigenfrequency $\nu \equiv \sigma/2\pi$ is plotted as summation of ν_1 and $\Delta\nu$, where ν_1 and $\Delta\nu$ are the ordinate and the abscissa, respectively. To first order, the asymptotic formula (9.1) predicts the equi-distant frequency spectrum, and hence individual p-modes lie on a straight line on the Echelle diagram. Figure 11.8 shows the eigenfrequency obtained by various groups in the Echelle diagram with cut of 135 μHz. The general pattern of observed frequencies are roughly in agreement with the theoretical expectation, and the oscillations detected in the integrated sunlight are now identified as high order p-modes with low degrees l. There still remains, however, slight discrepancy between the observed frequencies and the theoretically calculated frequencies. Figure 11.9 shows the variation of the frequency differences between $l = 0$ and $l = 2$ modes and between $l = 1$ and $l = 3$ modes. The upper panel shows the results of the standard solar models by various groups, which deviate systematically from the observed values that are shown in the lower panel.

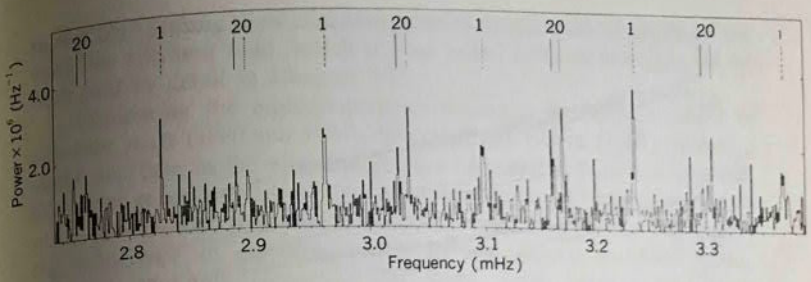

Fig. 11.7 Power spectrum from ACRIM total irradiance data. The frequencies measured by the Birmingham group are shown for comparison (from Woodard and Hudson, 1983b).

The gap between low l and high l p-modes in detection of solar oscillations was filled by Duvall and Harvey's (1983) Doppler-shift observation for velocity fields. They observed a one-dimensional solar image produced by a cylindrical lens. By using the lens to average the sun's image in a direction perpendicular to its rotation axis, they eliminated high-angular-order spherical harmonics to leave mainly zonal harmonics with $m = 0$. Averaging the sun's image in a direction

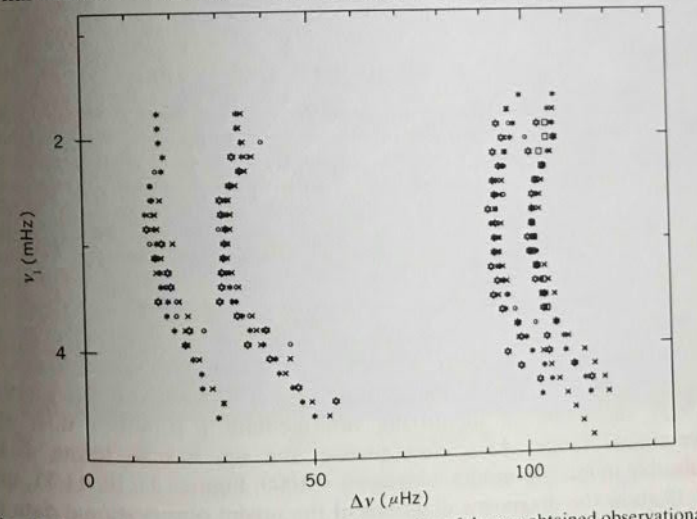

Fig. 11.8 Echelle diagram showing eigenfrequencies of the sun obtained observationally by various groups. The frequencies ν are plotted in the form of ν_1 and $\Delta\nu$ where ν_1 is the ordinate with a step of 135 μHz and $\Delta\nu$ is the abscissa. Taken from Gelly, Fossat, Grec, and Schmieder (1988).

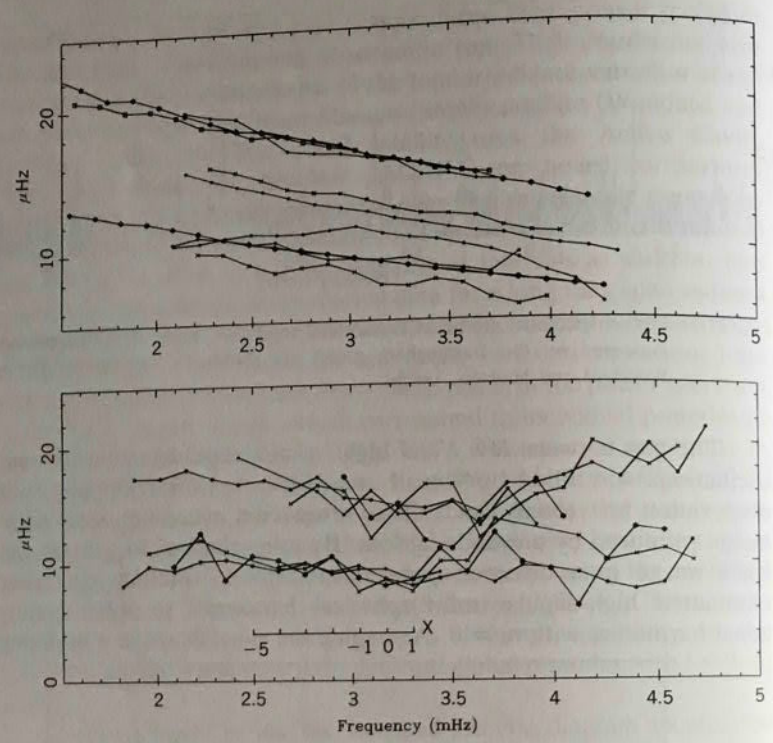

Fig. 11.9 Comparison of observational frequencies with theoretically calculated eigenfrequencies of standard solar models of various groups. The lower panel shows variation of observed frequency difference between $l = 0$ modes and $l = 2$ modes ($\nu_{l=0} - \nu_{l=2}$; lower part) and that between $l = 1$ modes and $l = 3$ modes ($\nu_{l=1} - \nu_{l=3}$; upper part) as a function of frequency. The upper panel shows the same as the lower panel but for various theoretical standard solar models. Authors on the upper panel are: (×) Shibahashi and Osaki (1981b), (•) Ulrich and Rhodes (1983), (○) Shibahashi, Noels, and Gabriel (1983), (□) Lebreton, Berthomieu, and Provost (1987). (After Gelly et al., 1988.)

parallel to the rotation axis, in contrast, leaves mainly information on sectoral ($|m| = l$) modes. By analyzing these data Duvall and Harvey (1983) succeeded in identifying intermediate l p-modes near the five-minute range. As a consequence, the sun is now found to be pulsating in many p-modes with $l = 0 \sim 1000$. Figures 11.10, 11.11, and 11.12 show the diagnostic diagrams of the recent observational data by Duvall, Harvey, Libbrecht, Popp, and Pomerantz (1988), where the ordinate is $\nu \equiv \sigma/2\pi$ and the abscissa is the harmonic degree l. The tremendous number of detected eigenmodes of the sun provides us the

possibility of using these eigenfrequencies to probe the interior of the sun; this research field, which is now called helioseismology, will be discussed in detail in Chapter VII.

Comparing the eigenfrequencies observed by SMM/ACRIM in separate years (1980 and 1984), Woodard and Noyes (1985) noticed a slight decrease in the eigenfrequencies of p-modes with low degrees. Such long-term variation of the eigenfrequencies has been examined by other groups, but the results are conflicting. Two groups reported a slight increase of eigenfrequencies of low degree p-modes (Isaak, Jefferies, McLeod, New, van der Raay, Pallé, Régulo, and Roca Cortés, 1988; Rhodes, Woodard, Cacciani, Tomczyk, Korzennik, and

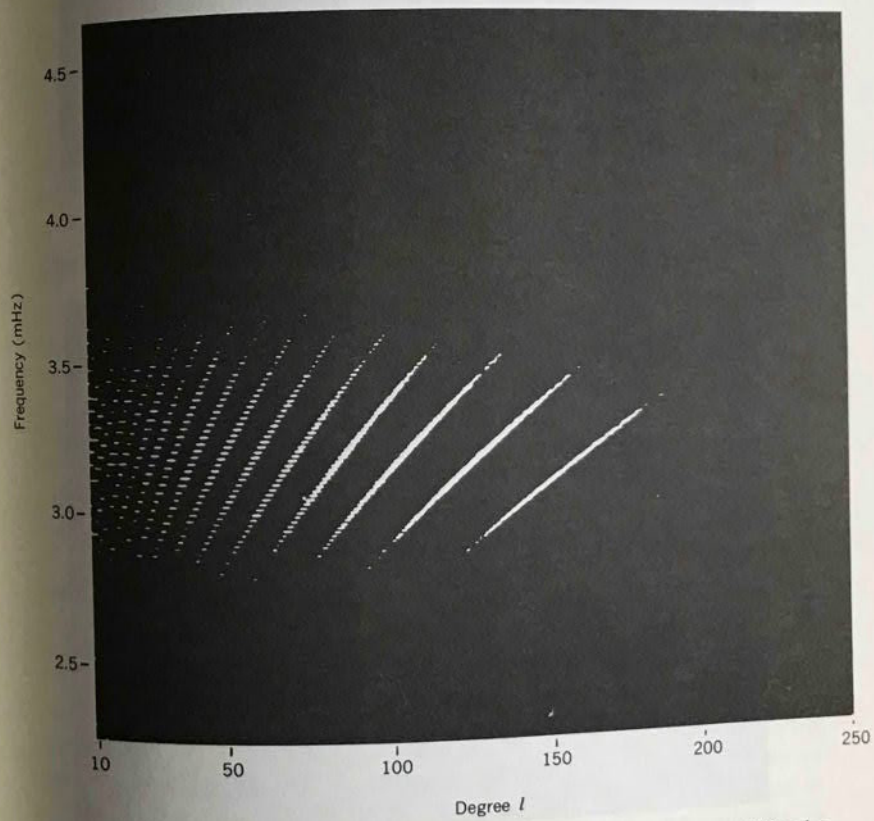

Fig. 11.10 The (l, ν)-diagram for the recent observational data in the range of $10 \leq l \leq 250$ by Duvall et al. (1988), where ν is the frequency given by $\nu \equiv \sigma/2\pi$.

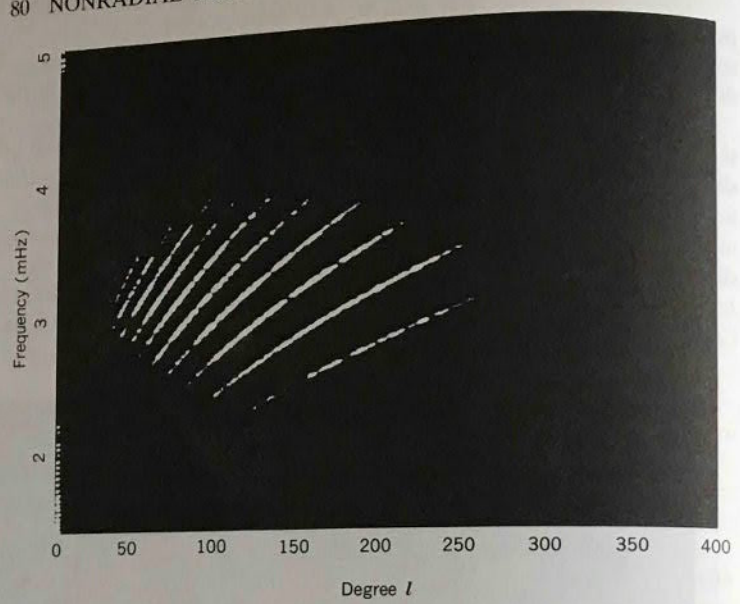

Fig. 11.11 The same as Fig. 11.10 but for $0 \leq l \leq 400$. (After Duvall et al. 1988.)

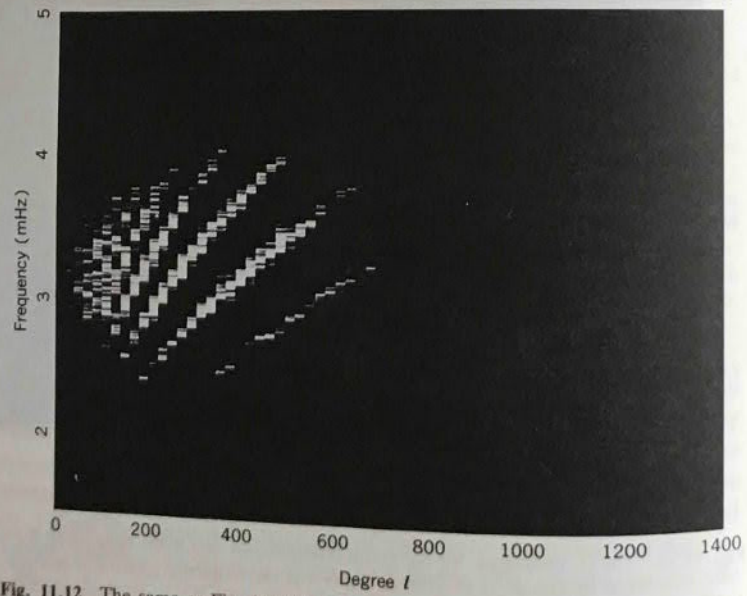

Fig. 11.12 The same as Fig. 11.10 but for $0 \leq l \leq 1400$. (After Duvall et al. 1988.)

Ulrich, 1988), while other two groups reached the opposite conclusion (Gelly, Fossat, and Grec, 1988; Henning and Scherrer, 1988).

We can use frequency differences of modes having the same n and l but different m to measure the solar rotation rate, in particular the variation of the rotation rate with the depth. Let us consider nonradial oscillations of the eastward- and westward-traveling waves with $m = \pm l$. In a rotating star, those waves traveling in the same direction as the rotation have higher frequencies than those traveling in the opposite direction, and their frequency difference due to this rotational splitting is, in the reference frame at rest,

$$\Delta\sigma \approx 2|m|\Omega. \tag{11.7}$$

Here the C_{nl}-term, which is due to the Coriolis force effect, has been neglected, since it is negligible for high wave-number modes like the solar five-minute oscillation (see Section 19). In the case of differential rotation, Ω in equation (11.7) may be understood as the angular velocity of rotation averaged with the eigenfunctions of the relevant modes. Since different modes are trapped at different depths, we can in principle probe the variation of the rotation rate with depth. Duvall and Harvey's (1984) detection of the frequency difference between sectoral modes and the corresponding zonal modes was soon applied to measure the rotation rate in the sun. This is an example of the product of helioseismology (see Chapter VII).

The observations described above are essentially one-dimensional in space—that is, they are based either on the sunlight integrated over some part of the solar disk or on a one-dimensional device (e.g., Reticon array). The fully two-dimensional observations of the solar disk enable us to identify both the degree l and the azimuthal order m of a mode. In order to perform such a two-dimensional observation, many researchers devised various narrow-band filters and instruments such as Fourier tachometers based on the Michelson interferometer (Brown, 1984), magneto-optical filters (Cacciani and Fofi, 1978; Cacciani and Rhodes, 1984; Rhodes, Cacciani, Blamont, Tomczyk, Ulrich, and Howard, 1988), Fabry-Perot filters (Rust, Appourchaux, and Hill, 1988), and birefringent filters in combination with a KD*P electro-optical crystal (Libbrecht and Zirin, 1986). Identification of both the quantum numbers l and m and measurement of eigenfrequencies of various tesseral modes by means of these instruments can be used to measure the variation of the rotation rate with the latitude in addition to that with the depth. In the case of differential rotation with respect to both depth and latitude, Ω in equation (11.7) should be regarded as the angular velocity of rotation averaged over both depth and latitude with

the eigenfunctions of the relevant modes. Since the latitude at which a mode, is concentrated is dependent on the azimuthal order m, we can probe the variation of the rotation rate with latitude. Recent results will be discussed in Chapter VII.

11.2 Long Period Oscillations

Several groups have reported that they have detected long-period global pulsations of the sun, whose periods are in the range of g-modes. If the identification of g-modes in the sun is real, it will provide important information about the stratification in the radiative core of the sun (see Chapter VII). However, the detection of long period oscillations has itself not yet been established. Indeed, negative results for the existence of these oscillations in the sun have also been reported by other groups, and there have been controversies over the very existence of long period global solar oscillations.

Henry Hill and his collaborators had been measuring solar oblateness in order to test Einstein's theory of general relativity over the Brans-Dicke theory. In the course of their study, they discovered fluctuations of solar diameter with a period near 50 min, together with nine higher frequencies of oscillation (Brown, Stebbins, and Hill, 1978). Later, they found some other long period oscillations whose periods are in the range of those of g-modes, together with short period oscillations in the p-mode range (Hill, 1985; Hill, Tash, and Padin, 1986). By measuring diameters of the solar disk in various directions and taking their correlation, they identified the degree l and the azimuthal order m. The radial order n is estimated from the period after identifying the degree l.

Severny, Kotov, and Tsap (1976, 1980, 1983), at the Crimean Observatory, by modifying their magnetograph to measure the Doppler velocity difference between the solar disk center and the limb, have discovered periodic fluctuations in the difference between line of sight velocities at the poles and the disk center with a period of 2 hr 40 min and an amplitude of about 2 m s^{-1}. The magnetograph at Stanford University has also been modified similarly, and the 2 hr 40 min periodicity was confirmed by a group at Stanford (Scherrer and Wilcox, 1983). The joint observations by the Stanford and Crimean groups showed that the oscillation lasts quite stably (Scherrer, Wilcox, Kotov, Severny, and Tsap, 1979, 1980). There are some other peaks in the power spectrum of the data of these groups, though the amplitudes are smaller than the peak of the 2 hr 40 min periodicity. Delache and Scherrer (1983) analyzed the Stanford data and tried the mode identification of those components in the following way: According to

the asymptotic theory, the period Π_{nl} of a g-mode with a low degree l ($n \gg l \simeq 1$) is, to first order, given by

$$\Pi_{nl} \simeq (n+l/2+\epsilon)\Pi_0/\sqrt{l(l+1)}, \tag{11.8}$$

with

$$\Pi_0 \equiv 2\pi^2 \left[\int_0^{r_*} N/r \, dr\right]^{-1}, \tag{11.9}$$

where r_* is the radius at the bottom of the convective envelope and N is the Brunt-Väisälä frequency. On the basis of this formula, Delache and Scherrer (1983) searched for peaks having uniformly spaced periods in the power spectrum with respect to $\Pi/\sqrt{l(l+1)}$ by assuming $l = 1$ or 2 or 3 and parametrizing the value of Π_0, and found them. Fröhlich and Delache (1984) and Isaak, van der Raay, Pallé, Roca Cortés and Delache (1984) also used the same technique to determine g-mode oscillations from the low frequency spectra of the SMM data and of the Birmingham group data, respectively. The values of Π_0 thus obtained were $\Pi_0 \simeq 38.6$ min from the Stanford data, $\Pi_0 \simeq 41.2$ min for the Birmingham data, and $\Pi_0 \simeq 38.6$ min for the SMM data.

The detection and the modal analysis of these long-period oscillations described above have not yet been well confirmed, and there still remain controversies. More reliable observations in the future will be necessary to confirm the existence of the long-period oscillations.

Chapter III

BASIC EQUATIONS AND ADIABATIC OSCILLATIONS

12. General Remarks

The associative development of theory and observation is important in astrophysics as in all other sciences. This importance has to be particularly emphasized in the study of nonradial oscillations in various types of stars, because much of the observational evidence is indirect or requires theoretical interpretation and analysis.

In this chapter, we first derive the basic equations of nonradial oscillations of stars. The basic equations governing nonradial oscillations are equations of conservation of mass, momentum, and energy, as usual (Section 13). The basic equations are then linearized for the normal mode analysis of nonradial oscillation. There generally are convection zones in stars. The coupling between convection and oscillation is very complicated, and the treatment of oscillation in the presence of convection is postponed to Section 20. The theoretical treatment is also restricted in this chapter to a spherically symmetric radiative star without rotation and magnetic field, except in Section 19.

The mathematical and physical properties of linear, adiabatic nonradial oscillations are discussed in Sections 13–20. They are: the orthogonality of the modes and the variational principle (Section 14), wave trapping (Section 15), asymptotic WKBJ analysis (Section 16), mode classification (Section 17), the numerical method (Section 18), the influence of rotation and magnetic field (Section 19), and convection (Section 20).

The Eulerian (fixed-position) perturbation of the gravitational potential is generally small in nonradial oscillations. Theoretical discussions become greatly simplified by the Cowling (1941) approximation in which it is neglected (Section 15). The physical justification for the Cowling approximation is that the contribution of one part of the medium to the gravitational potential perturbation is largely canceled in nonradial oscillations by the contribution of the other part of the

medium. The Cowling approximation is also good wherever the homology invariant U ($\equiv 4\pi\rho r^3/M_r$) of the stellar structure theory is small, even for radial pulsations. In nonradial oscillations, the error introduced by the Cowling approximation is not entirely negligible (although small) for the low overtones (small n) of the dipole ($l = 1$) and quadrupole ($l = 2$) g-modes. For the p-modes, the oscillation itself is unimportant where the homology invariant U is large. We will use the Cowling approximation for most of the theoretical discussions, since simplicity is more desirable than accuracy. The numerical work, however, does not need to be restricted to this approximation, as we can take advantage of the electronic computer.

A high degree of adiabaticity has been argued for in the first chapter in terms of the free-fall time and the Helmholtz-Kelvin time given by

$$\tau_{ff} \simeq (R^3/GM)^{1/2} = 0.443(M/M_\odot)^{-1/2}(R/R_\odot)^{3/2} \text{ hr} \quad (12.1)$$

and

$$\tau_{HK} \simeq GM^2/(RL) = 3.1 \times 10^7 (M/M_\odot)^2 (R/R_\odot)^{-1}(L/L_\odot)^{-1} \text{yr}, \quad (12.2)$$

where the symbols have their usual meanings. These are the dynamical and thermal time scales of a star as a whole. The fundamental oscillation time scale τ_{osc} defined by the travel time of a sound wave from the center to the surface is the same order of magnitude as the free fall time τ_{ff} because of the virial theorem describing the overall hydrostatic equilibrium of a star. There are, however, two cases in which nonadiabaticity is important and the time scales must be considered locally. One is the stellar outer envelope, where the local thermal time scale becomes comparable to or smaller than the dynamical time. The other is the wave propagation region or the trapping zone in which the excitation or damping mechanism operates. If the adiabaticity is achieved locally to a high degree of accuracy, an approximation using the adiabatic solution to estimate the growth (or damping) rate (quasi-adiabatic approximation) can give the correct result. If not, the full nonadiabatic treatment should be employed.

The local dynamical and thermal time scales are given by

$$\tau_{dyn} = H/c \quad \text{and} \quad \tau_{th} = \kappa\rho H^2/[c_*(1 - \beta)], \quad (12.3)$$

where c denotes the speed of sound, c_* the speed of light, κ the opacity; H stands for the characteristic length scale of oscillations, and it is given by the smaller of the following two scales: the pressure scale height, H_p, and the local wavelength of oscillations. The thermal time scale τ_{th} is valid for the radiative zone where $(\kappa\rho)^{-1}$ is the photon mean free path and $c_*(\kappa\rho H)^{-1}$ is the average speed of photon diffusion (for optically thick H, $1 - \beta$ denotes the ratio of the radiation pressure to the total pressure). The factor $1 - \beta$ is added to the expression of the thermal time scale because it measures the ratio of the radiation energy density to the total internal energy density of gas and radiation. The dynamical time scale given above is valid for perturbation of pressure-wave type. The reciprocal of the Brunt-Väisälä frequency, N^{-1}, is also a kind of dynamical time scale, but it takes account of the degree of local dynamical stability as well and is proper for perturbation of gravity-wave type.

The degree of adiabaticity is measured by $\sigma\tau_{th}$ compared with unity, or, roughly, by the ratio τ_{th}/τ_{dyn}, which is $\kappa\rho H(c/c_*)/(1 - \beta)$ for a trapped wave mode. The adiabatic approximation is normally sufficient to discuss the dynamical characteristics of the oscillations except in the atmosphere. However, for the study of the nonadiabatic effects, the numerical accuracy of the quasi-adiabatic approximation is not guaranteed in the outer envelope of a star, especially for giants and supergiants. This has already been noticed by Zhevakin (1953), who established the κ-mechanism in the HeII ionization zone as the principal cause of the Cepheid pulsation. In the present chapter, the dynamical properties of the adiabatic oscillations will be discussed; discussion of the nonadiabatic thermal properties will be postponed to the following two chapters.

13. Basic Equation

13.1 Equations of Hydrodynamics

The basic equations that describe deformations and oscillations of a star are equations of hydrodynamics. General discussions and derivations of equations of hydrodynamcis will not be given here as they may be found in various textbooks of fluid mechanics and astrophysics.

The basic equations of hydrodynamics are equations of conservation of mass, momentum, and energy, which are given by

$$\frac{\partial\rho}{\partial t} + \nabla\cdot(\rho\boldsymbol{u}) = 0, \quad (13.1)$$

$$\rho\left(\frac{\partial}{\partial t} + \boldsymbol{u}\cdot\nabla\right)\boldsymbol{u} = \rho\boldsymbol{f} - \nabla p - \rho\nabla\Phi + \text{div}\,\mathscr{D}, \quad (13.2)$$

and

$$\rho T\left(\frac{\partial}{\partial t} + \boldsymbol{u}\cdot\nabla\right)S = \rho(\varepsilon_N + \varepsilon_V) - \nabla\cdot\boldsymbol{F}_R, \quad (13.3)$$

where ρ denotes the density, p the pressure, T the temperature, $\boldsymbol{u}$ the fluid velocity, S the specific entropy, Φ the gravitational potential, $\boldsymbol{f}$ the electro-magnetic and external forces, $\mathscr{S}$ the viscous stress tensor, ε_N the nuclear energy generation rate, ε_V the viscous heat generation, $\boldsymbol{F}_R$ the radiative energy flux, ∇ the gradient operator.

There are convection zones in most stars, either in the interior or in the outer envelope. The convective motion in stars is considered to be in a state of fully developed turbulence. When convection is present, the treatment of stellar oscillation becomes rather difficult because the separation of the velocity into convective motion and oscillation and their mutual interaction are very complicated. We restrict ourselves to the case without convection in most of this chapter. The treatment in the presence of convection will be deferred and it will be discussed separately in Section 20. Equation (13.2) is the Navier-Stokes equation for a viscous fluid. However, the viscous term (the last term of the right-hand side of equation [13.2]) is generally small in the stellar interior, and we neglect it and also the ε_V term in equation (13.3) in most of this monograph. When convection exists, the turbulent viscosity may be important. We also omit the term $\boldsymbol{f}$ in equation (13.2) except for some special cases and consider non-magnetic self-gravitating systems. Equation (13.2) may then be reduced to the Euler equation for an inviscid flow:

$$\rho\left(\frac{\partial}{\partial t} + \boldsymbol{v}\cdot\nabla\right)\boldsymbol{v} = -\nabla p - \rho\nabla\Phi, \tag{13.4}$$

where the velocity without turbulent convection is denoted as $\boldsymbol{v}$ in order to distinguish it from the general form of $\boldsymbol{u}$ that may include turbulent convective velocity fields.

Supplementary equations are needed to complete the description of a system. The first one of them is the Poisson equation that relates the gravitational potential to the distribution of matter; it is written as

$$\nabla^2\Phi = 4\pi G\rho, \tag{13.5}$$

where G is the gravitational constant and ∇^2 is the Laplacian operator. The radiative flux is given by the radiative diffusion equation

$$\boldsymbol{F}_R = -K\nabla T, \tag{13.6}$$

where the radiative conductivity K is written in terms of opacity κ as

$$K = \frac{4ac_*}{3\kappa\rho}T^3, \tag{13.7}$$

a is the radiation density constant, and c_* the velocity of light. The

remaining supplementary equations are equations of state giving p (ρ, T) and S (ρ, T) and equations giving energy generation rate $\varepsilon_N(\rho,T)$ and the opacity κ (ρ, T) for a given chemical composition. The latter four equations will be introduced later, when they are necessary.

Let us now discuss the equilibrium state, upon which small perturbations of oscillations are superimposed. Here we consider a non-rotating, non-magnetic star without convection. By setting the time derivative and velocity equal to zero in equations (13.1)–(13.7) (i.e., $\partial/\partial t = 0$ and $\boldsymbol{u}_0 = 0$), we obtain

$$-\nabla p_0 - \rho_0\nabla\Phi_0 = 0, \tag{13.8}$$

$$\rho_0\varepsilon_{N,0} - \nabla\cdot\boldsymbol{F}_0 = 0, \tag{13.9}$$

$$\nabla^2\Phi_0 = 4\pi G\rho_0, \tag{13.10}$$

and

$$\boldsymbol{F}_0 = -K_0\nabla T_0, \tag{13.11}$$

where the subscript 0 denotes the unperturbed, equilibrium state.

Since the equilibrium state is spherically symmetric under the present assumption, equations (13.8)–(13.11) are rewritten in the spherical polar coordinates (r, θ, ϕ) as the standard form of equations of stellar structure:

$$\frac{dp}{dr} = -\rho g, \tag{13.12}$$

$$\frac{dM_r}{dr} = 4\pi r^2\rho, \tag{13.13}$$

$$\frac{dL_r}{dr} = 4\pi r^2\rho\varepsilon_N, \tag{13.14}$$

and

$$\frac{dT}{dr} = -\frac{3\kappa\rho}{4ac_*}\frac{1}{T^3}\frac{L_r}{4\pi r^2}, \tag{13.15}$$

where

$$g = \frac{GM_r}{r^2} \quad \text{and} \quad L_r = 4\pi r^2 F \tag{13.16}$$

are the local gravitational acceleration and the radiative luminosity, respectively, and M_r is the mass within the sphere of radius r. Here the

subscript 0 is omitted for simplicity.

Equation (13.15) is valid only when the energy transport is by radiation. When convection is present, the convective energy flux must be included. The energy flux is then the sum of the radiative and convective fluxes:

$$F = F_R + F_C \tag{13.17}$$

and

$$L_r = 4\pi r^2 (F_R + F_C). \tag{13.18}$$

Convective flux results from an averaging process of energy equation (13.3) over regions containing the turbulent eddies of maximum size. It is most often described based on the so-called mixing-length formalism of stellar convection.

13.2 Equations of Oscillation

Let us now derive basic equations of linear oscillations. To do so, we consider the "unperturbed" equilibrium state of a star and superimpose on it "small" perturbations. We assume in the linear theory that all perturbations are sufficiently small so that only terms in the first-order in perturbations are retained while those higher than the second are neglected.

There are two different ways to express perturbation: the Eulerian form and the Lagrangian form. The Eulerian perturbation is defined as a perturbation of a physical quantity at a given position, denoted by prime, while the Lagrangian perturbation is defined by that for a given fluid element, denoted by a symbol δ. A physical quantity f is therefore expressed by either

$$f(\boldsymbol{r},t) = f_0(\boldsymbol{r}) + f'(\boldsymbol{r},t) \tag{13.19}$$

or

$$f(\boldsymbol{r},t) = f_0(\boldsymbol{r}_0) + \delta f(\boldsymbol{r}_0,t). \tag{13.20}$$

The Lagrangian and Eulerian perturbations are related to each other by

$$\delta f(\boldsymbol{r},t) = f'(\boldsymbol{r},t) + \boldsymbol{\xi}\cdot\nabla f_0(\boldsymbol{r}) \tag{13.21}$$

to the first order in the displacement, $\boldsymbol{\xi}$,

$$\boldsymbol{\xi} \equiv \boldsymbol{r} - \boldsymbol{r}_0, \tag{13.22}$$

where $\boldsymbol{r}$ in equation (13.22) denotes the Lagrangian position variable of a given fluid element which is at $\boldsymbol{r} = \boldsymbol{r}_0$ in the equilibrium state. The corresponding time variations are denoted by $d\delta f(\boldsymbol{r},t)/dt$ and $\partial f'(\boldsymbol{r},t)/\partial t$,

where

$$\frac{d}{dt} = \frac{\partial}{\partial t} + \boldsymbol{v}\cdot\nabla \tag{13.23}$$

and

$$\boldsymbol{v} = \frac{d\boldsymbol{r}}{dt}. \tag{13.24}$$

In the general case when the unperturbed state has a steady flow with $\boldsymbol{v} \neq 0$, such as the case of a rotating star, we derive a relation between the Eulerian and Lagrangian perturbations of velocity vector. We first note that from the definition of $\boldsymbol{v}$ and $\boldsymbol{\xi}$

$$\begin{aligned}\delta\boldsymbol{v} &= \boldsymbol{v}(\boldsymbol{r}_0+\boldsymbol{\xi}) - \boldsymbol{v}_0(\boldsymbol{r}_0)\\ &= \frac{d\boldsymbol{r}}{dt} - \frac{d\boldsymbol{r}_0}{dt} = \frac{d\boldsymbol{\xi}}{dt}\\ &= \frac{\partial\boldsymbol{\xi}}{\partial t} + (\boldsymbol{v}\cdot\nabla)\boldsymbol{\xi}\\ &\approx \frac{\partial\boldsymbol{\xi}}{\partial t} + (\boldsymbol{v}_0\cdot\nabla)\boldsymbol{\xi}.\end{aligned} \tag{13.25}$$

We have therefore

$$\begin{aligned}\boldsymbol{v}' &= \delta\boldsymbol{v} - (\boldsymbol{\xi}\cdot\nabla)\boldsymbol{v}_0\\ &= \frac{\partial\boldsymbol{\xi}}{\partial t} + (\boldsymbol{v}_0\cdot\nabla)\boldsymbol{\xi} - (\boldsymbol{\xi}\cdot\nabla)\boldsymbol{v}_0.\end{aligned} \tag{13.26}$$

This relation will be used later in the case of a rotating star.

When no motion exits in the unperturbed state (i.e., $\boldsymbol{v}_0 = 0$), we have simply

$$\boldsymbol{v}' = \delta\boldsymbol{v} = \frac{\partial\boldsymbol{\xi}}{\partial t} = \frac{d\boldsymbol{\xi}}{dt}. \tag{13.27}$$

In what follows in this chapter, we write this perturbed velocity vector as $\boldsymbol{v}$ unless there is confusion.

With the above preparations, the set of the linearized basic equations is derived in the Eulerian form as follows:

$$\frac{\partial\rho'}{\partial t} + \nabla\cdot(\rho_0\boldsymbol{v}) = 0, \tag{13.28}$$

$$\rho_0 \frac{\partial \boldsymbol{v}}{\partial t} + \nabla p' + \rho_0 \nabla \Phi' + \rho' \nabla \Phi_0 = 0, \tag{13.29}$$

$$\rho_0 T_0 \frac{\partial}{\partial t}(S' + \boldsymbol{\xi}\cdot\nabla S_0) = (\rho \varepsilon_N)' - \nabla\cdot\boldsymbol{F}', \tag{13.30}$$

$$\nabla^2 \Phi' = 4\pi G \rho', \tag{13.31}$$

and

$$\boldsymbol{F}' = -K_0 \nabla T' - K' \nabla T_0. \tag{13.32}$$

Equations (13.28)–(13.32) are linear, homogeneous, partial differential equations with respect to time t and space coordinates $\boldsymbol{r}$ for perturbed variables with prime (such as ρ', T', Φ', ...) and velocity vector $\boldsymbol{v}$ (or displacement $\boldsymbol{\xi}$). The coefficients of these partial differential equations include solely quantities at equilibrium such as ρ_0, T_0, ..., which are functions of radial coordinate r only:

$$\rho_0 = \rho_0(r), \quad T_0 = T_0(r), \quad \Phi_0 = \Phi_0(r), \ \ldots\ . \tag{13.33}$$

We may therefore separate the time t and write all the variables to be proportional to $\exp(i\sigma t)$ as explained in Section 4.

In what follows, we omit the subscript 0 for equilibrium quantities unless there is confusion. If we note $\boldsymbol{v} = i\sigma\boldsymbol{\xi}$, equation of continuity (13.28) is written as

$$\rho' + \nabla\cdot(\rho\boldsymbol{\xi}) = 0 \tag{13.34}$$

or

$$\delta\rho/\rho + \nabla\cdot\boldsymbol{\xi} = 0, \tag{13.35}$$

while the equation of motion (13.29) is written as

$$-\sigma^2\boldsymbol{\xi} + \frac{1}{\rho}\nabla p' + \nabla\Phi' + \frac{\rho'}{\rho}\nabla\Phi = 0 \tag{13.36}$$

or in radial and horizontal components:

$$-\sigma^2\xi_r + \frac{1}{\rho}\frac{\partial p'}{\partial r} + \frac{\partial \Phi'}{\partial r} + \frac{\rho'}{\rho}\frac{d\Phi}{dr} = 0 \tag{13.37}$$

and

$$-\sigma^2\boldsymbol{\xi}_\perp + \nabla_\perp\left(\frac{p'}{\rho} + \Phi'\right) = 0. \tag{13.38}$$

Here

$$\boldsymbol{\xi} = (\xi_r, \xi_\theta, \xi_\phi), \quad \boldsymbol{\xi}_\perp = (0, \xi_\theta, \xi_\phi),$$

and

$$\nabla_\perp = \frac{1}{r}\left(0, \frac{\partial}{\partial\theta}, \frac{1}{\sin\theta}\frac{\partial}{\partial\phi}\right) \tag{13.39}$$

is the horizontal component of the gradient operator in the spherical polar coordinates. Eliminating $\boldsymbol{\xi}_\perp$ from equation (13.35) by use of equation (13.38), we obtain

$$\frac{\delta\rho}{\rho} + \frac{1}{r^2}\frac{\partial}{\partial r}(r^2\xi_r) + \frac{1}{\sigma^2}\nabla_\perp^2\left(\frac{p'}{\rho} + \Phi'\right) = 0, \tag{13.40}$$

where

$$\nabla_\perp^2 = \frac{1}{r^2}\frac{1}{\sin^2\theta}\left[\sin\theta\frac{\partial}{\partial\theta}\left(\sin\theta\frac{\partial}{\partial\theta}\right) + \frac{\partial^2}{\partial\phi^2}\right]. \tag{13.41}$$

The Poisson equation (13.31) is similarly written as

$$\frac{1}{r^2}\frac{\partial}{\partial r}\left(r^2\frac{\partial\Phi'}{\partial r}\right) + \nabla_\perp^2\Phi' = 4\pi G\rho'. \tag{13.42}$$

Let us now express the density perturbation ρ' in terms of p', ξ_r, and δS. From the thermodynamic relation (see equations [13.83] and [13.89] below),

$$\frac{\delta\rho}{\rho} = \frac{1}{\Gamma_1}\frac{\delta p}{p} - \nabla_{ad}\frac{\rho T}{p}\delta S, \tag{13.43}$$

where

$$\Gamma_1 = \left(\frac{\partial \ln p}{\partial \ln\rho}\right)_S \text{ and } \nabla_{ad} = \left(\frac{\partial \ln T}{\partial \ln p}\right)_S, \tag{13.44}$$

we have that

$$\frac{\rho'}{\rho} = \frac{1}{\Gamma_1}\frac{p'}{p} - A\xi_r - \nabla_{ad}\frac{\rho T}{p}\delta S, \tag{13.45}$$

where the quantity A is the Schwarzschild discriminant preferentially used by Ledoux (Ledoux and Walraven, 1958) to denote the degree of convective instability (i.e., $A > 0$) or stability (i.e., $A < 0$), and it is related to the Brunt-Väisälä frequency N by

$$A = -N^2/g = \frac{d\ln\rho}{dr} - \frac{1}{\Gamma_1}\frac{d\ln p}{dr}. \tag{13.46}$$

Eliminating $\delta\rho$ and ρ' from equations (13.37), (13.40), and (13.42), we obtain

$$\frac{1}{\rho}\left(\frac{\partial}{\partial r}+\frac{\rho g}{\Gamma_1 p}\right)p'-(\sigma^2+gA)\xi_r+\frac{\partial\Phi'}{\partial r}=g\nabla_{ad}\frac{\rho T}{p}\delta S, \quad (13.47)$$

$$\frac{1}{r^2}\frac{\partial}{\partial r}(r^2\xi_r)+\frac{1}{\Gamma_1}\frac{d\ln p}{dr}\xi_r+\left(\frac{\rho}{\Gamma_1 p}+\frac{\nabla_\perp^2}{\sigma^2}\right)\frac{p'}{\rho}+\frac{1}{\sigma^2}\nabla_\perp^2\Phi'$$

$$=\nabla_{ad}\frac{\rho T}{p}\delta S, \quad (13.48)$$

and

$$\left(\frac{\partial}{r^2\partial r}r^2\frac{\partial}{\partial r}+\nabla_\perp^2\right)\Phi'-4\pi G\rho\left(\frac{p'}{\Gamma_1 p}-A\xi_r\right)=-4\pi G\nabla_{ad}\frac{\rho^2 T}{p}\delta S. \quad (13.49)$$

We similarly write the flux perturbation $\boldsymbol{F}'$ from equation (13.32) as

$$F_r'=-K\frac{\partial T'}{\partial r}-K'\frac{dT}{dr} \quad (13.50)$$

and

$$\boldsymbol{F}_\perp'=-K\nabla_\perp T'. \quad (13.51)$$

Substitution of these expressions into equation (13.30) yields

$$i\sigma\rho T\delta S=(\rho\varepsilon_N)'-\frac{1}{r^2}\frac{\partial}{\partial r}(r^2F_r')+\nabla_\perp^2(KT'). \quad (13.52)$$

The six equations [equations (13.47), (13.48), (13.49), (13.50), (13.52), and (13.84) below] are the basic equations for linear nonadiabatic nonradial oscillation with six variables [p', T', δS, ξ_r, Φ', and F_r']. In the adiabatic approximation, the right-hand sides of equations (13.47), (13.48), and (13.49) are neglected while equations (13.50)—(13.52) are not needed, and the former three equations determine the three unknowns ξ_r, p', and Φ'.

13.3 Wave Equations in Radial and Angular Directions

Equations (13.47), (13.48), (13.49), (13.50), and (13.52) and a supplementary equation (13.84) relating p', T' and δS (which is obtained from a thermodynamic relation) are the basic equations. The coefficients of these differential equations depend solely on r, and the one and only differential operator with respect to the angular variables θ and ϕ is $\nabla_\perp^2$. In this case, the separation of variables into radial and angular parts is possible for all the variables, with the angular

dependence of $Y(\theta,\phi)$ satisfying

$$[r^2\nabla_\perp^2+\Lambda]\,Y(\theta,\phi)=0, \quad (13.53)$$

where Λ is a constant. Similarly, the function $Y(\theta,\phi)$ admits the separation into the product of a colatitude function $\Theta(\theta)$ and an azimuth function. The azimuth function should be $\exp(im\phi)$ with an integer m for a normal mode owing to the periodicity with respect to the increase of ϕ by 2π. Thus, equation (13.53) is reduced to

$$\frac{d}{d\mu}\left[(1-\mu^2)\frac{d\Theta}{d\mu}\right]+\left(\Lambda-\frac{m^2}{1-\mu^2}\right)\Theta=0, \quad (13.54)$$

where $\mu=\cos\theta$. The solution of this equation is given by Ferrer's associated Legendre polynomial $P_\nu^m(\mu)$ and $Q_\nu^m(\mu)$ (see, e.g., Whittaker and Watson, 1965) with $\Lambda=\nu(\nu+1)$. However, the function Θ must be regular and single valued for $-1\le\mu\le1$, and $Q_\nu^m(\mu)$ is improper because of a logarithmic singularity at $\mu=1$. The function $P_\nu^m(\mu)$ also diverges at $\mu=-1$ unless ν is an integer. Thus, we have $\Theta(\theta)=P_l^m(\mu)$ with an integer l. Further, the integer m must be chosen as $|m|\le l$, since $P_l^m(\mu)$ is zero if $|m|>l$. We have, finally,

$$Y_l^m(\theta,\phi)\propto P_l^{|m|}(\mu)e^{im\phi}, \quad (13.55)$$

where $m=-l,\ -l+1,\ \ldots,\ l-1,\ l$, and

$$\Lambda=l(l+1)\quad (l:\text{integer}). \quad (13.56)$$

With the normalization

$$\int_0^{2\pi}\int_0^{\pi}Y_l^m(\theta,\phi)\,Y_{l'}^{m'}(\theta,\phi)\sin\theta\,d\theta\,d\phi=\delta_{ll'}\delta_{mm'}, \quad (13.57)$$

the orthogonal functions

$$Y_l^m(\theta,\phi)=(-1)^{(m+|m|)/2}\left[\frac{2l+1}{2\pi}\frac{(l-|m|)!}{(l+|m|)!}\right]^{1/2}P_l^{|m|}(\mu)e^{im\phi} \quad (13.58)$$

form a complete set of normalized orthogonal functions called spherical surface harmonics, where $\delta_{ll'}$ and $\delta_{mm'}$ are the Kronecker deltas. For a normal mode, the variables take the following form:

$$p'(t,r,\theta,\phi)=p'(r)Y_l^m(\theta,\phi)e^{i\sigma t}, \quad (13.59)$$

etc. Hereafter, we often use the same symbols to denote the radial part of the variables, say $p'(r)$, if no confusion will result.

The corresponding expression for the displacement vector $\boldsymbol{\xi}$ is given by

$$\boldsymbol{\xi} = \left[\xi_r(r),\ \xi_h(r)\frac{\partial}{\partial\theta},\ \xi_h(r)\frac{\partial}{\sin\theta\partial\phi}\right] Y_l^m(\theta,\phi)e^{i\sigma t}, \quad (13.60)$$

where ξ_h is given from equation (13.38) by

$$\xi_h = \frac{1}{\sigma^2 r}\left(\frac{p'}{\rho} + \Phi'\right). \quad (13.61)$$

The spherical surface harmonics of $l = 4$ are illustrated in Fig. 13.1. The sign in the gray regions is opposite to that in the other regions. In other words, on a given sphere of radius r, at a phase of positive velocity in the gray regions, the velocity is negative in the white regions. There exist l [$|m|$ azimuthal and $(l - |m|)$ latitudinal] border lines, whichever value the parameter takes. For a non-zero m, the pattern of oscillation propagates with a phase velocity $-\sigma/m$ in the azimuthal direction.

Assuming the forms of $\xi_r, p', \Phi', \delta S, T'$, and F_r' as given by like equation (13.59), we obtain a set of ordinary differential equations from equations (13.47)–(13.52) as follows:

$$\frac{1}{\rho}\frac{dp'}{dr} + \frac{g}{\rho c^2}p' + (N^2 - \sigma^2)\xi_r + \frac{d\Phi'}{dr} = g\nabla_{ad}\frac{\rho T}{p}\delta S, \quad (13.62)$$

$$\frac{1}{r^2}\frac{d}{dr}(r^2\xi_r) + \frac{1}{\Gamma_1}\frac{d\ln p}{dr}\xi_r + \left(1 - \frac{L_l^2}{\sigma^2}\right)\frac{p'}{\rho c^2} - \frac{l(l+1)}{\sigma^2 r^2}\Phi' = \nabla_{ad}\frac{\rho T}{p}\delta S, \quad (13.63)$$

$$\frac{1}{r^2}\frac{d}{dr}\left(r^2\frac{d\Phi'}{dr}\right) - \frac{l(l+1)}{r^2}\Phi' - 4\pi G\rho\left(\frac{p'}{\rho c^2} + \frac{N^2}{g}\xi_r\right) = -4\pi G\nabla_{ad}\frac{\rho^2 T}{p}\delta S, \quad (13.64)$$

$$K\frac{dT'}{dr} = -F_r' - K'\frac{dT}{dr}, \quad (13.65)$$

and

$$i\omega\rho T\delta S = (\rho\varepsilon_N)' - \frac{1}{r^2}\frac{d(r^2F_r')}{dr} - \frac{l(l+1)}{r^2}KT', \quad (13.66)$$

where $c = (\Gamma_1 p/\rho)^{1/2}$ is the sound velocity. L_l and N are the Lamb frequency and the Brunt-Väisälä frequency, respectively, and given by

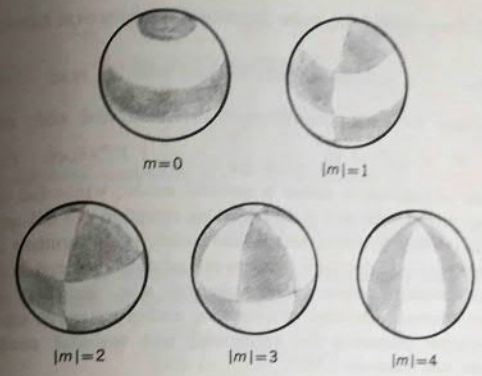

Fig. 13.1. Illustration of spherical surface harmonics $Y_l^m(\theta,\phi)$ with $l = 4$; see also Fig. 4.1.

$$L_l^2 = \frac{l(l+1)c^2}{r^2} \quad (13.67)$$

and

$$N^2 = -gA = g\left(\frac{1}{\Gamma_1}\frac{d\ln p}{dr} - \frac{d\ln\rho}{dr}\right). \quad (13.68)$$

They have appeared already in equations (4.9) and (4.11). Equations (13.62)–(13.66) are basic equations of linear nonadiabatic nonradial oscillations and equations (13.62)–(13.64) are those of linear adiabatic nonradial oscillations, with right-hand sides are neglected.

It is noted here that there exists a trivial solution to the basic equations of oscillations besides ordinary nonradial oscillation modes whose governing equations are discussed above. In this solution, eigenfrequency σ and all scalar variables are zero such that $\sigma = 0$ and $p', T', \rho', \Phi' = 0$ but velocity vector $\boldsymbol{v}$ is non-zero. To see this, we must go back to equations (13.28)–(13.32). We see from these equations that there exists a steady flow solution which satisfies $v_r = 0$ and

$$\nabla_\perp \cdot \boldsymbol{v}_\perp = 0, \quad (13.69)$$

that is, a horizontal eddy motion confined on the spherical surface. The solution of equation (13.69) is given by

$$\boldsymbol{v}_\perp = \nabla_\perp \times (Q\boldsymbol{e}_r), \quad (13.70)$$

where $\boldsymbol{e}_r$ is a unit vector in the radial direction and Q is any scalar

quantity. If we expand the scalar function Q by spherical harmonics as

$$Q = \sum_{l,m} Q_l^m(r)\, Y_l^m(\theta,\phi), \tag{13.71}$$

we then have for each component of the horizontal eddy motions

$$v_l^m = (Q_l^m/r)\left(0, \frac{1}{\sin\theta}\frac{\partial}{\partial\phi}, -\frac{\partial}{\partial\theta}\right) Y_l^m(\theta,\phi). \tag{13.72}$$

This form of solution is called a toroidal mode, while the ordinary oscillatory modes with $\sigma \neq 0$ described by equation (13.60) are called spheroidal modes. Toroidal modes are steady eddy motions and not oscillatory velocity fields, and thus are not of much interest in the case of a non-rotating, non-magnetic spherical star, but they become oscillatory modes in the case of a rotating and/or magnetic star. For a more detailed discussion on spheroidal and toroidal modes, see Aizenman and Smeyers (1977).

13.4 Some Useful Thermodynamic Relations

In treating the equations for nonradial oscillations we frequently need thermodynamic relations among the perturbations of the pressure, density, temperature, and entropy. Here, we summarize these thermodynamic relations, which will be used frequently in this monograph (for detailed derivations, see, e.g., Cox and Giuli, 1968, Chap. 9). In most cases, the periods of the nonradial oscillations are much shorter than the time scales of nucleosynthesis and material diffusion. Then, the Lagrangian perturbation of the chemical composition is negligibly small. This simplifies the thermodynamic relations very much. Therefore, in this subsection we discuss the interrelations among the Lagrangian perturbations of thermodynamic variables. The relations for the Eulerian perturbations may be obtained by use of the relation (13.21).

If the chemical composition does not change, any thermodynamic variable can be regarded as a function of two independent variables. If the matter density, ρ, and temperature, T, are chosen as the independent variables the pressure and entropy perturbations, δp and δS, are written as

$$\frac{\delta p}{p} = \chi_\rho \frac{\delta\rho}{\rho} + \chi_T \frac{\delta T}{T} \tag{13.73}$$

and

$$\delta S = c_v \frac{\delta T}{T} - c_v(\Gamma_3 - 1)\frac{\delta\rho}{\rho}, \tag{13.74}$$

where χ_ρ and χ_T are defined by

$$\chi_\rho = \left(\frac{\partial \ln p}{\partial \ln \rho}\right)_T \quad \text{and} \quad \chi_T = \left(\frac{\partial \ln p}{\partial \ln T}\right)_\rho, \tag{13.75}$$

the specific heat per unit mass at constant density, c_v, is defined by

$$c_v = T\left(\frac{\partial S}{\partial T}\right)_\rho, \tag{13.76}$$

and an adiabatic exponent $(\Gamma_3 - 1)$ is defined by

$$\Gamma_3 - 1 \equiv \left(\frac{\partial \ln T}{\partial \ln \rho}\right)_S = \frac{\chi_T}{c_v}\frac{p}{\rho T}. \tag{13.77}$$

The last relation of equation (13.77) was obtained by using one of the Maxwell relations of thermodynamics:*

$$\left(\frac{\partial T}{\partial \rho}\right)_S = \frac{1}{\rho^2}\left(\frac{\partial p}{\partial S}\right)_\rho. \tag{13.78}$$

If we regard the pressure, p, and temperature, T, as independent variables, we have

$$\frac{\delta\rho}{\rho} = \rho_p \frac{\delta p}{p} - \upsilon_T \frac{\delta T}{T} \tag{13.79}$$

and

$$\delta S = -c_p \nabla_{ad}\frac{\delta p}{p} + c_p \frac{\delta T}{T}, \tag{13.80}$$

where

$$\rho_p \equiv \left(\frac{\partial \ln \rho}{\partial \ln p}\right)_T = \frac{1}{\chi_\rho} \quad \text{and} \quad \upsilon_T \equiv -\left(\frac{\partial \ln \rho}{\partial \ln T}\right)_p = \frac{\chi_T}{\chi_\rho}, \tag{13.81}$$

and the adiabatic temperature gradient, ∇_{ad}, and the specific heat per unit mass at constant pressure c_p are defined as

$$\nabla_{ad} \equiv \left(\frac{\partial \ln T}{\partial \ln p}\right)_S \quad \text{and} \quad c_p \equiv T\left(\frac{\partial S}{\partial T}\right)_p. \tag{13.82}$$

Furthermore, if we regard pressure, p, and entropy, S, as the independent variables, we have

---

* This relation can be derived as follows: From the first law of thermodynamics, we have

$$dU = T dS + \frac{p}{\rho^2} d\rho,$$

where U denotes specific internal energy. Differentiating the above relations in terms of S and ρ, we obtain

$$\frac{\partial^2 U}{\partial\rho\partial S} = \frac{\partial^2 U}{\partial S\partial\rho} = \left(\frac{\partial T}{\partial \rho}\right)_S = \frac{1}{\rho^2}\left(\frac{\partial p}{\partial S}\right)_\rho.$$

$$\frac{\delta\rho}{\rho} = \frac{1}{\Gamma_1}\frac{\delta p}{p} - \frac{v_T}{c_p}\delta S \tag{13.83}$$

and

$$\frac{\delta T}{T} = \frac{\Gamma_2 - 1}{\Gamma_2}\frac{\delta p}{p} + \frac{\delta S}{c_p}, \tag{13.84}$$

where

$$\Gamma_1 \equiv \left(\frac{\partial \ln p}{\partial \ln \rho}\right)_S = \left(\frac{\partial \ln p}{\partial \ln \rho}\right)_T + \left(\frac{\partial \ln p}{\partial \ln T}\right)_\rho \left(\frac{\partial \ln T}{\partial \ln \rho}\right)_S$$

$$= \chi_\rho + \chi_T(\Gamma_3 - 1) \tag{13.85}$$

and

$$\frac{\Gamma_2 - 1}{\Gamma_2} \equiv \left(\frac{\partial \ln T}{\partial \ln p}\right)_S = \nabla_{ad} = \frac{\Gamma_3 - 1}{\Gamma_1}. \tag{13.86}$$

The ratio of the specific heats, γ, can be written as

$$\gamma \equiv \frac{c_p}{c_v} = \left(\frac{\partial S}{\partial T}\right)_p \left(\frac{\partial T}{\partial S}\right)_\rho$$

$$= \left(\frac{\partial S}{\partial p}\right)_T \left(\frac{\partial p}{\partial T}\right)_S \left(\frac{\partial T}{\partial \rho}\right)_S \left(\frac{\partial \rho}{\partial S}\right)_T = \left(\frac{\partial \rho}{\partial p}\right)_T \left(\frac{\partial p}{\partial \rho}\right)_S$$

$$= \frac{\Gamma_1}{\chi_\rho} = \rho_p \Gamma_1, \tag{13.87}$$

where the following cyclic relations are used:*

$$\left.\begin{aligned} \left(\frac{\partial S}{\partial T}\right)_p \left(\frac{\partial p}{\partial S}\right)_T \left(\frac{\partial T}{\partial p}\right)_S &= -1 \\ \left(\frac{\partial T}{\partial S}\right)_p \left(\frac{\partial \rho}{\partial T}\right)_S \left(\frac{\partial S}{\partial \rho}\right)_T &= -1. \end{aligned}\right\} \tag{13.88}$$

and

Using equations (13.77), (13.86), and (13.87), the quantity v_T/c_p in equattion (13.83) can be expressed as

$$\frac{v_T}{c_p} = \nabla_{ad}\frac{\rho T}{p}. \tag{13.89}$$

Let us now consider a mixture of ideal gas and radiation. The internal energy per unit mass, U, of such a system is

* Or the following expressions can be used:

$$\left(\frac{\partial S}{\partial T}\right)_p \left(\frac{\partial T}{\partial S}\right)_\rho = \frac{\partial(S,p)}{\partial(T,p)}\frac{\partial(T,\rho)}{\partial(S,\rho)} = \frac{\partial(T,\rho)}{\partial(T,p)}\frac{\partial(S,p)}{\partial(S,\rho)} = \left(\frac{\partial \rho}{\partial p}\right)_T \left(\frac{\partial p}{\partial \rho}\right)_S.$$

$$U = \frac{1}{\gamma_g - 1}\frac{k}{\mu m_u}T + \frac{a}{\rho}T^4, \tag{13.90}$$

where k, μ, m_u, and a denote the Boltzman constant, mean molecular weight, mass of the atomic mass unit, and radiation density constant, respectively, and γ_g is the ratio of the specific heat for the ideal gas; $\gamma_g = 5/3$ for a monoatomic gas. The total pressure is given as

$$p = p_{gas} + p_{rad} = \frac{k}{\mu m_u}\rho T + \frac{1}{3}aT^4. \tag{13.91}$$

For such a mixture of ideal gas and radiation we have

$$\chi_T = 4 - 3\beta, \quad \chi_\rho = \beta, \quad \rho_p = \frac{1}{\beta}, \quad v_T = \frac{4 - 3\beta}{\beta}, \tag{13.92}$$

$$c_v = \left[\frac{1}{\gamma_g - 1} + \frac{12(1-\beta)}{\beta}\right]\frac{k}{\mu m_u}, \tag{13.93}$$

$$\Gamma_1 = \beta + \frac{(4-3\beta)^2(\gamma_g - 1)}{\beta + 12(\gamma_g - 1)(1-\beta)}, \tag{13.94}$$

$$\Gamma_2 - 1 = \frac{(4-3\beta)(\gamma_g - 1)}{\beta^2 + 3(\gamma_g - 1)(1-\beta)(4+\beta)}, \tag{13.95}$$

and

$$\Gamma_3 - 1 = \frac{(4-3\beta)(\gamma_g - 1)}{\beta + 12(\gamma_g - 1)(1-\beta)}, \tag{13.96}$$

where

$$\beta \equiv p_{gas}/p. \tag{13.97}$$

The internal energy and the pressure of a completely degenerate gas are functions of density only and have no temperature dependence. Therefore, we have $\chi_T = 0$ and $v_T = 0$ for such a gas. There are two extreme states for a degenerate gas: nonrelativistic ($\log\rho \leq 7$) and relativistic degenerate ($\log\rho \geq 7$) states. For the nonrelativistically and completely degenerate gas, we have

$$U \propto \rho^{2/3} \quad \text{and} \quad p \propto \rho^{5/3}. \tag{13.98}$$

Then, we have

$$\chi_\rho = \Gamma_1 = \frac{5}{3} \tag{13.99}$$

for nonrelativistic complete degeneracy. For the relativistically and completely degenerate gas, we have

$$U \propto \rho^{1/3} \quad \text{and} \quad p \propto \rho^{4/3} \tag{13.100}$$

so that

$$\chi_\rho = \Gamma_1 = \frac{4}{3}. \tag{13.101}$$

Using thermodynamic relations, the Brunt-Väisälä frequency, N, defined by equation (13.68) is transformed to a form which is convenient for the numerical calculations. By definition, the square of the Brunt-Väisälä frequency, N^2, is given by

$$N^2 = -gA = -\frac{g}{r}\left(\frac{d\ln\rho}{d\ln r} - \frac{1}{\Gamma_1}\frac{d\ln p}{d\ln r}\right)$$
$$= -g\left(\frac{d\ln\rho}{dr} + \frac{g}{c^2}\right) = \frac{g}{r}V\left(\frac{d\ln\rho}{d\ln p} - \frac{1}{\Gamma_1}\right), \tag{13.102}$$

where $V(r)$ is the homology invariant defined by

$$V(r) \equiv -\frac{d\ln p}{d\ln r} = \frac{GM_r\rho}{rp}. \tag{13.103}$$

Since we are dealing with the spatial derivatives, we have to take into account possible change in the chemical composition. The matter density ρ may be written as

$$\rho = \rho(p, T, X_i), \tag{13.104}$$

where X_i ($i = 1, 2, \ldots, I$) represents the mass fraction of an element i, which satisfies the condition

$$\sum_{i=1}^{I} X_i = 1. \tag{13.105}$$

This relation reduces the number of the independent variables X_i to $(I-1)$. Then, we have

$$\frac{d\ln\rho}{d\ln p} = \left(\frac{\partial\ln\rho}{\partial\ln T}\right)_{\rho,X_i}\nabla + \left(\frac{\partial\ln\rho}{\partial\ln p}\right)_{T,X_i}$$
$$+ \sum_{i=1}^{I-1}\left(\frac{\partial\ln\rho}{\partial\ln X_i}\right)_{T,p,X_{j(\neq i)}}\frac{d\ln X_i}{d\ln p}, \tag{13.106}$$

where

$$\nabla \equiv \frac{d\ln T}{d\ln p}. \tag{13.107}$$

Furthermore, using the relation

$$\left(\frac{\partial\ln\rho}{\partial\ln p}\right)_{T,X_i} = \left(\frac{\partial\ln\rho}{\partial\ln p}\right)_{S,X_i} + \left(\frac{\partial\ln\rho}{\partial S}\right)_{p,X_i}\left(\frac{\partial S}{\partial\ln p}\right)_{T,X_i}$$
$$= \frac{1}{\Gamma_1} - \left(\frac{\partial\ln\rho}{\partial\ln T}\right)_{\rho,X_i}\nabla_{ad}, \tag{13.108}$$

we obtain

$$N^2 = \frac{gV}{r}\left[v_T(\nabla_{ad} - \nabla) + \sum_{i=1}^{I-1}\left(\frac{\partial\ln\rho}{\partial\ln X_i}\right)_{T,p,X_{j(\neq i)}}\frac{d\ln X_i}{d\ln p}\right]. \tag{13.109}$$

In the fully ionized region, the effect of the spatial gradient of chemical composition can be represented in terms of the gradient of the mean molecular weight, μ; i.e.,

$$\sum_{i=1}^{I-1}\left(\frac{\partial\ln\rho}{\partial\ln X_i}\right)_{T,p,X_{j(\neq i)}}\frac{d\ln X_i}{d\ln p} = \left(\frac{\partial\ln\rho}{\partial\ln\mu}\right)_{p,T}\frac{d\ln\mu}{d\ln p}, \tag{13.110}$$

where

$$\frac{1}{\mu} = \sum_{i=1}^{I}\frac{1+Z_i}{A_i} \approx 2X + \frac{3}{4}Y + \frac{Z}{2} \tag{13.111}$$

with the mass fractions of hydrogen, X, helium, Y, and heavy elements, Z. Therefore, if the pressure in the fully ionized region is approximated by ideal gas plus radiation pressure, the square of the the Brunt-Väisälä frequency, N^2, is reduced to

$$N^2 = \frac{gV}{r}\left[\frac{4-3\beta}{\beta}(\nabla_{ad} - \nabla) + \nabla_\mu\right], \tag{13.112}$$

where

$$\nabla_\mu \equiv \frac{d\ln\mu}{d\ln p}. \tag{13.113}$$

Equations (13.110) – (13.112) should not be used in a partially ionized region, because the gradient of mean molecular weight in the partially ionized region does not represent the gradient of chemical composition.

We have $N^2 = 0$ in the completely degenerate and chemically homogeneous region because $v_T = \chi_T/\chi_\rho = 0$ there.

14. Linear Adiabatic Oscillation as a Boundary Value Problem

14.1 Adiabatic Oscillation

The dynamical properties of stellar oscillations can be studied assuming that the specific entropy is conserved during the oscillations; i.e., $\delta S = 0$. In this approximation the perturbations of density can be expressed by the perturbation of pressure such as

$$\delta\rho = \delta p/c^2 \quad \text{or} \quad \rho' = p'/c^2 + \xi_r\rho N^2/g. \tag{14.1}$$

The basic equations (13.62)–(13.64) are reduced to

$$\frac{1}{r^2}\frac{d}{dr}(r^2\xi_r)-\frac{g}{c^2}\xi_r+\left(1-\frac{L_l^2}{\sigma^2}\right)\frac{p'}{\rho c^2}=\frac{l(l+1)}{\sigma^2 r^2}\Phi', \quad (14.2)$$

$$\frac{1}{\rho}\frac{dp'}{dr}+\frac{g}{\rho c^2}p'+(N^2-\sigma^2)\xi_r=-\frac{d\Phi'}{dr}, \quad (14.3)$$

and

$$\frac{1}{r^2}\frac{d}{dr}\left(r^2\frac{d\Phi'}{dr}\right)-\frac{l(l+1)}{r^2}\Phi'=4\pi G\rho\left(\frac{p'}{\rho c^2}+\frac{N^2}{g}\xi_r\right). \quad (14.4)$$

These equations with proper boundary conditions give a well-posed eigenvalue problem with an eigenvalue σ^2. We will consider the boundary conditions at the center ($r = 0$) and at the surface ($p = 0$), where the above equations are singular.

Near the origin $r \sim 0$, the quantities appearing in the above equations behave as follows: $g \sim 0$, $L_l^2 \propto r^{-2}$, $\rho \sim const$, $c^2 \sim const$, $N^2 \sim 0$, and $N^2/g \sim 0$. Therefore, equations (14.2)–(14.4) can be approximately written as

$$\frac{d}{dr}(r^2\xi_r)-\frac{l(l+1)}{\sigma^2}\left(\frac{p'}{\rho}+\Phi'\right)\approx 0, \quad (14.5)$$

$$\frac{1}{\rho}\frac{dp'}{dr}-\sigma^2\xi_r+\frac{d\Phi'}{dr}\approx 0, \quad (14.6)$$

and

$$\frac{d}{dr}\left(r^2\frac{d\Phi'}{dr}\right)-l(l+1)\Phi'\approx 0. \quad (14.7)$$

The general solution of equation (14.7) can be expressed as a linear combination of the two terms which are proportional to $r^{-(l+1)}$ and r^l, respectively. Because Φ' must be regular at the center, we adopt the solution $\Phi' \propto r^l$. Then, we have

$$\frac{d\Phi'}{dr}-\frac{l\Phi'}{r}=0 \quad \text{at} \quad r\sim 0. \quad (14.8)$$

Similarly, by considering the regularity at the center for the variables ξ_r and $(p'/\rho+\Phi')$ in equations (14.5) and (14.6), we obtain the relations, $\xi_r \propto r^{l-1}$ and $p' \propto r^l$, or, equivalently,

$$\xi_r-\frac{l}{\sigma^2 r}\left(\frac{p'}{\rho}+\Phi'\right)=0 \quad \text{at} \quad r\sim 0. \quad (14.9)$$

Equations (14.8) and (14.9) provide the boundary conditions at the center (see Section 18.1 for a different way to derive these equations). Since, as is easily verified, equations (14.2)–(14.4) are equivalent to a fourth-order differential equation with a single variable, the other two boundary conditions must be set at the surface. The physical boundary conditions are complicated because of the nonadiabaticity in the atmosphere. The oscillation must be solved in an atmosphere under conditions of no mechanical and thermal flux from outside. The relations among the variables at the base of the atmosphere where the adiabatic approximation is good must be taken as boundary conditions for the oscillation of the interior. However, we will postpone the discussion of physical boundary conditions to later sections and restrict ourselves here to the so-called zero-boundary conditions.

We assume that the pressure and the density become zero at the surface $r = R$. With oscillations, the stellar surface may be distorted, but still no pressure is acting from outside, and therefore,

$$\delta p = 0 \quad \text{at} \quad r = R. \quad (14.10)$$

Also, since $\rho = 0$ outside, equation (14.4) gives $\Phi' \propto r^{-(l+1)}$, or

$$\frac{d\Phi'}{dr}+\frac{(l+1)}{r}\Phi'=0 \quad \text{at} \quad r=R. \quad (14.11)$$

Equations (14.10) and (14.11) are the zero-boundary conditions (see Section 18.1 for more general discussion on the outer boundary conditions). Equations (14.2)–(14.4) and the boundary conditions (14.8)–(14.11) form a boundary value problem with σ^2 as an eigenvalue. Since neither the equations nor the boundary conditions involve the index m of the spherical surface harmonics, the eigenvalue σ^2 degenerates ($2l + 1$)-fold with respect to m.

The outer boundary condition (14.10) implies $\nabla\cdot\boldsymbol{\xi}\approx 0$ at the outer boundary. Combining this condition with equation (14.2), we obtain

$$\xi_r=\frac{p'}{g\rho} \quad \text{at} \quad r=R. \quad (14.12)$$

If Φ' is neglected (Cowling approximation; see Section 15.1 below), equation (14.12) is reduced to

$$\xi_r=\xi_h\frac{\sigma^2R^3}{GM} \quad \text{at} \quad r=R, \quad (14.13)$$

where the relation (13.61) was used. Equation (14.13) implies that the horizontal motion is much larger than the vertical motion for low frequency oscillations, or *vice versa*.

14.2 The Orthogonality of Eigenfunctions

The basic equations of linear adiabatic nonradial oscillations are reducible to a fourth-order differential equation, which is *not* a Strum-Liouville type, in contrast to the linear adiabatic radial pulsations (Section 14.4 below). In this section we shall discuss the orthogonality and the self-adjointness of linear adiabatic nonradial oscillations.

We will first show the orthogonality of eigenfunctions such that

$$\int_0^M \bar{\boldsymbol{\xi}}^* \cdot \boldsymbol{\xi} dM_r = \delta_{nn'} \delta_{ll'} \delta_{mm'} \int_0^R \rho[|\xi_r|^2 + l(l+1)|\xi_h|^2] r^2 dr, \quad (14.14)$$

where $\boldsymbol{\xi}$ and $\bar{\boldsymbol{\xi}}$ denote displacement eigenvectors belonging to the (n, l, m)- and (n', l', m')-modes, respectively, and an asterisk represents the complex conjugate. From equation (13.60), owing to equations (13.57) and (13.58), we obtain

$$\int_0^M \bar{\boldsymbol{\xi}}^* \cdot \boldsymbol{\xi} dM_r = \int_0^R \rho \bar{\xi}_r^* \xi_r r^2 dr \iint Y_l^m(\theta, \phi) Y_{l'}^{m'}(\theta, \phi)^* \sin\theta d\theta d\phi$$

$$+ \int_0^R \rho \bar{\xi}_h^* \xi_h r^2 dr \iint \left[\frac{\partial Y_l^m}{\partial \theta} \frac{\partial Y_{l'}^{m'*}}{\partial \theta} + \frac{1}{\sin^2\theta} \frac{\partial Y_l^m}{\partial \phi} \frac{\partial Y_{l'}^{m'*}}{\partial \phi} \right] \sin\theta d\theta d\phi$$

$$= \delta_{ll'} \delta_{mm'} \int_0^R \rho[\bar{\xi}_r^* \xi_r + l(l+1) \bar{\xi}_h^* \xi_h] r^2 dr. \quad (14.15)$$

It now remains to show that

$$I_{nn'} \equiv \int_0^R \rho[\xi_r \bar{\xi}_r^* + l(l+1) \xi_h \bar{\xi}_h^*] r^2 dr = 0 \quad \text{for} \quad n \neq n'. \quad (14.16)$$

Taking the scalar product of the equation of motion (13.36) with $\rho\bar{\boldsymbol{\xi}}^*$, we obtain

$$-\sigma^2 \rho \bar{\boldsymbol{\xi}}^* \cdot \boldsymbol{\xi} + \bar{\boldsymbol{\xi}}^* \cdot (\nabla p' + \rho' \nabla \Phi + \rho \nabla \Phi') = 0. \quad (14.17)$$

The following transformation will follow from equations (14.1)–(14.4) or their equivalent:

$$\sigma^2 \rho \bar{\boldsymbol{\xi}}^* \cdot \boldsymbol{\xi} - \nabla \cdot [p' \bar{\boldsymbol{\xi}}^* + \rho \Phi' \bar{\boldsymbol{\xi}}^* + (4\pi G)^{-1} \Phi' \nabla \bar{\Phi}'^*]$$

$$= \bar{\boldsymbol{\xi}}^* \cdot (\nabla p' + \rho' \nabla \Phi + \rho \nabla \Phi') - \nabla \cdot [p' \bar{\boldsymbol{\xi}}^* + \rho \Phi' \bar{\boldsymbol{\xi}}^* + (4\pi G)^{-1} \Phi' \nabla \bar{\Phi}'^*]$$

$$= -p' \nabla \cdot \bar{\boldsymbol{\xi}}^* + g \rho' \bar{\xi}_r^* - \Phi' \nabla \cdot (\rho \bar{\boldsymbol{\xi}}^*) - (4\pi G)^{-1} \nabla \cdot (\Phi' \nabla \bar{\Phi}'^*)$$

$$= p' \frac{\delta \bar{\rho}^*}{\rho} + \frac{g}{c^2} p' \bar{\xi}_r^* + N^2 \rho \xi_r \bar{\xi}_r^* + \Phi' \bar{\rho}'^* - (4\pi G)^{-1} \nabla \cdot (\Phi' \nabla \bar{\Phi}'^*)$$

$$= \frac{p'}{\rho c^2} \left(\delta \bar{p}^* - \frac{dp}{dr} \bar{\xi}_r^* \right) + N^2 \rho \xi_r \bar{\xi}_r^* + (4\pi G)^{-1} [\Phi' \nabla^2 \bar{\Phi}'^* - \nabla \cdot (\Phi' \nabla \bar{\Phi}'^*)]$$

$$= \frac{1}{\rho c^2} p' \bar{p}'^* + N^2 \rho \xi_r \bar{\xi}_r^* - (4\pi G)^{-1} \nabla \Phi' \cdot \nabla \bar{\Phi}'^*. \quad (14.18)$$

Integrating this equation over the whole volume of a star, we obtain

$$\sigma^2 I_{nn'} = \iiint \left(\frac{1}{\rho c^2} p' \bar{p}'^* + N^2 \rho \xi_r \bar{\xi}_r^* - \frac{1}{4\pi G} \nabla \Phi' \cdot \nabla \bar{\Phi}'^* \right) r^2 \sin\theta dr d\theta d\phi$$

$$- (4\pi G)^{-1} (l+1) \left[r \Phi' \bar{\Phi}'^* \right]_{r=R}, \quad (14.19)$$

where the last term is due to the following relation:

$$\iiint \nabla \cdot [p' \bar{\boldsymbol{\xi}}^* + \rho \Phi' \bar{\boldsymbol{\xi}}^* + (4\pi G)^{-1} \Phi' \nabla \bar{\Phi}'^*] r^2 \sin\theta dr d\theta d\phi$$

$$= (4\pi G)^{-1} \left[\iint \left(r^2 \Phi' \frac{\partial}{\partial r} \bar{\Phi}'^* \right) \sin\theta d\theta d\phi \right]_{r=R}$$

$$= -(4\pi G)^{-1} (l+1) \left[r \Phi' \bar{\Phi}'^* \right]_{r=R}, \quad (14.20)$$

by virtue of the zero-boundary conditions. The right-hand side of equation (14.19) is symmetric with respect to the eigenfunctions of the (n, l, m)- and (n', l', m')-modes, therefore, must be equal to $\sigma'^{2*} I_{nn'}$:

$$(\sigma^2 - \sigma'^{2*}) I_{nn'} = 0. \quad (14.21)$$

For the case of $n = n'$, this equation shows that $\sigma^2 = \sigma^{2*}$; i.e., the eigenvalue is real. When $n \neq n'$, $\sigma^2 \neq \sigma'^2$, in general, since the equations and the boundary conditions depend on n. Therefore, we obtain the orthogonality relation:

$$I_{nn'} = 0 \quad \text{for} \quad n \neq n', \quad (14.22)$$

if $\sigma^2 \neq \sigma'^2$. This means that the the system of equations (14.2)–(14.4) is self-adjoint.

Although there is no mathematical proof, to the authors' knowledge, the numerical results so far published suggest the nonexistence of degeneracy among the eigenfrequencies of adiabatic nonradial oscillations of a spherical star (i.e., $\sigma^2 = \sigma'^2$ only if $n = n'$). Even if the degeneracy exists, it is well known that an orthogonal set of functions can always be constructed (e.g., Schiff, 1955, § 10).

The eigenmodes with $\sigma^2 < 0$ are the dynamically unstable g$^-$-modes and those with $\sigma^2 > 0$ are the oscillatory modes. The set of eigenfunctions is usually assumed to form a complete set together with toroidal modes with $\sigma^2 = 0$ (see, e.g., Aizenman and Smeyers, 1977).

The relation between equation (14.18) and the wave energy conservation is noteworthy. For $n = n'$ and $l = l'$, the first term in the first line of equation (14.18) correspond to the kinetic energy of waves and the divergence term corresponds to the energy flux. The first and the second terms in the last line of equation (14.18) correspond to the potential energy of a pure pressure wave and that of a pure gravity wave, respectively. The third term in the last line of equation (14.18) may be regarded as the potential energy for perturbations caused by self-gravity, which plays an important role in the Jeans instability. This problem will be discussed again in Chapter V.

14.3 Variational Principle

It was first shown by Chandrasekhar (1964) that the eigenvalues of the adiabatic nonradial oscillations obey a variational principle. In this subsection we confirm the fact by using an operator representation for the linear adiabatic nonradial oscillations (Lynden-Bell and Ostriker, 1967; Cox, 1980). The formal solution of Poisson's equation for the Eulerian perturbation of the gravitational potential (13.31) is

$$\Phi'(\boldsymbol{r}) = -G\int_V \frac{\rho'(\boldsymbol{x})d^3\boldsymbol{x}}{|\boldsymbol{x}-\boldsymbol{r}|}. \tag{14.23}$$

Using equation (14.23), the continuity equation (13.28), and the adiabatic relation (14.1), the equation of motion (13.29) may be written as

$$\sigma^2\boldsymbol{\xi} = \mathscr{L}(\boldsymbol{\xi}), \tag{14.24}$$

where a linear operator $\mathscr{L}(\boldsymbol{\xi})$ is expressed as

$$\mathscr{L}(\boldsymbol{\xi}) \equiv \frac{1}{\rho^2}(\nabla p)\nabla\cdot(\rho\boldsymbol{\xi}) - \frac{1}{\rho}\nabla(\boldsymbol{\xi}\cdot\nabla p) - \frac{1}{\rho}\nabla(c^2\rho\nabla\cdot\boldsymbol{\xi})$$

$$+\nabla\left\{G\int_V \frac{\nabla_{\boldsymbol{x}}\cdot[\rho(\boldsymbol{x})\boldsymbol{\xi}(\boldsymbol{x})]d^3\boldsymbol{x}}{|\boldsymbol{x}-\boldsymbol{r}|}\right\}. \tag{14.25}$$

In deriving the last term in the above equation, it was assumed that the gas density ρ vanishes at the surface. Taking the scalar product of equation (14.24) with $\rho\boldsymbol{\xi}^*$ and integrating it throughout the stellar volume, we obtain

$$\sigma^2\int_0^M \boldsymbol{\xi}^*\cdot\boldsymbol{\xi}dM_r = \int_0^M \boldsymbol{\xi}^*\cdot\mathscr{L}(\boldsymbol{\xi})dM_r. \tag{14.26}$$

Comparing equation (14.26) with equation (14.19) shows the Hermiticity of the linear operator $\mathscr{L}$; i.e.

$$\int_0^M [\tilde{\boldsymbol{\xi}}^*\cdot\mathscr{L}(\boldsymbol{\xi})]dM_r = \int_0^M [\boldsymbol{\xi}\cdot\mathscr{L}(\tilde{\boldsymbol{\xi}}^*)]dM_r. \tag{14.27}$$

We note that since the zero-boundary condition was used in deriving equation (14.19), equation (14.27) for the Hermiticity of $\mathscr{L}$ is valid under the zero-boundary condition.

Now we apply a small variation on equation (14.26):

$$(\sigma^2+\Delta\sigma^2)\int_0^M (\boldsymbol{\xi}+\Delta\boldsymbol{\xi})^*\cdot(\boldsymbol{\xi}+\Delta\boldsymbol{\xi})dM_r$$

$$= \int_0^M (\boldsymbol{\xi}+\Delta\boldsymbol{\xi})^*\cdot\mathscr{L}(\boldsymbol{\xi}+\Delta\boldsymbol{\xi})dM_r, \tag{14.28}$$

where $\Delta\boldsymbol{\xi}$ and $\Delta\sigma^2$ are the variations in $\boldsymbol{\xi}$ and the corresponding variation in σ^2, respectively. Because of the linearity of the operator $\mathscr{L}$, we have $\mathscr{L}(\boldsymbol{\xi}+\Delta\boldsymbol{\xi}) = \mathscr{L}(\boldsymbol{\xi}) + \mathscr{L}(\Delta\boldsymbol{\xi})$. Using the Hermiticity of $\mathscr{L}$ and the relation (14.26) for the terms of $O(\Delta^0)$ and discarding the terms of $O(\Delta^2)$, we obtain from equation (14.28) the relation

$$\Delta\sigma^2\int_0^M \boldsymbol{\xi}^*\cdot\boldsymbol{\xi}dM_r = -\sigma^2\int_0^M (\boldsymbol{\xi}^*\cdot\Delta\boldsymbol{\xi}+\boldsymbol{\xi}\cdot\Delta\boldsymbol{\xi}^*)dM_r$$

$$+\int_0^M [\boldsymbol{\xi}^*\cdot\mathscr{L}(\Delta\boldsymbol{\xi})+\Delta\boldsymbol{\xi}^*\cdot\mathscr{L}(\boldsymbol{\xi})]dM_r$$

$$= -2\ \mathrm{Re}\left\{\int_0^M (\Delta\boldsymbol{\xi}^*)\cdot[\sigma^2\boldsymbol{\xi}-\mathscr{L}(\boldsymbol{\xi})]dM_r\right\}, \tag{14.29}$$

where Re means the real part of the indicated quantity. The right-hand side of equation (14.29) is equal to zero if σ is an eigenfrequency satisfying equation (14.24). Thus, we have proved that the eigenfrequencies obey a variational principle. The variational principle indicates that eigenfrequencies are determined more accurately than the eigenfunctions. This fact could be utilized to improve eigenfrequencies.

14.4 General Properties of Eigenfrequencies and Eigenfunctions

Some eigenvalues (square of oscillation frequencies) are shown in Fig. 14.1 for the polytrope with index 3 and $\Gamma_1 = 5/3$. In this figure the

square of the normalized eigenfrequencies ω^2 defined by

$$\omega^2 \equiv \sigma^2 \frac{R^3}{GM} \tag{14.30}$$

are plotted against l. There are two sequences of the eigenvalues. One of them tends to infinity as n increases for a given l:

$$\sigma_n^2 \to \infty \quad \text{as} \quad n \to \infty \quad \text{(p-mode)}, \tag{14.31}$$

and the other tends to zero:

$$\sigma_n^2 \to 0 \quad \text{as} \quad n \to \infty \quad \text{(g-mode)}. \tag{14.32}$$

For a given order n, the frequency is higher for the modes with larger l.

Figure 14.2 shows the eigenfunctions for the radial displacement, which are normalized at the surface for p-modes (solid curves) and at the center for g-modes (dashed curves). It is apparent that the relative amplitude of a p-mode (a g-mode) is large only in the outer (inner) part of the star. The f-mode, which has no node in the radial variation of the eigenfunction, has intermediate character between the p_1-mode and the

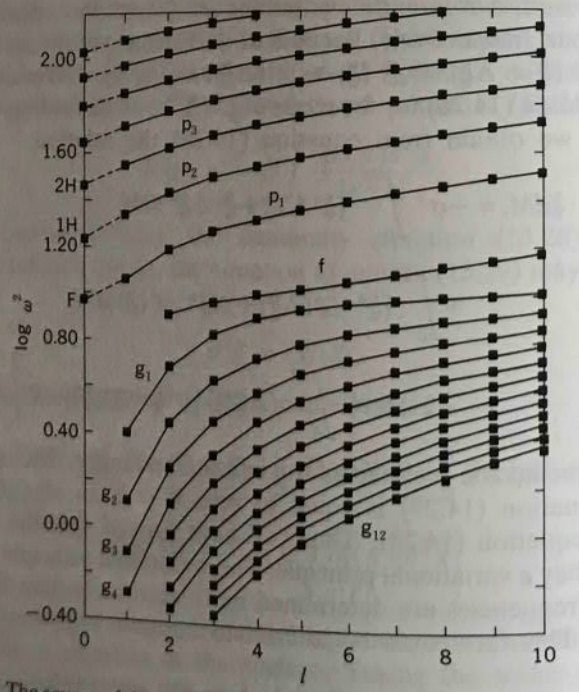

Fig. 14.1 The square of the dimensionless eigenfrequency, $\omega^2 (= \sigma^2 R^3/GM)$, versus the index l of spherical harmonics $Y_l^m(\theta,\phi)$ for the adiabatic pulsations of the polytrope with $N = 3$. The radial pulsations correspond to $l = 0$.

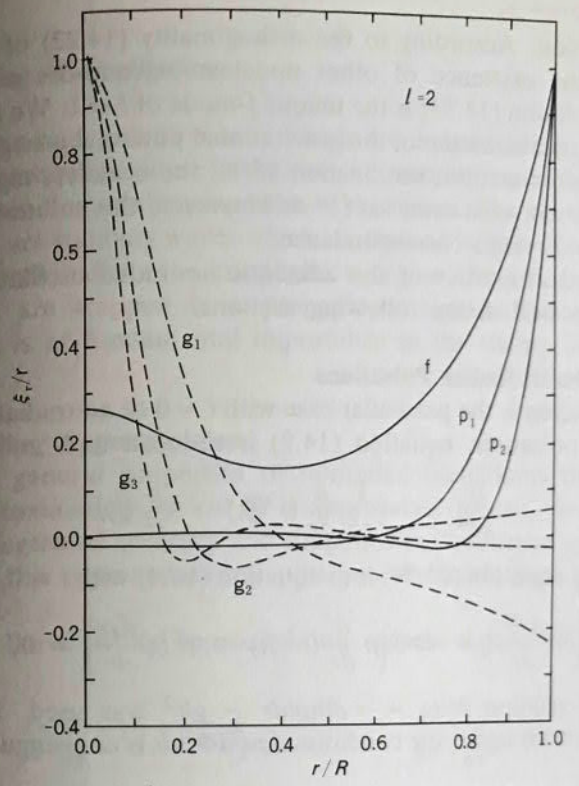

Fig. 14.2 Eigenfunctions of nonradial $l = 2$ pulsations of the $N = 3$ polytrope are plotted against the distance from the center. The solid curves are for the f- and p-modes, which are normalized at the surface, while the dashed curves are for the g-modes, which are normalized at the center.

g_1-mode.

We note that $\sigma = 0$ for the f-mode for $l = 1$. This mode corresponds to the trivial solution which describes a parallel displacement of the whole star. As is easily verified, a trivial solution exists for the set of equations (14.2)–(14.4) for $l = 1$ satisfying the boundary conditions (14.8)–(14.11):

$$\left.\begin{aligned} \xi_r &= \xi_h = \text{const.} \\ p' &= \rho g \xi_r; \qquad \text{i.e.,} \qquad \delta p = 0 \\ \Phi' &= -g\xi_r; \qquad \text{i.e.,} \qquad \delta\Phi = 0 \end{aligned}\right\} \tag{14.33}$$

$$\sigma^2 = 0.$$

This corresponds to the f-mode because there exists no node in the

radial direction. According to the orthogonality (14.22) of the eigenfunctions, the existence of other nodeless eigenmodes is inhibited. Thus, the solution (14.33) is the unique f-mode of $l = 1$. We note that if the Eulerian perturbation of the gravitational potential is neglected (the Cowling approximation; see Section 15.1), the nodeless eigensolution with $\sigma^2 \neq 0$ can exist even for $l = 1$. However, this solution is formal and has no physical correspondence.

Detailed properties of the adiabatic nonradial oscillation modes will be discussed in the following sections.

14.5 Adiabatic Radial Pulsations

Radial pulsation is the particular case with $l = 0$ of nonradial pulsation. For radial pulsations equation (14.2) is reduced to

$$\frac{p'}{\rho c^2} = -\frac{1}{r^2}\frac{d}{dr}(r^2\xi_r) + \frac{g}{c^2}\xi_r. \tag{14.34}$$

Substituting equation (14.34) into equation (14.4) with $l = 0$, we obtain

$$\frac{d}{dr}\left(r^2\frac{d\Phi'}{dr}\right) + 4\pi G\left[\rho\frac{d}{dr}(r^2\xi_r) + r^2\xi_r\frac{d\rho}{dr}\right] = 0, \tag{14.35}$$

where the relation $N^2/g = -d\ln\rho/dr - g/c^2$ was used. Integrating equation (14.35) under the condition that $d\Phi'/dr$ is non-singular at $r = 0$, we obtain

$$\frac{d\Phi'}{dr} + 4\pi G\rho\xi_r = 0. \tag{14.36}$$

Substituting equations (14.34) and (14.36) into equation (14.3) and using the relations for equilibrium structure such as (13.12) and (13.13), we finally obtain a standard differential equation of radial pulsations [equation (58.1) in Ledoux and Walraven, 1958]:

$$\frac{d}{dr}\left[\Gamma_1 pr^4\frac{d}{dr}\left(\frac{\xi_r}{r}\right)\right] + \left\{\sigma^2\rho r^4 + r^3\frac{d}{dr}[(3\Gamma_1 - 4)p]\right\}\left(\frac{\xi_r}{r}\right) = 0. \tag{14.37}$$

This equation with the boundary conditions (14.9) with $l = 0$ and (14.10) forms a Strum-Liouville type eigenvalue problem with the eigenvalue σ^2.

The mode with the smallest eigenvalue is called the fundamental mode, F, whose eigenfunction has no node in $0 \leq r \leq R$. The modes with n nodes are called the n-th harmonic mode, nH. The eigenfrequencies increase as the number of nodes of the eigenfunctions increases, as shown in Fig. 14.1. The properties of the eigenfunctions and eigenfrequencies are similar to those of nonradial p-modes.

15. Trapping of Oscillations

The acoustic and gravity waves which are responsible for nonradial oscillations are propagative in the radial direction only in the restricted regions depending on the properties of the waves. The global nonradial oscillations are standing waves which are formed by the reflection of the waves at both sides of a propagative region. In other words, the oscillations are trapped in a propagative region. The trapping of oscillations is of fundamental importance in the theory of nonradial oscillations.

15.1 Cowling Approximation

To discuss general properties of nonradial oscillations the Cowling (1941) approximation ($\Phi' = 0$) is appropriate to use, since it has a sufficient degree of accuracy and simplifies the treatment greatly. The accuracy of this approximation is quite good for modes with large values of n and l.

Using the Cowling approximation reduces equations (14.2) and (14.3) to

$$\frac{1}{r^2}\frac{d}{dr}(r^2\xi_r) - \frac{g}{c^2}\xi_r + \left(1 - \frac{L_l^2}{\sigma^2}\right)\frac{p'}{\rho c^2} = 0 \tag{15.1}$$

and

$$\frac{1}{\rho}\frac{dp'}{dr} + \frac{g}{\rho c^2}p' + (N^2 - \sigma^2)\xi_r = 0. \tag{15.2}$$

With the transformation of variables ξ_r and p' to new variables $\tilde{\xi}$ and $\tilde{\eta}$ defined by

$$\tilde{\xi} \equiv r^2\xi_r \exp\left(-\int_0^r \frac{g}{c^2}dr\right) \tag{15.3}$$

and

$$\tilde{\eta} \equiv \frac{p'}{\rho}\exp\left(-\int_0^r \frac{N^2}{g}dr\right) = \sigma^2 r\xi_h \exp\left(-\int_0^r \frac{N^2}{g}dr\right), \tag{15.4}$$

equations (15.1) and (15.2) result in a canonical form,

$$\frac{d\tilde{\xi}}{dr} = h(r)\frac{r^2}{c^2}\left(\frac{L_l^2}{\sigma^2} - 1\right)\tilde{\eta} \tag{15.5}$$

and

$$\frac{d\tilde{\eta}}{dr} = \frac{1}{r^2 h(r)}(\sigma^2 - N^2)\,\tilde{\xi}, \tag{15.6}$$

where

$$h(r) \equiv \exp\left[\int_0^r \left(\frac{N^2}{g} - \frac{g}{c^2} \right) dr \right] > 0. \qquad (15.7)$$

It should be noted that the equations of linear adiabatic nonradial oscillations are not the Sturm-Liouville type even in the Cowling approximation.

15.2 Local Analysis

Qualitative features of nonradial oscillations can be understood in the local treatment, in which the coefficients of equations (15.5) and (15.6) are assumed to be constant. In this approximation, we obtain

$$\tilde{\xi}(r),\ \tilde{\eta}(r) \propto \exp\ (ik_r r), \qquad (15.8)$$

where

$$k_r^2 = \sigma^{-2}c^{-2}(\sigma^2 - L_l^2)(\sigma^2 - N^2). \qquad (15.9)$$

Equation (15.9) is the dispersion relation, which relates the wave number to the frequency. The appearance of the Lamb frequency L_l [defined in equation (13.67)] and the Brunt-Väisälä frequency N as critical frequencies should be noted. If $\sigma^2 > L_l^2, N^2$ or $\sigma^2 < L_l^2, N^2$, the wave number k_r is real, and $k_r^2 > 0$. In such cases, waves can propagate in radial directions. If $N^2 > \sigma^2 > L_l^2$ or $L_l^2 > \sigma^2 > N^2$, the wave number k_r is purely imaginary, and $k_r^2 < 0$. The phase of the oscillation is spatially locked, and the amplitude changes exponentially with r. The wave energy flux over the spherical surface of radius r, which is $4\pi r^2 p' \xi_r$ and is proportional to $\xi\bar{\eta}^*$, also changes exponentially with r. Therefore, if the propagative zone or a source of waves exist interior (or exterior) to the imaginary k_r region, the solution exponentially increasing (or decreasing) with r should be omitted. Then the other solution describes the wave which is reflected and spatially damped as it goes into the imaginary k_r region. The wave is said to be *evanescent* in this region.

We now introduce the horizontal wave number k_h by

$$k_h^2 = l(l+1)/r^2 = L_l^2/c^2, \qquad (15.10)$$

for there are l nodal lines on the spherical surface of radius r, and $l\,(l+1)$ instead of l^2 is due to the spherical effect. The dispersion equation (15.9) is rewritten as

$$\sigma^4 - (N^2 + k^2c^2)\sigma^2 + N^2k_h^2c^2 = 0, \qquad (15.11)$$

where

$$k^2 = k_r^2 + k_h^2. \qquad (15.12)$$

Figure 15.1 illustrates the diagnostic diagram which represents the relation (15.11) on the (k_h^2, σ^2)-plane. In the hatched (G) and cross-hatched (P) regions, the quantity k_r^2 is positive, while it is negative in the other regions. For a given $k_r^2 \neq 0$, equation (15.11) is represented by two hyperbolas as shown in Fig. 15.1. The asymptotic lines are given by $\sigma^2 = N^2$ and $\sigma^2 = c^2k^2$. With $k_r^2 = 0$, we have

$$\sigma^2 = N^2 \qquad (15.13)$$

and

$$\sigma^2 = c^2k_h^2. \qquad (15.14)$$

Equations (15.13) and (15.14) represent the dispersion relations of the horizontally propagating gravity wave and the Lamb wave which is not propagative in the vertical direction, respectively.

There exist two kinds of restoring forces, pressure (mainly in the region P) and gravity (mainly in the region G). In fact, for $g \to 0$ (and hence $N^2 \to 0$), one root of equation (15.11) in the region P is given by $\sigma^2 \to c^2k^2$ and the other solution in the region G is given by $\sigma^2 \to N^2k_h^2/k^2 \to 0$. The former represents the acoustic wave due to the isotropic pressure and the latter shows the anisotropic nature of the gravity wave. As the radial wave number k_r becomes larger, the

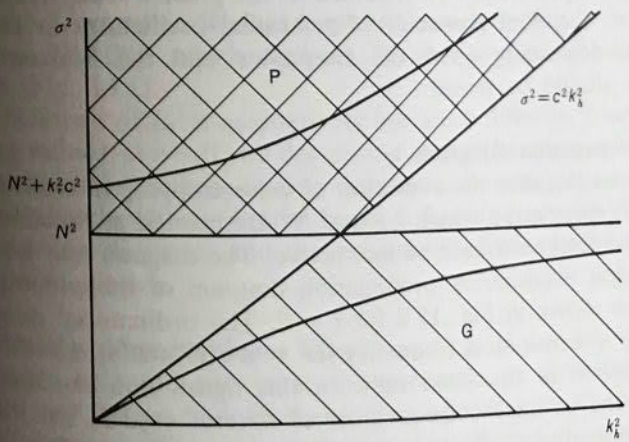

Fig. 15.1 Schematic diagnostic diagram for gravitoacoustic wave. The quantity k_r^2 is positive in the hatched region (G) and in the cross-hatched region (P), while it is negative in the other regions. The dispersion relation (15.11) is represented by the two hyperbolic lines on this diagram.

frequency of the acoustic modes becomes higher while that of the gravity waves becomes lower.

The group velocity $\boldsymbol{v}_{gr}$ and the phase velocity $\boldsymbol{v}_{ph}$ are given by

$$\boldsymbol{v}_{gr}=\frac{\partial\sigma}{\partial\boldsymbol{k}}=\frac{c^2\sigma}{2\sigma^2-(N^2+c^2k^2)}\left[k_r,\ \boldsymbol{k}_h\left(1-\frac{N^2}{\sigma^2}\right)\right] \quad (15.15)$$

and

$$\boldsymbol{v}_{ph}=\frac{\sigma}{\boldsymbol{k}}=\frac{\sigma}{k^2}(k_r,\ \boldsymbol{k}_h). \quad (15.16)$$

For the limiting acoustic wave ($g \to 0$, $\sigma = ck$), we have

$$\boldsymbol{v}_{gr}=\boldsymbol{v}_{ph}=c(\boldsymbol{k}/k), \quad (15.17)$$

representing an isotropic nondispersive propagation. For the limiting gravity wave ($g \to 0$ or $c \to \infty$: incompressible, $\sigma = Nk_h/k$), we have

$$\boldsymbol{v}_{gr}=\frac{Nk_r}{k^3}(-k_h,\ \frac{\boldsymbol{k}_h}{k_h}k_r) \text{ and } \boldsymbol{v}_{ph}=\frac{Nk_h}{k^3}(k_r,\ \boldsymbol{k}_h); \quad (15.18)$$

hence $\boldsymbol{v}_{gr} \perp \boldsymbol{v}_{ph}$ and the vertical components are the same in magnitude and opposite in direction.

It should be noted that equation (15.11) and Fig. 15.1 are not exact even for the isothermal plane-parallel atmosphere [see equation (11.3) and Fig. 11.2] in which k_r ($= k_z$) is really constant. However, the qualitative aspects are well revealed in the present local treatment. In particular, the dual character of nonradial oscillations in the stellar medium, depending upon the frequency and the horizontal wave number, should be noted.

15.3 Propagation Diagram

In order to visualize the condition of wave trapping in realistic stellar models, a diagram in which L_l^2 and N^2 are plotted as functions of the radial coordinate r should be instructive. The diagram may be called a propagation diagram. A propagation diagram of the polytrope with index 3 is shown in Fig. 15.2 for $l = 2$. The ordinate ω^2 denotes the square of dimensionless frequency [$\omega^2 = \sigma^2/(GM/R^3)$], and N^2 and L_l^2 are measured in the same unit. In this figure thin horizontal lines indicate the oscillation frequencies of several modes, and the small circles on the lines indicate loci of the nodes in $\xi_r(r)$ (*cf.* Figs. 14.1 and 14.2). The nodes for the p-modes and g-modes appear, respectively, in the P-type and G-type propagative zones, where $k_r^2 > 0$ [see equations (15.8) and (15.9)]. This figure clearly shows that the p-modes and g-modes are trapped in the P zone and the G zone, respectively. For

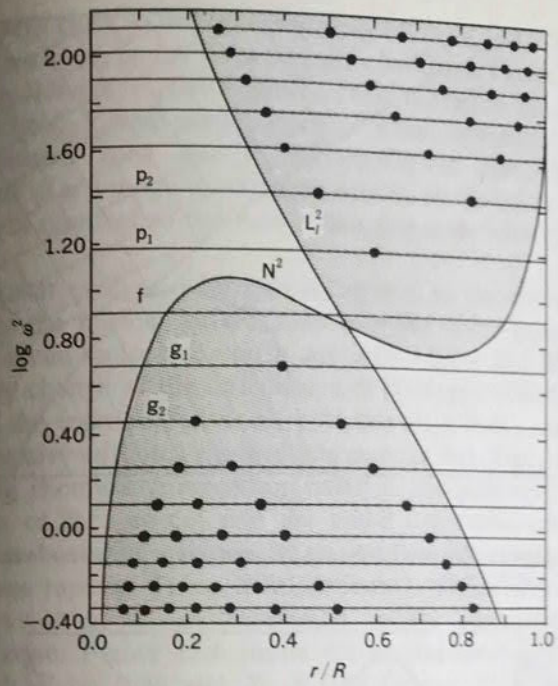

Fig. 15.2 Propagation diagram for the polytrope with index 3 in the case of $l = 2$. Some eigenfrequencies are indicated by thin horizontal lines, and the location of nodes is shown by circles.

larger l, the L_l^2-curve is displaced upward corresponding to the factor $L_l^2/L_{l=2}^2 = l(l+1)/6$, which explains the increase of ω^2 with l for p_n-modes (Fig. 14.1).

The behavior of L_l^2 is qualitatively not much different from star to star, being infinite at $r = 0$ and decreasing monotonically as r increases except in the chromosphere-corona transition. But the behavior of N^2 changes sensitively with evolution. In the following part we will discuss the propagation diagrams and the properties of nonradial modes of various stellar models.

15.3.1 Massive Main-Sequence Stars

Equation (13.112) indicates that the existence or nonexistence of convection and the gradient of chemical composition largely influence the distribution of N^2 in the stellar interior. Therefore, the spatial variation of N^2 changes significantly as the star evolves. Figure 15.3 illustrates the propagation diagram of $l = 2$ for a $10M_\odot$ zero-age main-sequence (ZAMS) model. This model has a convective core and a homogeneous chemical composition ($\nabla_\mu = 0$). The temperature

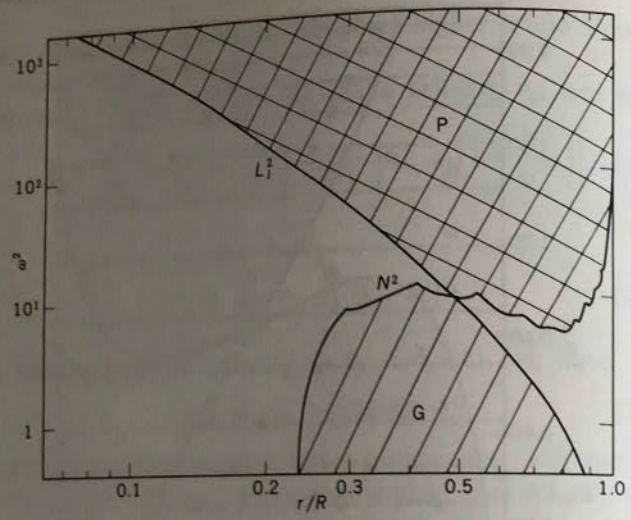

Fig. 15.3 Propagation diagram for the ZAMS model of a $10M_\odot$ star in the case of $l = 2$ ($X = 0.7$). Taken from Osaki (1975).

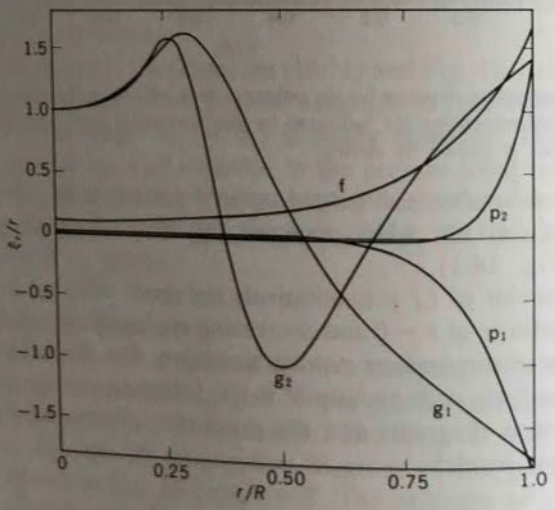

Fig. 15.4 Eigenfunctions of relative displacement in the radial direction ξ_r/r for $l = 2$ for the same model as Fig. 15.3. The normalization at the center is (1) $(\xi_r/r)_c = 1.0$ for g_1- and g_2-modes, (2) $(\xi_r/r)_c = 0.1$ for f-mode, (3) $(\xi_r/r)_c = 0.02$ for p_1-mode, and (4) $(\xi_r/r)_c = 0.005$ for p_2-mode. Note, however, that the energy density of oscillation is proportional to $\rho\xi_r^2$ (from Osaki,1975).

gradient is very close to the adiabatic value ($\nabla - \nabla_{ad} \simeq 10^{-6} \sim 10^{-7}$) in the convective core, and N^2 is practically zero there. Figure 15.4 shows the eigenfunctions of relative displacement in the radial direction ξ_r/r for $l = 2$ for the $10M_\odot$ ZAMS model. Because of the existence of a relatively large evanescent zone due to the convective core, the relative displacement of a g-mode is maximum at $r/R \sim 0.25$–0.3 rather than at the center, in contrast to the case of the polytrope with index 3 (Fig. 14.2).

As the star evolves, hydrogen is depleted in the central region as the result of the nuclear burning, and a highly stable zone due to the gradient of mean molecular weight develops. Figure 15.5 illustrates the evolutionary change of the distribution of hydrogen abundance X as a function of the fractional mass q ($= M_r/M$) for a $10M_\odot$ star. The fully mixed convective core in a massive star recedes with time, and the zone with varying chemical composition is left in the position between the outer edges of the present and the initial convective cores. This μ-gradient zone becomes wider as the star evolves. The central condensation increases rapidly. These features cause a characteristic change in the N^2-curve—that is, a trapezoidal profile associated with the μ-gradient zone. Figure 15.6 shows the propagation diagram for the models with $X_c = 0.48$ and $X_c = 0.07$, where X_c is the hydrogen abundance at the center. The μ-gradient zone acts like a potential well that may trap gravity waves. In these evolved models eigenmodes in the frequency range between the two maxima of the N^2-curve possess a dual

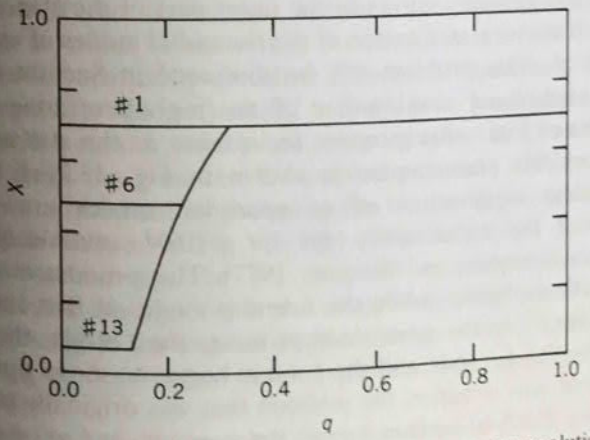

Fig. 15.5 The distribution of hydrogen inside a $10M_\odot$ star at various evolutionary stages.

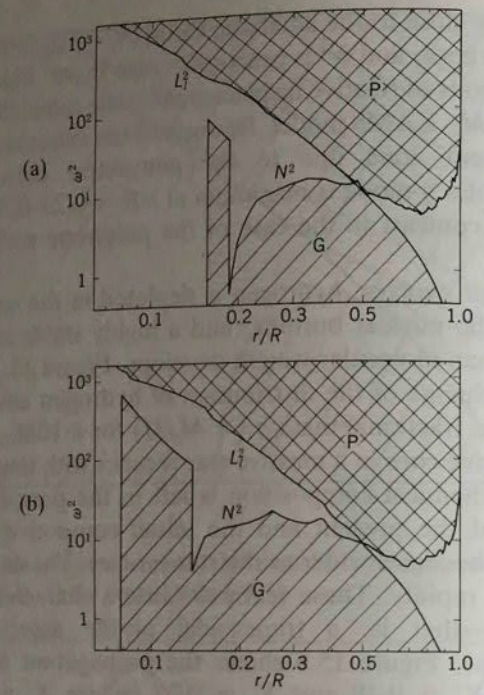

Fig. 15.6 Propagation diagrams for evolved $10M_\odot$ models, whose hydrogen distributions are shown in Fig. 15.5 [(a)$X_c = 0.48$ (model #6); (b)$X_c = 0.07$ (model #13)], in the case $l = 2$ (from Osaki, 1975).

character such that they behave like gravity waves in the μ-gradient zone, but like pressure waves in the outer part of the star. Because of this dual character classification of the nonradial modes of evolved stars is not trivial. This problem will be discussed in Section 17.

The evolutional development of the μ-gradient zone causes the frequencies of low order g-modes to increase as the star evolves. An example of this phenomenon is shown in Fig. 15.7(a), where the dimensionless eigenvalues ω^2 of nonradial modes are plotted as functions of the evolutionary age for a $16M_\odot$ main-sequence star (Aizenman, Smeyers, and Weigert, 1977). The g-modes move upward rapidly with evolution, while the f- and p-modes at first remain fairly constant in ω^2. As the g_1-mode approaches the f-mode, the f-mode is bumped by the g_1-mode and the f-mode begins to move upward while the g_1-mode now occupies the position that was originally occupied by the f-mode. The f-mode then bumps the p_1-mode, and so on. Aizenman et al. (1977) have shown that this phenomenon is essentially the same as the "avoided crossing" of modes of two coupled oscillators. One oscillator is identified as a gravity-wave oscillation trapped in the deep

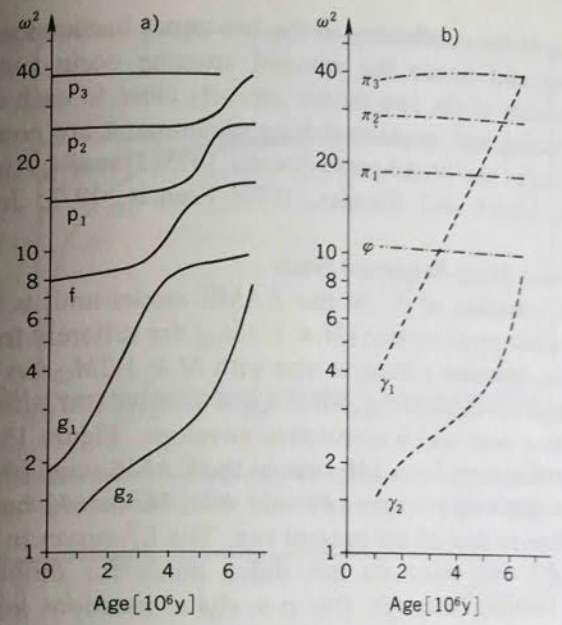

Fig. 15.7 Avoided crossing of eigenfrequencies with the evolutionary sequence of a $16M_\odot$ (after Aizenman et al., 1977): (a) for the full problem, (b) for the decoupled modes (see text for detail).

interior and the other is a p-wave oscillation trapped in the envelope. The avoided crossing is caused by the interaction between the two oscillations. Simple crossings between a g-mode and the f- or a g-mode would occur if the interaction between the two oscillations were suppressed. In order to show this, Aizenman et al. (1977) calculated eigenmodes for artificially modified differential equations. They dropped the terms $L_l^2 p'/(\sigma^2 \rho c^2)$ and $l(l+1)\Phi'/(\sigma^2 r^2)$ in equation (14.2) to obtain φ-and π-modes, which are, respectively, the f- and p-modes, decoupled from the g-modes. Decoupled g-modes, which were called γ-modes, were obtained by dropping the term $\sigma^2 \xi_r$ in equation (14.3). The result is shown in Fig. 15.7(b). The decoupled γ_1-mode now intersects, successively, the φ-, π_1-, and π_2-modes, and it is well demonstrated in the figure that the mode "bumping" phenomenon (or avoided crossing) in the original problem is due to the coupling between the pseudo g-modes trapped in the μ-gradient zone and the envelope f- and p-modes.

During the avoided crossing, the characters of the two modes are exchanged by the interaction of the two waves which occurs through the tunnel effect in the evanescent zone. The evanescent zone acts as a potential barrier. As the potential barrier becomes higher and/or wider,

the coupling of the oscillations in the two zones becomes weaker. Thus the coupling and hence the avoided crossing occur only when the eigenfrequencies of the two modes are very close to each other. These avoided crossing and mode-switching phenomena are common to the nonradial modes in a broad sense (Osaki, 1975; Hansen, Aizenman, and Ross, 1976; Ulrich and Rhodes, 1977; Francis, 1973; Jones, 1976).

15.3.2 Lower Main-Sequence Stars

The spatial variation of N^2 in the ZAMS model and its evolutionary change for a less massive star ($M \lesssim 1.2M_\odot$) are different from those for massive stars, because a massive star with $M \gtrsim 1.2M_\odot$ has a convective core and a radiative envelope, while a less massive star with $M \lesssim 1.2M_\odot$ has a radiative core and a convective envelope. Figure 15.8 shows the propagation diagrams for a $1M_\odot$ star at the ZAMS stage (#1) and at the advanced evolutionary stages (#2 and #3). Model #2 has an internal structure close to that of the present sun. The L_l^2-curves in Fig. 15.8 are of model #2, but they do not differ much for different models. Hydrogen burning through the p-p chain reactions results in the radiative core and hence the smooth μ-gradient zone, as shown in Fig. 15.9.

The condition of wave trapping in the outer envelope depends on the structure of the atmospheric layers. The adiabatic approximation is less adequate but still useful for most cases of interest. Figure 15.10 is a propagation diagram of the sun with particular emphasis on the

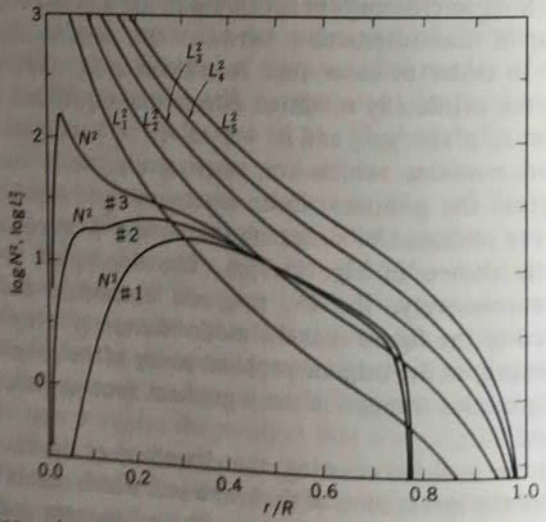

Fig. 15.8 Propagation diagram for models of a $1M_\odot$ star. The quantities N^2 and L_l^2 are measured in units of GM/R^3. After Shibahashi, Osaki, and Unno (1975).

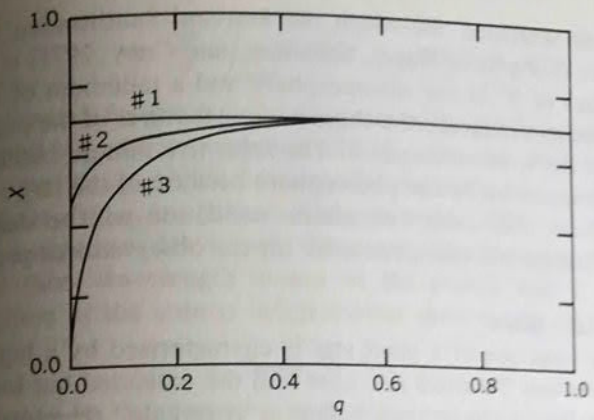

Fig. 15.9 The distribution of hydrogen inside a $1M_\odot$ star at various evolutionary stages. The propagation diagrams of these models are illustrated in Fig. 15.8.

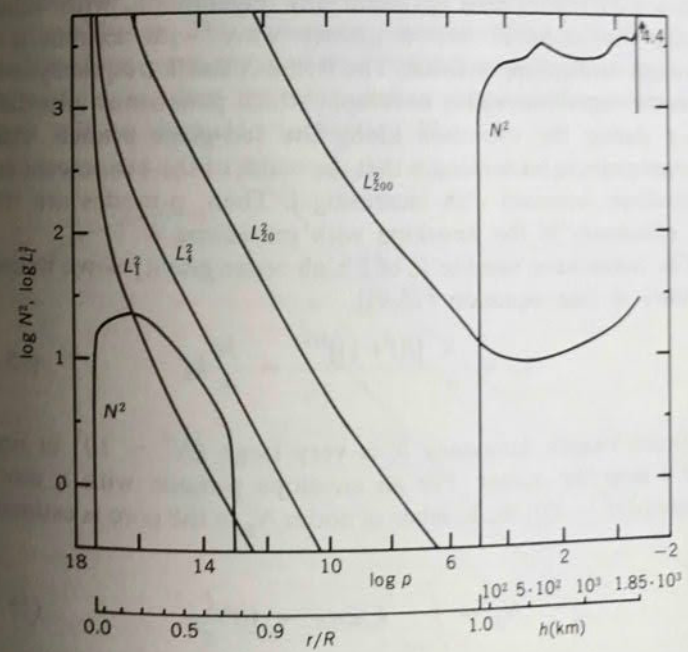

Fig. 15.10 The propagation diagram of a solar model. The Harvard-Smithsonian model atmosphere is adopted for the structure above the photosphere. The lower horizontal scale shows the relative radius (r/R) for the inside of the photosphere, and shows the height from the photosphere (h) in units of km.

atmospheric structure, for which the Harvard-Smithsonian reference atmosphere (Gingerich, Noyes, Kalkofen, and Cuny, 1971) is adopted. Large values of N^2 in the chromosphere and a minimum of L_l^2 in the temperature minimum are the characteristic features of the propagation diagram of the solar atmosphere. The solar five-minute oscillation ($\omega^2 \sim 10^3$) is trapped below the photosphere because of the large N^2 in the chromosphere. The solar five-minute oscillation will be discussed in detail in Chapter VII (see Section 11 for the observational properties).

15.3.3 Giant Stars

The stellar structure of a giant star is characterized by a high density contrast between the small size core and the extended but low density envelope (which is sometimes called a "core-halo" structure). Figure 15.11 shows the propagation diagram of a giant star model with $M = 5M_\odot$. We see from Fig. 15.11 that both N^2 and L_l^2 increase greatly with depth toward the center so that any eigenmode with moderate frequency, σ, behaves like a gravity wave with extremely short wavelength in the deep interior. The Brunt-Väisälä frequency is nearly zero in the outer convective envelope, which penetrates into the deep interior during the evolution along the red-giant branch. Another important point to be noticed is that the width of the evanescent zone in the envelope increases with increasing l. Then, p-modes are trapped more effectively in the envelope with increasing l.

The radial wave number k_r of a high order gravity wave in the core is written as [see equation (15.9)]

$$k_r \simeq \frac{N}{\sigma}\frac{[l(l+1)]^{1/2}}{r} = \frac{N}{\sigma}k_h. \tag{15.19}$$

The Brunt-Väisälä frequency N is very large ($N^2 \sim 10^7$ in units of GM/R^3) near the center. For an envelope p-mode with a moderate frequency ($\omega^2 \sim 10$), the number of nodes N_g in the core is estimated to be

$$N_g \sim \int_{core} k_r dr/\pi \sim 10^3 \frac{l}{\pi}. \tag{15.20}$$

The travel time, τ_{tr}, that it takes for a wave packet to traverse the core and to return to the envelope is accordingly very long and is given by

$$\tau_{tr} \sim 2\int_{core} \frac{dr}{|v_{gr,r}|} \sim 2\int_{core} \frac{k_r}{\sigma} dr$$

$$\sim \frac{2\pi}{\sigma}\int_{core} k_r dr/\pi \sim \text{period} \times N_g, \tag{15.21}$$

where $v_{gr,r}$ stands for the radial component of the group velocity of high order g-modes given in equation (15.18). On the other hand, the damping time, τ_{damp}, of nonradial oscillations in the core of a giant star is very short ($\tau_{damp} \sim$ period; Dziembowski, 1971) due to strong radiative dissipation. Obviously, this strong dissipation is due to the extremely short wavelength nature of the gravity waves. Since the damping time in the core is much shorter than the travel time, i.e.,

$$\tau_{damp} \ll \tau_{tr}, \tag{15.22}$$

the wave may be damped to a negligible intensity long before being reflected at the center. In such a situation, standing oscillations extending from the center to the surface are impossible (*cf.* Pesnell, 1984). However, there exists an evanescent zone between the core and the envelope P-zone. This evanescent zone acts like a partially reflecting wall for envelope p-modes, and thus "quasi"-standing wave oscillations are formed. A method to treat such a quasi-standing wave in the envelope will be discussed in Section 21.

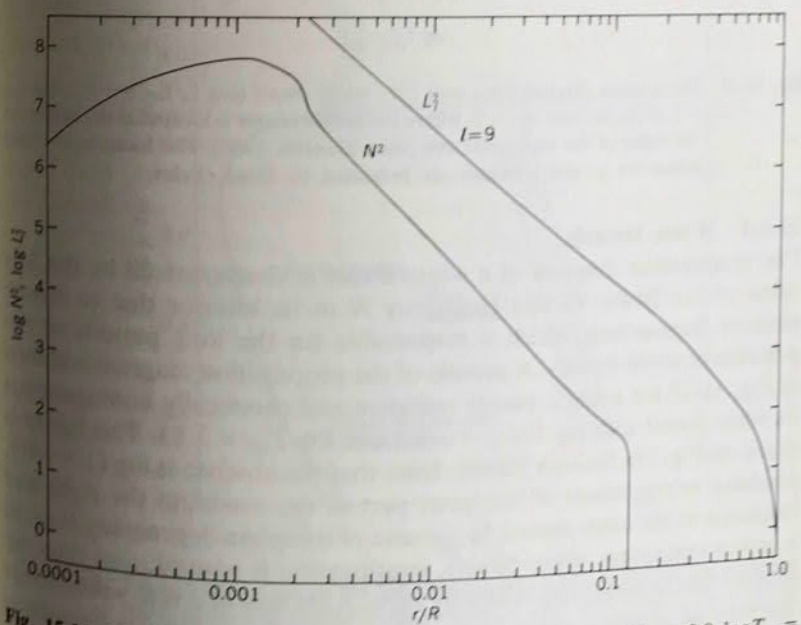

Fig. 15.11 Propagation diagram for a red giant model ($5M_\odot$, $\log L/L_\odot = 2.9$, $\log T_{eff} = 3.63$) in the case of $l = 9$. The quantities N^2 and L_l^2 are measured in units of GM/R^3 (after Shibahashi and Osaki, 1976b).

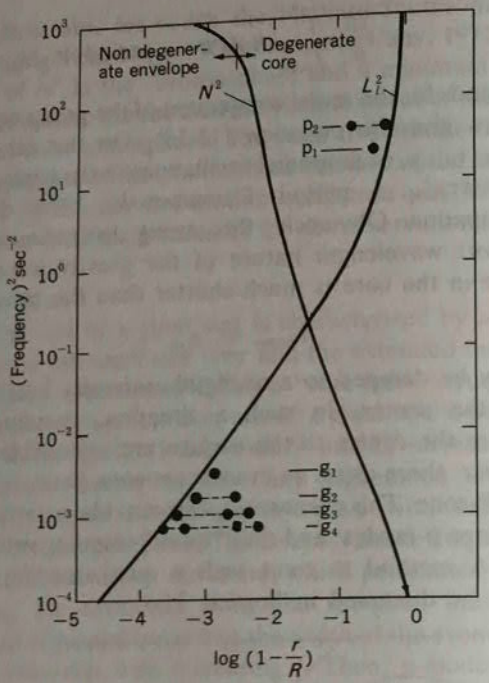

Fig. 15.12 Propagation diagram for a cool $1M_\odot$ white dwarf ($\log L/L_\odot = -4.2$, $\log T_{eff} = 3.83$) in the case of $l = 2$, where the stellar center is located at the origin (to the right) of the horizontal axis (after Hansen, 1980). The location of radial nodes for g- and p-modes are indicated by filled circles.

15.3.4 White Dwarfs

The propagation diagram of a white dwarf is characterized by the low value of the Brunt-Väisälä frequency N in its interior due to strong electron degeneracy, which is responsible for the long periods of the g-modes of white dwarfs. A sample of the propagation diagram is shown in Fig. 15.12 for a $1M_\odot$, purely radiative and chemically homogeneous Fe white dwarf with $\log L/L_\odot = -4.2$ and $\log T_{eff} = 3.83$. This figure is based on Fig.2 in Hansen (1980). Note that the abscissa is $\log(1 - r/R)$, resulting in placement of the inner part of the model to the right and emphasis of the outer layers. In the case of complete degeneracy (i.e., in a zero-temperature white dwarf), stratification is neutral, and thus the Brunt-Väisälä frequency is exactly zero. Although in a real white dwarf the internal temperature is finite and so is the Brunt-Väisälä frequency N, the value of N is extremely low in the degenerate core. The Brunt-Väisälä frequency increases drastically in the non-degenerate

radiative envelope. (It drops to zero in the thin surface convective zones due to the partial ionization of hydrogen and/or helium in a chemically stratified white dwarf.) The loci of nodes of the eigenfunctions of some g- and p-modes are also shown in Fig. 15.12. The low order g-modes of a white dwarf tend to be trapped in the outer envelope. On the other hand, the central concentration of a white dwarf is not high in general, and the Lamb frequency L_l varies gradually from infinity at the center to near zero at the surface. Consequently, the p-modes of lower harmonic degrees l have rather wide propagation zones ($\sigma^2 > N^2, L_l^2$), and their eigenfunctions have large amplitudes even in the deep interior. These properties of the p- and the g-modes are opposite to those for the other kind of star. The effect of a crystalline core of a cool white dwarf has been investigated by Hansen and Van Horn (1979).

Figure 15.13 illustrates the evolution of a star to the white dwarf phase. Losing most of its hydrogen-rich envelope in the asymptotic giant phase, a highly evolved star moves blueward in the HR diagram. After passing through the phase of planetary nebula nuclei, it enters into the white-dwarf cooling sequence. As we discussed in Section 10, nonradial g-mode oscillations are known to be excited in several phases of the

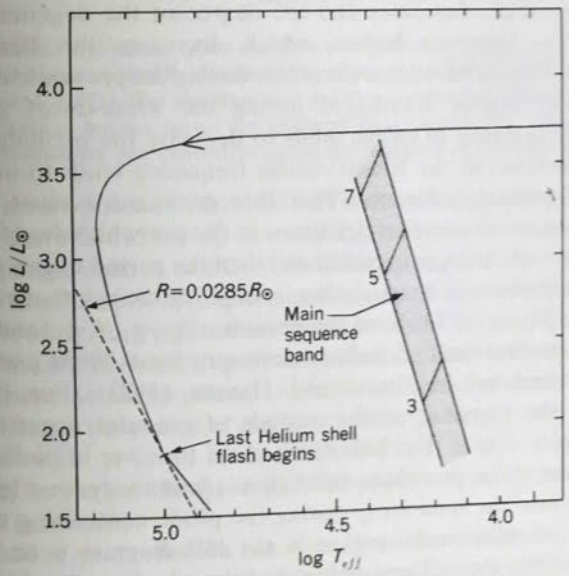

Fig. 15.13 Evolutionary track in the HR diagram of a $0.6M_\odot$ star from red supergiant phase to the white dwarf cooling sequence, after Iben (1982). Also shown are main sequence band and rough approximation to main sequence evolutionary tracks of 3, 5, $7M_\odot$ models. The dashed line indicates the location of constant radius for $0.0285R_\odot$.

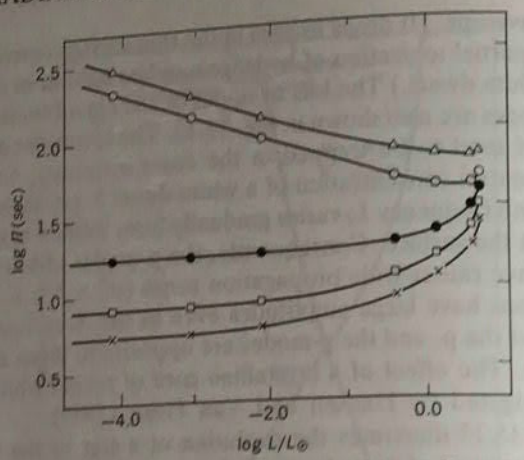

Fig. 15.14 Periods in seconds of the (top to bottom) g_1, g_2, f, p_1, and p_2-modes of nonradial quadrupole oscillations ($l = 2$) as functions of stellar luminosity for the $0.398M_\odot$ models (taken from Osaki and Hansen, 1973).

evolution from the planetary neblua nuclei phase to the cool white dwarf phase (ZZ Ceti or DAV stars). As the evolution proceeds, the core temperature decreases and the degree of the degeneracy of the electron gas becomes higher, which decreases the Brunt-Väisälä frequency. The stellar radius decreases during the pre-white dwarf stage but remains almost unchanged during the white-dwarf cooling sequence. A decrease in radius tends to decrease the oscillation period, while a decrease in the Brunt-Väisälä frequency tends to increase the periods of g-mode oscillations. Therefore, as the star evolves, the period of a g-mode oscillation first decreases in the pre-white dwarf phase due to the effect of decrease in radius and then the period begins to increase when the luminosity becomes low enough in the white-dwarf cooling sequence. Figure 15.14 shows the periods of g_2, g_1, f, p_1, and p_2-modes of $l = 2$ as functions of stellar luminosity for $0.398M_\odot$ white dwarf models calculated by Osaki and Hansen (1973). For this model sequence the turnover of the periods of g-modes occurs when the luminosity is $\sim 4L_\odot$. The luminosity at the turnover of period depends on the mass of the pre-white dwarf (lower luminosity for a less massive star), because the luminosity during the phase contracting toward the planetary nebulae nuclei region in the HR diagram is an increasing function of the mass. The numerical analysis by Kawaler, Hansen, and Winget (1985a) indicates that the periods of high order g-modes of a $0.95M_\odot$ pre-white dwarf model begin to increase when $L \sim 10^3 L_\odot$. On the other hand, analyzing the observed light curves, Winget, Kepler, Robinson, Nather, and O'Donoghue (1985) found that the period of a

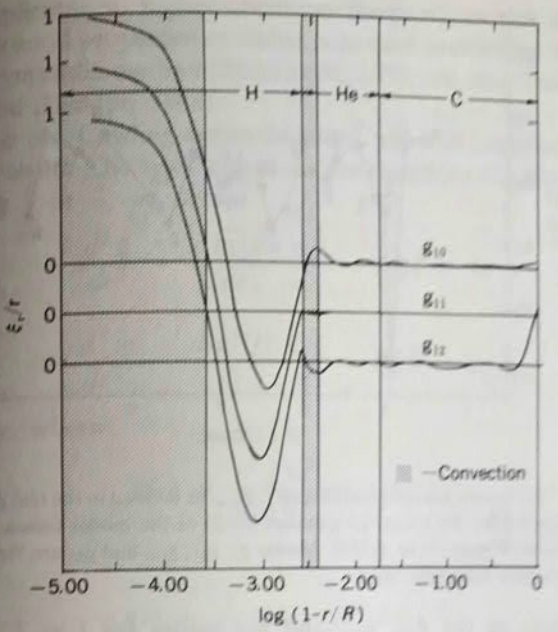

Fig. 15.15 Radial dependence of the eigenfunction ξ_r/r for the g_{10}, g_{11}, g_{12} modes ($l = 2$) of a compositionally stratified H/He/C white dwarf with $0.6M_\odot$, from Winget et al. (1981). The eigenfunctions are each normalized to unity at the stellar surface, but the curves are displaced from one another. The composition boundaries and convection zones are indicated by vertical divisions.

pre-white dwarf pulsator PG 1159–035 is decreasing. If the luminosity estimated for PG 1159–035, $L \sim 10^2 L_\odot$, is more or less valid, the observed period change of PG 1159–035 may suggest that the mass of this star is less than $0.95M_\odot$. One possible complexity is the helium shell flash. According to evolutionary models from the asymptotic giant branch to the white dwarf stage, the last helium flash occurs around the planetary nebulae nuclei phase. During a helium shell flash the stellar radius and hence the period of oscillations change largely on a time scale as short as $\sim 10^3$ yr (e.g., Iben, 1984). If PG 1159–035 is in a helium shell flash, its period change cannot be predicted as a function of its mass and luminosity.

The above properties do not depend on the detailed structure of white dwarfs. There are some interesting properties which depend on the composition stratification of the outer envelope of white dwarfs. Winget, Van Horn, and Hansen (1981) found that nonradial g-modes are selectively trapped in the chemically stratified envelope. Figure 15.15 (from Winget et al., 1981) shows the eigenfunctions for the radial

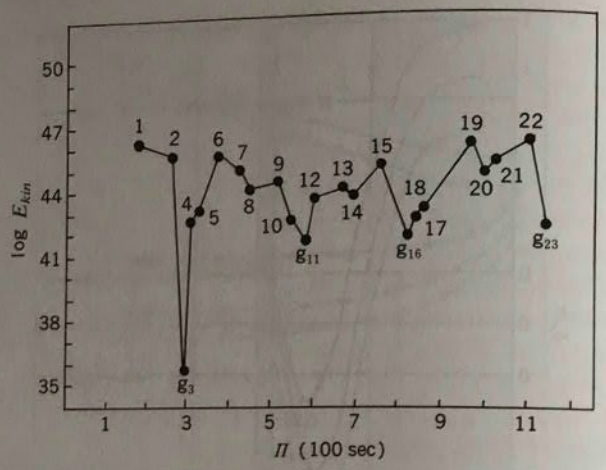

Fig. 15.16 The "kinetic energy of oscillation", E_{kin}, as defined in the text plotted against period for the lowest 23 g-modes ($l=2$) of the model shown in Fig. 15.15, from Winget, et al. (1981). Modes g_3, g_{11}, g_{16}, and g_{23} are "trapped" in the surface hydrogen layer.

displacements of the g_{10}, g_{11}, and g_{12} modes for $l = 2$, where the eigenfunctions are normalized to unity at the stellar surface. In this model the composition distribution at the interface is assumed to be discontinuous. In this figure, it is apparent that the amplitude in the core for g_{11} is small compared to those of g_{10} and g_{12}; i.e., the g_{11} mode is trapped in the white dwarf envelope. If a mode is trapped in the envelope, the kinetic energy of oscillations for a given amplitude at the surface, $E_{kin} = \frac{1}{2}\sigma^2 \int_0^M |\xi|^2 \, dM_r$ is small compared to the adjacent modes. Figure 15.16 shows the kinetic energy for several g-modes ($l = 2$). A mode with smaller E_{kin} can be considered to grow to observable amplitude more easily. Therefore, the trapping by the compositionally stratified envelope may be related to the groupings of the periods of ZZ Ceti stars. If this is true, the period of a ZZ Ceti star gives us information on the composition stratification of the outer envelope.

16. Modal Analysis by an Asymptotic Method

In the previous section we studied the local property and the qualitative characteristics of nonradial oscillation. To investigate them precisely for various modes in a realistic star, we need to solve the wave equations either by using numerical calculations or by using an asymptotic method. These two methods complement each other: the former is appropriate for lower overtones (small and intermediate n), while the

latter is applicable to higher overtones (large n). In this section, we study the general properties of stellar nonradial oscillations analytically using an asymptotic method (Shibahashi, 1979; see also Tassoul, 1980; Smeyers and Tassoul, 1988).

We use the Cowling approximation, which is accurate for large values of n and l. The basic equations are equations (15.5) and (15.6). Eliminating $\tilde{\xi}$ or $\tilde{\eta}$, we obtain

$$\frac{d^2\tilde{\xi}}{dr^2} - \frac{d\ln|P|}{dr}\frac{d\tilde{\xi}}{dr} - PQ\tilde{\xi} = 0 \qquad (16.1)$$

and

$$\frac{d^2\tilde{\eta}}{dr^2} - \frac{d\ln|Q|}{dr}\frac{d\tilde{\eta}}{dr} - PQ\tilde{\eta} = 0, \qquad (16.2)$$

respectively, where

$$P(r) = \frac{r^2}{c^2}\left(\frac{L_l^2}{\sigma^2} - 1\right)h(r) \qquad (16.3)$$

and

$$Q(r) = \frac{1}{r^2}(\sigma^2 - N^2)h(r)^{-1}. \qquad (16.4)$$

It should be noted that the zero value of $P(r)$ causes a regular singularity of equation (16.1) and not of equation (16.2), and the opposite is true for $Q(r)$. These equations should then be regarded as being complementary to each other. For the limiting case of $\sigma^2 \gg N^2$, equation (16.2) tends to the Sturm-Liouville type

$$\frac{d^2\tilde{\eta}}{dr^2} + \frac{d\ln(r^2h)}{dr}\frac{d\tilde{\eta}}{dr} - \frac{l(l+1)}{r^2}\tilde{\eta} = -\frac{\sigma^2}{c^2}\tilde{\eta}\,, \qquad (16.5)$$

and for the other limiting case of $\sigma^2 \ll N^2$, it tends to

$$\frac{d^2\tilde{\eta}}{dr^2} + \frac{d}{dr}\ln\left(\frac{r^2h}{N^2}\right)\frac{d\tilde{\eta}}{dr} - \frac{N^2}{c^2}\tilde{\eta} = -\frac{1}{\sigma^2}\frac{l(l+1)N^2}{r^2}\tilde{\eta}\,. \qquad (16.6)$$

Similarly, equation (16.1) tends to the Sturm-Liouville type

$$\frac{d^2\tilde{\xi}}{dr^2} + \frac{d}{dr}\ln\left(\frac{c^2}{r^2}h^{-1}\right)\frac{d\tilde{\xi}}{dr} - \frac{N^2}{c^2}\tilde{\xi} = -\frac{\sigma^2}{c^2}\tilde{\xi}\,, \qquad (16.7)$$

or

$$\frac{d^2\tilde{\xi}}{dr^2} + \frac{d}{dr}\ln(h^{-1})\frac{d\tilde{\xi}}{dr} - \frac{l(l+1)}{r^2}\tilde{\xi} = -\frac{1}{\sigma^2}\frac{l(l+1)N^2}{r^2}\tilde{\xi}\,, \qquad (16.8)$$

depending on whether $\sigma^2 \gg L_l^2$ or $\sigma^2 \ll L_l^2$. Since the only subsisting

term containing σ^2 is proportional to σ^2/c^2 in equations (16.5) and (16.7), their solutions must correspond to acoustic waves. On the other hand, the solutions of (16.6) and (16.8) correspond to gravity waves, for the frequency σ appears only in the form of $N^2[l(l+1)/r^2]/\sigma^2 = N^2k_h^2/\sigma^2$.

For convenience, we introduce the new variables v and w, defined by

$$v \equiv \tilde{\xi}|P|^{-1/2}\rho_c^{1/2} = \rho^{1/2}cr\left(\left|1-\frac{L_l^2}{\sigma^2}\right|\right)^{-1/2}\xi_r \qquad (16.9)$$

and

$$w \equiv \tilde{\eta}|Q|^{-1/2}\rho_c^{1/2} = \rho^{-1/2}r(|N^2-\sigma^2|)^{-1/2}p' , \qquad (16.10)$$

where ρ_c denotes the density at the stellar center. The basic equations (15.5) and (15.6) are then reduced to a pair of turning-point equations,

$$\frac{d^2v}{dr^2} + [k_r^2 - f(P)]v = 0 \qquad (16.11)$$

and

$$\frac{d^2w}{dr^2} + [k_r^2 - f(Q)]w = 0, \qquad (16.12)$$

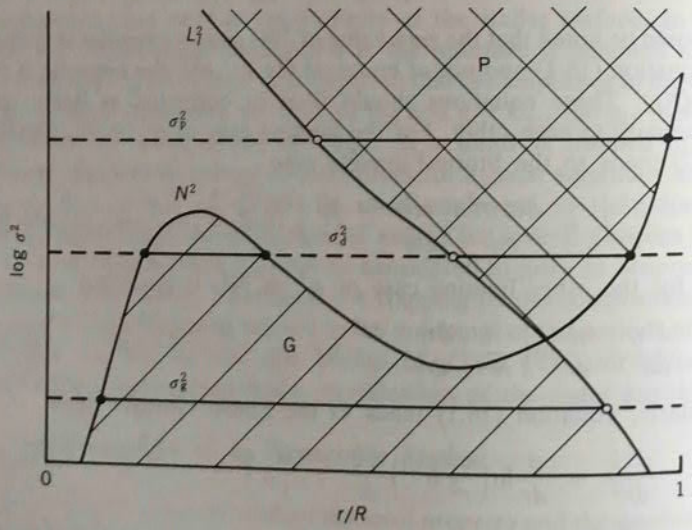

Fig. 16.1 Schematic propagation diagram of an idealized stellar model. The hatched region is the gravity-wave propagation zone and the cross-hatched region is the acoustic-wave propagation zone. Frequencies of three kinds of modes are indicated by the horizontal bars. Turning points of equations (16.11) and (16.12) are indicated by filled circles and open circles, respectively.

with $k_r^2 = -PQ$ given by equation (15.9) and

$$f(x) \equiv |x|^{1/2}\frac{d^2|x|^{-1/2}}{dr^2} \qquad (16.13)$$

The turning points are the points at which $k_r^2 - f(P) = 0$ and $k_r^2 - f(Q) = 0$ for equations (16.11) and (16.12), respectively.

Let us consider an idealized stellar model whose propagation diagram is illustrated in Fig. 16.1. For simplicity, we neglect the second terms in the brackets in the left-hand sides of equations (16.11) and (16.12), which are negligibly small compared with the first terms k_r^2 almost everywhere except near the singular points and the stellar surface. This approximation is especially valid for oscillations with short wavelengths in the radial direction. In this approximation, the singular points for one of these equations, at which $P = 0$ and $Q = 0$, respectively, coincide with the turning points for the other. Although such a coincidence is not necessarily required for the following discussion, it will simplify the mathematical treatment. In Fig. 16.1, the turning points of equations (16.11) and (16.12) are indicated by filled circles and open circles, respectively, at three kinds of frequencies. The hatched region is the gravity-wave propagation zone, in which $P > 0$, $Q < 0$ so that $k_r^2 > 0$, and the cross-hatched region, is the acoustic-wave propagation zone, in which $P < 0$, $Q > 0$ so that $k_r^2 > 0$. The other region is the evanescent zone, in which $k_r^2 < 0$.

We will solve the basic turning-point equations in terms of Airy functions by dividing the stellar interior into regions each having only one turning point, and then use asymptotic forms of Airy functions to join these regions in order to obtain a complete eigenfunction. The turning-point equation (16.12) is used to obtain the form of w near singular points for equation (16.11), at which $\sigma^2 = L_l^2$, and to deduce the form of v from dw/dr; conversely, equation (16.11) is used to obtain the solution of equation (16.12) near its singular points, at which $\sigma^2 = N^2$.

In the case of a high frequency denoted by σ_p in Fig. 16.1, an acoustic-wave propagation zone extends from a turning point r_a to another turning point r_b ($r_a < r_b$). To obtain the function w in the region containing the turning point r_a—that is, for $0 \le r < r_b$—it is appropriate to introduce a Liouville transformation, which transforms variables (w, r) to (W, ζ), by

$$\zeta \equiv \left(\frac{dr}{d\zeta}\right)^2 [k_r^2 - f(Q)] = \left(\frac{dr}{d\zeta}\right)^2 k_r^2 \qquad (16.14)$$

and

$$W \equiv \left(\left|\frac{dr}{d\zeta}\right|\right)^{-1/2} w \tag{16.15}$$

(see, e.g., Oliver, 1954; Langer, 1959). Then, it is readily verified that W satisfies the equation

$$\frac{d^2W}{d\zeta^2} + \left[\zeta - f\left(\frac{dr}{d\zeta}\right)\right]W = 0 \ , \tag{16.16}$$

where $f(x)$ is the regular function defined by (16.13). To the first approximation in which $f(dr/d\zeta)$ is neglected, the solution W is represented by

$$W = aAi(\zeta) + bBi(\zeta) \ , \tag{16.17}$$

where $Ai(\zeta)$ and $Bi(\zeta)$ denote the Airy functions of the first kind and of the second kind, respectively, which are related to Bessel functions of 1/3 order as

$$\left.\begin{aligned} Ai(\zeta) &= \frac{1}{3}\left[\zeta^{1/2}J_{-1/3}\left(\frac{2}{3}\zeta^{3/2}\right) + \zeta^{1/2}J_{1/3}\left(\frac{2}{3}\zeta^{3/2}\right)\right] \\ Bi(\zeta) &= \frac{1}{\sqrt{3}}\left[\zeta^{1/2}J_{-1/3}\left(\frac{2}{3}\zeta^{3/2}\right) - \zeta^{1/2}J_{1/3}\left(\frac{2}{3}\zeta^{3/2}\right)\right] \end{aligned}\right\} \tag{16.18}$$

and a, b are constant coefficients. For large values of $|\zeta|$, Airy functions take the asymptotic forms given by

$$\left.\begin{aligned} Ai(\zeta) &\sim \frac{1}{2\sqrt{\pi}}(-\zeta)^{-1/4}\exp\left[-\frac{2}{3}(-\zeta)^{3/2}\right] \\ Bi(\zeta) &\sim \frac{1}{\sqrt{\pi}}(-\zeta)^{-1/4}\exp\left[\frac{2}{3}(-\zeta)^{3/2}\right] \end{aligned}\right\} \tag{16.19}$$

for $\zeta < 0$, and

$$\left.\begin{aligned} Ai(\zeta) &\sim \frac{1}{\sqrt{\pi}}\zeta^{-1/4}\cos\left[\frac{2}{3}\zeta^{3/2} - \frac{\pi}{4}\right] \\ Bi(\zeta) &\sim -\frac{1}{\sqrt{\pi}}\zeta^{-1/4}\sin\left[\frac{2}{3}\zeta^{3/2} - \frac{\pi}{4}\right] \end{aligned}\right\} \tag{16.20}$$

for $\zeta > 0$. The combination of equations (16.14), (16.15), and (16.17) leads to the form of the function w

$$w = |k_r|^{-1/2}\left(\left|\frac{3}{2}\int_{r_a}^{r}|k_r|dr\right|\right)^{1/6}[aAi(\zeta) + bBi(\zeta)] \ , \tag{16.21}$$

where ζ is given by

$$\zeta = \mathrm{sgn}(k_r^2)\left(\left|\frac{3}{2}\int_{r_a}^{r}|k_r|dr\right|\right)^{2/3} \tag{16.22}$$

and the symbol $\mathrm{sgn}(x) \equiv |x|/x$ means the sign of function x. Substituting equations (16.19) and (16.20) into equation (16.21), we obtain the asymptotic form of the function w which is written as

$$w \sim \begin{cases} \dfrac{a}{2\sqrt{\pi}}\dfrac{1}{\sqrt{\kappa}}\exp\left(-\displaystyle\int_r^{r_a}\kappa dr\right) + \dfrac{b}{\sqrt{\pi}}\dfrac{1}{\sqrt{\kappa}}\exp\left(\displaystyle\int_r^{r_a}\kappa dr\right) & \text{for } r \ll r_a \\ \dfrac{a}{\sqrt{\pi}}\dfrac{1}{\sqrt{k_r}}\cos\left(\displaystyle\int_{r_a}^{r}k_r dr - \frac{\pi}{4}\right) - \dfrac{b}{\sqrt{\pi}}\dfrac{1}{\sqrt{k_r}}\sin\left(\displaystyle\int_{r_a}^{r}k_r dr - \frac{\pi}{4}\right) & \text{for } r_a \ll r, \end{cases} \tag{16.23}$$

with $\kappa^2 \equiv -k_r^2$. The coefficient b must be equal to zero for the regularity of the function w at the center $r = 0$. Otherwise the upper second term in the right-hand side of equation (16.23) diverges at $r = 0$, because $\kappa \approx [l(l+1)]^{1/2}/r$ in the region $r \ll r_a$ as a result of the inequality $N^2 \ll \sigma^2 \ll L_l^2$. To the same approximation as used for equation (16.23), equation (15.6) can be written as

$$\begin{aligned} v &= \mathrm{sgn}(Q)|k_r|^{-1}\left(\frac{dw}{dr} + \frac{1}{2}\frac{d\ln|Q|}{dr}w\right) \\ &\simeq \mathrm{sgn}(Q)|k_r|^{-1}\frac{dw}{dr} \ . \end{aligned} \tag{16.24}$$

Substituting equation (16.23) with $b = 0$ into (16.24), we obtain the asymptotic form of the function v for $r \gg r_a$

$$v \sim -\frac{a}{\sqrt{\pi}}\frac{1}{\sqrt{k_r}}\sin\left(\int_{r_a}^{r}k_r dr - \frac{\pi}{4}\right) \ . \tag{16.25}$$

In a similar way, equation (16.11) is used to obtain the function v for $r_a < r$. The function v takes the asymptotic form given by

$$v \sim \begin{cases} \dfrac{c}{\sqrt{\pi}}\dfrac{1}{\sqrt{k_r}}\cos\left(\displaystyle\int_r^{r_b}k_r dr - \frac{\pi}{4}\right) - \dfrac{d}{\sqrt{\pi}}\dfrac{1}{\sqrt{k_r}}\sin\left(\displaystyle\int_r^{r_b}k_r dr - \frac{\pi}{4}\right) & \text{for } r_a \ll r \ll r_b \\ \dfrac{c}{2\sqrt{\pi}}\dfrac{1}{\sqrt{\kappa}}\exp\left(-\displaystyle\int_{r_b}^{r}\kappa dr\right) + \dfrac{d}{\sqrt{\pi}}\dfrac{1}{\sqrt{\kappa}}\exp\left(\displaystyle\int_{r_b}^{r}\kappa dr\right) & \text{for } r_b \ll r \end{cases} \tag{16.26}$$

with two constant coefficients c and d. The asymptotic form of the function w is reduced from equation (16.26) to

$$w \sim -\frac{c}{\sqrt{\pi}}\frac{1}{\sqrt{k_r}}\sin\left(\int_r^{r_b} k_r dr - \frac{\pi}{4}\right) - \frac{d}{\sqrt{\pi}}\frac{1}{\sqrt{k_r}}\cos\left(\int_r^{r_b} k_r dr - \frac{\pi}{4}\right) \tag{16.27}$$

for $r_a \ll r \ll r_b$. Two kinds of asymptotic expression of the functions v and w for $r_a \ll r \ll r_b$ must agree with each other. Eliminating the coefficient d from the combination of equations (16.23) (with $b = 0$) and (16.27), and from that of equations (16.25) and (16.26), we obtain

$$c = -a\sin\left(\int_{r_a}^{r_b} k_r dr - \frac{\pi}{2}\right). \tag{16.28}$$

Similarly, we obtain

$$d = -a\cos\left(\int_{r_a}^{r_b} k_r dr - \frac{\pi}{2}\right). \tag{16.29}$$

In the expression of v for $r_b \ll r$ given by equation (16.26) the term with the coefficient c in the right-hand side represents the evanescent wave coming from the stellar interior. But the second term with the coefficient d represents the wave coming from the outside of the star and must then vanish. We set $d = 0$ as the outer boundary condition of equation (16.11) or (16.12). As seen from equation (16.29), the condition for $d = 0$ is satisfied if and only if

$$\int_{r_a}^{r_b} k_r dr = n\pi \tag{16.30}$$

with an integer n. This is the condition for eigenoscillation corresponding to Bohr-Sommerfeld's quantization rule in quantum mechanics. It should be noted that the right-hand side of equation (16.30) is not $(n + 1/2)\pi$ as in the latter quantization rule, but $n\pi$. This is due to the different properties of the two evanescent zones ($r < r_a$ and $r_b < r$) as a result of the different combination of signs of P and Q there.

The coefficients b and d are equal to zero, and the coefficient c is equal to $(-1)^n a$ as a result of the condition (16.30). There are n nodes of the function of v, which correspond to nodes of the function ξ_r in the propagation zone. Such eigenmodes are classified as p_n-modes after the number of nodes of the function ξ_r.

The quantization rule (16.30) leads to the eigenfrequency σ_n of the p_n-mode (Gough, 1986c; Smeyers, Briers, Tassoul, Degryse, Polfliet, and Van Hoolst, 1988). The outer turning point r_b is, in most cases, very close to the photosphere. So we approximate $r_b \approx R$ and replace the upper boundary of the integral in equation (16.30) by R. By estimating quantity k_r in the propagation zone to be

$$k_r \approx \begin{cases} \sigma/c & \text{for } r_a \ll r \ll R \\ c^{-1}(\sigma^2 - L_l^2)^{1/2} & \text{for } r \sim r_a, \end{cases} \tag{16.31}$$

and by substituting it into equation (16.30), we obtain

$$\int_{r_a}^{r^*} c^{-1}(\sigma^2 - L_l^2)^{1/2} dr + \sigma\int_{r^*}^{R} c^{-1} dr = n\pi, \tag{16.32}$$

where r^* is a radial distance below which the sound velocity is almost equal to its value at the center c_0. We assume that, for $r > r^*$, the ratio L_l^2/σ^2 may be neglected in comparison to unity. By integrating the first term in the left-hand side of equation (16.32) we have

$$\sigma\int_{r_a}^{r^*} c^{-1}\left[1 - \frac{l(l+1)c^2}{\sigma^2 r^2}\right]^{1/2} dr$$

$$\approx \sigma c_0^{-1}\left[(r^{*2} - r_a^2)^{1/2} - \sigma^{-1}[l(l+1)]^{1/2} c_0 \cos^{-1}(r_a/r^*)\right]. \tag{16.33}$$

In the case of a high overtone ($n \gg 1$) with low degree ($l \sim 1$) p-mode, the inner turning point r_a is very close to the stellar center, and then we set $r_a \approx 0$ so that

$$\sigma\int_{r_a}^{r^*} c^{-1}\left[1 - \frac{l(l+1)c^2}{\sigma^2 r^2}\right]^{1/2} dr$$

$$\approx \sigma\int_0^{r^*} c^{-1} dr - [l(l+1)]^{1/2}\pi/2. \tag{16.34}$$

Adding the second integral in the left-hand side of equation (16.32), we obtain the eigenfrequency σ_{nl} of the p_n-mode

$$\sigma_{nl} \approx 2\pi\nu_0(n + l/2 + \epsilon), \tag{16.35}$$

where

$$\nu_0 = \left[2\int_0^R \frac{1}{c} dr\right]^{-1} \tag{16.36}$$

and ϵ is a constant. This formula is valid for high overtone p-modes with low degree (Vandakurov, 1967; Tassoul, 1980; Smeyers and Tassoul, 1988).

In the case of an oscillation with a low frequency denoted by σ_g in Fig. 16.1, the procedure for obtaining eigenfunctions is the same as in

the case of the acoustic mode with a high frequency σ_p. Let r_a and r_b be the radial coordinates of the two turning points ($r_a<r_b$). The final results of asymptotic forms of eigenfunctions are given by

$$v\sim\begin{cases}\dfrac{a}{2\sqrt{\pi}}\dfrac{1}{\sqrt{\kappa}}\exp\left(-\displaystyle\int_r^{r_a}\kappa dr\right) & \text{for } r\ll r_a\\[2ex] \dfrac{a}{\sqrt{\pi}}\dfrac{1}{\sqrt{k_r}}\cos\left(\displaystyle\int_{r_a}^{r}k_r dr-\frac{\pi}{4}\right)\\[2ex] \quad=\dfrac{a}{\sqrt{\pi}}\dfrac{(-1)^{n+1}}{\sqrt{k_r}}\sin\left(\displaystyle\int_r^{r_b}k_r dr-\frac{\pi}{4}\right) & \text{for } r_a\ll r\ll r_b\\[2ex] \dfrac{a}{2\sqrt{\pi}}\dfrac{(-1)^n}{\sqrt{\kappa}}\exp\left(-\displaystyle\int_{r_b}^{r}\kappa dr\right) & \text{for } r_b\ll r\end{cases}\tag{16.37}$$

and

$$w\sim\begin{cases}\dfrac{a}{2\sqrt{\pi}}\dfrac{1}{\sqrt{\kappa}}\exp\left(-\displaystyle\int_r^{r_a}\kappa dr\right) & \text{for } r\ll r_a\\[2ex] -\dfrac{a}{\sqrt{\pi}}\dfrac{1}{\sqrt{k_r}}\sin\left(\displaystyle\int_{r_a}^{r}k_r dr-\frac{\pi}{4}\right)\\[2ex] \quad=\dfrac{a}{\sqrt{\pi}}\dfrac{(-1)^n}{\sqrt{k_r}}\cos\left(\displaystyle\int_r^{r_b}k_r dr-\frac{\pi}{4}\right) & \text{for } r_a\ll r\ll r_b\\[2ex] \dfrac{a}{2\sqrt{\pi}}\dfrac{(-1)^n}{\sqrt{\kappa}}\exp\left(-\displaystyle\int_{r_b}^{r}\kappa dr\right) & \text{for } r_b\ll r,\end{cases}\tag{16.38}$$

and the eigenvalue condition is

$$\int_{r_a}^{r_b}k_r dr = n\pi.\tag{16.39}$$

with an integer n. Such eigenmodes are classified as g_n-modes after the number of nodes, n, of the eigenfunction v. Estimating the quantity k_r to be

$$k_r\approx\frac{L_l N}{\sigma c}=\frac{[l(l+1)]^{1/2}N}{r}\frac{1}{\sigma}\tag{16.40}$$

in the region $r_a\ll r\ll r_b$ using the inequality $\sigma^2\ll L_l^2$, we obtain

$$\sigma_n\approx\frac{[l(l+1)]^{1/2}}{n\pi}\int_{r_a}^{r_b}\frac{N}{r}dr.\tag{16.41}$$

This formula for σ_n is, however, formal, since the turning point r_a depends strongly on the frequency σ_n itself in usual cases. For the case of higher-gravity modes with low frequencies in a massive star in the main-sequence stage, r_a and r_b correspond to the outer edge of the convective core and the stellar surface, respectively, and are practically independent of σ_n.

Eigensolution properties can be most clearly depicted in the phase diagram. If we plot the solution in the (v, w)-plane, starting from the stellar center and proceeding toward the surface, it describes a curve. This is the phase diagram, and its path is called the phase path. For simplicity, we use the asymptotic forms of Airy functions even near the turning points. The combination of equation (16.24) and the corresponding equation for w then leads to

$$\frac{dv}{dw}=\text{sgn}\,(PQ)\frac{w}{v}\,.\tag{16.42}$$

The phase point thus moves along a path given by

$$v^2+\text{sgn}\,(k_r^2)w^2=\text{const.},\tag{16.43}$$

which is a circle in a propagating zone and a hyperbola in an evanescent zone. If the functions v and w are expressed in terms of the polar coordinates as

$$\begin{pmatrix}v\\w\end{pmatrix}=R(r)\begin{pmatrix}\cos\lambda(r)\\\sin\lambda(r)\end{pmatrix},\tag{16.44}$$

the functions $R(r)$ and $\lambda(r)$ obey

$$\frac{d\ln R}{dr}=|k_r|[\text{sgn}(P)+\text{sgn}(Q)]\cos\lambda\sin\lambda\tag{16.45}$$

and

$$\frac{d\lambda}{dr}=|k_r|[-\text{sgn}(P)\sin^2\lambda+\text{sgn}(Q)\cos^2\lambda]\,.\tag{16.46}$$

The general behavior of the phase diagram is easy to see from these equations. The phase point moves clockwise around the origin in a gravity-wave zone where $P>0$ and $Q<0$, while it moves counterclockwise in an acoustic-wave zone where $P<0$ and $Q>0$. It moves along a hyperbola from the second or the fourth quadrant to the first or the third quadrant in an evanescent zone in which both P and Q

are positive, and in the opposite direction in an evanescent zone in which both P and Q are negative. The characteristic movement is schematically shown in Fig. 16.2. The inner boundary condition requires the phase point to start from the origin and to move along the straight line $v = w$ in the innermost evanescent zone ($P > 0$ and $Q > 0$ there). On the other hand, the phase point is required to move to the origin along the line $v = w$ in the outermost evanescent zone ($P < 0$ and $Q < 0$). This is possible only for certain discrete values of σ^2. These values are eigenvalues, and the corresponding solutions are eigensolutions. Figure 16.3 shows the phase diagrams of a g-mode and a p-mode. It is clearly seen that the phase point starts from the origin and moves along the line $v = w$ until it reaches at the inner edge of the propagation zone ($r = r_a$). For the case of g-mode with frequency σ_g, the phase point rotates clockwise around the origin in the propagation zone, and it finally moves along the line $v = w$ in the outermost evanescent zone ($r_b < r$). On the other hand, for the case of p-mode with frequency σ_p, it rotates counterclockwise in the propagation zone as shown in Fig. 16.3. It is clearly seen that the phase in the asymptotic form of v given by

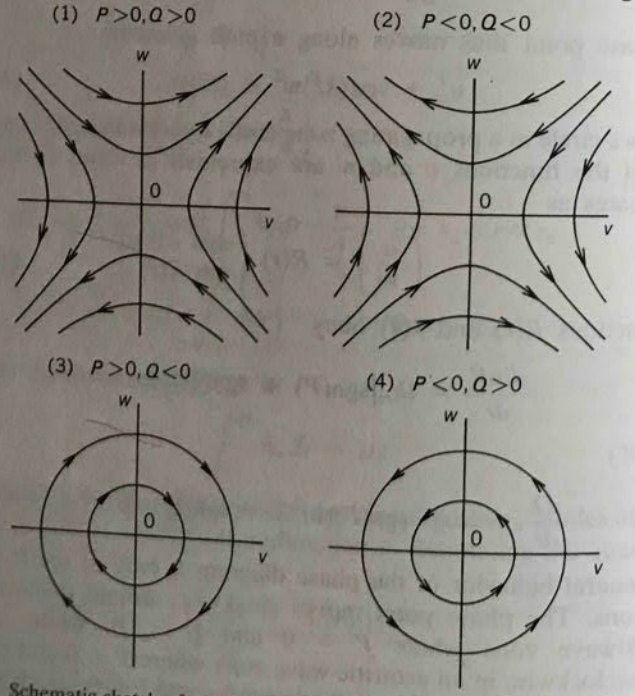

Fig. 16.2 Schematic sketch of phase paths for two kinds of evanescent waves [(1) and (2)], gravity waves (3), and acoustic waves (4).

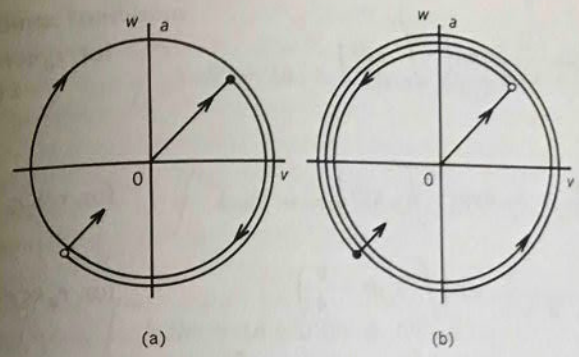

Fig. 16.3 Schematic phase diagrams of a simple g-mode [left; (a)] and of a simple p-mode [right; (b)]. Filled circles indicate turning points of equations (16.11) and (16.12), respectively.

equation (16.25) corresponds to the phase angle measured clockwise from the phase point at $r = r_a$. Conditions (16.30) and (16.39) are then interpreted as the conditions requiring the phase point of an eigenmode to move along the line $v = w$ in both the innermost and the outermost evanescent zones.

In the case of a mode with such a frequency σ_d as is shown in Fig. 16.1, there are four turning points. Let the radial coordinates of these points be r_a, r_b, r_c, and r_d ($r_a < r_b < r_c < r_d$). The manipulation for obtaining the eigenfunctions and the eigenvalue condition is lengthy but parallel to that used in the case of simple modes. The final results of asymptotic forms of eigenfunctions are given by

$$
v \sim \begin{cases}
\dfrac{a}{2\sqrt{\pi}} \dfrac{1}{\sqrt{\kappa}} \exp\left(-\displaystyle\int_r^{r_a} \kappa dr\right) & \text{for } r \ll r_a \\
\dfrac{a}{\sqrt{\pi}} \dfrac{1}{\sqrt{k_r}} \cos\left(\displaystyle\int_{r_a}^{r} k_r dr - \dfrac{\pi}{4}\right) & \text{for } r_a \ll r \ll r_b \\
\dfrac{a}{2\sqrt{\pi}} \dfrac{1}{\sqrt{\kappa}} \sin\left(\displaystyle\int_{r_a}^{r_b} k_r dr\right) \exp\left(-\displaystyle\int_{r_b}^{r} \kappa dr\right) & \\
\quad + \dfrac{a}{\sqrt{\pi}} \dfrac{1}{\sqrt{\kappa}} \cos\left(\displaystyle\int_{r_a}^{r_b} k_r dr\right) \exp\left(\displaystyle\int_{r_b}^{r} \kappa dr\right) & \text{for } r_b \ll r \ll r_c \\
\dfrac{c}{\sqrt{\pi}} \dfrac{1}{\sqrt{k_r}} \cos\left(\displaystyle\int_r^{r_d} k_r dr - \dfrac{\pi}{4}\right) & \text{for } r_c \ll r \ll r_d
\end{cases}
$$

$$\left|\ \frac{c}{2\sqrt{\pi}}\frac{1}{\sqrt{\kappa}}\exp\left(-\int_{r_d}^{r}\kappa dr\right) \qquad \text{for } r_d \ll r \right. \tag{16.47}$$

and

$$w\sim\begin{cases} \dfrac{a}{2\sqrt{\pi}}\dfrac{1}{\sqrt{\kappa}}\exp\left(-\displaystyle\int_{r}^{r_a}\kappa dr\right) & \text{for } r \ll r_a \\ -\dfrac{a}{\sqrt{\pi}}\dfrac{1}{\sqrt{k_r}}\sin\left(\displaystyle\int_{r_a}^{r}k_r dr-\frac{\pi}{4}\right) & \text{for } r_a \ll r \ll r_b \\ -\dfrac{a}{2\sqrt{\pi}}\dfrac{1}{\sqrt{\kappa}}\sin\left(\displaystyle\int_{r_a}^{r_b}k_r dr\right)\exp\left(-\displaystyle\int_{r_b}^{r}\kappa dr\right) & \\ \quad +\dfrac{a}{\sqrt{\pi}}\dfrac{1}{\sqrt{\kappa}}\cos\left(\displaystyle\int_{r_a}^{r_b}k_r dr\right)\exp\left(\displaystyle\int_{r_b}^{r}\kappa dr\right) & \text{for } r_b \ll r \ll r_c \\ -\dfrac{c}{\sqrt{\pi}}\dfrac{1}{\sqrt{k_r}}\sin\left(\displaystyle\int_{r}^{r_d}k_r dr-\frac{\pi}{4}\right) & \text{for } r_c \ll r \ll r_d \\ \dfrac{c}{2\sqrt{\pi}}\dfrac{1}{\sqrt{\kappa}}\exp\left(-\displaystyle\int_{r_d}^{r}\kappa dr\right) & \text{for } r_d \ll r, \end{cases} \tag{16.48}$$

where two constants a and c are related each other by a condition

$$c=a\left[2\cos\left(\int_{r_a}^{r_b}k_r dr\right)\cos\left(\int_{r_c}^{r_d}k_r dr\right)\exp\left(\int_{r_b}^{r_c}\kappa dr\right)\right.$$
$$\left.+\frac{1}{2}\sin\left(\int_{r_a}^{r_b}k_r dr\right)\sin\left(\int_{r_c}^{r_d}k_r dr\right)\exp\left(-\int_{r_b}^{r_c}\kappa dr\right)\right], \tag{16.49}$$

and the eigenvalue condition is given by

$$\cot\left(\int_{r_a}^{r_b}k_r dr\right)\tan\left(\int_{r_c}^{r_d}k_r dr\right)=\frac{1}{4}\exp\left(-2\int_{r_b}^{r_c}\kappa dr\right). \tag{16.50}$$

The quantity κ in the evanescent zone is estimated as $\kappa \approx [l\,(l+1)]^{1/2}/r$ if $N^2 \ll \sigma^2 \ll L_l^2$. The right-hand side of equation (16.50) is then given by

$$\frac{1}{4}\exp\left(-2\int_{r_b}^{r_c}\kappa dr\right)\approx\frac{1}{4}(r_c/r_b)^{-2l}\ , \tag{16.51}$$

and is estimated as $10^{-l} \ll 1$ if $r_c/r_b \approx 3$ in typical cases (Shibahashi and Osaki, 1976a). Let this small quantity be ϵ $(0 < \epsilon \ll 1)$. In this case, one

of the three conditions

$$\int_{r_a}^{r_b}k_r dr \approx (n\ +\ 1/2)\pi\ +\ O(\epsilon), \tag{16.52}$$

or

$$\int_{r_c}^{r_d}k_r dr \approx m\pi\ +\ O(\epsilon)\ , \tag{16.53}$$

or

$$\left.\begin{aligned}\int_{r_a}^{r_b}k_r dr &\approx (n+1/2)\pi\ \pm\ O(\sqrt{\epsilon}) \\ \int_{r_c}^{r_d}k_r dr &\approx m\pi\ \mp\ O(\sqrt{\epsilon})\end{aligned}\right\}, \tag{16.54}$$

with integers n and m must be satisfied in order for the value of the left-hand side of equation (16.50) to be negligibly small. It should be noted that conditions (16.52) and (16.53) cannot simultaneously satisfy the eigenvalue condition (16.50), of which the right-hand side is of the order of magnitude of ϵ.

When condition (16.52) holds, the order of magnitude of the coefficient c is $(-1)^{n+m}(r_c/r_b)^{-l}a$. Since the kinetic energy of the oscillation $(\sigma^2\rho r^2\xi^2)$ is proportional to $v^2 + w^2$, the ratio of the energies trapped within the inner propagation zone $(r_a < r < r_b)$ and the outer propagation zone $(r_c<r<r_d)$ is evaluated by a^2/c^2, that is:

$$\frac{(\rho r^2\xi^2)_{\text{inner zone}}}{(\rho r^2\xi^2)_{\text{outer zone}}} \approx (r_c/r_b)^{2l}\ , \tag{16.55}$$

and it is estimated as 10^{+l} if $r_c/r_b \approx 3$. We find in Section 17.2 that this estimate is in good agreement with the numerical results of Shibahashi and Osaki (1976a). In this case, the oscillation is mainly associated with the gravity-wave propagation zone $(r_a < r < r_b)$. On the other hand, when condition (16.53) holds, the left-hand side of equation (16.55) is approximated by $(r_c/r_b)^{-2l}$ and the oscillation is effectively trapped in the acoustic-wave propagation zone $(r_c < r < r_d)$. Condition (16.52) is then regarded as the mode trapping condition for the gravity-wave propagation zone, while (16.53) is regarded as that for the acoustic-wave propagation zone. Condition (16.52) includes a half-integer as in Bohr-Sommerfeld's quantization rule because the evanescent zones on both sides of the gravity-wave propagation zone have the same combination of signs of P and Q in this case. It should be noted that the left-hand sides of equations (16.52) and (16.53) are not exactly equal to

$(n + 1/2)\pi$ and $m\pi$, respectively.

When condition (16.54) holds, a mode-mixing phenomenon occurs. The absolute value of the coefficient c is the same order of magnitude as that of the coefficient a. The kinetic energy of the oscillation trapped within one of the propagation zones is therefore the same order of magnitude as that trapped in the other, and the mode behaves like a trapped gravity wave in the inner gravity-wave zone and like a trapped acoustic wave in the envelope. Condition (16.54) is then regarded as a mode-mixing condition.

Let us consider an eigenfrequency satisfying either (16.52) or (16.53) for a given model. Suppose the frequency gradually increases. At first, conditions (16.52)–(16.54) all break down. The wave number k_r in the gravity-wave zone ($\sigma < N, L_l$) decreases as a result of equation (16.40), and the extent of the gravity-wave zone is shortened. Therefore, the integral of k_r over the segment $[r_a, r_b]$ monotonically decreases. On the other hand, the integral of k_r in the gravity-wave zone soon comes close to $(n - 1/2)\pi$, or that in the acoustic-wave zone becomes close to $(m + 1)\pi$, and one of the eigenvalue conditions (16.52), (16.53) will be satisfied again. However, if both the integrals of k_r simultaneously approach $(n - 1/2)\pi$ and $(m + 1)\pi$ accidentally, the eigenvalue condition (16.54) is satisfied neither by conditions (16.52) nor (16.53) but by condition (16.54). In such a case there are two eigenvalues, which are slightly different, corresponding to the pair of signs ($\pm$) in equation (16.54). This means that accidental degeneracies of the modes never occur, but a pair of mixed character modes appear whenever two eigenvalues draw near. This property causes stepwise variation (or "avoided crossing," cf. Gabriel and Scuflaire, 1979) in eigenfrequency with increasing l for a fixed model, which has also been found in the case of terrestrial atmospheric oscillations (see, e.g., Francis, 1973; Jones, 1976).

Figure 16.4 shows the phase diagrams of two kinds of combined modes. The phase point starts from the origin and moves along the line of $v = w$ until it reaches the inner edge of the gravity-wave zone ($r = r_a$). Moving around clockwise in the gravity-wave zone ($r_a < r < r_b$), it reaches the inner edge of the middle evanescent zone ($r = r_b$). If condition (16.52) is met, the phase point at $r = r_b$ is on the second or the fourth quadrant. Then it moves inward along the hyperbola in the evanescent zone ($r_b < r < r_c$) as seen in Fig. 16.4(a). After moving around counterclockwise in the acoustic-wave zone ($r_c < r < r_s$), it moves along the line $v = w$ to satisfy the outer boundary condition. On the other hand, if condition (16.53) is satisfied, the phase point moves along a path such as is shown in Fig. 16.4(b). The phase diagram of such

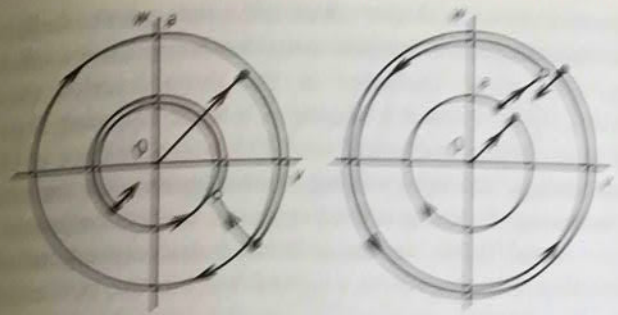

(a) (b)

Fig. 16.4 Schematic phase diagrams of a well-trapped mode in the inner gravity-wave zone [left; (a)] and of a well-trapped mode in the outer acoustic-wave zone [right; (b)].

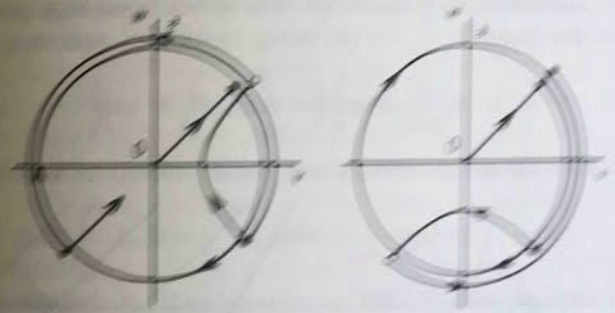

(a) (b)

Fig. 16.5 Phase diagrams of two kinds of mixed-character modes. Their frequencies and properties are very near but slightly different. The frequency of the mode on the left (a) is slightly higher than that of the mode on the right (b).

eigenmodes for a massive star is seen in Shibahashi and Osaki (1976a), in which the coordinates $(\xi_r/r, l\xi_h/r)$ are used instead of (v, w).

When condition (16.54) is satisfied, the phase point moves along a path such as shown in Figs. 16.5(a) or 16.5(b), depending on whether the sign is positive or negative for the last term in the right-hand side of the second equations (16.54). The radius of the phase track is naturally the same order of magnitude for both propagation zones.

In some massive evolved stars the lower-gravity modes trapped in the inner gravity-wave zone have such high frequencies that waves cannot be reflected at the outer boundary, and they take on progressive-wave character in the envelope (see Section 18; Shibahashi and Osaki, 1976b). Also, the higher-gravity modes of low frequencies may not be reflected at the outer boundary (see Section 18). In some giant stars, the

acoustic waves trapped in the envelope cannot reach the stellar center as a result of strong radiative dissipation in the deep interior, and they also show progressive-wave character in the deep interior (see Section 15.3.3; Osaki, 1977). In such a situation, a wave trapping region should be treated as an isolated pulsating unit with wave leakage in the form of a progressive wave. Strictly speaking, such eigenmodes are not standing waves. However, if an evanescent zone exists between the two propagation zones, those modes still have discrete eigenfrequencies, and the situation is analogous to a virtual level in the potential problem in quantum mechanics.

Assume a nonradial mode with such an eigenfrequency $\sigma_{\bar{G},\mathrm{low}}$ as shown in the propagation diagram of Fig. 16.6. The oscillation is trapped in the inner gravity-wave zone and leaks outward in the form of a progressive acoustic wave in the envelope. We denote three turning points as r_a, r_b, and r_c ($r_a < r_b < r_c$). The outer boundary condition is then set in the form of

$$v,\ w \propto \frac{1}{\sqrt{k_r}} \exp\left[i\left(-\int_{r_c}^{r} k_r dr + \sigma t\right)\right] \qquad (16.56)$$

for $r_c \ll r$, since the group velocity and phase velocity of acoustic waves

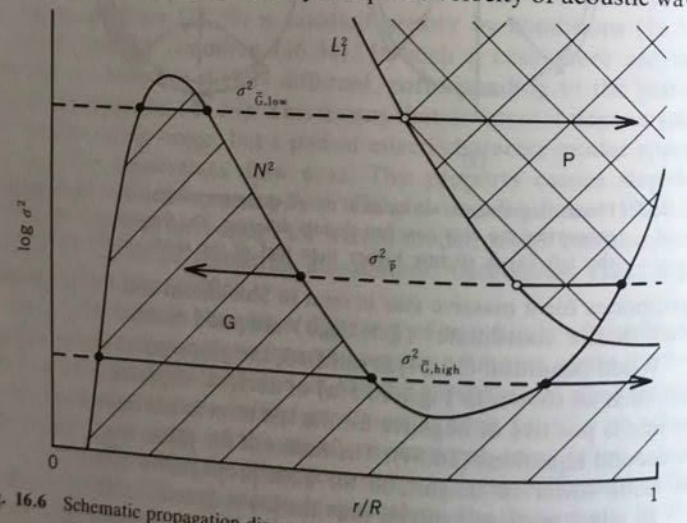

Fig. 16.6 Schematic propagation diagram of an idealized stellar model in an advanced stage. Frequencies of various kinds of modes having progressive-wave character are indicated by the horizontal bars. Turning points of equations (16.11) and (16.12) are indicated by filled circles and open circles, respectively. The arrows indicate the directions of leakage of wave energy, which are those of group velocity of progressive waves.

in the radial direction have the same sign. After some manipulation similar to that used previously we obtain the eigenvalue condition

$$\tan\left(\int_{r_a}^{r_b} k_r dr - \frac{\pi}{2}\right) \exp\left(2\int_{r_b}^{r_c} \kappa dr\right) = -\frac{i}{4} . \qquad (16.57)$$

The eigenvalue σ is complex even in the adiabatic approximation as a result of leakage of wave energy. In the gravity-wave zone the wave number k_r is then reduced from equation (16.40) to

$$k_r = k_\mathrm{R} + ik_\mathrm{I} \approx \frac{NL_l}{c}\left(\frac{1}{\sigma_\mathrm{R}} - i\frac{\sigma_\mathrm{I}}{\sigma_\mathrm{R}^2}\right) , \qquad (16.58)$$

where σ_R and σ_I are the real part and the imaginary part of σ, respectively. On the other hand, the quantity κ is estimated as the real quantity $\kappa \approx [l\,(l+1)]^{1/2}/r$ in the evanescent region $r_b < r < r_c$. After substituting equation (16.58) into equation (16.57) we obtain new forms of the eigenvalue condition given by

$$\int_{r_a}^{r_b} k_\mathrm{R} dr = \left(n + \frac{1}{2}\right)\pi \qquad (16.59)$$

and

$$\tanh\int_{r_a}^{r_b} k_\mathrm{I} dr \approx \int_{r_a}^{r_b} k_\mathrm{I} dr = -\frac{1}{4}\exp\left(-2\int_{r_b}^{r_c} \kappa dr\right) \qquad (16.60)$$

with an integer n. The condition (16.59) corresponds to Bohr-Sommerfeld's quantization rule, and equation (16.60) represents the effect of leakage. Using equations (16.58) and (16.59), equation (16.60) is rewritten as

$$\frac{\sigma_\mathrm{I}}{\sigma_\mathrm{R}} \approx \frac{1}{4}\frac{1}{(n+1/2)\pi}\exp\left(-2\int_{r_b}^{r_c} \kappa dr\right)$$

$$\approx \frac{1}{4}\frac{1}{(n+1/2)\pi}\left(\frac{r_c}{r_b}\right)^{-2l} . \qquad (16.61)$$

Since the temporal dependence of the functions v and w is $\exp(i\sigma t)$, this equation represents the damping rate as a result of wave leakage. The right-hand side of equation (16.61) is estimated as $10^{-l} \ll 1$ if $r_c/r_b \approx 3$ in typical cases (see Shibahashi and Osaki, 1976b).

In some evolved stars, higher gravity modes trapped in the inner gravity-wave zone with frequencies $\sigma_{\bar{G},\mathrm{high}}$ as shown in Fig. 16.6 leak outward in the form of progressive gravity waves in the envelope. In such a case, the outer boundary condition must then be set in a form similar to equation (16.56) except for the sign in front of the integral;

the group velocity and phase velocity of gravity waves in the radial direction have the opposite sign. The eigenvalue condition and the damping rate are naturally the same forms as those of equations (16.59) and (16.61).

The effect of wave leakage into the stellar deep interior upon the acoustic modes trapped in the envelope is dealt with in a similar way. Assume a nonradial mode with such an eigenfrequency σ_p as shown in Fig. 16.6. We denote three turning points r_b, r_c, and r_d ($r_b < r_c < r_d$). The oscillation is trapped in the envelope and takes on progressive gravity-wave character in the region $r < r_b$. Choosing the inward progressive wave, we must set the inner boundary condition at

$$v,\ w \propto \frac{1}{\sqrt{k_r}} \exp\left[i\left(\int_r^{r_b} k_r dr + \sigma t\right)\right] \tag{16.62}$$

for $r \ll r_b$. After some manipulation we obtain the eigenvalue condition

$$\tan\left(\int_{r_c}^{r_d} k_r dr\right) \exp\left(2\int_{r_b}^{r_c} \kappa dr\right) = \frac{i}{4} . \tag{16.63}$$

Using the approximate form of the wave number in the acoustic wave zone $k_r = k_R + ik_I \approx (\sigma_R + i\sigma_I)/c$, we finally obtain another form of the eigenvalue condition given by

$$\int_{r_c}^{r_d} k_r dr = m\pi \tag{16.64}$$

with an integer m, and the damping rate given by

$$\frac{\sigma_I}{\sigma_R} \approx \frac{1}{4}\frac{1}{m\pi} \exp\left(-2\int_{r_b}^{r_c} \kappa dr\right)$$

$$\approx \frac{1}{4}\frac{1}{m\pi}\left(\frac{r_c}{r_b}\right)^{-2l} . \tag{16.65}$$

The effect of wave leakage upon the damping rate is then estimated as 10^{-l} if $r_c/r_b \approx 3$. This estimate is in good agreement with the result of numerical calculations (Osaki, 1977).

In treating a pair of turning-point equations (16.11) and (16.12), we have assumed that the values of N^2 and L_l^2 vary slowly in the stellar interior—that is, $|k_r^2| \gg |f(P)|, |f(Q)|$. In some realistic stellar models this assumption breaks down, because the Brunt-Väisälä frequency N^2 may sharply vary at the edge of the convective region. The turning points $[k_r^2 - f(P) = 0]$ of equation (16.11) then do not strictly coincide with the singular points of equation (16.12), at which $\sigma^2 = N^2$. The value of N^2 can, however, vary slowly in the other parts. Therefore, the present treatment can be valid even in such a case, if the first exact equality in equation (16.14) is used for the variable ζ.

In the above analysis, we have used asymptotic forms of Airy functions. But, in order for this approximation to be valid, the turning points must be well separated. In other words, there must be many oscillations of the wave functions in the propagation zone, and the evanescent zone must extend widely. Therefore, the treatment used here is especially valid for eigenmodes having many nodes in the radial direction with large l of spherical harmonics $Y_l^m(\theta, \phi)$. However, the qualitative aspects of the present modal analysis can be valid even for lower harmonics and overtones.

17. Modal Classification

We have seen in previous sections that linear adiabatic nonradial oscillations show different physical and geometrical characteristics depending upon the frequency and the horizontal wave number. There are g- and p-mode sequences of eigenfrequencies and an f-mode (except for the case of $l = 1$) for a given l. The g- and p-mode sequences are attributed to the G and P propagation zones, respectively (see Fig. 15.3). Classifying nonradial oscillation modes is easy for a simple stellar structure such as a less centrally condensed polytrope or a zero-age main-sequence star, because only one propagation zone is responsible for a given eigenfrequency (except for an f-mode) and the frequency ranges of the g- and the p-modes are separated clearly (see Figs. 15.2 and 15.3). As the evolution proceeds, however, the maximum value of the Brunt-Väisälä frequency in the core increases, which leads to avoided crossings between a g-mode and a p-mode (or f-mode) as discussed in Section 15.3.1. The frequency ranges for the G-type and P-type propagation zones come to overlap with each other. In such cases, the classification of nonradial eigenmodes is not trivial. We will discuss how to classify the nonradial oscillation modes in an evolved star.

17.1 Phase Diagram and Generalized Cowling Nomenclature

In the previous section, it has been shown that if we plot an eigenfunction in the (v, w) diagram the point moves counterclockwise around the origin in the acoustic-wave (P) zone while it moves clockwise in a gravity-wave (G) zone as r increases. Thus, it is convenient to use a phase diagram in classifying nonradial oscillation modes. We use the (ξ_r, ξ_h) phase diagram rather than the (v, w) diagram because the former is directly related to the eigenfunction of displacement vector. The two

phase diagrams have the same general properties, because in the Cowling approximation, ξ_r and ξ_h are related to v and w through

$$\xi_r = f_1(r,\sigma)v \tag{17.1}$$

and

$$\xi_h = f_2(r,\sigma)w \tag{17.2}$$

with positive-definite functions $f_1(r,\sigma)$ and $f_2(r,\sigma)$ given by

$$f_1(r,\sigma) = \rho^{-1/2}c^{-1}r^{-1}(|1-L_l^2/\sigma^2|)^{1/2} \tag{17.3}$$

and

$$f_2(r,\sigma) = \sigma^{-2}\rho^{-1/2}r^{-2}(|N^2 - \sigma^2|)^{1/2}. \tag{17.4}$$

A sample of the (ξ_r, ξ_h) phase diagram is shown in Fig. 17.1 for the five lowest modes (g_2, g_1, f, p_1, p_2) of $l = 2$ for the ZAMS model of a $10M_\odot$ star, whose propagation diagram and eigenfunctions for ξ_r are shown in Figs. 15.3 and 15.4, respectively. In Fig. 17.1 the open circle indicates the stellar center and filled circles indicate the stellar surface. Obviously, in the phase diagram the curves for g-modes and p-modes cross the line of $\xi_r = 0$ (i.e., at a node of ξ_r) clockwise and counterclockwise, respectively.

Figure 17.2 shows the main-sequence evolution in the HR diagram for the $10M_\odot$ star whose propagation diagrams at some evolutionary stages were shown in Figs. 15.3 and 15.6. The numbers along the evolutionary track indicate the model numbers counted from the ZAMS stage. The propagation diagrams in Figs. 15.6(a) and (b) are for the models of Nos. 4 and 13, respectively. As the evolution proceeds, the Brunt-Väisälä frequency in the stellar interior increases due to the

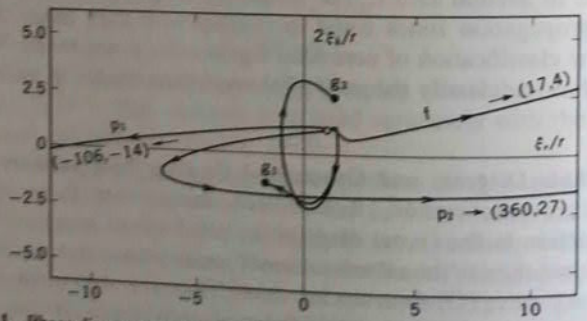

Fig. 17.1 Phase diagram showing the five lowest modes (g_2, g_1, f, p_1, p_2) of $l = 2$ for the ZAMS model with $M = 10M_\odot$. The phase points at the surface are (17,4) for f-mode, (-106, -14) for p_1-mode, and (360,27) for p_2-mode (after Osaki, 1975).

increase of the central condensation and the formation of a μ-gradient zone (see Fig. 15.6), and the frequencies of g-modes increase. Avoided crossings of modes occur when the star evolves enough (see Section 15.3.1). In such an evolved star, the frequency ranges for the G-type and P-type propagation zones overlap significantly. The eigenfunction for the mode whose frequency falls in the overlapped range has extra nodes. These modes with extra nodes correspond to the modes with frequencies like σ_d, shown in Fig. 16.1, which have two propagation zones.

Figure 17.3 shows eigenfunctions of the relative radial displacement ξ_r/r for the lowest three modes of $l = 2$ for the evolved model of Fig. 16.5(b) (model No.13; see Fig. 17.2). The eigenvalues $\omega^2[\equiv \sigma^2/(GM/R^3)]$ of these three modes are 27.2, 22.6, and 11.2, respectively. These modes can be continuously connected to p_1-, f-, and g_1-modes, respectively, of the ZAMS model as shown in Fig. 17.4, where eigenvalues ω^2 are plotted against the model numbers. The existence of extra nodes is apparent in Fig. 17.3. Such extra nodes also appear in eigenfunctions for polytropic models with high central condensation (Owen, 1957; Robe, 1968), in which the maximum of the Brunt-Väisälä frequency in the core region is significantly larger than the minimum frequency of the P zone in the outer part.

The phase diagrams for these modes are shown in Fig. 17.5. They behave like gravity waves in the μ-gradient zone but like acoustic waves in the outer part of the star. We can classify nodes of the eigenfunction

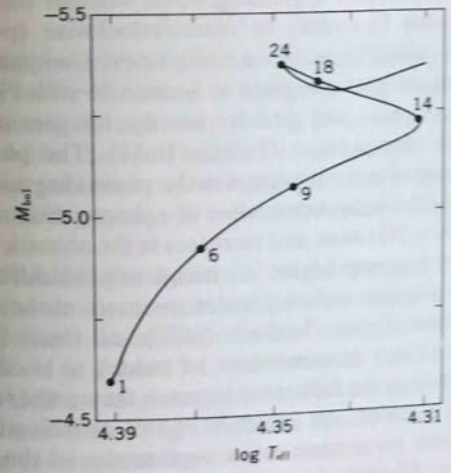

Fig. 17.2 Evolutionary track of a $10M_\odot$ star near the main sequence (from Osaki, 1976).

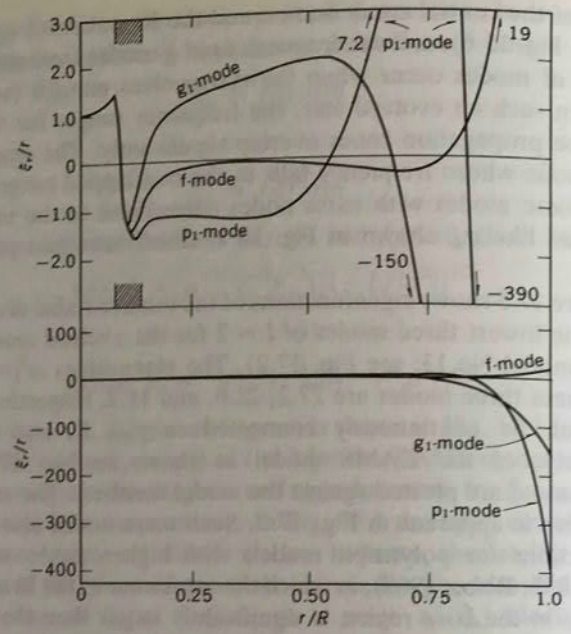

Fig. 17.3 Eigenfunctions of the relative radial displacement ξ_r/r for the same model as in Fig. 15.6 (b).The upper figure shows details of eigenfunctions in the inner part, while the lower figure does the same in the outer part. The hatched area indicates the zone with a varying chemical composition (from Osaki, 1975).

into g-nodes and p-nodes, depending upon whether the phase point is traveling clockwise (g-nodes) or counterclockwise (p-nodes) at the crossings of the axis $\xi_r/r = 0$, as r increases. Comparing asymptotic expressions of eigenfunctions given in Section 16 with Fig. 17.5, we see that the numbers of p- and g-nodes are the integers m and n in the right-hand sides of equations (16.52)–(16.54). The phase angle (the angle at which eigenfunction sweeps in the phase diagram as r increases from the inner to the outer boundaries of a propagation zone) decreases in the gravity-wave (G) zone and increases in the acoustic-wave (P) zone as the frequency becomes higher. Consequently the difference between the number of p-nodes and of g-nodes increases monotonically as the frequency becomes higher. Scuflaire (1974) and Osaki (1975) generalized Cowling's (1941) nomenclature of modes to oscillations having extra nodes by taking the difference between the number of p-nodes and the number of g-nodes. An example of this classification is given in Table 17.1, which gives consecutive eigenmodes of the $10M_\odot$ No. 13 model (see Figs. 15.6(b), 17.4) for $l = 2$ in order of increasing $\omega^2[= \sigma^2/(GM/R^3)]$. The third column shows the number of g-nodes, N_g, and

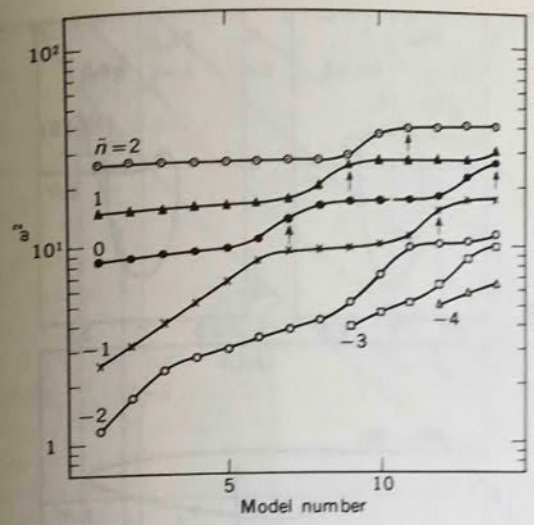

Fig. 17.4 The variation in dimensionless eigenvalues of nonradial modes ($l = 2$) with the evolutionary model sequence (after Osaki, 1975). The abscissa is the model number (see, Fig. 17.2). The arrows indicate the model where a new pair of nodes appears for a given mode. They are models Nos. 7 and 14 for $\bar{n} = 0$ mode, model No. 9 for $\bar{n} = 1$ mode, model No. 11 for $\bar{n} = 2$ mode, and model No. 12 for $\bar{n} = -1$ mode. As for the definition of $\bar{n}$, see equation (17.5).

the fourth column shows the number of p-nodes, N_p. We find that their difference,

$$\bar{n} = N_p - N_g, \tag{17.5}$$

is monotonic with respect to ω^2 and conserved during the evolutionary change of the stellar structure as shown in Fig.17.4. Therefore, the number $\bar{n}$ defined in equation (17.5) is suitable as the index of classification, while the total number of nodes (the second column of Table 17.1) does not behave as well. By using this nomenclature, we can easily pick up all the modes in a given frequency range for a given l.

17.2 Mode Classification Based on Modal Property

The weakness of the nomenclature discussed above is that it does not necessarily represent the characteristic of the mode. For example, the mode with $\bar{n} = -1$ in Table 17.1, which has the same ordinal number $\bar{n}$ as g_1 of the ZAMS model, has eigenvalue ω^2 similar to that of p_1-mode of the ZAMS model (see Fig. 17.4) and should have the character of p_1-mode in the envelope, as discussed in Section 15.3.1. As explained in Section 16, if the two propagation zones are widely separated by an intermediate evanescent zone, oscillation modes can be classified into

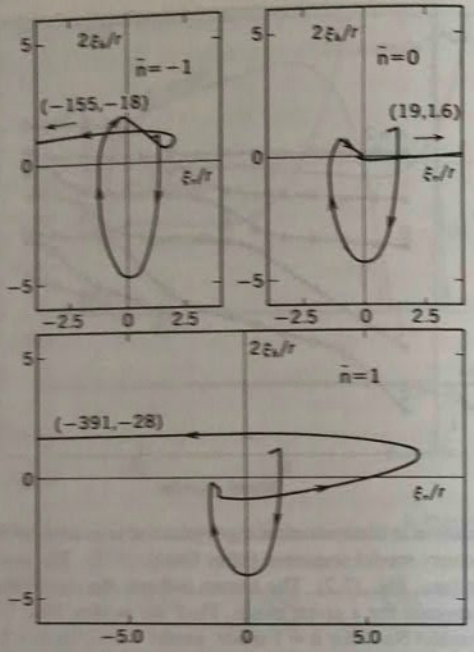

Fig. 17.5 Phase diagrams for the modes shown in Fig. 17.3 (after Osaki, 1975). The modes denoted as $\bar{n} = -1, 0$, and 1 correspond to g_1-, f-, and p_1-modes in Fig. 17.3, respectively. The phase points at the surface are $(-155, -18)$ for the $\bar{n} = 1$ mode, (19, 1.6) for the $\bar{n} = 0$ mode, and $(-391, -28)$ for the $\bar{n} = 1$ mode. As for the definition of $\bar{n}$, see equation (17.5).

Table 17.1 Relation between the number of nodes and the ordinal number $\bar{n}$ for the nonradial oscillations of $l=2$ for the $10M_\odot$ model whose propagation diagram is shown in Fig. 15.6b.

ω^2	Total number of nodes	N_g	N_p	$\bar{n}$ $(N_p - N_g)$
5.859	4	4	0	−4
8.698	3	3	0	−3
10.62	2	2	0	−2
17.18	3	2	1	−1
22.58	2	1	1	0
27.24	3	1	2	1
40.07	4	1	3	2
55.86	5	1	4	3
74.31	6	1	5	4
88.57	5	0	5	5
96.71	6	0	6	6
120.5	7	0	7	7

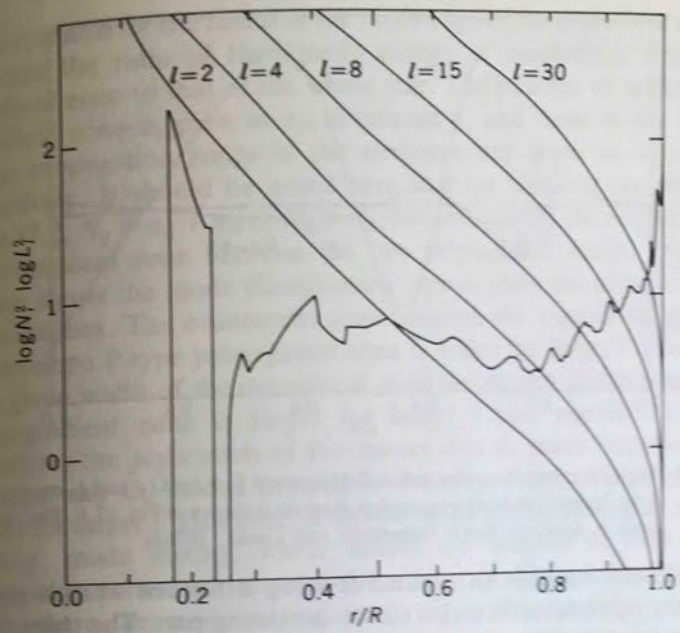

Fig. 17.6 Propagation diagram for an evolved model of a $30M_\odot$ star. The quantities N^2 and L_l^2 are measured in units of GM/R^3 (from Shibahashi and Osaki, 1976a).

two types by observing their mainly trapped propagation zones. (When the frequencies of two modes are similar, an avoided crossing occurs and the modes are trapped in both propagation zones; the modes, then, have mixed character.) Shibahashi and Osaki (1976a) introduced a classification scheme based on the characteristic in the main trapping zone. In this classification $\bar{G}_n$ indicates the mode trapped mainly in the μ-gradient zone having n g-nodes there and $\bar{P}_m$ denotes the mode trapped in the envelope acoustic-wave (P) zone having m p-nodes there. The symbol $\bar{g}_n$ is used for the mode trapped mainly in the envelope G zone separated from the "μ-gradient G zone". The overbar represents classification based on the characteristic in the main trapping zone. According to this classification, the modes with $\bar{n} = 1, 0, -1$, and -2 in Table 17.1, for example, are classified as $\bar{p}_2$-, $\bar{G}_2$-, $\bar{p}_1$-, and $\bar{f}$-modes, respectively. Comparing Fig. 17.5 with a phase diagram for the ZAMS model, Fig. 17.1, we see that the $\bar{f}$- and $\bar{p}_n$-modes have the same physical property as the f- and p_n-modes of the ZAMS (simple) model. In Fig. 17.4, the parts which show gradual increase in frequency with evolution correspond to the modes trapped in the envelope (i.e., $\bar{g}_n$-, $\bar{f}$-, and $\bar{p}_n$-modes), while the rapidly increasing parts (for example, $\bar{n} = -1$ modes between model Nos. 2 and 6, $\bar{n} = -2$ modes between model Nos. 9 and 11, etc.) correspond to $\bar{G}_n$ modes, whose frequencies tend to zero

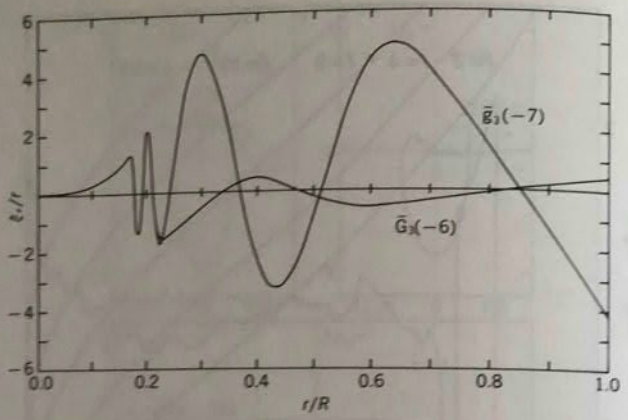

Fig. 17.7 Eigenfunctions of relative radial displacement ξ_r/r for $\bar{G}_3$- and $\bar{g}_3$-modes of $l = 4$ for the model whose propagation diagram is shown in Fig. 17.6. The ordinate scale is arbitrary (from Shibahashi and Osaki, 1976a).

for the ZAMS model. An avoided crossing is formed when a rapidly increasing part intersects with a slowly increasing part. The characteristic behavior in the lower frequency part (i.e., avoided crossings between $\bar{G}_n$ modes and $\bar{g}_n$ modes) is more clearly seen in Fig. 1 of Roth and Weigert (1979).

The propagation diagram of nonradial oscillations for an evolved $30M_\odot$ star is shown in Fig. 17.6. This model consists of the homogeneous convective core, the μ-gradient zone, the thin convective shell just outside the original convective core, and the radiative envelope. Since the thin convective shell behaves like an evanescent zone, the gravity waves with low frequencies are divided into modes trapped mainly in the μ-gradient zone ($\bar{G}_n$ modes) and those trapped in the envelope G zone ($\bar{g}_n$ modes). Figure 17.7 shows eigenfunctions of the relative radial displacement ξ_r/r for the $\bar{G}_3$- and $\bar{g}_3$-modes of $l = 4$ for the model shown in Fig. 17.6. The difference between the two modes is clearly seen. Numbers in parentheses in this figure are the ordinal numbers $\bar{n}$ defined by equation (17.5).

The results of numerical calculations are summarized in Table 17.2 for various values of l for the $30M_\odot$ model. The column headings in this table are the ordinal number of modes $\bar{n}$, the number of nodes of gravity-wave and pressure-wave type N_g and N_p, respectively, and the dimensionless eigenvalue defined by $\omega^2 = \sigma^2 R^3/GM$. The quantity Δ in column 5 is defined by

$$\Delta = \frac{\int_0^{r_s} \rho|\boldsymbol{\xi}|^2 4\pi r^2 dr}{\int_0^{R} \rho|\boldsymbol{\xi}|^2 4\pi r^2 dr}, \qquad (17.6)$$

where r_s stands for the radius at the outer edge of the μ-gradient zone. It measures the ratio of the kinetic energy of oscillations within the μ-gradient zone to that of the whole star. The number of nodes in the μ-gradient zone is given as $n_{\bar{G}}$ in column 6, and those in the G- and P-type propagation zones in the envelope are given as $n_{\bar{g}}$ and $n_{\bar{p}}$, respectively. It should be noted here that for some of the modes in Table 17.2, $N_g \neq n_{\bar{g}} + n_{\bar{G}}$ or $N_p \neq n_{\bar{p}}$, because one of the nodes exists in the evanescent zone between the two propagation zones. The ninth column shows the mode classification representing the physical nature of oscillations. The evanescent zone between the μ-gradient zone and the envelope P-type propagation zone is wider for larger l. Moreover, for a given width of the evanescent zone the degree of the trapping in the μ-gradient zone is larger for larger l [see equation (16.55)]. Therefore, the separation of the modes into $\bar{p}_n$ mode trapped in the envelope and $\bar{G}_n$-modes trapped in the μ-gradient zone is generally clearer for larger l. However, it should be noted that during an avoided crossing, mode mixing, where modes are trapped in both of the propagation zones, occurs even for a large l, although the frequency range where the mode mixing occurs is smaller for larger l.

Figure 17.8 shows the relation between eigenfrequencies ω^2 and l for modes specified in our classification scheme, and it corresponds to the diagnostic diagram shown in Fig. 15.1 because $k_h = [l(l+1)]^{1/2}/r$. The envelope modes of $\bar{p}_n$, $\bar{f}$, and $\bar{g}_n$ are connected by solid lines, while gravity modes $\bar{G}_n$ trapped in the μ-gradient zone are connected by dashed lines. The saturation effect of eigenfrequencies is seen for the envelope gravity-modes $\bar{g}_n$ at a moderate value of l, but not for $\bar{G}_n$-modes until $\omega^2 \sim 100$ ($l \gtrsim 30$). The reason for the difference is that the profile of N^2 in the μ-gradient zone has a narrow but high peak with $N^2_{max} \simeq 100$, while in the envelope N^2 shows a wide but moderately high plateau with $N^2 \simeq 8$ (Fig. 17.6). The dispersion relation for pure internal gravity waves, $\sigma = Nk_h/k$ (see subsection 15.2), indicates that saturation will occur when $k_h \gtrsim k_r$. Since $k_h \sim l/r$ and $k_r \sim \pi/\Delta r$ where Δr stands for the width of the G-type propagation zone, the condition for the occurrence of the saturation is reduced to $l \gtrsim \pi r/\Delta r$. The difference in the saturation effect of eigenmodes between $\bar{G}_n$ and $\bar{g}_n$-modes is thus caused by the difference in the width of the propagation zone and the maximum value of N^2. It should be noted that the diagnostic diagram (Fig. 17.8) gives information on the internal structure of the star; therefore, it is the basis of helio- and asteroseismology (see Chapter VII).

To specify nonradial modes, we shall hereafter utilize both the generalized Cowling classification based on the ordinal number $\bar{n}$ and

Table 17.2 Pulsational properties for nonradial modes of the evolved $30M_\odot$ model whose propagation diagram is shown in Fig. 17.6.

$\hat{n}$	N_g	N_p	ω^2	Δ	$n_{\bar{G}}$	$n_{\bar{g}}$	$n_{\bar{p}}$	Mode
l=2:								
1	0	1	17.28	0.476	**0***	0	1	$\bar{G}_0$
0	1	1	14.04	0.269	0	0	**1**	$\bar{p}_1$
−1	1	0	8.121	0.404×10^{-1}	1	**0**	0	$\bar{f}$
−2	2	0	2.548	0.731	**1**	1	0	$\bar{G}_1$
l=4:								
1	1	2	29.30	0.853	**0**	0	2	$\bar{G}_0$
0	1	1	19.93	0.165×10^{-2}	1	0	**1**	$\bar{p}_1$
−1	1	0	10.15	0.122×10^{-2}	1	**0**	0	$\bar{f}$
−2	2	0	6.562	0.824	**1**	0	0	$\bar{G}_1$
l=8:								
2	0	2	46.58	0.975	**0**	0	2	$\bar{G}_0$
1	1	2	41.36	0.851×10^{-6}	0	0	**2**	$\bar{p}_2$
0	1	1	26.68	0.112×10^{-6}	1	0	**1**	$\bar{p}_1$
−1	1	0	15.44	0.907	**1**	0	0	$\bar{G}_1$
l=15:								
2	0	2	64.13	1.00	**0**	0	2	$\bar{G}_0$
1	1	2	57.40	0.882×10^{-14}	1	0	**2**	$\bar{p}_2$
0	1	1	37.80	0.293×10^{-14}	1	0	**1**	$\bar{p}_1$
−1	1	0	28.99	0.983	**1**	0	0	$\bar{G}_1$
−2	2	0	20.51	0.726×10^{-14}	2	**0**	0	$\bar{f}$
−3	3	0	16.58	0.935	**2**	1	0	$\bar{G}_2$
−4	4	0	10.81	0.921	**3**	1	0	$\bar{G}_3$
−5	5	0	7.167	0.947	**4**	1	0	$\bar{G}_4$
−6	6	0	6.368	0.243×10^{-3}	4	1	0	$\bar{g}_1$
−7	7	0	5.160	0.921×10^{-3}	5	**2**	0	$\bar{g}_2$
−8	8	0	4.950	0.960	**5**	3	0	$\bar{G}_5$
−9	9	0	3.823	0.356×10^{-2}	6	**3**	0	$\bar{g}_3$
−10	10	0	3.570	0.958	**6**	4	0	$\bar{G}_6$
l=30:								
1	2	2	83.61	1.00	**0**	0	2	$\bar{G}_0$
0	1	1	61.69	0.881×10^{-36}	1	0	**1**	$\bar{p}_1$
−1	1	0	49.20	1.00	**1**	0	0	$\bar{G}_1$
−2	2	0	35.02	0.380×10^{-35}	2	**0**	0	$\bar{f}$

*Numbers boldface are used for the mode identification in column 9.

the classification based on the oscillation property in the mainly trapped zone, depending on the problem and on the degree of trapping of eigenmodes to a certain zone. These two different classifications are complementary.

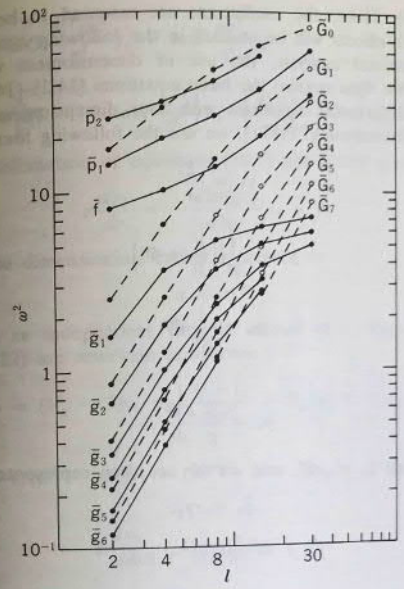

Fig. 17.8 Variation in dimensionless eigenvalues ω^2 of various modes with the degree l for the same model as in Figs. 17.6 and 17.7 (from Shibahashi and Osaki, 1976a). The solid lines: envelope $\bar{p}$-, $\bar{f}$-, $\bar{g}$-modes; the dashed lines: $\bar{G}$-modes. Filled circles and open circles indicate vibrationally stable and unstable modes, respectively (see Chapter V).

18. Numerical Method

18.1 Dimensionless Formulation of Equations and Boundary Conditions

In contrast to the asymptotic method which is suitable for qualitative study and has better adaptability to higher overtone oscillations, numerical investigation can give high accuracy, especially for the study of lower overtone oscillations with realistic stellar models.

In this section, the Cowling approximation is not adopted, and the full fourth-order differential equations or an equivalent set of simultaneous equations are treated. The basic equations are equations

(14.2)–(14.4). Here, the oscillations are assumed to be adiabatic. Nonadiabatic effects will be studied in the following chapter.

In numerical analysis, the use of dimensionless variables is preferred. We thus rewrite the basic equations (14.2)–(14.4) in four first-order differential equations with four dimensionless variables. Following Dziembowski (1971), we use the following four variables:

$$y_1 = \frac{\xi_r}{r}, \tag{18.1}$$

$$y_2 = \frac{1}{gr}\left(\frac{p'}{\rho} + \Phi'\right), \tag{18.2}$$

$$y_3 = \frac{1}{gr}\Phi', \tag{18.3}$$

and

$$y_4 = \frac{1}{g}\frac{d\Phi'}{dr}. \tag{18.4}$$

The variables ξ_r, p', Φ', and $d\Phi'/dr$ are then represented by

$$\xi_r = ry_1, \tag{18.5}$$

$$p' = \rho gr(y_2 - y_3), \tag{18.6}$$

$$\Phi' = gry_3, \tag{18.7}$$

and

$$\frac{d\Phi}{dr} = gy_4. \tag{18.8}$$

The substitution of (18.5)–(18.8) into equations (14.2), (14.3), and (14.4) gives

$$r\frac{dy_1}{dr} = \left(\frac{gr}{c^2} - 3\right)y_1 + \frac{gr}{c^2}\left(\frac{L_l^2}{\sigma^2} - 1\right)y_2 + \frac{gr}{c^2}y_3, \tag{18.9}$$

$$r\frac{dy_2}{dr} = -(N^2 - \sigma^2)\frac{r}{g}y_1 - \left[\frac{gr}{c^2} + \frac{d\ln(\rho g)}{d\ln r} + 1\right]y_2 + \left(\frac{gr}{c^2} + \frac{d\ln\rho}{d\ln r}\right)y_3, \tag{18.10}$$

and

$$r\frac{dy_4}{dr} = 4\pi G\frac{N^2\rho r^2}{g^2}y_1 + 4\pi G\frac{\rho r^2}{c^2}y_2 + \left[l(l+1) - 4\pi G\frac{\rho r^2}{c^2}\right]y_3 - \left[\frac{d\ln(gr)}{d\ln r} + 1\right]y_4, \tag{18.11}$$

and the combination of equations (18.7) and (18.8) gives

$$r\frac{dy_3}{dr} = -\frac{d\ln(gr)}{d\ln r}y_3 + y_4. \tag{18.12}$$

Further, the dimensionless radius x defined by

$$x = r/R \tag{18.13}$$

is used as an independent variable instead of r. Then, equations (18.9)–(18.12) are rewritten as follows:

$$x\frac{dy_1}{dx} = (V_g - 3)y_1 + \left[\frac{l(l+1)}{c_1\omega^2} - V_g\right]y_2 + V_g y_3, \tag{18.14}$$

$$x\frac{dy_2}{dx} = (c_1\omega^2 - A^*)y_1 + (A^* - U + 1)y_2 - A^* y_3, \tag{18.15}$$

$$x\frac{dy_3}{dx} = (1 - U)y_3 + y_4, \tag{18.16}$$

and

$$x\frac{dy_4}{dx} = UA^* y_1 + UV_g y_2 + [l(l+1) - UV_g]y_3 - Uy_4, \tag{18.17}$$

where

$$V_g = \frac{V}{\Gamma_1} = -\frac{1}{\Gamma_1}\frac{d\ln p}{d\ln r} = \frac{gr}{c^2}, \quad U \equiv \frac{d\ln M_r}{d\ln r} = \frac{4\pi\rho r^3}{M_r}, \tag{18.18}$$

$$c_1 \equiv (r/R)^3/(M_r/M), \tag{18.19}$$

$$\omega^2 = \sigma^2 R^3/(GM), \tag{18.20}$$

and

$$A^* \equiv -rA = rg^{-1}N^2. \tag{18.21}$$

In this way, the basic equations of linear adiabatic nonradial oscillation are reduced to simultaneous first-order differential equations (18.14)–(18.17), in which the coefficients are expressed in terms of

dimensionless stellar equilibrium quantities.

These equations form an eigenvalue problem with their proper boundary conditions. The boundary conditions were briefly examined in Section 14. However, the discussion will be more precise here, and the use of the present dimensionless variables is more convenient for actual computations.

If the oscillation is seriously nonadiabatic in the atmosphere, the adiabatic solution should be terminated at the interface where the interface conditions require the continuity of y_1, y_2, y_3, and y_4. In this procedure, we can first solve the oscillation in the atmosphere with the appropriate surface boundary conditions and then derive two asymptotic relations among y_1, y_2, y_3, and y_4, that are satisfied towards the adiabatic interior by eliminating arbitrary constants of integration. This is the basic idea of deriving the two outer boundary conditions for the interior oscillations. However, since the conditions of oscillation differ greatly from one mode of oscillation to another and from one star to another, we will outline here the procedure of deriving the boundary conditions taking, as an example, the simplest case where the oscillation is adiabatic all the way to the atmosphere (*cf.* Section 14.1 and Section 21).

Near the center, dimensionless quantities of stellar equilibrium structure approach their central values as follows:

$$\left.\begin{aligned} U &\to 3 + O(x^2) \\ V &\to 0 + O(x^2) \\ A^* &\to 0 + O(x^2) \end{aligned}\right\} \quad \text{as} \quad x \to 0. \tag{18.22}$$

Equations (18.14)–(18.17) may then be regarded as differential equations with constant coefficients near the center:

$$x\frac{d}{dx}\begin{pmatrix} y_1 \\ y_2 \\ y_3 \\ y_4 \end{pmatrix} = (a_{ij})\begin{pmatrix} y_1 \\ y_2 \\ y_3 \\ y_4 \end{pmatrix} \tag{18.23}$$

with the constant coefficient matrix

$$(a_{ij}) = \begin{pmatrix} -3 & \frac{l(l+1)}{c_1\omega^2} & 0 & 0 \\ c_1\omega^2 & -2 & 0 & 0 \\ 0 & 0 & -2 & 1 \\ 0 & 0 & l(l+1) & -3 \end{pmatrix} \tag{18.24}$$

The characteristic equation

$$\det(a_{ij} - \lambda\delta_{ij}) = 0, \tag{18.25}$$

determines two double roots given by

$$\lambda_1 = l-2 \quad \text{and} \quad \lambda_2 = -(l+3). \tag{18.26}$$

The general solution of equation (18.23) is now given by

$$y_i = (A_i + B_i \ln x)x^{\lambda_1} + (C_i + D_i \ln x)x^{\lambda_2}, \quad (i = 1, 2, 3, 4), \tag{18.27}$$

where A_i and B_i denote eigenvectors associated with λ_1 while C_i and D_i are those associated with λ_2. Since eigensolutions have to be regular at the center ($x = 0$), the vectors B_i, C_i, and D_i should vanish:

$$B_i \equiv 0 \quad \text{and} \quad C_i = D_i \equiv 0. \tag{18.28}$$

Then, eliminating x^{λ_2} from equation (18.27), we finally obtain two homogeneous relations near the center, which are given by

$$\frac{c_1\omega^2}{l}y_1 - y_2 = 0 \tag{18.29}$$

and

$$ly_3 - y_4 = 0. \tag{18.30}$$

These are the two inner boundary conditions. In these conditions variables appear separately in pairs of (y_1, y_2) and (y_3, y_4), owing to the matrix (a_{ij}) which is semi-diagonal.

The proper outer boundary conditions can similarly be obtained. Owing to the surface (assumed quasi-isothermal) properties that

$$\left.\begin{aligned} U &\to 0, \quad V_g \to V_g(x=1) \\ A^* &\to A^*(x=1), \quad c_1 \to 1 \end{aligned}\right\} \quad \text{as} \quad x \to 1, \tag{18.31}$$

equations (18.14)–(18.17) are reduced to differential equations with constant coefficients near the surface, given by

$$x\frac{d}{dx}\begin{pmatrix} y_1 \\ y_2 \\ y_3 \\ y_4 \end{pmatrix} = (b_{ij})\begin{pmatrix} y_1 \\ y_2 \\ y_3 \\ y_4 \end{pmatrix} \tag{18.32}$$

with

$$(b_{ij}) = \begin{pmatrix} V_g-3 & l(l+1)/\omega^2-V_g & V_g & 0 \\ \omega^2-A^* & 1+A^* & -A^* & 0 \\ 0 & 0 & 1 & 1 \\ 0 & 0 & l(l+1) & 0 \end{pmatrix} \tag{18.33}$$

The characteristic values of the matrix (b_{ij}) are

$$\left.\begin{aligned} \lambda_1 &= -l, \\ \lambda_2 &= l+1, \\ \text{and} \\ \lambda_\pm &= \frac{1}{2}[(V_g + A^* - 2) \pm \gamma^{1/2}], \end{aligned}\right\} \tag{18.34}$$

where

$$\gamma = (A^*-V_g+4)^2 + 4[l(l+1)/\omega^2 - V_g](\omega^2 - A^*). \tag{18.35}$$

The general solution of equation (18.32) is then given by

$$\begin{pmatrix} y_1 \\ y_2 \\ y_3 \\ y_4 \end{pmatrix} = A_3 \begin{pmatrix} \alpha_1 \\ \alpha_2 \\ 1 \\ -(l+1) \end{pmatrix} x^{-l} + B_3 \begin{pmatrix} \beta_1 \\ \beta_2 \\ 1 \\ l \end{pmatrix} x^{l+1}$$

$$+ C_1 \begin{pmatrix} 1 \\ \frac{\lambda_- - b_{11}}{b_{12}} \\ 0 \\ 0 \end{pmatrix} x^{\lambda_-} + D_1 \begin{pmatrix} 1 \\ \frac{\lambda_+ - b_{11}}{b_{12}} \\ 0 \\ 0 \end{pmatrix} x^{\lambda_+}, \tag{18.36}$$

where

$$\alpha_1 = \frac{b_{12}b_{23} - b_{13}(b_{22}+l)}{(b_{11}+l)(b_{22}+l) - b_{12}b_{21}}, \tag{18.37}$$

$$\alpha_2 = \frac{b_{21}b_{13} - b_{23}(b_{11}+l)}{(b_{11}+l)(b_{22}+l) - b_{21}b_{21}}, \tag{18.38}$$

$$\beta_1 = \frac{b_{12}b_{23} - b_{13}(b_{22}-l-1)}{(b_{11}-l-1)(b_{22}-l-1) - b_{12}b_{21}}, \tag{18.39}$$

and

$$\beta_2 = \frac{b_{21}b_{13} - b_{23}(b_{11}-l-1)}{(b_{11}-l-1)(b_{22}-l-1) - b_{12}b_{21}}. \tag{18.40}$$

Here the coefficient B_3 should be set equal to zero:

$$B_3 = 0, \tag{18.41}$$

in order for the potential perturbation y_3 not to increase outward.

The kinetic energy density of the oscillation, $e_K (\equiv \sigma^2 \rho |\boldsymbol{\xi}|^2)$, is related to x, y_1, y_2 as

$$e_K \propto x^{-(A^*+V_g-2)} \left[y_1^2 + \frac{l(l+1)}{\omega^2} y_2^2 \right], \tag{18.42}$$

since

$$\rho \propto x^{-(A^*+V_g)}. \tag{18.43}$$

For the solutions associated with $\lambda = \lambda_\pm$, the kinetic energy density is then given by

$$e_K \propto x^{-(A^*+V_g-2)} x^{2\lambda_\pm} = x^{\pm\sqrt{\gamma}}, \tag{18.44}$$

and oscillations near the surface are evanescent waves or propagating waves depending on whether $\gamma > 0$ or $\gamma < 0$. The roots of $\gamma = 0$ give two critical frequencies ω_{c_1} and ω_{c_2} ($\omega_{c_1} < \omega_{c_2}$):

$$\gamma = -\frac{4V_g}{\omega^2}(\omega^2 - \omega_{c_1}^2)(\omega^2 - \omega_{c_2}^2). \tag{18.35'}$$

If the frequency ω is lower than ω_{c_2} and higher than ω_{c_1} ($\omega_{c_1} < \omega < \omega_{c_2}$), the quantity γ is positive and the oscillations associated with $\lambda = \lambda_\pm$ are evanescent. On the other hand, the quantity γ is negative, and solutions associated with $\lambda = \lambda_\pm$ represent progressive waves, if $\omega < \omega_{c_1}$ or $\omega_{c_2} < \omega$. These critical frequencies ω_{c_1} and ω_{c_2} are similar to N and L_l of the local analysis in Section 15. The difference, however, results from the existence of the first term in the right-hand side of equation (18.35), because of the fact that $h(r)$ defined by (15.7) is not a constant as assumed in Section 15. Thus the critical frequencies ω_{c_1} and ω_{c_2} represent the critical frequencies for propagating gravity waves and for propagating acoustic waves near the surface, respectively.

If the eigenfrequency ω is between these critical frequencies ($\gamma > 0$), the kinetic energy density of the λ_+-solution monotonically increases outward while that of the λ_--solution monotonically decreases. Therefore, the λ_+-solution should be rejected, and

$$D_1 = 0. \tag{18.45}$$

Eliminating x^{-l} and $x^{\lambda-}$ from equation (18.36) with $B_3 = D_1 = 0$, we finally obtain two homogeneous relations among y_1, y_2, y_3, and y_4 as follows:

$$(l + 1)y_3 + y_4 = 0 \tag{18.46}$$

and

$$\frac{\lambda_- - b_{11}}{b_{12}} y_1 - y_2 - \left[\frac{\alpha_1(\lambda_- - b_{11})}{b_{12}} - \alpha_2\right] y_3 = 0. \tag{18.47}$$

These are the two outer boundary conditions in the case of $\omega_{c_1} < \omega < \omega_{c_2}$. Equations (18.46) and (18.47) are the potential boundary condition and the mechanical boundary condition, respectively.

If the inequalities

$$A^*, V_g \gg \omega^2, l(l+1)/\omega^2, 1 \tag{18.48}$$

are satisfied, the mechanical boundary condition (18.47) may be somewhat simplified. In the limit of the zero-boundary ($A^*, V_g \to \infty$) in which the density and pressure vanish at the stellar surface, the mechanical outer boundary condition (18.47) turns out to be

$$y_1 - y_2 + y_3 = 0. \tag{18.49}$$

This condition is readily reduced to the free boundary condition

$$\delta p = 0. \tag{18.50}$$

On the other hand, if the surface pressure is finite, the condition (18.47) is simplified to

$$y_1\{1 + [l(l + 1)/\omega^2 - 4 - \omega^2]/V\} - y_2 + y_3\{1 + [l(l + 1)/\omega^2 - l - 1]/V\} = 0, \tag{18.51}$$

which is accurate to the first order in V^{-1}. This form of the condition was utilized by Dziembowski (1971) and by Osaki and Hansen (1973).

If the frequency ω is either higher than ω_{c_2} or lower than ω_{c_1}, the quantity γ is negative and the waves cannot be reflected at the boundary. Since the temporal dependence of the oscillations is taken as $\exp(i\sigma t)$, the λ_-- and λ_+-solutions represent waves whose phases propagate upward and downward, respectively. It should be remembered here that the group velocity and the phase velocity in the radial direction have the same sign in acoustic waves but have the opposite sign in gravity waves (Section 15). Because we consider stellar free oscillations, the inward propagation of wave energy from the outer boundary should be rejected. Thus for acoustic waves with $\omega > \omega_{c_2}$, the solution associated with λ_+ is improper, so that

$$D_1 = 0, \tag{18.52}$$

and the mechanical outer boundary condition for $\omega > \omega_{c_2}$ is obtained as

$$\frac{\lambda_- - b_{11}}{b_{12}} y_1 - y_2 - \left[\frac{\alpha_1(\lambda_- - b_{11})}{b_{12}} - \alpha_2\right] y_2 = 0. \tag{18.53}$$

Since the quantity λ_- appearing in equation (18.53) is a complex quantity, given by

$$\lambda_- = \frac{1}{2}[(V_g + A^* - 2) - i|\gamma|^{1/2}], \tag{18.54}$$

the eigenvalue ω^2 and eigenfunctions y_i are also complex even in the adiabatic approximation. This is due to the leakage of the wave energy from the system in the form of progressive waves. On the other hand, for gravity waves with $\omega < \omega_{c_1}$, the solution associated with λ_- should be rejected so that

$$C_1 = 0. \tag{18.55}$$

The corresponding mechanical outer boundary condition is then given by

$$\frac{\lambda_+ - b_{11}}{b_{12}} y_1 - y_2 - \left[\frac{\alpha_1(\lambda_+ - b_{11})}{b_{12}} - \alpha_2\right] y_3 = 0 \tag{18.56}$$

with

$$\lambda_+ = \frac{1}{2}[(V_g + A^* - 2) + i|\gamma|^{1/2}]. \tag{18.57}$$

Thus the four proper boundary conditions of the differential equations (18.14)–(18.17) are now explicitly given by the two inner boundary conditions (18.29) and (18.30) and a set of the outer boundary conditions consisting of equation (18.46) and one of the conditions (18.47), (18.53), and (18.56) depending on the frequency of the oscillation ω.

18.2 Method of Calculation

To solve boundary value problems numerically, we may successively integrate the differential equations from each of the boundaries to a fitting point, regarding the boundary conditions as the initial conditions, until the two kinds of values of functions y_i at the fitting point agree with

each other by the correct choice of the eigenvalue. On the other hand, the relaxation method usually called the Henyey method (Henyey, Forbes, and Gould, 1964) is powerful in solving boundary value problems like the construction of stellar models (*cf.* Kippenhahn, Weigert, and Hoffmeister, 1967), and it can also be applied to stellar oscillation problems (*cf.* Baker, Moore, and Spiegel, 1971). In this subsection, we describe the algorism of the Henyey method of solving the eigenvalue problem of stellar oscillations.

Dividing the region of independent variable x by N mesh points ($x_n; n = 1,2,..., N$), we have a system of $4(N-1)$ difference equations from the four linear differential equations (18.14)–(18.17). These difference equations are then regarded as linear algebraic equations for $4N+1$ unknowns, *viz.*, the correction $\delta\omega^2$ to the assumed $\omega^{2(0)}$ and the corrections $\delta y_i(x_n)$ to the assumed $y_i^{(0)}(x_n)$. The four boundary conditions plus a normalization condition, say,

$$y_1 = 1, \tag{18.58}$$

at the outermost mesh point, together with $4(N-1)$ difference equations, form a system of $4N+1$ algebraic equations for $4N+1$ unknowns. We can successively iterate this procedure until all the correction terms become small enough. Thus both the eigenvalue ω^2 and the corresponding eigenfunctions $y_i(x_n)$ are obtained simultaneously.

Now we will consider more precisely how the Henyey-type relaxation method is applied to stellar oscillation problems. To make application to other problems easier, we discuss the method of solving eigenvalue problems of I first-order differential equations and K eigenvalues λ. For simplicity, the symbol y_i^n is used for $y_i(x_n)$. The set of the I differential equations $dy_i/dx = f_i(y_j;\lambda_k)$; $(i,j = 1,2,..., I; k = 1,..., K)$ is approximated by the corresponding difference equations given by

$$\frac{y_i^{n+1}-y_i^n}{\Delta x_n} = (1-\theta_i)f_i(y_j^{n+1};\lambda_k) + \theta_i f_i(y_j^n;\lambda_k), \tag{18.59}$$

for $i, j = 1, ..., I$ and $k = 1, ..., K$, where

$$\Delta x_n = x_{n+1} - x_n; \quad n = 1, 2, ..., N-1, \tag{18.60}$$

and θ_i is a real constant lying in the interval $0 \le \theta_i \le 1$. For better accuracy, $\theta_i = 0.5$ is adopted if no numerical instability occurs (see Section 24). To solve the eigenvalue problem with I first-order differential equations and K eigenvalues, the number of boundary conditions should be $I + K = L$ including the normalization conditions. Let L_I and $L - L_I$ be the numbers of the inner and the outer boundary conditions, respectively ($L_I < I$). Then, the inner and the outer boundary conditions can be written in the forms

$$g_l(y_i^1;\ \lambda_k) = 0; \quad l = 1, 2, ..., L_I \tag{18.61}$$

and

$$g_l(y_i^N;\ \lambda_k) = 0; \quad l = L_I+1, L_I+2, ..., L, \tag{18.62}$$

respectively, where $i = 1, 2,..., I$ and $k = 1, 2,..., K$.

Let $\bar{y}_i$ be trial eigenfunctions and $\bar{\lambda}_k$ be trial eigenvalues. We assume that the true eigenfunctions and eigenvalues are given by

$$y_i^n = \bar{y}_i^n + \delta y_i^n; \quad i = 1,2,...,I; \quad n = 1,2,...,N, \tag{18.63}$$

and

$$\lambda_k = \bar{\lambda}_k + \delta\lambda_k; \quad k = 1, 2, ..., K. \tag{18.64}$$

We define

$$\bar{f}_i^n = f_i(\bar{y}_j^n;\bar{\lambda}_k); \quad i, j = 1, 2, ..., I; \quad n = 1, 2, ..., N;$$
$$k = 1, 2, ..., K, \tag{18.65}$$

$$\bar{g}_l^1 = g_l(\bar{y}_i^1;\bar{\lambda}_k); \quad l = 1, 2, ..., L_I, \tag{18.66}$$

$$\bar{g}_l^N = g_l(\bar{y}_i^N;\bar{\lambda}_k); \quad l = L_I+1, L_I+2, ..., L, \tag{18.67}$$

$$F_{ij}^n = \frac{\partial \bar{f}_i^n}{\partial \bar{y}_j^n}, \quad L_{ik}^n = \frac{\partial \bar{f}_i^n}{\partial \bar{\lambda}_k}, \tag{18.68}$$

$$G_{ij}^1 = \frac{\partial \bar{g}_l^1}{\partial \bar{y}_j^1}, \ \Lambda_{lk}^1 = \frac{\partial \bar{g}_l^1}{\partial \bar{\lambda}_k}; \ l = 1,2,..., L_I, \tag{18.69}$$

and

$$G_{ij}^N = \frac{\partial \bar{g}_l^N}{\partial \bar{y}_j^N}, \ \Lambda_{lk}^N = \frac{\partial \bar{g}_l^N}{\partial \bar{\lambda}_k}; \ l = L_I+1, L_I+2, ..., L. \tag{18.70}$$

Substituting the forms (18.63) and (18.64) into equations (18.59), (18.61),and (18.62), and discarding all terms containing products of the δy_i^n and the $\delta\lambda_k$, we obtain the following $I \times N + K$ equations:

$$A_{ij}^n \delta y_j^{n+1} + B_{ij}^n \delta y_j^n + M_{ik}^n \delta\lambda_k + d_i^n = 0; \ n = 1,2,..., N-1, \tag{18.71}$$

$$G_{ij}^1 \delta y_j^1 + \Lambda_{lk}^1 \delta\lambda_k + \bar{g}_l^1 = 0; \ l = 1,2,..., L_I, \tag{18.72}$$

and

$$G_{ij}^{N}\delta y_j^{N}+A_{ik}^{N}\delta\lambda_k+\bar{g}_i^{N}=0;\ l=L_l+1,\ L_l+2,\ldots,\ L, \quad (18.73)$$

where the Einstein summation convention is used for j and k,

$$A_{ij}^{n} = \Delta x_n(1-\theta_i)F_{ij}^{n+1}-\delta_{ij}, \quad (18.74)$$

$$B_{ij}^{n} = \Delta x_n\theta_i F_{ij}^{n}+\delta_{ij}, \quad (18.75)$$

$$M_{ik}^{n} = \Delta x_n[(1-\theta_i)L_{ik}^{n+1}+\theta_i L_{ik}^{n}], \quad (18.76)$$

and

$$d_i^{n}=-(\bar{y}_i^{n+1}-\bar{y}_i^{n})+\Delta x_n[(1-\theta_i)\bar{f}_i^{n+1}+\theta_i\bar{f}_i^{n}], \quad (18.77)$$

where δ_{ij} denotes Kronecker's delta. At a first glance, the system of the equations looks too large to be solved by matrix inversion. But there are many zero elements in the coefficient matrix, and the Henyey-type relaxation method makes use of this characteristic property.

First, we consider a set of I equations which consists of the L_I equations (18.72) and $I-L_I$ equations from (18.71) (for example, $i=1, 2, \ldots, I-L_I$). The set of equations may be written as

$$(\boldsymbol{P}_1)\begin{pmatrix}\delta y_1^1\\ \delta y_2^1\\ \vdots\\ \delta y_I^1\end{pmatrix}=(\boldsymbol{Q}_1)\begin{pmatrix}\delta y_1^2\\ \delta y_2^2\\ \vdots\\ \delta y_I^2\end{pmatrix}+(\boldsymbol{q}_1)\begin{pmatrix}\delta\lambda_1\\ \delta\lambda_2\\ \vdots\\ \delta\lambda_K\\ 1\end{pmatrix}, \quad (18.78)$$

where

$$(\boldsymbol{P}_1)=\begin{pmatrix} G_{11}^1 & G_{12}^1 & \cdots & G_{1I}^1\\ G_{21}^1 & G_{22}^1 & \cdots & G_{2I}^1\\ \vdots & \vdots & \ddots & \vdots\\ G_{L_I1}^1 & G_{L_I2}^1 & \cdots & G_{L_II}^1\\ B_{11}^1 & B_{12}^1 & \cdots & B_{1I}^1\\ B_{21}^1 & B_{22}^1 & \cdots & B_{2I}^1\\ \vdots & \vdots & \ddots & \vdots\\ B_{(I-L_I)1}^1 & B_{(I-L_I)2}^1 & \cdots & B_{(I-L_I)I}^1\end{pmatrix}, \quad (18.79)$$

$$(Q_1)_{ij}=\begin{cases}0 & \text{for } i=1,2,\ldots,L_I \text{ and } j=1,2,\ldots,I;\\ -A_{(i-L_I)j}^1 & \text{for } i=L_I+1,\ L_I+2,\ldots,I \text{ and } j=1,2,\ldots,I,\end{cases} \quad (18.80)$$

and

$$(q_1)=\begin{pmatrix} -\Lambda_{11}^1 & -\Lambda_{12}^1 & \cdots & -\Lambda_{1K}^1 & -\bar{g}_1^1\\ -\Lambda_{21}^1 & -\Lambda_{22}^1 & \cdots & -\Lambda_{2K}^1 & -\bar{g}_2^1\\ \vdots & \vdots & \ddots & \vdots & \vdots\\ -\Lambda_{L_I1}^1 & -\Lambda_{L_I2}^1 & \cdots & -\Lambda_{L_IK}^1 & -\bar{g}_{L_I}^1\\ -M_{11}^1 & -M_{12}^1 & \cdots & -M_{1K}^1 & -d_1^1\\ -M_{21}^1 & -M_{22}^1 & \cdots & -M_{2K}^1 & -d_2^1\\ \vdots & \vdots & \ddots & \vdots & \vdots\\ -M_{(I-L_I)1}^1 & -M_{(I-L_I)2}^1 & \cdots & -M_{(I-L_I)K}^1 & -d_{(I-L_I)}^1\end{pmatrix}. \quad (18.81)$$

This set of I equations includes $2I+K$ unknowns δy_i^1, δy_i^2 ($i=1, 2, \ldots, I$), and $\delta\lambda_k$ ($k=1, 2, \ldots, K$) so that I unknowns are expressed by linear combinations of the other $I+K$ unknowns; i.e.,

$$\begin{pmatrix}\delta y_1^1\\ \delta y_2^1\\ \vdots\\ \delta y_I^1\end{pmatrix}=(\boldsymbol{R}_1)\begin{pmatrix}\delta y_1^2\\ \delta y_2^2\\ \vdots\\ \delta y_I^2\end{pmatrix}+(\boldsymbol{r}_1)\begin{pmatrix}\delta\lambda_1\\ \delta\lambda_2\\ \vdots\\ \delta\lambda_K\\ 1\end{pmatrix}, \quad (18.82)$$

where

$$(\boldsymbol{R}_1) = (\boldsymbol{P}_1)^{-1}(\boldsymbol{Q}_1), \quad (18.83)$$

$$(\boldsymbol{r}_1) = (\boldsymbol{P}_1)^{-1}(\boldsymbol{q}_1), \quad (18.84)$$

and $(\boldsymbol{P}_1)^{-1}$ denotes the inverse matrix of $(\boldsymbol{P}_1)$.

Next, we combine the remaining L_I equations ($i=I-L_I+1, I-L_I+2, \ldots, I$) in (18.71) for $n=1$ and the first $(I-L_I)$ equations ($i=1, 2, \ldots, I-L_I$) in (18.71) for $n=2$. This set of equations can be written as

$$(S_1)\begin{pmatrix}\delta y_1^1\\ \delta y_2^1\\ \vdots\\ \delta y_I^1\end{pmatrix}+(P_2)\begin{pmatrix}\delta y_1^2\\ \delta y_2^2\\ \vdots\\ \delta y_I^2\end{pmatrix}=(Q_2)\begin{pmatrix}\delta y_1^3\\ \delta y_2^3\\ \vdots\\ \delta y_I^3\end{pmatrix}+(q_2)\begin{pmatrix}\delta\lambda_1\\ \delta\lambda_2\\ \vdots\\ \delta\lambda_K\\ 1\end{pmatrix}, \tag{18.85}$$

where

$$(S_1)_{ij}=\begin{cases}B^1_{(I-L_I+i)j} & \text{for } i=1,2,\ldots,L_I \text{ and } j=1,2,\ldots,I;\\ 0 & \text{for } i=L_I+1,\ L_I+2,\ldots,I \text{ and } j=1,2,\ldots,I,\end{cases} \tag{18.86}$$

$$(P_2)=\begin{pmatrix}A^1_{(I-L_I+1)1} & A^1_{(I-L_I+1)2} & \cdots & A^1_{(I-L_I+1)I}\\ A^1_{(I-L_I+2)1} & A^1_{(I-L_I+2)2} & \cdots & A^1_{(I-L_I+2)I}\\ \vdots & \vdots & \ddots & \vdots\\ A^1_{I1} & A^1_{I2} & \cdots & A^1_{II}\\ B^2_{11} & B^2_{12} & \cdots & B^2_{1I}\\ B^2_{21} & B^2_{22} & \cdots & B^2_{2I}\\ \vdots & \vdots & \ddots & \vdots\\ B^2_{(I-L_I)1} & B^2_{(I-L_I)2} & \cdots & B^2_{(I-L_I)I}\end{pmatrix}, \tag{18.87}$$

$$(Q_2)_{ij}=\begin{cases}0 & \text{for } i=1,2,\ldots,L_I \text{ and } j=1,2,\ldots,I;\\ -A^2_{(I-L_I)j} & \text{for } i=L_I+1,\ L_I+2,\ldots,I \text{ and } j=1,2,\ldots,I,\end{cases} \tag{18.88}$$

and

$$(q_2)=\begin{pmatrix}-M^1_{(I-L_I+1)1} & -M^1_{(I-L_I+1)2} & \cdots & -M^1_{(I-L_I+1)K} & -d^1_{(I-L_I+1)}\\ -M^1_{(I-L_I+2)1} & -M^1_{(I-L_I+2)2} & \cdots & -M^1_{(I-L_I+2)K} & -d^1_{(I-L_I+2)}\\ \vdots & \vdots & \ddots & \vdots & \vdots\\ -M^1_{I1} & -M^1_{I2} & \cdots & -M^1_{IK} & -d^1_I\\ -M^2_{11} & -M^2_{12} & \cdots & -M^2_{1K} & -d^2_1\\ -M^2_{21} & -M^2_{22} & \cdots & -M^2_{2K} & -d^2_2\\ \vdots & \vdots & \ddots & \vdots & \vdots\\ -M^2_{(I-L_I)1} & -M^2_{(I-L_I)2} & \cdots & -M^2_{(I-L_I)K} & -d^2_{(I-L_I)}\end{pmatrix}. \tag{18.89}$$

Substituting (18.82) into (18.85), we obtain

$$\begin{pmatrix}\delta y_1^2\\ \delta y_2^2\\ \vdots\\ \delta y_I^2\end{pmatrix}=(R_2)\begin{pmatrix}\delta y_1^3\\ \delta y_2^3\\ \vdots\\ \delta y_I^3\end{pmatrix}+(r_2)\begin{pmatrix}\delta\lambda_1\\ \delta\lambda_2\\ \vdots\\ \delta\lambda_K\\ 1\end{pmatrix}, \tag{18.90}$$

where the matrices (R_2) and (r_2) are defined by

$$(R_2)=[(S_1)(R_1)+(P_2)]^{-1}(Q_2) \tag{18.91}$$

and

$$(r_2)=[(S_1)(R_1)+(P_2)]^{-1}[(q_2)-(S_1)(r_1)]. \tag{18.92}$$

Equation (18.90) can be generalized as

$$\begin{pmatrix}\delta y_1^n\\ \delta y_2^n\\ \vdots\\ \delta y_I^n\end{pmatrix}=(R_n)\begin{pmatrix}\delta y_1^{n+1}\\ \delta y_2^{n+1}\\ \vdots\\ \delta y_I^{n+1}\end{pmatrix}+(r_n)\begin{pmatrix}\delta\lambda_1\\ \delta\lambda_2\\ \vdots\\ \delta\lambda_K\\ 1\end{pmatrix}, \tag{18.93}$$

with

$$(R_n)=[(S_{n-1})(R_{n-1})+(P_n)]^{-1}(Q_n) \tag{18.94}$$

and

$$(r_n)=[(S_{n-1})(R_{n-1})+(P_n)]^{-1}[(q_n)-(S_{n-1})(r_{n-1})], \tag{18.95}$$

where

$$(S_{n-1})_{ij}=\begin{cases}B^{n-1}_{(I-L_I+i)j} & \text{for } i=1,2,\ldots,L_I \text{ and } j=1,2,\ldots,I;\\ 0 & \text{for } i=L_I+1,\ L_I+2,\ldots,I \text{ and } j=1,2,\ldots,I.\end{cases} \tag{18.96}$$

$$(P_n) = \begin{pmatrix} A^{n-1}_{(I-L_I+1)1} & A^{n-1}_{(I-L_I+1)2} & \cdots & A^{n-1}_{(I-L_I+1)I} \\ A^{n-1}_{(I-L_I+2)1} & A^{n-1}_{(I-L_I+2)2} & \cdots & A^{n-1}_{(I-L_I+2)I} \\ \vdots & \vdots & \ddots & \vdots \\ A^{n-1}_{I1} & A^{n-1}_{I2} & \cdots & A^{n-1}_{II} \\ B^{n}_{11} & B^{n}_{12} & \cdots & B^{n}_{1I} \\ B^{n}_{21} & B^{n}_{22} & \cdots & B^{n}_{2I} \\ \vdots & \vdots & \ddots & \vdots \\ B^{n}_{(I-L_I)1} & B^{n}_{(I-L_I)2} & \cdots & B^{n}_{(I-L_I)I} \end{pmatrix}, \tag{18.97}$$

$$(Q_n)_{ij} = \begin{cases} 0 & \text{for } i=1,2,\ldots,L_I \text{ and } j=1,2,\ldots,I; \\ -A^{n}_{(i-L_I)j} & \text{for } i=L_I+1,\ L_I+2,\ldots,I \text{ and } j=1,2,\ldots,I, \end{cases} \tag{18.98}$$

and

$$(q_2) = \begin{pmatrix} -M^{n-1}_{(I-L_I+1)1} & -M^{n-1}_{(I-L_I+1)2} & \cdots & -M^{n-1}_{(I-L_I+1)K} & -d^{n-1}_{(I-L_I+1)} \\ -M^{n-1}_{(I-L_I+2)1} & -M^{n-1}_{(I-L_I+2)2} & \cdots & -M^{n-1}_{(I-L_I+2)K} & -d^{n-1}_{(I-L_I+2)} \\ \vdots & \vdots & \ddots & \vdots & \vdots \\ -M^{n-1}_{I1} & -M^{n-1}_{I2} & \cdots & -M^{n-1}_{IK} & -d^{n-1}_{I} \\ -M^{n}_{11} & -M^{n}_{12} & \cdots & -M^{n}_{1K} & -d^{n}_{1} \\ -M^{n}_{21} & -M^{n}_{22} & \cdots & -M^{n}_{2K} & -d^{n}_{2} \\ \vdots & \vdots & \ddots & \vdots & \vdots \\ -M^{n}_{(I-L_I)1} & -M^{n}_{(I-L_I)2} & \cdots & -M^{n}_{(I-L_I)K} & -d^{n}_{(I-L_I)} \end{pmatrix}. \tag{18.99}$$

At the outermost mesh point $n = N$, combining the remaining L_I equations in (18.71) for $n = N - 1$ with $L - L_I$ outer boundary conditions in (18.62) we obtain

$$(\Sigma)\begin{pmatrix} \delta y^{N-1}_1 \\ \delta y^{N-1}_2 \\ \vdots \\ \delta y^{N-1}_I \end{pmatrix} + (\Pi)\begin{pmatrix} \delta y^{N}_1 \\ \delta y^{N}_2 \\ \vdots \\ \delta y^{N}_I \end{pmatrix} = (w)\begin{pmatrix} \delta\lambda_1 \\ \delta\lambda_2 \\ \vdots \\ \delta\lambda_K \\ 1 \end{pmatrix}, \tag{18.100}$$

where

$$\Sigma_{ij} = \begin{cases} B^{N-1}_{(I-L_I+i)j} & \text{for } i=1,2,\ldots,L_I \text{ and } j=1,2,\ldots,I; \\ 0 & \text{for } i=L_I+1,\ L_I+2,\ldots,I \text{ and } j=1,2,\ldots,I, \end{cases} \tag{18.101}$$

$$(\Pi) = \begin{pmatrix} A^{N-1}_{(I-L_I+1)1} & A^{N-1}_{(I-L_I+1)2} & \cdots & A^{N-1}_{(I-L_I+1)I} \\ A^{N-1}_{(I-L_I+2)1} & A^{N-1}_{(I-L_I+2)2} & \cdots & A^{N-1}_{(I-L_I+2)I} \\ \vdots & \vdots & \ddots & \vdots \\ A^{N-1}_{I1} & A^{N-1}_{I2} & \cdots & A^{N-1}_{II} \\ G^{N}_{(L_I+1)1} & G^{N}_{(L_I+1)2} & \cdots & G^{N}_{(L_I+1)I} \\ G^{N}_{(L_I+2)1} & G^{N}_{(L_I+2)2} & \cdots & G^{N}_{(L_I+2)I} \\ \vdots & \vdots & \ddots & \vdots \\ G^{N}_{L1} & G^{N}_{L2} & \cdots & G^{N}_{LI} \end{pmatrix}, \tag{18.102}$$

and

$$(w) = \begin{pmatrix} -M^{N-1}_{(I-L_I+1)1} & -M^{N-1}_{(I-L_I+1)2} & \cdots & -M^{N-1}_{(I-L_I+1)K} & -d^{N-1}_{(I-L_I+1)} \\ -M^{N-1}_{(I-L_I+2)1} & -M^{N-1}_{(I-L_I+2)2} & \cdots & -M^{N-1}_{(I-L_I+2)K} & -d^{N-1}_{(I-L_I+2)} \\ \vdots & \vdots & \ddots & \vdots & \vdots \\ -M^{N-1}_{I1} & -M^{N-1}_{I2} & \cdots & -M^{N-1}_{IK} & -d^{N-1}_{I} \\ -\Lambda^{N}_{(L_I+1)1} & -\Lambda^{N}_{(L_I+1)2} & \cdots & -\Lambda^{N}_{(L_I+1)K} & -\tilde{g}^{N}_{(L_I+1)} \\ -\Lambda^{N}_{(L_I+2)1} & -\Lambda^{N}_{(L_I+2)2} & \cdots & -\Lambda^{N}_{(L_I+2)K} & -\tilde{g}^{N}_{(L_I+2)} \\ \vdots & \vdots & \ddots & \vdots & \vdots \\ -\Lambda^{N}_{L1} & -\Lambda^{N}_{L2} & \cdots & -\Lambda^{N}_{LK} & -\tilde{g}^{N}_{L} \end{pmatrix}. \tag{18.103}$$

Substituting equation (18.93) with $n = N - 1$ into equation (18.100) yields

$$[(\Sigma)(R_{N-1})+(\Pi)]\begin{pmatrix} \delta y^{N}_1 \\ \delta y^{N}_2 \\ \vdots \\ \delta y^{N}_I \end{pmatrix} = [(w)-(\Sigma)(r_{N-1})]\begin{pmatrix} \delta\lambda_1 \\ \delta\lambda_2 \\ \vdots \\ \delta\lambda_K \\ 1 \end{pmatrix}, \tag{18.104}$$

or

$$(\mathbf{Z})\begin{pmatrix} \delta y_1^N \\ \delta y_2^N \\ \vdots \\ \delta y_I^N \\ \delta\lambda_1 \\ \delta\lambda_2 \\ \vdots \\ \delta\lambda_K \end{pmatrix} = (\boldsymbol{c}) \tag{18.105}$$

with the $(I+K)$-th order square matrix $(\mathbf{Z})$ whose elements are given by

$$Z_{ij} = \begin{cases} [(\Sigma)(R_{N-1})+(\Pi)]_{ij} & \text{for } j=1,2,\ldots,I; \\ [(\Sigma)(r_{N-1})-(w)]_{i(j-I)} & \text{for } j=I+1,\ I+2,\ldots,I+K, \end{cases} \tag{18.106}$$

for $i = 1, 2, \ldots, I+K(=L)$, and the column vector $(\boldsymbol{c})$ given by

$$c_i=[(w)-(\Sigma)(r_{N-1})]_{i(K+1)};\ i=1,\ 2,\ldots,I+K. \tag{18.107}$$

Applying the inverse matrix of $(\mathbf{Z})$ to equation (18.105), we obtain

$$\begin{pmatrix} \delta y_1^N \\ \delta y_2^N \\ \vdots \\ \delta y_I^N \\ \delta\lambda_1 \\ \delta\lambda_2 \\ \vdots \\ \delta\lambda_K \end{pmatrix} = (\mathbf{Z})^{-1}(\boldsymbol{c}). \tag{18.108}$$

Thus the solutions for the outermost mesh point, δy_i^N $(i = 1,2,\ldots, I)$ and $\delta\lambda_k$ $(k = 1,2,\ldots, K)$, are obtained. Inserting these solutions into the recurrence relation (18.93) with $n = N-1$, we obtain the solutions for $n = N-1$, δy_i^{N-1}. By the same procedure, the solutions for the inner mesh points, δy_i^n, are successively obtained. Inserting these solutions into equations (18.63) and (18.64), we obtain the corrected values for y_i^n and λ_k. Unless the entire system of the equations is linear in all dependent variables, y_i^n, and eigenvalues, λ_k, however, the corrected y_i^n and λ_k will not be true solutions of equations (18.59), (18.61), and (18.62), but simply better approximations. Since the system of

equations for nonradial oscillations is nonlinear in terms of the eigenvalue (oscillation frequency), we have to iterate the procedure until the corrections, δy_i^n and $\delta\lambda_k$, become sufficiently small.

To adopt the Henyey-type relaxation method, starting trial eigenvalues and eigenfunctions are needed. The convergence of this relaxation depends on how good the initial guesses of eigenvalues and eigenfunctions are (and on the degree of nonlinearity of the system of equations). Castor (1971) invented the following method of making a good guess in solving the radial pulsation problem. If we set aside one of the boundary conditions while keeping the normalization condition, we can solve this system of equations with an arbitrary value of ω^2. (No iteration is necessary in this case, because the system of equations is linear in terms of unknowns.) We then substitute this solution into the excluded boundary condition. In general, the condition is not satisfied for the arbitrary ω^2, but the numerical value associated with the boundary condition serves as a discriminant for eigenvalues of the original system. Once we get a reasonably good initial guess of the eigenvalue and corresponding eigenfunctions, we can use the relaxation code to obtain solutions for the full system. This method is applicable also to the nonradial oscillation problem. For instance, we choose the potential boundary condition (18.46) as a discriminant,

$$D(\omega^2; y_i^N) \equiv (l+1)y_3^N + y_4^N, \tag{18.109}$$

which becomes zero if and only if ω^2 is one of the eigenvalues. We evaluate D for various values of ω^2 and use the value of ω^2 near the zero points of D as an initial guess of the eigenvalue. To calculate the discriminant D, unknowns are only y_i^n, in terms of which the system of equations is linear, so that any values for the initial trial value for y_i^n can be adopted and the solutions for a given value of ω^2 are obtained without an iteration.

An example of the behavior of D as a function of ω^2 is shown in Fig. 18.1 for a white dwarf model (from Osaki and Hansen, 1973). With the help of the discriminant we shall not miss any eigenmodes. In some cases, however, the discriminant given by equation (18.109) does not behave smoothly as in Fig. 18.1. Very often, zero points of D are very close to singular points, where $D = \pm\infty$. Such singularity is caused by that the function y_i takes zero by accident for the given value of ω^2 at the mesh point where the normalization condition is applied. In order to avoid the problem, we only have to evaluate the discriminant with a different normalization. That is, better behavior of the discriminant is obtained if we adopt the deviation from the boundary condition divided by y_i^1 as the discriminant, if the normalization condition is applied to the

outer most mesh point. Sometimes a good discriminant can be obtained by using an inner boundary condition.

In the cases of progressive boundary conditions (18.53) or (18.56) and of nonadiabatic oscillations (Chapter IV), the eigenvalues and eigenfunctions are complex quantities. Such problems can be solved either by applying the algorism of complex numbers in the above formulations or by separating the complex variables into real and imaginary parts to form a system of $2I$ real dependent variables and $2K$ real eigenvalues. In either cases, the discriminant D depends on the real and the imaginary parts of ω so that it is difficult to obtain good trial functions and eigenfunctions by using the discriminant. In most cases, however, the imaginary part is so small compared to the real part that we can use adiabatic real solutions with the reflective boundary conditions as trial solutions of the problem.

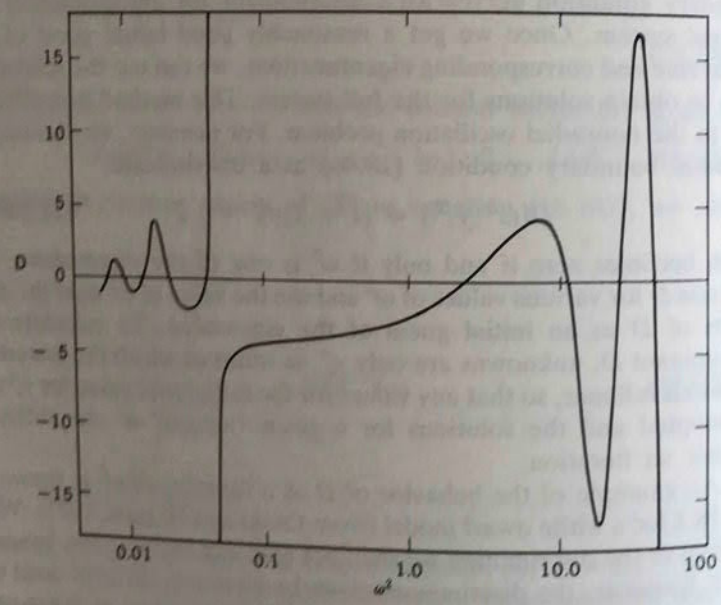

Fig. 18.1 Behavior of the discriminant given in equation (18.109) as a function of ω^2 for a white dwarf model of $0.398M_\odot$ (from Osaki and Hansen, 1973).

19. The Influence of Velocity Field and Magnetic Field as Treated by Perturbation Theory

19.1 Perturbation Equations

So far we have considered linear, adiabatic oscillations of a nonrotating star with no magnetic field. However, real stars rotate to a greater or lesser degree and have magnetic fields. Their influence on nonradial oscillations sometimes has to be taken into account. For example, the beat phenomena of early type O, B variables are well explained by the nonradial oscillations of rotating stars, and the rapid oscillations in Ap stars are interpreted as nonradial oscillations of rotating, magnetic stars, as discussed in Chapter II. However, since the theory has been complicated for the case of rapid rotation or strong magnetic field except in some special cases, we shall consider here the effects of a slow rotation and a weak magnetic field upon nonradial oscillations in a case where the equilibrium structure can be taken as spherically symmetric. The influence of rotation will be discussed in greater detail in Chapter VI.

The equation of motion in the presence of a velocity field and a magnetic field $\boldsymbol{B}$ in a rotating frame of angular velocity $\boldsymbol{\Omega}_0$ is given by

$$\frac{\partial \boldsymbol{v}}{\partial t}+(\boldsymbol{v}\cdot\nabla)\boldsymbol{v}+2\boldsymbol{\Omega}_0\times\boldsymbol{v}+\boldsymbol{\Omega}_0\times\boldsymbol{\Omega}_0\times\boldsymbol{r}$$

$$=-\nabla\Phi-\frac{1}{\rho}\nabla p+\frac{1}{4\pi\rho}(\nabla\times\boldsymbol{B})\times\boldsymbol{B}, \tag{19.1}$$

where $\boldsymbol{B}$ is described in the MHD approximation by

$$\frac{\partial \boldsymbol{B}}{\partial t}=\nabla\times(\boldsymbol{v}\times\boldsymbol{B}). \tag{19.2}$$

In equation (19.1), the third and fourth terms in the left-hand side represent the Coriolis force and the centrifugal force, respectively. We suppose the equilibrium velocity field $\boldsymbol{v}_0$ and the equilibrium magnetic field $\boldsymbol{B}_0$ are steady so that

$$\frac{\partial \boldsymbol{v}_0}{\partial t}=0 \tag{19.3}$$

and

$$\frac{\partial \boldsymbol{B}_0}{\partial t}=0. \tag{19.4}$$

The unperturbed state without oscillations is then described by

$$(\boldsymbol{v}_0\cdot\nabla)\boldsymbol{v}_0+2\boldsymbol{\Omega}_0\times\boldsymbol{v}_0+\boldsymbol{\Omega}_0\times\boldsymbol{\Omega}_0\times\boldsymbol{r}$$

$$=-\nabla\Phi_0-\frac{1}{\rho_0}\nabla p_0+\frac{1}{4\pi\rho_0}(\nabla\times\boldsymbol{B}_0)\times\boldsymbol{B}_0 \tag{19.5}$$

and, if the velocity field is solenoidal,

$$(\boldsymbol{B}_0\cdot\nabla)\boldsymbol{v}_0-(\boldsymbol{v}_0\cdot\nabla)\boldsymbol{B}_0=0\ , \tag{19.6}$$

while the linearized equations are

$$\frac{\partial\boldsymbol{v}'}{\partial t}+(\boldsymbol{v}_0\cdot\nabla)\boldsymbol{v}'+(\boldsymbol{v}'\cdot\nabla)\boldsymbol{v}_0+2\boldsymbol{\Omega}_0\times\boldsymbol{v}'$$

$$=-\nabla\Phi'+\frac{\rho'}{\rho_0^2}\left[\nabla p_0-\frac{1}{4\pi}(\nabla\times\boldsymbol{B}_0)\times\boldsymbol{B}_0\right]-\frac{1}{\rho_0}\nabla p'$$

$$+\frac{1}{4\pi}\frac{1}{\rho_0}[(\nabla\times\boldsymbol{B}')\times\boldsymbol{B}_0+(\nabla\times\boldsymbol{B}_0)\times\boldsymbol{B}'] \tag{19.7}$$

and

$$\frac{\partial\boldsymbol{B}'}{\partial t}=\nabla\times(\boldsymbol{v}'\times\boldsymbol{B}_0)+\nabla\times(\boldsymbol{v}_0\times\boldsymbol{B}')\ , \tag{19.8}$$

where the prime denotes the Eulerian perturbation. Hereafter, the suffix 0 for the equilibrium quantities is omitted for simplicity. The Eulerian perturbation of velocity $\boldsymbol{v}'$ is related with the displacement vector $\boldsymbol{\xi}$ by equation (13.26). We set the temporal dependence of eigenfunctions as $\exp(i\sigma t)$ in the rotating frame. Substitution of equation (13.26) into (19.7), with the help of the linearized equations describing the mass-conservation and the adiabatic energy conservation, gives (*cf.* Lynden-Bell and Ostriker, 1967; Gough and Taylor, 1984; Dziembowski and Goode, 1984)

$$\nabla[(p-\rho c^2)\nabla\cdot\boldsymbol{\xi}-\boldsymbol{\xi}\cdot\nabla p]-p\nabla(\nabla\cdot\boldsymbol{\xi})+\rho^{-1}(\boldsymbol{\xi}\cdot\nabla\rho)\nabla p$$

$$-\rho\sigma^2\boldsymbol{\xi}+\rho\nabla\Phi'+2i\sigma\rho[\boldsymbol{\Omega}_0\times\boldsymbol{\xi}+(\boldsymbol{v}\cdot\nabla)\boldsymbol{\xi}]$$

$$+\rho\left[(\boldsymbol{v}\cdot\nabla)^2\boldsymbol{\xi}-2\boldsymbol{\Omega}_0\times[(\boldsymbol{\xi}\cdot\nabla)\boldsymbol{v}-(\boldsymbol{v}\cdot\nabla)\boldsymbol{\xi}]-(\boldsymbol{\xi}\cdot\nabla)(\boldsymbol{v}\cdot\nabla)\boldsymbol{v}\right]$$

$$+(4\pi)^{-1}\left[[\rho^{-1}(\boldsymbol{\xi}\cdot\nabla)\rho+\nabla\cdot\boldsymbol{\xi}]\boldsymbol{B}\times(\nabla\times\boldsymbol{B})\right.$$

$$\left.-[(\nabla\times\boldsymbol{B}')\times\boldsymbol{B}+(\nabla\times\boldsymbol{B})\times\boldsymbol{B}']\right]=0, \tag{19.9}$$

which is symbolically writtten as

$$\mathscr{L}(\boldsymbol{\xi})-\sigma^2\boldsymbol{\xi}+\sigma\boldsymbol{M}(\boldsymbol{\xi})+\boldsymbol{N}(\boldsymbol{\xi})+\boldsymbol{B}(\boldsymbol{\xi})=0\ , \tag{19.10}$$

where the operator $\mathscr{L}(\boldsymbol{\xi})$ is defined by equation (14.25) and

$$\boldsymbol{M}(\boldsymbol{\xi})=2i[\boldsymbol{\Omega}_0\times\boldsymbol{\xi}+(\boldsymbol{v}\cdot\nabla)\boldsymbol{\xi}]\ , \tag{19.11}$$

$$\boldsymbol{N}(\boldsymbol{\xi})=(\boldsymbol{v}\cdot\nabla)^2\boldsymbol{\xi}-2\boldsymbol{\Omega}_0\times[(\boldsymbol{\xi}\cdot\nabla)\boldsymbol{v}-(\boldsymbol{v}\cdot\nabla)\boldsymbol{\xi}]-(\boldsymbol{\xi}\cdot\nabla)(\boldsymbol{v}\cdot\nabla)\boldsymbol{v}, \tag{19.12}$$

and

$$\boldsymbol{B}(\boldsymbol{\xi})\equiv(4\pi\rho)^{-1}\left[[\rho^{-1}(\boldsymbol{\xi}\cdot\nabla)\rho+\nabla\cdot\boldsymbol{\xi}]\boldsymbol{B}\times(\nabla\times\boldsymbol{B})\right.$$

$$\left.-[(\nabla\times\boldsymbol{B}')\times\boldsymbol{B}+[(\nabla\times\boldsymbol{B})\times\boldsymbol{B}']\right]\ . \tag{19.13}$$

Here, $\boldsymbol{B}'$ is related to $\boldsymbol{\xi}$ through equations (19.8) and (13.26). Besides the influence upon the equilibrium structure, the effect of the presence of the unperturbed velocity field appears in the operators $\boldsymbol{M}$ and $\boldsymbol{N}$, and the effect of the magnetic field appears in the operator $\boldsymbol{B}$.

We regard the effects of velocity fields and magnetic field on the equilibrium structure and on the oscillations as small perturbations, and expand any equilibrium quantity such as ρ, the eigenfunctions, and eigenfrequencies as

$$\rho=\rho^{(0)}+\rho^{(1)}+\dots\ , \tag{19.14}$$

$$\boldsymbol{\xi}=\boldsymbol{\xi}^{(0)}+\boldsymbol{\xi}^{(1)}+\dots\ , \tag{19.15}$$

and

$$\sigma=\sigma^{(0)}+\sigma^{(1)}+\dots\ . \tag{19.16}$$

Substituting (19.14)–(19.16) into (19.10) and neglecting the terms of the first and higher orders, we obtain

$$\mathscr{L}^{(0)}(\boldsymbol{\xi}^{(0)})-\sigma^{(0)2}\boldsymbol{\xi}^{(0)}=0\ . \tag{19.17}$$

Similarly, discarding of the second and higher orders yields

$$\mathscr{L}^{(0)}(\boldsymbol{\xi}^{(1)})+\mathscr{L}^{(1)}(\boldsymbol{\xi}^{(0)})-\sigma^{(0)2}\boldsymbol{\xi}^{(1)}-2\sigma^{(0)}\sigma^{(1)}\boldsymbol{\xi}^{(0)}$$

$$+\sigma^{(0)}\boldsymbol{M}^{(0)}(\boldsymbol{\xi}^{(0)})+\boldsymbol{B}^{(0)}(\boldsymbol{\xi}^{(0)})=0\ . \tag{19.18}$$

Here, the operators with a superscript, such as $\mathscr{L}^{(1)}$, are operators consisting of equilibrium quantities of the first order. As seen in equations (19.5) and (19.9), the magnetic field affects both the

equilibrium structure and the oscillations in the same order of magnitude. The equilibrium structure is no longer spherically symmetric, and the small departure from spherical symmetry is represented in terms of $\mathscr{L}^{(1)}$ and $\boldsymbol{B}^{(0)}$. In contrast, velocity fields (relative to an inertial frame) affect the equilibrium structure in the second order, while their effects on the oscillations appear even in the first order. The operator $\boldsymbol{N}^{(0)}$ represents the departure from the spherical symmetry, but it is of the second order, and then we do not discuss it in this section.

The solution of equation (19.17) gives the eigenmodes of a non-rotating non-magnetic star, which are represented in terms of spherical harmonics $Y_l^m(\theta,\phi)$. Since such a star is spherically symmetric, there remains a freedom for the choice of the polar axis, $\theta = 0$. Here we arbitrarily set the axis and let $\{\boldsymbol{\xi}_{nlm}\}$ be the set of eigensolutions with the eigenfrequency $\sigma_{nl}^{(0)}$ given by equation (19.17). The eigenfrequencies with a fixed set of (n, l) are degenerate with respect to the azimuthal order $m\,(m = -l,\ldots,l)$.

If we take account of the effects of $\boldsymbol{v}_0$ and $\boldsymbol{B}$, the star is no longer spherically symmetric and its normal modes have a specified direction. The zero-order eigenfunction of equation (19.10) must satisfy both equations (19.17) and (19.18). Let us now consider the (n, l) multiplets and represent the zero-order eigenfunction $\boldsymbol{\xi}^{(0)}$ in terms of the set of $\{\boldsymbol{\xi}_{nlm}\}$:

$$\boldsymbol{\xi}^{(0)} = \sum_{m=-l}^{l} \alpha_m \boldsymbol{\xi}_{nlm} \ . \tag{19.19}$$

The set of combination coefficients $\{\alpha_m\}$ should be uniquely determined for $\boldsymbol{\xi}^{(0)}$ to satisfy both equations (19.17) and (19.18). Also we expand the perturbed displacement $\boldsymbol{\xi}^{(1)}$ in terms of $\{\boldsymbol{\xi}_{nlm}\}$ as

$$\boldsymbol{\xi}^{(1)} = \sum_{m'} {\sum_{n'\,l'}}' \beta_{n'l'm'} \boldsymbol{\xi}_{n'l'm'} + \sum_{l'\,m'} \gamma_{l'm'}(r) \boldsymbol{\eta}_{l'm'} \ . \tag{19.20}$$

In the first term on the right-hand side of equation (19.20), $\{\beta_{n'l'm'}\}$ is a set of constants and Σ' means the summation over n' and l' except for $(n', l') = (n, l)$. In considering the perturbation in the eigenfunctions, we must include, for the completeness of the eigenfunctions, toroidal modes $\boldsymbol{\eta}_{lm}$ with $\sigma^{(0)} = 0$ given by (*cf.* see Section 13; Aizenman and Smeyers, 1977)

$$\boldsymbol{\eta}_{l'm'} \equiv \frac{1}{[l'(l'+1)]^{1/2}} \left(0,\ \frac{1}{\sin\theta}\frac{\partial}{\partial\phi},\ -\frac{\partial}{\partial\theta}\right) Y_{l'}^{m'}(\theta,\phi) \ . \tag{19.21}$$

The second term on the right-hand side of equation (19.20) represents contributions from these toroidal modes, and $\{\gamma_{l'm'}\}$ is a set of functions of r.

In the following, we derive the expansion coefficients of $\boldsymbol{\xi}^{(0)}$ and $\boldsymbol{\xi}^{(1)}$: $\{\alpha_m\}$, $\{\beta_{n'l'm'}\}$, and $\{\gamma_{l'm'}\}$. Substituting equations (19.19) and (19.20) into equation (19.18) and then integrating over the whole volume after multiplying by $\boldsymbol{\xi}^*_{n''l''m''}$ with an arbitrary set $(n''l''m'')$, we obtain

$$\begin{aligned}
&-2\sigma_{nl}^{(0)}\sigma^{(1)}\delta_{n''n}\delta_{l''l}\delta_{m''m}\alpha_m I_{nl} + \sum_m \alpha_m \int_0^M \boldsymbol{\xi}^*_{n''l''m''}\cdot\mathscr{L}^{(1)}(\boldsymbol{\xi}_{nlm})dM_r \\
&+ {\sum_{m'}}{\sum_{n'\,l'}}' \left(\sigma_{n'l'}^{(0)2} - \sigma_{nl}^{(0)2}\right)\delta_{n''n'}\delta_{l''l'}\delta_{m''m'}\beta_{n'l'm'} I_{n'l'} \\
&+ \sigma_{nl}^{(0)} \sum_m \alpha_m \int_0^M \boldsymbol{\xi}^*_{n''l''m''}\cdot\boldsymbol{M}^{(0)}(\boldsymbol{\xi}_{nlm})dM_r \\
&+ \sum_m \alpha_m \int_0^M \boldsymbol{\xi}^*_{n''l''m''}\cdot\boldsymbol{B}^{(0)}(\boldsymbol{\xi}_{nlm})dM_r = 0 \ .
\end{aligned} \tag{19.22}$$

Here, δ_{ij} is the Kronecker delta,

$$I_{nl} \equiv \int_0^M |\boldsymbol{\xi}_{nlm}|^2 dM_r \ , \tag{19.23}$$

and we have used the orthogonality of $\boldsymbol{\xi}_{nlm}$, equation (14.14) and

$$\int_0^M \boldsymbol{\xi}^*_{n''l''m''}\cdot\boldsymbol{\eta}_{l'm'}dM_r = 0 \ . \tag{19.24}$$

For $(n'', l'') = (n, l)$, equation (19.22) is reduced to

$$\sum_{m=-l}^{l} (\boldsymbol{O}_{m''m} - \sigma^{(1)}\delta_{m''m})\alpha_m = 0 \tag{19.25}$$

for $m'' = -l, \ldots, l$ (Dziembowski and Goode, 1985, 1986), where

$$\boldsymbol{O}_{m''m} \equiv \boldsymbol{M}_{m''m} + \boldsymbol{B}_{m''m} \ , \tag{19.26}$$

$$\boldsymbol{M}_{m''m} \equiv \frac{1}{2I_{nl}} \int_0^M \boldsymbol{\xi}^*_{nlm''}\cdot\boldsymbol{M}^{(0)}(\boldsymbol{\xi}_{nlm})dM_r \ , \tag{19.27}$$

and

$$\boldsymbol{B}_{m''m} \equiv \frac{1}{2\sigma_{nl}^{(0)}I_{nl}} \int_0^M \boldsymbol{\xi}^*_{nlm''}\cdot[\boldsymbol{B}^{(0)}(\boldsymbol{\xi}_{nlm}) + \mathscr{L}^{(1)}(\boldsymbol{\xi}_{nlm})]dM_r \ . \tag{19.28}$$

Equation (19.25) means that the $2l + 1$ eigenvalues $\sigma^{(1)}$ are the

characteristic values of the matrix $\boldsymbol{O} \equiv (\boldsymbol{O}_{m''m})$ and the combination coefficients α_m are the corresponding eigenvectors of the matrix. We rewrite equation (19.25) in a matrix form:

$$\boldsymbol{O}\boldsymbol{\alpha} = \boldsymbol{\alpha}\boldsymbol{\Lambda} , \tag{19.29}$$

where the matrix $\boldsymbol{\alpha}$ consists of the eigenvectors, and the matrix $\boldsymbol{\Lambda} \equiv (\Lambda_{m''m}) = (\sigma_m^{(1)} \delta_{m''m})$ is a diagonal matrix consisting of the characteristic values.

The expansion coefficients for $\xi^{(1)}$ are obtained as follows. For $(n'', l'') = (n', l')$, equation (19.22) is reduced to

$$\begin{aligned} &\beta_{n'l'm'}\left(\sigma_{n'l'}^{(0)2} - \sigma_{nl}^{(0)2}\right) I_{n'l'} \\ &+ \sum_m \alpha_m \left\{ \sigma_{nl}^{(0)} \int_0^M \xi_{n'l'm'}^* \cdot \boldsymbol{M}^{(0)}(\xi_{nlm}) dM_r \right. \\ &\left. + \int_0^M \xi_{n'l'm'}^* \cdot [\boldsymbol{B}^{(0)}(\xi_{nlm}) + \mathscr{L}^{(1)}(\xi_{nlm})] dM_r \right\} = 0 . \end{aligned} \tag{19.30}$$

Then

$$\begin{aligned} \beta_{n'l'm'} &= [\sigma_{nl}^{(0)2} - \sigma_{n'l'}^{(0)2}]^{-1} I_{n'l'}^{-1} \\ &\times \sum_m \alpha_m \left\{ \sigma_{nl}^{(0)} \int_0^M \xi_{n'l'm'}^* \cdot \boldsymbol{M}^{(0)}(\xi_{nlm}) dM_r \right. \\ &\left. + \int_0^M \xi_{n'l'm'}^* \cdot [\boldsymbol{B}^{(0)}(\xi_{nlm}) + \mathscr{L}^{(1)}(\xi_{nlm})] dM_r \right\} . \end{aligned} \tag{19.31}$$

Similarly, by substituting equations (19.19) and (19.20) into equation (19.18) and integrating over the whole volume after multiplying $\eta_{l'm'}^*$, we obtain

$$\begin{aligned} \gamma_{l'm'} &= \sigma_{n'l'}^{(0)-2} \\ &\times \sum_m \alpha_m \left\{ \sigma_{nl}^{(0)} \int_0^M \eta_{l'm'}^* \cdot \boldsymbol{M}^{(0)}(\xi_{nlm}) dM_r \right. \\ &\left. + \int_0^M \eta_{l'm'}^* \cdot [\boldsymbol{B}^{(0)}(\xi_{nlm}) + \mathscr{L}^{(1)}(\xi_{nlm})] dM_r \right\} . \end{aligned} \tag{19.32}$$

Here we have used

$$\int_0^M |\eta_{l'm'}|^2 dM_r = 1. \tag{19.33}$$

19.2 Influence of Rotation on Spheroidal Modes

In evaluating the operator $\boldsymbol{M}^{(0)}(\xi_{nlm})$ in equation (19.27), we suppose the equilibrium velocity field $\boldsymbol{v}_0$ is due to the rotation of the star. Let us suppose the magnetic effect is much smaller than the effect of the rotation and investigate the effect of the rotation in this subsection. The assumption may be justified in most cases. The equilibrium velocity field is given by

$$\boldsymbol{v}_0 = \boldsymbol{\Omega} \times \boldsymbol{r} = (0,\ 0,\ r\Omega \sin\theta) , \tag{19.34}$$

where the angular velocity $\boldsymbol{\Omega}$ of the star at equilibrium measured in the rotating frame with an angular velocity $\boldsymbol{\Omega}_0$ is assumed to be axially symmetric so that

$$\boldsymbol{\Omega} = [\Omega(r,\theta)\cos\theta,\ -\Omega(r,\theta)\sin\theta,\ 0] . \tag{19.35}$$

We consider the problem in a rotating frame whose rotational axis is identical with the rotational axis of the star. Using the relations among the unit vectors

$$\frac{\partial \boldsymbol{e}_r}{\partial \phi} = \boldsymbol{e}_\phi \sin\theta , \tag{19.36}$$

$$\frac{\partial \boldsymbol{e}_\theta}{\partial \phi} = \boldsymbol{e}_\phi \cos\theta , \tag{19.37}$$

and

$$\frac{\partial \boldsymbol{e}_\phi}{\partial \phi} = -\boldsymbol{e}_r \sin\theta - \boldsymbol{e}_\theta \cos\theta , \tag{19.38}$$

we obtain

$$\begin{aligned} \frac{1}{2}\xi_{m''}^* \cdot \boldsymbol{M}^{(0)}(\xi_m) &= -m\Omega \xi_{m''}^* \cdot \xi_m - i(\Omega+\Omega_0)\xi_{m'',r}^* \xi_{m,\phi} \sin\theta \\ &\quad - i(\Omega+\Omega_0)\xi_{m'',\theta}^* \xi_{m,\phi} \cos\theta \\ &\quad + i(\Omega+\Omega_0)\xi_{m'',\phi}^* (\xi_{m,r}\sin\theta + \xi_{m,\theta}\cos\theta) , \end{aligned} \tag{19.39}$$

where Ω_0 denotes the angular velocity of the rotating frame. Here the suffixes n and l representing the multiplets ξ_{nlm} are omitted for

simplicity, and the suffixes r, θ, and ϕ mean the r-, θ-, and ϕ-component of $\boldsymbol{\xi}$ measured in the spherical polar coordinates, of which $\theta = 0$ is taken as the direction of the rotational axis, and the azimuthal dependence of $\boldsymbol{\xi}_{nlm}$ is taken as $\exp(im\phi)$. Then, if we take the polar angles (θ, ϕ) with respect to the rotational axis of the star as a base for $\boldsymbol{\xi}_{nlm}$, the integral of equation (19.39) over the whole star is reduced to

$$\frac{1}{2}\int_0^M \boldsymbol{\xi}^*_{nlm''}\cdot\boldsymbol{M}^{(0)}(\boldsymbol{\xi}_{nlm})dM_r=\delta_{m''m}m\times\left\{\Omega_0\int_0^R\rho(r)r^2(2\xi_r\xi_h+\xi_h^2)dr\right.$$

$$+\frac{2l+1}{2}\frac{(l-|m|)!}{(l+|m|)!}\int_{\theta=0}^{\pi}\int_{r=0}^{R}\rho(r)r^2\Omega(r,\theta)$$

$$\times\left[(-\xi_r^2+2\xi_r\xi_h)(P_l^{|m|})^2+\right.$$

$$\left.\left.+\xi_h^2\left[2P_l^{|m|}\frac{dP_l^{|m|}}{d\theta}\frac{\cos\theta}{\sin\theta}-\left(\frac{dP_l^{|m|}}{d\theta}\right)^2-\frac{m^2}{\sin^2\theta}(P_l^{|m|})^2\right]\right]dr\sin\theta d\theta\right\}, \tag{19.40}$$

while the denominator of $\boldsymbol{M}_{m''m}$, I_{nl}, is given by

$$\int_0^M|\boldsymbol{\xi}^{(0)}|^2dM_r=\int_0^R\rho(r)r^2[\xi_r^2+l(l+1)\xi_h^2]dr\ . \tag{19.41}$$

Equation (19.40) means that the matrix $\boldsymbol{M}\equiv(\boldsymbol{M}_{m''m})$ is diagonal:

$$\boldsymbol{M}_{m''m}\equiv\sigma_m^{(1)rot}\delta_{m''m}\ . \tag{19.42}$$

As a consequence, the eigenvector matrix $\boldsymbol{\alpha}$ is the unit matrix. That is, the zero-order eigenfunction is given by a single spherical harmonic $Y_l^m(\theta,\phi)$. The perturbation in eigenfrequency of the mode labeled by m due to the rotation measured in the rotating frame of the angular frequency Ω_0 is given by (Hansen, Cox, and Van Horn, 1977)

$$\sigma_m^{(1)rot}=m\times\left\{\Omega_0\int_0^R\rho(r)r^2(2\xi_r\xi_h+\xi_h^2)dr\right.$$

$$+\frac{2l+1}{2}\frac{(l-|m|)!}{(l+|m|)!}\int_{\theta=0}^{\pi}\int_{r=0}^{R}\rho(r)r^2\Omega(r,\theta)$$

$$\times\left[(-\xi_r^2+2\xi_r\xi_h)(P_l^{|m|})^2\right.$$

$$\left.\left.+\xi_h^2\left[2P_l^{|m|}\frac{dP_l^{|m|}}{d\theta}\frac{\cos\theta}{\sin\theta}-\left(\frac{dP_l^{|m|}}{d\theta}\right)^2-\frac{m^2}{\sin^2\theta}(P_l^{|m|})^2\right]\right]dr\sin\theta d\theta\right\}$$

$$\times\left[\int_0^R\rho(r)r^2[\xi_r^2+l(l+1)\xi_h^2]dr\ \right]^{-1}\ . \tag{19.43}$$

With the help of the properties of spherical harmonics $Y_l^m(\theta,\phi)$, the integral of equation (19.43) is rewritten in another useful form (Cuypers, 1980):

$$\sigma_m^{(1)rot}=m\times\left\{\Omega_0\int_0^R\rho(r)r^2(2\xi_r\xi_h+\xi_h^2)dr\right.$$

$$+\frac{2l+1}{2}\frac{(l-|m|)!}{(l+|m|)!}\int_{r=0}^{R}\rho(r)r^2\left[\int_{\theta=0}^{\pi}(P_l^{|m|})^2\left\{\Omega(r,\theta)\sin\theta\right.\right.$$

$$\times\left(2\xi_r\xi_h-\xi_r^2+\xi_h^2[1-l(l+1)]\right)$$

$$\left.\left.-\left(\frac{3}{2}\frac{\partial\Omega}{\partial\theta}\cos\theta+\frac{1}{2}\frac{\partial^2\Omega}{\partial\theta^2}\sin\theta\right)\xi_h^2\right\}d\theta\right]dr\Bigg\}$$

$$\times\left[\int_0^R\rho(r)r^2[\xi_r^2+l(l+1)\xi_h^2]dr\ \right]^{-1}\ . \tag{19.44}$$

The perturbation in frequency in an inertial frame is given by equation (19.43) or (19.44) with $\Omega_0 = 0$. As seen from equation (19.43), the perturbation in frequency due to the rotation is dependent on the index m of the spherical surface harmonics $Y_l^m(\theta,\phi)$. Thus, the $(2l+1)$-fold degeneracy is resolved by rotation. This result is similar to the Zeeman effect of magnetic field in which m is the magnetic quantum number.

It may be instructive to consider some simple cases. In a case of uniform rotation $\Omega = \text{const.}$, equation (19.44) leads the perturbation in frequency in an inertial frame of $\Omega_0 = 0$ (Cowling and Newing, 1949; Ledoux, 1951):

$$\sigma_{nlm}^{(1)rot}\big|_{\text{inertial frame}}=-m(1-C_{nl})\Omega\ , \tag{19.45}$$

where

$$C_{nl}=\frac{\int_0^R\rho r^2[2\xi_r\xi_h+\xi_h^2]dr}{\int_0^R\rho r^2[\xi_r^2+l(l+1)\xi_h^2]dr} \tag{19.46}$$

is a constant depending on the model and on the mode considered. The perturbation in frequency is proportional to the rotational angular

velocity Ω and to the azimuthal order m. A nonradial mode with $m \neq 0$ travels around the polar axis with a phase velocity $-\sigma_m/m = -\sigma^{(0)}/m + (1 - C_{nl})\Omega$. In the reference frame co-rotating with the star ($\Omega = 0$), the frequencies of traveling waves are

$$\sigma_{nlm}|_{\text{co-rotating frame}} = \sigma_{nl}^{(0)} + mC_{nl}\,\Omega_0 \ , \qquad (19.47)$$

and they are lower or higher than the frequency (undisturbed by rotation) of the standing wave with $m = 0$, depending upon whether the traveling directions are the same or opposite to the rotation. In the case of p-modes, with an increase in the radial order n, since the radial displacement ξ_r comes to dominate over the horizontal displacement ξ_h, the quantity C_{nl} tends to zero. In the case of g-modes, in contrast, it tends to $1/[l(l+1)]$, since ξ_h becomes the dominant term with increasingly higher overtones.

In the case of $\Omega(r,\theta) = \Omega(r)$, equation (19.44) leads to

$$\sigma_m^{(1)rot} = m\left\{C_{nl}\,\Omega_0 - \frac{\int_0^R \rho r^2 \Omega(r)\left[\xi_r^2 - 2\xi_r\,\xi_h - \xi_h^2[1 - l(l+1)]\right]dr}{\int_0^R \rho r^2[\xi_r^2 + l(l+1)\xi_h^2]dr}\right\}. \qquad (19.48)$$

Again, the perturbation in frequency is linearly proportional to the azimuthal order m. In other cases, in general, the perturbation in eigenfrequency $\sigma_m^{(1)}$ depends on m in more complicated forms.

19.3 The r Modes

In a non-rotating non-magnetic spherical star, the toroidal vector fields of velocity correspond to the trivial solution with zero frequency for the adiabatic linear nonradial oscillations as discussed in Section 13.3. However, the toroidal displacement vector must be incorporated with usual spheroidal displacements to represent an arbitrary displacement [see equation (19.20)]. In a rotating star, the toroidal modes become non-trivial, having oscillation frequencies of the order of the rotation frequency (Papaloizou and Pringle, 1978). These modes are called r-modes (or quasi-toroidal modes). The character of the r-modes is similar to Rossby waves which appear in the Earth's atmosphere or oceans (see, e.g., Greenspan, 1969; Chapter VI).

In this subsection, we assume uniform rotation and nonexistence of magnetic field, and use the co-rotating frame, $\Omega = 0$. The angular frequency of oscillation in an inertial frame is obtained by adding $-m\Omega_0$ to the angular frequency in the corotating frame. For a uniformly rotating non-magnetic star, equation (19.10) is, in the co-rotating frame, reduced to

$$\mathcal{L}(\boldsymbol{\xi}) - \sigma^2\boldsymbol{\xi} + 2i\sigma\boldsymbol{\Omega}_0 \times \boldsymbol{\xi} = 0 \ . \qquad (19.49)$$

The frequency of toroidal modes is zero in a non-rotating star ($\sigma^{(0)} = 0$), which is equivalent to the relation

$$\mathcal{L}^{(0)}(\boldsymbol{\xi}^{(0)}) = 0 \qquad (19.50)$$

for a toroidal displacement $\boldsymbol{\xi}^{(0)}$. Because of $\sigma^{(0)} = 0$, however, we cannot use equation (19.18) for the r-modes.

Toroidal velocity fields have no radial velocity but have non-zero radial component of vorticity (the curl of velocity), while spheroidal velocity fields have finite radial velocity but no radial component of vorticity. Therefore, the toroidal velocity fields do not disturb the equilibrium configuration of a non-rotating non-magnetic star. This is the reason why the toroidal displacements have zero angular frequency (see Section 13) in a non-rotating spherical star. However, in a rotating star, the radial component of vorticity interacts with the Coriolis force and disturbs the equilibrium structure of the star. This is the reason for the existence of the r-mode oscillations with finite angular frequency. In discussing the characteristic of the r-modes, it is instructive to separate equation (19.49), which consists of three component equations, into the following three equations:

$$\sigma^2(\nabla_\perp \times \boldsymbol{\xi})_r - 2i\sigma[\boldsymbol{\Omega}_0(\nabla_\perp \cdot \boldsymbol{\xi}) - (\boldsymbol{\Omega}_0 \cdot \nabla_\perp)\boldsymbol{\xi}]_r = [\nabla_\perp \times \mathcal{L}(\boldsymbol{\xi})]_r , \qquad (19.51)$$

$$\sigma^2 \nabla_\perp \cdot \boldsymbol{\xi} + 2i\sigma\boldsymbol{\Omega}_0 \cdot (\nabla_\perp \times \boldsymbol{\xi}) = \nabla_\perp \cdot \mathcal{L}(\boldsymbol{\xi}) , \qquad (19.52)$$

and

$$2i\sigma\Omega_0 \sin\theta\,\xi_\phi = [\mathcal{L}(\boldsymbol{\xi})]_r - \sigma^2\xi_r , \qquad (19.53)$$

where equation (19.51) is the r-component of the operation $\nabla_\perp \times$ as applied to equation (19.49), equation (19.52) is obtained by applying operation $\nabla_\perp \cdot$ to equation (19.49), and equation (19.53) is the r-component of equation (19.49). Since $[\nabla_\perp \times \mathcal{L}^{(0)}(\boldsymbol{\xi})]_r = 0$ for any displacement vector $\boldsymbol{\xi}$, the non-zero terms of the right-hand side of equation (19.51) are associated with deformation of the equilibrium structure due to rotation and are of the order of Ω_0^2; i.e.,

$$[\nabla \times \mathcal{L}(\boldsymbol{\xi})]_r = -\frac{1}{r^2}\frac{\partial p}{\partial \theta}\frac{1}{\sin\theta}\frac{\partial}{\partial \phi}\left[\frac{1}{\rho^2}\nabla \cdot (\rho\boldsymbol{\xi})\right]$$

$$+ \frac{1}{r^2\rho^2}\frac{\partial \rho}{\partial \theta}\frac{1}{\sin\theta}\frac{\partial}{\partial \phi}[\boldsymbol{\xi} \cdot \nabla p + c^2\rho\nabla \cdot \boldsymbol{\xi}] . \qquad (19.54)$$

Let us consider an r-mode whose zero-order displacement vector is proportional to the toroidal vector η_{lm}, and assume the displacement vector as

$$\xi = \alpha(r)\eta_{lm} + \sum_{n'l'} \beta_{n'l'm}\xi_{n'l'm} + \sum_{l'}{}' \gamma_{l'}(r)\eta_{l'm} \ , \qquad (19.55)$$

where the form of the toroidal vector η_{lm} is given by equation (19.21), and $\xi_{n'l'm}$ represents the zero-order eigenfunction for the spheroidal mode with quantum numbers $n'l'm$. The leading terms in equation (19.51) are of the order of Ω_0^2 because σ is $O(\Omega_0)$. When equation (19.55) is substituted into equation (19.51), the leading terms are written as

$$\sigma^{(0)2}\alpha(r)(\nabla_\perp \times \eta_{lm})_r + 2i\sigma^{(1)}\alpha(r)(\boldsymbol{\Omega}_0 \cdot \nabla_\perp \eta_{lm})_r = 0. \qquad (19.56)$$

Using in the above equation the expression for η_{lm} given by equation (19.21), we obtain

$$\sigma^{(1)}\left[\sigma^{(1)} - \frac{2m\Omega_0}{l(l+1)}\right]\alpha(r)\sqrt{l(l+1)}Y_l^m = 0. \qquad (19.57)$$

Then we obtain the non-zero eigenvalue of an r-mode as

$$\sigma^{(1)} = \frac{2m\Omega_0}{l(l+1)} \ , \qquad (19.58)$$

which is identical to the angular frequency for Rossby (or planetary) waves (Longuet-Higgins, 1964; Chapter VI).

Equation (19.58) indicates that in the co-rotating frame the r-modes propagate counter to the stellar rotation in the azimuthal direction (i.e., retrograde waves in the co-rotating frame), because (ϕ, t)-dependence of the eigenfunction is approximately written as $\exp\{im[\phi + \frac{2\Omega_0}{l(l+1)}t]\}$. Note that the leading term of eigenfrequency of the r-modes is determined only by the angular dependence of the radial component of vorticity and rotation of the star [see equation (19.56)]. To the order of Ω_0, the eigenfrequency of the r-modes is independent of the radial dependence of the eigenfunction, $\alpha(r)$. In this sense, the eigenfrequency is infinitely degenerate to the order of Ω_0. This degeneracy is resolved when we consider the higher order terms.

When we substitute equation (19.55) into equation (19.53), which states that the radial component of the Coriolis force must be balanced by the effect of spheroidal displacement, we find

$$\beta_{n'l'm} = O(\Omega_0^2) \ . \qquad (19.59)$$

Moreover, if we substitute equation (19.55) into equation (19.51) again and take into account the higher order terms, we obtain

$$-\sigma^{(1)}\sigma^{(2)}\sqrt{l(l+1)}\alpha(r)Y_l^m + 2i\sigma^{(1)}\Omega_0 \sum_{n'l'} \beta_{n'l'm}\left[-\xi_h l(l+1)\cos\theta Y_l^m + (\xi_r + \xi_h)\sin\theta\frac{\partial Y_l^m}{\partial\theta}\right] = \sum_{n'l'} \beta_{n'l'm}\left[\nabla_\perp \times \mathscr{L}^{(1)}(\xi_{n'l'm})\right]_r \ . \qquad (19.60)$$

Since $[\nabla_\perp \times \mathscr{L}^{(1)}(\xi_{n'l'm})]_r = O(\Omega_0^2)$, we obtain

$$\sigma^{(2)} = O(\Omega_0^3) \ , \qquad (19.61)$$

(Papaloizou and Pringle, 1978). The value of $\sigma^{(2)}$ is determined as the eigenvalue in the numerical calculation to obtain radial dependence of the toroidal displacement $\alpha(r)$. We note that in determining $\sigma^{(2)}$ and $\alpha(r)$ the spheroidal components with $l' = l \pm 1$ must be incorporated. But $\gamma_l'(r)$ is not necessary to obtain $\sigma^{(2)}$. Further discussions on the properties of r-modes are given in, e.g., Provost, Berthomieu, and Rocca (1981), Smeyers, Craeynest, and Martens (1981), and Saio (1982). The overstability of r-modes in slowly rotating stars was investigated by Saio (1982) and Berthomieu and Provost (1983).

19.4 Influence of Magnetic Fields

Next, we consider the magnetic effect. Let us suppose the magnetic effect dominates over the effect of the rotation. The rapidly oscillating Ap stars seem to fulfill this condition (see Section 9). In contrast to the case of rotation in which the effect on stellar equilibrium configuration appears in the order of Ω^2 but the effect on the oscillations appears in the order of Ω, the effect of magnetic field appears as a term of $\mathscr{L}^{(1)}$ in equation (19.18) in the order of B^2 both in the equilibrium configuration and in the oscillations. Therefore, in a general case, a detailed equilibrium model is needed for consistency in order to consider the influence of magnetic field on the stellar nonradial oscillations. The only exception is the case of force-free equilibrium fields in which $(\nabla \times \boldsymbol{B}) \times \boldsymbol{B} = 0$.

However, in the absence of the unperturbed velocity field, if we take the polar angles (θ, ϕ) with respect to the magnetic axis of the star as a base for $\{\xi_{nlm}\}$, the matrix $\boldsymbol{B} \equiv (\boldsymbol{B}_{m''m})$ is diagonal:

$$\boldsymbol{B}_{m''m} = \sigma_{|m|}^{(1)mag}\delta_{m''m} \ , \qquad (19.62)$$

and the zero-order eigenfunction is given by a single spherical harmonic $Y_l^m(\theta, \phi)$. For a potential field $(\nabla \times \boldsymbol{B} = 0)$, $\sigma_{|m|}^{(1)mag}$ is given by

$$\sigma_m^{(1)mag} = \frac{1}{8\pi\sigma_{nl}^{(0)}I_{nl}}\int_0^M \rho^{-1}|\boldsymbol{B}'|^2 dM_r \ , \qquad (19.63)$$

if the energy loss $[(\boldsymbol{\xi}^{(0)}\times\boldsymbol{B})\times\boldsymbol{B}']$ from the surface is absent. In the case of a dipole field,

$$\boldsymbol{B}=B_0\nabla(r^{-2}\cos\theta)=B_0(2r^{-3}\cos\theta\boldsymbol{e}_r+r^{-3}\sin\theta\boldsymbol{e}_\theta)\ , \qquad (19.64)$$

equation (19.63) is reduced to

$$\sigma_m^{(1)mag}=\frac{B_0^2}{8\pi\sigma_{nl}^{(0)}}\frac{\displaystyle\int_0^M\rho^{-1}\beta_{lm}\,dM_r}{\displaystyle\int_0^M(\xi_r^{(0)2}+l_1^2\xi_r^{(0)2})dM_r}, \qquad (19.65)$$

where

$$\beta_{lm}=(l_1^2\xi_h^{(0)}-2\xi_r^{(0)})^2\Delta_0+(l_1^2\xi_h^{(0)}-2\xi_r^{(0)})(\xi_h^{(0)}-\xi_r^{(0)})(1-3\Delta_0)$$

$$+(\xi_h^{(0)}-\xi_r^{(0)})^2\Delta_1+\left[\frac{d}{dr}(r\xi_r^{(0)})\right]^2(1-\Delta_0)$$

$$+\frac{d}{dr}(r\xi_r^{(0)})\frac{d}{dr}(r\xi_r^{(0)})(1-3\Delta_0)+\left[\frac{d}{dr}(r\xi_h^{(0)})\right]^2(l_1^2-m^2-\Delta_1)$$

$$-2\xi_h\frac{d}{dr}[r(\xi_r^{(0)}+\xi_h^{(0)})]m^2+\xi_h^{(0)2}l_1^2m^2,$$

$$l_1^2=l(l+1),\quad \Delta_0=\frac{2(l_1^2-m^2)-1}{(2l-1)(2l+3)},$$

and

$$\Delta_1=\frac{2l_1^4-m^2(2l_1^2+3)}{(2l-1)(2l+3)}. \qquad (19.66)$$

19.5 Nonradial Oscillations in a Rotating Magnetic Star

Some Ap stars posses strong magnetic fields whose symmetric axis is inclined to the rotational axis of the star. The observed magnetic field strength then varies with the rotational phase of the star. As described in Section 9, rapid oscillations have recently been discovered in some of these stars, and these oscillations look like axisymmetric dipole modes whose symmetric axis is identical with the magnetic axis which itself is inclined to the rotational axis of the star. We consider in this subsection the nonradial oscillations in a rotating magnetic star by taking into account both the effects of the rotation and the magnetic fields upon oscillation.

The basic equation to solve is equation (19.25). As seen in equations (19.26)–(19.28), the expression of matrixes $\boldsymbol{O}$, $\boldsymbol{M}$, and $\boldsymbol{B}$ are

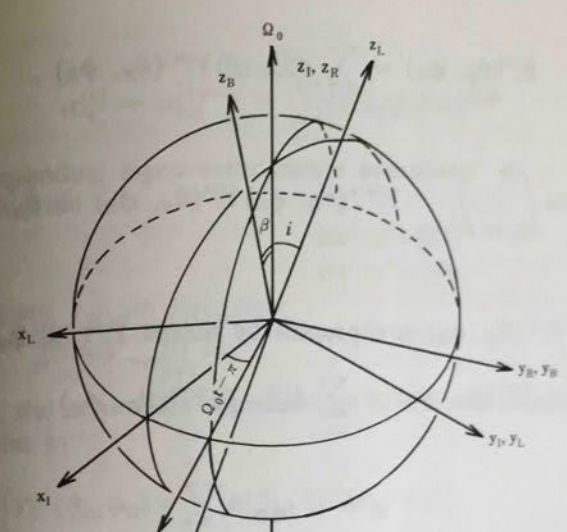

Fig. 19.1 Geometry of various frames: $(x_i, y_i, z_i) = (r\sin\theta_i\cos\phi_i, r\sin\theta_i\sin\phi_i, r\cos\theta_i)$, $(i = B, R, I, L)$. The transformation formula of spherical harmonics is given by means of the so-called Euler angles and the explicit form is given by equations (19.68), (19.86), and (19.88).

dependent on the choice of the base of eigenfunctions—that is, they are dependent on the choice of coordinates. Let us now suppose that the effect of the magnetic field dominates that of rotation. In such a case, it is more convenient to adopt a reference frame co-rotating with the magnetic axis with the angular velocity Ω_0, and to choose $Y_l^m(\theta_B, \phi_B)$ to describe the eigenfunctions rather than to use $Y_l^m(\theta_R, \phi_R)$, where (θ_B, ϕ_B) and (θ_R, ϕ_R) are coordinates in the co-rotating frame and $\theta_B = 0$ and $\theta_R = 0$ are the directions of the magnetic axis and the rotation axis, respectively. The angle between these two axes is denoted by β (see Fig. 19.1). In the following, we derive the expression of the matrix $\boldsymbol{O}$ by means of the coordinates (θ_B, ϕ_B).

Let us first obtain the expression of $\boldsymbol{M}$, the component of $\boldsymbol{O}$ due to the rotation, by means of the coordinates (θ_B, ϕ_B). As was noted in the previous subsection 19.2, in the (θ_R, ϕ_R) frame

$$\boldsymbol{M}^{(R)}\boldsymbol{\alpha}^{(R)}=\boldsymbol{\alpha}^{(R)}\boldsymbol{\Lambda}. \qquad (19.67)$$

Here the quantities with superscript (R) represent those expressed in the (θ_R, ϕ_R) frame co-rotating with the magnetic axis, and $\boldsymbol{\Lambda} = (\sigma_m^{(1)rot}\delta_{m''m})$. The spherical harmonics with respect to (θ_B, ϕ_B), $Y_l^m(\theta_B, \phi_B)$, are expanded by means of $Y_l^{m'}(\theta_R, \phi_R)$ as

$$Y_l^m(\theta_B,\ \phi_B) = \sum_{m'=-l}^{l} d^{(l)}_{mm'}(\beta)\, Y_l^{m'}(\theta_R,\ \phi_R)\ , \qquad (19.68)$$

where

$$d^{(l)}_{mm'}(\beta) \equiv \int_{\phi_B=0}^{2\pi}\int_{\theta_B=0}^{\pi} Y_l^{m'*}(\theta_R,\ \phi_R)\, Y_l^m(\theta_B,\ \phi_B)\, \sin\theta_B d\theta_B d\phi_B . \qquad (19.69)$$

Inversely, $Y_l^{m'}(\theta_R,\ \phi_R)$ is expressed by means $Y_l^m(\theta_B,\ \phi_B)$ as

$$Y_l^{m'}(\theta_R,\ \phi_R) = \sum_{m=-l}^{l} d^{(l)}_{mm'}(\beta)\, Y_l^m(\theta_B,\ \phi_B)\ . \qquad (19.70)$$

Hence

$$\boldsymbol{\alpha}^{(R)} = {}^t\boldsymbol{d}\boldsymbol{\alpha}^{(B)}\ , \qquad (19.71)$$

where the matrix $\boldsymbol{d}$ consists of $d^{(l)}_{mm'}(\beta)$, superscript t means the transposed matrix, and superscript (B) means the expression in the $(\theta_B,\ \phi_B)$ frame. It should be noted that

$$\boldsymbol{d}^{-1} = {}^t\boldsymbol{d}\ . \qquad (19.72)$$

Substituting equation (19.71) into equation (19.67) and then multiplying $\boldsymbol{d}$ from the left-hand side, we obtain

$$\boldsymbol{d}\boldsymbol{M}^{(R)\,t}\boldsymbol{d}\boldsymbol{\alpha}^{(B)} = \boldsymbol{\alpha}^{(B)}\boldsymbol{\Lambda}\ . \qquad (19.73)$$

The right-hand side of equation (19.73) should be $\boldsymbol{M}^{(B)}\boldsymbol{\alpha}^{(B)}$, and hence

$$\boldsymbol{M}^{(B)} = \boldsymbol{d}\boldsymbol{M}^{(R)\,t}\boldsymbol{d}\ . \qquad (19.74)$$

Since $\boldsymbol{M}^{(R)}$ is diagonal and is given by equation (19.42),

$$\boldsymbol{M}^{(B)}_{m''m} = \sum_{k=-l}^{l} d^{(l)}_{m''k}(\beta)\, d^{(l)}_{mk}(\beta)\, \sigma_k^{(1)rot}\ . \qquad (19.75)$$

By adding equations (19.62) and (19.75), we eventually obtain the expression of the matrix $\boldsymbol{O}^{(B)}$ in the $(\theta_B,\ \phi_B)$ frame (Dziembowski and Goode, 1985, 1986; Kurtz and Shibahashi, 1986):

$$\boldsymbol{O}^{(B)}_{m''m} = \sigma^{(1)mag}_{|m|}\delta_{m''m} + \sum_{k=-l}^{l} d^{(l)}_{m''k}(\beta)\, d^{(l)}_{mk}(\beta)\, \sigma_k^{(1)rot}\ . \qquad (19.76)$$

The off-diagonal components of the matrix $\boldsymbol{O}^{(B)}$ are of the order of $\sigma^{(1)rot}$ and therefore they do not contribute to the eigenvalue to the order of $\sigma^{(1)rot}$. The eigenvalues are given by the diagonal components

of $\boldsymbol{O}^{(B)}$:

$$\sigma_m^{(1)} \approx \sigma^{(1)mag}_{|m|} + \sum_{k=-l}^{l} [d^{(l)}_{mk}(\beta)]^2 \sigma_k^{(1)rot}\ . \qquad (19.77)$$

The corresponding eigenvector matrix consists of

$$\alpha^{(B)}_{m''m} = \begin{cases} 1 & \text{for } m'' = m\ ; \\ 0 & \text{for } m'' = -m; \\ \dfrac{\sum_{k=-l}^{l} d^{(l)}_{m''k}(\beta) d^{(l)}_{mk}(\beta)\, \sigma_k^{(1)rot}}{\sigma^{(1)mag}_{|m|} - \sigma^{(1)\ mag}_{|m''|}} & \text{for } m'' \neq \pm m\ . \end{cases} \qquad (19.78)$$

Therefore, the zero-order eigenfunction of a slowly rotating magnetic star is given by

$$\xi^{(0)} \propto \Big[Y_l^m(\theta_B, \phi_B) + {\sum_{m''=-l}^{l}}'' \alpha^{(B)}_{m''m} Y_l^{m''}(\theta_B,\ \phi_B) \Big] \times \exp\Big[i\Big(\sigma^{(0)} + \sigma^{(1)mag}_{|m|} + \sum_{k=-l}^{l} [d^{(l)}_{mk}(\beta)]^2 \sigma_k^{(1)rot} \Big) t \Big]. \qquad (19.79)$$

In a case of uniform rotation, $\sigma_k^{(1)rot}$ measured in the reference frame co-rotating with the star with angular velocity Ω_0 is

$$\sigma_k^{(1)rot} = k\, C_{nl}\, \Omega_0, \qquad (19.80)$$

which is obtained by substitution of $\Omega = 0$ into equation (19.44). Since, as Aizenman, Hansen, Cox, and Pesnell (1984) showed,

$$\sum_{k=-l}^{l} [d^{(l)}_{mk}(\beta)]^2 k\Omega_0 = m\, C_{nl}\, \Omega_0 \cos\beta\ , \qquad (19.81)$$

$$\sigma_m^{(1)} \approx \sigma^{(1)mag}_{|m|} + m\, C_{nl}\, \Omega_0 \cos\beta\ . \qquad (19.82)$$

The eigenvector matrix is then given by

$$\alpha^{(B)}_{m''m} \approx \begin{cases} 1 & \text{for } m'' = m\ ; \\ 0 & \text{for } m'' = -m; \\ \dfrac{\left[\sum_{k=-l}^{l} k d^{(l)}_{m''k}(\beta) d^{(l)}_{mk}(\beta) \right] C_{nl}\, \Omega_0}{\sigma^{(1)mag}_{|m|} - \sigma^{(1)mag}_{|m''|}} & \text{for } m'' \neq \pm m\ . \end{cases} \qquad (19.83)$$

Therefore the zero-order eigenfunction of a slowly rotating magnetic star is given by

$$\xi^{(0)} \propto \Big[Y_l^m(\theta_B,\ \phi_B) + {\sum_{m''=-l}^{l}}'' \alpha^{(B)}_{m''m} Y_l^{m''}(\theta_B,\ \phi_B) \Big]$$

$$\times \exp\left[i(\sigma^{(0)} + \sigma^{(1)mag}_{|m|} + m\, C_{nl}\, \Omega_0 \cos\beta)t\right] \qquad (19.84)$$

for $m = -l, \ldots, l$, where Σ'' means the summation over m'' except for $m'' = \pm m$.

The observable luminosity variation due to a single mode labelled by m is obtained by rewriting the eigenfunction in an inertial frame and integrating over the visible disc (see Fig. 19.1). As a first step, we transform the spherical harmonics $Y_l^m(\theta_B, \phi_B)$ into $Y_l^{m'}(\theta_R, \phi_R)$ in the co-rotating frame using equation (19.68). In the co-rotating frame, the perturbed physical quantities $f'(\mathbf{r}, t)$ of the single mode are given by

$$f'_{nlm}(\mathbf{r},t) = f'_{nl}(r) \sum_{m''} \sum_{m'} \alpha^{(B)}_{m''m}\, d^{(l)}_{m''m'}(\beta) Y_l^{m'}(\theta_R, \phi_R) \exp[i(\sigma^{(0)}_{nl} + \sigma^{(1)}_m)t]. \qquad (19.85)$$

Next we move from the co-rotating frame to an inertial frame, whose polar axis coincides with the rotation axis of the star (see Fig. 19.1 and Table 19.1). Let (θ_I, ϕ_I) be the coordinates of the inertial frame. Then, since

$$\begin{aligned} Y_l^m(\theta_I, \phi_I) &= Y_l^m(\theta_R, \phi_R) \exp[im(\Omega_0 t - \pi)] \\ &= (-1)^m Y_l^m(\theta_R, \phi_R) \exp(im\,\Omega_0 t), \end{aligned} \qquad (19.86)$$

where $t=0$ is chosen as the time when the magnetic pole is the closest to the line-of-sight, the eigenfunctions are rewritten as

$$\begin{aligned} f'_{nlm}(\mathbf{r},t) = f'_{nl}(r) \sum_{m''} \sum_{m'} (-1)^{m'} \alpha^{(B)}_{m''m}\, d^{(l)}_{m''m'}(\beta) Y_l^{m'}(\theta_I, \phi_I) \\ \times \exp[i(\sigma^{(0)}_{nl} + \sigma^{(1)}_m - m'\Omega_0)t]. \end{aligned} \qquad (19.87)$$

We transform the coordinates (θ_I, ϕ_I) into another set of coordinates (θ_L, ϕ_L) in the inertial frame, where $\theta_L = 0$ coincides with the line-of-sight. Since

$$Y_l^m(\theta_I, \phi_I) = \sum_{m'=-l}^{l} d^{(l)}_{mm'}(i)\, Y_l^{m'}(\theta_L, \phi_L), \qquad (19.88)$$

where i denotes the angle between the rotation axis of the star and the line-of-sight (see Fig. 19.1),

$$f'_{nlm}(\mathbf{r},t) = f'_{nl}(r) \sum_{m''} \sum_{m'} (-1)^{m'} \alpha^{(B)}_{m''m} d^{(l)}_{m''m'}(\beta) \sum_{m'''} d^{(l)}_{m'm'''}(i)\, Y_l^{m'''}(\theta_L, \phi_L)$$

$$\times \exp[i(\sigma^{(0)}_{nl} + \sigma^{(1)}_m - m'\Omega_0)t]. \qquad (19.89)$$

Integration of equation (19.89) over the visible disc, $\theta_L = [0, \pi/2]$ and $\phi_L = [0, 2\pi]$, leads to obvservable luminosity variation due to the single mode. Since

$$\int_0^{2\pi} Y_l^{m'''}(\theta_L, \phi_L)\, d\phi_L = 0 \qquad (19.90)$$

except for $m''' = 0$, we eventually obtain an expression for the observable luminosity variation:

$$\begin{aligned} \Delta L_{obs} \propto \sum_{m''} \sum_{m'} (-1)^{m'} \alpha^{(B)}_{m''m} d^{(l)}_{m''m'}(\beta)\, d^{(l)}_{m'0}(i)\, Y_l^0(\theta_L, \phi_L) \\ \times \exp[i(\sigma^{(0)}_{nl} + \sigma^{(1)}_m - m'\Omega_0)t]. \end{aligned} \qquad (19.91)$$

In cases of a uniform rotation, equation (19.91) is reduced to

$$\begin{aligned} \Delta L_{obs} \propto \sum_{m'=-l}^{l} (-1)^{m'} \Big\{ & d^{(l)}_{mm'}(\beta) \\ & + C_{nl}\,\Omega_0 \sum_{m''=-l}^{l}{}'' \frac{d^{(l)}_{m''m'}(\beta)}{\sigma^{(1)mag}_{|m|} - \sigma^{(1)mag}_{|m''|}} \Big[\sum_{k=-l}^{l} k d^{(l)}_{m''k}(\beta) d^{(l)}_{mk}(\beta) \Big] \Big\} \\ & \times d^{(l)}_{m'0}(i) \cos\{[\sigma^{(0)}_{nl} + \sigma^{(1)mag}_{|m|} + m\, C_{nl}\,\Omega_0 \cos\beta - m'\Omega_0]t\}\ . \end{aligned} \qquad (19.92)$$

The form of matrix $\boldsymbol{d}$ for $l=1$ can be seen in Edmonds (1957), and those for $l=2$ and $l=3$ are given in Shibahashi (1986). Equation (19.92) will be applied to the observations of the rapidly oscillating Ap stars in Section 43.

Table 19.1 Relations among various coordinates and the transforming formulae.

θ-axis	Magnetic axis		Rotation axis		Line-of-sight
Rotating frame	(θ_B, ϕ_B)	$\xrightarrow{(19.68)}$	(θ_R, ϕ_R)		
			$\downarrow$ (19.86)		
Inertial frame			(θ_I, ϕ_I)	$\xrightarrow{(19.88)}$	(θ_L, ϕ_L)

20. *Influence of Convection*

20.1 Influence of Convection

In most stars, there are convection zones either in the interior or in the outer envelope. Convection in stars should be in a state of fully developed turbulence because of its high Reynolds number. Our main concern, however, is the influence of its large-scale statistical average. The corresponding mathematical description will be the coarse graining average in which fluctuations on a smaller scale than a certain grain size are smoothed out. In nonradial oscillations, wave lengths may not always be longer than the characteristic scale of turbulent convection, which is supposed to be of the order of the scale height. We will, however, treat here those cases in which the wave length of the oscillation is much larger than the scale height, by taking a grain size large enough to smooth out the convective pattern. The influence of convection on the oscillation is described by the spatial average of the nonlinear couplings in the momentum and energy exchange that can be prescribed in analogy with the viscosity and the thermal conduction.

The basic equations governing the convection-pulsation system are given by equations (13.1)–(13.3). We will, however, represent the above prescription explicitly by introducing the turbulent Reynolds stress $\mathscr{P}_t$ and the turbulent conductive flux $\boldsymbol{F}_K$ in equations of momentum and energy conservation. Let us first define the mass-centered velocity, $\boldsymbol{w}$, by

$$\rho \boldsymbol{u} = \bar{\rho}\boldsymbol{w}, \tag{20.1}$$

and decompose it in the average (oscillation) velocity, $\boldsymbol{v}$, and the turbulent (convection) velocity, $\boldsymbol{V}$,

$$\boldsymbol{w} = \boldsymbol{v} + \boldsymbol{V}, \quad \boldsymbol{v} = \bar{\boldsymbol{w}}, \tag{20.2}$$

where the overbar denotes the local spatial average. Likewise, other symbols are decomposed into

$$\boldsymbol{u}=\bar{\boldsymbol{u}}+\boldsymbol{u}_C,\ p=\bar{p}+p_C,\ \rho=\bar{\rho}+\rho_C,\ \text{etc.}, \tag{20.3}$$

where subscript C, represents the convection. We define $\mathscr{P}_t$ and $\boldsymbol{F}_k$ by

$$(\mathscr{P}_t)_{ij} = <\bar{\rho}u_{Ci}V_{tj}> = <\bar{\rho}u_iV_{tj}> \tag{20.4}$$

and

$$\boldsymbol{F}_K = <\bar{\rho}\,(h_C+\boldsymbol{u}_C^2/2)\,\boldsymbol{V}_t> = <\bar{\rho}\,(h+\boldsymbol{u}^2/2)\,\boldsymbol{V}_t>, \tag{20.5}$$

where the convective turbulent velocity $\boldsymbol{V}$ has been decomposed

virtually into the laminar convection $\boldsymbol{V}_l$ generating no viscosity or conduction and the turbulent motion $\boldsymbol{V}_t$ generating viscosity and conduction We will, however, omit the subscript l from $\boldsymbol{V}_l$ hereafter, following the renormalization technique sometimes used for the evaluation of turbulent diffusivities (Nakano, 1972). Then, the basic equations (13.1)–(13.3) are rewritten in the following form:

$$\frac{\partial \rho}{\partial t} + \nabla\cdot(\rho\boldsymbol{u}) = 0, \tag{20.6}$$

$$\frac{\partial \rho \boldsymbol{u}}{\partial t} + \operatorname{div}(\rho\boldsymbol{u}\boldsymbol{u}) = -\nabla p - \rho\nabla\Phi - \operatorname{div}\mathscr{P}_t(\boldsymbol{u}), \tag{20.7}$$

and

$$\rho T\left[\frac{\partial S}{\partial t} + (\boldsymbol{u}\cdot\nabla)S\right] = \rho(\varepsilon_N+\varepsilon_V) - p_t\nabla\cdot\boldsymbol{u} - \nabla\cdot(\boldsymbol{F}_R+\boldsymbol{F}_K), \tag{20.8}$$

where

$$(\mathscr{P}_t)_{ij} = p_t\delta_{ij} - (\mathscr{S}_t)_{ij} = p_t\delta_{ij} - \mu_t\sigma_{ij}, \tag{20.9}$$

$$p_t = \frac{1}{3}<\bar{\rho}\boldsymbol{V}^2>,\ \sigma_{ij} = \frac{\partial u_i}{\partial x_j} + \frac{\partial u_j}{\partial x_i} - \frac{2}{3}(\nabla\cdot\boldsymbol{u})\delta_{ij}, \tag{20.10}$$

$$\rho\varepsilon_V = \operatorname{grad}\boldsymbol{u}\cdot\mathscr{S}_t(\boldsymbol{u}), \tag{20.11}$$

$$\boldsymbol{F}_K = -\kappa_t\nabla[(p+p_t)/\bar{\rho}], \tag{20.12}$$

with

$$\mu_t = f_v\bar{\rho}\sqrt{<\boldsymbol{V}>^2}l_t,\quad \kappa_t = f_K\bar{\rho}\sqrt{<\boldsymbol{V}>^2}l_t, \tag{20.13}$$

l_t being the mixing length, $f_v \sim 0.1$, and $f_K = 2.5\,f_v$. The factors f_v and f_K are somewhat uncertain (however, see Unno (1987) and references therein). Anisotropy of μ_t is important in the theory of stellar differential rotation and circulation [see, e.g., Durney (1987)], but is disregarded in equations (20.9) and (20.10). The explicit forms of $\mathscr{P}_t$ and $\boldsymbol{F}_K$ in equations (20.9) and (20.12) are due to the gradient diffusion approximation in analogy with that of molecular diffusivities. That is, the specific moment, $\boldsymbol{u}$ (the specific enthalpy, h, under constant pressure), is transported by mass flux, $\bar{\rho}\boldsymbol{V}$, in all directions so that the net momentum (thermal energy) transport should be proportional to the gradient of $\boldsymbol{u}$, (T). In the renormalization, it may appear that the contribution $(\rho\boldsymbol{V}\boldsymbol{V})$ in equation (20.7) is counted twice. But the turbulent diffusivities introduced by the gradient diffusion approxima-

tion treats essentially the moment $\boldsymbol{u}$ of one mean-free-time earlier, and the nonlinear inertia of the laminar flow is not included in $\mathscr{P}_t$. Therefore, the renormalization takes care of the nonlinear effect in smaller scales by the turbulent diffusivity, while retaining the nonlinear effect in larger scales as before. The analogy betweewn turbulence and molecular motions in the momentum diffusion are thus prescribed. In the same spirit, three terms, $-p_t\nabla\cdot\boldsymbol{u}$, $\rho\varepsilon_V$, and $-\nabla\cdot\boldsymbol{F}_K$, have been added in equation (20.8). The term, $-p_t\nabla\cdot\boldsymbol{u}$, represents the work done by the motion against the turbulent pressure gradient, $\rho\varepsilon_V$ denotes the viscous dissipation due to the turbulent viscosity, and $\boldsymbol{F}_K$ given by equation (20.5) as the small scale convection is deformed by the renormalization technique (Nakano, 1972) to be the turbulence counterpart of the molecular thermal conduction, which has been neglected compared with $\boldsymbol{F}_R$ in equation (20.12). The form of $\boldsymbol{F}_K$ in equation (20.12) is due to the gradient diffusion approximation of $\mathscr{J}_t(\boldsymbol{u})$. The introduction of p_t and ε_V in equation (20.8) is for consistency with the introduction of $\mathscr{P}_t$ in equation (20.7), which is necessary also when numerical computations are performed with the use of artificial viscosity. To show this, we derive the equation of the kinetic energy conservation from equation (20.7) by multiplying $\boldsymbol{u}$ scalarly,

$$\frac{\partial}{\partial t}\left(\frac{1}{2}\rho\boldsymbol{u}^2\right)+\nabla\cdot\left(\frac{1}{2}\rho\boldsymbol{u}^2\boldsymbol{u}\right)=-\boldsymbol{u}\cdot\nabla(p+p_t)-\rho\boldsymbol{u}\cdot\nabla\Phi+\boldsymbol{u}\cdot\operatorname{div}\mathscr{J}_t(\boldsymbol{u}). \tag{20.14}$$

Then the thermal energy conservation, equation (20.8), is transformed into

$$\frac{\partial}{\partial t}(\rho U)+\nabla\cdot(\rho h\boldsymbol{u})-\boldsymbol{u}\cdot\nabla(p+p_t)=\rho(\varepsilon_N+\varepsilon_V)-\nabla\cdot(\boldsymbol{F}_R+\boldsymbol{F}_K), \tag{20.15}$$

where use has been made of the thermodynamic relation

$$TdS = dU + pd(1/\rho) = dh - (1/\rho)dp, \tag{20.16}$$

and of a useful formula derived from the continuity (20.6), that is,

$$\rho(d/dt)Q = (\partial/\partial t)(\rho Q) + \nabla\cdot(\rho Q\boldsymbol{u}) , \tag{20.17}$$

for an arbitrary quantity Q. Adding equations (20.14) and (20.15), we obtain the total energy conservation,

$$\frac{\partial}{\partial t}\left[\rho\left(U+\frac{\boldsymbol{u}^2}{2}\right)\right]+\nabla\cdot\left[\rho\left(h+\frac{\boldsymbol{u}^2}{2}\right)\boldsymbol{u}\right]+\rho\boldsymbol{u}\cdot\nabla\Phi$$

$$=\rho\varepsilon_N-\nabla\cdot[\boldsymbol{F}_R+\boldsymbol{F}_K+\boldsymbol{u}\cdot\mathscr{P}_t(\boldsymbol{u})], \tag{20.18}$$

where $\boldsymbol{u}\cdot\mathscr{P}_t(\boldsymbol{u})$ represents the kinetic energy flux transported by the turbulent viscous stress. The work against the turbulent pressure, p_t, cancels in equation (20.18) by decreasing the kinetic energy but increasing the thermal energy.

The coarse grain average of equations (20.6), (20.7), and (20.18) gives

$$\frac{\partial\bar\rho}{\partial t}+\nabla\cdot(\bar\rho\boldsymbol{v})=0, \tag{20.19}$$

$$\bar\rho\left(\frac{\partial}{\partial t}+\boldsymbol{v}\cdot\nabla\right)\boldsymbol{v}+\nabla(\bar p+p_t)+\bar\rho\nabla\Phi=\operatorname{div}\mathscr{J}_t(\boldsymbol{v}), \tag{20.20}$$

and

$$\frac{\partial}{\partial t}\left[\bar\rho\left(\bar U+\frac{\boldsymbol{v}^2}{2}\right)\right]+\nabla\cdot\left[\bar\rho\left(\bar h+\frac{\boldsymbol{v}^2}{2}\right)\boldsymbol{v}\right]+\bar\rho\boldsymbol{v}\cdot\nabla\Phi$$

$$=\overline{\rho\epsilon_N}-\nabla\cdot[\bar{\boldsymbol{F}}_R+\bar{\boldsymbol{F}}_C]-\frac{\partial}{\partial t}\left\langle\frac{1}{2}\bar\rho\boldsymbol{V}^2\right\rangle-\nabla\cdot[\boldsymbol{F}_K+\boldsymbol{u}\cdot\mathscr{P}_t(\boldsymbol{v})], \tag{20.21}$$

where the convective flux,

$$\boldsymbol{F}_C=\left\langle\bar\rho\left(h+\frac{\boldsymbol{u}^2}{2}\right)\boldsymbol{V}\right\rangle, \tag{20.22}$$

absorbs the turbulence contribution $<\boldsymbol{V}\cdot\mathscr{P}_t(\boldsymbol{V})>$ in $<\boldsymbol{u}\cdot\mathscr{P}_t(\boldsymbol{u})>$, and $\bar\rho\,\bar{\boldsymbol{u}}\,\boldsymbol{v}$ and $\overline{\rho U}$ are approximated by $\bar\rho\boldsymbol{v}\boldsymbol{v}$ and $\bar\rho\bar U$, respectively. The thermal energy equation of the average motion is obtained from equation (20.21) by subtracting the kinetic energy part, [$\boldsymbol{v}\cdot$equation (20.20)], in the following form:

$$\bar\rho\bar T\left(\frac{\partial}{\partial t}+\boldsymbol{v}\cdot\nabla\right)(\bar S+\bar S_t)=\bar\rho(\bar\varepsilon_N+\bar\varepsilon_V)-\nabla\cdot(\bar{\boldsymbol{F}}_R+\bar{\boldsymbol{F}}_C), \tag{20.23}$$

where the entropy of the turbulent motion $\bar S_t$ is defined by

$$\bar\rho\bar T\left(\frac{\partial}{\partial t}+\boldsymbol{v}\cdot\nabla\right)\bar S_t=\frac{\partial}{\partial t}\left\langle\frac{1}{2}\rho\boldsymbol{V}^2\right\rangle+\nabla\cdot\boldsymbol{F}_K+p_t\nabla\cdot\boldsymbol{v} \tag{20.24}$$

in analogy with the thermodynamic relation (20.16).

These equations describe the hydrodynamics of a general flow associated with turbulent convection. For unperturbed state ($\partial/\partial t=0$), with rotation or circulation velocity $\boldsymbol{v}_0$, we obtain, from equations (20.19)–(20.23),

$$\nabla\cdot(\rho_0 \boldsymbol{v}_0) = 0, \tag{20.25}$$

$$(1+\delta_1)\nabla p_0+\rho_0\nabla\Phi_0=-\rho_0(\boldsymbol{v}_0\cdot\nabla)\boldsymbol{v}_0+\mathrm{div}[\mu_t\sigma(\boldsymbol{v}_0)], \tag{20.26}$$

and

$$\nabla\cdot(\boldsymbol{F}_{R,0}+\boldsymbol{F}_{C,0})-\rho_0(\varepsilon_{N,0}+\varepsilon_{V,0})=-(1+\delta_2)\rho_0 T_0\boldsymbol{v}_0\cdot\nabla S_0, \tag{20.27}$$

where

$$\delta_1 = p_t/\bar{p} \quad \text{and} \quad \delta_2 = \bar{S}_t/\bar{S}, \tag{20.28}$$

and subscript 0 denotes the unperturbed state. For a spherical symmetric star without rotation and circulation ($\boldsymbol{v}_0 = 0$), equations (20.26) and (20.27) are reduced to

$$(1+\delta_1)\frac{dp_0}{dr} + \rho_0 g = 0, \tag{20.29}$$

and

$$\frac{dL_r}{dr} - 4\pi r^2\rho_0\epsilon_{N,0} = 0. \tag{20.30}$$

Equations (20.19), (20.20), and (20.24) are also the basic equations governing oscillations under the influence of turbulent convection. The latter influence appears as $\boldsymbol{F}_C, p_t, \bar{S}_t$ and μ_t in $\mathscr{J}_t$ and $\bar{\varepsilon}_t$ through equations (20.9) and (20.11). The $\bar{\varepsilon}_V$-term is crucial in accretion disk physics (Shakura and Sunyaev, 1973), but it is small in stellar oscillations and is neglected hereafter. The linearized equations of oscillation are then obtained in the following form:

$$\rho' + \nabla\cdot(\rho_0\boldsymbol{\xi}) = 0\ , \tag{20.31}$$

$$\rho_0\frac{\partial^2\boldsymbol{\xi}}{\partial t^2}+(1+\delta_1)\nabla p'+\rho'\nabla\Phi_0+\rho_0\nabla\Phi'=\mathrm{div}[\mu_t\sigma(\boldsymbol{v})], \tag{20.32}$$

and

$$(1+\delta_2)\rho_0 T_0\frac{\partial}{\partial t}(S'+\boldsymbol{\xi}\cdot\nabla S_0)=(\rho\varepsilon_N)'-\nabla\cdot(\boldsymbol{F}_R'+\boldsymbol{F}_C'). \tag{20.33}$$

The turbulence corrections, δ_1 and δ_2, are troublesome to estimate precisely. These corrections, being small in any case, are taken here to be constant under the assumption that turbulent motions behave similarly to thermal motions in the course of oscillation. For μ_t, only the equilibrium value is needed, but the evaluation of $\boldsymbol{F}_C'$ requires the solution of time-dependent convection induced by oscillation. The adiabatic oscillation is described by equations (20.31)–(20.33) with the right-hand sides put equal to zero. In that case, the influence of convection appears only through δ_1 and δ_2, which are normally small.

20.2 Convection in Oscillating Medium

Equations governing the convection superposed on the oscillation can be obtained by subtracting the coarse grain average from the basic equations. For instance, subtracting equation (20.19) from equation (20.6), we obtain

$$\frac{\partial\rho_C}{\partial t} + \nabla\cdot(\bar{\rho}\boldsymbol{V}) = 0\ . \tag{20.34}$$

For simplicity, however, we employ the anelastic approximation (Ogura and Phillips,1962) for stellar convection,

$$\nabla\cdot(\bar{\rho}\boldsymbol{V}) = 0\ , \tag{20.35a}$$

suppressing acoustic waves, or even the Boussinesq approximation ($\rho_C=0$, $\bar{\rho}=$const.) for qualitative studies,

$$\nabla\cdot\boldsymbol{V} = 0\ . \tag{20.35b}$$

The monentum conservation in convection, [(20.7)–(20.20)], is given by

$$\bar{\rho}\left[\frac{\partial}{\partial t} + (\boldsymbol{v}+\boldsymbol{V})\cdot\nabla\right]\boldsymbol{V} + \bar{\rho}(\boldsymbol{V}\cdot\nabla)\boldsymbol{v}$$

$$= -\nabla p_C - \rho_C(\nabla\Phi+\dot{\boldsymbol{v}}) + \mathrm{div}\,\mathscr{J}_t(\boldsymbol{V})\ , \tag{20.36}$$

where

$$\dot{\boldsymbol{v}} = \left(\frac{\partial}{\partial t} + \boldsymbol{v}\cdot\nabla\right)\boldsymbol{v}\ . \tag{20.37}$$

The density excess ρ_C in buoyancy is approximated in the Boussinesq approximation by

$$\rho_C = -v_T\frac{\rho_0}{T_0}T_C\ . \tag{20.38}$$

The derivation of the thermal energy conservation for convection is somewhat involved. Using the approximation $\delta_2 = S_t/S =$ const., we rewrite equation (20.15) in the following form:

$$(1+\delta_2)\rho T\left(\frac{\partial}{\partial t} + \boldsymbol{u}\cdot\nabla\right) S = \rho\varepsilon_N - \nabla\cdot\boldsymbol{F}_R , \qquad (20.39)$$

in comparison with the corresponding average equation (20.23),

$$(1+\delta_2)\bar{\rho}\bar{T}\left(\frac{\partial}{\partial t} + \boldsymbol{v}\cdot\nabla\right)\bar{S} = \overline{\rho\varepsilon_N} - \nabla\cdot(\bar{\boldsymbol{F}}_R + \bar{\boldsymbol{F}}_C), \qquad (20.40)$$

where $\bar{\varepsilon}_V$ is neglected. Here, the turbulence entropy S_t has been assumed to be similar in form to $\bar{S}_t$ in equation (20.24), as follows:

$$\rho T\left(\frac{\partial}{\partial t} + \boldsymbol{u}\cdot\nabla\right) S_t = -\rho\varepsilon_V + \nabla\cdot\boldsymbol{F}_K + p_t\nabla\cdot\boldsymbol{u}, \qquad (20.41)$$

although we will not use such an expression to estimate δ_2. Subtracting equation (20.40) from equation (20.39) side by side, we obtain

$$(1+\delta_2)\overline{\rho T}\left[\left(\frac{\partial}{\partial t} + \boldsymbol{v}\cdot\nabla\right)S_C + \boldsymbol{V}\cdot\nabla\bar{S}\right] = (\overline{\rho\varepsilon_N})_C - \nabla\cdot(\boldsymbol{F}_{R,C} + \boldsymbol{F}_{K,C}), \qquad (20.42)$$

where the radiative flux from a convective element, $\boldsymbol{F}_{R,C}$, and the conductive flux of convection energy, $\boldsymbol{F}_{K,C}$, are given by

$$\boldsymbol{F}_{R,C} = -K\nabla T_C, \qquad K = (4/3)(ac*\bar{T}^3/\kappa\bar{\rho}), \qquad (20.43)$$

$$\boldsymbol{F}_{K,C} = (1+\delta_2)(\bar{\rho}\bar{T}S_C\boldsymbol{V}) - \bar{\boldsymbol{F}}_C = -\kappa_t c_p \nabla T_C, \qquad (20.44)$$

where the last expression is due to the same vein of approximation as the gradient diffusion approximation. Equation (20.42) is further simplified in the Boussinesq approximation in which (dp_C) is neglected in the thermodynamic relation,

$$\bar{T}dS_C = c_p(dT_C - \nabla_{ad}\frac{\bar{T}}{\bar{p}}dp_C), \qquad (20.45)$$

since the convection is an unstable gravity mode which is the slow mode having small pressure perturbation, p_C. We then have

$$c_p^*\left[\left(\frac{\partial}{\partial t} + \bar{\boldsymbol{v}}\cdot\nabla\right)T_C + \boldsymbol{V}\cdot\left(\nabla\bar{T} - \nabla_{ad}\frac{\bar{T}}{\bar{p}}\nabla\bar{p}\right)\right]$$

$$= \varepsilon_{N,C} - \frac{1}{\bar{\rho}}\nabla\cdot(\boldsymbol{F}_{R,C} + \boldsymbol{F}_{K,C}), \qquad (20.46)$$

where

$$c_p^* = (1 + \delta_2)c_p . \qquad (20.47)$$

Following Xiong (1978), we now employ the statistical theory of turbulent convection to study the convection-oscillation coupling. With the aid of equation (20.35), we construct a closed set of equations for energy densities X, Y, and Z, defined by

$$X = (1/2)<\bar{\rho}V^2> = (3/2)p_t , \qquad (20.48)$$

$$Y = (c_p/\bar{T})^{1/2}<\rho T_C V_z> , \qquad (20.49)$$

$$Z = (1/2)(c_p/\bar{T})<\bar{\rho}T_C^2> , \qquad (20.50)$$

arranging equations (20.36) and (20.46). To make this possible, we use several approximations:

(A1) Spatial structure of a convective element is practically unchanged by the presence of oscillation and is approximated by that of the stationary Rayleigh-Bernard convective cell with free boundaries.

(A2) Turbulence is isotropic, and its characteristic scale is much smaller than the wave length of the oscillation.

(A3) The third-order correlation ($<\bar{\rho}\boldsymbol{V}^2\boldsymbol{V}>$, for example) is estimated by use of the gradient diffusion approximation.

From equation (20.36), we obtain the kinetic energy equation of convection,

$$\bar{d}_t X - \nabla\cdot[(\mu_t/\bar{\rho})\nabla X] + p_t\nabla\cdot\boldsymbol{v}$$

$$= -\nabla\cdot\boldsymbol{F}_{CW} + v_T[(g+\dot{v}_z)/(c_p\bar{T})^{1/2}]Y - 2(\mu_t/\bar{\rho})k^2X, \qquad (20.51)$$

where

$$\bar{d}_t = (\partial/\partial t) + \boldsymbol{v}\cdot\nabla, \qquad (20.52)$$

the second term on the *l.h.s.* is due to the approximation (A3) for $<\bar{\rho}(\boldsymbol{V}^2/2)\boldsymbol{V}>$, and the wave flux, $\boldsymbol{F}_{CW} = <p_C\boldsymbol{V}>$, associated with convection can be neglected on account of the approximation (A2) and the Boussinesq approximation unless the convection is oscillatory with magnetic field or rotation. From the z-component of equation (20.36) and equation (20.46), we obtain

$$\bar{d}_t Y + (\partial V_z/\partial z)Y + (c_p/\bar{T})^{1/2}p_t[(\partial\bar{T}/\partial z) - \nabla_{ad}(\bar{T}/\bar{p})(\partial\bar{p}/\partial z)]$$

$$-\nabla\cdot[(\kappa_t/\bar{\rho})\nabla Y] = 2v_T^*[(g+\dot{v}_z)/(c_p\bar{T})^{1/2}]Z$$

$$+\left\{\frac{\varepsilon_N\varepsilon_T}{c_p\bar{T}} - \left[\left(\frac{K}{c_p} + \mu_t + \kappa_t\right)/\bar{\rho}\right]k^2\right\}Y, \qquad (20.53)$$

where the term, $(c_p/\bar{T})^{1/2} < \bar{\rho} T_C (\boldsymbol{V}\cdot\nabla) V_z >$, on the *l.h.s.* has been neglected with the approximation (A.2),

$$v_T^* = v_T - < c_p T_C (\partial p_C/\partial z) > / [(g+\dot{v}_z) Z] \approx v_T - (1/3) \tag{20.54}$$

by the approximation (A.2), k denotes the representative wave number of a convective element, (e.g. $k=\sqrt{3}\pi/l_t$) and $\varepsilon_{N,C}$ has been approximately

$$\varepsilon_{N,C} = \varepsilon_N \varepsilon_T (T_C/\bar{T}). \tag{20.55}$$

Multiplying equation (20.46) by $(\bar{\rho}/\bar{T})T_C$, we obtain

$$\bar{d}_t Z + (c_p \bar{T}^{1/2})[\partial \ln \bar{T}/\partial z - \nabla_{ad} \partial \ln \bar{p}/\partial z] Y - 2\nabla\cdot[(\kappa_t/\bar{\rho})\nabla Z]$$

$$= \{2(\varepsilon_N \varepsilon_T / c_p \bar{T}) - [(K/c_p\bar{\rho}) + (\kappa_t/\bar{\rho})] k^2\} Z, \tag{20.56}$$

where the difference between c_p and c_p^* has been neglected for simplicity. The nonlocal effects represented by the second term of equation (20.51), the fourth term of equation (20.53) and the third term of equation (20.56) are important in the penetrative convection (Unno, Kondo, and Xiong, 1985) but are small compared with the corresponding diffusivity terms (the last term in each equation) in the main body of the convection zone. Since we have adopted the Boussinesq approximation which is consistent with the local theory (Spiegel and Veronis, 1960), these nonlocal effects will be neglected hereafter.

Summarizing the result, we have

$$[\bar{d}_t + (2/3)\nabla\cdot\boldsymbol{v} + 2(\mu_t/\bar{\rho})k^2] X = v_T (g+\dot{v}_z)(c_p\bar{T})^{-1/2} Y, \tag{20.57}$$

$$[\bar{d}_t + (\partial v_z/\partial z) - (c_p\bar{T})^{-1}\varepsilon_N \varepsilon_T + (c_p^{-1}K + \mu_t + \kappa_t)(k^2/\bar{\rho})] Y$$

$$= 2 v_T^* (g+\dot{v}_z)(c_p\bar{T})^{-1/2} Z - (2/3)(c_p\bar{T})^{1/2}(\bar{\nabla} - \nabla_{ad})(\partial \ln \bar{p}/\partial z) X, \tag{20.58}$$

and

$$[\bar{d}_t - 2(c_p\bar{T})^{-1}\varepsilon_N \varepsilon_T + 2(c_p^{-1}K + \kappa_t)(k^2/\bar{\rho})] Z$$

$$= -(c_p\bar{T})^{1/2}(\bar{\nabla} - \nabla_{ad})(\partial \ln \bar{p}/\partial z) Y, \tag{20.59}$$

where

$$\bar{\nabla} = \partial \ln \bar{T}/\partial \ln \bar{p}. \tag{20.60}$$

These equations are nonlinear in X, Y, Z because of μ_t and κ_t that are proportional to $X^{1/2}$. Without oscillation, they are reduced to

$$[(\partial/\partial t) + 2(\mu_t/\rho_0)k^2] X = v_T g (c_p T_0)^{-1/2} Y, \tag{20.61}$$

$$[(\partial/\partial t) - (c_p T_0)^{-1}\varepsilon_N \varepsilon_T + (c_p^{-1}K + \mu_t + \kappa_t)(k^2/\rho_0)] Y$$

$$= 2 v_T^* g (c_p T_0)^{-1/2} Z + (2/3)(c_p T_0)^{1/2}(\nabla - \nabla_{ad}) H_p^{-1} X, \tag{20.62}$$

and

$$[(\partial/\partial t) - 2(c_p T_0)^{-1}\varepsilon_N \varepsilon_T + 2(c_p^{-1}K + \kappa_t)(k^2/\rho_0)] Z$$

$$= (c_p T_0)^{1/2}(\nabla - \nabla_{ad}) H_p^{-1} Y, \tag{20.63}$$

where H_p denotes the pressure scale height,

$$H_p = -\left(\frac{\partial \ln p_0}{\partial z}\right)^{-1}. \tag{20.64}$$

In the convective core ($\varepsilon_N \neq 0$), the convection is unstable until the turbulent conductivity κ_t is increased to satisfy the following stability criterion:

$$\rho_0 \varepsilon_N \varepsilon_T - c_p T_0 (\kappa_t + c_p^{-1} K) k^2 \leq 0, \tag{20.65}$$

in which the equality gives the amplitude of the steady state. In the convective envelope ($\varepsilon_N = 0$), the system is stable and settled to the steady state given by

$$2(c_p T_0)^{1/2} \mu_{t0} k^2 X_0 = v_T g \rho_0 Y_0, \tag{20.66}$$

$$(c_p T_0)^{1/2}(c_p^{-1}K + \mu_{t0} + \kappa_{t0}) k^2 Y_0$$

$$= 2 v_T^* g \rho_0 Z_0 + (2/3)(c_p \rho_0 T_0)(\nabla - \nabla_{ad}) H_p^{-1} X_0, \tag{20.67}$$

and

$$2(c_p^{-1}K - \kappa_{t0}) k^2 Z_0 = (c_p T_0)^{1/2}(\nabla - \nabla_{ad}) \rho_0 H_p^{-1} Y_0, \tag{20.68}$$

where subscript 0 represents the equilibrium convection. The solution of these equations are equivalent to that of the local mixing length theory (Vitense, 1953).

Equations (20.58)–(20.59) govern the convection in the presence of oscillation, while equations (20.66)–(20.68) describe the convection in the absence of rotation. To study the convection-pulsation coupling, we need to calculate $\boldsymbol{F}_C'$ in equation (20.33). Solving linearized equations of (20.57)–(20.59) for Y', we obtain F_{Cz}'. The derivation of this and other components of $\boldsymbol{F}_C'$ will be made in Section 30.

Chapter IV

NONADIABATIC OSCILLATIONS

21. Basic Equations of Fully Nonadiabatic Oscillations

As discussed in the previous chapter, dynamically stable adiabatic oscillations in a non-rotating and non-magnetic spherical star are strictly periodic. In mathematical terms, the eigenfrequencies and eigenfunctions are purely real. Oscillations in nature are, however, inevitably nonadiabatic; i.e., energy exchange among mass elements occurs during oscillations, and governs the vibrational stability (amplitude growth or decay) of the star. This corresponds to the fact that the eigenfrequencies and eigenfunctions are complex (non-real) in the mathematical description of linear nonadiabatic oscillations. The fact that the eigenvalue and eigenfunctions become complex due to nonadiabaticity is recognized by looking at the linearized equation of energy conservation (13.66), which includes a coefficient of complex number, because the equation of energy conservation involves a first-order time derivative. Since we express, in this monograph, the temporal dependence of perturbed quantities as $\exp(i\sigma t)$, the amplitude of oscillations grows if the imaginary part of the angular frequency σ is negative.

21.1 Differential Equations

In order to obtain the eigenfrequencies and eigenfunctions of linear nonadiabatic oscillations, we have to incorporate the equations of energy conservation and the flux equation (13.65) and (13.66). Although these equations are written in terms of the Eulerian perturbations of nuclear energy generation rate ε_N, radiative flux $\boldsymbol{F}_R$, etc., it is convenient, in practice, to use the Lagrangian perturbations. One reason for this is that if we use the Lagrangian perturbations of nuclear energy generation rate and opacity κ, we do not need to consider the dependence of these quantities on the chemical composition, which is conserved in a mass element because the oscillation periods are, in most cases, much shorter than the time scale of

nucleosynthesis or the time scale of particle diffusion. The linearized perturbation equation of energy conservation may be written as

$$T\frac{d\,\delta S}{dt} = \delta\varepsilon_N - \delta\left(\frac{1}{\rho}\nabla\cdot\boldsymbol{F}\right), \tag{21.1}$$

where energy flux $\boldsymbol{F}$ includes the radiative and the convective fluxes [*cf.* equations (13.17) and (20.23)]. The first and second terms in the right-hand side of equation (21.1) represent, respectively, the energy gain (or loss) due to the excess (or deficient) energy generation and the energy loss (or gain) due to the excess (or deficient) energy outflow. Using the equation of mass conservation (13.35), the latter term can be written in a different form:

$$\begin{aligned} -\delta\left(\frac{1}{\rho}\nabla\cdot\boldsymbol{F}\right) &= \frac{1}{\rho}\left[\frac{\delta\rho}{\rho}\nabla\cdot\boldsymbol{F} - \delta(\nabla\cdot\boldsymbol{F})\right] \\ &= \frac{1}{\rho}[-(\nabla\cdot\boldsymbol{\xi})(\nabla\cdot\boldsymbol{F}) - \nabla\cdot\boldsymbol{F}' - (\boldsymbol{\xi}\cdot\nabla)(\nabla\cdot\boldsymbol{F})] \\ &= -\frac{1}{\rho}\nabla\cdot[\boldsymbol{F}' + \boldsymbol{\xi}(\nabla\cdot\boldsymbol{F})]. \end{aligned} \tag{21.2}$$

In the following we use the fact that the energy flux has only a radial component in the equilibrium structure (i.e., $\boldsymbol{F}=F_r\boldsymbol{e}_r$). Furthermore, writing the flux perturbation as

$$\boldsymbol{F}' = F_r'\boldsymbol{e}_r + \boldsymbol{F}_\perp', \tag{21.3}$$

with $\boldsymbol{F}_\perp'$ being the horizontal component of the flux perturbation, we define the luminosity perturbation δL_r as

$$\delta L_r = 4\pi r^2\left(\delta F_r + 2\frac{\xi_r}{r}F_r\right), \tag{21.4}$$

which represents the perturbation in the spherically symmetric part of energy flow. Then equation (21.2) leads to

$$-\delta\left(\frac{1}{\rho}\nabla\cdot\boldsymbol{F}\right) + \frac{\partial\,\delta L_r}{\partial M_r} = -\frac{1}{\rho}\nabla\cdot\boldsymbol{F}_\perp' + l(l+1)\frac{\xi_h}{r}\frac{dL_r}{dM_r}, \tag{21.5}$$

where L_r is the total (convective plus radiative) luminosity at r as defined by equation (13.18). The terms in the right-hand side of equation (21.5) represent the effect of the non-spherical perturbation in energy flux.

Here we face a serious difficulty in treating perturbation of energy flux. In general, energy flux consists of radiative and convective fluxes.

However, time-dependent convection theory, which is necessary to calculate perturbations of the convective flux, has not been fully developed. Although some attempts to include perturbations of the convective flux have been made (e.g., Unno, 1967, 1977; Gabriel, Scuflaire, Noels, and Boury, 1975; Gough, 1976; Xiong, 1978; Baker and Gough, 1979; Gonczi and Osaki, 1980; Saio, 1980; Gonczi, 1982; Stellingwerf, 1984), the treatments are very complex and include several uncertain points (see Sections 20 and 30). Therefore, in most of the investigations of nonadiabatic nonradial pulsation, the perturbation of the convective flux is neglected for simplicity. This neglect is sometimes called a "frozen convection" approximation. This name is, however, somewhat misleading, because this treatment is not necessarily an approximation even in the cases where the oscillation period is much shorter than the turnover time of the largest convective eddies.

In order to avoid complexity, we neglect perturbations of the convective flux in this chapter. (The time-dependent convection theory is discussed in Sections 20 and 30.) There are several ways to neglect perturbations of convective flux. For example, if we set $\delta L_C = 0$ and $\boldsymbol{F}_{C\perp}' = 0$, equation (21.5) becomes

$$-\delta\left(\frac{1}{\rho}\nabla\cdot\boldsymbol{F}\right) = -\frac{\partial\,\delta L_R}{\partial M_r} - \frac{1}{\rho}\nabla\cdot\boldsymbol{F}_{R\perp}' + l(l+1)\frac{\xi_h}{r}\frac{dL_r}{dM_r}, \tag{21.6}$$

where the radiative luminosity L_R and the convective luminosity L_C at r are given by $L_R = 4\pi r^2 F_{R,r}$ and $L_C = 4\pi r^2 F_{C,r}$ respectively. If we set $\delta\left(\frac{1}{\rho}\nabla\cdot\boldsymbol{F}_C\right) = 0$, equation (21.5) becomes

$$-\delta\left(\frac{1}{\rho}\nabla\cdot\boldsymbol{F}\right) = -\frac{\partial\,\delta L_R}{\partial M_r} - \frac{1}{\rho}\nabla\cdot\boldsymbol{F}_{R\perp}' + l(l+1)\frac{\xi_h}{r}\frac{dL_R}{dM_r}. \tag{21.7}$$

Furthermore, if we assume $\delta(\nabla\cdot\boldsymbol{F}_C)=0$, equation (21.5) becomes

$$-\delta\left(\frac{1}{\rho}\nabla\cdot\boldsymbol{F}\right) = -\frac{\partial\,\delta L_R}{\partial M_r} - \frac{1}{\rho}\nabla\cdot\boldsymbol{F}_{R\perp}' + l(l+1)\frac{\xi_h}{r}\frac{dL_r}{dM_r} - \frac{\partial(r^2\xi_r)}{r^2\partial r}\frac{dL_C}{dM_r}. \tag{21.8}$$

Other ways are also possible. Although we have no convincing scientific reason to prefer one relation to the others, we choose the expression in equation (21.6) in the following discussions in this chapter. Before we proceed further, we should caution that using any of the above approximations can cause a fictitious excitation effect near the bottom of the convective zone. Special attention must be paid to this phenomenon in performing a nonadiabatic analysis.

In the diffusion approximation the radiative flux is given by equation (13.6), and its linearized form is given by equations (13.50) and (13.51) with the Eulerian perturbations of the physical variables. Transforming the Eulerian perturbations to the Lagrangian perturbations and using the fact that the perturbed quantities are proportional to a spherical harmonic $Y_l^m(\theta,\phi)$, we obtain

$$\delta F_{R,r} = F_R\left[-\frac{\delta\kappa}{\kappa}+2\frac{\xi_r}{r}-l(l+1)\frac{\xi_h}{r}+4\frac{\delta T}{T}+\frac{d(\frac{\delta T}{T})/d\ln r}{d\ln T/d\ln r}\right] \tag{21.9}$$

and

$$\nabla\cdot\boldsymbol{F}'_{R\perp} = -\frac{F_R}{d\ln T/d\ln r}\frac{l(l+1)}{r}\frac{T'}{T}, \tag{21.10}$$

where F_R denotes the radiative flux in the equilibrium state.

Thus the differential equations for the radial part of eigenfunctions of the fully nonadiabatic nonradial linear oscillations given in equations (13.62)–(13.66) can be written as

$$\frac{d}{dr}\left(\frac{p'}{\rho}+\Phi'\right)-\frac{N^2}{g}\frac{p'}{\rho}+(N^2-\sigma^2)\xi_r = g\upsilon_T\frac{\delta S}{c_p}, \tag{21.11}$$

$$\frac{1}{r^2}\frac{d}{dr}(r^2\xi_r)+\frac{1}{\Gamma_1}\frac{d\ln p}{dr}\xi_r+\left(1-\frac{L_l^2}{\sigma^2}\right)\frac{p'}{\rho c^2}-\frac{l(l+1)}{\sigma^2 r^2}\Phi' = \upsilon_T\frac{\delta S}{c_p}, \tag{21.12}$$

$$\frac{1}{r^2}\frac{d}{dr}\left(r^2\frac{d\Phi'}{dr}\right)-\frac{l(l+1)}{r^2}\Phi'-4\pi G\rho\left(\frac{p'}{\rho c^2}+\frac{N^2}{g}\xi_r\right) = -4\pi G\rho\upsilon_T\frac{\delta S}{c_p}, \tag{21.13}$$

$$i\sigma T\delta S = \delta\varepsilon_N-\frac{d\delta L_R}{dM_r}+\frac{l(l+1)}{d\ln T/d\ln r}\frac{F_R}{\rho r}\frac{\delta T}{T}+l(l+1)\left(\frac{\xi_h}{r}\frac{dL_r}{dM_r}-\frac{\xi_r}{r}\frac{L_R}{4\pi r^3\rho}\right), \tag{21.14}$$

and

$$\frac{\delta L_R}{L_R} = -\frac{\delta\kappa}{\kappa}+4\frac{\xi_r}{r}-l(l+1)\frac{\xi_h}{r}+4\frac{\delta T}{T}+\frac{d(\frac{\delta T}{T})/d\ln r}{d\ln T/d\ln r}. \tag{21.15}$$

The relation between δT and δS is obtained from a thermodynamic relation [equation (13.80)]:

$$\delta S = c_p\left(\frac{\delta T}{T}-\nabla_{ad}\frac{\delta p}{p}\right), \tag{21.16}$$

and ξ_h is related with $(p'/\rho+\Phi')$ by equation (13.61). The perturbations of opacity and nuclear energy generation rate may be represented as functions of δp and δS:

$$\frac{\delta\kappa}{\kappa} = \kappa_T\frac{\delta T}{T}+\kappa_\rho\frac{\delta\rho}{\rho} = \kappa_{ad}\frac{\delta p}{p}+\kappa_S\frac{\delta S}{c_p} \tag{21.17}$$

and

$$\frac{\delta\varepsilon_N}{\varepsilon_N} = \varepsilon_T\frac{\delta T}{T}+\varepsilon_\rho\frac{\delta\rho}{\rho} = \varepsilon_{ad}\frac{\delta p}{p}+\varepsilon_S\frac{\delta S}{c_p}, \tag{21.18}$$

where

$$\left.\begin{aligned}\kappa_T &= \left(\frac{\partial\ln\kappa}{\partial\ln T}\right)_\rho, \qquad \kappa_\rho = \left(\frac{\partial\ln\kappa}{\partial\ln\rho}\right)_T,\\ \kappa_{ad} &= \left(\frac{\partial\ln\kappa}{\partial\ln p}\right)_S = \kappa_T\nabla_{ad}+\frac{\kappa_\rho}{\Gamma_1},\\ \kappa_S &= c_p\left(\frac{\partial\ln\kappa}{\partial S}\right)_p = \kappa_T-\upsilon_T\kappa_\rho,\end{aligned}\right\} \tag{21.19}$$

and

$$\left.\begin{aligned}\varepsilon_T &= \left(\frac{\partial\ln\varepsilon_N}{\partial\ln T}\right)_\rho, \qquad \varepsilon_\rho = \left(\frac{\partial\ln\varepsilon_N}{\partial\ln\rho}\right)_T,\\ \varepsilon_{ad} &= \left(\frac{\partial\ln\varepsilon_N}{\partial\ln p}\right)_S = \varepsilon_T\nabla_{ad}+\frac{\varepsilon_\rho}{\Gamma_1},\end{aligned}\right\} \tag{21.20}$$

$$\varepsilon_S = c_p\left(\frac{\partial \ln \varepsilon_N}{\partial S}\right)_p = \varepsilon_T - v_T\varepsilon_\rho .$$

In deriving the above relations we assumed that the chemical composition of a mass element is conserved during the oscillations. This assumption is justified because in most cases the period of oscillations is much shorter than the time scales of nucleosynthesis and particle diffusion. When the time scale of nucleosynthesis is comparable to the period of oscillation, more careful treatment is necessary to obtain the expression for $\delta\varepsilon_N$ (see e.g., Cox, 1955; Kawaler, 1988a).

Thus, linear nonadiabatic nonradial oscillations are described by six (four if the Cowling approximation is employed) first-order differential equations of the complex variables.

21.2 Reflective Boundary Conditions

The six differential equations discussed above and six boundary conditions form an eigenvalue problem with a complex eigenvalue σ. In this subsection, as a natural choice, we discuss three inner boundary conditions and three outer boundary conditions. In the deep interior of a star, the thermal time-scale must be extremely long compared to the oscillation periods. The adiabatic condition is nearly perfectly satisfied for oscillations there. Therefore, the inner boundary conditions for the mechanical variables such as Φ', ξ_r, and p' are the same as those discussed in Section 14. These are $\Phi' \propto r^l$, $\xi_r \propto r^{l-1}$, and $p' \propto r^l$ near the center. Using these relations, equations (21.11)–(21.13) can be reduced to

$$\xi_r - \frac{l}{\sigma^2 r}\left(\frac{p'}{\rho} + \Phi'\right) = 0 \qquad (21.21)$$

and

$$\frac{d\Phi'}{dr} = \frac{l\Phi'}{r}, \qquad (21.22)$$

near the center. Another central boundary condition may be chosen as

$$\delta S = 0. \qquad (21.23)$$

If oscillations are well trapped in the envelope of the star, the inner boundary may be set somewhere between the center and the bottom of the oscillating envelope. Since in this case the oscillation amplitude is negligibly small, we can use simple inner boundary conditions such as $\xi_r = 0$, $\Phi' = 0$, and $\delta S = 0$ (or $\delta L_R/L_R = 0$). We note that for many cases of the oscillations well trapped in the envelope, the Cowling approximation is a good approximation and the system of the differential equations can be reduced to four first-order differential equations.

Since the outer boundary of a star is ill defined, some difficulties arise in setting the outer boundary conditions for oscillations. In this subsection we will discuss simple boundary conditions, assuming that the pressure and the density near the surface decrease steeply outward. In this case we can use a reflective outer boundary condition for the pressure perturbation:

$$\delta p = 0 \quad \text{at} \quad r = R. \qquad (21.24)$$

The outer boundary condition for the perturbation of the gravitational potential is obtained from the condition of continuity at the surface:

$$\frac{d\Phi'}{dr} + (l+1)\frac{\Phi'}{r} = 0 \quad \text{at} \quad r = R. \qquad (21.25)$$

Above two conditions are the same as those for adiabatic conditions. If the radiation pressure is dominant at the outer boundary, the first assumption that the pressure decreases steeply outward may not be allowable. In such a case more careful treatment is necessary, and replacing δp with δp_{gas} (p_{gas}; gas pressure) in equation (21.24) is probably better (see Shibahashi and Osaki, 1981a).

Another condition can be given by using the fact that there is no (or negligible) inward radiative flux at the surface:

$$F_R = f_E J = f_E \frac{\sigma_{rad}}{\pi} T^4, \qquad (21.26)$$

where J is the mean intensity and f_E the Eddington factor, which is reduced to 2π in the Eddington approximation. Perturbing equation (21.26) in a Lagrangian sense gives

$$\frac{\delta F_R}{F_R} = \frac{\delta f_E}{f_E} + 4\frac{\delta T}{T}. \qquad (21.27)$$

In order to obtain the perturbation of the Eddington factor δf_E, however, it is necessary to solve nonlocal radiative transfer incorporating perturbations due to nonradial oscillations. Since this is a very difficult problem (see Christensen-Dalsgaard and Frandsen, 1983a), this term is not taken into account for simplicity in this chapter.

21.3 Progressive-wave Boundary Conditions in the Core of a Red-Giant Star

As mentioned in Section 15.3.3, in the nondegenerate core of a red-giant star the Brunt-Väisälä frequency N is extremely large ($N^2 \sim$

10^7 in units of GM/R^3). Therefore, in such a star, any eigenmode with a moderate eigenfrequency behaves like a short wavelength gravity wave in the core. The radial wavelength is on the order of a thousandth of the core radius in the inner part of the core. Since the wave traveling time through the core is extremely long, the damping time is much shorter than the traveling time [see equations (15.21) and (15.22)], which means that waves traveling toward the center are damped before reaching and being reflected near the center. Then, a nearly standing wave cannot be formed in the core, and the wave penetrating from the envelope propagation zone through the evanescent zone is absorbed in the core without being reflected (*cf.* Pesnell, 1984). In other words, kinetic energy of p-modes trapped in the envelope leaks into the core. In such a case it is convenient to set a progressive-wave boundary condition at the outer part of the core propagation zone (Osaki, 1977; Dziembowski, 1977a) rather than obtaining eigenfunctions throughout the core by resolving their thousand spatial oscillations.

Since the thermal time scale is very long in the core of a star, we can safely use the local adiabatic condition in the outer part of the core. Furthermore, for g-waves with short radial wavelength in the core the Cowling approximation may be used. Since the vertical component of the group velocity of gravity waves has opposite sign to that of the phase velocity (Section 15.2), the inwardly propagating wave has an outward phase velocity. An asymptotic form of inwardly propagating adiabatic gravity waves with $\sigma^2 \ll N^2$ is given, under the Cowling approximation, by equation (16.62), which may be rewritten as

$$\xi_r r^2 \simeq \frac{\sqrt{l(l+1)}}{\sigma}\frac{v}{\sqrt{\rho}} \simeq \text{const}\cdot\frac{1}{\sqrt{\rho}\,k_r}\exp\left[i\left(\sigma t - \int^r k_r dr\right)\right]. \tag{21.28}$$

The radial wave number k_r is given for high-order g-waves as [see eq. (15.19)]

$$k_r \simeq \frac{N L_l}{\sigma c} = \frac{\sqrt{l(l+1)}N}{\sigma r} \quad \text{for} \quad \sigma^2 \ll N^2 . \tag{21.29}$$

Differentiating equation (21.28) with respect to r, we obtain

$$\frac{1}{r^2}\frac{d(r^2\xi_r)}{dr} = -\left[ik_r + \frac{1}{2}\left(\frac{d\ln\rho}{dr} + \frac{d\ln k_r}{dr}\right)\right]\xi_r . \tag{21.30}$$

Substituting equation (21.30) into equation (21.12) with $\Phi' = 0$ and $\delta S = 0$, we obtain the mechanical boundary condition

$$\frac{1}{2}\left(2ik_r - \frac{1}{r} - \frac{N^2}{g} + \frac{g}{c^2} + \frac{d\ln N}{dr}\right)\xi_r = \left(1 - \frac{L_l^2}{\sigma^2}\right)\frac{p'}{\rho c^2} . \tag{21.31}$$

The other inner boundary condition, under the Cowling approximation, can be chosen as

$$\delta S = 0 . \tag{21.32}$$

Equations (21.31) and (21.32) form a set of progressive-wave inner boundary conditions for p-modes trapped in the envelope of a red-giant star with highly condensed nondegenerate core.

22. *Weakly Nonadiabatic Nonradial Oscillations*

22.1 Degree of Nonadiabaticity

The ratio of thermal to dynamical time scales is one of the most important parameters that govern the nonadiabaticity (entropy perturbation) of stellar oscillations. This fact is apparent in the dimensionless equation of energy conservation. Multiplying equation (21.14) by $(\rho r/F_R) = 4\pi r^3\rho/L_R$, we obtain a dimensionless form of the linearized equation of energy conservation,

$$i\omega\frac{\tau_{th}}{\tau_{dyn}}\frac{\delta S}{c_p} = \frac{4\pi r^3\rho}{L_R}\left(\delta\varepsilon_N - \frac{d\,\delta L_R}{dM_r}\right) + \frac{l(l+1)}{d\ln T/d\ln r}\frac{T'}{T}$$
$$+ l(l+1)\frac{\xi_h}{r}\frac{4\pi r^3\rho}{L_R}\frac{dL_r}{dM_r} , \tag{22.1}$$

where the thermal timescale τ_{th} and the dynamical timescale τ_{dyn} are defined as

$$\tau_{th} = \frac{4\pi r^3\rho c_p T}{L_R} \quad \text{and} \quad \tau_{dyn} = \sqrt{\frac{R^3}{GM}} . \tag{22.2}$$

Equation (22.1) indicates that for a given energy excess [the right-hand side of equation (22.1)] the entropy perturbation is smaller for larger τ_{th}/τ_{dyn}. Figure 22.1 shows τ_{th}/τ_{dyn} as a function of the fractional radius r/R for massive zero-age main-sequence stars of $7M_\odot$ ($\log L/L_\odot = 3.25$) and $20M_\odot$ ($\log L/L_\odot = 4.64$). The ratio τ_{th}/τ_{dyn} is very large in the interior of a star except near the stellar surface. Since τ_{th} is proportional to the mass to luminosity ratio M/L, τ_{th}/τ_{dyn} in the $7M_\odot$ model is larger than in the $20M_\odot$ model for a given r/R. Nonadiabatic eigenfunctions of the f-mode with $l = 2$ are shown in Fig. 22.2 taken from Saio and Cox (1980) for the same models. The amplitude of the entropy perturbation is appreciable only near the surface, where the ratio τ_{th}/τ_{dyn} is

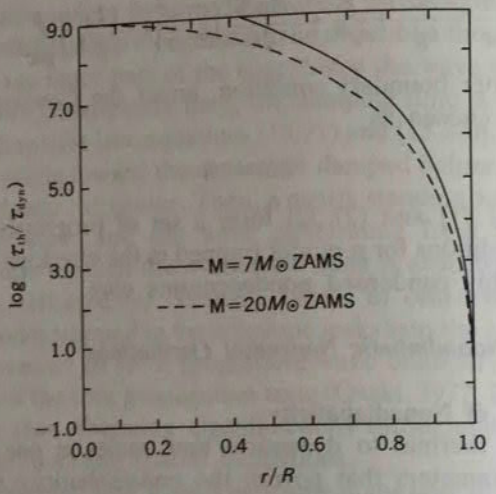

Fig. 22.1 The ratio of thermal to dynamical time scales, τ_{th}/τ_{dyn} versus fractional radius, r/R, in massive zero-age main-sequence stars.

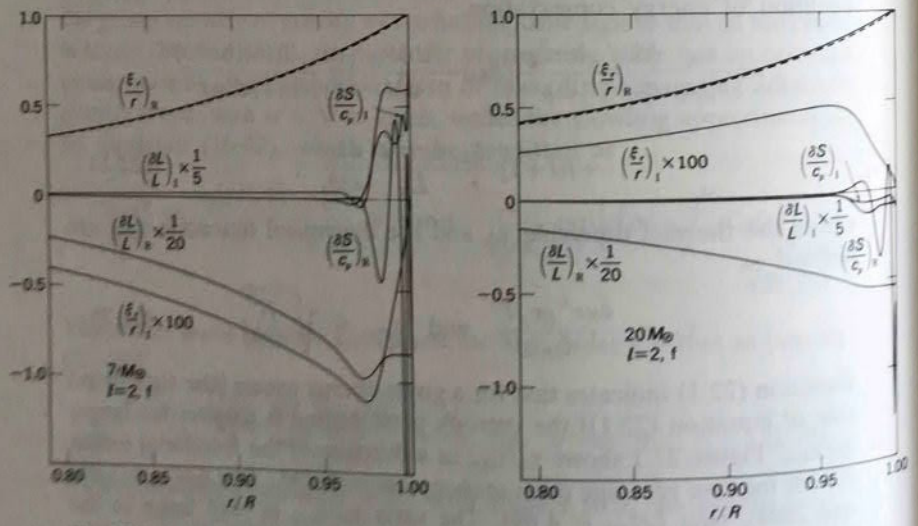

Fig. 22.2 Eigenfunctions of ξ_r/r, $\delta L/L_R$, and $\delta S/c_p$ for the f-mode with $l = 2$ in the ZAMS models of (a) $7M_\odot$ and (b) $20M_\odot$ (taken from Saio and Cox, 1980). They are normalized by $\xi_r/r = 1$ at $r/R = 1$. The two arrows indicate the positions of peaks in the opacity in the He^+ ionization zone and around $T = 1.5\times10^5$ K (see section 28).

comparable to or less than unity. The eigenfunction for the radial displacement is almost identical to the adiabatic one shown by the dashed lines in Fig. 22.2. In most of the stellar interior, oscillations are almost adiabatic. Thus, the adiabatic period of oscillation is, in many cases, a very good approximation for the period of nonadiabatic oscillation.

In a highly evolved star with a low M/L the value of τ_{th}/τ_{dyn} could be small enough for nonadiabatic oscillations to significantly deviate from the adiabatic ones. Even for large τ_{th}/τ_{dyn} large entropy perturbation is possible in the following cases. Equation (22.1) indicates that the entropy perturbation could be large if the dimensionless frequency ω is very low. This corresponds to a thermal (or secular) mode for which the imaginary part is much larger than the real part of the eigenfrequency. The secular mode will not be discussed in this article (see e.g., Hansen, 1978). Another possibility is having a large value for the right-hand side of equation (22.1), which can be realized if the radial wavelength is very short or if l is very large. Such oscillations, in which dynamical and thermal effects couple strongly, have peculiar properties. We will discuss very nonadiabatic oscillations in Section 23.

22.2 Quasi-adiabatic Approximation

When τ_{th}/τ_{dyn} ($\equiv c_4$) is very large, entropy perturbation is, in most cases, so small that the real part of the angular frequency is essentially the same as its adiabatic value. In such cases, we can use a quasi-adiabatic approximation, in which the terms of $O(c_4^{-2})$ are discarded. In the following part of this section we discuss the properties of weakly nonadiabatic oscillations by using the quasi-adiabatic approximation as well as the Cowling approximation.

In the quasi-adiabatic approximation, equations for nonadiabatic nonradial oscillations can be reduced to forms similar to those for adiabatic oscillations. Let us first express the entropy perturbation as a function of ξ_r and p'. First of all we need to express the luminosity perturbation as a function of ξ_r and p' to substitute into equation (22.1). It is apparent from equation (22.1) that $\delta S/c_p$ is the order of c_4^{-1}. Therefore, we need the expression for $\delta L_R/L_R$ only to the order of c_4^0; i.e., we can neglect nonadiabaticity in equation (21.15) and in the right-hand side of equation (22.1). Recalling that $\xi_h = p'/(\sigma^2 r\rho)$ under the Cowling approximation and using the relations (21.16)–(21.17) without the terms proportional to δS, we obtain from equation (21.15)

$$\frac{\delta L_R}{L_R} = \left(4\nabla_{ad} - \kappa_{ad} - \frac{1}{V\nabla}\frac{d\,\nabla_{ad}}{d\ln r}\right)\frac{\delta p}{p} + 4\frac{\xi_r}{r} - \frac{l(l+1)}{\sigma^2 r^2}\frac{p'}{\rho}$$

$$-\frac{\nabla_{ad}}{V\nabla}\frac{d}{d\ln r}\left(\frac{\delta p}{p}\right)+O(c_4^{-1}), \tag{22.3}$$

where $c_4 \equiv \tau_{th}/\tau_{dyn}$ [equation (22.2)] and ∇ is defined by (13.107). In order to eliminate the term with $d(\delta p/p)/d\ln r$ in equation (22.3), we use the relations for adiabatic oscillation given in equations (15.1) and (15.2);

$$\frac{1}{V}\frac{d}{d\ln r}\left(\frac{\delta p}{p}\right)=\frac{1}{V}\frac{d}{d\ln r}\left(\frac{\rho}{p}\frac{p'}{\rho}-V\frac{\xi_r}{r}\right)$$

$$=\frac{\rho}{p}\left(1-\frac{L_l^2}{\Gamma_1\sigma^2}\right)\frac{p'}{\rho}+\left(4-V-U+\frac{r\sigma^2}{g}\right)\frac{\xi_r}{r}+O(c_4^{-1}). \tag{22.4}$$

Substituting equation (22.4) into equation (22.3), we obtain

$$\frac{\delta L_R}{L_R} = D_1\xi_r + D_2\frac{p'}{\rho} + O(c_4^{-1}), \tag{22.5}$$

where

$$D_1\equiv\left[4+V(\kappa_{ad}-4\nabla_{ad})+\frac{\nabla_{ad}}{\nabla}\left(\frac{d\ln\nabla_{ad}}{d\ln r}-4+V+U-\frac{r\sigma^2}{g}\right)\right]r^{-1} \tag{22.6}$$

and

$$D_2\equiv-\frac{\rho}{p}\left(\kappa_{ad}-4\nabla_{ad}+\frac{\nabla_{ad}}{V\nabla}\frac{d\ln\nabla_{ad}}{d\ln r}+\frac{\nabla_{ad}}{\nabla}\right)+\left(\frac{\nabla_{ad}}{\nabla}-1\right)\frac{l(l+1)}{\sigma^2r^2}. \tag{22.7}$$

If we substitute equation (22.5) into equation (22.1), we have terms proportional to $d\xi_r/dM_r$ and $d(p'/\rho)/dM_r$. To eliminate these terms we again use relations for adiabatic oscillations given in equations (15.1) and (15.2). After some manipulation, we can express the entropy perturbation in terms of ξ_r and p' as

$$\frac{\delta S}{c_p} = i\frac{D_3}{\omega c_4}\xi_r + i\frac{D_4}{\omega c_4}\frac{p'}{\rho} + O(c_4^{-2}), \tag{22.8}$$

where D_3 and D_4 are defined by

$$D_3\equiv\frac{4\pi r^3\rho}{L_R}\left(\frac{\varepsilon_N\varepsilon_{ad}V}{r}+\frac{dL_R}{dM_r}D_1\right)+l(l+1)\frac{\nabla-\nabla_{ad}}{r\nabla}-D_1\left(3-\frac{rg}{c^2}\right)+\frac{dD_1}{d\ln r}$$

$$-D_2(N^2-\sigma^2)r \tag{22.9}$$

and

$$D_4\equiv\frac{4\pi r^3\rho}{L_R}\left(D_2\frac{dL_R}{dM_r}-\frac{\rho}{p}\varepsilon_N\varepsilon_{ad}\right)-\frac{l(l+1)}{\sigma^2r^2}\frac{4\pi r^3\rho\varepsilon_N}{L_R}+\frac{l(l+1)}{gr}\frac{\nabla_{ad}}{\nabla}$$

$$-\frac{rD_1}{c^2}\left(1-\frac{L_l^2}{\sigma^2}\right)+D_2\frac{rN^2}{g}+\frac{dD_2}{d\ln r}, \tag{22.10}$$

respectively, and ω is the dimensionless frequency, $\sigma/(GM/R^3)^{1/2}$. The relation $\varepsilon_N = dL_r/dM_r$ was used in equation (22.10).

Substituting equation (22.8) into equations (21.11) and (21.12), we obtain equations for nonadiabatic nonradial pulsations under the quasiadiabatic and the Cowling approximations:

$$\frac{1}{r^2}\frac{d(r^2\xi_r)}{dr}-\left(\frac{g}{c^2}+i\frac{D_3v_T}{\omega c_4}\right)\xi_r$$

$$+\left[\left(1-\frac{L_l^2}{\sigma^2}\right)\frac{1}{c^2}-i\frac{D_4v_T}{\omega c_4}\right]\frac{p'}{\rho}=O(c_4^{-2}) \tag{22.11}$$

and

$$\frac{d}{dr}\left(\frac{p'}{\rho}\right)-\left(\frac{N^2}{g}+i\frac{D_4gv_T}{\omega c_4}\right)\frac{p'}{\rho}$$

$$+\left(N^2-\sigma^2-i\frac{D_3gv_T}{\omega c_4}\right)\xi_r=O(c_4^{-2}). \tag{22.12}$$

Since these equations are similar to equations (15.1) and (15.2) for adiabatic oscillation, we can use a way similar to that used in Sections 15 and 16 to discuss properties of quasi-adiabatic nonradial pulsations. Following the discussion in Section 15.1, we introduce new variables $\tilde{\xi}_N$ and $\tilde{\eta}_N$ as follows:

$$\tilde{\xi}_N \equiv r^2\xi_r\exp\left[-\int_0^r\left(\frac{g}{c^2}+i\frac{D_3v_T}{\omega c_4}\right)dr\right] \tag{22.13}$$

and

$$\tilde{\eta}_N \equiv \frac{p'}{\rho}\exp\left[-\int_0^r\left(\frac{N^2}{g}+i\frac{D_4gv_T}{\omega c_4}\right)dr\right], \tag{22.14}$$

where the subscript N is used to distinguish variables for nonadiabatic oscillations from those for the adiabatic oscillations used in Sections 15

and 16. Using these variables in equations (22.11) and (22.12), we obtain a canonical form of the differential equations:

$$\frac{d\bar{\xi}_N}{dr} = h_N(r)\frac{r^2}{c^2}\left(\frac{L_l^2}{\sigma^2}-1+i\frac{D_4c^2v_T}{\omega c_4}\right)\bar{\eta}_N \qquad (22.15)$$

and

$$\frac{d\bar{\eta}_N}{dr} = \frac{1}{r^2h_N(r)}\left(\sigma^2-N^2+i\frac{D_3gv_T}{\omega c_4}\right)\bar{\xi}_N, \qquad (22.16)$$

where the terms of $O(c_4^{-2})$ are neglected and $h_N(r)$ is defined as

$$h_N(r) \equiv \exp\left\{\int_0^r\left[\frac{N^2}{g}-\frac{g}{c^2}+i\frac{v_T}{\omega c_4}(gD_4-D_3)\right]dr\right\}. \qquad (22.17)$$

These equations are quasi-adiabatic versions of canonical equations (15.5)–(15.7) for adiabatic oscillations under the Cowling approximation. Furthermore, eliminating $\bar{\xi}_N$ or $\bar{\eta}_N$ from equations (22.15) and (22.16), we obtain the second order differential equations

$$\frac{d^2\bar{\xi}_N}{dr^2}-\frac{1}{P_N}\frac{dP_N}{dr}\frac{d\bar{\xi}_N}{dr}-P_NQ_N\bar{\xi}_N = 0 \qquad (22.18)$$

and

$$\frac{d^2\bar{\eta}_N}{dr^2}-\frac{1}{Q_N}\frac{dQ_N}{dr}\frac{d\bar{\eta}_N}{dr}-P_NQ_N\bar{\eta}_N = 0, \qquad (22.19)$$

where P_N and Q_N are defined as

$$P_N \equiv \frac{r^2h_N(r)}{c^2}\left(\frac{L_l^2}{\sigma^2}-1+i\frac{D_4c^2v_T}{\omega c_4}\right) \qquad (22.20)$$

and

$$Q_N \equiv \frac{1}{r^2h_N(r)}\left(\sigma^2-N^2+i\frac{D_3gv_T}{\omega c_4}\right), \qquad (22.21)$$

respectively. Equations (22.18) and (22.19) are quasi-adiabatic versions of equations (16.1) and (16.2). Equations (22.15)–(22.21) are used in an asymptotic analysis given in the following subsection.

22.3 Asymptotic Analysis

Because equations (22.18) and (22.19) have the same forms as equations (16.1) and (16.2), respectively, for adiabatic oscillations, we can use a parallel argument here with that given in Section 16. Using a procedure similar to that given in Section 16 (Lee, 1985a) with WKBJ-type solutions for equations (22.18) and (22.19), we obtain, after some

manipulation, eigenvalue conditions for high order nonradial pulsations as

$$\int_{r_a}^{r_b}\mathrm{Re}(k_r)dr = n\pi \qquad (22.22)$$

and

$$\int_{r_a}^{r_b}\mathrm{Im}(k_r)dr = 0\,, \qquad (22.23)$$

where $\mathrm{Re}(k_r)$ and $\mathrm{Im}(k_r)$ are the real and the imaginary parts, respectively, of the radial wave number and r_a and r_b are the radii at the inner and outer boundaries, respectively, of a propagation zone. (Note that r_a and r_b depend on the oscillation frequency as well as the equilibrium structure of the star.) Under the quasi-adiabatic approximation the radial wave number k_r is given by

$$k_r^2 = -P_NQ_N = -\frac{1}{c^2}\left(\sigma^2-N^2+i\frac{D_3gv_T}{\omega c_4}\right)\left(\frac{L_l^2}{\sigma^2}-1+i\frac{D_4c^2v_T}{\omega c_4}\right). \qquad (22.24)$$

Or, using the fact that the imaginary part of the eigenfrequency, σ_I, is much smaller than the real part, σ_R, equation (22.24) is written as

$$k_r^2 \simeq -\frac{1}{c^2}\left[\sigma_R^2-N^2+i\left(\frac{D_3gv_T}{\omega_Rc_4}+2\sigma_I\sigma_R\right)\right] \times\left[\frac{L_l^2}{\sigma_R^2}-1+i\left(\frac{D_4c^2v_T}{\omega_Rc_4}-2\frac{L_l^2}{\sigma_R^2}\frac{\sigma_I}{\sigma_R}\right)\right], \qquad (22.25)$$

where ω_R means the real part of the dimensionless frequency ω.

For high order g-modes ($\sigma_R^2 \ll N^2, L_l^2$), we obtain from equation (22.25)

$$k_r \simeq \frac{L_lN}{\sigma_Rc}\left\{1+i\left[\frac{v_T}{2\omega_Rc_4}\left(\frac{\sigma_R^2D_4c^2}{L_l^2}-\frac{D_3g}{N^2r}\right)-\frac{\sigma_I}{\sigma_R}\right]\right\}. \qquad (22.26)$$

From the eigenvalue condition for the real part of k_r given in equation (22.22), we obtain

$$\sigma_R = \frac{\sqrt{l(l+1)}}{n\pi}\int_{r_a}^{r_b}\frac{N}{r}dr. \qquad (22.27)$$

This equation is the same as the expression for the adiabatic frequency for high order g-modes given by (16.41), which indicates that the effect of nonadiabaticity on the real part of the eigenfrequency is of the order

of c_4^{-2}. From the eigenvalue condition given by equation (22.23) for the imaginary part of k_r we obtain

$$\frac{\sigma_I}{\sigma_R}=\frac{1}{2}\int_{r_a}^{r_b}\left[\frac{\sigma_R^2 D_4 Nr}{l(l+1)}-\frac{D_3 g}{Nr}\right]\frac{v_T}{\omega_R c_4}dr\left[\int_{r_a}^{r_b}\frac{N}{r}dr\right]^{-1}. \quad (22.28)$$

Thus, the imaginary part of the eigenfrequency, σ_I, which determines the growth- or decay-time of oscillation is a quantity of the order of c_4^{-1}.

For high order p-modes ($\sigma_R^2 \gg L_l^2, N^2$), the radial wave number k_r is reduced to

$$k_r \simeq \frac{\sigma_R}{c}\left\{1+i\left[\frac{\sigma_I}{\sigma_R}+\frac{v_T}{2\omega_R c_4}\left(\frac{D_3 g}{\sigma_R^2}-D_4 c^2\right)\right]\right\}. \quad (22.29)$$

In this case, from the eigenvalue condition for the real part of k_r given in equation (22.22), we obtain

$$\sigma_R = n\pi\left[\int_{r_a}^{r_b}\frac{dr}{c}\right]^{-1}. \quad (22.30)$$

Again, the nonadiabatic effect on the real part of the eigenfrequency is of the order of c_4^{-2}. From the eigenvalue condition for the imaginary part of k_r given by equation (22.23), we obtain

$$\frac{\sigma_I}{\sigma_R}=\frac{1}{2}\int_{r_a}^{r_b}\left(D_4 c-\frac{D_3 g}{\sigma_R^2 c}\right)\frac{v_T}{\omega_R c_4}dr\left[\int_{r_a}^{r_b}\frac{dr}{c}\right]^{-1}. \quad (22.31)$$

Thus, the first order correction from nonadiabaticity appears in the imaginary part of the eigenfrequency which governs growth or decay of the oscillation. Discussion on the modes which have two propagation zones is given by Lee (1985a). Asymptotic analysis without using the quasi-adiabatic approximation is discussed by Dziembowski (1977a).

23. *Very Nonadiabatic Nonradial Oscillations*

For stars with $L/M \gtrsim 10^4 L_\odot/M_\odot$, τ_{th}/τ_{dyn} is so small in the envelope that radial pulsations or nonradial oscillations trapped in the envelope are very nonadiabatic. In this case, it is difficult to identify oscillation modes, because there is no one-to-one correspondence between the adiabatic and nonadiabatic eigenfrequencies. Because of this complexity, investigation on very nonadiabatic nonradial oscillations is not yet well developed.

One way to investigate the properties of very nonadiabatic oscillations is to artificially change the effect of the nonadiabaticity and see what happens during the continuous change of the degree of nonadiabaticity. Shibahashi and Osaki (1981a) used the procedure in

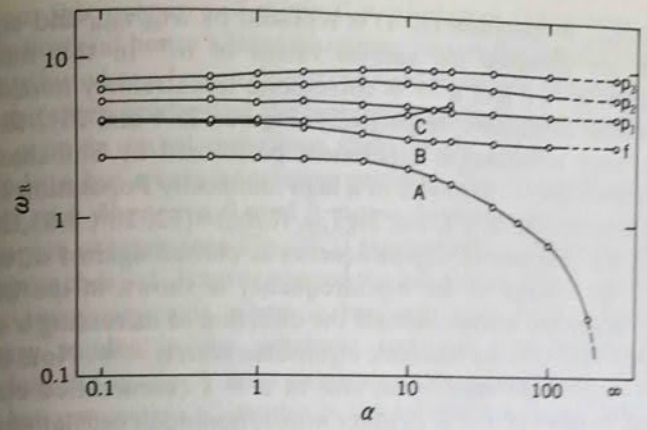

Fig. 23.1 Variation in real part ω_R of nondimensional eigenfrequencies for nonradial pulsations with $l = 10$ with the multiplying factor α to the thermal time scale (from Shibahashi and Osaki, 1981a).

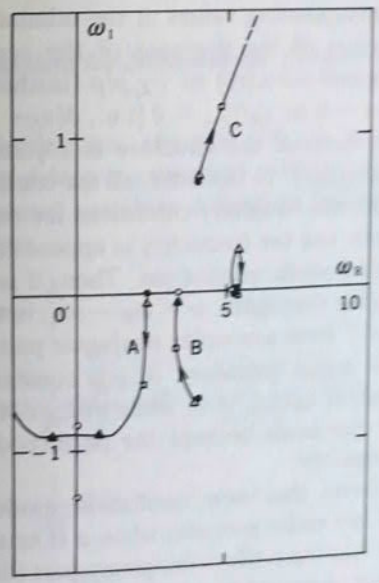

Fig. 23.2 Loci of complex eigenvalues in the complex ω-plane with the variation of α for some nonradial modes shown in Fig. 23.1 (from Shibahashi and Osaki, 1981a). Symbols indicate $\alpha = 0$ (filled circles), $\alpha = 1$ (open triangles), $\alpha = 10$ (open squares), $\alpha = 100$ (filled triangles), and $\alpha = \infty$ (open circles).

which τ_{th}/τ_{dyn} in equation (22.1) is replaced by $\alpha\tau_{th}/\tau_{dyn}$ and eigenfrequencies are obtained for various values of α.* In this numerical experiment, $\alpha \to 0$ and $\alpha \to \infty$ correspond to extremely nonadiabatic and adiabatic conditions, respectively. Figures 23.1 and 23.2 show the result of such a numerical experiment performed by Shibahashi and Osaki (1981a) for l= 10 modes of a high luminosity Population I model with parameters $(M/M_\odot, L/L_\odot, \log T_{eff}, R/R_\odot)$=(12, 10^5, 3.85, 207). In Fig. 23.1 the real part of eigenfrequency is plotted against α, while in Fig. 23.2 the change of the eigenfrequency is shown in the complex ω-plane, where the arrows indicate the direction of increasing α and the open circle indicates the adiabatic eigenvalue with $\alpha = \infty$. Note that the complex eigenfrequencies in the case of $\alpha = 1$ (unmodified case) are very close to those of $\alpha = 0$. In other words, nonradial oscillations of the unmodified model with $l = 10$ are extremely nonadiabatic.

The eigenfrequencies of the modes corresponding to the adiabatic p_1-, p_2-, and p_3- modes do not vary very much with a large variation in α. The frequencies of higher order p-modes at the limit of $\alpha = 0$ tend to be smaller than the corresponding values at the adiabatic limit ($\alpha = \infty$). This is a manifestation of the decrease of the sound velocity from $\sqrt{\Gamma_1 p/\rho}$ (adiabatic sound velocity) to $\sqrt{\chi_\rho p/\rho}$ (isothermal sound velocity). In the limit of $\alpha = 0$ or $\tau_{th}/\tau_{dyn} = 0$ [i.e., $\delta(\varepsilon_N - \rho^{-1}\nabla\cdot\boldsymbol{F}) = 0$], no thermal wave exists because the structure is adjusted to the thermal equilibrium instantaneously. In this limit, all the coefficients of the basic differential equations and boundary conditions for nonradial pulsations become real numbers, and the frequency ω appears only in the form of ω^2 as in the case of adiabatic oscillations. Then, if $\omega = \omega_R + i\omega_I$ is an eigenvalue, its complex conjugate, $\omega = \omega_R - i\omega_I$, is also an eigenvalue. In fact, modes B and C form a complex conjugate pair in the limit of $\alpha = 0$. We note that for radial pulsation, δL_R is constant in space in the envelope in the limit of $\tau_{th}/\tau_{dyn} = 0$, while $d\delta L_R/dM_r \neq 0$ in the same limit for nonradial pulsations because the perturbed radiation field is not spherically symmetric.

Figure 23.1 shows that new oscillation modes enter into the frequency range of low order p-modes when α is smaller than ~ 10 for this model. Mode C has the positive imaginary part (damped oscillation) of frequency which is comparable to the real part for any α. In the limit of $\alpha = 0$, the eigenfrequency of mode C is the complex conjugate to the eigenfrequency of mode B, which continuously changes to adiabatic f-mode as α changes to infinity. The imaginary and real parts of the eigenfrequency of mode C increase rapidly as α increases in the range of

* The same experiment was applied to nonadiabatic radial pulsations by Saio, Wheeler, and Cox (1984).

>1. From this property of mode C it is inferred that a large entropy perturbation and hence a large imaginary part of the frequency of mode C are attributed to a large value of the right-hand side of equation (22.1) due to the steep gradient of the luminosity perturbation. Similar modes appear even in radial pulsations (Saio et al., 1984).

Mode A has a very interesting property. The frequency of mode A is purely real when $\alpha = 0$, and it moves downward nearly vertically in the complex ω-plane (see Fig. 23.2) as α increases. When its imaginary part approaches -1, it turns toward the imaginary axis. It finally settles on the imaginary axis when α becomes very large. Since purely imaginary modes in the adiabatic limit are convectively unstable g^--modes, the mode A must originate from a convective mode. This model has convective g^--modes in the adiabatic case, because it has a convectively unstable zone due to hydrogen ionization, which is located just below the photosphere. This interpretation may well be supported, because the eigenfunction of the mode A in the case of overstable oscillation with a finite but non-zero α is trapped in the convective zone.

24. *Numerical Method for Nonadiabatic Analysis of Nonradial Oscillations*

As in the adiabatic case (Section 18), it is convenient to use nondimensional variables in numerical analyses. As a simple extension of the nondimensional variables defined in Section 18, we choose the following variables:

$$y_1 = \frac{\xi_r}{r}, \tag{24.1}$$

$$y_2 = \frac{1}{gr}\left(\frac{p'}{\rho} + \Phi'\right) \quad \left[= \frac{\sigma^2 r}{g}\frac{\xi_h}{r}\right], \tag{24.2}$$

$$y_3 = \frac{1}{gr}\Phi', \tag{24.3}$$

$$y_4 = \frac{1}{g}\frac{d\Phi'}{dr}, \tag{24.4}$$

$$y_5 = \frac{\delta S}{c_p}, \tag{24.5}$$

and

$$y_6 = \frac{\delta L_R}{L_R}, \tag{24.6}$$

where y_1, y_2, y_3, and y_4 are the same as Dziembowski's (1971) variables used in his adiabatic analysis. We choose the entropy perturbation rather than the temperature perturbation as the fifth variable for the following reason: Although the nonadiabatic effect is considerable in the outer part of a star, the thermal time scale is much longer than the period of the oscillations in the deep interior. Thus the oscillations are almost adiabatic in the deep interior of the star, where the independence between the temperature and pressure perturbations tends to be lost numerically. Therefore, choosing the entropy perturbation tends to cause less trouble in the nonadiabatic analysis.

Using the variables defined in equations (24.1)–(24.6), the differential equations of linear nonadiabatic nonradial oscillations (21.11)–(21.15) are written as

$$\frac{dy_1}{d\ln r} = (V_g - 3)y_1 + \left[\frac{l(l+1)}{c_1\omega^2} - V_g\right]y_2 + V_g y_3 + v_T y_5, \tag{24.7}$$

$$\frac{dy_2}{d\ln r} = (c_1\omega^2 - A^*)y_1 + (A^* - U + 1)y_2 - A^* y_3 + v_T y_5, \tag{24.8}$$

$$\frac{dy_3}{d\ln r} = (1 - U)y_3 + y_4, \tag{24.9}$$

$$\frac{dy_4}{d\ln r} = UA^* y_1 + UV_g y_2 + [l(l+1) - UV_g]y_3 - Uy_4 - Uv_T y_5, \tag{24.10}$$

$$\begin{aligned}\frac{dy_5}{d\ln r} = {} & V[\nabla_{ad}(U - c_1\omega^2) - 4(\nabla_{ad} - \nabla) + c_2]y_1 \\ & + V\left[\frac{l(l+1)}{c_1\omega^2}(\nabla_{ad} - \nabla) - c_2\right]y_2 + Vc_2 y_3 + V\nabla_{ad} y_4 \\ & + V\nabla(4 - \kappa_S)y_5 - V\nabla y_6,\end{aligned} \tag{24.11}$$

and

$$\frac{dy_6}{d\ln r} = \left[l(l+1)\frac{\nabla_{ad} - \nabla}{\nabla} - \varepsilon_{ad}c_3 V\right]y_1 + \left[\varepsilon_{ad}c_3 V - l(l+1)\left(\frac{\nabla_{ad}}{\nabla} + \frac{c_3}{c_1\omega^2}\right)\right]y_2$$

$$+\left[l(l+1)\frac{\nabla_{ad}}{\nabla} - \varepsilon_{ad}c_3 V\right]y_3 + \left[c_3\varepsilon_S - \frac{l(l+1)}{V\nabla} - i\omega c_4\right]y_5 - \frac{d\ln L_R}{d\ln r}y_6, \tag{24.12}$$

where

$$c_2 = (\kappa_{ad} - 4\nabla_{ad})V\nabla + \nabla_{ad}\left(\frac{d\ln\nabla_{ad}}{d\ln r} + V\right), \tag{24.13}$$

$$c_3 = \frac{4\pi r^3\rho\varepsilon_N}{L_R}, \tag{24.14}$$

$$c_4 = \frac{4\pi r^3\rho T c_p}{L_R}\sqrt{\frac{GM}{R^3}}, \tag{24.15}$$

and c_1, V_g, and A^* are defined by equations (18.19), (18.18), and (18.21), respectively. The quantity c_4 represents the ratio of a local thermal time scale to the free-fall time scale of the star and have a large value in the deep interior of the star ($>10^5$).

The central boundary conditions (21.21)–(21.23) are given by

$$y_1 = ly_2/(c_1\omega^2), \tag{24.16}$$

$$y_4 = ly_3, \tag{24.17}$$

and

$$y_5 = 0 \tag{24.18}$$

near the center.

The outer boundary conditions (21.24), (21.25), and (21.27) are written as

$$y_1\{1 + [l(l+1)/\omega^2 - 4 - \omega^2/V\} - y_2 + y_3\{1 + [l(l+1)/\omega^2 - l - 1]/V\} = 0, \tag{24.19}$$

$$(l+1)y_3 + y_4 = 0, \tag{24.20}$$

and

$$(2 - 4\nabla_{ad}V)y_1 + 4\nabla_{ad}V(y_2 - y_3) + 4y_5 - y_6 = \tag{24.21}$$

at $r = R$. The terms proportional to V^{-1} are retained in the mechanical boundary condition in equation (24.19) [*cf.* equation (18.51)], because these terms become leading terms when equation (24.19) is substituted

into equation (24.21).

A Henyey-type relaxation method as described in Section 18.2 can be used to obtain the eigenvalue ω and eigenfunctions $y_i(r)$. In the core of a star the thermal time scale is so long compared to the oscillation time scale that numerical instability sometimes occurs in the entropy perturbation, y_5. The amplitude of the numerical instability is, in many cases, very small because the entropy perturbation is negligibly small there, so that the numerical instability has no practical effect on the results. Sometimes, however, the amplitude of the numerical instability could be large enough to disturb eigenfunctions of other quantities. This difficulty can be avoided by using the method invented by Sugimoto (1970) for calculations of stellar evolution: In the Henyey-method a differential equation

$$\frac{dy_i}{dx} = f_i(x, y_j) \tag{24.22}$$

is converted to a difference equation

$$\frac{y_i^{n+1} - y_i^n}{x_{n+1} - x_n} = (1-\theta_i) f_i^{n+1} + \theta_i f_i^n, \tag{24.23}$$

where n indicates quantities at the n-th grid point. The average weight, θ_i, is usually set at 0.5 (centered difference scheme) for better accuracy. According to Sugimoto's (1970) prescription, the numerical instability is suppressed if we adopt $(\theta_5, \theta_6) = (1,0)$ or $= (0,1)$. Since adopting $(\theta_5, \theta_6) = (0.5, 0.5)$ is better for accuracy, a better way may be adopting $(\theta_5, \theta_6) = (1,0)$ or $(0,1)$ in the deep interior (in the region where c_4 is greater than, say, 10^4) and $= (0.5, 0.5)$ in the outer region.

In applying a Henyey-type relaxation scheme to solve the eigenvalue problem we sometimes encounter a difficulty, in that the matrix $\boldsymbol{P}_1$ in (18.78) is singular. In equation (18.78) three inner boundary conditions and three difference equations are incorporated to obtain the relation between the corrections for the eigenfunctions at the innermost grid point and at the second grid point [equation (18.82)]. If we adopt the three inner boundary conditions given in equations (24.16)–(24.18) and choose three difference equations which correspond to equations (24.7)–(24.9), for example, to construct a matrix equation such as equation (18.78), then all the elements in the 6th column of the matrix $\boldsymbol{P}_1$ are zero and $\boldsymbol{P}_1$ does not have its inverse matrix. This occurs because the variable y_6 does not appear in any of those equations. This difficulty can be easily avoided by changing the order of equations so that all the variables appear in equation (18.78). For example, we can exchange between equations (24.9) and (24.11) or (24.12).

If the nonadiabatic effect is small (i.e., $\omega_I/\omega_R \ll 1$, where ω_I and ω_R are the imaginary part and real part of the nondimensional frequency ω), adiabatic solutions for the eigenfrequency and eigenfunctions can be used for trial values in the Henyey-type relaxation method described in Section 18.2. However, for a very nonadiabatic case the real part of the eigenfrequency could be far from the adiabatic eigenfrequency. Furthermore, since there is no one-to-one correspondence between the adiabatic and nonadiabatic eigenvalues, it is not certain whether all the eigenvalues have been picked up for a certain region in the complex (ω_R, ω_I)-plane. A way to obtain a good initial guess of complex eigenvalue is to use Castor's (1971) method (see Section 18.2) generalized to complex variables, in which one boundary condition is set aside in integrating differential equations for a trial eigenvalue, and the boundary condition is used as the discriminant to see whether the trial eigenvalue is close enough to a true eigenvalue.

In addition to generalization of Castor's (1971) method to complex variables, Dziembowski (1977a) and Shibahashi and Osaki (1981a) invented a method of seaching for all the eigenvalues in a given region of (ω_R,ω_I)-plane by introducing concept of mapping as follows. In their method, a discriminant $D(\omega)$ is produced from a boundary condition. The discriminant is zero for an eigenvalue $\tilde{\omega}$; i.e.,

$$D(\tilde{\omega}) = 0, \tag{24.24}$$

and $D(\omega)$ must not have singular points in the parameter area considered (see below). Let us consider the mapping from the complex ω-plane to the complex D-plane. A closed loop in the ω-plane is mapped into a closed loop in the D-plane. If the closed loop in the D-plane winds n-times around the origin, there exist n eigenvalues inside the loop of the ω-plane. Figure 24.1 illustrates such a mapping from the ω-plane to the D-plane. The large rectangle $ABCD$ on the ω-plane is mapped to the closed curve $A'B'C'D'$ on the D-plane which winds around the origin once. By dividing the large rectangle into two by a straight line EF, we find that an eigenvalue exists inside the rectangle $AEFD$ but not inside the rectangle $EBCF$.

This can be understood as follows: If $D(\omega)$ is a regular function, and there are J eigenvalues $\tilde{\omega}_j$ $(j = 1,2,\ldots, J)$ [i.e., J zero points of $D(\omega)$], the discriminant $D(\omega)$ can be written as

$$D(\omega) \propto \prod_{j=1}^{J} (\omega - \tilde{\omega}_j). \tag{24.25}$$

Let arg (z) be the angle which the direction from the origin to the point z makes with the real axis in the complex plane. Then we have

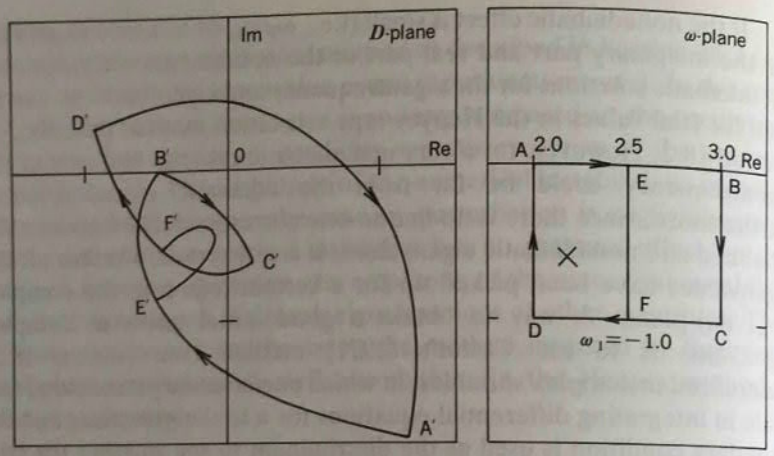

Fig. 24.1 Mapping from the ω-plane to the D-plane. The cross ($\times$) in the ω-plane indicates an eigenfrequency for which $D(\tilde{\omega}) = 0$ (from Shibahashi and Osaki, 1981a).

$$\arg[D(\omega)] = \sum_{j=1}^{J} \arg(\omega - \tilde{\omega}_j) + \text{const.} \tag{24.26}$$

It can be shown that when ω makes a closed loop C in the complex ω-plane, the net change in arg $(\omega-\tilde{\omega}_j)$ is 2π if $\tilde{\omega}_j$ is within the loop and zero if $\tilde{\omega}_j$ is outside the loop C. This can be expressed as

$$\oint_C d[\arg(\omega - \tilde{\omega}_j)] = \begin{cases} 2\pi & \text{if } \tilde{\omega}_j \text{ is within the loop } C; \\ 0 & \text{if } \tilde{\omega}_j \text{ is outside the loop } C. \end{cases} \tag{24.27}$$

Therefore, we have

$$\frac{1}{2\pi}\oint_C d[\arg(D)] = \text{the number of eigenvalues within the loop } C. \tag{24.28}$$

Thus, the winding number around the origin in the D-plane corresponds to the number of eigenvalues within the loop of the ω-plane. It should be noted, however, that if the discriminant $D(\omega)$ has singularities within the loop C, the above relation does not hold. For example, if there is a pole within the loop C, it decreases the value of the integral in equation (24.28) by -2π; i.e., it decreases the winding number in the D-plane by one.

Chapter V

EXCITATION AND DAMPING OF OSCILLATIONS

25. *Energy Equation and Work Integral*

The vibrational stability, as well as the dynamical and thermal stability, is the problem of the exchange from one type of energy to another in a system. Therefore, the energy equation provides us with the basis of a theory with which the physical mechanisms of various kinds of instabilities can be considered. From the basic equations (13.1)–(13.4), an equation describing the total energy conservation is derived in what follows. In this section, the viscous terms are neglected owing to their smallness in the basic equations, as discussed in Section 13. The equation of conservation of mechanical energy can be obtained by taking the scalar product of equation (13.4) with $\boldsymbol{v}$,

$$\rho\frac{d}{dt}\left(\frac{1}{2}v^2\right) = -\boldsymbol{v}\cdot\nabla p - \rho\boldsymbol{v}\cdot\nabla\Phi. \tag{25.1}$$

Using the first law of thermodyndmics,

$$TdS = dU + pd\left(\frac{1}{\rho}\right), \tag{25.2}$$

equation (13.3) (i.e., equation of conservation of thermal energy) can be reduced to

$$\rho\frac{dU}{dt} + \nabla\cdot(p\boldsymbol{v}) - \boldsymbol{v}\cdot\nabla p = \rho\varepsilon_N - \nabla\cdot\boldsymbol{F}, \tag{25.3}$$

where U denotes specific internal energy. In deriving equation (25.3), the continuity equation (13.1) has been used and the radiative flux $\boldsymbol{F}_R$ has been replaced by the total flux $\boldsymbol{F}$ [see equations (13.17) and (20.23)].

Adding equations (25.1) and (25.3) to eliminate $\boldsymbol{v}\cdot\nabla p$, we obtain the total energy conservation

$$\rho\frac{d}{dt}\left(\frac{1}{2}v^2 + U\right) + \nabla\cdot(p\boldsymbol{v} + \boldsymbol{F}) + \rho\boldsymbol{v}\cdot\nabla\Phi = \rho\varepsilon_N. \tag{25.4}$$

Noting that

$$\int_0^M \boldsymbol{v}\cdot\nabla\Phi dM_r = -\int_0^M dM_r \frac{d\boldsymbol{r}}{dt}\frac{d}{d\boldsymbol{r}}\int_0^M \frac{GdM_r'}{|\boldsymbol{r}-\boldsymbol{r}'|}$$

$$= -\iint dM_r dM_r' \frac{d\boldsymbol{r}}{dt}\frac{\partial}{\partial \boldsymbol{r}}\left(\frac{G}{|\boldsymbol{r}-\boldsymbol{r}'|}\right)$$

$$= -\iint dM_r dM_r' \frac{1}{2}\left(\frac{d\boldsymbol{r}}{dt}\frac{\partial}{\partial \boldsymbol{r}} + \frac{d\boldsymbol{r}'}{dt}\frac{\partial}{\partial \boldsymbol{r}'}\right)\frac{G}{|\boldsymbol{r}-\boldsymbol{r}'|}$$

$$= -\frac{1}{2}\iint dM_r dM_r' \frac{d}{dt}\left(\frac{G}{|\boldsymbol{r}-\boldsymbol{r}'|}\right)$$

$$= -\frac{1}{2}\frac{d}{dt}\iint \frac{GdM_r dM_r'}{|\boldsymbol{r}-\boldsymbol{r}'|}$$

$$= \frac{1}{2}\frac{d}{dt}\int_0^M \Phi dM_r, \tag{25.5}$$

we integrate equation (25.4) over the whole volume of a star, obtaining

$$\frac{dE}{dt} = \int_0^M \left(\varepsilon_N - \frac{1}{\rho}\nabla\cdot\boldsymbol{F}\right)dM_r - \int_{r=R} p\boldsymbol{v}\cdot d\boldsymbol{S}$$

$$= \int_0^M T\frac{dS}{dt}dM_r - \int_{r=R} p\boldsymbol{v}\cdot d\boldsymbol{S}, \tag{25.6}$$

where E denotes the total energy of the star

$$E = \int_0^M \left(\frac{1}{2}v^2 + \frac{1}{2}\Phi + U\right)dM_r. \tag{25.7}$$

In obtaining equation (25.6), we assumed that the total mass is conserved. Equation (25.6) expresses the energy theorem. The total energy E consists of the kinetic, potential, and internal energies. The factor 1/2 in the potential energy in equation (25.7) is due to the characteristics of the self-gravitating system as seen from equation (25.5). The energy theorem states that change in the total energy of a system is caused by either nuclear energy generation ε_N in the interior or loss of radiative flux $\boldsymbol{F}$ at the surface or the outgoing wave flux $p\boldsymbol{v}$, if no work is done from the outside.

As mentioned in the beginning, at least one form of energy increases or decreases monotonically with time for an unstable situation. For the dynamical instability, the first integral in the

right-hand side of equation (25.6) can be neglected since the dynamical time scale in a star is usually much shorter than the thermal time scale. If the surface integral vanishes (as is usually the case in a star), kinetic energy must increase at the expense of the potential and/or internal energy. Therefore, if an equilibrium state has an adiabatically accessible neighboring state having less potential and/or internal energy, the equilibrium state is dynamically unstable. The Jeans gravitational instability and the convective instability are examples of radial and nonradial dynamical instabilities, respectively. In stable situations, disturbances are subject to acoustic and gravity waves or oscillations.

In the case of thermal instability, the system can be treated as hydrostatic with zero kinetic energy in the time scale considered. We note that thermal instability could also occur as overstability (see, e.g., Unno, 1975b). When a star has no energy source ($\varepsilon_N = 0$), radiation loss through the surface leads to the Kelvin contraction of the star.

To study vibrational instability, the kinetic energy must be included. Vibrational instability is characterized by the existence of a periodicity in the temporal behavior of perturbations. Integrating equation (25.6) over one period of oscillation, we obtain

$$\oint \frac{dE}{dt}dt = \oint dt\int_0^M \left(\varepsilon_N - \frac{1}{\rho}\nabla\cdot\boldsymbol{F}\right)dM_r - \oint dt\int_{r=R} p\boldsymbol{v}\cdot d\boldsymbol{S}$$

$$= \oint dt\int_0^M T\frac{dS}{dt}dM_r - \oint dt\int_{r=R} p\boldsymbol{v}\cdot d\boldsymbol{S}, \tag{25.8}$$

where $\oint dt$ indicates the integration over one period of oscillation. It is useful to introduce the work integral W, which is defined as the increase of the total energy E over one period of oscillation. The work integral W is given by the first term in the right-hand side of equation (25.8) for a real star if the pressure goes to zero at the surface (no shock waves going outward). For a nearly strictly periodic oscillation (i.e., $\oint \delta T dt \simeq 0$ and $\oint \delta S dt \simeq 0$) W is given as (Eddington, 1926)

$$W = \oint \frac{dE}{dt}dt = \oint dt\int_0^M T\frac{dS}{dt}dM_r = \oint dt\int_0^M \delta T\frac{d\delta S}{dt}dM_r$$

$$= \oint dt\int_0^M \frac{\delta T}{T}\delta\left(\varepsilon_N - \frac{1}{\rho}\nabla\cdot\boldsymbol{F}\right)dM_r. \tag{25.9}$$

If W is positive, the star is vibrationally unstable. The energy increase is provided from photon energy, which is originally produced by nuclear reactions in the core. In other words, oscillation is generated if photon energy is efficiently converted to kinetic energy through a certain

mechanism. Equation (25.9) can be understood to express an energy production through a completely periodic change, which resembles the energy production of a Carnot-type heat engine.

Equation (25.8) indicates that if a finite value can artificially be given to the surface pressure, a strictly periodic oscillation can be produced by equating the first term in the right-hand side to the second term. This corresponds to a strictly periodic imaginary oscillation, in which all the excitation effect is consumed by the work done on the artificially placed matter above the stellar surface. The work integral W can also be defined as the amount of energy which must be removed from the star in order for the star to oscillate strictly periodically (i.e., with constant amplitude). Baker and Kippenhahn (1962) introduced $W(r)$ defined by

$$W(r)=\oint dt\int_S p\boldsymbol{v}\cdot d\boldsymbol{S}(r)=\oint dt\int_0^{M_r}\frac{1}{\rho}\nabla\cdot(p\boldsymbol{v})dM_r \qquad (25.10)$$

for oscillations artificially enforced to be strictly periodic. It represents the work done on the overlying layer by the sphere of radius r, and its surface value is W.

Both of the formulae for W are applicable to nonlinear periodic oscillations and also to linear stability analysis. In the former case, W may represent the nonlinear shock dissipation; in the latter case, the condition $W>0$ expresses the vibrational instability.

In the linear stability problem, the bilinear form of the energy theorem (25.6) is often useful to investigate the restoring forces and excitation mechanisms of oscillation. Following Eckart (1960), we rearrange the basic equations (13.28), (13.29), and (13.83) in such a way as giving the partial time derivatives $\partial\boldsymbol{v}/\partial t$, $\partial p'/\partial t$, and $\partial(p'-c^2\rho')/\partial t$; multiply these equations by $\rho\boldsymbol{v}$, $p'/(\Gamma_1 p)$, and $g^2(p'-c^2\rho')/(\rho c^4N^2)$, respectively; and add them. After somewhat lengthy manipulations, the result turns out to be

$$\frac{\partial}{\partial t}(\rho e_W)+\nabla\cdot\boldsymbol{F}_W=\rho\delta T\frac{\partial\delta S}{\partial t}-\Phi'\frac{\partial\rho'}{\partial t}, \qquad (25.11)$$

where the wave energy per unit mass, e_W, is defined as

$$e_W=\frac{1}{2}\left\{v^2+\left(\frac{p'}{\rho c}\right)^2+\left(\frac{g}{N}\right)^2\left[\left(\frac{p'}{\Gamma_1 p}-\frac{\rho'}{\rho}\right)^2-\frac{\nabla}{\nabla_{ad}}\left(v_T\frac{\delta S}{c_p}\right)^2\right]\right\}, \qquad (25.12)$$

and

$$\boldsymbol{F}_W=p'\boldsymbol{v}+\rho\boldsymbol{v}\Phi'. \qquad (25.13)$$

We can replace $\partial/\partial t$ by d/dt in equation (25.11) because the difference appears only in higher order terms. The second term in the right-hand side of equation (25.11) can be incorporated into the global wave energy E_W by integrating equation (25.11) over the whole volume of the star; i.e.,

$$\frac{dE_W}{dt}=\int_0^{M_r}\delta T\frac{d\delta S}{dt}dM_r-\int_S \boldsymbol{F}_W\cdot d\boldsymbol{S}, \qquad (25.14)$$

where

$$E_W=\int_0^{M}\left(e_W+\frac{1}{2}\frac{\rho'}{\rho}\Phi'\right)dM_r. \qquad (25.15)$$

This equation states that change in the wave energy of a star is caused by nonadiabatic processes in the interior and by the outgoing wave flux $\boldsymbol{F}_W$ at the surface. The first term in e_W is the kinetic energy and the other terms represent the potential energies corresponding to the various restoring forces. If there is a negative potential energy, monotonically unstable modes could exist, because the kinetic energy can increase without changing the total energy. For example, a dynamically unstable convective mode (or g^--mode) arises if $N^2<0$ somewhere in the stellar interior, due to the exchange of energy between the first and the third term in the right-hand side of equation (25.12). In the case of an acoustic wave, the second term in e_W is dominant, and the wave energy averaged over one period is equi-partitioned into kinetic energy $(1/2)v^2$ and acoustic potential energy $(1/2)(p'/\rho c)^2$. When the third term is dominant, the internal gravity wave ($N^2>0$) or the convective mode ($N^2<0$) appears. The term proportional to $(\delta S)^2$ is related to nonadiabatic effect. Although this term cannot be discussed independently of the right-hand side of equation (25.11), equation (25.12) suggests that if this term is so large as to make the square bracket negative, the convective mode ($N^2<0$) could become oscillatory. This phenomenon seems to be related to the vibrationary unstable mode which was obtained and was traced to a convective mode in the adiabatic limit by Shibahashi and Osaki (1981a) (see also Section 23).

The direct derivation of work integral W from equation (25.14) is convenient for linear stability analysis:

$$W=\oint dt\frac{dE_W}{dt}=\oint dt\left[\int_0^{M}\delta T\frac{d\delta S}{dt}dM_r-\int_S \boldsymbol{F}_W\cdot d\boldsymbol{S}\right]$$
$$=\oint dt\left[\int_0^{M}\frac{\delta T}{T}\delta\left(\varepsilon_N-\frac{1}{\rho}\nabla\cdot\boldsymbol{F}\right)dM_r-\int_{r=R}(p'+\rho\Phi')\,\boldsymbol{v}\cdot d\boldsymbol{S}\right]. \qquad (25.16)$$

This is equivalent to the linear version of Eddington's work integral (25.8) if the surface integral vanishes. The work integral W is related to the growth rate σ_I of amplitude of oscillation, which is the imaginary part of $\sigma(\sigma = \sigma_R + i\sigma_I)$:

$$\sigma_I = -\frac{1}{2}\frac{W/E_W}{\Pi}, \tag{25.17}$$

where Π denotes the period. The factor 1/2 comes from the fact that the energy is proportional to the square of amplitude. We consider that $|\sigma_I/\sigma_R| \ll 1$, since the ratio is of the order of magnitude of the dynamical to thermal time-scale ratio. Then, $\Pi = 2\pi\sigma_R^{-1}$. The total energy of oscillation E_W is twice the time average of the kinetic energy since there is equi-partition of the kinetic and potential energies of oscillation in the time average:

$$E_W = \int_0^M \langle v^2 \rangle_{AV}\, dM_r = \frac{\sigma_R^2}{2}\int_0^M \boldsymbol{\xi}\cdot\boldsymbol{\xi}^*\, dM_r = \frac{\sigma_R^2}{2}\int_0^M |\boldsymbol{\xi}|^2 dM_r. \tag{25.18}$$

Then, we have

$$\sigma_I = -\frac{1}{2\pi\sigma_R} W\left[\int_0^M |\boldsymbol{\xi}|^2 dM_r\right]^{-1}. \tag{25.19}$$

There are several alternative expressions of W. The physical mechanisms of excitation and damping may best be studied with equation (25.16). However, for linear nonadiabatic numerical calculation, equation (25.10) is sometimes more convenient. We have

$$W(r) = \oint dt \int_S \mathrm{Re}(\delta p)\,\mathrm{Re}\left(\frac{d\xi_r}{dt}\right) dS = 4\pi r^2 \oint \mathrm{Re}(\delta p)\,\mathrm{Re}(i\sigma_R \xi_r)\, dt$$

$$= 4\pi r^2 \sigma_R \oint \left(\frac{\delta p + \delta p^*}{2}\right)\left(\frac{i\xi_r - i\xi_r^*}{2}\right) dt$$

$$= -4\pi^2 r^2 \mathrm{Im}(\delta p^* \xi_r). \tag{25.20}$$

The term proportional to Re $(\delta p \xi_r)$ does not appear in the last line of equation (25.20), because it has the temporal dependence $\exp(2i\sigma_R t)$ and hence becomes zero by the integral over one period. As discussed before, equations (25.10) and (25.20) are applicable to the oscillation which is artificially enforced to be purely periodic. In the linear analysis, we can use equation (25.20) in the following way. First, we obtain an adiabatic eigenfrequency σ_{ad} by a numerical analysis based on the method disussed in Section 18. Then we solve the equations of

nonadiabatic oscillations assuming that the temporal dependence is $\exp(i\sigma_R t)$ with $\sigma_R = \sigma_{ad}$. In solving the equations of nonadiabatic oscillations, the outer mechanical boundary condition ($\delta p \to 0$ near the surface) is disregarded. Then, we evaluate the work integral in equation (25.20) by using the solution obtained in this way. Note that since the solution does not satisfy the outer mechanical boundary condition, $W = W(R)$ has a finite value. Baker and Kippenhahn (1962) used this formula for radial pulsations, but it can be used as well for nonradial oscillations, as was done by Ando and Osaki (1975). The work integral for nonradial oscillations with the energy leakage at a boundary was discussed by Osaki (1977).

There are two reasons why the work integral is useful in the numerical analysis. One way it is useful is to check the consistency of the imaginary part of the eigenvalue σ_I between the direct nonadiabatic numerical calculation and the evaluation by use of the work integral in equation (25.19). For a quasi-adiabatic analysis σ_I is obtained only by using the work integral in the form of equation (25.16). [Note that equation (25.20) is only for nonadiabatic analyses.] The other reason to use the work integral is to see where the excitation and damping zones are located in the stellar interior. If $W(r)$ or dW/dr is plotted as a function of the position in the stellar interior, dW/dr is positive in an excitation zone and negative in a damping zone.

We restrict ourselves to discussing the work integral in a spherically symmetric star. However, it should be noted that, in some kinds of stars such as Ap stars, deviation from the spherical symmetry or chemical inhomogeneity should be taken into account (*cf.* Dziembowski, 1984b).

26. *Work Integral in Quasi-Adiabatic Approximation*

26.1 Work Integral for Quasi-Adiabatic Analyses

In quasi-adiabatic analysis the work integral W is estimated by using adiabatic eigenfunctions as well as adiabatic relations. In this case we should evaluate the work integral W by using the expression given in equation (25.16). Let us decompose W into W_N, W_F, and W_C, which are related to the perturbations of nuclear energy generation rate, radiative flux, and convective flux, respectively:

$$W = W_N + W_F + W_C \tag{26.1}$$

with

$$W_N = \frac{\pi}{\sigma_R}\int_0^M \frac{\delta T^*}{T}\delta\varepsilon_N dM_r, \tag{26.2}$$

$$W_F=\frac{\pi}{\sigma_R}\int_0^M \frac{\delta T^*}{T}\left[-\frac{d\delta L_R}{dM_r}+\frac{l(l+1)}{d\ln T/d\ln r}\frac{F_R}{\rho r}\frac{\delta T}{T}\right.$$

$$\left.+l(l+1)\left(\frac{\xi_h}{r}\frac{dL_r}{dM_r}-\frac{\xi_r}{r}\frac{F_R}{\rho r}\right)\right]dM_r, \tag{26.3}$$

and

$$W_C=\frac{\pi}{\sigma_R}\int_0^M \frac{\delta T^*}{T}\left(-\frac{d\delta L_C}{dM_r}-\frac{1}{\rho}\nabla\cdot\boldsymbol{F}'_{C\perp}\right)dM_r, \tag{26.4}$$

where we neglected the surface integral $\int \boldsymbol{F}_W\cdot d\boldsymbol{S}$ representing the energy loss by the outgoing wave which vanishes for the trapped oscillation. In the following discussion in this section we neglect the effect of the perturbation of convective flux, W_C, which will be discussed in Section 30. The manner of decomposing terms into W_F and W_C depends on how to neglect the effect of the perturbation of convective flux. The above decomposition is due to the convention chosen in Chapter IV ($\boldsymbol{F}'_{C\perp}$ and $\delta L_C = 0$).

The complex conjugate of δT appears in equations (26.2)–(26.4) because we have integrated over the period of oscillation [cf. equation (25.20)]. In the following part of this section, however, we consider that physical variables represent only radial dependence [see equation (13.59)]. In this case, the mass element dM_r is regarded as an abbreviation for $4\pi\rho r^2 dr$. Furthermore, we assume that adiabatic eigenvalues and eigenfunctions are purely real, which is true in most cases. Therefore, for example, $\delta T^*\delta T$ will be written as $(\delta T)^2$ in the following discussion.

In evaluating W_F we can use equation (21.15) for δL_R, as well as adiabatic relations. However, Osaki (1976) claimed that a numerical inaccuracy could arise in evaluating the luminosity perturbation because of a numerical cancellation effect. For example, the eigenfunctions of higher g-modes in evolved models oscillate spatially very rapidly and have many nodes in the μ-gradient zone just outside the convective core. In such a case, the third and last terms in the right-hand side of equation (21.15) become very large there, and they have opposite signs that largely cancel each other out. If we calculate the $d(\delta T/T)/d\ln r$ term by a direct numerical differentiation of $\delta T/T$ given at discrete mesh points, it will be subject to some numerical inaccuracy, which is in turn magnified by the cancellation effect. To avoid this numerical difficulty, we rewrite the term involving the derivative of the temperature perturbation by using the basic differential equations of adiabatic oscillation. After some manipulation we obtain

$$\frac{\delta L_R}{L_R}=4\frac{\xi_r}{r}+\left[4-\kappa_T-(\Gamma_3-1)^{-1}\kappa_\rho\right]\frac{\delta T}{T}+\frac{\nabla_{ad}-\nabla}{\nabla}\frac{l(l+1)}{\sigma^2 r^2}\left(\frac{p'}{\rho}+\Phi'\right)$$

$$-\frac{1}{\nabla}\left(1+\frac{1}{V}\frac{d\ln\nabla_{ad}}{d\ln r}\right)\frac{\delta T}{T}+\frac{\nabla_{ad}}{\nabla}\left[(U-c_1\omega^2-4)\frac{\xi_r}{r}+\frac{1}{g}\frac{d\Phi'}{dr}\right], \tag{26.5}$$

where the relation $\xi_h=(p'/\rho+\Phi')/(\sigma^2 r)$ was used [equation (13.61)]. The homology invariants U and V, and c_1 are defined in equations (18.18) and (18.19), respectively. Equation (26.5) does not involve any numerical differentiation of perturbation variables since $y_4=(1/g)d\Phi'/dr$ is the fourth variable of the basic adiabatic oscillation (see Section 18.1).

The luminosity perturbation calculated in this manner may be seriously in error in the outer envelope of a star, because the thermal time scale is short there and hence the nonadiabatic effect is large. To avoid this difficulty the integration in equation (26.3) should be terminated at a radius where the order-of-magnitude relation

$$\omega\frac{\tau_{th}}{\tau_{dyn}}\sim 1 \tag{26.6}$$

is satisfied [see equation (22.1) and Cox (1974, §10)], where τ_{th} and τ_{dyn} are defined in equation (22.2).

26.2 Excitation Mechanisms

In order to reveal the qualitative nature of excitation or damping mechanisms of nonradial oscillations, we analyze, in this subsection, the work integral W by using the quasi-adiabatic and Cowling ($\Phi'=0$) approximations. Except for some possible nonadiabatic mechanisms, all the important excitation and damping mechanisms should be revealed in this way.

In quasi-adiabatic analysis the integral W is estimated by using adiabatic eigenfunctions as well as adiabatic relations. In this approximation equation (26.2) reduces to

$$W_N=\frac{\pi}{\sigma}\int_0^R \varepsilon_N\frac{\varepsilon_{ad}}{\nabla_{ad}}\left(\frac{\delta T}{T}\right)^2 4\pi r^2\rho dr$$

$$=\frac{\pi}{\sigma}\int_0^R \varepsilon_N\left(\varepsilon_T+\frac{\varepsilon_\rho}{\Gamma_3-1}\right)\left(\frac{\delta T}{T}\right)^2 4\pi r^2\rho dr. \tag{26.7}$$

This equation shows that the temperature and density dependence (both are positive) of nuclear energy generation rate always have a destabilizing effect. This excitation is called the *ε-mechanism*.

We are going to modify the expression for W_F given by equations (26.3) and (26.5) to a form in which all the terms are proportional to $(\delta T/T)^2$ or $[d(\delta T/T)/dr]^2$. In order to do so we have to express p', ξ_r in terms of $\delta T/T$ and $d(\delta T/T)/dr$. For the sake of simplicity, we assume that the adiabatic temperature gradient ∇_{ad} is constant. From the relation between the Eulerian and the Lagrangian perturbations we have

$$\frac{p'}{p}=\frac{\delta p}{p}-\frac{\xi_r}{r}\frac{d\ln p}{d\ln r}\simeq\frac{1}{\nabla_{ad}}\frac{\delta T}{T}+\frac{\xi_r}{r}V. \tag{26.8}$$

Using equations (15.1) and (15.2) with equation (26.8), we obtain

$$\frac{\xi_r}{r}\simeq(\nabla_{ad}\alpha_0)^{-1}\left[\left(\frac{L_l^2}{\Gamma_1\sigma^2}-1\right)\frac{\delta T}{T}+H_p\frac{d}{dr}\left(\frac{\delta T}{T}\right)\right], \tag{26.9}$$

where

$$\alpha_0\equiv 4-U-\frac{l(l+1)}{c_1\omega^2}+c_1\omega^2, \tag{26.10}$$

and the Lamb frequency L_l^2 is defined in equation (13.67). Substituting equations (26.8) and (26.9) into equation (26.5), we obtain

$$\frac{\delta L_R}{L_R}\simeq\alpha_1\frac{\delta T}{T}+\left(\frac{\nabla-\nabla_{ad}}{\nabla}-\frac{c_1\omega^2-U}{\alpha_0}\right)\frac{H_p}{\nabla_{ad}}\frac{d}{dr}\left(\frac{\delta T}{T}\right), \tag{26.11}$$

where

$$\alpha_1\equiv 4-\frac{1}{\nabla_{ad}}-\kappa_T-\frac{\kappa_\rho}{\Gamma_3-1}+\left(1-\frac{L_l^2}{\Gamma_1\sigma^2}\right)\left(\frac{c_1\omega^2-U}{\alpha_0\nabla_{ad}}\right). \tag{26.12}$$

Substituting these equations and disregarding Φ', we obtain, after lengthy manipulations, an approximate expression for W_F:

$$\begin{aligned}\frac{\sigma}{\pi}W_F\simeq&-\frac{1}{2}\left[\alpha_1 L_R\left(\frac{\delta T}{T}\right)^2\right]_{r=R}-\frac{1}{2}\int_0^R dr\left(\frac{\delta T}{T}\right)^2\frac{d}{dr}(\alpha_1 L_R)\\&+\int_0^R dr L_R\frac{H_p}{\nabla_{ad}}\left(\frac{\nabla-\nabla_{ad}}{\nabla}-\frac{c_1\omega^2-U}{\alpha_0}\right)\left\{\left[\frac{d}{dr}\left(\frac{\delta T}{T}\right)\right]^2+\frac{l(l+1)}{r^2}\left(\frac{\delta T}{T}\right)^2\right\}\\&+l(l+1)\int_0^R dr\left(\frac{\delta T}{T}\right)^2\frac{1}{\nabla_{ad}}\left[\frac{4-V}{\alpha_0 V}\left(\frac{1}{c_1\omega^2}\frac{dL_r}{dr}-\frac{L_R}{r}\right)\right.\\&\left.+\frac{c_1\omega^2-U}{c_1\omega^2\alpha_0 V}\frac{dL_r}{dr}+\frac{1}{2}\frac{d}{dr}\left(\frac{c_1\omega^2 L_R-dL_r/d\ln r}{c_1\omega^2\alpha_0 V}\right)\right],\end{aligned} \tag{26.13}$$

where L_r and L_R are, respectively, the total and the radiative luminosities at r.

The first and the second terms in the right-hand side of equation (26.13) describe the *κ-mechanism*. In the outer envelope in the radiative equilibrium, L_R is constant and the κ-mechanism works for driving an oscillation if

$$\frac{d}{dr}\left(\kappa_T+\frac{\kappa_\rho}{\Gamma_3-1}\right)>0. \tag{26.14}$$

If a region in the stellar envelope satisfies this condition, radiative flux from the stellar interior is blocked by the effect of the temperature and density dependence of opacity. The blocked energy is converted to the energy of the oscillation. The value of κ_T increases in the inner part of an ionization zone and decreases in the outer part. Therefore, the excitation and damping zones due to the κ-mechanism are located in, respectively, the inner and outer parts of the ionization zone. In an ionization zone an adiabatic exponent (Γ_3-1) (>0) is minimum. This spatial variation of (Γ_3-1) enhances the effect of the κ-mechanism. This effect is sometimes called the *γ-mechanism* (see Cox, Cox, Olsen, King, and Eilers, 1966).

We note that the condition for the κ-mechanism given in inequality (26.14) is different from the condition derived in a one-zone model (Baker, 1966). In the one-zone model, the value of $[\kappa_T+(\Gamma_3-1)^{-1}\kappa_\rho]$ is important rather than its spatial derivative. This is because the second term in the right-hand side of equation (26.13) does not appear in the one-zone model, and the opacity derivatives, κ_T and κ_ρ, appear in a term similar to the first term.

The sign of α_1 affects the driving or damping when L_R is not constant. However, we have to be cautious if a strong driving or damping is found in a zone in which L_R changes due to a variation in the convective energy flux. Because we are neglecting the effect of the perturbation of the convective flux, such an excitation or damping could be fictitious.

The second line of equation (26.13) arises from the radiative diffusions of the thermal energy of oscillating gaseous elements. For high order g-modes $(c_1\omega^2-U)/\alpha_0$ is very small. This indicates that a superadiabatic region $(\nabla>\nabla_{ad})$ excites high order g-modes. This excitation mechanism is called the *δ-mechanism* in this monograph. This excitation effect was first demonstrated by Cowling (1957), who showed the overstability of g-modes for the superadiabatic stratification of plasma stabilized by the existence of horizontal magnetic fields. The same mechanism has been proposed for the excitation mechanism of rapid oscillations of Ap stars by Shibahashi (1983). If the superadiabatic

region is stabilized by a spatial gradient of the mean molecular weight, the δ-mechanism corresponds to Kato's (1966) mechanism. The δ-mechanism does not exist for p-modes or radial pulsations, because in such cases $[(\nabla-\nabla_{ad})\nabla^{-1}-(c_1\omega^2-U)\alpha_0^{-1}]$ reduces to $\sim -\nabla_{ad}/\nabla$. This term causes radiative damping for p-modes and radial pulsations irrespective of the sign of $(\nabla-\nabla_{ad})$.

These excitation mechanisms will be discussed in detail in the following sections.

27. The ε-Mechanism

The physical mechanisms and the positions in stars of the excitation of the radial pulsation have been investigated in detail (see Cox, 1967, 1974; King and Cox, 1968). The situation is similar for nonradial oscillations in some respects, but there are also significant differences. The ε-mechanism to be discussed in this section is much the same for both radial and nonradial oscillations, except that the condition of the trapping of oscillation in the interior is favorable for some g-modes.

The ε-mechanism is usually unimportant for radial pulsation because of the much smaller amplitude of oscillation in the interior than in the envelope. Exceptions are the case of $\Gamma_1\sim 4/3$ and stars of less central condensation. Very massive and supermassive stars (Ledoux, 1941; Osaki, 1966) are in the first category, and the upper mass limit of main sequence stars is extensively studied in this connection (see e.g., Ledoux, 1978; Ledoux, Noels, and Boury, 1982). Also, radial fundamental modes of Wolf-Rayet star models are excited by the ε-mechanism of the central helium burning (Maeder, 1985; Cox and Cahn, 1988). Less massive dwarfs of polytropic index 1.5 belong to the second category (Gabriel, 1964). In those two situations, stabilities are tested also for nonradial oscillations (Noels, Boury, Scuflaire, and Gabriel, 1974; Aizenman, Hansen, and Ross, 1975). However, the excitation of nonradial modes in the Wolf-Rayet stars is still controversial (see, e.g., Scuflaire and Noels, 1986; Cox and Cahn, 1988).

The importance of the ε-mechanism is emphasized for nonradial g-modes, since the overstability is not restricted to special kinds of models. In the latter part of this section we will discuss g-modes excited by the ε-mechanism for various stellar models. We will first discuss the temperature dependence of ε_N for the p-p chain reactions as an example.

27.1 p-p Chain Reactions

The work W_N defined in equation (26.2) is always positive and

contributes to excitation of oscillations. The physical reason is that the entropy time-derivative is in phase with the temperature increase because of the temperature sensitivity of the nuclear energy generation. It should be noted that the values of ε_T and ε_ρ depend on the time scale under consideration and are different from those calculated from the equilibrium ε_N. Let us take an example of the p-p chain reactions represented as follows (*cf.* Reeves, 1965):

$$^1\mathrm{H}(^1\mathrm{H},e^+\nu)^2\mathrm{H}(^1\mathrm{H},\gamma)^3\mathrm{He}(^3\mathrm{He},2^1\mathrm{H})^4\mathrm{He} \quad \text{(PPI)}$$

$$^3\mathrm{He}(^4\mathrm{He},\gamma)^7\mathrm{Be}(e^-,\nu)^7\mathrm{Li}(^1\mathrm{H},\gamma)^8\mathrm{Be}\rightarrow 2^4\mathrm{He} \quad \text{(PPII)} \qquad (27.1)$$

$$^7\mathrm{Be}(^1\mathrm{H},\gamma)^8\mathrm{B}(,e^+\nu)^8\mathrm{Be}\rightarrow 2^4\mathrm{He}, \quad \text{(PPIII)}$$

where, e.g., $^2\mathrm{H}(^1\mathrm{H},\gamma)^3\mathrm{He}$ means the ^{3}He formation from ^{2}H by the ^{1}H capture followed by γ-ray emission. Let N_j, C_{jk}, and Q_{jk} be the number density of nuclei with the atomic weight j (j = e means electron), the reaction rate of the j- and k-nuclei, and the energy generated (minus neutrino loss) by a single reaction, respectively. The asterisk will stand for ^{7}Li in order to distinguish it from ^{7}Be. The ^{8}B- and ^{8}Be-decays are assumed to occur instantaneously. Then, we have

$$\rho\varepsilon_N=\frac{1}{2}N_1^2C_{11}Q_{11}+N_2N_1C_{21}Q_{21}+N_3\left(\frac{1}{2}N_3C_{33}Q_{33}+N_4C_{34}Q_{34}\right)$$
$$+N_7(N_eC_{7e}Q_{7e}+N_1C_{71}Q_{71})+N_7^*N_1C_{71}^*Q_{71}^*, \qquad (27.2)$$

$$\frac{\partial N_1}{\partial t}+\nabla\cdot(N_1\boldsymbol{v})=-N_1^2C_{11}-N_1N_2C_{21}+N_3^2C_{33}$$
$$-N_1N_3^*C_{71}^*-N_1N_7C_{71}, \qquad (27.3)$$

$$\frac{\partial N_2}{\partial t}+\nabla\cdot(N_2\boldsymbol{v})=\frac{1}{2}N_1^2C_{11}-N_1N_2C_{21}, \qquad (27.4)$$

$$\frac{\partial N_3}{\partial t}+\nabla\cdot(N_3\boldsymbol{v})=N_1N_2C_{21}-N_3(N_3C_{33}+N_4C_{34}), \qquad (27.5)$$

$$\frac{\partial N_4}{\partial t}+\nabla\cdot(N_4\boldsymbol{v})=\frac{1}{2}N_3^2C_{33}-N_3N_4C_{34}+2N_1N_3^*C_{71}^*$$
$$+2N_1N_7C_{71}, \qquad (27.6)$$

$$\frac{\partial N_7}{\partial t}+\nabla\cdot(N_7\boldsymbol{v})=N_3N_4C_{34}-N_7(N_eC_{7e}+N_1C_{71}), \quad (27.7)$$

$$\frac{\partial N_7^*}{\partial t}+\nabla\cdot(N_7^*\boldsymbol{v})=N_7N_eC_{7e}-N_7^*N_1C_{71}^*, \quad (27.8)$$

where C_{jk}'s are the function of temperature and $Q_{11}=1.179$, $Q_{21}=5.493$, $Q_{33}=12.859$, $Q_{34}=1.587$, $Q_{7e}=0.06$, $Q_{71}=10.9$, and $Q_{71}^*=17.347$ (in MeV) (Reeves, 1965). A factor 1/2 appears for reactions of identical particles since $N_j^2C_{jj}$ counts a single reaction twice; a factor 2 appears in the rate equations (27.3)–(27.8) if two identical particles are integrated or created by a single reaction, and in some terms these two factors cancel each other out.

The terms on the left sides of equations (27.3)–(27.8) can be comparable to the terms on the right sides, if the oscillation period and the time scales of reactions are of the same order of magnitude. In that case, δN_j (and therefore $\delta\varepsilon_N$) is not in phase with $\delta\rho$ or δT, and the analysis becomes rather complicated. Fortunately, that is not the case ordinarily, at least for the main reactions. Now, we consider the situation where the lifetime of ^{2}H is much shorter and those of other elements are much longer than the oscillation period. Then, we have

$$N_2=\frac{1}{2}N_1(C_{11}/C_{21}) \quad (27.9)$$

from equation (27.4) and

$$\frac{\delta N_1}{N_1}=\frac{\delta N_3}{N_3}=\frac{\delta N_4}{N_4}=\frac{\delta N_7}{N_7}=\frac{\delta N_7^*}{N_7^*}=\frac{\delta\rho}{\rho} \quad (27.10)$$

from the other equations. Equilibrium relations are derived if the right sides of equations (27.4), (27.5), (27.7), and (27.8) are set to be zero. In addition to equation (27.9), we obtain

$$N_{3E}^2=\frac{b_{\rm I}}{2}N_1^2\left(\frac{C_{11}}{C_{33}}\right)_E,\quad N_{3E}=\frac{1-b_{\rm I}}{2}\frac{N_1^2}{N_4}\left(\frac{C_{11}}{C_{34}}\right)_E, \quad (27.11)$$

$$N_{7E}=\frac{b_{\rm II}}{2}\frac{N_1^2}{N_e}\left(\frac{C_{11}}{C_{7e}}\right)_E=\frac{b_{\rm III}}{2}N_1\left(\frac{C_{11}}{C_{71}}\right)_E,\quad N_{7E}^*=\frac{b_{\rm II}}{2}N_1\left(\frac{C_{11}}{C_{71}^*}\right)_E, \quad (27.12)$$

and

$$-\dot N_{1E}=4\dot N_{4E}=(2-b_{\rm I})N_1^2C_{11E}, \quad (27.13)$$

where the branching factors $b_{\rm I}$, $b_{\rm II}$, and $b_{\rm III}$ satisfy

$$b_{\rm I}+b_{\rm II}+b_{\rm III}=1, \quad (27.14)$$

$$(1-b_{\rm I})^2/b_{\rm I}=2(N_4/N_1)^2\,(C_{34}^2/C_{11}C_{33})_E, \quad (27.15)$$

$$b_{\rm III}/b_{\rm II}=(N_1/N_e)\,(C_{71}/C_{7e})_E, \quad (27.16)$$

and the subscript E denotes the equilibrium.

Taking the Lagrange variation of equation (27.2) and using equations (27.9)–(27.12), we obtain

$$\frac{\delta\varepsilon_N}{\varepsilon_N}=\varepsilon_\rho\frac{\delta\rho}{\rho}+\varepsilon_T\frac{\delta T}{T}=\frac{\delta\rho}{\rho}+\sum_{ij}\nu_{ij}f_{ij}\frac{\delta T}{T}, \quad (27.17)$$

where

$$\nu_{ij}\equiv\frac{d\ln C_{ij}}{d\ln T},\quad f_{ij}\equiv\frac{b_{ij}Q_{ij}}{\Sigma_{ij}b_{ij}Q_{ij}}. \quad (27.18)$$

Here b_{ij} denotes the branching factor (1, $b_{\rm I}$, $b_{\rm II}$, or $b_{\rm III}$) of the ij-reaction, and the summation excludes the very rapid reactions (^{1}H capture by ^{2}H, β-decay, etc.), but the associated energies (e.g., Q_{21}) should be added to the energies of the preceding reactions. The result (27.17) is true also for the inclusion of the CNO cycle, if the branching factors are redefined properly. We note that the CNO cycle involves relatively slow β-decay, whose lifetime (order of minutes) could be comparable to the oscillation period. In such a case, a more complex treatment is necessary [see Cox (1955) and Kawaler (1988a)].

For the solar interior g-modes, contribution to ε_T arises mostly from the ^{3}He+^{3}He-reaction. Since we obtain

$$\nu_{11}=11.270(T/10^6)^{-1/3}-2/3,\quad f_{11}=0.509, \quad (27.19)$$

and

$$\nu_{33}=40.925(T/10^6)^{-1/3}-2/3,\quad f_{33}=0.491, \quad (27.20)$$

ε_T becomes 11.32 at $T=10^7K$ in contrast to the equilibrium $\varepsilon_T(=\nu_{11}=4.56)$. This increase in ε_T is crucial for the overstability of less massive dwarfs (Noels et al., 1974).

27.2 Excitation of g-Modes of Lower Main-Sequence Stars

The internal structure of lower main-sequence stars with masses $M<1.2M_\odot$ is characterized by the radiative core and the convective envelope. We discuss in this subsection the stability of nonradial g-mode oscillations of the sun as a typical example. The possibility of excitation

of low-order g-modes in the sun due to the ε-mechanism of the high temperature dependence of ^{3}He + ^{3}He reaction was first discussed by Dilke and Gough (1972). They suggested that if the amplitude of g-modes grows sufficiently, it could lead to intermittent mixing of the core and a temporary depression of the solar neutrino flux. Unno (1975a) discussed the most favorable modes for the overstability by taking into account the property of wave trapping for nonradial oscillations. Three groups (Christensen-Dalsgaard, Dilke, and Gough, 1974; Shibahashi, Osaki, and Unno, 1975; Boury, Gabriel, Noels, Scuflaire, and Ledoux, 1975) have examined this suggestion independently by a global stability analysis of relevant modes for the realistic solar evolutionary sequence, and they have confirmed that some low-order g-modes may become unstable due to the ε-mechanism.

A large value of the temperature derivative of energy generation rate ε_T is essential in order for the ε-mechanism to work. The variations of ε_T and ε_N as well as hydrogen and ^{3}He mass fractions in a solar model are shown in Fig. 27.1. Due to the existence of the ^{3}He+ ^{3}He reaction in the p-p chain reactions, the effective value of ε_T is raised to ~ 11 from $4-5$ for the p-p reaction itself. (The rapid increase of ε_T very near the center is due to the increase of the contribution from the CN cycle.)

Figure 27.2 shows work integrals for g_1- and g_2-modes of $l = 1$ for a $1M_\odot$ model slightly younger than the present sun as well as the eigenfunctions of the radial displacement and temperature perturbation. Rapid increase in W_N in the core indicates the existence of the ε-mechanism. The gradual decrease of W is due to radiative damping. In the convective zone the work integrals are shown by dashed lines. A fictitious excitation exists at the bottom of the envelope convection zone, because the effect of perturbation of convective flux is not

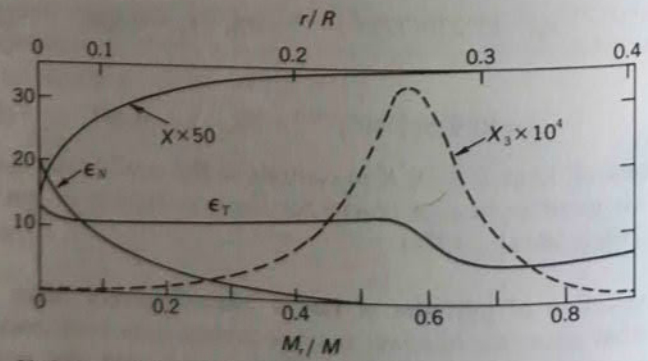

Fig. 27.1 Variations of the nuclear energy generation rate, ε_N (in units of erg s^{-1} g^{-1}), and its temperature derivative, ε_T, and the mass fractions of hydrogen, X, and ^{3}He as functions of $M_r(\leq 0.9M_\odot)$.

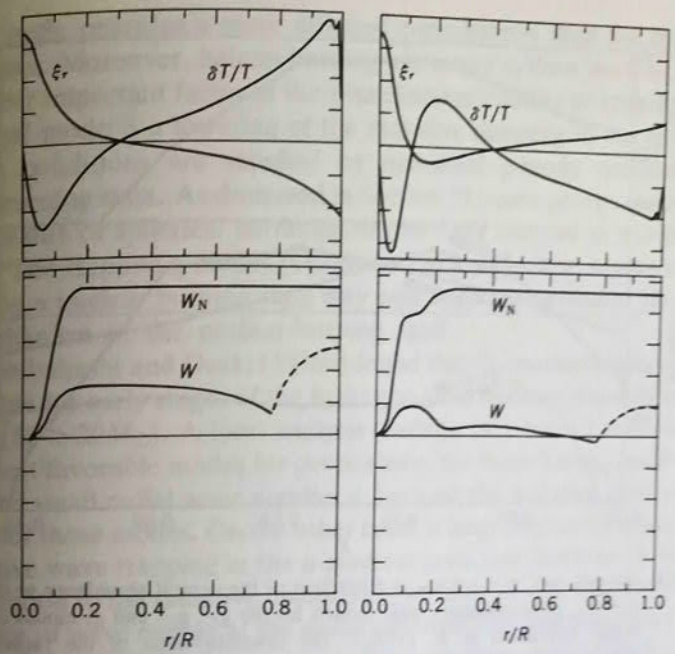

Fig. 27.2 Displacement in the radial direction, ξ_r, the Lagrangian temperature perturbation, $\delta T/T$, and the work integral, W, for the g_1-mode (left) and the g_2-mode (right) of $l = 1$ in a $1M_\odot$ model [after Shibahashi et al. (1975)]. The effect of excitation due to the ε-mechanism, W_N, is also shown. Variations in W in the outer convection zone are shown by dashed lines. Normalizations are arbitrary.

included. This false excitation prevents us from obtaining a definitive answer on the stability of low-order g-modes of the sun and lower main-sequence stars. If the stability is determined by the work integral terminated at the top of the radiative zone (i.e., $r/R \simeq 0.78$), the g_1-mode in Fig. 27.2 is unstable with a growth time of $\sim 10^7$yr, while the g_2-mode is stable. The results of stability determined by using such "truncated" work integrals are shown in Fig. 27.3 for various evolutionary stages, where the growth rate, $\eta = -\sigma_I/\sigma_R$, is plotted against the hydrogen mass fraction at the center (X_c). As seen in this figure, the g_1- and g_2-modes of $l = 1$ are unstable in some early phases of evolution. However, before the star evolves to the present sun ($X_c < 0.45$), these g-modes become stable because relative amplitude in the core decreases due to the increase of the central condensation.

Since the lower main-sequence stars have essentially the same structure as the solar models, one may naturally expect that low-order g-modes of these stars are unstable. This was confirmed for $0.5M_\odot$, and $1.1M_\odot$ models by Noels et al. (1974) and Noels, Boury, Gabriel, and

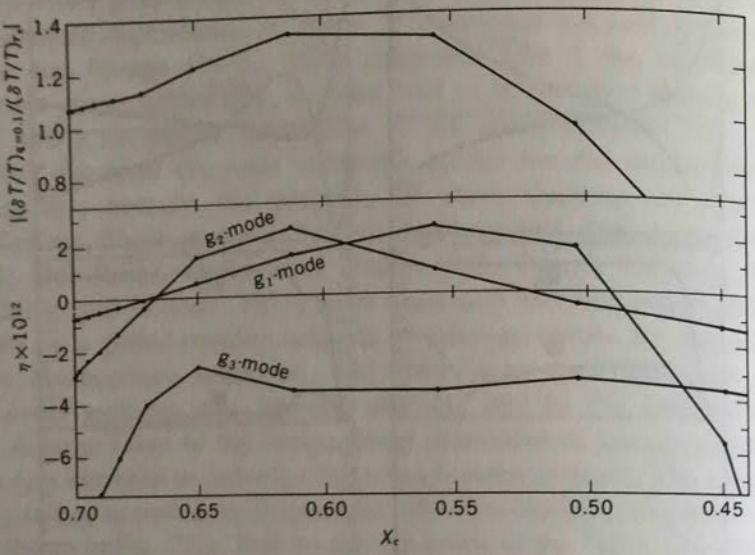

Fig. 27.3 Growth rate, $\eta = -\sigma_I/\sigma_R$ as a function of the central abundance at the center, X_C, of evolutionary solar models for the g_1-, g_2-, and g_3-modes of $l = 1$ [after Shibahashi et al. (1975)]. The absolute value of the ratio of the temperature perturbation at $M_r = 0.1M_\odot$ to that at the base of the convective envelope for the g_1-mode of $l = 1$ is also shown in the upper panel.

Scuflaire (1976).

As noted above, the effect of the outer convective zone introduces uncertainty into the stability of low-order g-modes. Using the time-dependent convection theory derived by Unno (1967) and extended by Gabriel, Scuflaire, Noels, and Boury (1975), Saio (1980) examined the stability of low-order g-modes of the sun by a fully nonadiabatic analysis. He found that a low-order g-mode of $l = 1$ with a period of about 80 min is unstable even in the present sun due to the ε-mechanism in the core and the κ-mechanism (see section 28) in the hydrogen ionization zone. The existence of unstable low-order g-modes in the present sun is interesting because detections of some solar long period oscillations, including the 160 min oscillation, have been claimed (see Section 11.2). However, it must be cautioned that since the balance between excitation and damping is rather delicate, the stability result may be modified significantly when a better time-dependent convection theory is developed.

27.3 Excitation of g-Modes in Shell-Burning Stars

The ε-mechanism is stronger for nuclear reactions with larger temperature sensitivity (i.e., larger ε_T). Therefore, for hydrogen burning, the

CNO cycle provides a more efficient ε-mechanism than the p-p chain reactions. Moreover, helium burning has larger ε_T than the CNO cycle. Another important factor in the ε-mechanism's ability to actually excite a global mode is a lowering of the radiative damping in the envelope. These conditions are satisfied by nonradial g-mode oscillations in shell-burning stars. As discussed in Section 17, some gravity modes with large value of spherical harmonic degree l are trapped in a μ-gradient zone. The trapped g-modes ($\bar{G}_n$-modes) in a μ-gradient zone accompanied by a nuclear burning shell may well become overstable due to the ε-mechanism of the nuclear-burning shell.

Shibahashi and Osaki (1976b) found that $\bar{G}_0$-modes with $l \sim 10$ are unstable for early stages of the hydrogen-shell burning phase of massive stars ($M \geq 20M_\odot$). A local analysis (Section 29.1 below) indicates that the most favorable modes for overstability are those having small values of l and small radial wave number n, because the radiative dissipation is least for those modes. On the other hand, a large degree l is required for effective wave trapping in the μ-gradient zone (see Sections 16 and 17). In addition to the radiative dissipation, we have to take into account the leakage of wave energy at the stellar photosphere. Since the peak value of the Brunt-Väisälä frequency in the μ-gradient zone is much higher than that at the surface for stars in the shell-hydrogen-burning stage, low order $\bar{G}$-modes behave like p-modes in the outer envelope and have frequencies larger than the critical frequency necessary for the acoustic wave to be reflected at the surface. These modes have progressive-wave character in the atmosphere. Because of the existence of a wide evanescent zone between the μ-gradient G-zone and the envelope P-zone, most of the wave energy is reflected, but a small fraction of the wave energy leaks through the photosphere. Such oscillations can be treated by using the progressive-wave outer boundary condition as discussed in Sections 16 and 18, or by using the reflective boundary condition and estimating separately the amount of energy leakage from the eigenfunctions. The latter method was adopted by Shibahashi and Osaki (1976b) in their quasi-adiabatic analysis. The effect of the energy leakage on the work integral may be estimated as

$$W_{leak} = -\frac{2\pi^2}{\Pi}\int \frac{1}{2}\rho|\boldsymbol{\xi}|^2 c dS, \tag{27.21}$$

where Π and c denote the period of oscillation and the sound velocity, respectively, and the integration is taken over the stellar surface. The total work integral to determine stability is obtained by $W + W_{leak}$.

A summary of the stability analysis for $\bar{G}_0$-modes by Shibahashi and Osaki (1976b) is given in Table 27.1. In this table a negative value

Table 27.1 Pulsational properties of $\bar{G}_0$-modes in early hydrogen-shell-burning phase

$M/M_\odot$	$\log\frac{L}{L_\odot}$	$\log T_{eff}$	l	ω^2	Π(hr)	τ_{damp}(yr)	W/W_N	W_{leak}/W_N
5	2.96	4.180	5	477.5	0.527	1.6	0.16	-1.3×10^{2}
			6	525.4	0.486	2.0×10^{-1}	−0.09	-9.3×10^{1}
11	4.18	4.372	7	499.2	0.761	8.2	0.09	-5.0×10^{2}
			8	531.8	0.737	1.2×10^{1}	−0.13	-3.3×10^{2}
20	4.94	4.486	9	569.0	0.898	1.9×10^{3}	0.21	-9.3×10^{-1}
			10	593.9	0.879	-6.1×10^{4}	0.06	-3.5×10^{-2}
			11	616.0	0.863	1.6×10^{4}	−0.10	-1.5×10^{-3}
40	5.60	4.582	10	430.3	1.16	1.6×10^{3}	0.46	−1.7
			11	450.1	1.14	-5.9×10^{3}	0.37	-2.9×10^{-2}
			12	468.1	1.11	-7.8×10^{3}	0.25	-8.7×10^{-4}
			13	484.7	1.09	-1.5×10^{4}	0.13	-3.1×10^{-5}
			14	500.1	1.08	-4.5×10^{5}	0.004	-1.1×10^{-6}
			15	514.3	1.06	1.4×10^{4}	−0.14	-3.9×10^{-8}

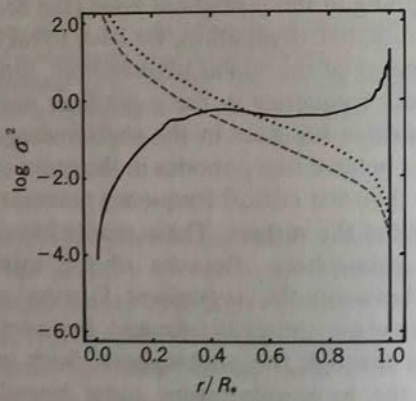

Fig. 27.4 Propagation diagram for a pre-white dwarf model with $0.95M_\odot$ at log $(L/L_\odot) = 3.10$ (from Kawaler, Hansen, Winget, 1985a). The solid line is the square of the Brunt-Väisälä frequency, N^2 in units of s^{-2}. The dashed line is the square of the Lamb frequency, L_l^2, for $l = 1$; the dotted line, for $l = 2$.

for the damping time of oscillation τ_{damp} indicates that the corresponding mode is overstable. Overstable G_0-modes were found only for models with $M \geqq 20M_\odot$. They did not find any overstable higher order gravity modes, $\bar{G}_n$, with $n \geq 1$. The stability of modes with large n is explained by the increase of radiative dissipation in the propagative zone. Note that for some modes W_{leak} is comparable to W and is the main stabilizing agent for the ε-mechanism.

The overstability of G_0-modes occurs only in the earliest stage of shell hydrogen burning. In a later stage the relative amplitude of a

$\bar{G}_0$-mode in the nuclear burning region decreases because the position of the peak of the Brunt-Väisälä frequency shifts from the μ-gradient zone to the core and the peak value increases with the evolution of stars. This change in the Brunt-Väisälä frequency is in turn caused by the following two factors: the structure of the core changes from convective to isothermal, and the central condensation of the models increases very rapidly with evolution.

When the core evolves sufficiently and the electron gas partially degenerates, the Brunt-Väisälä frequency decreases there and the above disadvantage for the ε-mechanism disappears. Overstable g-modes driven by the ε-mechanism have been found for models of planetary nebulae nuclei (Kawaler, Winget, Hansen, and Iben, 1986; Kawaler, 1988a), of hot white dwarfs (DeGregoria, 1977), and of

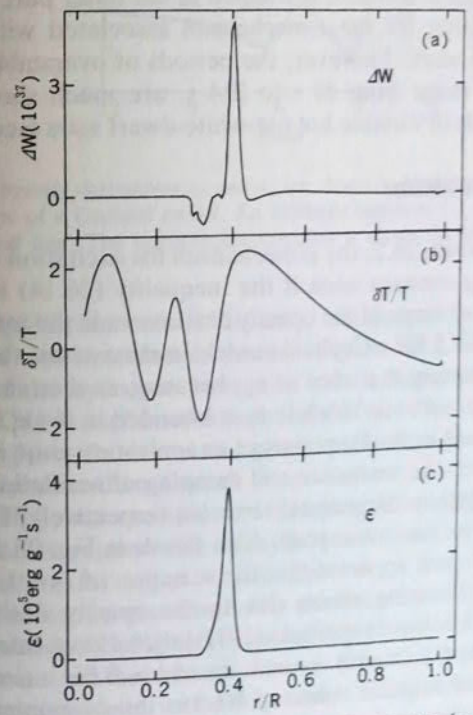

Fig. 27.5 (a)Work done as a function of fractional radius for the $l = 1$, g_5-mode in a $0.60M_\odot$ hydrogen-deficient pre-white dwarf model at log $L/L_\odot = 3.208$.
(b)The relative Lagrangian temperature perturbation for the mode described in (a).
(c)The energy generation rate ε_N as a function of fractional radius. The sharp peak is the helium-burning shell. The unis in (a) and (b) are arbitrary. (From Kawaler et al., 1986.)

accreting white dwarfs (Sienkiewicz, 1980). Figure 27.4 shows an example of the propagation diagram for a hot pre-white dwarf star (Kawaler et al., 1985a). In this case the G-wave zone in the core is bounded by the Lamb frequency L_l^2 rather than by N^2 in contrast to the case of the early shell-hydrogen-burning phase (see above). Therefore, lower l value is appropriate not only to suppress the radiative damping in the G-wave zone but also to trap a g-mode in the core. Actually, for these models g-modes with low values of l are overstable.

A sample unstable mode of $l = 1$ for a hot pre-white-dwarf model (Kawaler et al., 1986) is shown in Figure 27.5, in which the derivative of the work integral ΔW ($=dW/dM_r$), the eigenfunction for temperature perturbation, and the nuclear energy generation rate are shown as functions of the fractional radius. This mode, whose dimensionless angular frequency ω is $\simeq 0.9$, is trapped in the outer part of the core, a favorable condition for the ε-mechanism associated with the helium shell burning to work. However, the periods of overstable modes thus excited, which range from 50 s to 214 s, are much shorter than the observed periods of variable hot pre-white-dwarf stars (see Section 10).

28. *The κ-Mechanism*

As shown in Section 26.2, the κ-mechanism for excitation of oscillations works in an L_R constant zone if the inequality (26.14) is satisfied. A sample of the variations of the opacity derivatives in the interior of a star is given in Fig. 28.1 for a Cepheid model. In most cases, the variation of κ_T is more important than that of κ_ρ, because, as seen in Fig. 28.1, κ_T changes from ~ -4 to ~ 12 while κ_ρ is bounded in $0 < \kappa_\rho \lesssim 1$. Since κ_T increases outward in the inner part of an ionization zone and decreases in the outer part, the excitation and damping of oscillations due to the effect of the opacity derivatives occur in, respectively, the inner and outer parts of the ionization zone. Also shown in Fig. 28.1 is $\Gamma_3 - 1$ by the dashed line. It is apparent that the variation of $\Gamma_3 - 1$ enhances the excitation and damping effects due to the opacity derivatives.

Figure 28.2 [taken from Osaki (1977)] shows work integral $W(r)$ for $\bar{\text{f}}$- ($\omega = 3.02$) and $\bar{\text{p}}_1$-modes ($\omega = 4.46$) of $l = 7$ for a similar Cepheid model. Constant negative values of $W(r)$ in the deep interior show the energy leakage due to the progressive gravity waves from the envelope to the core (see Sections 15.3.3 and 21.3). Two distinctive excitation zones (where $dW/dr > 0$) are recognized in these figures. One excitation zone is associated with the hydrogen and first helium ionization zone around $\log p \simeq 3.7$ and the other with the second helium ionization zone around $\log p \simeq 4.8$. The relative importance of the two excitation zones

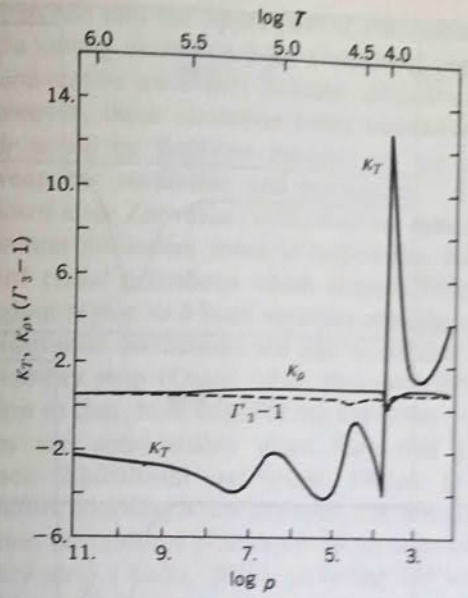

Fig. 28.1 The opacity derivatives κ_T and κ_ρ are shown as functions of $\log p$ in the envelope of a Cepheid model. An adiabatic exponent $\Gamma_3 - 1$ is shown by the dashed line. The temperature variation is shown on the upper horizontal axis.

in a given equilibrium model depends mainly on the distribution of amplitude of the oscillation mode. Figure 28.2 shows that the importance of the hydrogen ionization zone is larger for $\bar{\text{p}}_1$-mode than for $\bar{\text{f}}$-mode. This is explained mainly by the fact that the amplitude of oscillation of $\bar{\text{p}}_1$-mode decreases more rapidly from the stellar surface toward the interior than that of $\bar{\text{f}}$-mode.

In Fig. 28.2, no excitation or damping is recognized above the excitation zone associated with the hydrogen ionization zone; i.e., $W(r)$ is nearly constant for $\log p < 3.6$. This occurs because of a strong nonadiabatic effect on the luminosity perturbation. The thermal time scale [see equation (22.2)] decreases rapidly toward the stellar surface with a decrease of the matter density (Fig. 22.1). The linearized equation of energy conservation [equation (22.1)] indicates that in the stellar envelope ($dL_r/dM_r = 0$) the Lagrangian perturbation of the radiative luminosity, δL_R, is constant in the limit of $\tau_{th}/\tau_{dyn} = 0$. In this limit, no excitation or damping of oscillation occurs [see equation (26.3)]; i.e., $W(r)$ is constant. The strongly nonadiabatic exterior is separated from the quasi-adiabatic interior by a transition region whose location in the stellar envelope is determined by the order-of-magnitude

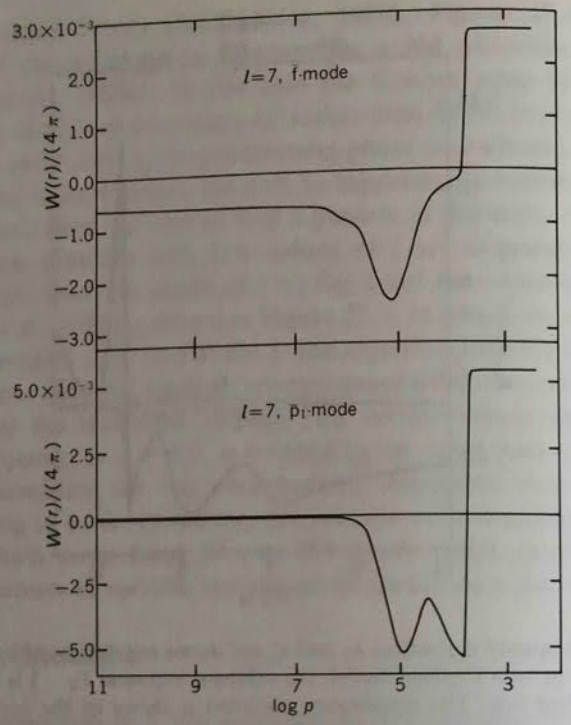

Fig. 28.2 The work integral $W(r)$ normalized by E_W is shown for the nonradial f-mode (upper panel) and the p_1-mode (lower panel) of $l = 7$ in a Cepheid model [from Osaki (1977)].

relation given in equation (26.6). Since the decrease of τ_{th} with r is very rapid, the location of the transition region depends on the oscillation modes only very weakly. For both of the oscillation modes shown in Fig. 28.2, the transition region is located in the hydrogen ionization zone. Because of the existence of the transition zone, the damping zone expected (in the quasi-adiabatic analysis) in the outer part of the hydrogen ionization zone is suppressed (i.e., heat capacity is too small there). Depending on the equilibrium models and the oscillation mode, the transition region could be located in the second helium ionization zone. In such a case the effect of the hydrogen ionization zone on the stability of the oscillation is suppressed.

In many cases, an ionization zone exists in a convective zone because of the high opacity in the ionization zone and low adiabatic temperature gradient. The gradient of the radiative luminosity, dL_R/dr, in the upper part of the ionization zone is positive due to the decrease of the convective energy flux there. Then it is possible that $d(L_R\alpha_1)/dr<0$ because $\alpha_1 < 0$ usually there [see equation (26.13)]. In this case the

excitation zone extends into the upper part of the ionization zone. On the other hand, a strong excitation zone sometimes appears near the bottom of the convective envelope, because $dL_R/dr<0$ and usually $\alpha_1>0$ there. However, these excitation zones associated with a finite value of dL_R/dr could be fictitious because we are neglecting the interaction between the oscillation and convection.

It is well known after Zhevakin (1953) that the κ-mechanism in the hydrogen and helium ionization zones is responsible for the Cepheid instability strip of radial pulsations which extends from the classical Cepheids in the giant region to δ Scuti variables near the main sequence (see Fig. 5.1). Nonradial oscillations are also overstable for models in the Cepheid instability strip (Osaki, 1977; Dziembowski, 1977a; Lee, 1985b). In addition to that, blue edges of the instability region for some nonradial modes are considerably bluer than that for the radial fundamental mode (Shibahashi and Osaki, 1981a). If the effect of convection-oscillation coupling is not included, the κ-mechanism due to hydrogen ionization destabilizes p-modes even for stars redder than the Cepheid instability strip (Ando, 1976), including the sun (Ando and Osaki, 1975). Since these stars have well developed convective envelopes, however, the effect of convection-oscillation coupling is expected to affect the stability results. The true excitation mechanism for the five-minute oscillation of the sun is still controversial (see Section 42).

Moreover, the κ-mechanism in the hydrogen ionization zone is responsible for the excitation of nonradial g-modes of the ZZ Ceti variables (variable DA white dwarfs; DAV stars) (Dziembowski and Koester, 1981; Dolez and Vauclair, 1981; Winget, Van Horn, Tassoul, Hansen, Fontaine, and Carroll, 1982a; Cox, Starrfield, Kidman, and Pesnell, 1987). Also, it has been established that overstable g-modes of variable DB (helium envelope) white dwarfs are excited by the κ-mechanism in the second helium ionization zone (Winget, Van Horn, Tassoul, Hansen, and Fontaine, 1983a).

The κ-mechanism associated with hydrogen and helium ionization zones does not work for massive main-sequence stars such as the β Cephei stars because in such a star, the transition region is located interior to the ionization zones. Stellingwerf (1978) found that the κ-mechanism associated with an opacity bump at a temperature close to 1.5×10^5 K has a considerable effect on the stability of radial pulsations in massive stars. This opacity bump originates from the coincidence of the frequency maxium of the radiation flux with the second ionization edge of helium at 54.4 eV (Stellingwerf, 1979). Figure 28.3 illustrates the variation of κ_{ad} defined in equation (21.19) against the temperature

of an equilibrium model of $12M_\odot$. The existence of the peak of κ_{ad} associated with the opacity bump is apparent. Although a larger peak is associated with the He II ionization zone ($\log T \simeq 4.5$), the density is too low for this zone to affect the stability of radial or nonradial pulsations.

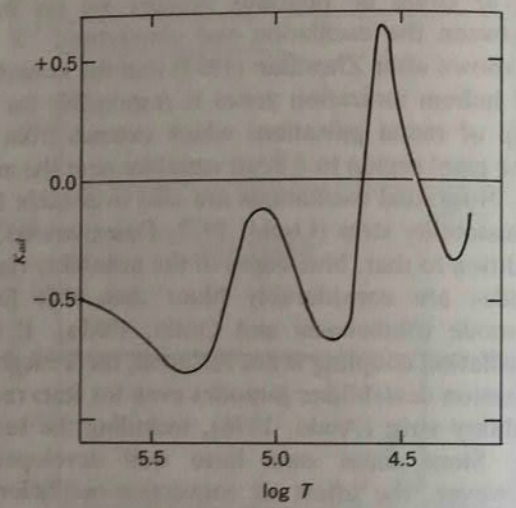

Fig. 28.3 Variation in the opacity derivative κ_{ad} with the depth ($\log T$) of an equilibrium model ($M = 12M_\odot$, $M_{bol} = -5$, and $\log T_{eff} = 4.3$) [after Lee and Osaki (1982)].

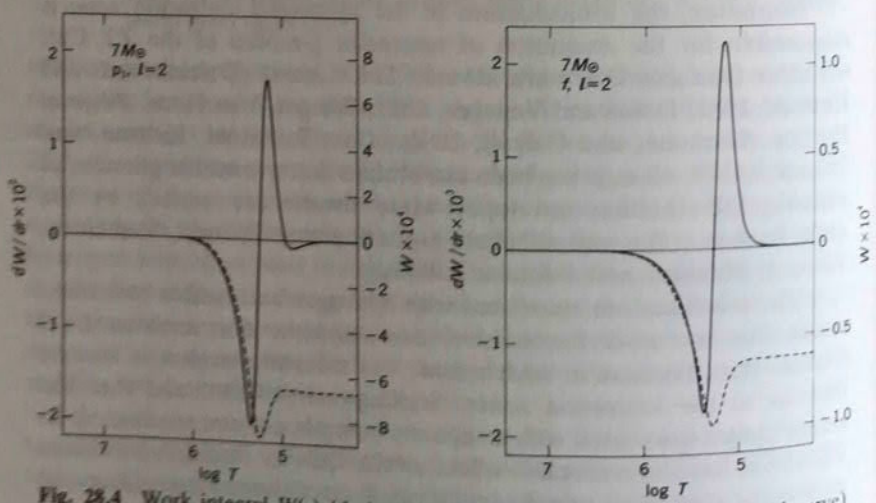

Fig. 28.4 Work integral $W(r)$ (dashed line) and its derivative $dW(r)/dr$ (solid curve) versus $\log T$ for (a) $\tilde{p}_1$ and (b) f mode ($l = 2$) of a main-sequence model ($7M_\odot$, $M_{bol} = -3.93$, and $\log T_{eff} = 4.24$) [from Saio and Cox (1980)]. The normalization of W and dW/dr is arbitrary.

This figure indicates that an excitation zone should exist in the range of $5.1 \lesssim \log T \lesssim 5.3$, where $d\kappa_{ad}/dr$ is positive. An example of the work integral for f-mode in a massive star of $7M_\odot$ is shown in Fig. 28.4. There exists an excitation zone at the place expected from Fig. 28.3. However, the strength of the excitation is not enough to excite radial pulsations (Stellingwerf, 1978) or nonradial oscillations (Saio and Cox, 1980; Lee and Osaki, 1982).

The κ-mechanism associated with the ionization of carbon and oxygen is also possible. Since the ionization of the K-shell electrons occurs in a high temperature region ($T \sim 10^6$K), the κ-mechanism could be effective for the excitation of oscillations in very hot stars. This mechanism is, however, ineffective in most stars, because oscillations in the region with $T \sim 10^6$K are usually almost perfectly adiabatic, and the amounts of carbon and oxygen are very small. A possible exception is the case of very hot pre-white-dwarf stars ($T_{eff} \sim 10^5$K), including planetary nebula nuclei. Some of these stars are nonradial pulsators called DOV stars (see Section 10). The effective temperatures of these stars are high enough for the oscillation in the ionization zone to be weakly nonadiabatic. Since most of the hydrogen-rich matter of these stars has been lost, carbon/oxygen matter produced by helium burning could be located in the temperature region of $T \sim 10^6$K. In such a case the κ-mechanism associated with the ionization of the K-shell electrons of carbon/oxygen can excite global oscillations, as has been confirmed in nonadiabatic analyses by Starrfield, Cox, Hodson, and Pesnell (1983), and Starrfield, Cox, Kidman, and Pesnell (1984, 1985).

The rapidly oscillating Ap stars are at the lower portion of the Cepheid instability strip on the HR diagram (see Section 9). Hence it may be quite natural to suppose that the κ-mechanism is responsible for the excitation of those oscillations as in the case of classical Cepheids. However, the diffusion hypothesis, which has been widely accepted for explaining the chemical peculiarity of Ap stars, suggests that helium settles deeply so that there is no helium ionization zone. If so, the κ-mechanism associated with the helium ionization zones does not work. Matthews (1988) suggested the κ-mechanism associated with silicon as a possible excitation mechanism for the rapid oscillations in Ap stars. Silicon is expected to be abundant in the envelope of an Ap star. The ionization potential of Si IV is 45.1 eV. Since it is close to that of He II, 54.4 eV, if the instability strip due to the κ-mechanism of Si IV exists, it is expected to overlap with, but be slightly cooler than, the Cepheid instability strip. All the rapidly oscillating Ap stars so far discovered are cool Ap/Fp stars located in the red portion of the Cepheid instability strip, and this fact seems to confirm Matthews'

(1988) suggestion. However, whether or not the abundance of silicon is enough for the κ-mechanism is not certain. Further quantitative studies are needed. On the other hand, Dolez, Gough, and Vauclair (1988) suggest that helium accumulates in the magnetic polar regions of an Ap star and that the κ-mechanism associated with helium may be responsible for the excitation of the rapid oscillations in Ap stars.

29. *The δ-Mechanism*

29.1 Local Analysis

The δ-mechanism (or the Cowling mechanism) for excitation of g-modes appears in the work integral given in equation (26.13). A better understanding of this mechanism may be obtained by a local analysis. We will discuss, in this subsection, mainly the δ-mechanism for high order g-modes including the effect of magnetic fields under the perfect MHD condition (but neglecting the effect of rotation). To simplify the analysis we use the Boussinesq approximation, in which density is treated as a constant in the equation of continuity and in the equation of motion except for the buoyancy term (Oberbeck, 1879; Boussinesq, 1903; see also, e.g., Drazin and Reid, 1981). Because of this approximation, the acoustic modes are eliminated and the discussion will be limited to the gravity wave and secular modes.

Let us suppose a plane-parallel, gravitationally stratified layer of fluid in hydrostatic and radiative equilibrium (i.e., $\boldsymbol{F}_C = \boldsymbol{v}_0 = 0$) with a spatially uniform magnetic field. Then, in the Boussinesq approximation, the basic equations of oscillation (13.28), (19.7), (13.30), and (19.8) are reduced to

$$\nabla\cdot\boldsymbol{\xi}=0, \tag{29.1}$$

$$\frac{\partial^2\boldsymbol{\xi}}{\partial t^2}=-\frac{1}{\rho}\nabla\left(p'+\frac{\boldsymbol{B}\cdot\boldsymbol{B}'}{4\pi}\right)-\frac{\rho'}{\rho}\nabla\Phi+\frac{(\boldsymbol{B}\cdot\nabla)\boldsymbol{B}'}{4\pi\rho}, \tag{29.2}$$

$$c_pT\frac{\partial}{\partial t}\left[\frac{T'}{T}-\frac{\xi_z}{H_p}(\nabla-\nabla_{ad})\right]=\varepsilon'_N+\frac{1}{\rho}[\nabla\cdot(K\nabla T)]', \tag{29.3}$$

and

$$\frac{\partial\boldsymbol{B}'}{\partial t}=(\boldsymbol{B}\cdot\nabla)\frac{\partial\boldsymbol{\xi}}{\partial t}, \tag{29.4}$$

where ∇, ∇_{ad}, and K have been defined by equations (13.107), (13.82), and (13.7), respectively, and H_p denotes the pressure scale height.

For the fully ionized ideal gas with radiation fields, the Eulerian perturbation of density ρ' is given as

$$\frac{\rho'}{\rho}=-v_T\frac{T'}{T}+\xi_z H_p^{-1}\left(\frac{\partial\ln\rho}{\partial\ln\mu}\right)_{p,T}\nabla_\mu$$

$$=-\frac{4-3\beta}{\beta}\frac{T'}{T}+\xi_z H_p^{-1}\nabla_\mu, \tag{29.5}$$

where ∇_μ is defined by equation (13.113), β is the ratio of the gas pressure to the total pressure, and the Eulerian perturbation of pressure is neglected. The ∇_μ term in equation (29.5) is necessary for representing the effect of inhomogeneous chemical composition in the core.

We consider the higher overtones of gravity waves whose wavelengths in the vertical direction are much shorter than the density and pressure scale heights. This does not mean that the fluid is incompressible, but it does imply that the density variations are very small. This is the situation appropriate for the Boussinesq approximation, in which the density variations are taken into account only in the term of the buoyancy, and the pressure perturbation p' is neglected in the energy equation (29.3) (Spiegel and Veronis, 1960). The temporal and spatial dependence of the perturbation on an arbitrary quantity f is taken as

$$f'(t,x,y,z)=f'\cdot\exp[i(k_xx+k_yy+k_zz)+st]. \tag{29.6}$$

Equations (29.1) and (29.2) are then reduced to

$$ik_x\xi_x+ik_y\xi_y+ik_z\xi_z=0, \tag{29.7}$$

$$s^2\xi_x=-\frac{ik_x}{\rho}\left[p'+\frac{i\boldsymbol{B}\cdot\boldsymbol{k}}{4\pi}(\boldsymbol{B}\cdot\boldsymbol{\xi})\right]-\frac{(\boldsymbol{B}\cdot\boldsymbol{k})^2}{4\pi\rho}\xi_x, \tag{29.8}$$

$$s^2\xi_y=-\frac{ik_y}{\rho}\left[p'+\frac{i\boldsymbol{B}\cdot\boldsymbol{k}}{4\pi}(\boldsymbol{B}\cdot\boldsymbol{\xi})\right]-\frac{(\boldsymbol{B}\cdot\boldsymbol{k})^2}{4\pi\rho}\xi_y, \tag{29.9}$$

and

$$s^2\xi_z=-\frac{ik_z}{\rho}\left[p'+\frac{i\boldsymbol{B}\cdot\boldsymbol{k}}{4\pi}(\boldsymbol{B}\cdot\boldsymbol{\xi})\right]-\frac{(\boldsymbol{B}\cdot\boldsymbol{k})^2}{4\pi\rho}\xi_z$$

$$+g\left(\frac{4-3\beta}{\beta}\frac{T'}{T}-\nabla_\mu\frac{\xi_z}{H_p}\right). \tag{29.10}$$

If the highest order in wave number k is retained in the radiative loss term, equation (29.3) is led to

$$s\left[\frac{T'}{T}-\frac{\xi_z}{H_p}(\nabla-\nabla_{ad})\right]=\left(\frac{\varepsilon_N}{c_pT}\varepsilon_T-\frac{K}{c_p\rho}k^2\right)\frac{T'}{T}, \quad (29.11)$$

where

$$k^2=k_x^2+k_y^2+k_z^2, \quad (29.12)$$

and only the temperature dependence of ε_N has been taken into account. Equations (29.7) – (29.11) form a set of linear algebraic equations for variables ξ_x, ξ_y, ξ_z, p'/ρ, and T'/T. The determinant of the coefficient matrix must be zero for the existence of a non-trivial solution:

$$\begin{vmatrix} ik_x & ik_y & ik_z & 0 & 0 \\ s^2+\sigma_A^2-b_1B_xk_x & -b_1B_yk_x & -b_1B_zk_x & ik_x & 0 \\ -b_1B_xk_y & s^2+\sigma_A^2-b_1B_yk_y & -b_1B_zk_y & ik_y & 0 \\ -b_1B_xk_z & -b_1B_yk_z & s^2+\sigma_A^2-b_1B_zk_z+\frac{g\nabla_\mu}{H_p} & ik_z & -g\frac{4-3\beta}{\beta} \\ 0 & 0 & -sH_p^{-1}(\nabla-\nabla_{ad}) & 0 & s-g_N+l_R \end{vmatrix}=0, \quad (29.13)$$

where

$$g_N=\varepsilon_N\varepsilon_T/(c_pT), \qquad l_R=Kk^2/(c_p\rho), \quad (29.14)$$

$$\sigma_A^2=\frac{(\boldsymbol{B}\cdot\boldsymbol{k})^2}{4\pi\rho}, \quad \text{and} \quad b_1=\frac{\boldsymbol{B}\cdot\boldsymbol{k}}{4\pi\rho}. \quad (29.15)$$

This equation gives the dispersion relation (*cf.* Ledoux, 1974)

$$(s^2+\sigma_A^2)\left\{s^3-(g_N-l_R)s^2+\left(\frac{k_h^2}{k^2}N^2+\sigma_A^2\right)s - \left(\frac{k_h^2}{k^2}\frac{g}{H_p}\nabla_\mu+\sigma_A^2\right)(g_N-l_R)\right\}=0, \quad (29.16)$$

where k_h is the horizontal wave number defined by

$$k_h^2=k_x^2+k_y^2, \quad (29.17)$$

and N^2 denotes the square of the Brunt-Väisälä frequency which is expressed, in the present approximation, as $N^2=gH_p^{-1}[(4-3\beta)\beta^{-1}\times(\nabla_{ad}-\nabla)+\nabla_\mu]$ [equation (13.112)].

For weak nonadiabaticity, which is usually the case, the roots of equation (29.16) are given by

$$s_{1,2}\simeq\pm i\left(\frac{k_h^2}{k^2}N^2+\sigma_A^2\right)^{\frac{1}{2}}$$

$$+\frac{1}{2}(l_R-g_N)\frac{g}{H_p}\frac{k_h^2}{k^2}\frac{4-3\beta}{\beta}(\nabla-\nabla_{ad})\left(N^2\frac{k_h^2}{k^2}+\sigma_A^2\right)^{-1} \quad (29.18)$$

and

$$s_3\simeq-(l_R-g_N)\left(\frac{g}{H_p}\nabla_\mu\frac{k_h^2}{k^2}+\sigma_A^2\right)\left(N^2\frac{k_h^2}{k^2}+\sigma_A^2\right)^{-1}, \quad (29.19)$$

in addition, $s=\pm i\sigma_A$, which correspond to the Alfven wave. The interpretation of the conditions for the convective instability ($N^2<0$), the thermal instablity ($s_3>0$), and the g-mode overstability [$\mathrm{Re}\,(s_{1,2})>0$] is self-revealing in the above equations.

29.1.1 Kato's Mechanism

Let us discuss first the case without a magnetic field. In this case equation (29.16) is reduced to

$$s^3-(g_N-l_R)s^2+\frac{k_h^2}{k^2}N^2s-\frac{k_h^2}{k^2}\frac{g}{H_p}\nabla_\mu(g_N-l_R)=0. \quad (29.20)$$

Let the coefficients of equation (29.20) be denoted successively by 1, a_1, a_2, and a_3. Then, the necessary and sufficient conditions for stability [$\mathrm{Re}\,(s)<0$] are given by the Hurwitz criterion which states $a_1>0$, $a_1a_2-a_3>0$, and $a_3>0$, or, equivalently, $a_2>0$, $a_1a_2-a_3>0$, and $a_3>0$. The dynamical instability is the violation of $a_2>0$, or

$$\nabla-\nabla_{ad}-\frac{\beta}{4-3\beta}\nabla_\mu>0, \quad (29.21)$$

which is often called the Ledoux (1947) criterion for the convective instability. The condition of thermal instability is $a_1<0$ for the radial mode ($k_h=0$) and $a_3<0$ for the nonradial mode ($k_h\neq0$). The condition is identical for both cases in the present local theory, if $\nabla_\mu>0$:

$$g_N>l_R. \quad (29.22)$$

On the other hand, the condition

$$l_R>g_N \quad \text{and} \quad \nabla_\mu<0 \quad (29.23)$$

is that of thermal instability for nonradial perturbations with an adverse μ-gradient. The condition (29.22) is only approximate for the radial mode, since the pressure perturbation has been neglected. The exception may be the thermal instability of the shell source model (Schwarzschild and Härm, 1965; Weigert, 1966) in which the pressure perturbation is less important (*cf.* Hōshi, 1968; Unno, 1970, 1975b). The nonradial thermal mode does not exist if $\nabla_\mu=0$, since the

hydrostatic condition requires the pressure and the density perturbations to be spherically symmetric and a nonradial temperature perturbation must be associated with a perturbation of the mean molecular weight (Kippenhahn, 1967; Rosenbluth and Bahcall, 1973; Richstone, 1974; Gabriel and Noels, 1976a).

The condition of the vibrational instability, $(a_1 a_2 - a_3 < 0)$, is reduced, for the thermally stable case, to

$$\nabla - \nabla_{ad} > 0. \tag{29.24}$$

The semiconvective zones in massive stars ($M > 10M_\odot$) appear by the condition that

$$\nabla_{ad} + \frac{\beta}{4-3\beta}\nabla_\mu > \nabla > \nabla_{ad} \tag{29.25}$$

(*cf.* Schwarzschild and Härm, 1958). However, this condition is nothing but the g-mode overstability, as pointed out by Kato (1966). A similar situation was first studied by Veronis (1965) in the salinity convection. In this monograph, following the above definition, the semiconvective zone may be understood as a zone of varying molecular weight having a superadiabatic temperature gradient which is dynamically stabilized by a μ-gradient. This definition has been adopted commonly by workers on stellar stability, but it is slightly different from that used by those working on stellar evolution.

The physical reason for the overstable convection in a semiconvective zone (Kato, 1966) is the radiative Cowling mechanism discussed in Section 26. It is a very efficient mechanism of excitation, especially for higher harmonics and high overtone modes (large k, hence large l_R). However, as pointed out by Gabriel (1969) and Auré (1971), the overstable convection is the gravity wave which may propagate to the outer radiative zone and be damped before being reflected back to the evanescent zone. The global stability analysis for the overstable convection will be discussed in Subsection 29.2.

29.1.2 Magnetic Overstability

In the uniform sector of a magnetic field, the angular frequency of oscillation is given by

$$\sigma = \left(N^2 \frac{k_h^2}{k^2} + \sigma_A^2\right)^{1/2}, \tag{29.26}$$

and the wave is called a "magneto-gravity wave." The second term in the right-hand side of equation (29.26) gives the frequency of the Alfvén mode, whose restoring force is the magnetic tension. Equation (29.26)

means that the layer may be dynamically stable even if $N^2 < 0$. However, if the temperature gradient is superadiabatic, the dynamically stable layer is overstable as seen in equation (29.18). Whether the motion in the layer is monotonically growing ($\sigma^2 < 0$) or overstable [$\sigma^2 > 0$ and $\mathrm{Re}(s_{1,2}) > 0$] is dependent on the superadiabaticity and the Alfvén frequency σ_A which itself is dependent on the wavenumber $\boldsymbol{k}$ and the magnetic field $\boldsymbol{B}$. The possibility of magnetic overstability was first discussed by Cowling (1957). Shibahashi (1983) suggested magnetic overstability as the cause of rapid oscillations in Ap stars. He supposed that there is a superadiabatic layer, in which $N^2 < 0$, associated with hydrogen and helium ionization zones and that the magnetic field is a dipole field—that is, the magnetic field is almost vertical at the magnetic polar regions and almost horizontal at the magnetic equator of the star. He then considered the motion having a short wavelength in the vertical direction but a long wavelength in the horizontal direction as in the case of high order p-modes with low degree. Since $\boldsymbol{B}\cdot\boldsymbol{k}$ is large in the magnetic polar regions, the motion may be oscillatory and overstable because of $\nabla - \nabla_{ad} > 0$. The frequency is of the order of the observed frequencies of the rapid oscillations in Ap stars if it is estimated as

$$\sigma^2 \approx \sigma_A^2 \simeq 10^{-4}\left(\frac{\rho}{10^{-7}\,\mathrm{g\,cm^{-3}}}\right)^{-1}\left(\frac{B}{10^3\,\mathrm{G}}\right)^2\left(\frac{k}{10^{-8}\,\mathrm{cm^{-1}}}\right)^2 \mathrm{s}^{-2}. \tag{29.27}$$

On the other hand, the motion is supposed to be convectively unstable ($\sigma^2 < 0$) in the magnetic equator of the star, because $\boldsymbol{B}\cdot\boldsymbol{k}$ is small there. An instructive explanation of the magnetic overstability as a possible mechanism for the rapid oscillations in Ap stars was given by Cox (1984). Shibahashi (1983) suggested that some nonlinear mode coupling may induce a global mode, as observed, from the overstable motion restricted in the magnetic polar regions. However, his suggestion is based on local analysis, and thus extension of a global formulation is highly desirable (*cf.* Biront, Goossens, Cousens, and Mestel, 1982; Campbell and Papaloizou, 1986). Moreover, treatment without the Boussinesq approximation is necessary (*cf.* Hermans, Goossens, Kerner, and Lerbringer, 1988).

29.1.3 The δ-Mechanism in a Rotating Star

So far we have discussed the δ-mechanism in a non-rotating star. The discussion based on local analysis is easily extended to the axially symmetric modes of a rotating star (Goldreich and Schubert, 1967; Fricke, 1968). Some useful conditions for stability have been well known: the sufficient conditions for the dynamical stability are collectively called the Solberg-Hoiland criterion and the instability

associated with the violation of the sufficient condition for the secular stability is known as Goldreich-Schubert-Fricke instability. Readers who are interested in these instabilities should consult several reviews, e.g., Fricke and Kippenhahn (1972).

The overstability can be studied by local analysis in a dynamically stable case. The physical cause of the overstability is the δ-mechanism. The sufficient conditions for stability,

$$\rho^{-1}\nabla p\cdot(\nabla_{ad}\nabla\ln p-\nabla\ln T)>0 \tag{29.28}$$

and

$$\rho^{-1}\nabla p\times(\nabla_{ad}\nabla\ln p-\nabla\ln T)=0, \tag{29.29}$$

were obtained by Shibahashi (1980) and were intensively discussed by Knobloch and Spruit (1983). Rotation does not influence directly the vibrational stability criterion, although it affects the stellar geometrical configuration. In the case of a spherically symmetric star, the condition (29.28) inhibiting the overstability becomes

$$\nabla_{ad}-\nabla>0, \tag{29.30}$$

as shown by Kato (1966) (see subsection 29.1.1), and the condition (29.29) is automatically satisfied. Condition (29.29) requires that the direction of the effective gravity force must be parallel to the direction of subadiabatic temperature gradient for the vibrational stability. The instability induced by the breakdown of condition (29.29) is closely related to the baroclinic instability in the dynamic meteorology. Knobloch and Spruit (1983) named the vibrational instability "ABCD instability," in an abbreviation of "Axisymmetric, BaroClinic, Diffusive instability." In the case of hydrostatic equilibrium and $\nabla\ln\rho\times\nabla\ln\mu=0$, condition (29.29) is satisfied if and only if the centrifugal force is the gradient of a potential—that is, if the rotation law is cylindrical. This condition is the same as one of the two conditions for secular stability in the absence of μ-gradient. Therefore, if the rotation is not cylindrical, both secular instability and vibrational instability may occur. A global formulation is desirable.

29.2 Global Analysis of g-Modes in Semiconvective Zone

During the main sequence evolution, semiconvection appears in a star more massive than $10M_\odot$. Schwarzschild and Härm (1958) noticed that the boundary of the convective core of a massive main-sequence star moved outward with evolution and that physical inconsistency occurred if the whole convective region was chemically homogenized. Between the convective core and the radiative envelope they inserted a

semiconvective zone, in which the distribution of the chemical composition was adjusted by a partial mixing to satisfy the convective neutrality by a criterion

$$\nabla=\nabla_{rad}=\nabla_{ad}, \tag{29.31}$$

where ∇_{rad} represents the temperature gradient expected when all energy is transported by radiation. Equation (29.31) indicates that all energy is assumed to be transported by radiation in the semiconvective zone. However, Sakashita and Hayashi (1959) pointed out that the criterion for the convective neutrality in the existence of the chemical composition gradient should be Ledoux's criterion [i.e., $N^2=0$ in equation (13.112)]

$$\nabla=\nabla_{rad}=\nabla_{ad}+\frac{\beta}{4-3\beta}\nabla_\mu. \tag{29.32}$$

The treatment of the semiconvective zone in very massive stars is important because it affects their later evolution significantly. There has been considerable controversy as to which criterion should be used and how partial or complete mixing is achieved. Equation (29.32) is the criterion of dynamical stability, and thus it is the criterion for ordinary convection. However, as discussed in the preceding subsection, even when the medium is dynamically stable in the sense of equation (29.32), overstable convection occurs in a medium of varying molecular weight if the temperature gradient is superadiabatic; i.e., $\nabla>\nabla_{ad}$. This was first pointed out by the local stability analysis of Kato (1966). Strictly speaking, overstable convection is a problem of vibrational instability of nonradial g-modes, and it can be settled only by global stability analysis of a whole star. Gabriel (1969) and Auré (1971) criticized Kato's (1966) result because it was a local treatment. They argued that the dissipation in the outer radiative zone was strong enough to damp locally overstable convection and that vibrational instability of g-modes might not occur. On the other hand, as discussed in Sections 15–17, one of the most important characteristics of nonradial oscillations is a wave-trapping phenomenon. In particular, the μ-gradient zone left behind by the receding convective core in massive stars behaves like an ideal potential well that traps gravity waves. The effect of wave trapping was not considered in the studies of Gabriel (1969) and Auré (1971), because it was not well known at that time. Shibahashi and Osaki (1976a), Scuflaire, Noels, Gabriel, and Boury (1976), and Gabriel and Noels (1976b) have studied the vibrational stability of gravity modes in massive stars with semiconvective zones, and they have confirmed by a global stability analysis that some gravity modes trapped in the

μ-gradient zones are in fact overstable due to Kato's (1966) mechanism. A summary of Shibahashi and Osaki's (1976a) analysis is given.

Evolutionary models used in the stability analysis were those for stars of $30M_\odot$ and $15M_\odot$ with the initial chemical composition $X = 0.70$ and $Z = 0.03$. Ledoux's (1947) criterion for convective stability (i.e., $N^2 > 0$ for stability) was used and no partial mixing was assumed to occur to construct the semiconvective zone, for the purpose was to examine the possible overstability that may cause mixing. Here, the semiconvective zone is defined as the region where a composition gradient exists and the temperature gradient ∇ is larger than ∇_{ad} but smaller than $\nabla_{ad} + \beta(4-3\beta)^{-1}\nabla_\mu$. Figure 29.1 shows the variation of the extent of the superadiabatic layer in the μ-gradient zone (shown by hatched regions) with evolution. Equilibrium models in the core hydrogen-burning stage consist of the homogeneous convective core, the μ-gradient zone formed by the retreating convective core where the temperature gradient is mostly superadiabatic (i.e., semiconvective zone in the present definition), and the radiative envelope. The extent of the semiconvection zone is larger in more massive stars.

The stability was examined using the quasi-adiabatic approximation for the models 21 for both the $30M_\odot$ and the $15M_\odot$ star. The degree of superadiabaticity is illustrated in Fig. 29.2. It is typically $\nabla - \nabla_{ad} \simeq 0.01$

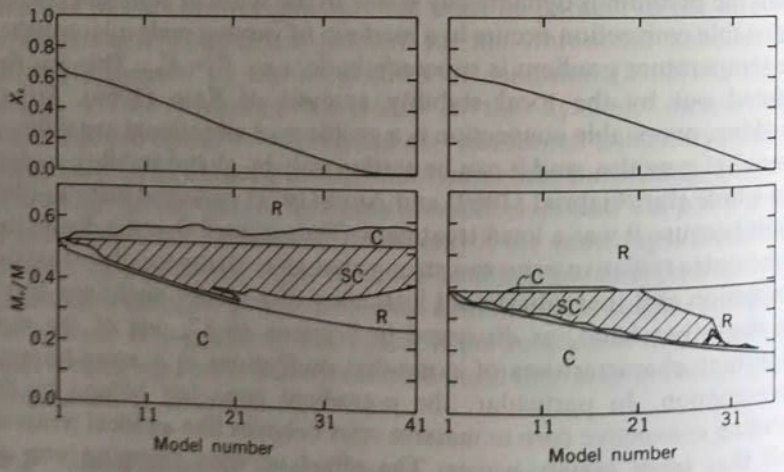

Fig. 29.1 Structural changes with evolution for a $30M_\odot$ star (left) and a $15M_\odot$ star (right) [after Shibahashi and Osaki (1976a)]. The abscissa is the model number of evolutionary sequence. The upper figures show variation in the central hydrogen abundance X_c. The symbols in the figure are: C, the convective zone where material is well mixed and homogeneous with $\nabla = \nabla_{ad}$; R, the radiative zone where $\nabla < \nabla_{ad}$; SC (hactched region), the semiconvective zone where $\nabla_{ad} < \nabla < \nabla_{ad} + [\beta/(4-3\beta)]\nabla_\mu$.

for the $30M_\odot$ star, and $\nabla - \nabla_{ad} \simeq 0.002$ for the $15M_\odot$ star. The propagation diagram for the $30M_\odot$ model is given in Fig. 17.6. In a star with a well-developed μ-gradient zone there exist $\bar{G}_n$-modes well trapped in the μ-gradient zone as discussed in Section 17. Shibahashi and Osaki (1976a) found that some $\bar{G}_n$-modes for large l are overstable with the growth time of $10^3 - 10^4$yr. Among the modes for the $30M_\odot$ star listed in Table 17.2, $\bar{G}_n$-modes with $n = 1, 2\ldots, 6$ and $l = 15$ and all $\bar{G}_n$-modes with $l = 30$ are found to be overstable (see also Fig. 17.8). The eigenfunctions of $\bar{G}_n$-modes have large amplitude only in the μ-gradient zone, so that Kato's (1966) mechanism for the overstability in the semiconvective zone works effectively. Since the wave trapping is incomplete for smaller l (see Table 17.2), $\bar{G}_n$-modes for smaller l tend to be stabilized by the effect of radiative damping in the envelope. No overstable mode was found for $l \leq 4$ for the $30M_\odot$ star.

For the $15M_\odot$ star, superadiabaticity in the semiconvective zone is small compared with the $30M_\odot$ star, as seen in Fig. 29.2, so that the destabilizing effect is correspondingly weak. For the $15M_\odot$ star, only $\bar{G}_3$- and $\bar{G}_4$-modes for $l = 15$ are overstable with the growth time of $\sim 10^4$yr, and all modes are stable for $l \leq 8$. Roughly speaking, the magnitude of the destabilizing effect may be represented by a product of $(\nabla - \nabla_{ad})$ and $l(l+1)$ as seen in equation (29.18), because $l_R \propto k^2 = (N^2/\sigma^2)k_h^2 \propto l(l+1)$. This is consistent with the numerical result that the lowest l for which unstable modes are found is $l = 15$ for the $15M_\odot$ star and $l = 8$ for the $30M_\odot$ star, because $(\nabla - \nabla_{ad})$ in the $15M_\odot$ star is about one-fifth of that in the $30M_\odot$ star.

The e-folding time of oscillations for unstable modes is typically 10^3

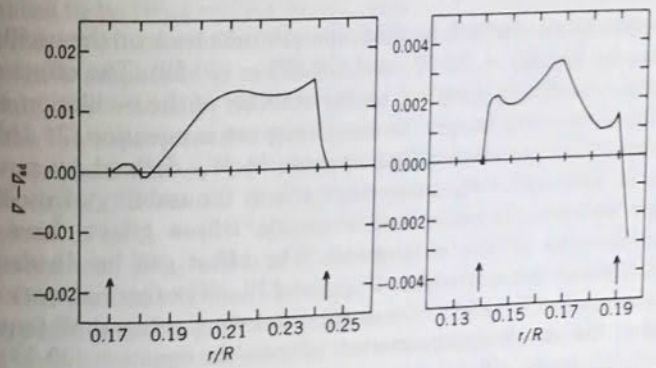

Fig 29.2 Superadiabaticity in temperature gradient $\nabla - \nabla_{ad}$ in the μ-gradient zone of model No. 21 of the $30M_\odot$ star (left) and of model No. 21 of the $15M_\odot$ star (right). The arrows show the inner and outer boundaries of the μ-gradient zone [after Shibahashi and Osaki (1976a)].

-10^4yr, which is shorter than the evolutionary time of the stars. In general, modes having larger l are more unstable. Since the molecular and radiative viscosities are not important in the stellar interior, we expect that overstable convection grows to a finite amplitude (Stevenson, 1979) and that some kind of mixing occurs. In this sense, Schwarzschild and Härm's (1958) criterion in equation (29.31) is preferable to Ledoux's (1947) criterion in equation (29.32) (*cf.* Langer, El Eid, and Fricke, 1985), although the model with penetraive convection constructed by use of the non-local mixing length theory (Xiong, 1985) may be more realistic.

Semiconvective zones are present in stars of about $1M_\odot$ as well as in massive stars. As a small convective core in such stars expands due to the growing importance of the CNO cycle, the opacity is larger at the outer side of the convective core boundary than at its inner side. Therefore in such models a shallow semiconvective zone [i.e., $\nabla_{ad} < \nabla < \nabla_{ad} + \beta(4-3\beta)^{-1}\nabla_\mu$] is found just above the convective core. Gabriel and Noels (1977) studied the vibrational stability of some g-modes of large l in stars of 1, 1.1, and $1.5M_\odot$ during central hydrogen burning. Most of these models have been found to be stable, instabilities occur in only two models of the $1.1M_\odot$ sequence. This is because semiconvective zones in such stars are shallow and the degree of superadiabaticity is small. Baglin (1971) also discussed overstability of the semiconvective zone in a white dwarf where the μ-gradient was formed due to the gravitational settling of elements.

30. *Convection*

Convection fluctuates with oscillation and works back on the oscillation, as shown by (20.31) – (20.33) and (20.57) – (20.59). The effect of the convection-oscillation coupling on the stability of the oscillation is seen explicitly in the work integral such as that given in equation (25.16). The perturbation of convective flux appears in W_C defined by equation (26.4). In addition to W_C convection affects the stability of oscillation through turbulent pressure and viscosity, whose effects have been neglected so far in this monograph. The effect can be divided into mechanical and thermal works, W_{mech} and W_{th}. The thermal work W_{th} is evaluated as $\delta_2\,(1+\delta_2)^{-1}$ times the total work integral W [equation (26.1)] in the rough approximation adopted in equation (20.33). The mechanical work, W_{mech}, arises due to the Reynolds stress [see equations (20.7) and (20.32)]:

$$W_{mech}=-\frac{\pi}{\sigma}\int_0^M \rho^{-1}\mathrm{Re}\left[\boldsymbol{v}'^*\cdot\ \mathrm{div}\ \mathscr{P}_t'\right]dM_r. \tag{30.1}$$

We assume that

$$-\mathrm{div}\ \mathscr{P}_t=-\nabla p_t+\nabla(\mu_t\nabla\cdot\boldsymbol{v})+(\nabla\cdot\mu_t\nabla)\boldsymbol{v} \tag{30.2}$$

as suggested by the mixing length theory (*cf.* Unno, 1969), in which the turbulent convection is simulated to molecular motion in producing diffusive processes, where μ_t represents the turbulent viscosity defined in equation (20.13). Then we can express W_{mech} as

$$W_{mech}=W_{pr}+W_{str}, \tag{30.3}$$

where

$$W_{pr}=-\frac{\pi}{\sigma}\int_0^M\frac{1}{\rho}\mathrm{Re}(\boldsymbol{v}'^*\cdot\nabla p_t')dM_r=\pi\int_0^M\frac{1}{\rho}\mathrm{Im}\ (p_t'\nabla\cdot\boldsymbol{\xi}^*)dM_r \tag{30.4}$$

and

$$W_{str}=\frac{\pi}{\sigma}\int_0^M\frac{1}{\rho}\mathrm{Re}\left[\boldsymbol{v}'^*\cdot\nabla(\mu_t\nabla\cdot\boldsymbol{v}')+\boldsymbol{v}'^*\cdot(\nabla\cdot\mu_t\nabla)\boldsymbol{v}')\right]dM_r$$

$$=-\pi\sigma\int_0^M\frac{\mu_t}{\rho}(|\nabla\cdot\boldsymbol{\xi}|^2+|\nabla\boldsymbol{\xi}|^2)dM_r, \tag{30.5}$$

where the ij-component of $\nabla\boldsymbol{\xi}$ is $\partial\xi_j/\partial x_i$ in Cartesian coordinates. The work by viscous stresses W_{str} is always negative, but the evaluation of the work by the turbulent pressure W_{pr} is possible when the time-dependent convection is solved. The order of magnitude of W_{pr} is estimated to be $|W_{pr}|\sim\langle V\rangle^2M_C\alpha^2$, where $\langle V\rangle$ denotes the representative velocity of convection, M_C the mass of the convection zone, and α the relative amplitude of oscillation, *viz.*, $|\nabla\cdot\boldsymbol{\xi}|$ or $|\delta\rho/\rho|$. Likewise, we estimate the viscosity work as $|W_{str}|\sim(\sigma\tau_C)\langle V\rangle^2M_C\alpha^2$, where τ_C denotes the representative time scale of convection, $l_t/\langle V\rangle$. Here we have assumed that $\mu_t\sim\rho\langle V\rangle l_t$, l_t being the mixing length. Since the luminosity L is mainly due to the convective flux and is roughly estimated to be $L\sim\langle V\rangle^2M_C/\tau_C$, both W_{pr} and W_{str} are not negligible compared with $|W_{th}|$ which is of the order of $L\alpha^2/\sigma$, depending on the $\sigma\tau_C$ value and on whether the wave is trapped in the convection zone. Thus, positive and negative contributions to the work integral are of the same order of magnitude even in the most favorable case of overstability; the coupling between convection and oscillation has to be taken into account in stability analysis, although the time-dependent convection theory has not been so well established.

Convection-pulsation coupling has been formulated by Unno

(1967, 1977), by Gabriel, Scuflaire, Noels, and Boury (1975), and by Xiong (1978). The effect must be important in late-type stars with extended outer convective envelopes (Baker and Gough, 1979; Gonczi and Osaki, 1980; Gonczi, 1982). For solar five-minute oscillations, the problem has been discussed by Antia, Chitre, and Narasimha (1982) and Gabriel (1988). The excitation mechanism of the five-minute oscillation is still somewhat controversial (see Section 42).

The influence of convection on oscillation appears in equations (20.32) and (20.33) through the quantities δ_1, δ_2, μ_t, and $\boldsymbol{F}'_C$. The effect of turbulent pressure and energy in the form described by δ_1 and δ_2 in equations (20.32) and (20.33) is adequate when $\sigma\tau_C \gg 1$ and hence $|W_{pr}| \ll |W_{str}|$, as discussed in Section 20. In the opposite case of $\sigma\tau_C \ll 1$, we have $|W_{pr}| \ll |W_{th}|$. Therefore, we can take δ_1 and δ_2 to be small corrections that may be neglected in the qualitative study. For μ_t, only the equilibrium value is needed, as discussed above. The convective flux $\boldsymbol{F}_C$ is given by equation (20.22),

$$\boldsymbol{F}_{C,0}=\left\langle \rho_0\left(h_C+\frac{V^2}{2}\right)\boldsymbol{V}\right\rangle=\langle c_p\rho_0 T_C \boldsymbol{V}\rangle_0-(\kappa_t/2)\nabla(\langle \boldsymbol{V}^2\rangle_0)$$

$$=[(c_pT_0)^{1/2}Y_0-\kappa_t(d/dr)\,(X_0/\rho_0)]\boldsymbol{e}_r, \tag{30.6}$$

where $\boldsymbol{e}_r(=\nabla r)$ denotes the unit vector in the radial direction, and the second term has been reduced by use of the gradient diffusion approximation. To derive the perturbation of the convective flux, $\boldsymbol{F}'_C$, it is convenient to use the gradient diffusion approximation from the beginning so that

$$\begin{aligned}
\boldsymbol{F}'_C&=-[\kappa_t\nabla(c_p\langle T_C^2\rangle^{1/2}+(1/2)\langle V^2\rangle)]'\\
&=(\kappa'_t/\kappa_t)\boldsymbol{F}_{C,0}-\kappa_t\nabla[(2c_pT/\rho)^{1/2}Z^{1/2}+\rho^{-1/2}X]'\\
&=(\kappa'_t/\kappa_t)\boldsymbol{F}_{C,0}-(\kappa_t/2)\nabla\left[(2c_pT_0Z_0/\rho_0)^{1/2}\left(\frac{Z'}{Z_0}+\frac{(c_pT)'}{c_pT_0}-\frac{\rho'}{\rho_0}\right)\right.\\
&\quad\left.+(X_0^2/\rho_0)^{1/2}\left(2\frac{X'}{X_0}-\frac{\rho'}{\rho_0}\right)\right].
\end{aligned} \tag{30.7}$$

Thus, only the evaluation of κ'_t, X', and Z' remains in the problem of convection oscillation coupling.

The eddy conductivity, κ_t, is proportional to $(\bar{\rho}X)^{1/2}l_t$ as expressed by equation (20.13), and, therefore,

$$\kappa'_t/\kappa_t=\mu'_t/\mu_t=(1/2)[(X'/X_0)+(\rho'/\rho_0)+2(l'_t/l_t)]. \tag{30.8}$$

The relative perturbation of the mixing length, l'_t/l_t, however, requires some consideration. Gough (1976) treated this problem in the time-dependent mixing-length theory. Here, a simple qualitative approach (Unno, 1977) to determine l'_t/l_t will be introduced. We treat the Lagrangian perturbation,

$$\delta l_t/l_t=l'_t/l_t+(d\ln H_p/dr)\xi_r=l'_t/l_t-(\nabla/H_p)\xi_r, \tag{30.9}$$

since the mixing length is a concept concerned with the transport of conserving quantities.

Let us assume that a convective element born at time t' has a mixing length equal to the instantaneous local scale height $H_p(=-\partial r/\partial\ln p)$ initially and evolves according to the law ρl_t^3 = constant during its lifetime τ_C. Then, the relative excess $\delta l_t/l_t$ is given by $(\delta H_p/H_p)e^{i\sigma t'}$ at its birth and will be further increased by $(-1/3)(\delta\rho/\rho)(e^{i\sigma t}-e^{i\sigma t'})$, where $\delta\rho/\rho$ at time t is written as $(\delta\rho/\rho)e^{i\sigma t}$, explicitly expressing the time dependence. For the average convective element, we obtain

$$\frac{\delta l_t}{l_t}e^{i\sigma t}=\int_0^\infty\left\{\frac{\delta H_p}{H_p}e^{i\sigma t'}-\frac{1}{3}\frac{\delta\rho}{\rho}(e^{i\sigma t}-e^{i\sigma t'})\right\}$$

$$\times\ \exp\left(-\frac{t-t'}{\tau_C}\right)\frac{d(t-t')}{\tau_C} \tag{30.10}$$

or

$$\frac{\delta l_t}{l_t}=\frac{1}{1+i\sigma\tau_C}\left(\frac{\delta H_p}{H_p}-\frac{i\sigma\tau_C}{3}\frac{\delta\rho}{\rho}\right), \tag{30.11}$$

assuming a constant birth rate and constant lifetime for the convective elements. The variation of H_p is calculated from its definition,

$$\frac{\delta H_p}{H_p}=\frac{\partial\xi_r}{\partial r}+H_p\frac{\partial}{\partial r}\left(\frac{\delta p}{p}\right). \tag{30.12}$$

The formulation is now completed, if we assume

$$\tau_C\simeq\left(\frac{\kappa_t}{\rho}k^2\right)^{-1}\simeq\left(\frac{\mu_t}{\rho}k^2\right)^{-1} \tag{30.13}$$

in equation (30.11) where k denotes the representative wave number of a convective element (see Section 20).

Thus, the problem of the convection-oscillation coupling is reduced to the problem of evaluating X' and Z' from the basic equations (20.57)–(20.59) of convection under the influence of oscillation, as it should be.

Linearizing equation (20.57)–(20.59), we have

$$[i\sigma+(2/3)\nabla\cdot\xi+D_1]X'+(i\sigma\xi_r D_r+D_1')X_0$$
$$=B_1Y'+B_1'Y_0, \tag{30.14}$$

$$[i\sigma+(1+D_r\xi_r)+D_2]Y'+(i\sigma\xi_r D_r+D_2')Y_0$$
$$=B_2Z'+B_2'Z_0+B_3X'+B_3'X_0, \tag{30.15}$$

and

$$[i\sigma+D_3]Z'+(i\sigma\xi_r D_r+D_3')Z_0 =(2/3)[B_3Y'+B_3'Y_0], \tag{30.16}$$

where ε_N has been neglected in the outer convective zone,

$$D_r=\partial/\partial r, \tag{30.17}$$

$$D_1=2(\mu_t/\rho_0)k^2, \quad D_1'=D_1[(\mu_t'/\mu_t)-(\rho'/\rho_0)-2(l_t'/l_t)], \tag{30.18}$$

$$\left.\begin{aligned} D_2&=2\frac{c_p^{-1}K+\mu_t+\kappa_t}{\rho_0}k^2, \\ \frac{D_2'}{D_2}&=\frac{(c_p^{-1}K)'+\mu_t'+\kappa_t'}{c_p^{-1}K+\mu_t+\kappa_t}-\frac{\rho'}{\rho_0}-2\frac{l_t'}{l_t}, \end{aligned}\right\} \tag{30.19}$$

$$D_3=2\frac{c_p^{-1}K+\kappa_t}{\rho_0}k^2, \quad \frac{D_3'}{D_3}=\frac{(c_p^{-1}K)'+\kappa_t'}{c_p^{-1}K+\kappa_t}-\frac{\rho'}{\rho_0}-2\frac{l_t'}{l_t}, \tag{30.20}$$

$$B_1=v_T g(c_pT_0)^{-1/2}, \quad B_1'=B_1\left[i\sigma\frac{\xi_r}{g}-\frac{1}{2}\frac{T'}{T_0}\right], \tag{30.21}$$

$$B_2=2v_T^* g(c_pT_0)^{-1/2}, \quad B_2'=B_1\left[i\sigma\frac{\xi_r}{g}-\frac{1}{2}\frac{T'}{T_0}\right], \tag{30.22}$$

$$\left.\begin{aligned} B_3&=(2/3)(c_pT_0)^{1/2}(\nabla-\nabla_{ad})/H, \\ B_3'&=B_3\left[\frac{\nabla'-\nabla'_{ad}}{\nabla_0-\nabla_{ad}}-\frac{1}{2}\frac{T'}{T_0}\right], \end{aligned}\right\} \tag{30.23}$$

and

$$\nabla'=(\nabla_0/H)\left[D_r\left(\frac{p'}{p_0}\right)-\nabla_0^{-1}D_r\left(\frac{T'}{T_0}\right)\right]. \tag{30.24}$$

Solving equations (30.14)–(30.16), we obtain X', Y', and Z'. With the values of X', Y', and Z', the Eulerian perturbation of convective flux, F_C', can be calculated by use of equation (30.7). Thus, we can evaluate the work integral due to convective flux, W_C.

The dynamical convection-oscillation coupling appearing as W_{pr} and W_{str} arises where $\sigma\tau_C \sim 1$. However, the phase relation between $\delta l_t/l_t$ and $\delta\rho/\rho$ is rather complicated in the computation of W_{pr} and W_{str}. The result will be stabilizing or destabilizing, depending on the mode of oscillation and on the stellar model. Numerical investigation seems to be necessary. It should also be noted that the theory of the stellar convection zone is still very incomplete for both the time-independent and dependent cases and that an exact nonlocal theory avoiding the use of the mixing length is very much desired.

Chapter VI

NONRADIAL OSCILLATIONS OF ROTATING STARS

31. Introductory Remarks

In a non-rotating non-magnetic spherical star, no force is exerted on a non-divergent flow along a level surface. This corresponds to the existence of the trivial solution with toroidal flow discussed in Section 13. If the star rotates, the conservation law of angular momentum plays an essential role in fluid motions in the star, and the toroidal flow can no longer be steady. When we describe fluid motions in a rotating star using an inertial frame, the effect of rotation appears in the inertial term $\boldsymbol{v}\cdot\nabla\boldsymbol{v}$ in the momentum equation [see equation (13.4)], where $\boldsymbol{v}$ is composed of rotation $\boldsymbol{\Omega}\times\boldsymbol{r}$ and perturbation of velocity $\boldsymbol{v}'$ with $\boldsymbol{\Omega}$ being the angular velocity of the stellar rotation. This inertial term appears as two kinds of fictitious forces: the Coriolis force and the centrifugal force in the momentum equation in the co-rotating frame. The centrifugal force in a uniformly rotating star, which may be written in the form of a potential force $\nabla(|\boldsymbol{\Omega}\times\boldsymbol{r}|^2/2)$, can be treated together with the gravitational force. The latitudinal dependence of effective gravity (true gravity plus centrifugal force) deforms the equilibrium structure of the star, which in turn modifies oscillation frequencies. Since the linearized momentum equation can be written in a form in which the effect of the centrifugal force appears only through the modification of the distribution of the equilibrium structure, a new type of wave is not expected from the centrifugal force. Equilibrium structures of rotating stars are extensively discussed in an excellent monograph by Tassoul (1978).

On the other hand, the Coriolis force, $-2\boldsymbol{\Omega}\times\boldsymbol{v}'$, has a form which does not exist in a nonrotating nonmagnetic star. The Coriolis force not only modifies the oscillation frequencies of g-, p-, and f-modes but also generates new waves: Rossby-type waves and inertial waves, all of which are sometimes called inertial waves inclusively. The r-mode, which is the global Rossby wave, was introduced in Section 19. We will discuss, in Section 33 by using a local analysis, the mechanism of the

r-mode oscillation and its relation to the prototype Rossby wave which is familiar in geophysics. We will also discuss other inertial waves including a wave which is generated by a mechanism similar to that of the Rossby wave. Waves in a rotating fluid are extensively discussed in the literature of geophysics. The authors found books by Greenspan (1968) and by Pedlosky (1979), for example, useful.

We discussed the effect of rotation on the oscillation frequencies of spheroidal modes (g-, f-, and p-modes) in Section 19 by using a perturbation analysis with a small parameter of the ratio of the rotation frequency to the oscillation frequency (Ω/σ). The perturbation analysis is not applicable to the case of $\Omega/\sigma \gtrsim 1$. This chapter discusses such oscillations strongly modified by rotation, in which many peculiar phenomena arise.

In contrast to the effect of rotation on nonradial oscillations, nonradial oscillations in a rotating star can affect the equilibrium distribution of the angular momentum, because nonaxisymmetric nonradial oscillations can transport angular momentum from place to place when they are nonconservative (i.e., when there exists effect of dissipation and/or leaky boundary conditions). This effect may be important for the evolution of stellar rotation. This basic mechanism will be described in Section 36.

32. Basic Equations

The basic equations that describe oscillations of a rotating star are equations of hydrodynamics given by (13.1)–(13.3). As in Section 13, we restrict ourselves in this chapter to the case without turbulent convection and magnetic field. The basic equations of hydrodynamics are then given by

$$\frac{\partial \rho}{\partial t} + \nabla \cdot (\rho \boldsymbol{v}) = 0, \tag{32.1}$$

$$\rho \left(\frac{\partial}{\partial t} + \boldsymbol{v} \cdot \nabla \right) \boldsymbol{v} = -\nabla p - \rho \nabla \Phi , \tag{32.2}$$

and

$$\rho T \left(\frac{\partial}{\partial t} + \boldsymbol{v} \cdot \nabla \right) S = \rho \varepsilon_N - \nabla \cdot \boldsymbol{F}_R , \tag{32.3}$$

where the velocity without turbulent convection is denoted by $\boldsymbol{v}$. By setting the time derivative to zero in equations (32.1)–(32.3), we obtain equations governing the equilibrium state:

$$\nabla \cdot (\rho_0 \boldsymbol{v}_0) = 0 , \tag{32.4}$$

$$(\boldsymbol{v}_0 \cdot \nabla) \boldsymbol{v}_0 = -\frac{1}{\rho_0} \nabla p_0 - \nabla \Phi_0 , \tag{32.5}$$

and

$$\rho_0 T_0 (\boldsymbol{v}_0 \cdot \nabla) S_0 = \rho_0 \varepsilon_{N,0} - \nabla \cdot \boldsymbol{F}_{R,0} , \tag{32.6}$$

where the subscript 0 denotes the equilibrium state. Let us now discuss the equilibrium state with the velocity due to rotation,

$$\boldsymbol{v}_0 = \boldsymbol{\Omega} \times \boldsymbol{r} , \tag{32.7}$$

where $\boldsymbol{\Omega}$ denotes the angular velocity of a star at equilibrium. We assume $\boldsymbol{\Omega}$ is axially symmetric so that

$$\boldsymbol{\Omega} = [\Omega(r,\theta)\cos\theta, \ -\Omega(r,\theta)\sin\theta, \ 0] \tag{32.8}$$

in the spherical polar coordinates. We suppose that the equilibrium state is also axially symmetric. Since the equilibrium velocity field is solenoidal,

$$\nabla \cdot \boldsymbol{v}_0 = 0 , \tag{32.9}$$

and the scalar product of $\boldsymbol{v}_0$ with a gradient of any scalar quantity f leads to

$$\boldsymbol{v}_0 \cdot \nabla f = \Omega \frac{\partial f}{\partial \varphi} , \tag{32.10}$$

equation (32.4) is automatically satisfied, and equation (32.6) is reduced to equation (13.9). Equation (32.5) is reduced to

$$\boldsymbol{\Omega} \times \boldsymbol{\Omega} \times \boldsymbol{r} = -\frac{1}{\rho_0} \nabla p_0 - \nabla \Phi_0 , \tag{32.11}$$

where the left-hand side represents the centrifugal force.

The linearized basic equations are derived in the Eulerian form as follows:

$$\frac{\partial \rho'}{\partial t} + \nabla \cdot (\rho_0 \boldsymbol{v}' + \rho' \boldsymbol{v}_0) = 0 , \tag{32.12}$$

$$\rho_0 \left[\frac{\partial \boldsymbol{v}'}{\partial t} + (\boldsymbol{v}_0 \cdot \nabla) \boldsymbol{v}' + (\boldsymbol{v}' \cdot \nabla) \boldsymbol{v}_0 \right] + \rho' (\boldsymbol{v}_0 \cdot \nabla) \boldsymbol{v}_0 = -\nabla p' - \rho' \nabla \Phi_0 - \rho_0 \nabla \Phi' , \tag{32.13}$$

and

$$\rho_0 T_0\left[\frac{\partial S'}{\partial t}+(\boldsymbol{v}_0\cdot\nabla)S'+(\boldsymbol{v}'\cdot\nabla)S_0\right]+(\rho T)'(\boldsymbol{v}_0\cdot\nabla)S_0$$
$$=(\rho\varepsilon_N)'-\nabla\cdot\boldsymbol{F}'_R. \tag{32.14}$$

With the help of equations (32.9) and (32.10), the linearized mass-conservation equation (32.12) and energy equation (32.14) are reduced to

$$\left(\frac{\partial}{\partial t}+\Omega\frac{\partial}{\partial\phi}\right)\rho'+\nabla\cdot(\rho_0\boldsymbol{v}')=0, \tag{32.15}$$

and

$$\rho_0 T_0\left[\left(\frac{\partial}{\partial t}+\Omega\frac{\partial}{\partial\phi}\right)S'+(\boldsymbol{v}\cdot\nabla)S_0\right]=(\rho\varepsilon_N)'-\nabla\cdot\boldsymbol{F}'_R, \tag{32.16}$$

respectively. The operator $(\partial/\partial t+\Omega\partial/\partial\phi)$ appearing in the above equations represents the temporal derivative referring to a local rotating frame with the angular velocity Ω. Inserting equations (32.7) and (32.5) into the linearized equation of motion (32.13), and using the relations among the unit vectors (19.36)–(19.38), we obtain

$$\left[\left(\frac{\partial}{\partial t}+\Omega\frac{\partial}{\partial\phi}\right)v'_i\right]\boldsymbol{e}_i+2\boldsymbol{\Omega}\times\boldsymbol{v}'+(\boldsymbol{v}'\cdot\nabla\boldsymbol{\Omega})r\sin\theta\boldsymbol{e}_\phi$$
$$=-\frac{1}{\rho_0}\nabla p'-\nabla\Phi'+\frac{\rho'}{\rho_0^2}\nabla p_0. \tag{32.17}$$

The first term in the left-hand side of equation (32.17) represents the time derivative of the velocity referring to a local rotating frame; the second term stands for the Coriolis force, and the third term is due to differential rotation. The Eulerian velocity perturbation $\boldsymbol{v}'$ is related to the displacement $\boldsymbol{\xi}$, with the help of (13.26), (32.7), (32.10), and (19.36)–(19.38), by

$$\boldsymbol{v}'=\left[\left(\frac{\partial}{\partial t}+\Omega\frac{\partial}{\partial\phi}\right)\xi_i\right]\boldsymbol{e}_i-(\boldsymbol{\xi}\cdot\nabla\boldsymbol{\Omega})r\sin\theta\boldsymbol{e}_\phi. \tag{32.18}$$

Supplementary equations are needed to complete the description of a system. They are the same as those given in Section 13. For example, the Poisson equation is given by

$$\nabla^2\Phi'=4\pi G\rho' \ . \tag{32.19}$$

From equation (13.83), the Lagrangian entropy perturbation is represented in terms of the Lagrangian density perturbation and the Lagrangian pressure perturbation as

$$\frac{\delta\rho}{\rho_0}-\frac{1}{\Gamma_1}\frac{\delta p}{p_0}=-\frac{v_T}{c_p}\delta S \ . \tag{32.20}$$

By using relations between Lagrangian perturbations and Eulerian perturbations given by equations (13.21) and (32.18), we represent the entropy perturbation in terms of the Eulerian density and pressure perturbations:

$$\left(\frac{\partial}{\partial t}+\Omega\frac{\partial}{\partial\phi}\right)\left(\frac{\rho'}{\rho_0}-\frac{p'}{\Gamma_1 p_0}\right)+\boldsymbol{v}'\cdot\left(\nabla\ln\rho_0-\frac{1}{\Gamma_1}\nabla\ln p_0\right)$$
$$=-\frac{v_T}{c_p}\left(\frac{\partial}{\partial t}+\Omega\frac{\partial}{\partial\phi}\right)\delta S. \tag{32.21}$$

Equations (32.15)–(32.19), (13.50), (13.51), and (13.84) are the basic equations for linear nonadiabatic nonradial oscillation in rotating stars. In the adiabatic approximation, equations (13.50) and (13.51) are not needed, and the right-hand sides of equations (32.16) and (32.21) are neglected.

It is instructive to describe a fluid motion in terms of vorticity defined by

$$\boldsymbol{\omega}\equiv\nabla\times\boldsymbol{v} \ , \tag{32.22}$$

which represents the local and instantaneous rate of rotation of the fluid. Let us derive an equation governing the change of vorticity. Taking the curl of equation of motion (32.2), we obtain

$$\frac{\partial\boldsymbol{\omega}}{\partial t}+\nabla\times(\boldsymbol{\omega}\times\boldsymbol{v})+\nabla\times\left(\frac{1}{\rho}\nabla p\right)=0. \tag{32.23}$$

In deriving equation (32.23), we have used well-known formulae in vector analysis,

$$\frac{1}{2}\nabla|\boldsymbol{v}|^2=\boldsymbol{v}\times(\nabla\times\boldsymbol{v})+(\boldsymbol{v}\cdot\nabla)\boldsymbol{v} \tag{32.24}$$

and

$$\nabla\times(\nabla\Phi)=0. \tag{32.25}$$

Since

$$\nabla\cdot\boldsymbol{\omega}=\nabla\cdot(\nabla\times\boldsymbol{v})\equiv 0, \tag{32.26}$$

the second term of equation (32.23) is rewritten as

$$\nabla\times(\boldsymbol{\omega}\times\boldsymbol{v})=(\boldsymbol{v}\cdot\nabla)\boldsymbol{\omega}-(\boldsymbol{\omega}\cdot\nabla)\boldsymbol{v}+(\nabla\cdot\boldsymbol{v})\boldsymbol{\omega}. \tag{32.27}$$

Then, equation (32.23) is reduced to

$$\left(\frac{\partial}{\partial t}+\boldsymbol{v}\cdot\nabla\right)\boldsymbol{\omega}-(\boldsymbol{\omega}\cdot\nabla)\boldsymbol{v}+(\nabla\cdot\boldsymbol{v})\boldsymbol{\omega}+\nabla\times\left(\frac{1}{\rho}\nabla p\right)=0. \quad (32.28)$$

In combining equations (32.1) and (32.28), we obtain

$$\left(\frac{\partial}{\partial t}+\boldsymbol{v}\cdot\nabla\right)\frac{\boldsymbol{\omega}}{\rho}-\left(\frac{\boldsymbol{\omega}}{\rho}\cdot\nabla\right)\boldsymbol{v}+\frac{1}{\rho}\nabla\times\left(\frac{1}{\rho}\nabla p\right)=0. \quad (32.29)$$

We can rewrite the term of $\rho^{-1}\nabla p$ in the above equation in terms of enthalpy and entropy as

$$\frac{1}{\rho}\nabla p=\nabla h-T\nabla S \quad (32.30)$$

by using a thermodynamic relation

$$dh=TdS+\frac{dp}{\rho}, \quad (32.31)$$

where h denotes the enthalpy. Then, the third term in equation (32.29) is rewritten in terms of the temperature gradient and the entropy gradient as

$$\nabla\times(\rho^{-1}\nabla p)=-\nabla\times(T\nabla S)=-\nabla T\times\nabla S. \quad (32.32)$$

Hence, the vorticity equation (32.29) can be written as

$$\left(\frac{\partial}{\partial t}+\boldsymbol{v}\cdot\nabla\right)\frac{\boldsymbol{\omega}}{\rho}-\left(\frac{\boldsymbol{\omega}}{\rho}\cdot\nabla\right)\boldsymbol{v}-\frac{1}{\rho}\nabla T\times\nabla S=0. \quad (32.33)$$

The vorticity equation (32.33) is useful to understand the physical nature of the waves caused by rotation of the fluid, and is used in the following section.

By substituting the equilibrium quantities such as ρ_0, p_0, and $\boldsymbol{v}_0$ into equation (32.29), we obtain an equation governing the equilibrium state:

$$(\boldsymbol{v}_0\cdot\nabla)\frac{\boldsymbol{\omega}_0}{\rho_0}-\left(\frac{\boldsymbol{\omega}_0}{\rho_0}\cdot\nabla\right)\boldsymbol{v}_0+\frac{1}{\rho_0}\nabla\times\left(\frac{1}{\rho_0}\nabla p_0\right)=0, \quad (32.34)$$

where

$$\boldsymbol{\omega}_0\equiv\nabla\times\boldsymbol{v}_0=\nabla\times(\boldsymbol{\Omega}\times\boldsymbol{r})=2\boldsymbol{\Omega}. \quad (32.35)$$

The first term of equation (32.34) is zero because of equations (32.7), (32.8), (32.10), and (32.35). Then equation (32.34) is reduced to

$$-(2\boldsymbol{\Omega}\cdot\nabla)(\boldsymbol{\Omega}\times\boldsymbol{r})+\nabla\times\left(\frac{1}{\rho_0}\nabla p_0\right)=0. \quad (32.36)$$

If the rotation law is cylindrical ($\partial\Omega/\partial z=0$) or uniform, equation (32.36) leads to

$$\nabla\rho_0\times\nabla p_0=0, \quad (32.37)$$

which means that the isobaric surface and the isopycnic surface coincide. The fluid layer in this case is called "barotropic." Otherwise the condition (32.37) is not satisfied, and the isobaric and the isopycnic surfaces are inclined each other. The fluid layer in this situation is called "baroclinic."

The linearized equation of vorticity equation (32.28) is given by

$$\left[\left(\frac{\partial}{\partial t}+\Omega\frac{\partial}{\partial\phi}\right)\omega_i'\right]\boldsymbol{e}_i+(\boldsymbol{\omega}'\cdot\nabla\Omega)r\sin\theta\boldsymbol{e}_\phi+(\boldsymbol{v}'\cdot\nabla)2\boldsymbol{\Omega}-(2\boldsymbol{\Omega}\cdot\nabla)\boldsymbol{v}'$$
$$+(\nabla\cdot\boldsymbol{v}')2\boldsymbol{\Omega}+\nabla\times\left(\frac{1}{\rho}\nabla p\right)=0. \quad (32.38)$$

In what follows, we omit subscript 0 for equilibrium quantities unless there is confusion.

33. Local Analysis

Prior to the full discussion of the oscillations in the rotating stars, it is instructive to examine locally the effect of uniform rotation on oscillations. This enables us to understand the basic physical aspects of the waves newly introduced by rotation.

33.1 Dispersion Relation

To make the local analysis tractable, some simplifications are employed. We assume the rotation is uniform. The adiabaticity is also assumed for disturbances. We adopt the Cowling approximation and discard the perturbation of the gravitational potential. The simplified forms of equations (32.15), (32.21), and (32.17) are

$$\frac{D\rho'}{Dt}+\nabla\cdot(\rho\boldsymbol{v}')=0, \quad (33.1)$$

$$\frac{D\rho'}{Dt}-\frac{1}{c^2}\frac{Dp'}{Dt}+\rho\boldsymbol{v}'\cdot\boldsymbol{A}=0, \quad (33.2)$$

and

$$\frac{Dv_i'}{Dt}\boldsymbol{e}_i+2\boldsymbol{\Omega}\times\boldsymbol{v}'=-\frac{1}{\rho}\nabla p'+\frac{\rho'}{\rho^2}\nabla p, \quad (33.3)$$

where

$$\frac{D}{Dt}\equiv\frac{\partial}{\partial t}+\Omega\frac{\partial}{\partial\phi} \tag{33.4}$$

denotes time derivative following the unperturbed rotation, and

$$\boldsymbol{A}\equiv\nabla\ln\rho-\frac{1}{\Gamma_1}\nabla\ln p. \tag{33.5}$$

The temporal and spatial dependence of any perturbed quantities are assumed to be proportional to $\exp[i(\sigma t+\boldsymbol{k}\cdot\boldsymbol{r})]$, in which the angular frequency σ should be defined in a rotating frame. The perturbed elements are assumed to have small dimensions compared with the scale length of equilibrium pressure, density, etc., and the effect of sphericity is neglected. The resulting equations then become

$$i\sigma\frac{\rho'}{\rho}+i\boldsymbol{k}\cdot\boldsymbol{v}'=0, \tag{33.6}$$

$$i\sigma\frac{\rho'}{\rho}-\frac{i\sigma}{c^2}\frac{p'}{\rho}+\boldsymbol{v}'\cdot\boldsymbol{A}=0, \tag{33.7}$$

and

$$i\sigma\boldsymbol{v}'+2\boldsymbol{\Omega}\times\boldsymbol{v}'=-ik\frac{p'}{\rho}+\left(\frac{1}{\rho}\nabla p\right)\frac{\rho'}{\rho}. \tag{33.8}$$

Equations (33.6)–(33.8) form a set of linear simultaneous algebraic equations for variables ρ'/ρ, p'/ρ, and $\boldsymbol{v}'$, and its characteristic equation gives a dispersion relation

$$\sigma\left[\frac{\sigma^4}{c^2}-\left\{k^2+\frac{4\Omega^2}{c^2}+i(\boldsymbol{k}\cdot\nabla\ln\rho)\right\}\sigma^2-\left\{\boldsymbol{k}\cdot[2\boldsymbol{\Omega}\times\nabla\ln(\rho/p^{2/\Gamma_1})]\right\}\sigma+\left\{N^2k_\perp^2+(2\boldsymbol{\Omega}\cdot\boldsymbol{k})^2+i(2\boldsymbol{\Omega}\cdot\boldsymbol{k})(2\boldsymbol{\Omega}\cdot\nabla\ln\rho)\right\}\right]=0, \tag{33.9}$$

where

$$N^2=\rho^{-1}\nabla p\cdot\boldsymbol{A} \tag{33.10}$$

denotes the square of the Brunt-Väisälä frequency and $\boldsymbol{k}_\perp$ denotes the horizontal component of the wave number vector which is perpendicular to the apparent gravity. In deriving equation (33.9), we have used the barotropic relation given by equation (32.37), which is consistent with the uniform rotation.

The orders of magnitude of the three terms in the first brace as the coefficient of σ^2 in equation (33.9) are $O(k^2)$, $O(\Omega^2/c^2)$, and $O(k/H_p)$, where H_p denotes the characteristic scale height of equilibrium

quantities. We suppose

$$k^2\gg\Omega^2/c^2\gg k/H_p, \tag{33.11}$$

which is justified in most cases in the stellar interior. Let ϵ be

$$\epsilon\equiv\frac{\Omega^2}{k^2c^2}, \tag{33.12}$$

and we suppose

$$\frac{1}{kH_p}\sim O(\epsilon^2). \tag{33.13}$$

The coefficient of σ^1 in equation (33.9) is dependent on the direction of the wavenumber vector, but it is, at maximum, of the order of $\epsilon^{3/2}k^3c$, and the three terms in the third brace in equation (33.9) are, at maximum, of the order of $N^2k^4c^2$, ϵk^4c^2, and $\epsilon^3k^4c^2$, respectively. The imaginary parts in the two brace brackets in equation (33.9) make the wavenumber $\boldsymbol{k}$ complex, which leads to a slow variation of amplitude of disturbance with depth corresponding to the density variation with depth (attenuation effect). According to the above assumption (33.11), this effect is small enough to neglect compared with the scale of perturbations. Whether the third term or the fourth term in the square bracket in equation (33.9) is larger is dependent on the direction of the wavenumber vector. Thus we retain both terms, though we neglect the last term in the third brace in equation (33.9).

In a limiting case of

$$|N^2k_\perp^2+(2\boldsymbol{\Omega}\cdot\boldsymbol{k})^2|\gg kc\left|\boldsymbol{k}\cdot[2\boldsymbol{\Omega}\times\ln(\rho/p^{2/\Gamma_1})]\right|, \tag{33.14}$$

equation (33.9) is reduced to

$$\sigma\left[\frac{\sigma^4}{c^2}-k^2\sigma^2+\{N^2k_\perp^2+(2\boldsymbol{\Omega}\cdot\boldsymbol{k})^2\}\right]=0. \tag{33.15}$$

Equation (33.15) leads to the following modes:

$$\sigma^2\simeq k^2c^2 \tag{33.16}$$

and

$$\sigma^2\simeq\frac{N^2k_\perp^2+(2\boldsymbol{\Omega}\cdot\boldsymbol{k})^2}{k^2}. \tag{33.17}$$

Equation (33.16) represents a pair of high-frequency acoustic modes, and equation (33.17) represents a pair of low-frequency modes related with rotation and buoyancy. We call the mode given by equation (33.17)

the inertia-gravity wave. In the case of $\Omega=0$, the inertia-gravity wave tends to a simple gravity wave:

$$\sigma^2=\frac{N^2k_\perp^2}{k^2} . \tag{33.18}$$

In the case of $N^2=0$, the inertia-gravity wave is reduced to

$$\sigma^2=\frac{(2\boldsymbol{\Omega}\cdot\boldsymbol{k})^2}{k^2} , \tag{33.19}$$

which is called the inertial wave. It should be noted that equation (33.17) describes oscillatory motion even if $N^2<0$ when $(2\boldsymbol{\Omega}\cdot\boldsymbol{k})^2$ is large enough.

In the other limiting case of

$$|N^2k_\perp^2+(2\boldsymbol{\Omega}\cdot\boldsymbol{k})^2|\ll kc\left|\boldsymbol{k}\cdot[2\boldsymbol{\Omega}\times\nabla\ln(\rho/p^{2/\Gamma_1})]\right| , \tag{33.20}$$

the inertia-gravity wave disappears. Instead, equation (33.9) leads to

$$\sigma^2\left[\frac{\sigma^3}{c^2}-\sigma k^2-\{\boldsymbol{k}\cdot[2\boldsymbol{\Omega}\times\nabla\ln(\rho/p^{2/\Gamma_1})]\}\right]\simeq 0. \tag{33.21}$$

This equation gives

$$\sigma^2\simeq c^2k^2 \tag{33.22}$$

and

$$\sigma\simeq-\frac{\boldsymbol{k}\cdot[2\boldsymbol{\Omega}\times\nabla\ln(\rho/p^{2/\Gamma_1})]}{k^2} . \tag{33.23}$$

The latter mode propagates in the direction of rotation (prograde), since $\nabla\ln(\rho/p^{2/\Gamma_1})$ is usually toward the stellar center throughout a star.

In general cases, the dispersion relation (33.9) provides a pair of high-frequency acoustic modes

$$\sigma^2\simeq k^2c^2+4\Omega^2 , \tag{33.24}$$

a pair of low-frequency modes with mixed characters of inertia-gravity wave and low-frequency prograde wave

$$\sigma\simeq-\frac{1}{2k^2}\left\{\boldsymbol{k}\cdot[2\boldsymbol{\Omega}\times\nabla\ln(\rho/p^{2/\Gamma_1})]\right\}$$
$$\pm\frac{1}{2k^2}\left[\left\{\boldsymbol{k}\cdot[2\boldsymbol{\Omega}\times\nabla\ln(\rho/p^{2/\Gamma_1})]\right\}^2+4k^2[N^2k_\perp^2+(2\boldsymbol{\Omega}\cdot\boldsymbol{k})^2]\right]^{1/2} , \tag{33.25}$$

and a unique zero-frequency mode. Equation (33.25) gives a pair of complex conjugate frequencies if N^2 is negative and $|N^2|$ is large enough, which are the overstable convection modes propagating in the direction of rotation of the star.

In the following subsections, we discuss the physical properties of each mode.

33.2 Zero-Frequency Mode : Geostrophic Motion

There always exists a zero-frequency mode, whose frequency measured in an inertial frame is the same as the rotation frequency of the star. In this case, equation (33.7) is reduced to

$$\boldsymbol{v}'\cdot\boldsymbol{A}=0 , \tag{33.26}$$

and this means that the motion is horizontal. Equation (33.6) leads to

$$\boldsymbol{k}\cdot\boldsymbol{v}'=0 . \tag{33.27}$$

The momentum equation (33.8) gives

$$[2\boldsymbol{\Omega}\times\boldsymbol{v}']_\perp=-\frac{1}{\rho}\nabla_\perp p' , \tag{33.28}$$

which means that the horizontal component of the Coriolis force is in balance with the horizontal gradient of pressure. This mode is called "geostrophic mode" or "geostrophic motion" in geophysics.

33.3 Inertial Wave

Pure inertial waves are waves in the homentropic fluid layer ($N^2=0$) whose restoring force comes from the Coriolis force. To discuss the physical properties, the Boussinesq approximation is convenient. In this approximation, equations (33.6) and (33.7) are shown to be

$$\boldsymbol{k}\cdot\boldsymbol{v}'=0 \tag{33.29}$$

and

$$i\sigma\frac{\rho'}{\rho}+\boldsymbol{v}'\cdot\boldsymbol{A}=0 , \tag{33.30}$$

respectively. Since we consider the homentropic layer,

$$\boldsymbol{A}=0 , \tag{33.31}$$

so that equation (33.30) means the Eulerian density perturbation is zero. Then the equation of motion is reduced to

$$\frac{D\boldsymbol{v}'}{Dt}=-2\boldsymbol{\Omega}\times\boldsymbol{v}'-i\frac{p'}{\rho}\boldsymbol{k} . \tag{33.32}$$

As easily seen from equation (33.29), the motion of the inertial wave is perpendicular to the wavenumber vector $\boldsymbol{k}$. Therefore, the scalar product of equation (33.32) and $\boldsymbol{v}'$ leads to

$$\boldsymbol{v}' \cdot \frac{D\boldsymbol{v}'}{Dt} = 0 \ , \tag{33.33}$$

which means that the direction of acceleration is perpendicular to the direction of motion. This indicates that the particle motion of the internal wave has a circular orbit.

33.4 Low-Frequency Prograde Wave

The characteristics of the mode given by equation (33.23) can clearly be seen in the case of

$$\boldsymbol{\Omega} \cdot \boldsymbol{k} = 0 \tag{33.34}$$

in a homentropic layer

$$\nabla S = 0 \ . \tag{33.35}$$

In this case, the nature of the wave in consideration is clearly separated from that of the inertial wave, and equation (33.23) gives

$$\sigma = -\frac{\boldsymbol{k} \cdot [2\boldsymbol{\Omega} \times \nabla \ln \rho]}{k^2} \ . \tag{33.36}$$

The mode given by equation (33.36) cannot be obtained from the dispersion relation derived with the use of the Boussinesq approximation. But if we adopt the anelastic approximation instead of the Boussinesq approximation, we can obtain it (Ando, 1989). This is because the density variation of a fluid element with its movement in the stratified medium is essential in the physical property of this mode. Ando (1985) and Ishibashi and Ando (1985, 1986) showed numerically the existence of such a mode even without anelastic approximation.

In the following, we discuss the dynamic property of this mode by examining the linearized vorticity equation (32.38). Since we assume the rotation is uniform, the second term of equation (32.38) disappears. We discard the third term of equation (32.38) by supposing the rotation is uniform and by discarding the curvature of the coordinates. Due to assumption (33.34), the fourth term of equation (32.38) is zero. With the help of equation (32.32), the sixth term of equation (32.38) is reduced to

$$\nabla \times (\rho^{-1} \nabla p)' = -\nabla T' \times \nabla S - \nabla T \times \nabla S' \ . \tag{33.37}$$

It becomes zero because of equation (33.35) and $S' = 0$ which is derived from the assumption of the adiabatic perturbation in the homentropic layer. Therefore, in the present situation, insofar as we approximate

$$(2\boldsymbol{\Omega} \cdot \nabla)\boldsymbol{v}' \simeq i(2\boldsymbol{\Omega} \cdot \boldsymbol{k})\boldsymbol{v}' , \tag{33.38}$$

the linearized vorticity equation is given by

$$\frac{D\omega_i'}{Dt}\boldsymbol{e}_i + (\nabla \cdot \boldsymbol{v}')2\boldsymbol{\Omega} = 0 \ . \tag{33.39}$$

In the case of uniform rotation, the Eulerian perturbation of vorticity is equal to its Lagrangian perturbation:

$$\delta\boldsymbol{\omega} \equiv \boldsymbol{\omega}' + (\boldsymbol{\xi} \cdot \nabla)2\boldsymbol{\Omega} = \boldsymbol{\omega}' \ . \tag{33.40}$$

Since

$$\nabla \cdot \boldsymbol{v}' = -d\ln\rho/dt \ , \tag{33.41}$$

where $d/dt \equiv \partial/\partial t + \boldsymbol{v} \cdot \nabla$ denotes the Lagrangian derivative, equation (33.39) gives

$$\frac{D\,\delta\omega_i}{Dt}\boldsymbol{e}_i - \frac{d\ln\rho}{dt}2\boldsymbol{\Omega} = 0 \ . \tag{33.42}$$

Using equation (33.42), we can understand the mechanism of this wave. If a fluid element at a point (say point A) on the equatorial plane moves toward the center, a positive vorticity is generated as a result of increase of density of the element. The flow associated with this vorticity pushes a fluid element at a point (say point B) just east (larger ϕ; the direction of the stellar rotation) of point A toward the center. As before, the element at point B attains a positive vorticity. The flow associated with the vorticity pushes a fluid element at a point (say point C) just east of point B toward the center, while it pushes the element of point A toward its original position. In this way, the restoring force is exerted to point A and the phase of perturbation propagates eastward from A, B, C, ... ; i.e., in the direction of the stellar rotation (Ishibashi and Ando, 1986). Thus, the mechanism of the wave generation is similar to the Rossby wave which will be discussed in the next subsection.

Therefore, it is concluded that the essential dynamic aspect of this mode is the conservation of vorticity. It is now quite clear why this mode cannot be retained in the Boussinesq approximation, in which the density variation is taken into account only in buoyancy, not in the variation of volume of a fluid element.

Equation (33.25) indicates that the real part of the frequency of overstable convection is the same as the frequency of the low frequency prograde wave considered in this subsection. Therefore, the nature of

propagation of overstable convection modes is caused by the conservation of vorticity as in the present case.

33.5 Rossby Wave

So far we have discarded the effect of curvature of the stratification. If we take it into account, a new type of wave appears, which is called the Rossby wave. The prototype of the Rossby wave is generated essentially by rotation and the curvature of the stratification. To make our discussion simpler, we consider a slowly and uniformly rotating spherical star, in which the centrifugal force is negligible. One way to extract purely rotational effect separated from gravity is to consider the radial component of vorticity associated with a motion on a level surface. The radial component of the linearized vorticity equation (32.38) is written as

$$i\sigma\frac{1}{r}\left(\frac{\partial v'_\phi}{\partial\theta}-\frac{1}{\sin\theta}\frac{\partial v'_\theta}{\partial\phi}\right)+2\Omega_r(\nabla\cdot\boldsymbol{v}')-[2\boldsymbol{\Omega}\cdot\nabla\boldsymbol{v}']_r=0. \quad (33.43)$$

We suppose that the vertical velocity is much smaller than the horizontal one; i.e.,

$$|v'_r|\ll|v'_\theta|,|v'_\phi| \ . \quad (33.44)$$

Furthermore, we use the Boussinesq approximation, which is a good approximation for a low-frequency wave:

$$\nabla\cdot\boldsymbol{v}'\simeq\frac{1}{r}\left(\frac{\partial v'_\theta}{\partial\theta}+\frac{1}{\sin\theta}\frac{\partial v'_\phi}{\partial\phi}\right)=0. \quad (33.45)$$

Under these conditions equation (33.43) is reduced to

$$i\sigma\frac{1}{r}\left(\frac{\partial v'_\phi}{\partial\theta}-\frac{1}{\sin\theta}\frac{\partial v'_\theta}{\partial\phi}\right)-\frac{2\Omega\sin\theta}{r}v'_\theta=0. \quad (33.46)$$

Since

$$\frac{d(2\Omega\cos\theta)}{dt}=(\boldsymbol{v}_0+\boldsymbol{v}')\cdot\nabla(2\Omega\cos\theta)=\frac{v'_\theta}{r}\frac{\partial(2\Omega\cos\theta)}{\partial\theta}$$
$$=-\frac{2\Omega\sin\theta v'_\theta}{r} \quad (33.47)$$

and the Lagrangian and the Eulerian perturbations of vorticity are the same in the case of uniform rotation as shown in equation (33.40), equation (33.46) can be written as

$$\frac{d}{dt}(\zeta+2\Omega\cos\theta)=0, \quad (33.48)$$

where the radial component of the Lagrangian perturbation of vorticity ζ is defined as

$$\zeta\equiv\delta\omega_r=\omega'_r=\frac{1}{r}\left(\frac{\partial v'_\phi}{\partial\theta}-\frac{1}{\sin\theta}\frac{\partial v'_\theta}{\partial\phi}\right). \quad (33.49)$$

Note that $\Omega\cos\theta$ is the radial component of the angular velocity of rotation and that $(\zeta+2\Omega\cos\theta)$ is the radial component of total vorticity seen in an inertial frame. Then equation (33.48) means that the radial component of vorticity is conserved with the motion.

Let us define a local Cartesian coordinate (x, y, z) as

$$dx=rd\theta,\ dy=r\sin\theta d\phi,\ dz=dr, \quad (33.50)$$

and

$$v'_x=v'_\theta,\ v'_y=v'_\phi,\ v'_z=v'_r. \quad (33.51)$$

In this coordinate system equations (33.45) and (33.46) are, respectively, written as

$$\frac{\partial v'_x}{\partial x}+\frac{\partial v'_y}{\partial y}=0 \quad (33.52)$$

and

$$i\sigma\left(\frac{\partial v'_y}{\partial x}-\frac{\partial v'_x}{\partial y}\right)+2\frac{\partial\Omega_z}{\partial x}v'_x=0, \quad (33.53)$$

where

$$\Omega_z\equiv\Omega\cos\theta. \quad (33.54)$$

Assuming that the spatial dependence of the wave is expressed as $\exp(ik_xx+ik_yy)$, we obtain from equations (33.52) and (33.53)

$$\sigma=-2\frac{\partial\Omega_z}{\partial x}\frac{k_y}{k_x^2+k_y^2}. \quad (33.55)$$

This gives the angular frequency of the "local" Rossby wave, which was first derived by Rossby (1939). In geophysics, the latitudinal derivative of the Coriolis parameter, $-2\partial\Omega_z/\partial x(=2\Omega\sin\theta)$, is called 'beta', and the approximation in which the 'beta' is treated as a constant is called 'beta-plane' approximation. We note that the Rossby wave cannot be obtained by simply replacing the curl of equation (33.8) by $[i\boldsymbol{k}\times(33.8)]$, because the geometric effect plays the essential role of the Rossby wave while such an operation misses the latitudinal dependence of the unit vector in the radial direction.

Equation (33.55) indicates that the Rossby wave is a retrograde (in

the co-rotating frame) wave generated by the latitudinal dependence of the vertical component of the angular velocity of rotation. The mechanism by which the Rossby wave is generated can be understood based on the conservation law in equation (33.48) as follows: Let us consider a series of points on a latitudinal line on the northern hemisphere ($0<\theta<\pi/2$). We call the points A, B, C, ... in the order of decreasing ϕ (or decreasing y) direction. Suppose that a fluid element at point A moved toward the pole of rotation (northward). According to equation (33.48), the element should get a negative value of ζ at the displaced position. Thus generated flow (whirl) pushes the fluid element at point B northward. Then, a negative ζ is generated at the position displaced from point B as at the element from point A. The flow generated around B pushes point C northward and pushes point A southward. The latter effect works as the restoring force for point A. In this way the Rossby wave is generated and its phase propagates in the decreasing ϕ direction; that is, it retrogrades in the co-rotating frame.

The angular frequency of the global Rossby wave can be obtained by introducing the stream function ψ such that

$$v'_\theta \equiv -\frac{1}{r\sin\theta}\frac{\partial\psi}{\partial\phi} \tag{33.56}$$

and

$$v'_\phi \equiv \frac{1}{r}\frac{\partial\psi}{\partial\theta}. \tag{33.57}$$

The velocity fields given above satisfy equation (33.45) automatically. Substituting equations (33.56) and (33.57) into equation (33.46), we obtain

$$i\sigma\nabla_1^2\psi+\frac{2\Omega}{r^2}\frac{\partial\psi}{\partial\phi}=0. \tag{33.58}$$

If the angular dependence of the stream function ψ is given by a spherical harmonic, $Y_l^m(\theta,\phi)$, equation (33.58) yields

$$\sigma=\frac{2m\Omega}{l(l+1)}. \tag{33.59}$$

This corresponds to the r-mode discussed in Section 19.3. The exact analogy between equations (33.55) and (33.59) becomes apparent when we recognize that $l(l+1)$ and m correspond to $k_x^2+k_y^2$ and $k_y\sin\theta$, respectively. This confirms that the cause of the r-mode is the same as that of the prototype Rossby wave.

We note here that the conservation of the specific total vorticity

plays an essential role in generating both the prototype Rossby wave and the low-frequency prograde wave discussed in the previous subsection. The restoring force arises due to the latitudinal dependence of the vertical component of the equilibrium vorticity for the former wave, and it is due to the density stratification of the equilibrium state for the latter mode. In this sense, the low-frequency prograde wave discussed in the previous subsection is sometimes called the "generalized Rossby wave" in geophysics.

34. Global Analysis

One of the conspicuous effects of rotation on the global nonradial oscillations is the well-known m-splitting of the oscillation frequency, in which an oscillation frequency designated by (n,l) in a nonrotating star is split into equally spaced $(2l+1)$ frequencies in the existence of rotation (Section 19). The m-splitting is derived as the first-order term in a perturbation analysis, in which the ratio of the rotational angular frequency to the pulsation angular frequency (in the co-rotating frame), Ω/σ_c, is assumed to be much smaller than unity. (In the following part of this chapter, the subscript c is attached to oscillation frequencies in the co-rotating frame.) Extending such an analysis to the second order is straightforward but very complex (Chlebowsky, 1978; Saio, 1981; Smeyers and Martens, 1983; Martens and Smeyers, 1986) because the effect of deformation of the equilibrium structure due to the centrifugal force may be the same order of $(\Omega/\sigma_c)^2$. The fraction of the rotational deformation of the equilibrium structure is on the order of $\Omega^2/(GM/R^3)$. Since the frequencies of the p-modes are larger than $(GM/R^3)^{1/2}$ (see Section 14), the effect of the deformation must be included in the second-order analysis for the p-modes. If the second-order effect is included, the frequencies are not equally spaced even in the case of uniform rotation, while the first-order effect leads to an unequally spaced m-splitting only if the rotation frequency has a latitudinal dependence (Section 19; Hansen, Cox, and Van Horn, 1977). In the case of $\Omega/\sigma_c \gtrsim 1$, a perturbation analysis is not applicable, for which rotation makes qualitative modifications in the properties of the nonradial pulsations. For example, the angular dependence of the variations of a nonradial oscillation mode cannot be described by a single spherical harmonic, $Y_l^m(\theta,\phi)$. In other words, a pulsation mode in a rotating star cannot be referred to by a set of (l,m). In this section we discuss such low-frequency adiabatic nonradial pulsations of rotating stars.

34.1 Differential Equations

We use spherical harmonics $Y_l^m(\theta,\phi)$ to describe the θ- and ϕ-dependence of the perturbations. Then, only m-value can be assigned; in other words, only the ϕ-dependence, $\exp(im\phi)$, can be assumed. For a given value of m, the perturbed quantities should be expressed by a summation of the components which are proportional to $Y_l^m(\theta,\phi)$ with $l \geq |m|$. We write the displacement vector $\boldsymbol{\xi}$ for a nonradial oscillation mode with a given m as

$$\frac{\boldsymbol{\xi}}{r}=\sum_{l=|m|}^{l=\infty}\left\{\mathbf{e}_r\Xi_l(r)+\mathbf{e}_\theta\left[H_l(r)\frac{\partial}{\partial\theta}+T_l(r)\frac{1}{\sin\theta}\frac{\partial}{\partial\phi}\right]\right.$$

$$\left.+\mathbf{e}_\phi\left[H_l(r)\frac{1}{\sin\theta}\frac{\partial}{\partial\phi}-T_l(r)\frac{\partial}{\partial\theta}\right]\right\}Y_l^m(\theta,\phi)\exp(i\sigma t), \quad (34.1)$$

where $\mathbf{e}_r$, $\mathbf{e}_\theta$, and $\mathbf{e}_\phi$ are the unit vectors in r-, θ-, and ϕ-directions, respectively, and σ represents the angular freqency of oscillation seen in an inertial frame. The terms proportional to $H_l(r)$ and $T_l(r)$ are, respectively, the spheroidal and the toroidal components of the horizontal motion. The perturbation of any scalar quantity, $f'(r,\theta,\phi,t)$, is expressed as

$$f'(r,\theta,\phi,t)=\sum_{l=|m|}^{l=\infty}f_l'(r)Y_l^m(\theta,\phi)\exp(i\sigma t). \quad (34.2)$$

For low-frequency oscillations ($\sigma_c<\sqrt{GM/R^3}$), the effect of the deformation of the equilibrium structure [$\propto\Omega^2/(GM/R^3)$] is small compared to the terms proportional to $(\Omega/\sigma_c)^2$ which originate from the Coriolis force. Therefore, we can assume that the equilibrium structure is spherically symmetric. Moreover, we assume that the angular velocity of rotation Ω is a function only of the distance from the stellar center. To describe adiabatic nonradial oscillations, we use the continuity equation (32.15), the momentum equation (32.17), the Poisson equation (32.19), and the adiabatic relation obtained from equation (32.20) by setting $\delta S=0$. In treating the horizontal components of the momentum equation, it is more convenient to use the equation obtained by taking the divergence in the θ- and ϕ-directions of equation (32.17) [i.e., $\nabla_\perp\cdot$(32.17)] and the equation for the radial component of vorticity [i.e., the r-component of equation (32.38)] rather than using equation (32.17) itself for the horizontal components. If we substitute equations (34.1) and (34.2) into those equations, we obtain a set of equations which contain not only terms whose θ- and ϕ-dependences are expressed by $Y_l^m(\theta,\phi)$ but also terms proportional to $\cos\theta Y_l^m(\theta,\phi)$ or $\sin\theta\partial Y_l^m(\theta,\phi)/\partial\theta$, etc. To treat the latter terms, the following relations

of spherical harmonics are useful:

$$\sin\theta\frac{\partial Y_l^m(\theta,\phi)}{\partial\theta}=lJ_{l+1}^m Y_l^m(\theta,\phi)-(l+1)J_l^m Y_{l-1}^m(\theta,\phi) \quad (34.3)$$

and

$$\cos\theta Y_l^m(\theta,\phi)=J_{l+1}^m Y_{l+1}^m(\theta,\phi)+J_l^m Y_{l-1}^m(\theta,\phi), \quad (34.4)$$

where

$$J_l^m=\begin{cases}\left[\dfrac{l^2-m^2}{(4l^2-1)}\right]^{1/2}, & \text{if } l>|m|;\\ 0, & \text{if } l\leq|m|.\end{cases} \quad (34.5)$$

We define the variables y_i^l's ($i=1, 2, 3, 4$) as

$$y_1^l=\Xi_l(r),\ y_2^l=\frac{1}{gr}\left(\frac{p_l'}{\rho}+\Phi_l'\right),\ y_3^l=\frac{\Phi_l'}{gr},\ y_4^l=\frac{1}{g}\frac{d\Phi_l'}{dr}, \quad (34.6)$$

where the variables with superscript or subscript l represent the radial variations of the terms proportional to $Y_l^m(\theta,\phi)$ [see equations (34.1) and (34.2)]. Then, the governing equations for low frequency nonradial oscillations of a rotating star are written in the form of the following infinitely coupled differential equations:

$$\frac{dy_1^l}{d\ln r}=(V_g-3)y_1^l-V_g(y_2^l-y_3^l)+l(l+1)H_l, \quad (34.7)$$

$$\frac{dy_2^l}{d\ln r}=\left\{c_1\omega_c^2+rA-c_1\frac{d\hat{\Omega}^2}{d\ln r}[1-(J_{l+1}^m)^2-(J_l^m)^2]\right\}y_1^l+(1-U-rA)y_2^l$$

$$+rAy_3^l-2mc_1\omega_c\hat{\Omega}H_l-2ic_1\omega_c\hat{\Omega}[(l-1)J_l^m T_{l-1}-(l+2)J_{l+1}^m T_{l+1}]$$

$$+c_1\frac{d\hat{\Omega}^2}{d\ln r}(J_{l-1}^m J_l^m y_1^{l-2}+J_{l+2}^m J_{l+1}^m y_1^{l+2}), \quad (34.8)$$

$$[l(l+1)-m\eta]H_l-i\eta[T_{l-1}(l^2-1)J_l^m+iT_{l+1}l(l+2)J_{l+1}^m]$$

$$=\left\{m\eta+\frac{1}{\omega_c^2}\frac{d\hat{\Omega}^2}{d\ln r}[1-(l+3)(J_{l+1}^m)^2+(l-2)(J_l^m)^2]\right\}y_1^l$$

$$+l(l+1)\frac{y_2^l}{c_1\omega_c^2}-\frac{1}{\omega_c^2}\frac{d\hat{\Omega}^2}{d\ln r}[(l+1)J_{l-1}^m J_l^m y_1^{l-2}$$

$$-lJ_{l+2}^m J_{l+1}^m y_1^{l+2}], \quad (34.9)$$

$$i[(l+1)(l+2)-m\eta]T_{l+1}-\eta[l(l+2)J^m_{l+1}H_l+(l+1)(l+3)J^m_{l+2}H_{l+2}]$$

$$=-\eta[(l+2)J^m_{l+1}y^l_1-(l+1)J^m_{l+2}y^{l+2}_1]+\frac{m}{\omega_c^2}\frac{d\hat{\Omega}^2}{d\ln r}(J^m_{l+1}y^l_1+J^m_{l+2}y^{l+2}_1), \tag{34.10}$$

$$\frac{dy^l_3}{d\ln r}=(1-U)y^l_3+y^l_4, \tag{34.11}$$

and

$$\frac{dy^l_4}{d\ln r}=-rAUy^l_1+V_gUy^l_2+[l(l+1)-V_gU]y^l_3-Uy^l_4, \tag{34.12}$$

where i is the imaginary unit, $\hat{\Omega}$ is the dimensionless rotation frequency defined by

$$\hat{\Omega}=\Omega\sqrt{R^3/GM}, \tag{34.13}$$

ω_c denotes the dimensionless oscillation frequency in the frame rotating with Ω given by

$$\omega_c\equiv\omega+m\hat{\Omega}, \tag{34.14}$$

and η is defined by

$$\eta=\frac{2\Omega}{\sigma_c}=\frac{2\hat{\Omega}}{\omega_c}. \tag{34.15}$$

We note that equations (34.9) and (34.10) are algebraic equations originating from the momentum equations for horizonontal motion. If there is no rotation ($\Omega=0$), equations (34.9) and (34.10) are reduced to $H_l=y^l_2/(c_1\omega^2)$ and $T_{l+1}=0$, respectively. In this case the variables belonging to each of l are decoupled from others, so that equations (34.7), (34.8), (34.11), and (34.12) are reduced to usual equations of adiabatic nonradial oscillations (18.14)–(18.17) for y^l_1, y^l_2, y^l_3, and y^l_4.

For a finite rotational angular frequency Ω, equation (34.8) indicates that the spheroidal components associated with l couple with toroidal components $T_{l\pm1}$. Furthermore, equations (34.9) and (34.10) indicate that the toroidal components $T_{l\pm1}$ couple with the spheroidal components associated with l and $l\pm2$. Thus, we have two independent sets of infinitely coupled equations; one consists of the spheroidal variables, $\{y^l_i(i=1, 2, 3, 4)\}$ and $\{H_l\}$, and the toroidal components $\{T_{l+1}\}$ associated with $l=|m|, |m|+2, \ldots$; and the other set consists of

the spheroidal variables $\{y^l_i(i=1, 2, 3, 4)\}$ and $\{H_l\}$, and the toroidal components $\{T_{l-1}\}$ associated with $l=|m|+1, |m|+3, \ldots$. We call, for the sake of convenience, the former even-modes and the latter odd-modes. We note that the r- and ϕ-components of displacement vector, ξ_r and ξ_ϕ, are symmetric to the equator and the θ-component, ξ_θ, is antisymmetric for even modes, while ξ_r and ξ_ϕ are antisymmetric and ξ_θ symmetric for odd modes.

In the following discussions we assume, for simplicity, that rotation is uniform ($\Omega=$ constant) and that the Eulerian perturbation of the gravitational potential is negligible (the Cowling approximation). Let us introduce the column vectors with infinite dimensions, $\boldsymbol{Y}_1$, $\boldsymbol{Y}_2$, $\boldsymbol{H}$, and $\boldsymbol{T}$, whose j-th ($j=1,2,\ldots,\infty$) elements are given by y^l_1, y^l_2, H_l, and $T_{l'}$, respectively, where

$$\begin{cases} l=|m|+2(j-1), & l'=|m|+2j-1 \quad \text{for even modes;} \\ l=|m|+2j-1, & l'=|m|+2(j-1) \quad \text{for odd modes.} \end{cases} \tag{34.16}$$

Then equations (34.7)–(34.10) are written in slightly simpler forms:

$$\frac{d\boldsymbol{Y}_1}{d\ln r}=(V_g-3)\boldsymbol{Y}_1-V_g\boldsymbol{Y}_2+\boldsymbol{\Lambda H}, \tag{34.17}$$

$$\frac{d\boldsymbol{Y}_2}{d\ln r}=(c_1\omega_c^2+rA)\boldsymbol{Y}_1+(1-U-rA)\boldsymbol{Y}_2-2mc_1\omega_c\hat{\Omega}\boldsymbol{H}-2ic_1\omega_c\hat{\Omega}\boldsymbol{C}\,\boldsymbol{T}, \tag{34.18}$$

$$\boldsymbol{LH}-i\eta\tilde{\boldsymbol{M}}\,\boldsymbol{T}=\frac{\boldsymbol{Y}_2}{c_1\omega_c^2}+m\eta\boldsymbol{\Lambda}^{-1}\boldsymbol{Y}_1, \tag{34.19}$$

and

$$-\eta\boldsymbol{MH}+i\tilde{\boldsymbol{L}}\boldsymbol{T}=-\eta\boldsymbol{KY}_1. \tag{34.20}$$

The j-th elements ($j=1,2,\ldots,\infty$) of the diagonal matrices $\boldsymbol{\Lambda}$, $\boldsymbol{L}$, $\tilde{\boldsymbol{L}}$, are given by

$$\left.\begin{aligned} &\Lambda_{jj}=l(l+1), \quad L_{jj}=1-\frac{m\eta}{l(l+1)}, \\ &\tilde{L}_{jj}=\begin{cases} 1-\dfrac{m\eta}{(l+1)(l+2)} & \text{for even modes;} \\ 1-\dfrac{m\eta}{l(l-1)} & \text{for odd modes.} \end{cases} \end{aligned}\right\} \tag{34.21}$$

The non-zero elements of the infinite bi-diagonal matrices $\boldsymbol{C}$, $\boldsymbol{K}$, $\boldsymbol{M}$, and $\tilde{\boldsymbol{M}}$ are defined by

$$\left.\begin{aligned} &C_{jj}=-(l+2)J^m_{l+1}, \quad C_{(j+1)j}=(l+1)J^m_{l+2}, \\ &K_{jj}=\frac{J^m_{l+1}}{l+1}, \qquad K_{j(j+1)}=-\frac{J^m_{l+2}}{l+2}, \\ &M_{jj}=\frac{l}{l+1}J^m_{l+1}, \quad M_{j(j+1)}=\frac{l+3}{l+2}J^m_{l+2}, \\ &\tilde{M}_{jj}=\frac{l+2}{l+1}J^m_{l+1}, \quad \tilde{M}_{(j+1)j}=\frac{l+1}{l+2}J^m_{l+2} \end{aligned}\right\} \text{for even modes,} \quad (34.22)$$

and

$$\left.\begin{aligned} &C_{jj}=(l+1)J^m_l, \quad C_{j(j+1)}=-(l+2)J^m_{l+1}, \\ &K_{jj}=-\frac{J^m_l}{l}, \qquad K_{(j+1)j}=\frac{J^m_{l+1}}{l+1}, \\ &M_{jj}=\frac{l+1}{l}J^m_l, \quad M_{(j+1)j}=\frac{l}{l+1}J^m_{l+1}, \\ &\tilde{M}_{jj}=\frac{l-1}{l}J^m_l, \quad \tilde{M}_{j(j+1)}=\frac{l+2}{l+1}J^m_{l+1} \end{aligned}\right\} \text{for odd modes.} \quad (34.23)$$

The usual boundary conditions for adiabatic nonradial pulsations (Sections 12.2, 16.1) may be used; i.e., ξ is regular at the center, and $\delta p=0$ at the surface. In a numerical analysis, a truncated system of the above infinite series of differential equations is solved with the boundary conditions as an eigenvalue problem. We note, however, that a different approach is also possible using a general variational principle (Clement, 1986; Unno and Saio, 1987).

34.2 Numerical Analysis for g- and r-Modes

In order to calculate eigenfrequencies and eigenfunctions we have to truncate the infinite series of terms in equations (34.1) and (34.2). Here, we use a drastic truncation for the sake of simplicity by taking into account only the first two components for each mode. In other words, we assume that the angular dependence of perturbed quantities is approximately represented by a linear combination of two spherical

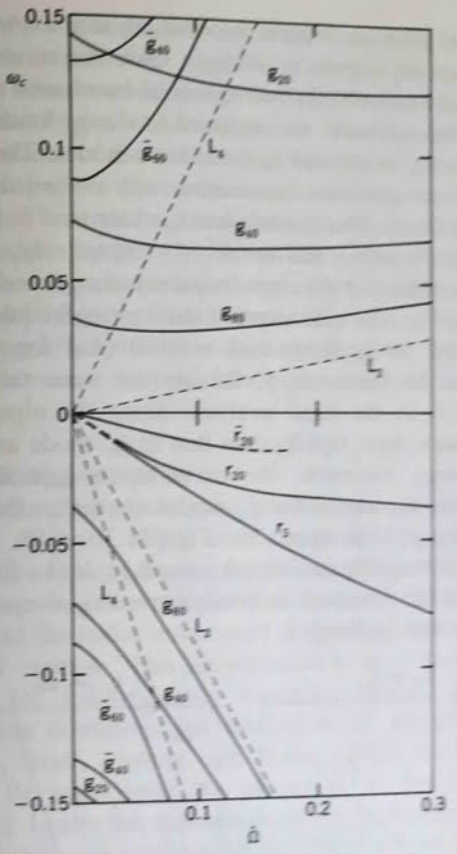

Fig. 34.1 Dimensionless eigenfrequencies in the co-rotating frame for even modes with $m=-2$ are plotted as functions of the rotation frequency. The dashed lines labeled L_2 and L_4 are asymptotic lines for the g_m-modes and the $\tilde{g}_m$-modes, respectively (taken from Lee and Saio, 1987a).

harmonics; i.e., the spheroidal variables associated with $Y^m_{|m|}$ and $Y^m_{|m|+2}$ and toroidal components associated with $Y^m_{|m|+1}$ and $Y^m_{|m|+3}$ are included in an even mode, and the spheroidal variables associated with $Y^m_{|m|+1}$ and $Y^m_{|m|+3}$ and the toroidal components associated with $Y^m_{|m|}$ and $Y^m_{|m|+2}$ are included in an odd mode.

A sample of numerical results is given in Fig. 34.1 for even modes with $m=-2$ of a $10M_\odot$ zero-age main-sequence model (Lee and Saio, 1987a). In this figure, dimensionless angular frequencies of g- and r-modes in the co-rotating frame are shown as functions of the dimensionless rotation angular frequency, $\hat{\Omega}$. There are two series for each type of mode. This corresponds to the fact that in the absence of

rotation, there exist an infinite number of series corresponding to different l values for a given m ($l \geq |m|$). Only two series appear in the numerical result because only two spherical harmonics are included in this analysis. We call these two series of modes g_n-mode and $\tilde{g}_n$-mode for g-modes and r_n-mode and $\tilde{r}_n$-mode for r-modes. The g_n-mode and $\tilde{g}_n$-mode tend to g_n-modes associated with $l=|m|$ and $l=|m|+2$, respectively, as $\Omega \to 0$. The r_n-mode and $\tilde{r}_n$-mode tend to toroidal modes associated with $l=|m|+1$ and $l=|m|+3$, respectively, as $\Omega \to 0$.

In a non-rotating star the eigenfrequency of a g_n-mode tends to zero as $n \to \infty$, while Fig. 34.1 indicates that the limiting frequency is not zero but $\sim 0.1\hat{\Omega}$ (L_2) for g_n-mode and $\sim 1.05\hat{\Omega}$ (L_4) for $\tilde{g}_n$-mode. This corresponds to the existence of the inertial wave term $(2\boldsymbol{\Omega}\cdot\boldsymbol{k})^2$ in equation (33.17) in the local analysis. Since the eigenfrequency of $\tilde{g}_n$-mode increases more rapidly than that of $g_{n'}$-mode as the rotational angular frequency increases, the curve for a $\tilde{g}_n$-mode in the ($\hat{\Omega}$, ω_c)-plane crosses the curves for $g_{n'}$-modes. Actually, the crossings are "avoided crossings," as shown in Fig. 34.2, which magnifies the crossings of two prograde modes: (a) g_{20} and $\tilde{g}_{40}$ at $\hat{\Omega} \simeq 0.03$, and (b) g_{20} and $\tilde{g}_{60}$ at $\hat{\Omega} \simeq 0.085$. Through an avoided crossing, the properties of the normal modes are exchanged.

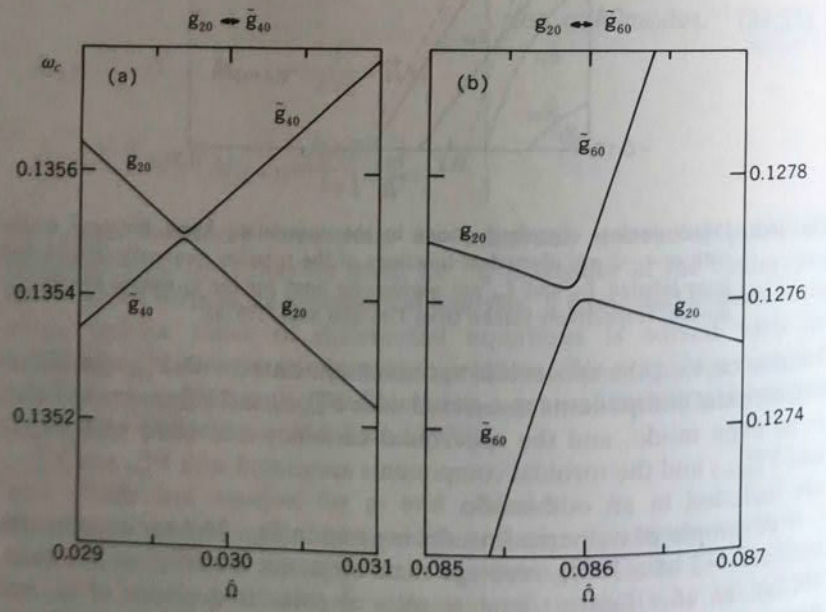

Fig. 34.2 Large-scale views of selected regions of Fig. 34.1 to show the avoided crossings (a) between g_{20} and $\tilde{g}_{40}$ and (b) between g_{20} and $\tilde{g}_{60}$ (taken from Lee and Saio, 1987a).

The r-modes are retrograde waves in the co-rotating frame; i.e., the eigenfrequency is negative for negative m. In the limit of $\hat{\Omega} \to 0$, the frequency of an r-mode tends to $\omega_0 \equiv 2m\hat{\Omega}/[l'(l'+1)]$, where $l'=|m|+1$ for an r_n-mode and $l'=|m|+3$ for an $\tilde{r}_n$-mode. The limiting frequency for $\hat{\Omega} \to 0$ is independent of the radial wave number n (see section 19.3). The absolute value of the eigenfrequency for a finite rotation frequency is less than $|\omega_0|$. This trend is consistent with the numerical results of perturbation analysis by Provost, Berthomieu, and Rocca (1981) and Saio (1982). Since in our discussion the effect of deformation of the equilibrium model due to rotation is neglected, the true value of $|\omega_c|$ for r_5 is probably larger than the value shown in Fig. 34.2. The effect of the deformation is, however, very small for higher overtone modes (Provost et al., 1981).

34.3 Traditional Approximation

The term "traditional approximation" is often used in the literature of geophysics (e.g., Eckart, 1960). In this approximation the horizontal component of the angular velocity of rotation, $-\Omega \sin\theta \boldsymbol{e}_\theta$, is neglected. Physically, this means that we neglect the Coriolis force associated with radial motion and the radial component of the Coriolis force associated with horizontal motion. This approximation is a reasonably good approximation for low-frequency nonradial modes, in which the horizontal motion dominates the oscillation. In astrophysics, Berthomieu, Gonczi, Graff, Provost, and Rocca (1978) reached the same approximation by considering the properties of the low frequency nonradial modes. Under this approximation the governing equations for nonradial oscillations are considerably simplified and can be reduced to forms similar to the equations for a non-rotating spherical star. Thus, employing the traditional approximation helps us to understand the qualitative character of nonradial oscillations of a rotating star. However, we must keep in mind that this approximation can cause some difficulty near the stellar center, where the radial motion is comparable with the horizontal motion even for low frequency modes.

34.3.1 Equations

The last two terms in equation (34.18) arise from the radial component of the Coriolis force associated with the horizontal motions. The last terms of equations (34.19) and (34.20) arise from the horizontal components of the Coriolis force associated with the radial component of velocity. These four terms are discarded in the traditional approximation. Thus, under the traditional approximation, equations (34.17)–(34.20) are reduced to

$$\frac{d\boldsymbol{Y}_1}{d\ln r}=(V_g-3)\boldsymbol{Y}_1+\left(\frac{\boldsymbol{W}}{c_1\omega_c^2}-V_g\right)\boldsymbol{Y}_2, \tag{34.24}$$

$$\frac{d\boldsymbol{Y}_2}{d\ln r}=(c_1\omega_c^2+rA)\boldsymbol{Y}_1+(1-U-rA)\boldsymbol{Y}_2, \tag{34.25}$$

$$\boldsymbol{H}=\boldsymbol{\Lambda}^{-1}\boldsymbol{W}\frac{\boldsymbol{Y}_2}{c_1\omega_c^2}, \tag{34.26}$$

and

$$i\,\boldsymbol{T}=\eta\bar{\boldsymbol{L}}^{-1}\boldsymbol{M}\boldsymbol{H}, \tag{34.27}$$

where $\boldsymbol{W}$ is a symmetric tridiagonal matrix defined by

$$\boldsymbol{W}=\boldsymbol{\Lambda}(\boldsymbol{L}-\eta^2\bar{\boldsymbol{M}}\bar{\boldsymbol{L}}^{-1}\boldsymbol{M})^{-1}, \tag{34.28}$$

or the elements of the matrix $\boldsymbol{W}^{-1}$ are given by

$$(\boldsymbol{W}^{-1})_{jj}=\frac{1}{l(l+1)}\left\{1-\frac{m\eta}{l(l+1)}-\frac{\eta^2(l^2-1)(J_l^m)^2}{l^2[1-\frac{m\eta}{l(l-1)}]}\right.$$

$$\left.-\frac{\eta^2 l(l+2)(J_{l+1}^m)^2}{(l+1)^2[1-\frac{m\eta}{(l+1)(l+2)}]}\right\}, \tag{34.29}$$

and

$$(\boldsymbol{W}^{-1})_{j(j+1)}=(\boldsymbol{W}^{-1})_{(j+1)j}=-\eta^2 J_{l+1}^m J_{l+2}^m/[(l+1)(l+2)-m\eta], \tag{34.30}$$

where the relation between j and l is given by equation (34.16). To the first order in $\hat{\Omega}/\omega_c$ the j-th diagonal element of the matrix $\boldsymbol{W}$ is $l(l+1)+m\eta$. The off-diagonal elements consist of the terms of the order of $(\hat{\Omega}/\omega_c)^2$, which cause coupling among the terms proportional to $Y_l^m(\theta,\phi)$ with different l [see equations (34.1) and (34.2)]. This shows that expanding the perturbation in spherical harmonics $Y_l^m(\theta,\phi)$ is not the best way for nonradial pulsations with $\hat{\Omega}/\omega_c \gtrsim 1$. It is more convenient to change the basis, which will bring the matrix $\boldsymbol{W}$ into a diagonal matrix and lead to a decoupled system of equations.

Let $\boldsymbol{B}$ be the matrix which diagonalizes the matrix $\boldsymbol{W}$. Since the matrix $\boldsymbol{W}$ is a symmetric real matrix for a real pulsation frequency, $\boldsymbol{B}$ is a unitary matrix; i.e., ${}^t\boldsymbol{B}\boldsymbol{B}=\boldsymbol{I}$, where ${}^t\boldsymbol{B}$ $(=\boldsymbol{B}^{-1})$ and $\boldsymbol{I}$ stand for the transposed matrix of $\boldsymbol{B}$ and the identity matrix with infinite dimensions, respectively. Multiplying equations (34.24) and (34.25) by $\boldsymbol{B}^{-1}$ from the left, we obtain

$$\frac{d\boldsymbol{Z}_1}{d\ln r}=(V_g-3)\boldsymbol{Z}_1+\left(\frac{\boldsymbol{D}}{c_1\omega_c^2}-V_g\right)\boldsymbol{Z}_2, \tag{34.31}$$

and

$$\frac{d\boldsymbol{Z}_2}{d\ln r}=(c_1\omega_c^2+rA)\boldsymbol{Z}_1+(1-U-rA)\boldsymbol{Z}_2, \tag{34.32}$$

where

$$\boldsymbol{Z}_1=\boldsymbol{B}^{-1}\boldsymbol{Y}_1 \quad \text{and} \quad \boldsymbol{Z}_2=\boldsymbol{B}^{-1}\boldsymbol{Y}_2, \tag{34.33}$$

and the matrix $\boldsymbol{D}$ is the diagonal matrix given by

$$\boldsymbol{D}=\boldsymbol{B}^{-1}\boldsymbol{W}\boldsymbol{B}. \tag{34.34}$$

Writing the j-th components of the column vecotors $\boldsymbol{Z}_1$ and $\boldsymbol{Z}_2$ as Z_1^j and Z_2^j, respectively, we rewrite equations (34.31) and (34.32) as

$$\frac{dZ_1^j}{d\ln r}=(V_g-3)Z_1^j+\left(\frac{\lambda_j^{(m)}}{c_1\omega_c^2}-V_g\right)Z_2^j \tag{34.35}$$

and

$$\frac{dZ_2^j}{d\ln r}=(c_1\omega_c^2+rA)Z_1^j+(1-U-rA)Z_2^j\,, \tag{34.36}$$

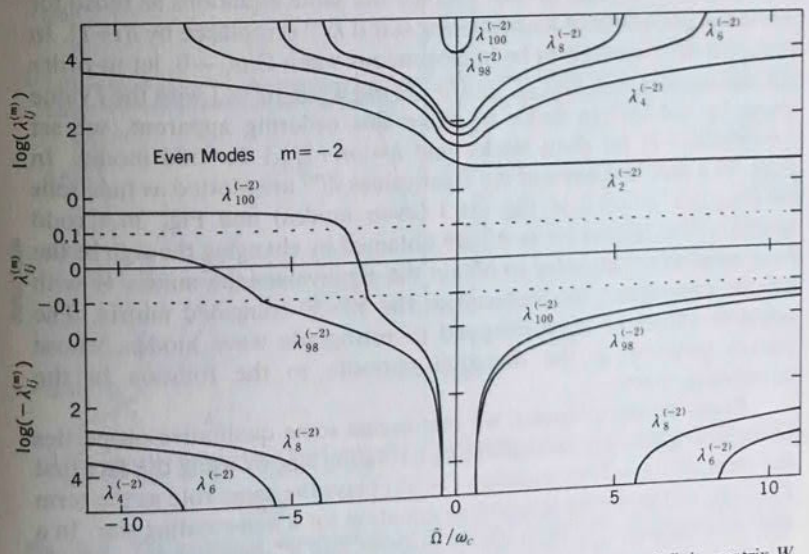

Fig. 34.3 Some eigenvalues $\lambda_j^{(m)}$ of 50×50 truncated matrix for the infinite matrix W are shown as functions of $\hat{\Omega}/\omega_c$ for even modes with $m=-2$. Here, $l_j=2j$.

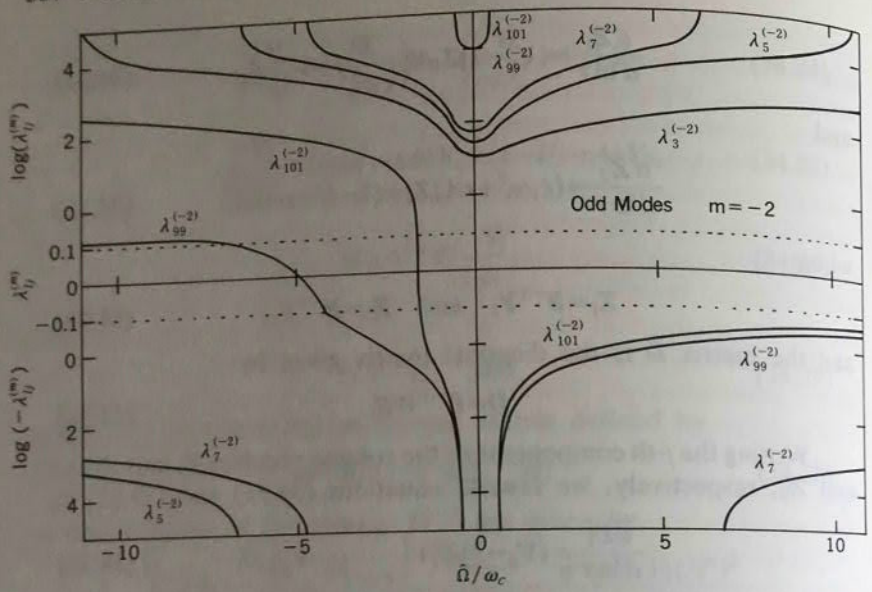

Fig. 34.4 Same as Fig. 34.3 but for odd modes with $m=-2$. Here, $l_j=2j+1$.

where $\lambda_j^{(m)}$ denotes the j-th eigenvalue of the diagonal matrix $\boldsymbol{D}$ with $l_j=|m|+2(j-1)$ for even modes and $l_j=|m|+2j-1$ for odd modes. Equations (34.35) and (34.36) become the same equations as those for nonradial pulsations of a nonrotating star if $\lambda_j^{(m)}$ is replaced by $l(l+1)$. In order for the notations to be homogeneous when $\hat{\Omega}/\omega_c\to 0$, let us order the eigenvalues such that $\lambda_j^{(m)}\approx l(l+1)+m\eta$ when $|\eta|\ll 1$ with the l value given by (34.16). In order to make this ordering apparent, we set $l_j=|m|+2(j-1)$ for even modes and $l_j=|m|+2j-1$ for odd modes. In Figs. 34.3 and 34.4 some of the eigenvalues $\lambda_j^{(m)}$ are plotted as functions of $\hat{\Omega}/\omega_c$ for $m=-2$ in Fig. 34.3 (even modes) and Fig. 34.4 (odd modes). (The figures for $m=2$ are obtained by changing the sign of the horizontal axis.) In order to obtain the eigenvalues the matrix $\boldsymbol{W}$ with infinite dimensions was reduced to the 50×50 truncated matrix. The negative values of ω_c correspond to retrograde wave modes, whose phases progress in the direction opposite to the rotation in the co-rotating frame.

Based on these figures, we can discuss some qualitative properties of the low-frequency oscillations of a rotating star by using the fact that the term $\lambda_j^{(m)}/(c_1\omega_c^2)$ in equation (34.35) plays the same role as the term $l(l+1)/(c_1\omega^2)$ in the corresponding equation for a non-rotating star. In a non-rotating star $l(l+1)$ is always positive and g$^+$-modes have positvie ω^2 while g$^-$-modes (convective modes) have negative ω^2 (i.e., ω is purely imaginary). For low-frequency oscillations of a rotating star,

positive values of $\lambda_j^{(m)}$ give g$^+$-modes similar to the usual g$^+$-modes of non-rotating stars, while the existence of negative values of $\lambda_j^{(m)}$ makes it possible for g$^-$-modes to have real frequency ($\omega_c^2>0$). This may be understood as meaning that rotation completely stabilizes some convective modes [see equation (33.17)]. For $\hat{\Omega}/\omega_c>0$, the change of sign of a $\lambda_j^{(m)}$ occurs through a singular point. The value of $\hat{\Omega}/\omega_c$ at the singular point is smaller for the eigenvalue $\lambda_j^{(m)}$ with larger j. In the negative region of $\hat{\Omega}/\omega_c$, $\lambda_j^{(m)}$ changes its sign twice, once through a singular point and once through zero. The zero points of $\lambda_j^{(m)}$'s are due to the poles of the elements of the matrix $\boldsymbol{W}^{-1}$ [equations (34.29) and (34.30)]. These points correspond to the largest frequencies of r-modes (global Rossby waves), $|2m\Omega/[l'(l'+1)]|$, for the toroidal velocity fields

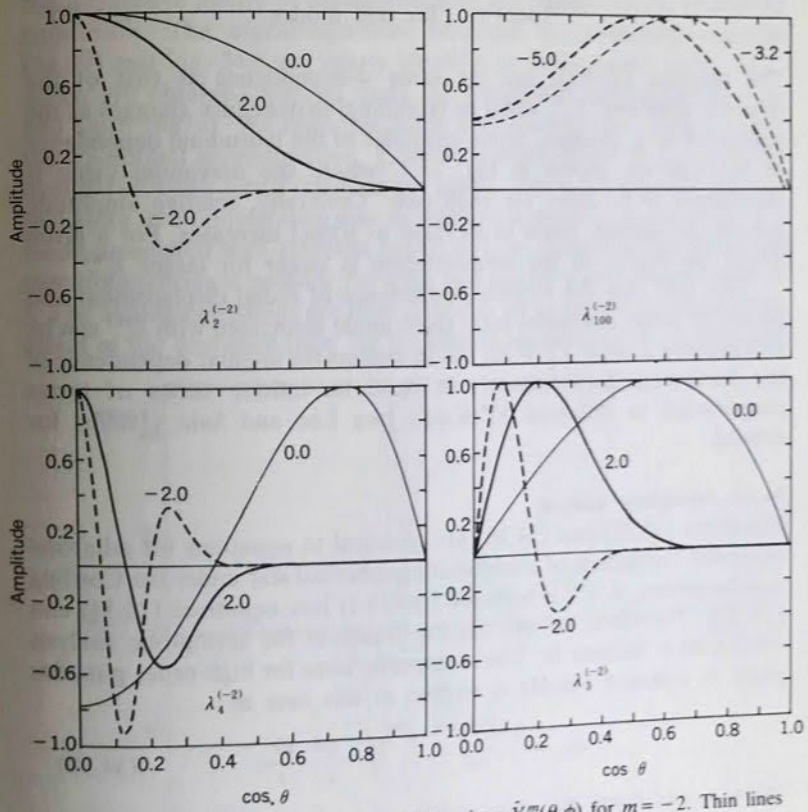

Fig. 34.5 The latitudinal dependencies of functions $\hat{Y}_{l_j}^m(\theta,\phi)$ for $m=-2$. Thin lines correspond to the case of no rotation. The thick solid and dashed lines are for the prograde and retrograde modes, respectively, in the co-rotating frame. The numbers along the lines indicate the values of $\hat{\Omega}/\omega_c$.

proportional to spherical harmonics $Y_l^m(\theta,\phi)$. The eigenvalue $\lambda_j^{(m)}$ has a positive value for a large negative value of Ω/ω_c, which corresponds to the existence of the Rossby waves (or r-modes in astrophysics).

The transformation from $\mathbf{Y}_1$ and $\mathbf{Y}_2$ to $\mathbf{Z}_1$ and $\mathbf{Z}_2$ in equation (34.33) corresponds to changing the basis of the expansions in (34.1) and (34.2). The new basis is composed of linear combinations of spherical harmonics, defined by

$$\tilde{Y}_{l_j}^m(\theta,\phi)=\sum_{i=1}^{\infty} B_{ij} Y_{\mu+2i-2}^m(\theta,\phi), \tag{34.37}$$

where μ is defined by

$$\mu=\begin{cases} |m| & \text{for even modes;} \\ |m|+1 & \text{for odd modes.} \end{cases} \tag{34.38}$$

The function $\tilde{Y}_{l_j}^m(\theta,\phi)$ has the same ϕ-dependence as that of the spherical harmonic Y_l^m, while its latitudinal dependence changes as the parameter $\hat{\Omega}/\omega_c$ changes. Some examples of the latitudinal dependence of $\tilde{Y}_{l_j}^m(\theta,\phi)$ are shown in Fig. 34.5, where the maximum value is normalized to be unity for each case. Generally, relative amplitude around the equator tends to increase as $|\hat{\Omega}/\omega_c|$ increases. For a given $|\hat{\Omega}/\omega_c|$ the degree of the concentration is larger for larger $\lambda_{l_j}^{(m)}$.

We note that the angular dependence of radial displacement and perturbed scalar quantities for a given mode associated with $\lambda_{l_j}^{(m)}$ can be expressed by a single $\tilde{Y}_{l_j}^m(\theta,\phi)$; but to express the angular dependence of the horizontal displacement, we need an infinite series of terms proportional to different $\tilde{Y}_{l_j}^m(\theta,\phi)$'s [see Lee and Saio (1989b) for details].

34.3.2 Asymptotic Analysis

Equations (34.35) and (34.36) are identical to equations for adiabatic nonradial oscillations of a nonrotating spherical star under the Cowling approximation, if $\lambda_{l_j}^{(m)}$ is replaced by $l(l+1)$ [see equations (18.14) and (18.15)]. Therefore, we can use the results of the asymptotic analysis developed in Section 16. The asymptotic form for high-order g-modes given in equation (16.41) is written in this case as

$$\omega_{c,n}\simeq\frac{(\lambda_{l_j}^{(m)})^{1/2}}{n\pi}\int_{r_a}^{r_b}\sqrt{-\frac{rA}{c_1}}\frac{dr}{r}, \tag{34.39}$$

where r_a and r_b are the inner and the outer boundaries of the G-wave zone, respectively. For high-order g-modes of a massive main sequence star, which has a convective core and a radiative envelope, r_a is approximately the radius of the outer boundary of the convective core and r_b the radius of the star. Since $\lambda_{l_j}^{(m)}$ is a function of $\hat{\Omega}/\omega_c$, we can obtain the angular frequencies of high order g-modes combining equation (34.39) with the $\hat{\Omega}/\omega_c$-$\lambda_{l_j}^{(m)}$ relation such as is shown in Figs. 34.2 and 34.3. Equation (34.39) is also used for r-modes, which correspond to retrograde waves with small positive $\lambda_{l_j}^{(m)}$. Since they have positive values of $\lambda_{l_j}^{(m)}$, the boundaries of the propagation zone are the same as those for g-modes.

In order to compare the numerical results obtained by using asymptotic analysis with those shown in Fig. 34.1, only two components of spherical harmonics are included. Figure 34.6 shows $\lambda_{l_j}^{(m)}$ versus $\hat{\Omega}/\omega_c$ for this case. A comparison between Figs. 34.6 and 34.3 indicates that the qualitative nature of oscillations does not depend on the manner of truncation. The eigenfrequencies obtained by combining equation (34.39) and Fig. 34.6 are nearly identical to those shown in Fig. 34.1, which are obtained without using the traditional approximation (Lee and Saio, 1987a). We note that since in the asymptotic analysis under the traditional approximation, $\tilde{g}_m$-mode is independent of g_m-mode, no avoided crossing occurs (they simply cross). This is analogous to the fact that since in a non-rotating star an oscillation mode is independent of a mode associated with different values of l, an accidental degeneracy of eigenfrequencies is possible between two modes with different value of l. The avoided crossings are reproduced in an asymptotic analysis if the effect of the deviation from the traditional approximation is taken into

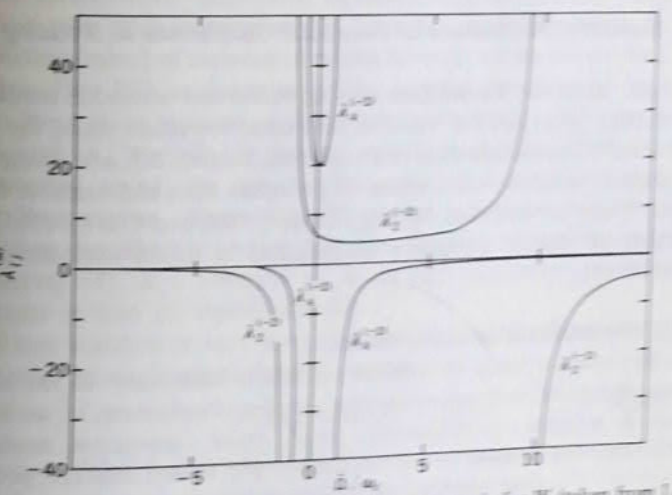

Fig. 34.6 Same as Fig. 34.3 but for the 2×2 truncated matrix for W (taken from Lee and Saio, 1987a). Here, $l=2$.

account (Lee and Saio, 1989a).

Using Fig. 34.6, we can interpret the qualitative property of eigenfrequencies shown in Fig. 34.1. At $\Omega=0$, $\lambda_2^{(-2)}=6$ and $\lambda_4^{(-2)}=20$. Therefore, g_n- and $\tilde{g}_n$-modes in Fig. 34.1 are associated with $\lambda_2^{(-2)}$ and $\lambda_4^{(-2)}$, respectively. As seen in Fig. 34.6, $\lambda_2^{(-2)}$ has singular points at $\hat{\Omega}/\omega_c \simeq 10$ and $\hat{\Omega}/\omega_c \simeq -1.3$, while $\lambda_4^{(-2)}$ has singular points at $\hat{\Omega}/\omega_c \simeq 0.95$ and at $\hat{\Omega}/\omega_c \simeq -0.6$. At these singular points $\lambda_j^{(m)}$ changes its sign. The singular points for $\lambda_2^{(-2)}$ and $\lambda_4^{(-2)}$ correspond to the asymptotic lines L_2, and L_4, respectively, in Fig. 34.1. In other words, the singular points correspond to the low-frequency cut-off of gravity waves for a rotating star, because in a frequency range where λ_j^m is negative, waves are not propagative in the radiative equilibrium zone ($-rA = rN^2/g > 0$) [see equation (34.39)]. Below the cut-off frequency waves are propagative in a convective zone. Such a wave correponds to a convective (g^--) mode which is stabilized by the existence of rotation. The stabilized convective mode trapped in the convective core in a massive main sequence star becomes overstable when it couples with a g-mode in the envelope (Section 35 below).

In the retrograde wave region ($\omega_c<0$) in Fig. 34.6, $\lambda_j^{(m)}$'s have zero points at $\hat{\Omega}/\omega_c = l'(l'+1)/(2m)$ with $l' = |m| + 1$ and $|m| + 3$. The zero point corresponds to the high-frequency cut-off for r-modes. For a given rotation angular frequency, the Rossby waves with angular frequency $|\omega_c|$ smaller than the high-frequency cut-off are propagative in the radiative equilibrium zone.

35. Excitation Mechanisms of Nonradial Oscillations in Rotating Stars

Various excitation mechanisms of both radial and nonradial oscillations have been proposed for massive near-main-sequence stars, for which the usual κ-mechanism does not work (see Section 28), and discussed in connection with the variabilities of β Cephei stars and variable B-type stars. These are reviewed by, e.g., Osaki (1982) and Cox (1985). In this section we discuss excitation mechanisms in which rotation plays a crucial role.

35.1 Overstable Convective Modes

Stellar rotation tends to stabilize convective instability. In the analysis using the traditional approximation developed in Section 34, we learned that if rotation is sufficiently rapid, some convective modes are stabilized and become purely oscillatory. For slower rotation, perturbations in a region with a superadiabatic temperature gradient are overstable. In other words, some periodicity exists in a convective zone

in a rotating star. Usually, these perturbations are confined to the convective zone. To extract the periodic motion from the convective core, Osaki (1974) considered a resonance coupling between the overstable convection in the core of a massive star and a nonradial oscillation mode in the envelope. Osaki (1974) proposed this mechanism as the excitation mechanism for β Cephei stars. If a star has a rapidly spinning core compared to the envelope, the angular frequency of a large-scale overstable convective mode may coincide with the angular frequency of a nonradial f-mode in the envelope, which has a similar angular frequency to those of β Cephei stars. In addition to the β Cephei stars, many B-type stars have been found to be variable, with periods longer than those of β Cephei stars (see Section 8). Since rotation and a convective core are common to these stars, Osaki's (1974) mechanism is a promising candidate for the excitation mechanism of the nonradial oscillations in these stars. Furthermore, because the periods of variability of the variable B stars are comparable to typical rotation periods of these stars, a large differential rotation between the core and envelope is not necessary in explaining these variations by Osaki's (1974) excitation mechanism.

Lee and Saio (1986) confirmed that Osaki's mechanism actually works for a uniformly rotating massive star. They solved the differential equations (34.7)–(34.12) assuming uniform rotation for a $10M_\odot$ zero-age main-sequence model, in which the superadiabatic temperature gradient, $\nabla - \nabla_{ad}$, in the convective core is assumed to be 10^{-3}. The infinite series of the differential equations was truncated by including the first two spherical harmonics. Complex eigenfrequencies (in the co-rotating frame) of convective modes for even modes are shown (solid lines) in Fig. 35.1 as functions of the angular frequency of rotation. When there is no rotation, a convective mode has a purely imaginary frequency; i.e., it grows (or decays) exponentially. For a finite value of the rotation speed, the angular frequency of a convective mode is generally complex. Since the differential equations and boundary conditions described in Section 34.1 have purely real coefficients (after eliminating i), if a complex ω_c is an eigenfrequency, its complex conjugate is also an eigenfrequency.

When rotation is very slow, the real part of the frequency of a convective mode is approximately written as

$$\omega_{cR} \simeq m C_{nl} \hat{\Omega} \tag{35.1}$$

in the co-rotating frame, where C_{nl} (>0) is a numerical constant which depends on the eigenfunction of the convective mode for $\hat{\Omega}=0$ [see equations (19.46) and (19.47)]. Therefore, for a sufficiently small $\hat{\Omega}$, an

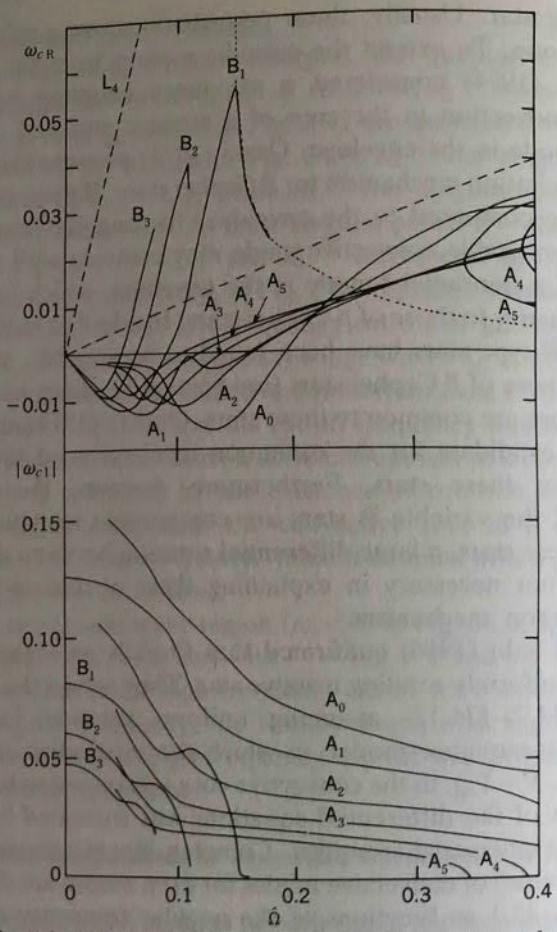

Fig. 35.1 Dimensionless eigenfrequencies in the co-rotating frame for overstable and stable convective modes for $m=-2$ even modes as functions of the dimensionless rotation frequency (based on Lee and Saio, 1986). The abscissa is the rotation frequency, and the ordinate of the upper (lower) frame is the real (imaginary) part of the eigenfrequency. The dotted curve represents the eigenfrequency of a stable convective mode obtained by imposing zero-boundary conditions at the outer boundary of the convective core. The dashed lines labeled L_2 and L_4 have the same meanings as in Fig. 34.1.

overstable convective mode is a retrograde wave (travels opposite to rotation) in the co-rotating frame, as seen in the small $\hat{\Omega}$ part of Fig. 35.1. As $\hat{\Omega}$ increases, however, ω_{cR} becomes positive (prograde wave). These overstable convective modes are generally confined to the convective core and no motion penetrates into the outer envelope. If the confinement is maintained, the convective modes are completely stabilized when the rotation frequency is increased sufficiently. Examples of the transition from overstable to stable can be seen for the modes labeled A_4 and A_5 in Fig. 35.1. Since for a complex ω_c a curve in the $(\omega_{cR},\hat{\Omega})$-plane represents a complex and its complex conjugate eigenfrequencies, it appears that a curve branches off in the same plane when the convective mode is completely stabilized (i.e., ω_c becomes purely real).

The modes labeled B_n in Fig. 35.1 behave differently when $\hat{\Omega}$ is gradually increased. Before ω_{cR} attains a maximum, the eigenfunction is well confined in the convective core. With further increase in $\hat{\Omega}$, ω_{cR} and $|\omega_{cI}|$ decrease steeply and, more importantly, the relative amplitude in the outer envelope grows. In the envelope, the eigenfunction behaves as a g-mode with a large number of radial nodes. A sample of eigenfunctions for a mode which has large amplitude in the convective core and the outer envelope is given in Fig. 35.2, where the amplitude of radial displacement $|r\Xi_l|$ is shown as a function of the location in the stellar interior for the B_1 mode at $\hat{\Omega}=0.162$ ($\omega_{cR}=3.31\times10^{-2}$,

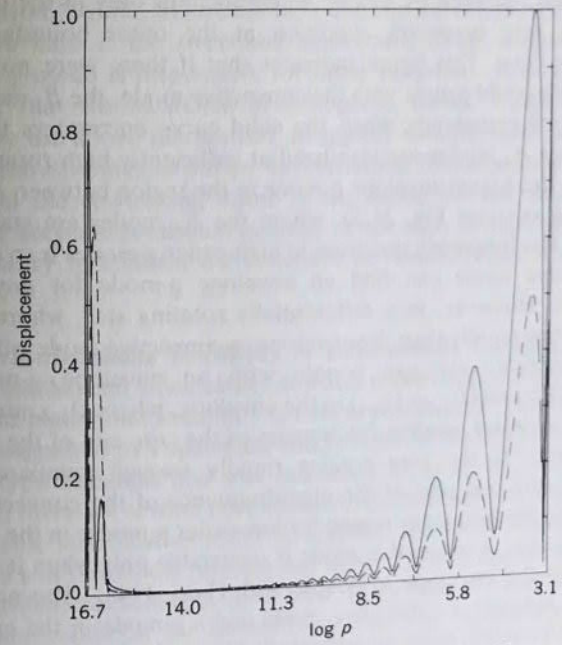

Fig. 35.2 The radial displacement $|r\Xi_l|$ of the even B_1-mode with $m=-2$ for $\hat{\Omega}=0.162$ is shown as a function of log p. The solid and broken curves indicate the components with $l=|m|$ and $l=|m|+2$, respectively. The short vertical line attached to the upper horizontal axis shows the location of the edge of the convective core.

$|\omega_{c1}|=4.40\times10^{-4}$). The solid and the broken curves indicate the components with $l=|m|$ and $l=|m|+2$, respectively. We note that at the surface the horizontal displacement is much larger than the radial displacement ($|H_{|m|}|/|\Xi_{|m|}|=7.8\times10^{2}$) and that the toroidal component is about 60% of the horizontal displacement for the spheroidal component. This phenomenon is the appearance of a mixed convective/g-mode by a resonance between a convective mode and an envelope g-mode, just as Osaki (1974) expected. Lee and Saio (1987b) found that this mode is overstable even if the nonadiabatic effect is included. Thus, this mechanism is a promising candidate for the excitation mechanism for variable B-type stars.

The coupling with an envelope mode is essential in order for a convective mode to be overstable for the rotation frequency larger than the value corresponding to the $\omega_{c\mathrm{R}}$ peak. If we solve the B_1 mode by suppressing the coupling with an envelope g-mode, we have purely real frequencies at the location shown by the dotted line in Fig. 35.1. This solution was obtained by solving eigenfunctions only in the convective core with zero boundary condition at the outer boundary of the convective core. This figure indicates that if there were no envelope mode which could couple with the convective mode, the B_1 mode would be stabilized completely when the solid curve encounters the dotted line, just as A_n modes are stabilized at sufficiently high rotation rates. Note that there is no envelope g-mode in the region between L_2 and the horizontal axis (see Fig. 34.1), where the A_n modes are stabilized by rotation. The frequency spectrum in high-order g-modes is so dense that a convective mode can find an envelope g-mode for any rotation frequency. However, in a differentially rotating star, where the core rotates more rapidly than the envelope, a convective mode with $\omega_{c\mathrm{R}}^{core}$ in the convective core can couple with an envelope g-mode with $\omega_{c\mathrm{R}}^{env}=\omega_{c\mathrm{R}}^{core}-m(\hat{\Omega}_{core}-\hat{\Omega}_{env})$ in the envelope, where $\hat{\Omega}_{core}$ and $\hat{\Omega}_{env}$ are the dimensionless rotation frequencies of the core and of the envelope, respectively. If the core rotates rapidly enough compared to the envelope, the real part of the eigenfrequency of the convective mode enters into the frequency region for low-order g-modes in the envelope. In such a case, a convective mode is overstable only when it can find a g-mode in the envelope to couple with (Lee, 1988). The necessity of coupling between a convective mode and a g-mode in the envelope is discussed in detail, using an asymptotic theory, by Lee and Saio (1989a), who also show that only prograde waves can be overstable as a result of the coupling.

In the above numerical analysis, a large superadiabatic temperature gradient $\nabla-\nabla_{ad}=10^{-3}$ in the convective core was assumed. The rotation frequency at the peak of $\omega_{c\mathrm{R}}$ of a B_n mode is proportional to $(\nabla-\nabla_{ad})^{1/2}$ [*cf.* equation (34.39)]. Therefore, if the true superadiabatic temperature gradient in the core is smaller than 10^{-3}, overstable convective modes coupled with envelope g-modes appear for rotation slower than that shown in Fig. 35.1.

In an observer's frame, the real part of angular frequency of the overstable convective mode coupled with an envelope g-mode is

$$\omega_{\mathrm{R}}=\omega_{c\mathrm{R}}^{core}-m\hat{\Omega}_{core}\simeq-m\hat{\Omega}_{core}\ , \tag{35.2}$$

because $\omega_{c\mathrm{R}}^{core}$ is very small compared to $m\hat{\Omega}_{core}$. Equation (35.2) indicates that if more than one oscillation period is detected for a star, each period corresponds to a mode with different m, and that m times the observed period associated with m is approximately independent of observed periods. These properties are just those observed for some variable B-type stars (e.g., Gies and Kullavanijaya, 1988). Observationally, the product of the observed period multiplied by m is called the "superperiod," while, theoretically, it must be the rotation period of the convective core if the overstable convective mode coupled with an envelope g-mode is responsible for these variations. It is fair to note, however, that the existence of retrograde waves, which cannot be excited by the above mechanism, in rapidly rotating stars is suspected (see Section 8). Since to obtain the oscillation frequency and the phase velocity in the co-rotating frame of the stellar surface, one needs to know the accurate rotational velocity of the star, further observations are necessary to confirm the existence or nonexistence of retrograde waves.

35.2 Kelvin-Helmholtz Instability in Differentially Rotating Stars

Another mechanism of instability in which rotation plays a crucial role is the Kelvin-Helmholtz instability (or shear instability). This mechanism was first suggested by Papaloizou and Pringle (1978) as a possible cause of early-type variables and was examined in detail by Ando (1981). However, there are several problems with this mechanism. One of them is that stable stratification tends to stabilize the shear instability. The interior of a differentially rotating star may be locally approximated as a plane stratified medium with shear flow. In the case of plane shear flow, a necessary condition for instability is that the Richardson number defined by

$$R_i=\frac{N^2}{(dU/dz)^2}, \tag{35.3}$$

is less than 1/4, where N denotes the Brunt-Väisälä frequency measuring

the stratification, while dU/dz measures the vertical shear. When applied to a rotating star, this condition shows that stratification stabilizes most of the differential rotation even in a rapidly rotating star. Furthermore, even if Kelvin-Helmholtz instability occurs somewhere, generated waves tend to change the rotation profile very rapidly in such a way as to suppress this instability.

36. Angular Momentum Transfer by Nonradial Oscillations

36.1 General Theory

We discussed the effect of rotation on nonradial oscillations in the previous sections of this chapter. In contrast, we will discuss, in this section, the effect of nonradial oscillations on rotation. One of the most important aspects of nonaxisymmetric ($m \neq 0$) nonradial oscillation is that they can transport angular momentum from one part of the star to another when they are nonconservative (i.e., when there exists an effect of dissipation or leaky boundary conditions). As reviewed by McIntyre (1980), the interaction of wave and mean flow (e.g., rotation) has long been familiar in many branches of science such as fluid dynamics, acoustics, and electromagnetics. The subject has been revitalized in geophysics by recent evidence that wave-induced streaming takes place on a very large scale in the earth's atmosphere and also perhaps in the atmosphere of Venus. Investigations of convection-rotation interaction in the sun may be classified into the same category. Nonradial oscillations were recently discovered in several rapidly rotating early-type stars (e.g., Be stars). Interaction between the nonradial oscillations and rapid rotation may play essential roles in various phenomena in these stars.

In order to discuss the effect of waves on rotation, we should start with a nonlinear momentum equation. The momentum equation (32.2) combined with the continuity equation (32.1) is written in the form

$$\frac{\partial(\rho \boldsymbol{v})}{\partial t} + \boldsymbol{v}\nabla\cdot(\rho\boldsymbol{v}) + \rho(\boldsymbol{v}\cdot\nabla)\boldsymbol{v} = -\nabla p - \rho\nabla\Phi, \tag{36.1}$$

and its ϕ-component is written in the conservation form of the angular momentum

$$\frac{\partial(\varpi\rho v_\phi)}{\partial t} + \nabla\cdot(\rho\varpi\boldsymbol{v}v_\phi) = -\frac{\partial p}{\partial\phi} - \rho\frac{\partial\Phi}{\partial\phi}, \tag{36.2}$$

where

$$\varpi \equiv r\sin\theta. \tag{36.3}$$

Let us decompose the physical quantities into the quantity averaged in the azimuthal direction and the residuals. For example, velocity may be written as

$$\boldsymbol{v} = \bar{\boldsymbol{v}} + \boldsymbol{V}, \tag{36.4}$$

where the overline means the zonal (ϕ-direction) average ($\bar{\boldsymbol{V}} = 0$). It should be remarked that $\boldsymbol{V}$ given by equation (36.4) is not necessarily small enough to be regarded as the linear perturbation of the velocity. We assume that the mean velocity field is only due to rotation; i.e.,

$$\bar{\boldsymbol{v}} = \boldsymbol{\Omega}\times\boldsymbol{r}. \tag{36.5}$$

[See Andrews and McIntyre (1978) for more general discussion.] After decomposing the other physical quantities into the azimuthally averaged values and the residuals, we take the zonal averages of equation (36.2) to obtain

$$\rho\frac{\partial\bar{h}}{\partial t} + \varpi\frac{\partial}{\partial t}\overline{(\rho' V_\phi)} + \nabla_l\cdot(h\overline{\rho'\boldsymbol{V}_p}) + \nabla_l\cdot(\varpi\rho\overline{V_\phi\boldsymbol{V}_p}) = -\overline{\rho'\frac{\partial\Phi'}{\partial\phi}}, \tag{36.6}$$

where the terms proportional to the zonal mean of the product of three perturbed quantities is discarded, and the overbar above ρ is dropped for simplicity. In equation (36.6) $\bar{h}$ is the specific angular momentum of rotation defined as

$$\bar{h} \equiv \varpi^2\Omega, \tag{36.7}$$

$\boldsymbol{V}_p$ is the poloidal component (i.e., r- and θ-components) of oscillatory velocity defined as

$$\boldsymbol{V}_p \equiv V_r\boldsymbol{e}_r + V_\theta\boldsymbol{e}_\theta\ , \tag{36.8}$$

and ∇_l is the poloidal component of the differential operator ∇; i.e.,

$$\nabla_l = \left(\frac{\partial}{\partial r},\ \frac{1}{r}\frac{\partial}{\partial\theta},\ 0\right). \tag{36.9}$$

Needless to say, the pressure gradient term does not appear in equation (36.6) because $\partial(\ldots)/\partial\phi = 0$. The last term in the left-hand side of equation (36.6) comes from the Reynolds stress, which represents here the divergence of the angular momentum flux. The right-hand side of equation (36.6) represents the effect of longitudinal torque generated by self-gravity. The second and the third terms in the left-hand side of equation (36.6) are expected to be small (Ando, 1981). In the following

discussion, we adopt the Cowling approximation ($\Phi'=0$), and take into account only leading terms in equation (36.6) for the sake of simplicity (*cf.* Ishibashi, 1987); i.e., we adopt

$$\rho\frac{\partial\tilde{h}}{\partial t}=-\nabla_l\cdot(\rho\varpi\overline{V_pV_\phi}). \tag{36.10}$$

Strictly speaking, nonlinear wave solutions for V_p and V_ϕ should be employed to evaluate the right-hand side of equation (36.10). However, in order to give clearly the physical interpretation for wave-induced forcing, we use only the linear perturbation of the velocity, and discarded the higher-order perturbation so that

$$V=v' , \tag{36.11}$$

where v' in the right-hand side is the linear perturbation of velocity in the sense used in the other sections ($|v'|/|v|\ll1$). Then the right-hand side of equation (36.10) denoted by τ can be estimated with the help of the basic equations for linear nonradial oscillations of rotating stars. These equations are given by equations (32.15), (32.17), and (32.21). If the wave motions are assumed to behave as $\exp[i(\sigma t+m\phi)]$, these equations lead to

$$i(\sigma+m\Omega)v'_p-\frac{2h}{\varpi^2}v'_\phi\nabla_l\varpi=-\frac{1}{\rho}\nabla_lp'+\frac{\rho'}{\rho^2}\nabla_lp, \tag{36.12}$$

$$i(\sigma+m\Omega)v'_\phi+\frac{1}{\varpi}v'_p\cdot\nabla\tilde{h}=-\frac{imp'}{\rho\varpi}, \tag{36.13}$$

$$i(\sigma+m\Omega)\left(\frac{\rho'}{\rho}-\frac{p'}{\Gamma_1p}+v_T\frac{\delta S}{c_p}\right)=-v'_p\cdot A, \tag{36.14}$$

and

$$i(\sigma+m\Omega)\rho'+\nabla_l\cdot(\rho v'_p)+\frac{im\rho}{\varpi}v'_\phi=0. \tag{36.15}$$

The overbars above the zonal averaged quantities are omitted here and in the subsequent discussions.

After some manipulation, we obtain

$$2\tau=-2\overline{\nabla_l\cdot(\rho\varpi v'_pv'_\phi)}=-\mathrm{Re}[\nabla_l\cdot(\rho\varpi v'_pv'^*_\phi)]$$

$$=\frac{2\rho^2\varpi^2}{\Gamma_1mp}(\sigma_R+m\Omega)\sigma_I|v'_\phi|^2-m\rho\mathrm{Im}\left[\frac{(v'_p\cdot\rho^{-1}\nabla_lp)v'^*_p\cdot A}{(\sigma^*+m\Omega)^2}\right]$$

$$-\frac{m\rho}{\varpi}\left(\frac{\rho\varpi^2}{m^2\Gamma_1p}-\frac{1}{|\sigma+m\Omega|^2}\right)\mathrm{Re}[(\sigma+m\Omega)v'_pv'^*_\phi]\cdot\nabla\tilde{h}$$

$$-\rho\mathrm{Im}\left[\frac{(v'_p\cdot A+v'_p\cdot\nabla_l)(v'^*_p\cdot\nabla\tilde{h})}{(\sigma^*+m\Omega)}\right]$$

$$+\rho\varpi\mathrm{Im}\left[v'^*_\phi(\sigma+m\Omega)v_T\frac{\delta S}{c_p}\right]+m\rho\mathrm{Re}\left[\frac{(v'_p\cdot\rho^{-1}\nabla_lp)v_T\delta S^*/c_p}{(\sigma^*+m\Omega)}\right], \tag{36.16}$$

where σ_R and σ_I are the real and imaginary parts, respectively, of eigenfrequency σ (*cf.* Ando, 1983). It is difficult to discuss the physical properties of equation (36.16) directly. We assume that the stars rotate slowly and the oscillation frequency is large enough (i.e., $\sigma_R\gg\Omega$). In this approximation, the first two terms and the last two terms dominate in the right-hand-most side of equation (36.16), and after some manipulation, equation (36.16) can be reduced, using the eigenfrequency and eigenfunction for a non-rotating star, to (Ando, 1983)

$$\tau=\tau_{ir}+\tau_{NA}, \tag{36.17}$$

where

$$\tau_{ir}=\sigma_R\sigma_Im\rho\left[\frac{l(l+1)|\sigma|^2}{L_l^2}|\xi_h|^2+\frac{N^2}{|\sigma|^2}|\xi_r|^2\right]|Y_l^m|^2 \tag{36.18}$$

and

$$\tau_{NA}=\frac{1}{2}mp\mathrm{Im}\left[\left(\frac{\delta p}{p}\right)^*\left(\frac{\delta\rho}{\rho}\right)\right]|Y_l^m|^2. \tag{36.19}$$

Here ξ_r and ξ_h are the radial and the horizontal components of the displacement, such that

$$(v'_p,v'_\phi)=i\sigma\left(\xi_r,\ \xi_h\frac{\partial}{\partial\theta},\ \xi_h\frac{\partial}{\sin\theta\partial\phi}\right)Y_l^m(\theta,\phi). \tag{36.20}$$

In the course of derivation of equation (36.19), the terms up to the order of σ_I/σ_R have been kept with the assumption of $|\sigma_I/\sigma_R|\ll1$.

The imaginary part σ_I of the eigenfrequency in τ_{ir} comes from the time derivative of the wave amplitude. Thus, this term may make a large contribution to the wave-induced forcing in the course of either wave passage, growing, or damping, while it becomes zero in the steady state limit. This term is called "wave transience" by McIntyre (1980). For example, a growing prograde wave ($m<0$, $\sigma_I<0$) propagating in the same direction as rotation can accelerate rotation. The τ_{NA} is similar to

the work integral discussed in Chapter V for each fluid element except for some factors including m. In the excitation region, wave energy is supplied through a thermal process, and the corresponding angular momentum is dredged up from, or deposited to, rotation depending on whether the wave is prograde or retrograde. In the dissipative region, the situation is similar, but the sense is reversed. In the stars, owing to the conservation of the total angular momentum, nonradial oscillations may accelerate rotation at one depth and latitude at the expense of a corresponding deceleration at another depth and latitude.

In the case of rigid rotation and/or strong differential rotation, the third and the fourth terms of the right-hand-most side of equation (36.16) might be important, and, under certain conditions, Kelvin-Helmholtz instabilities may occur, in which case the energy will be supplied from the rotation energy. The detailed discussion about the exchange among energy of pulsation, rotation, and gravity is given by Ando (1985).

36.2 Nonradial Oscillation as a Possible Excitation Mechanism for Be-Phenomena

It is now well known that Be stars eject their mass from the equatorial region quasi-periodically at intervals ranging from several years to some decades, and that this mass forms a cool gas disc around them. In the active mass-eruption phase, Be stars show Balmer line emissions. In the quiescent phase, they show normal B type spectra.

The mechanism of the episodic mass-loss in Be stars is as yet unknown. Previously, Be stars were presumed to be at break-up velocity and to eject their mass from the equator. However, it is now confirmed that there is no observational evidence that any Be star is at break-up velocity. Other mechanisms, such as magnetic fields, stellar winds, and mass accretion in close binary systems have also been proposed, but none succeeded in explaining all the key aspects of observations.

New detector devices such as Reticon and CCD systems have opened up the field of high-precision spectroscopy. Walker, Yang, and Fahlman (1979), Baade (1981), and Bolton (1982) discovered that several Be stars in addition to the well-known early type variables (β Cephei and 53 Persei variables) pulsate nonradially. In particular, Vogt and Penrod (1983) showed clearly the short-term variations with timescale of several hours in HeI 6678 absorption line of ζ Oph, in which a small "bump" travels from blue to red as shown in Fig. 8.1. A correlation between this short-term variability and long-term mass-loss activity in Be stars has been suspected. Vogt and Penrod (1983) pointed

out the possible mass-loss by shock waves generated by nonradial oscillations, and suggested that the pulsational energy in nonradial oscillations of ζ Oph is large enough for an ample amount of its envelope to be ejected.

Here the relation between nonradial oscillations and mass-loss in Be stars will be discussed from a different point of view. As discussed in the previous subsection, the prograde nonradial oscillations propagating in the same direction as rotation seen in the co-rotating frame accelerate rotation in the radiative damping region, while the retrograde nonradial oscillations decelerate it there. Osaki (1986a) discussed a possible mechanism of episodic mass-loss in Be stars by nonradial oscillations on this basis.

If we assume that prograde nonradial oscillations are excited in the deep interior of the star by some mechanism, angular momentum transported by nonradial oscillations is deposited near the surface due to dissipation. This may result in an increase in rotational velocity at the surface, leading eventually to the break-up velocity and to mass-loss at the equator. Once the mass-loss starts, nonradial oscillations will leak into the newly formed extended envelope and mass-loss may be accelerated. In the meantime, nonradial oscillations will be damped owing to increased dissipation in the extended envelope, and consequently the mass-loss will come to an end. The star remains quiet until new nonradial oscillations are built up to sufficient amplitude and a new episode begins.

This model only requires prograde nonradial oscillations, while the existence of retrograde nonradial oscillations is reported in some Be stars as well. Based on the working hypothesis that the actual observations reflect the fact that either prograde or retrograde nonradial oscillation is predominant in a certain phase of Be star, though both modes exist, the way these two nonradial oscillations modify the rotation profile in the envelope of Be stars has been investigated by Ando (1986). In this situation, wave-rotation interaction plays a crucial role.

It is very difficult to attack this problem generally. Following the assumptions given below, Ando (1986) formulated the time evolution of azimuthal velocity (rotation) $\overline{v_\phi}$ deviating from the uniform rotation at the equator by using equations (36.10) and (36.19). His assumptions are (1) this interaction is at work only near the equator; (2) a steady sectoral g-mode, which is composed of a superposition of a retrograde and a prograde traveling wave, is considered, and the effect of wave dissipation and excitation on rotation is taken into account; (3) quasi-adiabatic approximation is applied to estimate the radiative

damping of a wave; (4) eddy viscosity is introduced for the sake of simplicity as a relaxation mechanism of the strongly differential rotation, since the shear instability is too complicated to incorporate.

According to Ando's (1986) formulation, even uniform rotation is secularly unstable in the envelope of early-type stars, and there is a possibility that the rotation profile may vacillate quasi-periodically around uniform rotation. This kind of phenomenon is already recognized in meteorology as the quasi-biennial oscillation of the zonal wind in the tropical stratosphere.

In the 20 $M_\odot$ ZAMS model regarded as a simple Be star model, the oscillatory motion of the rotation profile was actually confirmed by Ando's (1986) numerical calculations. The time scale is inversely proportional to the wave energy. For the reasonable models of Be stars, it ranges from one year to several decades, which is in good agreement with the observational time span of Be episodic mass-loss. The amplitude of acceleration of $\overline{v_\phi}$ amounts to the order of phase speed of nonradial oscillations. It actually takes 10 km s^{-1} to 100 km s^{-1} depending on the period and m value of nonradial oscillations, which is large enough to push the surface velocity to the break-up velocity in the Be stars.

The two conspicuous observational aspects predicted by this model should be checked to confirm this model. One is the quasi-periodic variation (acceleration and deceleration) of the rotational velocity at the equator. The other is that a prograde nonradial oscillation is dominantly seen during the acceleration at the surface and a retrograde nonradial oscillation during the deceleration. Regarding the former aspect, more precise line-profile observations should be accumulated over the whole cycle of a Be episode. In any case, confirmation of both aspects is important, although it is a time-consuming task.

Chapter VII

HELIO– AND ASTEROSEISMOLOGY

37. Theoretical Overview

The identification of the solar five-minute oscillation as the global eigenmodes of the sun has opened a new field of research called "helioseismology," in which the observed oscillations are used to probe the solar internal structure, which can never be observed directly. Study of the solar internal structure by means of helioseismology is worth doing for the following purposes.

The detection of solar neutrinos was a unique method of examining the physical state of the central region of the sun. The observed flux of solar neutrinos is only 1/3 of the theoretical expectation based on the standard solar model, and this inconsistency has been an unsolved problem in astrophysics. Helioseismology provides another diagnosis of the solar internal structure and is expected to yield a useful key to solving the solar neutrino problem.

Since helioseismology can diagnose a wide range of the solar interior, it is a powerful tool in studying the structure and evolution of the sun. Though rotation is considered an important factor governing stellar structure, the internal rotation of stars and its evolution have not yet been definitely understood. We will be able to defin the internal rotation law of the sun through helioseismology. Rotation is one of the key factors of solar and stellar activity. The knowledge of solar internal rotation will be helpful in understanding the solar dynamo and activity.

Solar internal rotation is related to a famous test of Einstein's theory of general relativity. According to Einstein's theory, the perihelion of Mercury precesses, and its theoretically expected value is consistent with the observed value. However, if the sun has a rapidly rotating core, the gravitational field is deformed, and this affects Mercury's perihelion. If we take this effect into account, Einstein's prediction might become inconsistent with the observed value. Hence, in order to conclude whether Einstein's theory is correct or not, we have

to know the solar internal rotation rate. It is not so easy to measure the deformation of the solar disk shape due to the centrifugal force from the circular disk, and the information on solar internal rotation derived from the solar oscillations is more reliable. Hence, helioseismology provides a unique test of Einstein's theory of general relativity.

In this chapter, we discuss various aspects of helioseismology after overviewing the sun as a pulsator in the next section. These aspects include observational technique and data reduction (Section 39), the forward problem (Section 40), the inverse problem (Section 41), and the excitation mechanism (Section 42). We also discuss, in Section 43, the stellar version of seismology called "asteroseismology," which is still in its infancy but is expected to develop in the near future. There are many useful reviews and proceedings of conferences on helio- and asteroseismology. Since these fields are rapidly developing, readers should also consult these soures. For example, as reviews, see Leibacher and Stein (1981), Christensen-Dalsgaard (1982b, 1984a), Gough (1982, 1985b), Scherrer (1982), Deubner and Gough (1984), Christensen-Dalsgaard, Gough, and Toomre (1985b), Leibacher, Noyes, Toomre, and Ulrich (1985), Brown, Mihalas, and Rhodes (1986), and Libbrecht (1988c); for proceedings, see Hill and Dziembowski (1980), Gough (1983, 1986a), Belvedere and Paternó (1983), Ulrich, Harvey, Rhodes, and Toomre (1984), Durney and Sofia (1987), Christensen-Dalsgaard and Frandsen (1988), and Rolfe (1988).

38. The Sun as a Pulsator

Let us consider the characteristics of the sun as a pulsator. As seen in Chapter III, the oscillation property of a star is represented by the internal distribution of Brunt-Väisälä frequency and that of the sound velocity. As the sun has a convective envelope, the square of the Brunt-Väisälä frequency is negative there. Insofar as we suppose a standard evolution theory of the sun, the μ-gradient zone induced by nuclear evolution leads to a gradual plateau of the Brunt-Väisälä frequency near the solar core. The maximum of the plateau is about 0.4 mHz. Hence, all the g-modes have frequencies lower than about 0.4 mHz, and the frequencies of g-modes concentrate on the peak frequency with the increase of the degree l. As the frequency of a low order g-mode becomes higher with increasing l, it comes to be close to that of the f-mode with the same l, which is approximately given by (Gough, 1980)

$$\sigma_l^2 \simeq (GM/R^3)l \,. \tag{38.1}$$

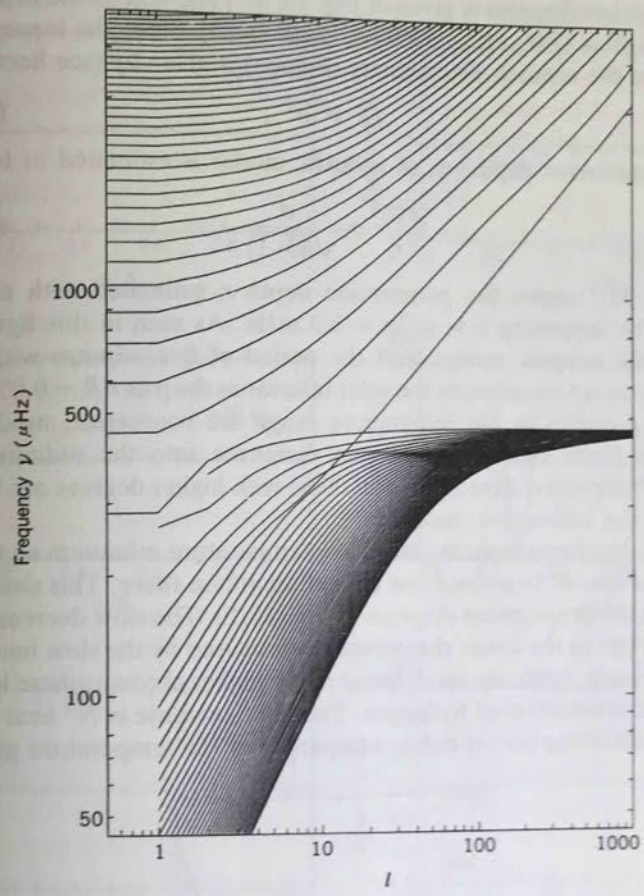

Fig. 38.1 The (l, ν)-diagram of a standard model, where $\nu \equiv \sigma/2\pi$. "Avoided crossings" of the f-mode and some g-modes are realized near $l = 7 \sim 18$. From Christensen-Dalsgaard (1986).

As noted in Sections 15 and 16, however, degeneracy of these modes never occurs, but "avoided crossing" is realized. Figure 38.1 shows the (l, ν)-diagram of a standard solar model, and we can see the "avoided crossings" near $l \simeq 7 - 18$.

The sound velocity increases with the depth and reaches its maximum near $r/R \approx 0.1$. In the deeper interior, since the mean molecular weight becomes larger because of the increase of helium produced by the nuclear reaction, the sound velocity slightly decreases. The Lamb frequency, however, being proportional to the sound velocity over the radial distance, monotonically increases toward the center. The

propagation diagram is given in Fig. 15.10. [The unit of the ordinate of Fig. 15.10 is $GM_\odot/R_\odot^3$ ($=3.9349 \times 10^{-7}\mathrm{s}^{-2}$)]. Since the inner turning point of the acoustic mode cavity (P-zone) is given by (see Section 15)

$$L_l^2 = \sigma^2 , \tag{38.2}$$

the penetration depth, r_t, of acoustic modes is estimated in terms of

$$\frac{c(r_t)}{r_t} = \frac{\sigma}{\sqrt{l(l+1)}} . \tag{38.3}$$

Figure 38.2 shows the penetration depth r_t estimated with equation (38.3) by supposing $\nu \equiv \sigma/2\pi = 3.3$ mHz. As seen in this figure, the nonradial acoustic modes with the period of five minutes with $l = 1$ provide us information on the solar interior as deep as $r/R \sim 0.05$. As far as the p-modes in the five-minute range are concerned, modes with degrees lower than about 60 can penetrate into the radiative zone beneath the convective zone, and those with higher degrees are trapped within the convective zone.

In the chromosphere, there is a temperature minimum so that the acoustic cut-off frequency has a local minimum there. This situation is seen in the propagation diagram of Fig. 15.10. The slow decrease in N^2 with height in the lower chromosphere is caused by the slow increase in temperature, while the small hump in the higher chromosphere is due to the ionization effect of hydrogen. The rapid increase in N^2 near the top of the chromosphere is due to steepening of the temperature gradient.

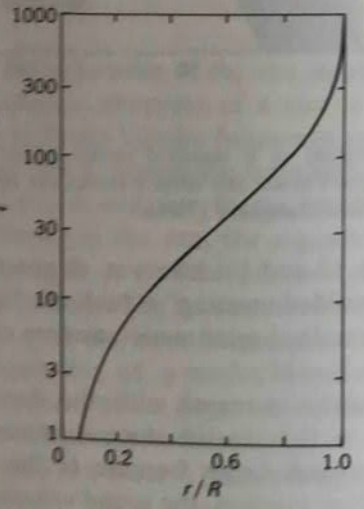

Fig. 38.2 The penetration depth r_t of nonradial p-modes of frequency $\nu \equiv \sigma/2\pi = 3.3$ mHz as a function of l estimated from equation (38.3).

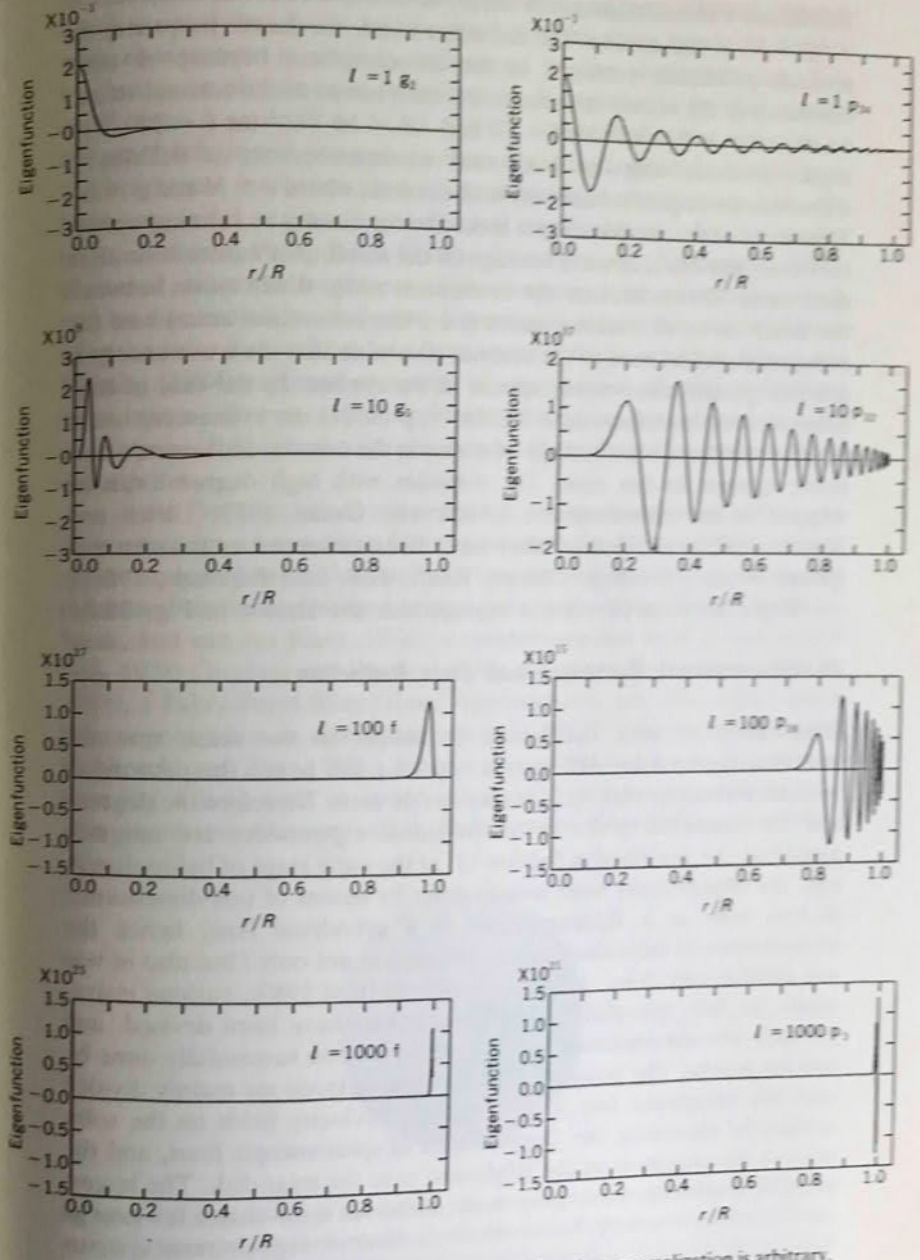

Fig. 38.3 Eigenfunction $p^{1/2}\xi_r$ of various eigenmodes, where normalization is arbitrary.

The Brunt-Väisälä frequency N finally settles to a constant value of $1.4 \times 10^{-3}\text{s}^{-1}$ in the corona. On the other hand, the Lamb frequency L_l remains practically constant in the chromosphere because of near constancy of the sound velocity, and it then jumps to the coronal value, which is $2.5 \times 10^{-3}\text{s}^{-1}$ for $l = 10$ and $4.8 \times 10^{-2}\text{s}^{-1}$ for $l = 200$. For higher p-modes with low horizontal wavenumbers $k_h \leq 0.2\text{Mm}^{-1}$, waves can propagate acoustically in the corona where $\sigma > N$ and $\sigma > L_l$. Thus some of the wave energy is leaked to the corona by running waves. However, the effect of wave leakage on the stability of modes is small in most cases. This is because the evanescent zone, which exists between the inner cavity of acoustic waves (i.e., the convection zone) and the outer propagation zone of the corona, is so wide that the wave energy is reduced greatly when waves appear in the corona. In the case of high horizontal wavenumbers $k_h \geq 0.2\text{Mm}^{-1}$, p-modes are evanescent in the corona, and there is no leakage of waves in the corona. However, a new mode appears in this case: The p-modes with high degree l can be trapped in the chromosphere (Ando and Osaki, 1977; Ulrich and Rhodes, 1977), and indeed they have been observed as the chromospheric modes (Deming, Glenar, Käufl, Hill, and Espenak, 1986).

Eigenfunctions of various eigenmodes are shown in Fig. 38.3.

39. Observational Technique and Data Reduction

Observation of solar oscillations is unique in the sense that the two-dimensional solar disk can be resolved and hence the patterns of oscillations on the solar surface are directly seen. Therefore the degree l and the azimuthal order m of individual eigenmodes are uniquely identified. As described in Section 11, at the early stage of helioseismology, the observations were mainly done by means of one-dimensional devices such as a Reticon array or a cylindrical lens; hence the identification of individual modes differing in not only l but also m was not satisfactorily done. However, since the mid 1980s, various instruments for fully two-dimensional observations have been devised, and the fully two-dimensional observations have been successfully done by various groups. The possible observational methods are mainly divided into two categories: one is observation of velocity fields on the solar surface by measuring the Doppler shift of spectroscopic lines, and the other is measurement of the brightness over the solar disk. The largest velocity amplitude of a single p-mode of the sun is less than a few tens of centimeters per second. Some extremely accurate measurement systems have been devised, and fully two-dimensional Doppler shift observations over the solar disk have already succeeded and will be performed

systematically at several places all over the world [e.g., GONG (Global Oscillations Network Group)-project]. On the other hand, the brightness observation is strongly influenced by the sky conditions. The brightness amplitude of an individual mode included in the five-minute oscillations is as small as $\Delta L/L \sim 10^{-6}$, which means that variation in the sky background prevents us from detecting individual modes from the brightness oscillation. Indeed, ground-based observations have not been successful in detecting such small amplitudes of individual modes (e.g., Jimenez, Pallé, Roca Cortés, Domingo, and Korzennik, 1987). However, since the brightness observation has some advantages which will be discussed later, fully two-dimensional observations of brightness over the solar disk will be done from space in the near future. Noyes and Rhodes (1984) reported prospects of observations of solar oscillations from space. Brown (1988) reviews techniques for observing solar oscillations. Readers should also consult these works for more detailed description.

In the Doppler velocity observation, the most important instrument is an excellent narrow-band filter to measure the Doppler shift of some spectroscopic lines. Various instruments have been devised: the resonance scattering method using a magnetic optical device (Brookes, Isaak, and van der Raay, 1978), a magneto-optical filter (Cacciani and Fofi, 1978; Cacciani and Rhodes, 1984), a Fourier Tachometer (Brown, 1984), a Fabry-Perot filter (Rust, Appourchaux, and Hill, 1988), and a birefringent filter in combination with a KD*P electro-optical crystal (Libbrecht and Zirin, 1986). Since it is essential to have an observation covering a long time in order to get high-frequency resolution, the instruments must be very stable. Furthermore, since the largest velocity

Fig. 39.1 A velocity image of the sun, made using the Doppler effect. Bright is approaching, dark receding, with the total range in velocity being about 3 km s^{-1}. The gradient shows the solar rotation, and the mottling outlines supergranulation. After Libbrecht et al. (1986).

amplitude of a single p-mode of the sun is less than a few tens of centimeters per second, an extremely accurate measurement system is required. These instruments enable us to take two-dimensional solar images of very narrow bands of both wings of an appropriate spectroscopic line such as Ca $\lambda 6439$.

Figure 39.1 shows such a picture taken at the Big Bear Solar Observatory with a birefringent filter in combination with a KD*P electro-optical crystal set (Libbrecht, Popp, Kaufman, and Penn, 1986). The filter is set to pass only the light whose wavelength is at the wing of the spectroscopic line (see Fig. 39.2). Two-dimensional solar images at appropriate wavelengths of both the red wing and the blue wing are alternatively taken. The Doppler velocity v_D at a point on the solar disk is related with the intensity level of both wings by

$$\frac{I_+ - I_-}{I_+ + I_-} = -\left|\frac{d\ln I}{d\ln\lambda}\right| \frac{v_D}{c_*}, \tag{39.1}$$

where I_+ and I_- are the intensity level of the red wing and the blue wing of the line, respectively, $|d\ln I/d\ln\lambda|$ is the gradient at the wings, and c_* denotes the light speed (see Fig. 39.2). By comparing the intensity level of the picture taken by the red wing of the spectroscopic line and that taken by the blue wing of the same line, we can then measure the velocity in the line-of-sight direction at any place on the solar disk. The most dominant contribution comes from the solar rotation, and the spinning and the orbital motion of the earth also contribute to the

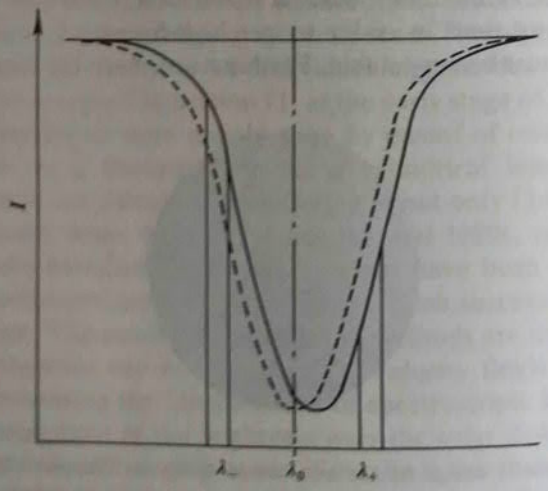

Fig. 39.2 A schematic picture of a spectroscopic-line profile and positions at which a narrow band filter is set.

Doppler shift of the line. The latter motions, however, are constant anywhere on the disk, and hence insofar as the relative velocity fields at places on the solar surface are concerned, we do not have to take account of these motions, while we do have to calibrate them in measuring the velocity due to the radial modes. The solar rotation is supposed to be axially symmetric. It is removable by averaging over a long time-span and by assuming spatial symmetry. The residual velocity field consists of oscillation patterns of eigenmodes and some other local velocity fields associated with granules. The oscillation velocity fields can be, in principle, distinguished from others by their spatial pattern and the temporal periods.

The following is the mathematical principle with which to extract information on individual modes from the observed velocity fields. For the sake of simplicity, we suppose that the rotational velocity of the earth has already been removed and there is no velocity field on the solar surface except for oscillations and the rotation. The velocity field associated with a single mode is given by

$$\boldsymbol{v}_{nlm} = \left[v_{r,n},\ v_{h,n}\frac{\partial}{\partial\theta},\ v_{h,n}\frac{\partial}{\sin\theta\partial\phi}\right] Y_l^m(\theta,\phi)\exp(i\sigma_{nlm}t). \tag{39.2}$$

The observed velocity field is only the line-of-sight component of the superposition of various eigenmodes differing in the quantum numbers n, l, and m and the rotational velocity of the sun. If we take into account of the angle between the solar equator and the line-of-sight, B_0, the line-of-sight velocity component is given by

$$\begin{aligned} v_D(x,y,t) &= \left[\sum_{nlm} \boldsymbol{v}_{nlm} + \boldsymbol{\Omega}\times\boldsymbol{r}\right]\cdot\boldsymbol{e}_{l.s.} \\ &= \sum_{nlm}\Big[v_{r,n}\,Y_l^m(\theta,\phi)\,(\cos B_0\sin\theta\sin\phi + \sin B_0\cos\theta) \\ &\quad + v_{h,n}\frac{\partial}{\partial\theta}Y_l^m(\theta,\phi)\,(\cos B_0\cos\theta\sin\phi - \sin B_0\sin\theta) \\ &\quad + v_{h,n}\frac{\partial}{\sin\theta\partial\phi}Y_l^m(\theta,\phi)\cos B_0\cos\phi\Big]\exp(i\sigma_{nlm}t) \\ &\quad + r\Omega\sin\theta\cos B_0\cos\phi, \end{aligned} \tag{39.3}$$

since the unit vector $\boldsymbol{e}_{l.s.}$ along the line-of-sight is given by

$$\boldsymbol{e}_{l.s.} = (\cos B_0\sin\theta\sin\phi + \sin B_0\cos\theta)\boldsymbol{e}_r$$

$$+(\cos B_0 \cos\theta \sin\phi - \sin B_0 \sin\theta)\mathbf{e}_\theta$$

$$+(\cos B_0 \cos\phi)\mathbf{e}_\phi\,, \tag{39.4}$$

where (θ, ϕ) are the spherical polar coordinates associated with the solar rotation axis. Here, (x, y) are the two-dimensional coordinates on the solar disk. We take the x-axis and y-axis along the westward direction and the northward direction, respectively, and assume the origin of $x = 0$ and $y = 0$ at the solar disk center. If we normalize the radius of the solar disk image as unity, then

$$x = \sin(\theta + B_0)\sin\phi \tag{39.5}$$

and

$$y = \cos(\theta + B_0)\,, \tag{39.6}$$

and inversely,

$$\theta = \cos^{-1} y - B_0 \tag{39.7}$$

and

$$\phi = \sin^{-1}[x/\sin(\cos^{-1} y)]\,. \tag{39.8}$$

We suppose that the solar rotation is steady and axisymmetric. Then we can distinguish the solar rotational velocity from the oscillation velocity field by taking a time average with a long time-span, and we can extract the velocity field due to the oscillations. That is, the line-of-sight component of the oscillatory velocity field at an arbitrary point (x, y) on the solar disk is given by

$$v_{D,osc}(x,y,t) = v_D(x,y,t) - \overline{v_D(x,y)}, \tag{39.9}$$

where $\overline{v_D(x,y)}$ means a time-average of $v_D(x,y,t)$ with a long time-span.

The next task is to identify each of individual mode by performing a spherical harmonic analysis with respect to space and a Fourier analysis with respect to time. The procedure for the spherical harmonic analysis is integration over the spherical surface after multiplying the complex conjugate of spherical harmonics. If the observable quantity due to a single mode is proportional to a single spherical harmonic and if we have all the data over the spherical surface, this analysis gives the amplitude of each spherical harmonic component. It should be noted here, however, that the line-of-sight component of oscillation velocity of an eigenmode is not given by a single spherical harmonic. Though the radial velocity component of an eigenmode is proportional to a spherical

harmonic, the horizontal component proportional to $\nabla_\perp Y_l^m(\theta, \phi)$ also contributes to the line-of-sight velocity and hence it causes some contamination in the spherical harmonic analysis. The ratio of the amplitude of the radial component of the velocity to that of the horizontal component at the surface is $l/\omega^2[\equiv l(GM_\odot/R_\odot^3)/\sigma^2]$, where the factor l comes from $\nabla_\perp$. In the case of five-minute oscillation, the ratio is about $10^{-3} \times l$. Furthermore, the visible solar disk is restricted to half of the solar surface. If we could see the whole surface of the sun, since the spherical harmonics consist of an orthogonal complete set, we could identify the unique quantum numbers l and m of each of the individual modes. However, as the available information is only on the visible half of the solar surface, a spherical harmonic analysis leads to some extra contamination in addition to the true values of l and m of an eigenmode. That is, the result obtained after such a procedure,

$$\tilde{v}(l,m,t) \equiv \int_0^\pi \int_0^\pi v_{D,osc}(x,y,t)\, Y_l^{m*}(\theta,\phi)\sin\theta d\theta d\phi\,, \tag{39.10}$$

is not exactly identical to the amplitude of the eigenmodes of the degree l and the azimuthal order m. However, this procedure is in practice one of the best. An alternative method is to take cross-correlation among the data of each (x, y) and search for a characteristic pattern of spherical harmonics (Christensen-Dalsgaard, 1984b; Duvall and Harvey, 1984).

Performing a Fourier analysis of $\tilde{v}(l, m, t)$ with respect to time, we distinguish individual eigenmodes belonging to the same degree l and the azimuthal order m but differing in the radial order n, since the eigenfrequencies differ:

$$\hat{v}(l,m,\sigma) = \int_0^\infty \tilde{v}(l,m,t)\exp(-i\sigma t)dt\,. \tag{39.11}$$

Figure 39.3 shows the result of this process obtained by Duvall, Harvey, Libbrecht, Popp, and Pomerantz (1988), which shows the amplitude $\hat{v}(l,m,\sigma)$ against $\nu = \sigma/2\pi$ for various values of l. Since the observational run is finite, there appear sidelobes around the peaks at the true eigenfrequencies. Furthermore, time gaps between consecutive observing times lead to aliasing noises; that is, there appear "false peaks" separated from each other by the frequency corresponding to the time gaps. Figures 11.9-11.12 show the (l, ν)-diagrams of the result thus obtained by Duvall et al. (1988). On those diagrams the eigenmodes differing in the azimuthal order m but with the same l and n are not distinguishable, because the m-splitting of frequencies is so minute.

The observation of brightness by broad-band photometry yields, on the other hand, a superposition of scalar eigenfunctions, each of which

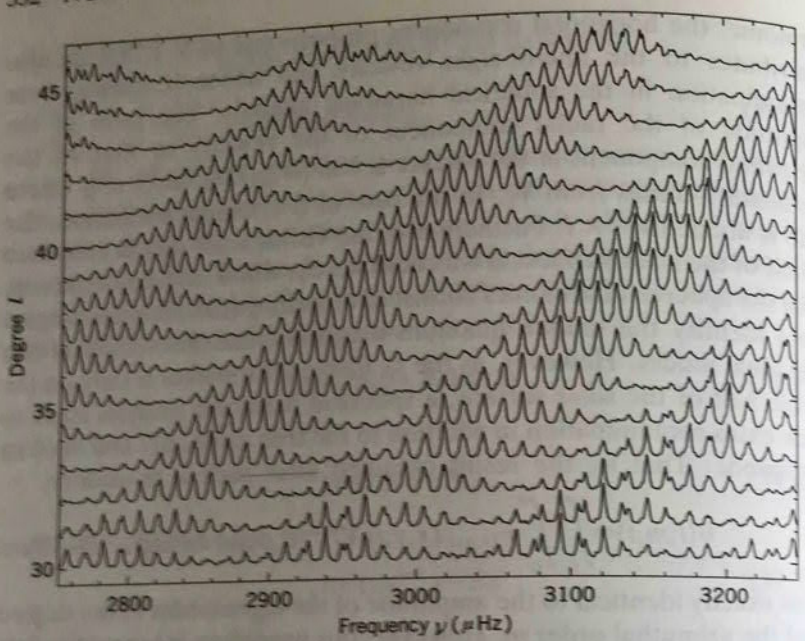

Fig. 39.3 Observed power spectra $\hat{v}(l,\nu)$ for the data obtained at the Big Bear Solar Observatory. From Duvall et al. (1988).

is proportional to a single spherical harmonic:

$$\Delta I(x,y,t)=\sum_{n,l,m}\Delta I_{nlm}(R)Y_l^m(\theta,\phi)\exp(i\sigma_{nlm}t). \qquad (39.12)$$

Here we assume that the effect of the limb darkening has been removed from ΔI. Therefore, in the ideal case of no noise, the brightness observation is advantageous in resolving individual eigenmodes to the Doppler velocity observation. If we could get the brightness distribution on the back half-side of the solar surface, spherical harmonic analysis would provide us the amplitude of individual eigenmodes, $\Delta I_{nlm}(R)$. Since the visible disk is, however, restricted to half of the solar surface, even in the brightness observation the individual eigenmodes cannot be completely resolved in a mathematical sense: the spherical harmonic analysis of only the visible half solar surface leads to

$$\hat{I}(l,m,t)=\int_0^{\pi}\int_0^{\pi}\Delta I(x,y,t)\;Y_l^{m*}(\theta,\phi)\;\sin\theta d\theta d\phi\,, \qquad (39.13)$$

which has some contamination in addition to the true amplitude due to the eigenmodes with the degree l and the azimuthal order m. We treat $\hat{I}(l, m, t)$ thus obtained as an approximation of $\Sigma\Delta I_{nlm}(R)\exp(i\sigma_{nlm}t)$. By performing a Fourier analysis with respect to time and by finding

notable peaks in the power spectrum, we eventually resolve individual eigenmodes:

$$\hat{I}(l,m,\sigma)=\int_0^{\infty}\tilde{I}(l,m,t)\exp(-i\sigma t)dt\,. \qquad (39.14)$$

Intensity observations around CaII K line have been performed and led to successful data (Duvall et al., 1988).

Resolving individual modes differing in m with the same value of (n, l) is important in order to investigate the solar internal rotation. To do so, an observational run as long as possible is desirable. The m-splitting caused by the solar rotation is invisible in Figs. 11.9-11.12. Figure 39.4 is a useful diagram to see the m-splitting of frequencies, on which m/l $(-1 \le m/l \le 1)$ is plotted against frequency $\nu \equiv \sigma/2\pi$ (Libbrecht, 1989). If the solar internal rotation is rigid, or if the angular velocity is only a function of r, the frequency splitting is linearly proportional to m (see Section 19) and hence the $(\nu, m/l)$-diagram shows straight lines. On the other hand, if the internal rotation depends also on the latitude, the frequency splitting is dependent on m in a more complicated way, and the $(\nu, m/l)$-diagram deviates from a straight line. From the shape on the $(\nu, m/l)$-diagram, we can outline the dependence of the solar internal rotation upon the latitude. If the equatorial zone rotates faster than the polar region, the derivative of a curve on the $(\nu, m/l)$-diagram becomes smaller with increase of $|m/l|$, since the modes with high azimuthal order are mainly trapped in the equatorial zone while those with low azimuthal order are concentrated within the polar regions. On the other hand, if the polar region is spinning faster than the equatorial zone, the inclination of the curve becomes steeper with increase of $|m/l|$. Figure 39.4 shows that the deviation from the straight line expected from the rotation rate at the equator on the photosphere is not so conspicuous. This indicates that the dependence of the solar internal rotation on the radial distance r and the latitude θ is not so significant. The data have been inverted to infer the solar internal rotation, and the inverted results show that the rotation rate in the convection zone is roughly independent of depth, showing a latitudinal differential rotation equal to that seen at the solar surface (Libbrecht, 1988d). Since the integrals in equation (19.44) giving the m-splitting of frequencies due to rotation are symmetric in m, the frequency perturbation for slow rotation is antisymmetric with respect to m. Thus, in the presence of latitudinal differential rotation we expect

$$\sigma_{nlm}-\sigma_{n0}=-\Omega_0 m+\Omega_2 m^3+\cdots, \qquad (39.15)$$

where Ω_0, Ω_2, ... are the expansion coefficients. The observed

m-splitting of frequency is sometimes represented by means of series expansion of Legendre functions [*cf.* Durney, Hill, and Goode (1988)]:

$$\sigma_{nlm} - \sigma_{nl0} = l\,(l+1)\sum_i a_i P_i(-m/l)\,, \qquad (39.16)$$

where a_i's are the expansion coefficients and P_i's are Legendre polynomials. These coefficients, fitted to various observational data of m-splitting, have been published by Brown (1985, 1986), Brown and Morrow (1987a, b), Duvall, Harvey, and Pomerantz (1986), Libbrecht (1986, 1989), and Rhodes, Cacciani, Woodard, Tomczyk, Korzennik, and Ulrich (1987). The coefficients a_2, a_4, ... should be zero if the solar structure is spherically symmetric and the values of a_2, a_4, ... have been recognized as a measure of accuracy of observations. However, Kuhn (1988) suggests that there is a possibility of $a_2 \neq 0$ and $a_4 \neq 0$, which indicates the anisotropy of solar structure. These data are used to infer the solar internal rotation by means of the inversion method (Korzennik, Cacciani, Rhodes, Tomczyk, and Ulrich, 1988).

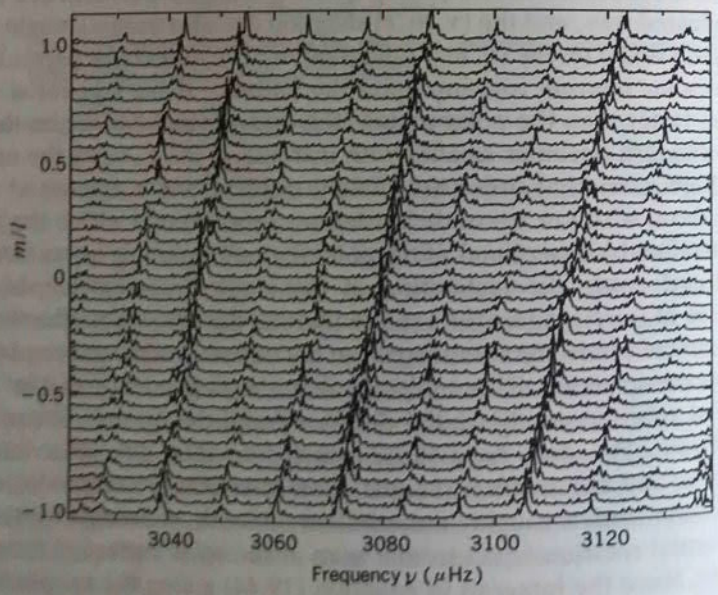

Fig. 39.4 Power spectra on the $(\nu, m/l)$-diagram. Each trace is a piece of a power spectrum for different m with $l = 20$. The peaks in the $m = 0$ spectra at $\nu =$ 3047, 3080, and 3114 μHz are from modes with $(n, l) = (15,19)$, $(15,20)$, and $(15,21)$, respectively. Note that $l = 19$ and 21 modes are contaminations due to the spherical harmonic analysis on half of the solar surface. Peaks at $\pm 11.6\mu$Hz are temporal sidelobes arising from the observing window. After Libbrecht (1989).

40. Forward Problem

As soon as the solar five-minute oscillation became recognized as a superposition of eigenmodes of the sun, attention was paid to the possibility of using this tremendous number of modes as diagnostics of the internal structure of the sun. There are two approaches to probing the solar structure using the oscillations. One of them is based on the so-called "forward problem," in which theoretical eigenfrequencies are calculated for a given equilibrium model of the sun. First, we construct a series of theoretical models of the sun with varying parameters, and then we calculate theoretical eigenfrequencies for each of the models by solving the equations of oscillations. The theoretical frequencies are compared with the observed frequencies, and then we search for the best fit model. The other approach is called the "inverse problem," in which functional forms of certain physical quantities of the sun are determined as the solutions of integral equations which are formulated with the observed eigenfrequencies. In this section, we discuss the forward problem, and the inverse problem is described in the next section.

Inference of the depth of the solar convection zone from the five-minute oscillation data is a good example of the forward problem. Five-minute oscillations with high degree do not penetrate into the sun very deeply. The order of magnitude of the effective depth, d, of the five-minute oscillation may be estimated by $d \sim \pi/k_h$ for the lowest p-modes because $\int_{R-d}^{R} k_r dr \sim \pi$ and $k_r \sim k_h$ for the p_1-mode. The observed power of the oscillations is conspicuous in the wavenumber range from $k_h \sim 0.2$ Mm^{-1} to 1 Mm^{-1} so that we can probe the subsurface layer with a depth of 3 to 15 Mm directly by the high-degree five-minute oscillations in this wavenumber range. These oscillations penetrate at least the superadiabatic boundary layer beneath which the solar convection zone is stratified almost adiabatically. Since the structure of this superadiabatic boundary layer determines the depth of the convection zone, we can in principle infer the depth of the solar convection zone from the five-minute oscillations, provided that the conventional convection theory is correct. As seen in Section 11, the observed ridges of the power of oscillations appear systematically below the theoretical eigenfrequencies calculated by Ando and Osaki (1975), which were based on the solar envelope model with $\alpha \equiv l_t/H_p = 1.0$ and the convection zone about 10^5km deep. Roughly speaking, the eigenfrequencies of p-modes are determined by the traveling time of the sound wave in the p-mode cavity. Hence, the fact that the eigenfrequen-

cies of the model are higher than those of the real sun means that the sound velocity in the convective zone of the model is higher than that of the real sun—that is, the temperature in the convective zone of the model is higher than that of the real sun. Since the surface temperature is fixed, the above fact indicates that the temperature gradient of the model is steeper than the real sun. This in turn means that the estimated convective energy transport used in the model is less efficient than in the real sun. As a consequence, the solar convective region should be deeper than expected by the model with $\alpha = 1.0$. Ulrich and Rhodes (1977) calculated eigenfrequencies of p-modes for the solar envelope models with different depths of the convection zone by varying the mixing length. Their results show that the convection zone is about 2×10^5 km deep. Their conclusion was confirmed by an independent calculation performed by a group of workers at Nice Observatory (Berthomieu, Cooper, Gough, Osaki, Provost, and Rocca, 1978). However, there remains a slight discrepancy between theory and observation in such a sense that the theoretical eigenfrequencies lie slightly above the observed ridges of power in the (k_h, σ)-diagram. In the above investigations of high degree p-modes, the varying parameter in constructing models is the depth of the convection zone.

Even for five-minute period range p-modes with degrees l lower than about 60 penetrate the radiative region beneath the convection zone. Therefore, we have to use models of the whole of the sun. Theory of stellar structure and evolution is one of the well-established research fields in astrophysics, and there is a standard recipe for computing a model of a star near the main sequence. A standard solar model is constructed in the following procedure: We first make a model of the sun at zero-age by assuming that the sun was chemically homogeneous at zero-age and then evolve it to its present age along the lines of the standard theory of stellar evolution. We suppose the sun to be spherically symmetric and ignore the effects of rotation and magnetic field. During evolution, the mass of the sun is assumed to be unchanged. As for the initial chemical abundance of the zero-age main-sequence model, we assume that the ratio of the mass fraction of heavy elements (Z) to that of hydrogen (X) is the same as the surface value of the present sun, and we adopt the spectroscopically observed value for the present sun as Z/X. The luminosity of a star for a given mass and an age is essentially determined by chemical abundance. We treat the initial abundance of the remaining element, helium, $Y = 1-X-Z$, as a parameter in order to adjust the luminosity of the model at the solar age to the present solar luminosity. The radius of the model at the solar age must be equal to the solar radius, and is strongly dependent on

efficiency of convection. However, there is uncertainty in theoretical treatment of convection, and there remains a parameter to determine the efficiency of energy transport by convection— a mixing length within the framework of the mixing-length theory. We treat the mixing length l_t as a parameter to adjust the radius of the model at the solar age to the solar radius. The two parameters, the initial helium abundance and mixing length, should be uniquely determined to adjust both the luminosity and the radius of the model to the solar luminosity and the solar radius. However, uncertainties in the input physics, such as nuclear reaction rates, opacity, and so on, lead to some tolerant range of parameters.

Once a solar model is constructed, its eigenfrequencies can be calculated by the procedure described in Section 18.

Figure 40.1 shows the comparison of the eigenfrequencies of a solar

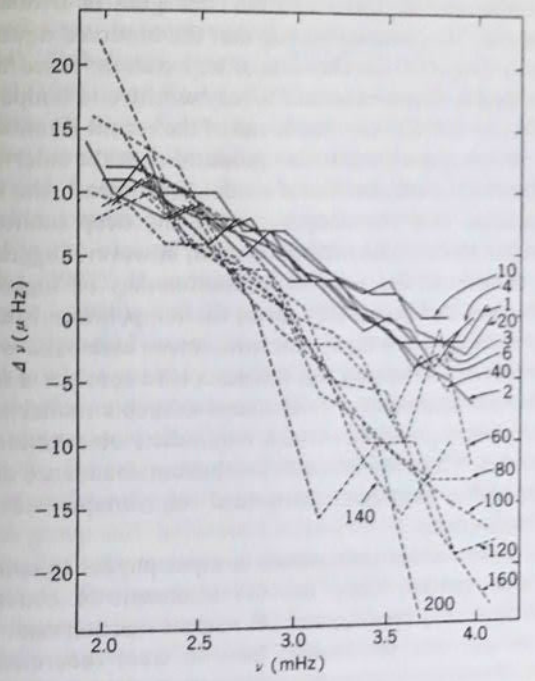

Fig. 40.1 Comparison of the theoretical eigenfrequencies of a standard solar model computed by Christensen-Dalsgaard (1982a) and the frequencies observed by Harvey and Duvall (1984). The ordinate and the abscissa are the frequency difference, $\nu_{obs} - \nu_{theory}$, and the frequency ν_{theory}, respectively. The modes belonging to the same degree l are connected with continuous ($l \leq 20$) and dashed ($l \geq 40$) lines. From Christensen-Dalsgaard and Gough (1984a).

model constructed by Christensen-Dalsgaard (1982a) by the standard procedure with the observed frequencies. As seen in this figure, there are some discrepancies in the sense that theoretical eigenfrequencies of low degree modes are lower than the observed values while those with high degree are slightly higher than the observed frequencies. As discussed previously, the fact that the eigenfrequencies of high degree p-modes of the model are higher than the observed frequencies means that the convection zone of the real sun is deeper than that of the model.

The p-modes with low degrees penetrate into the deep interior. The fact that the eigenfrequencies of p-modes with low degrees of the model are lower than the observed frequencies indicates that the sound velocity, and hence the temperature too, in the solar deep interior are higher than those of the model. This indication seems to be contradictory to the solar neutrino problem. The experiment of solar neutrino detection performed by Davis and his colleagues in Brookhaven has provided us with the puzzling finding that the observed neutrino flux is only about one-third of the theoretical expectation. Since the nuclear reaction producing boron neutrinos is very sensitive to temperature, the results of Davis's (1988) experiment and of the recent Kamiokande data (Totsuka, 1988) suggest that the temperature near the solar center may be lower than in the standard solar model. In contrast, the low degree p-modes indicate that the temperature in the deep interior may be higher than the model. The oscillation data, however, suggest only that the sound velocity in the solar deep interior may be higher than the model. This does not necessarily mean the temperature is also higher, since the sound velocity is higher for lower mean molecular weight. One of the possibilities for solving this dilemma is to consider a solar model with low helium abundance. It is found that this model results in a shallow convective envelope, which contradicts observations of high-degree p-modes. Thus, models with low helium abundance do not solve the discrepancies between theoretical eigenfrequencies and the observed frequencies.

There remain some ambiguities in input physics in constructing a standard solar model. They are (1) treatment of convection, (2) equation of state, (3) opacity, and (4) nuclear reaction rate. It is fair to say that we are not yet certain how to treat theoretically stellar convection. There are various ways in treating of convection other than the local mixing length theory (*cf.* Section 20). Ulrich and Rhodes (1984) and Ulrich (1986b) compared theoretical frequencies of p-modes in the five-minute range based on various convection theories and the observed frequencies. For the deep interior, the simplest equation of state may be that for the fully ionized perfect gas, and it is indeed often

adopted in computation of stellar structure and evolution. The equation of state for solar models used in helioseismology has to be more precise than in conventional stellar evolution theory, since the relative accuracy of observation in eigenfrequency is as minute as 10^{-4} and hence theoretical frequencies also must be calculated with the same degree of accuracy. The ionization degree based on Saha's equation in the deep interior is not quite 100%, though it is expected that very high pressure lowers the continuum level of an atom so that ionization is complete. The latter expectation introduces the concept of "pressure ionization" and it is formulated for practical use in some of the evolution codes (e.g., Eggleton, Faulkner, and Flannery, 1973). The high pressure changes the energy levels of discrete excitation states slightly. Ulrich (1982) introduced the concept of scattering state and of Plank-Larkin's partition function in the equation of state. By considering this as well as electron screening that leads the gas in the solar deep interior to the fully ionized state, he constructed a solar model. Ulrich and Rhodes (1983, 1984), Shibahashi, Noels, and Gabriel (1983), Noels, Scuflaire, and Gabriel (1984), and Kaisig, Knölker, and Stix (1984) also examined the equation of state following Ulrich (1982), and computed solar models. They compared the theoretical eigenfrequencies of the models with observed frequencies, but the discrepancies still remain. The Planck-Larkin partition function introduced by Ulrich is originally formulated in the case of pure hydrogen plasma. Däppen, Anderson, and Mihalas (1987), Hummer and Mihalas (1988), Mihalas, Däppen, and Hummer, (1988), and Däppen, Mihalas, Hummer, and Mihalas (1988a) have studied more extensively the equation of state and formulated in more practical cases. Opacity appears in the equation of radiative transfer among basic equations governing stellar equilibrium. Hence the temperature distribution in the radiative region is dependent on opacity. So far extensive calculation of opacity in a wide range of temperature and density has been performed by two major groups: the Los Alamos group and the Lawrence Livermore group. The calculation requires detailed information on atomic physics and is done with some approximations. The opacity calculated by these groups is not identical; but some discrepancies remain. Korzennik and Ulrich (1989) investigated the solar structure by the inverse problem approach and suggested that the opacity may be an important source of the discrepancy between the theoretical frequencies of models and the observed frequencies. As for the nuclear reaction rate, the cross-sections for pp- and pep-reactions are purely theoretical. The measurement of the cross-sections for other reactions has been done only for high energy regions, and one has to extrapolate cross-sections to the relevant energy. Another

problem with the standard solar models is that there are small differences among models calculated by different evolutionary codes even though the input physics is almost the same (e.g., see Dziembowski, Paternó, and Ventura, 1988). The causes of these differences are unclear, but they may be the differences of numerical computation schemes. Most of the stellar evolutionary codes were developed earlier than the opening of helioseismology, and numerical accuracy as high as the requirement of helioseismology, $\delta\sigma/\sigma < 10^{-4}$, was not required in stellar evolution theory at that time. Therefore, to define quantitatively the discrepancies between the real sun and a standard solar model, we have to examine carefully the accuracy of the evolutionary code itself as well as the input physics (Bachall and Urlich, 1988; Turck-Chièze, Cahen, Cassè, and Doom, 1988).

Apart from the tolerance of the input physics in constructing the standard solar models, we can extend the area of the parameters to find models yielding a better fit. Some groups of researchers have examined "non-standard" solar models by supposing material mixing (e.g., Ulrich and Rhodes, 1983) or turbulent diffusion (Berthomieu, Provost, and Schatzman, 1984; Lebreton, Berthomieu, Provost, and Schatzman, 1988) or the existence of exotic elementary particles (Spergel and Press, 1985; Gilliland, Faulkner, Press, and Spergel, 1986), WIMPs, which are described below. Since there remain discrepancies between theoretical frequencies of standard solar models and observed frequencies of the real sun, it is worthwhile to consider such "non-standard" solar models. Oscillations of solar models taking account of WIMPs were studied by Faulkner, Gough, and Vahia (1986), Däppen, Gilliland, and Christensen-Dalsgaard (1986), and Gilliland and Däppen (1988). WIMPs are weakly interacting massive particles, and their existence has been suggested from the standpoint of the grand unified theory for elementary particles and is used as a possible explanation for the missing mass problem of cosmology. If we suppose that WIMPs are spread over the universe, they are expected to be accumulated in the central regions of stars, where the density is so high that interaction with WIMPs and other particles is frequent. The WIMPs at the solar center are expected to increase the conductivity, and hence the temperature gradient near the solar center would be reduced. As a result, the temperature at the region responsible for the boron neutrino is expected to become lower, while the temperature near the center but outside the boron neutrino region is expected to become higher. Therefore, the boron neutrino production rate will be less than the standard theory and the eigenfrequencies of low degree p-modes will be higher. In this way the WIMPs solar models are expected to solve both the solar neutrino

problem and the discrepancies of observed eigenfrequencies of the sun and theoretical frequencies. More extensive studies will be done in relation to cosmology and the evolution of stars in general.

41. Inverse Problem

There is no definitely established guideline for constructing models other than the procedure for the standard solar model. Hence, even if we succeed in constructing a non-standard solar model providing a better fit to the observation of oscillations, we cannot exclude other possibilities for the solar structure. On the other hand, functional forms of certain physical quantities such as the sound velocity distribution can be directly determined by solving integral equations which are provided by eigenfrequencies. Such an approach is called the "inverse problem," which is an opposite approach to the "forward problem." Hence, in order to determine the solar internal structure using a seismological approach, the inverse problem would be more useful, and it may also be useful in clarifying the cause of the discrepancy between the real sun and the standard model.

There are various approaches to the inverse problem. They are divided into two categories: the inversion methods based on a reference model and those without any reference model. We first discuss the former in the next subsection, 41.1. The latter is described in subsection 41.2.

41.1 Inversion Methods Using a Reference Model

Let us first consider how to deduce the density structure of the sun by means of an inversion method. To do so, we first introduce a reference model, and, on the basis of the variational principle, we formulate an equation which gives the change in eigenfrequencies induced from virtual changes in the equilibrium structure. Then, by regarding this equation as an integral equation, of which the known function is the differences between the observed eigenfrequencies and the eigenfrequencies of the reference model and the unknown to be solved is the difference in physical quantities between the real sun and the reference model, we shall obtain the amounts of physical quantities that must be modified from the reference model to fit the observational data.

The practical procedure is as follows. From equation (14.24), adiabatic eigenfrequency is given by

$$\sigma^2 \int_0^M \boldsymbol{\xi}^* \cdot \boldsymbol{\xi} \, dM_r = \int_0^M \boldsymbol{\xi}^* \cdot \mathcal{L}(\boldsymbol{\xi}) \, dM_r. \tag{41.1}$$

Here $\mathscr{L}$ is an operator including the pressure and density of the equilibrium state and their derivatives. This equation implies that the eigenfrequencies are weighted averages of these equilibrium quantities with weighting functions dependent on the eigenfunctions $\boldsymbol{\xi}$. The observed eigenfrequencies are supposed to satisfy equation (41.1) where the equilibrium quantities in the operator $\mathscr{L}$ are those of the real sun. Eigenfrequencies σ_0^2 of a reference model satisfy also equation (41.1), but the operator $\mathscr{L}$ consists of quantities of the model (p_0, ρ_0, and their derivatives). We subtract these two equations and obtain an equation for $\Delta\sigma^2 \equiv \sigma^2 - \sigma_0^2$ as a linear functional of the differences of the physical quantities $\Delta p \equiv p - p_0$, $\Delta\rho \equiv \rho - \rho_0$, etc., if the reference model is close enough to the real sun. Imposing the constraint of hydrostatic equilibrium, we can express the equation for $\Delta\sigma^2$ only in terms of $\Delta\rho$ if we assume the equation of state is known. The resultant equation is symbolically written as

$$\frac{\Delta\sigma_{nl}^2}{\sigma_{nl}^2} = \int_0^R K_{nl}(\boldsymbol{X}_0, \boldsymbol{\xi}_0, r)\frac{\Delta\rho}{\rho}\,dr\,. \tag{41.2}$$

Here $\Delta\sigma_{nl}^2/\sigma_{nl}^2$ is a known while $\Delta\rho/\rho$ is an unknown, and $K_{nl}(\boldsymbol{X}_0, \boldsymbol{\xi}_0, r)$ is a sensitivity function, where $\boldsymbol{X}_0$ denotes some physical quantities of the reference model and $\boldsymbol{\xi}_0$ is the eigenfunction of the model. It should be recalled that equation (41.1) is stationary to variations in the functions $\boldsymbol{\xi}_{nl}$ (see Section 14). Hence, in the expession of $\Delta\sigma_{nl}^2$, the difference in the eigenfunction $\boldsymbol{\xi}$–$\boldsymbol{\xi}_0$ does not appear, but $\Delta\sigma_{nl}^2$ can be expressed in terms of $\boldsymbol{\xi}_0$ alone. A set of equation (41.2) for various modes can be regarded as an integral equation whose unknown and known functions are $\Delta\rho/\rho$ and $\Delta\sigma_{nl}^2/\sigma_{nl}^2$, respectively, and K_{nl} is the kernel. As for the kernel K_{nl}, if we have a good equilibrium model of the sun, it is theoretically calculated. At the moment, we suppose that the so-called standard model is sufficiently good to evaluate the kernel K_{nl}, and we regard the kernel of equation (41.2) as known. There are various ways to solve this equation, and in the following we outline the spectral expansion method, the method based on the Moore-Penrose generalized inverse matrix, and the Backus-Gilbert method.

Another important approach based on the inverse problem is to deduce the solar internal rotation from the m-splitting data of frequencies. Since there is no standard theoretical model of the stellar internal rotation, the forward problem approach is meaningless, and the inverse problem approach is the unique method of inferring the solar internal rotation. As noted in Section 14, in the case of non-rotating stars, eigenfrequencies of modes belonging to the same n and l degenerate with respect to the azimuthal order m. However, this

degeneracy is lifted in the presence of rotation, and eigenfrequencies of modes differing in m differ slightly in the form of equation (19.43). If we get eigenfrequencies of many modes differing in n, l, and m, we can regard equation (19.43) as an integral equation, whose known function is the frequency difference between the (n,l,m)-mode and the $(n, l,0)$-mode $\{\Delta\sigma_{nlm}\}$ while the unknown function is $\Omega(r,\theta)$. For the sake of simplicity, we consider here the case in which $\Omega(r,\theta)$ depends only on r. The integral equation is then written as

$$\Delta\sigma_{nlm} = \int_0^R K_{nlm}(\boldsymbol{X}_0, \boldsymbol{\xi}_0, r)\,\Omega(r)\;dr, \tag{41.3}$$

where K_{nlm} is the kernel corresponding to the terms in equation (19.43).

In what follows, we symbolically write the integral equations (41.2) and (41.3) as

$$w_i = \int_0^R K_i(\boldsymbol{X}_0, \boldsymbol{\xi}_0, r)\,u(r)dr, \tag{41.4}$$

where w_i is the observationally known data, K_i is the kernel, $u(r)$ is the unknown function to be solved, and i denotes the ordering suffix of the mode.

41.1.1 Spectral Expansion Method

A spectral expansion method is a familiar method of solving a linear inverse problem; it is called so since it provides the solution by means of an expansion in terms of the kernel. Let A_{ij} be

$$A_{ij} \equiv \int_0^R K_i K_j\,dr, \tag{41.5}$$

where i and j denote the ordering suffix of modes. The matrix A_{ij} thus defined is positive-definite and symmetric, and it can be diagonalized with an orthogonal matrix U_{ij}

$$\boldsymbol{A} = \boldsymbol{U}\boldsymbol{\Sigma}^t\boldsymbol{U}, \tag{41.6}$$

where $\boldsymbol{\Sigma}$ is a diagonal matrix whose elements are

$$\Sigma_{ij} = \lambda_i\,\delta_{ij}, \tag{41.7}$$

with

$$\lambda_1 \geq \lambda_2 \geq \ldots > 0. \tag{41.8}$$

Here δ_{ij} is Kronecker's delta and λ_i's are the singular values of the matrix $\boldsymbol{A}$.

Now consider the functions $\Psi_i(r)$ defined by

$$\Psi_i(r)=\lambda_i^{-1/2}\sum_j U_{ji}K_j(r)\,. \tag{41.9}$$

The set of $\Psi_i(r)$ is an orthonormal set:

$$\int_0^R \Psi_i\Psi_j\,dr=\delta_{ij}\,. \tag{41.10}$$

Therefore we may consider an expansion of the solution $u(r)$ in terms of them:

$$u(r)=\sum_i \alpha_i\,\Psi_i(r), \tag{41.11}$$

where the expansion coefficients α_i are given by

$$\alpha_i\equiv\int_0^R \Psi_i\,u(r)\,dr=\lambda_i^{-1/2}\sum_j U_{ji}\,w_j\,. \tag{41.12}$$

The standard error of each coefficient α_i is proportional to $\lambda_i^{-1/2}$. Then the uncertainty of α_i increases with decreasing λ_i. It should be noted here that the convergency of the expansion is not guaranteed.

This spectral expansion method has been quite often used in terrestrial seismology and has been applied in helioseismology (e.g. Gough, 1984c, 1985a; Korzennik, Cacciani, Rhodes, Tomczyk, and Ulrich, 1988; Korzennik and Ulrich, 1989).

One of the variations of this method was applied to Duvall and Harvey's (1984) observational data on frequency splitting by Duvall, Dziembowski, Goode, Gough, Harvey, and Leibacher (1984) and Leibacher (1984) to infer the solar internal rotation. The data are the frequency differences of sectoral modes $m = \pm l$ of various n and l. Since these sectoral modes have large amplitudes in the equatorial zone, we can infer the solar internal rotation near the equator by inverting these data. Duvall et al. (1984) and Leibacher (1984) employed a piecewise constant function,

$$\tilde{\Psi}_i(r)=\begin{cases}1, & \text{if } r_i<r<r_{i+1};\\ 0, & \text{otherwise,}\end{cases} \tag{41.13}$$

as an expansion basis rather than $\Psi(r)$ given by equation (41.9), since the function $\Psi(r)$ given by equation (41.9) oscillates with large amplitude in the surface regions. The inverted result is shown in Fig. 41.1. The dashed line is the equatorial angular velocity of the photosphere. The error bars represent the standard errors of the averages Ω_i arising from the estimated errors in the data. As seen in this figure, the solar internal rotation in the equatorial plane is nearly constant in $0.3 < r/R < 1.0$. The rotation rate is so slow that it cannot

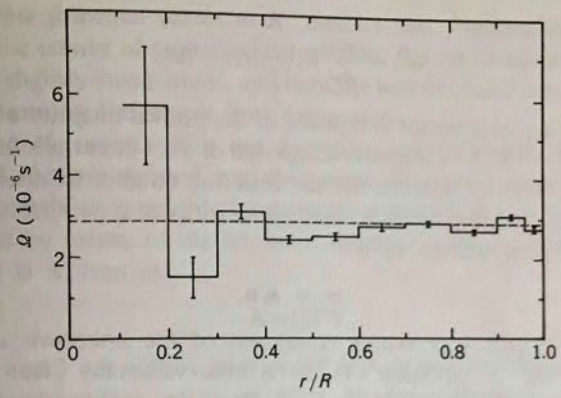

Fig. 41.1 Inferred rotation rate in the equatorial plane. The dashed line is at the equatorial angular velocity of the photosphere. The error bars represent the standard errors arising from the standard errors in the data of Duvall and Harvey (1984). After Duvall et al. (1984).

affect significantly the precession of Mercury's perihelion. Hence the observed value of the precession rate of Mercury's perihelion is consistent with Einstein's prediction based on his theory of general relativity (Duvall et al., 1984). The relatively large error bars in the deep interior are caused by the following facts: The observed quantities are the frequency differences between sectoral modes $\sigma_{n,l,l} - \sigma_{n,l,-l}$, which are proportional to l so that the significance of the observational error of low-degree modes is larger than that of high-degree modes. Since the modes penetrating into the deep interior are low-degree modes, the error bar of the inverted results in the deep interior is consequently larger than that in the outer part. Whether or not the dip near $r/R \simeq 0.25$ is real has not yet been certain. More recent data of m-splitting of frequencies are obtained by means of fully two-dimensional observations of the solar disk, and they are inverted to determine both the radial and latitudinal dependences of the solar internal rotation (see Section 39). The inverted results based on the 1986 data set taken by Libbrecht are seen in Libbrecht (1988d) and in Korzennik et al. (1988). The inverted results based on the Mt. Wilson data obtained by means of magneto-optical filter are presented by Korzennik et al. (1988).

41.1.2 Method Using the Moore-Penrose Generalized Inverse Matrix

We replace the integral in equation (41.4) with the summation by discretizing the radius R with N mesh points:

$$w_i = \sum_{j=1}^{N} K_i(r_j) u(r_j) \Delta r_j. \tag{41.14}$$

Let $\boldsymbol{w} \equiv \{w_i\}$ be a vector composed of the known quantity of i-modes. Also let $\boldsymbol{K} \equiv \{K_{ij}\}$ be a matrix composed of a set of kernels for i-modes times Δx_j, where j denotes the the ordering number of discrete mesh points of the fractional radius, that is, the suffix of x_j $(= r_j/R)$. Equation (41.14) is then written as

$$\boldsymbol{w} = \boldsymbol{K}\boldsymbol{u}, \tag{41.15}$$

where $\boldsymbol{u} \equiv \{u_j\}$ is a vector composed of the unknown $u(r_j)$. The left-hand side of equation (41.15) is observationally given, and the kernel matrix $\boldsymbol{K}$ is theoretically given. Then the problem becomes how to solve algebraic equation (41.15).

Let the dimension of $\boldsymbol{w}$ be $M \times 1$. Then the dimensions of $\boldsymbol{K}$ and $\boldsymbol{u}$ are $M \times N$ and $N \times 1$, respectively. The existence and uniqueness of a solution of the algebraic equation (41.15) depend on the rank $r(\leq min[M, N])$ of the matrix $\boldsymbol{K}$ and, in the case of $M > r$, on the consistency of the data $\boldsymbol{w}$. We classify the following four cases:

(a) $r = N$ and $\boldsymbol{w}$ consistent
(b) $r = N$ and $\boldsymbol{w}$ inconsistent
(c) $r < N$ and $\boldsymbol{w}$ consistent
(d) $r < N$ and $\boldsymbol{w}$ inconsistent.

In the case of (a), the solution is uniquely determined. No solution is given in the case of (b), but the least squares solution is uniquely determined. In the case of (c), there are an infinite number of $\boldsymbol{u}$ satisfying equation (41.15). In the case of (d), there is no solution, while even the least squares solution is not uniquely determined.

In the cases of (c) and (d), some prior information is required to select a solution (case (c)) and a least squares solution (case (d)) among possible solutions. A well-known way to do this is to choose the solution of minimal norm among an infinite number of solutions or least squares solutions, that is, to choose $\boldsymbol{u}$ which minimizes $|\boldsymbol{u}|^2$. The solution thus determined is called "the minimal norm solution" in the case of (c) and "the least squares minimal norm solution" in the case of (d). An example of the adoption of the least squares minimal norm solution in helioseismology is in Denis and Denis's (1984) attempt to infer the solar equilibrium structure.

It should be noted here that the kernels $K_{nl}(r)$ of high order p-modes are quite similar to each other near the outer part of the sun. In evaluating the rank of the matrix $\boldsymbol{K}$, we adopt a parameter ϵ; we regard numbers smaller than ϵ as zero to avoid getting practically

meaningless principal values of $\boldsymbol{K}$. Besides that, because of round-off error in the course of numerical calculation, the set of equation (41.15) becomes slightly inconsistent, and then the practical case corresponds to case (d) among the above four categories.

When the matrix $\boldsymbol{K}$ is not a regular square matrix, the inverse matrix of $\boldsymbol{K}$ is not defined, and then some alternative definition of the inverse matrix is required. In general, a matrix $\boldsymbol{K}$ can be uniquely expressed by means of the so-called singular value decomposition, in which $\boldsymbol{K}$ is written as

$$\boldsymbol{K} = \boldsymbol{U}\boldsymbol{\Sigma}{}^t\boldsymbol{V}, \tag{41.16}$$

where $\boldsymbol{U}$ and $\boldsymbol{V}$ are unitary matrices of $M \times M$ and $N \times N$, respectively, and $\boldsymbol{\Sigma}$ is a diagonal matrix of $M \times N$ whose elements are

$$\Sigma_{ij} = \begin{cases} \lambda_i \delta_{ij}, & \text{if } 1 \leq i \leq r; \\ 0, & \text{otherwise}, \end{cases} \tag{41.17}$$

with

$$\lambda_1 \geq \lambda_2 \geq \ldots \geq \lambda_r > 0. \tag{41.18}$$

Here δ_{ij} is Kronecker's delta and λ_i's are the singular values of the matrix, and they are given by the square root of eigenvalues of the square matrix ${}^t\boldsymbol{K}\boldsymbol{K}$, where ${}^t\boldsymbol{K}$ denotes the transposed matrix of $\boldsymbol{K}$.

By introducing this singular value decomposition, we rewite equation (41.15) as

$$\boldsymbol{\Sigma}\boldsymbol{u}' = \boldsymbol{w}', \tag{41.19}$$

where

$$\boldsymbol{u}' \equiv {}^t\boldsymbol{V}\boldsymbol{u} \tag{41.20}$$

and

$$\boldsymbol{w}' \equiv {}^t\boldsymbol{U}\boldsymbol{w}. \tag{41.21}$$

Let $\boldsymbol{\Sigma}^\dagger$ be a $N \times M$ matrix composed of

$$\Sigma^\dagger_{ij} \equiv \begin{cases} \lambda_i^{-1} \delta_{ij}, & \text{if } 1 \leq i \leq r; \\ 0, & \text{otherwise}. \end{cases} \tag{41.22}$$

Then it can be shown that

$$\boldsymbol{u}'_{LSMN} \equiv \boldsymbol{\Sigma}^\dagger \boldsymbol{w}' \tag{41.23}$$

is the least squares minimal norm solution of equation (41.19). As a consequence, the least squares minimal norm solution for $\boldsymbol{u}$ is given by

$$u_{LSMN} \equiv V\Sigma^{\dagger t}Uw$$

$$\equiv K^{\dagger}w, \qquad (41.24)$$

since unitary transformation keeps the norm unchanged. The matrix $K^{\dagger}$ is known as the Moore-Penrose generalized inverse matrix of K and it is obtained, in practice, through the singular value decomposition (Rao and Mitra, 1971). This type of generalized inverse matrix is useful, and Kozrennik et al. (1988) and Korzennik and Ulrich (1989) applied the generalized inverse matrix to the helioseismological inverse problem.

The least squares minimal norm solution is simple, but it is not always suitable in the context of helioseismology. The requirement of the "minimal norm" is not based on some physical arguments but is an *a priori* assumption. The solution shows some unrealistic fluctuation around the true value. To avoid such unrealistic fluctuation, Phillips (1962) introduced another alternative procedure in which a criterion for smoothness is satisfied for the solution. In their method, however, the solution is no longer one of the possible least squares solution, and the weighting factors for the the smoothness and for the least squares of the solution is arbitrary. Their method has been applied to the inverse problem of helioseismology by Jeffrey (1988). Sekii and Shibahashi (1988) propose another concept of the "least square maximal smoothness solution", which satisfies both the conditions of the least squares and those of the smoothest solution, and a mathematical procedure to obtain it.

41.1.3 Backus-Gilbert Method

Backus and Gilbert (1968) devised an inversion method by which well localized averages of the unknown function are given. By taking linear combinations of the data, we can compute any functionals of the form

$$w = \sum_i \beta_i w_i = \int_0^R \sum_i \beta_i K_i(\boldsymbol{X}_0, \boldsymbol{\xi}_0, r)\, u(r)dr, \qquad (41.25)$$

where β_i's are a set of constants. If the coefficients could be chosen so that $\sum_i \beta_i K_i(r)$ is a Dirac delta function centered at $r = r_0$, then w given by equation (41.25) would become $u(r)$ at $r = r_0$. Practically, if $\sum_i \beta_i K_i(r)$ resembles well the delta function, w leads to well localized averages of $u(r)$, centered at $r = r_0$. Backus and Gilbert (1970) showed how to choose β_i so that the functions of $\sum_i \beta_i K_i(r)$ are concentrated as much as possible on a chosen $r = r_0$ and small elsewhere. This method has been applied to helioseismology by Gough (1982), Duvall et al. (1984), and Hill, Gough, and Toomre (1984a,b) and discussed in detail by

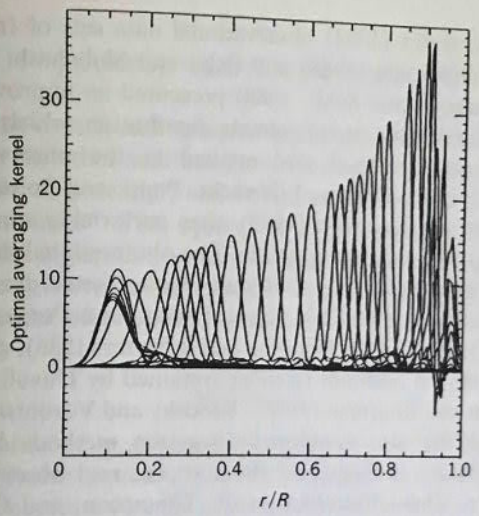

Fig. 41.2 An example of optimal averaging kernels $\sum_i \beta_i K_i(r)$ based on the kernels for the rotation. Normalization is $\int_0^R \sum_i \beta_i K_i(r)dr = 1$. After Christensen-Dalsgaard and Gough (1984a).

Christensen-Dalsgaard and Gough (1984a) and Gough (1984b,c, 1985a). Figure 41.2 shows examples of functions $\sum_i \beta_i K_i(r)$ based on the kernels for the rotational splitting of frequency. As seen in this figure, we can make the function w localize fairly well. One of the defects of this method is that the kernels for high overtones resemble each other and the function $\sum_i \beta_i K_i(r)$ is not satisfactorily localized at the outer part of the sun.

41.2 Asymptotic Inversion Method

Though those methods are promising, one of their defects is that uniqueness and convergency of the solution are not always satisfied. In order to avoid these problems, Brodsky and Levshin (1979) and Gough (1984a) developed another method based on an asymptotic expression of eigenfrequencies, from which an Abel type integral equation is derived. Brodsky and Levshin (1979) devised their method to apply it to torsional oscillations of the earth, and Gough (1984a, 1986b) first introduced the asymptotic inversion method in the field of helioseismology. The solution of the Abel type integral equation is analytically obtained, and hence the solution is unique insofar as the integral equation is numerically given. Gough's (1984a) method was applied by Christensen-Dalsgaard, Duvall, Gough, Harvey, and Rhodes (1985a) to determine the sound speed of the solar interior from Duvall's (1982) and

Harvey and Duvall's (1984) observational data sets of frequencies of oscillations. Shibahashi (1988) and Sekii and Shibahashi (1987, 1989; see also Shibahashi and Sekii, 1988) presented an improved inversion method of inferring the sound velocity distribution, which is also based on an asymptotic method and applied to the observational data compiled by Duvall, Harvey, Libbrecht, Popp, and Pomerantz (1988) and Libbrecht and Kaufman (1988) after performing some numerical simulations to evaluate its prospects. The observational data consist of those obtained by Pallé, Perez, Régulo, Roca Cortés, Isaak, McLeod, and van der Raay (1986a,b), Grec, Fossat, and Pomerantz (1983), Harvey and Duvall (1984), Henning and Scherrer (1986), and Libbrecht and Zirin (1986) in addition to those obtained by Duvall et al. (1988) and Libbrecht and Kaufman (1988). Brodsky and Vorontsov (1988) and Vorontsov (1988) also developed inversion methods based on an asymptotic theory, and applied them to the real observational data quoted above. Christensen-Dalsgaard, Thompson, and Gough (1988) and Kosovichev and Gough (1988) also tried to improve an asymptotic inversion method and inverted the above observational data. Gough (1984a) also formulated an asymptotic inversion method to infer the solar internal rotation; his method was discussed in Duvall et al. (1984), and was extended to the case of latitudinal differential rotation by Lee and Shibahashi (1986). In what follows we discuss the asymptotic inversion method of inferring the solar internal sound velocity distribution from p-mode data. The following description follows Shibahashi (1988) and Sekii and Shibahashi (1989).

41.2.1 Acoustic Potential and Acoustic Radius

The wave equation for linear, adiabatic, nonradial oscillations of stars is a fourth order differential equation with respect to the distance from the stellar center, r. But if we neglect the perturbation of gravitational potential, which is small enough except in the cases of low order and low degree modes, it becomes a second-order differential equation. Furthermore it tends to be a Sturm-Liouville type in the limiting cases of high order p-modes or high order g-modes, as was shown in Chapter III, Section 14. The resultant equation is further reduced to a form of the Schrödinger equation in quantum mechanics, which is, in the case of high order p-mode oscillations, formally written as

$$\frac{d^2}{dr^2}\psi_{nl}(r)+\frac{1}{c(r)^2}[\sigma_{nl}^2-\Phi_l(r)]\psi_{nl}(r)=0\,, \qquad (41.26)$$

where $\psi_{nl}(r)$ is the radial part of an eigenfunction ψ of a mode with radial order n and degree l, that is,

$$\psi(r,\theta,\phi,t)=\psi_{nl}(r)Y_l^m(\theta,\phi)\exp(i\sigma_{nl}t)\,, \qquad (41.27)$$

σ_{nl} denotes the corresponding eigenfrequency, and $c(r)$ means the sound velocity, and the other notations have their usual meanings. Here $\Phi_l(r)$ plays the role of potential, and hereafter we call the term $\Phi_l(r)$ the "acoustic potential." The square of eigenfrequency σ_{nl}^2 should be regarded as the eigenvalue in the potential. So the wave function ψ_{nl} has the propagating-wave character in the region of $\Phi_l(r)<\sigma_{nl}^2$, while it is evanescent in the other region, and the turning points $r=r_1$ and r_2 are the roots of

$$\Phi_l(r)=\sigma_{nl}^2\,. \qquad (41.28)$$

The exact forms of $\psi_{nl}(r)$ and $\Phi_l(r)$ depend on the approximations adopted to derive equation (41.26), but the acoustic potential can generally be expressed as the combination of the square of the Lamb frequency, $L_l^2\equiv l(l+1)c^2/r^2$, which is dominant in the deep interior of a star depending on the degree l of the mode, and the l-independent term $\Psi(r)$, which is related to the density scale height and dominates mainly in the outer part of a star:

$$\Phi_l(r)=l(l+1)c(r)^2/r^2+\Psi(r)\,. \qquad (41.29)$$

If we adopt the approximation used by Deubner and Gough (1984), ψ and $\Psi(r)$ are given by

$$\psi=\rho^{1/2}c^2\nabla\cdot\boldsymbol{\xi} \qquad (41.30)$$

and

$$\Psi(r)=c(r)^2\left[\frac{d}{dr}\left(\frac{1}{2H_\rho}\right)+\left(\frac{1}{2H_\rho}\right)^2\right], \qquad (41.31)$$

respectively, where $\boldsymbol{\xi}$ denotes the displacement vector, ρ the density, and H_ρ the density scale height. Figure 41.3 shows the acoustic potential Φ_l, expressed by equations (41.29) and (41.31), the Lamb frequency L_l^2 and the l-independent term Ψ as functions of acoustic radius τ, which is defined by

$$\tau(r)\equiv\int_0^r\frac{dr'}{c(r')}\,, \qquad (41.32)$$

for the model 1 for the sun of Shibahashi, Noels, and Gabriel (1983). Since the sound velocity $c(r)$ becomes faster with increasing depth, the Lamb frequency term dominates in the deep interior over the

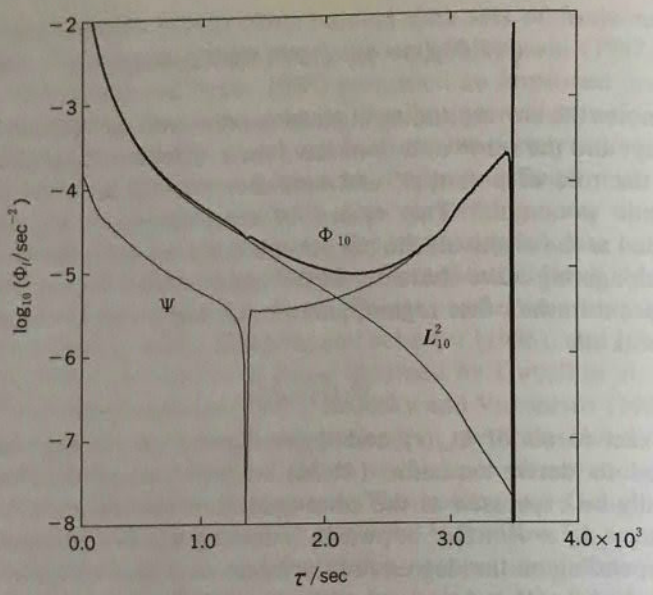

Fig. 41.3 Acoustic potential Φ_l (thick curve), the square of the Lamb frequency $L_l^2 = l(l+1)c(r)^2/r^2$ (thin curve) in the case of $l = 10$, and the l-independent part of the acoustic potential, $\Psi(r)$, given by equation (41.31) as functions of the acoustic radius τ. The sharp dip of Ψ is at the bottom of the convection zone. From Sekii and Shibahashi (1989).

l-independent term $\Psi(r)$. On the other hand, since the density scale height is small in the outer envelope, $\Psi(r)$ is the dominant term of the potential $\Phi_l(r)$ in the outer part. As the degree l decreases, $\Psi(r)$ comes to contribute more significantly to the acoustic potential.

41.2.2 Integral Equation

It should be noted here that neither the exact form of eigenfunction ψ_{nl} nor that of the l-independent part of the acoustic potential $\Psi(r)$ is necessary in the following analysis. Instead, only the following general characters of the acoustic potential are taken into account: i) $\Phi_l(r)$ is concave and has only one minimum in the region of space considered, and ii) the potential is dominated by the Lamb frequency in the deep interior, while it is almost independent of l in the outer part. The WKBJ asymptotic analysis of the wave equation (41.26) leads to the quantization rule

$$(n+\epsilon)\pi = \int_{r_1(\sigma_{nl}^2,l)}^{r_2(\sigma_{nl}^2,l)} [\sigma_{nl}^2 - \Phi_l(r)]^{1/2} \frac{dr}{c(r)} \qquad (41.33)$$

for the eigenmode of radial order n. Here, r_1 and r_2 are the inner and outer turning points at which the integrand of the right-hand side of equation (41.33) becomes zero. Since these turning points are determined by the frequency σ^2 if a form of the acoustic potential Φ_l is given, which itself is dependent on the degree of the mode l, we have written σ_{nl}^2 and l as the arguments of r_1 and r_2. The quantity ϵ represents a phase correction due to the reflection at the turning points, and it does not depend much on the mode.

Strictly speaking, this quantization rule gives only the relation between discrete eigenvalues σ_{nl} and the corresponding integers n and l. But, hereafter, we extend this relation to non-integers n and l by interpolation and treat equation (41.33) as a relation which gives a continuous function n of continuous variables l and σ^2, and omit suffix nl attached to σ. From observational data of the p-mode spectrum, we can identify the frequency σ, the degree l, and the order n of many modes so that such interpolation can be easily done.

41.2.3 Gough's Inversion Method

Gough (1984a, 1985a, 1986b) was the first to develop the inversion method based on the asymptotic theory to infer sound velocity distribution in the sun from the p-mode oscillations spectrum. As a first approximation, he disregarded the l-independent term in the acoustic potential $\Psi(r)$ and, instead, dealt with the data of whole l's together. He and Christensen-Dalsgaard et al. (1985a) then derived the relation

$$\frac{(n+\epsilon)\pi}{\sigma} = \int_{r_1}^{r_2} \left[\frac{r^2}{c(r)^2} - \frac{l(l+1)}{\sigma^2}\right]^{1/2} d\ln r \qquad (41.34)$$

by dividing the quantization rule (41.33) by σ. This relation reminds us of the so-called Duvall's relation which is empirically obtained from Duvall's (1982) observational data on p-modes and indicates that $(n+\alpha)/\sigma_{nl}$ is a function of $\sigma_{nl}/\sqrt{l(l+1)}$ with $\alpha \simeq 1.5$ (see Fig. 41.4). Indeed, Gough (1984b) and Christensen-Dalsgaard et al. (1985a) showed that Duvall's relation can be derived from equation (41.34) if we replace the upper limit of the integral in the left-hand side of equation (41.34) by R and choose an appropriate constant α in place of ϵ in equation (41.34) to absorb the influence of the replacement of the upper limit of the integral:

$$\frac{(n+\alpha)\pi}{\sigma} = \int_{r_1}^{R} \left[\frac{r^2}{c(r)^2} - \frac{l(l+1)}{\sigma^2}\right]^{1/2} d\ln r. \qquad (41.35)$$

They regarded $l(l+1)/\sigma^2$ as a continuous variable and $(n+\alpha)\pi/\sigma$ as a known continuous function of it. Then they regarded equation (41.35)

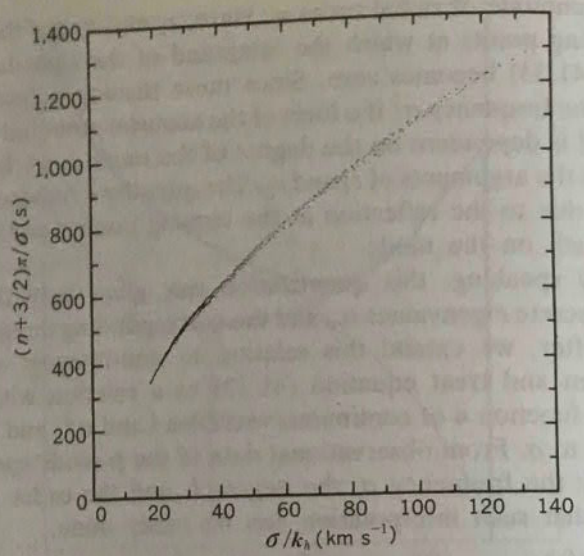

Fig. 41.4 The observed frequencies σ of solar p-modes can be reduced quite well to a single curve if plotted as $(n+\alpha)/\sigma$ vs $\sigma/\sqrt{l(l+1)}$. After Duvall (1982).

as an integral equation with the unknown to be solved r^2/c^2 and the known function $(n+\alpha)\pi/\sigma$. Differentiation of equation (41.35) with respect to $\sigma/\sqrt{l(l+1)}$ leads to an Abel's integral equation, which can be analytically inverted. The final solution is given by

$$\frac{r}{R}=\exp\left[-\frac{2}{\pi}\int_{c(R)/R}^{c(r)/r}\left(\frac{l(l+1)}{\sigma^2}-\frac{r^2}{c(r)^2}\right)^{-1/2}\frac{dF}{d[\sigma/\sqrt{l(l+1)}]}\,d[\sigma/\sqrt{l(l+1)}]\right], \tag{41.36}$$

where $F=F(\sigma/\sqrt{l(l+1)})$ denotes the left-hand side of equation (41.35). Equation (41.36) gives r for a given r/c.

Though the procedure outlined above is mathematically beautiful, disregard of the l-independent term $\Psi(r)$ in the acoustic potential $\Phi_l(r)$ makes the asymptotic treatment of the wave equation for low-degree modes inaccurate, since the l-independent term $\Psi(r)$ contributes significantly to the acoustic potential in the case of low degree l as seen in Fig. 41.3. Since it is such low degree modes that penetrate to the deep interior of the sun and provide us information from there, disregard of the l-independent term $\Psi(r)$ leads to the larger discrepancy between the inverted result of $c(r)$ and the true value.

41.2.4 Asymptotic Inversion Taking $\Psi(r)$ into Account

By transforming variables, we rewrite the right-hand side of equation (41.33) as an integral with respect to the level of the potential. As a first step to do so, we rewrite it as an integral with respect to the acoustic radius τ:

$$\int_{r_1}^{r_2}[\sigma^2-\Phi_l(r)]^{1/2}\frac{dr}{c(r)}=\int_{\tau_1(\sigma^2,l)}^{\tau_2(\sigma^2,l)}[\sigma^2-\Phi_l(r)]^{1/2}\,d\tau\,, \tag{41.37}$$

where τ_1 and τ_2 are the turning points corresponding to r_1 and r_2 measured in the acoustic radius, respectively — that is, $\tau_1=\tau(r_1)$ and $\tau_2=\tau(r_2)$. Here we have explicitly written again σ^2 and l as the arguments of the turning points τ_1 and τ_2. As the next step, we regard the coordinate τ as a function of Φ_l. It should be noted here that the function $\tau(\Phi_l)$ is two-valued; that is, each value of the acoustic potential corresponds to two different values of τ (see Fig. 41.5). Accordingly, the integral in the right-hand side of equation (41.37) must be divided into two parts before replacing $d\tau$ by $(d\tau/d\Phi_l)d\Phi_l$, one from $\tau=\tau_1$ to $\tau=\tau_0$ and the other from $\tau=\tau_0$ to $\tau=\tau_2$, where τ_0 is the acoustic radius at which the potential is the minimum value $\Phi_{l,min}$, i.e., $\Phi_l(\tau_0)=\Phi_{l,min}$:

$$\int_{\tau_1(\sigma^2,l)}^{\tau_2(\sigma^2,l)}[\sigma^2-\Phi_l(\tau)]^{1/2}\,d\tau=\int_{\tau_1(\sigma^2,l)}^{\tau_0(l)}[\sigma^2-\Phi_l(r)]^{1/2}\,d\tau_{\rm I}+\int_{\tau_0(l)}^{\tau_2(\sigma^2,l)}[\sigma^2-\Phi_l(\tau)]^{1/2}\,d\tau_{\rm II}\,. \tag{41.38}$$

where we have written the function $\tau(\Phi_l)$ in these two ranges as $\tau=\tau_{\rm I}(\Phi_l)$ and $\tau=\tau_{\rm II}(\Phi_l)$, respectively. Here, since the acoustic potential is dependent on l, the position of its minimum also depends on l, so that $\tau_0=\tau_0(l)$. We can now replace $d\tau_{\rm I}$ and $d\tau_{\rm II}$ by $(d\tau_{\rm I}/d\Phi_l)d\Phi_l$ and $(d\tau_{\rm II}/d\Phi_l)d\Phi_l$, respectively. The limits of integration with respect to Φ_l are evidently σ^2 and $\Phi_{l,min}$, so that

$$\int_{\tau_1(\sigma^2,l)}^{\tau_0(l)}[\sigma^2-\Phi_l(\tau)]^{1/2}\,d\tau_{\rm I}+\int_{\tau_0(l)}^{\tau_2(\sigma^2,l)}[\sigma^2-\Phi_l(\tau)]^{1/2}\,d\tau_{\rm II}=\int_{\Phi_{l,min}}^{\sigma^2}[\sigma^2-\Phi_l]^{1/2}\left(\frac{d\tau_{\rm II}}{d\Phi_l}-\frac{d\tau_{\rm I}}{d\Phi_l}\right)d\Phi_l\,. \tag{41.39}$$

We define the "acoustic length," $s(\Phi_l)$, as the distance measured in terms of acoustic radius between the two branches of the potential curve for a given l, $\tau_{\rm I}$ and $\tau_{\rm II}$, at a given level of the potential Φ_l:

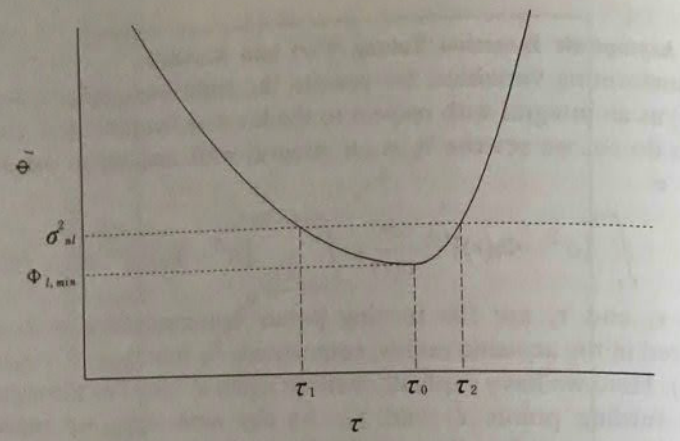

Fig. 41.5 A schematic picture of the acoustic potential $\Phi_l(\tau)$ for a given l. The function $\tau(\Phi_l)$ is two-valued.

$$s(\Phi_l)\equiv\int_{\tau_{\rm I}(\Phi_l)}^{\tau_0(l)} d\tau_{\rm I}+\int_{\tau_0(l)}^{\tau_{\rm II}(\Phi_l)} d\tau_{\rm II}\,. \tag{41.40}$$

With use of the acoustic length, the term $(d\tau_{\rm II}/d\Phi_l - d\tau_{\rm I}/d\Phi_l)$ in the right-hand side of equation (41.39) is simply written as $ds/d\Phi_l$, which represents the dependence of the distance between the two branches of the potential curve upon the potential level. Then, combining equations (41.33), (41.37), (41.38), (41.39), and (41.40), we eventually rewrite the quantization rule as

$$(n+\epsilon)\pi=\int_{\Phi_{l,\min}}^{\sigma^2}(\sigma^2-\Phi_l)^{1/2}\frac{ds}{d\Phi_l}d\Phi_l\,. \tag{41.41}$$

For a fixed l, the left-hand side of equation (41.41) is now regarded as a continuous, known function of σ^2, and hence equation (41.41) is regarded as an integral equation, in which the unknown to be solved is $ds/d\Phi_l$ and the kernel is $(\sigma^2-\Phi_l)^{1/2}$. Differentiation with respect to σ^2 leads equation (41.41) to an Abel type integral equation (Shibahashi, 1988),

$$2\pi\frac{\partial n(\sigma^2,l)}{\partial\sigma^2}=\int_{\Phi_{l,\min}}^{\sigma^2}(\sigma^2-\Phi_l)^{-1/2}\frac{ds}{d\Phi_l}d\Phi_l\,, \tag{41.42}$$

whose solution is analytically obtained. Here, we have assumed

$$\frac{\partial\epsilon}{\partial\sigma^2}\ll\frac{\partial n}{\partial\sigma^2} \tag{41.43}$$

and discarded $\partial\epsilon/\partial\sigma^2$.

In equation (41.42), the left-hand side is the known function which is obtained from observational data, the kernel is $(\sigma^2-\Phi_l)^{-1/2}$, and the unknown function to be solved is $ds/d\Phi_l$. The recipe for solving an Abel type integral equation is well known: Applying $\int_{\Phi_{l,\min}}^{\alpha}d\sigma^2$ to equation (41.42) with a parameter α after dividing it by $\sqrt{\alpha-\sigma^2}$, we obtain

$$\begin{aligned}&2\pi\int_{\Phi_{l,\min}}^{\alpha}\frac{\partial n}{\partial\sigma^2}(\alpha-\sigma^2)^{-1/2}d\sigma^2\\&=\int_{\Phi_{l,\min}}^{\alpha}\int_{\Phi_{l,\min}}^{\sigma^2}[(\sigma^2-\Phi_l)(\alpha-\sigma^2)]^{-1/2}\frac{ds}{d\Phi_l}d\Phi_l d\sigma^2\\&=\int_{\Phi_{l,\min}}^{\alpha}\frac{ds}{d\Phi_l}d\Phi_l\int_{\Phi_l}^{\alpha}[(\sigma^2-\Phi_l)(\alpha-\sigma^2)]^{-1/2}d\sigma^2\,.\end{aligned} \tag{41.44}$$

In the far right-hand side of this equation, we have changed the order of integration. The second integral in the far right-hand side of equation (41.44) is π, and equation (41.44) is then reduced to

$$2\int_{\Phi_{l,\min}}^{\alpha}\frac{\partial n}{\partial\sigma^2}(\alpha-\sigma^2)^{-1/2}d\sigma^2=\int_{\Phi_{l,\min}}^{\alpha}\frac{ds}{d\Phi_l}d\Phi_l=s(\alpha)\,. \tag{41.45}$$

By writing Φ_l in place of α, we eventually obtain the analytic solution of the Abel type integral equation:

$$s(\Phi_l)=2\int_{\Phi_{l,\min}}^{\Phi_l}\left[\frac{\partial n}{\partial\sigma^2}\right]_l(\Phi_l-\sigma^2)^{-1/2}d\sigma^2\,. \tag{41.46}$$

Since the acoustic length $s(\Phi_l)$ is the distance between the two branches of the potential curve determined by a given l, equation (41.46) gives the distance between the two turning points determined by both a form of the potential, which itself is dependent on l, and the level in the potential considered, $\Phi_l=\sigma^2$. Hence, hereafter, we regard the acoustic length as a function of both σ^2 and l, and we rewrite it with the two arguments

$$s(\sigma^2,l)=2\int_{\Phi_{l,\min}}^{\sigma^2}\left[\frac{\partial n}{\partial\sigma'^2}\right]_l(\sigma^2-\sigma'^2)^{-1/2}d\sigma'^2\,. \tag{41.47}$$

In this expression, σ^2 represents a level of the potential, l should be regarded as the parameter which determines the potential profile, and we write $d\sigma'^2$ in place of $d\sigma^2$ in equation (41.46). The acoustic length thus deduced from the integral equation is the time required for the sound wave of a given frequency σ to propagate between the two turning points:

$$s(\sigma^2,l)\equiv\int_{\tau_1}^{\tau_2} d\tau=\tau_2(\sigma^2,l)-\tau_1(\sigma^2,l)\,. \tag{41.48}$$

In equations (41.38)–(41.48), the minimum of the acoustic potential $\Phi_{l,min}$ is practically obtained by an extrapolation from a sequence of the square of observed frequencies with respect to the radial order n,

$$\Phi_{l,min}=\lim_{n\to 0}\sigma_{nl}^2\,, \tag{41.49}$$

for each value of l. The formula for extrapolation is not unique, but the final solution $s(\sigma^2, l)$ of the Abel type integral equation is not so significantly dependent on the manner of extrapolation.

41.2.5 Separation of Sound Velocity Term

The acoustic length $s(\sigma^2, l)$ is the length of the cut of the acoustic potential Φ_l for the degree l at the level of $\Phi_l=\sigma^2$ measured in terms of the acoustic radius. The acoustic potential itself consists of two terms, as shown in equation (41.29), of which the first is directly related to the sound velocity distribution. Since only that term depends on the degree l of modes, we can separate the sound velocity term by examining l-dependence of $s(\sigma^2, l)$ once we get the acoustic lengths for various values of l. It is convenient to use $l(l+1)$ instead of l as one of the arguments of s, since the acoustic potential Φ_l depends on the degree l only in terms of $l(l+1)$. So we write hereafter the acoustic length as $s=s(\sigma^2, L^2)$, where

$$L^2\equiv l(l+1)\,. \tag{41.50}$$

Differentiation of $s(\sigma^2, L^2)$ defined by equation (41.48) with respect to L^2 leads to

$$\frac{\partial s}{\partial L^2}=\frac{\partial\tau_2(\sigma^2,L^2)}{\partial L^2}-\frac{\partial\tau_1(\sigma^2,L^2)}{\partial L^2}$$

$$=\frac{1}{c(r_2)}\frac{\partial r_2}{\partial L^2}-\frac{1}{c(r_1)}\frac{\partial r_1}{\partial L^2}\,, \tag{41.51}$$

where $r_1(\sigma^2, L^2)$ and $r_2(\sigma^2, L^2)$ denote the radii of the inner and the outer turning points, respectively. Since the acoustic potential is generally dominated by the Lamb frequency in the deep interior and by the l-independent term in the outer envelope, as we note in the previous section, the inner and the outer turning points are at

$$\frac{L^2c^2(r_1)}{r_1^2}=\sigma^2 \tag{41.52}$$

and

$$\Psi(r_2)=\sigma^2\,, \tag{41.53}$$

respectively. Differentiating equations (41.52) and (41.53) with respect to L^2 while keeping σ^2 constant, we obtain

$$\left[\frac{\partial r_1}{\partial L^2}\right]_{\sigma^2}=-\frac{1}{2L^2}\frac{dr_1}{d\ln[c(r_1)/r_1]} \tag{41.54}$$

and

$$\left[\frac{\partial r_2}{\partial L^2}\right]_{\sigma^2}=0\,. \tag{41.55}$$

Substitution of equations (41.54) and (41.55) into equation (41.51) yields

$$\frac{d\ln r_1}{d[c(r_1)/r_1]}=2L^2\left[\frac{\partial s}{\partial L^2}\right]_{\sigma^2}\,. \tag{41.56}$$

The suffix 1 appearing in the left-hand side of equation (41.56) means that the quantities $c(r)$ and r should be evaluated at the inner turning point at which equation (41.52) is fulfilled. Then we rewrite equation (41.56) as

$$\left.\frac{d\ln r}{da(r)}\right|_{a(r)=\sigma/L}=2L^2\left[\frac{\partial s}{\partial L^2}\right]_{\sigma^2}\,, \tag{41.57}$$

where

$$a(r)\equiv c(r)/r\,. \tag{41.58}$$

The right-hand side of equation (41.57) can be evaluated by numerical differentiation of the acoustic length $s(\sigma^2, L^2)$ obtained by equation (41.47) as the solution of the integral equation (41.42). Then equation (41.57) provides the gradient of the sound velocity at the inner turning point of the mode. Once we get the acoustic lengths for various values of L^2 and σ^2, we then obtain $d\ln r/da$ as a function of a in a wide range in which the inner turning points of the modes are distributed, and we can regard equation (41.57) as a differential equation with respect to $r=r(a)$. By integrating it with an appropriate boundary condition, we get $r=r(a)$ and then eventually $c=c(r)$ from its inverse function.

The boundary condition for equation (41.57) should be given at the surface as

$$r=R \quad \text{at} \quad a=c(R)/R\,, \tag{41.59}$$

but it is in practice given as follows at the outermost point among the

turning points in hand, where $c = c(r)$ can be inferred from a theoretical model with little uncertainty. Since the outermost point is close enough to the surface, the sound velocity $c(r)$ is well approximated by

$$c^2(r) \propto \left(\frac{1}{r} - \frac{1}{R}\right). \tag{41.60}$$

Then the logarithmic derivative of $a(r) = c(r)/r$ with respect to r is estimated as

$$\frac{d\ln r}{d\ln a} \simeq -2(1 - r/R). \tag{41.61}$$

Equation (41.61) is useful to estimate the radial distance r/R of the outermost point corresponding to the smallest value of a.

41.2.6 An Alternative Complementary Inversion Method

We have extended the quantization rule between discrete eigenvalues and the corresponding integers to a continuous function of $n = n(\sigma^2, l)$, and have derived the integral equation (41.42), of which the known function is $\partial n/\partial\sigma^2$. In practice, we can estimate $\partial n/\partial\sigma^2$ from numerical differentiation of discrete eigenvalues σ^2_{nl} with respect to the radial order n while keeping l constant; $(\partial\sigma^2/\partial n)^{-1}$. In the case of a low degree l, insofar as the frequency σ is high enough, we can accurately calculate the numerical differentiation, since many radial overtones differing in n are available. However, in the case of a high degree $l (> 600)$, since the number of overtones differing in the radial order n for a given l is limited to only a few, such numerical differentiation of σ^2 with respect to n is in practice inaccurate.

So, in order to efficiently extract information from p-modes with high degree modes such as $l \geq 600$, we need to derive an alternative complementary integral equation in place of the integral equation (41.42). Differentiation of equation (41.41) with respect to l leads to

$$2\pi \frac{\partial n(\sigma^2, l)}{\partial l} = -(2l+1) \int_{\Phi_{l,min}}^{\sigma^2} (\sigma^2 - \Phi_l)^{-1/2} \frac{d\chi}{d\Phi_l} d\Phi_l, \tag{41.62}$$

where

$$\frac{d\chi}{d\Phi_l} \equiv \frac{c(r)^2}{r^2} \frac{ds}{d\Phi_l} = \frac{c(r)}{r^2} \frac{dr}{d\Phi_l(r)}, \tag{41.63}$$

since

$$\frac{\partial \Phi_l(r)}{\partial l} = (2l+1) \frac{c(r)^2}{r^2}. \tag{41.64}$$

Here, in estimating $\partial n/\partial l$, we have to first estimate the non-integer values of $n = n(\sigma^2, l)$ for each of l at any arbitrary values of σ^2 by interpolation with respect to both σ^2 and l. Such interpolation can be done even if there are only a few overtones, as in the case of high degree such as $l \geq 600$. The left-hand side of equation (41.62) is then observationally available, and it is regarded as a known function of σ^2 for a fixed l, which itself is obtained from observational data. Equation (41.62) is now regarded as an Abel-type integral equation with the unknown function to be solved $d\chi/d\Phi_l$ and the kernel $(\sigma^2 - \Phi_l)^{-1/2}$. The integral equation (41.62) can be analytically solved by a procedure similar to that described in the previous subsection, and the final solution is given as

$$\chi(\sigma^2, l) \equiv \int_{r_1}^{r_2} \frac{c(r)}{r^2} dr = -\frac{2}{(2l+1)} \int_{\Phi_{l,min}}^{\sigma^2} \left[\frac{\partial n}{\partial l}\right]_{\sigma^2} (\sigma^2 - \sigma'^2)^{-1/2} d\sigma'^2. \tag{41.65}$$

Here, since $\chi(\Phi_l)$ is determined by the level in consideration in the potential, which is itself determined by the degree l, we regard χ as a function of both σ^2 and l, and we rewrite it with the two arguments. Once we get $\chi(\sigma^2, l)$ for a wide range of l, by differentiating both sides of the second equality in equation (41.65), we obtain

$$\left.\frac{d\ln r}{d[a(r)^{-1}]}\right|_{a(r)=\sigma/L} = -\frac{2l(l+1)}{2l+1} \left[\frac{\partial \chi}{\partial l}\right]_{\sigma^2}. \tag{41.66}$$

which eventually gives the sound velocity distribution as equation (41.57) does.

If we use the following formula in order to estimate $\partial n/\partial\sigma^2$ for high degree modes such as $l > 600$, we may still use equation (41.42) even in the case of $l \geq 600$:

$$\frac{\partial n(\sigma^2, l)}{\partial \sigma^2} = -\frac{[\partial n(\sigma^2, l)/\partial l]_{\sigma^2}}{[\partial \sigma^2(n, l)/\partial l]_n}, \tag{41.67}$$

where the numerator is estimated by direct numerical differentiation and the denominator $\partial\sigma^2/\partial l$ can be easily estimated from the inclination of the curve connecting the modes of the fixed radial order n on the (l, ν)-diagram (or (k, σ)-diagram). One of the disadvantages in using equation (41.67) to estimate $\partial n(\sigma^2, l)/\partial\sigma^2$ is that we have to perform numerical differentiation twice. So we are better off using equation (41.62) rather than equation (41.42) with the help of equation (41.67).

41.2.7 Application to the Real Observational Data

The validity of the present asymptotic inversion method has been verified by Sekii and Shibahashi (1989) (see also Shibahashi and Sekii, 1988). They carried out numerical tests using a solar model and solved the inverse problem by regarding the theoretically calculated eigenfrequencies as the observed values to see how well the sound velocity distribution is reproduced. The practical procedure is the same as that used in the previous section 41.2.5. They used 1971 p-modes which are actually observed in the real sun. In order to determine the sensitivity of the method to the observational errors in eigenfrequencies, they prepared ten sets of simulate observational frequencies, which are distributed within the observed standard deviation around the true frequencies. Figure 41.6 shows the solutions together with the solution in the case of error-free data and the true sound velocity of the model. The ten sets of solutions are statistically distributed due to the statistical distribution of the frequency data itself around the solution in the case

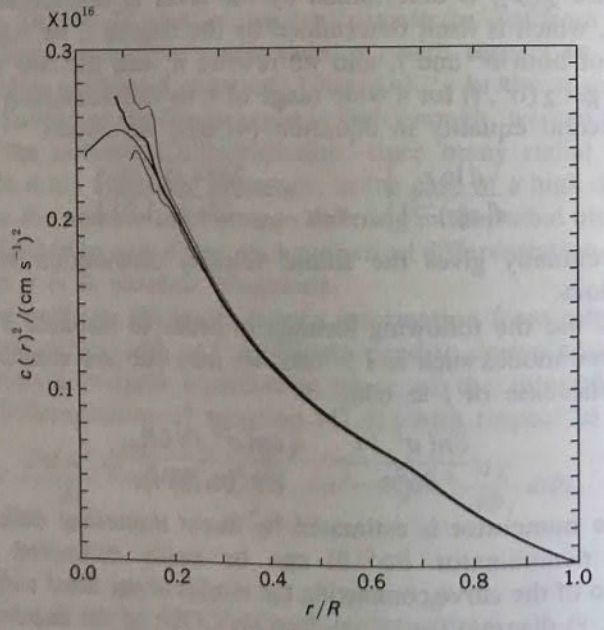

Fig. 41.6 The square of the sound velocity $c(r)^2$. The thin curves show the envelope of a set of solutions obtained by inversion of the erroneous data of eigenspectrum of 1971 p-modes. The thick curve shows the result of inversion of error-free eigenspectrum. The smooth thin curve shows the true value of the model, of which eigenspectrum of p-modes is used in the inverse problem. After Shibahashi and Sekii (1988).

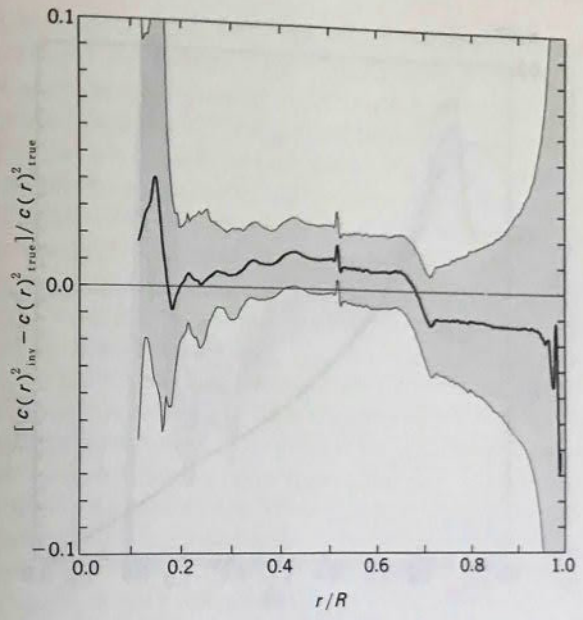

Fig. 41.7 The relative error of the squared sound velocity obtained as the solution of the inverse problem of p-mode oscillations in comparison with the true value of the model; $[c(r)^2_{\rm inv} - c(r)^2_{\rm true}]/c(r)^2_{\rm true}$. The thin curves show the envelope of a set of solutions obtained from the errorneous data of eigenspectrum of 1971 p-modes. The thick curve shows the result of inversion of error-free eigenspectrum. After Shibahashi and Sekii (1988).

of error-free data. The thin curves in this figure indicate the envelopes of the solutions, and they define the most reliable range for true sound velocity distribution. Figure 41.7 shows the relative difference between the true sound velocity distribution and the solutions deduced from the sets of p-mode spectrum. We see that the inversion method reproduces the true sound velocity in the range of $0.20 \leq r/R \leq 0.80$.

Since we have verified the usefulness of the present inversion method by performing numerical simulations, we now apply the method to the real observational data compiled by Duvall et al. (1988) and Libbrecht and Kaufman (1988). To estimate the error in the result of the deduced sound velocity distribution caused by observational error in the frequencies of modes, Shibahashi and Sekii (1988) constructed 72 sets of frequency spectra of 1971 modes in the range of $1 \leq l \leq 600$ by adding some amounts within the standard deviation to the reported frequencies. The thin curves of Fig. 41.8 show the envelopes of the set of sound velocity distribution deduced from each of the frequency spectra. We regard the belt surrounded by the envelopes in this figure as the reliable

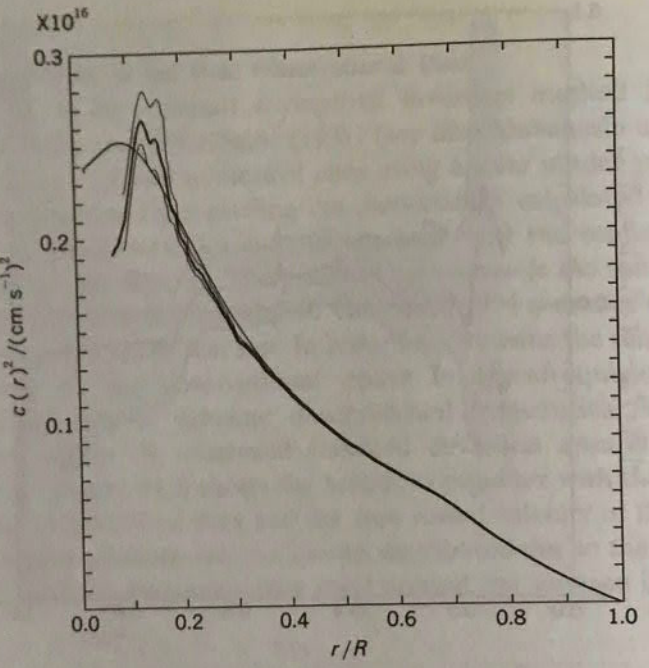

Fig. 41.8 The square of the sound velocity $c(r)^2$. The thick curve shows the inversion result from the observational data of 1971 modes compiled by Duvall et al. (1988) and Libbrecht and Kaufman (1988). The thin curves show the confidence level of 1σ due to the observational error in frequency spectrum. The smooth thin curve shows the value of a theoretical solar model of Shibahashi et al. (1983). After Shibahashi and Sekii (1988).

sound velocity inferred from the observational data which was compiled by Duvall et al. (1988) and Libbrecht and Kaufman (1988). The thick curve in the same figure indicates the sound velocity deduced from the reported frequencies without taking account of standard deviation. In the same figure, we plot the sound velocity distribution of the model 1 of Shibahashi et al. (1983). Figure 41.9 shows the difference between the sound velocity distribution deduced from the observational data and that of the theoretical model: $(c^2_{\rm inv} - c^2_{\rm model})/c^2_{\rm model}$. Since 72 statistical sets of frequency spectra have been used, the confidential level shown by these envelopes is estimated as 1σ. We find that the sound velocity $c(r)$ in the range of $0.20 \leq r/R \leq 0.40$ deduced from the p-mode spectrum is slower than that of the model.

As seen in Fig. 41.8, the gradient of the sound velocity $c(r)^2$ significantly varies near $r/R \simeq 0.70$, and this is the manifestation of the transition between the radiative core and the convective envelope (Christensen-Dalsgaard et al., 1985a). From the inversion of the

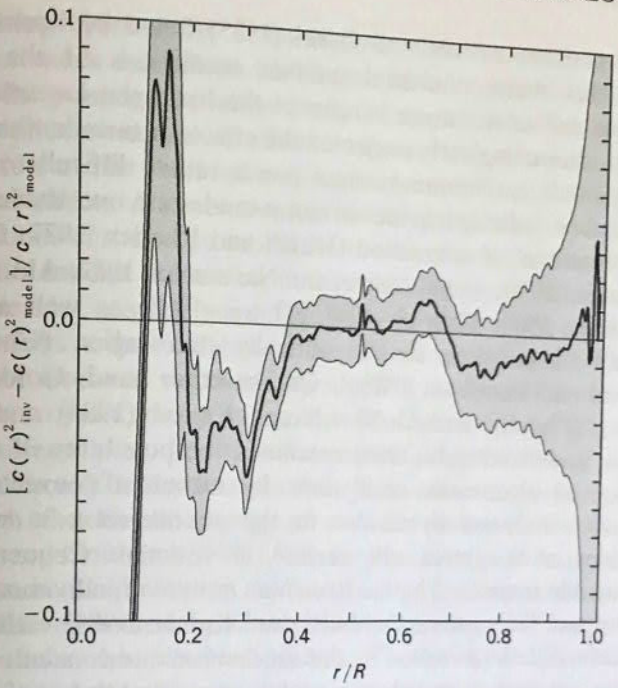

Fig. 41.9 The relative error of the squared sound velocity obtained as the solution of the inverse problem of p-mode oscillations in comparison with a theoretical model of Shibahashi et al. (1983); $[c(r)^2_{\rm inv} - c(r)^2_{\rm model}]/c(r)^2_{\rm model}$. The thick curve shows the inversion result from the observational data of 1971 modes compiled by Duvall et al. (1988) and Libbrecht and Kaufman (1988). The thin curves show the confidence level of 1σ due to observational error in the frequency spectrum. After Shibahashi and Sekii (1988).

observational data, we reach the same conclusion as that of the forward problem approach concerning the depth of the convective envelope — that is, the convective envelope is about 2.1×10^5 km deep (Christensen-Dalsgaard et al., 1985a). The gradient of the sound velocity also varies significantly very much at the ionization zone, and the amount of variation is dependent on the chemical abundance of the corresponding element. Gough (1984b) and Däppen and Gough (1984, 1986) derived a method of inferring the helium abundance by using the derivatives of the sound velocity.

42. *Excitation Mechanism*

For the excitation of observed oscillations, there exist two different models. One of the possibilities is the linear overstability of the eigenmodes, which is thought to be responsible for the pulsations of

Cepheid variables. Ando and Osaki (1975) found by linear stability analysis that many nonradial p-mode oscillations of the sun are overstable due to the κ-mechanism of the hydrogen ionization zone. However, they completely neglected the effects of turbulent convection on the p-mode oscillations because it was rather difficult to estimate them reliably. Indeed, whether or not p-modes are overstable depends on the treatment of convection (Ulrich and Rhodes, 1977; Goldreich and Keeley, 1977a; Antia, Chitre, and Narasimha, 1982; Antia, Chitre, and Gough, 1988; Gabriel, 1988; Chitre, 1988) as well as on the treatment of radiation in the optically thin region (Christensen-Dalsgaard and Frandsen, 1983a). On the other hand, Goldreich and Keeley (1977a, b), and Goldreich and Kumar (1988) and Kumar, Franklin, and Goldreich (1988) examined the possibility of stochastic excitation of eigenmode oscillations by turbulent convection. This mechanism is essentially similar to the phenomenon in which the oscillations of a system are excited at resonant frequencies and maintained at some level by the Brownian motion of individual particles that compose the system. Goldreich and Kumar (1988) estimated the energy of oscillations excited by this mechanism and concluded that the stochastic excitation model can explain the amplitudes of observed five-minute oscillations. The results might be, however, sensitive to the velocity of convection and the spectrum of the large eddies because they determine the absolute value of the energy of the resonant eddies. At present, it will be fair to say that the question of the excitation of the five-minute oscillation has not been settled yet.

We now compare the result of stability analysis with observations. If we discard the effects of turbulent convection on oscillations and adopt the Eddington approximation for the radiative transfer in the optically thin atmosphere, p-modes are overstable in wide ranges of n and l. For a given l the growth rate first increases with radial order of modes, but after reaching a maximum it decreases, and p-modes finally become stabilized for $\sigma \geq 0.03\ \mathrm{s}^{-1}$. The most unstable modes are those with a period around 300 s and with a wide range of degrees. The stabilization of higher p-modes is due to the strong radiative dissipation in the upper atmosphere. The general pattern of instability of p-modes appears in reasonable agreement with the distribution of observed power. However, f-modes almost always appear stable, because the excitation mechanism (κ-mechanism) does not operate for these modes due to their solenoidal nature (i.e., $\nabla \cdot \boldsymbol{\xi} \simeq 0$). On the other hand, observations show that the amplitudes of f-modes with high degree l are comparable with those of p-modes with the same range of l. This fact casts a serious suspicion on the justification of the hypothesis of

self-exciting overstability of oscillations. Observations show that the individual mode damps with the lifetime of the order of a few days. If we assume the p-modes are self-excited, the amplitudes of these modes will grow until some nonlinear effects suppress them. Some people claim, however, that the observed amplitudes seem too small to induce such nonlinear effects. A stochastic excitation hypothesis seems favorable for explanations of these two problems: the observation of f-modes and the lifetime of modes. According to this hypothesis, the turbulent convection generates acoustic noise, and acoustic noise in the sun's resonant cavity results in the excitation of the cavity's normal modes. The kinetic energy of modes is stochastically supplied by the turbulence, and the radiation works to damp the modes. The excited modes in this process are considered p-modes in the five-minute range because of the spectra of turbulence. These modes are thought to induce three-mode coupling, by which the kinetic energy of p-modes is transferred to f-modes (Kumar and Goldreich, 1989). The amplitudes of modes are determined by balance of power of turbulence and radiation damping. The amplitudes estimated by Goldreich and Keeley (1977b) were much smaller than the observed values. Goldreich and Kumar (1988) reinvestigated the efficiency of the generation of acoustic noise in the gravitationally stratified layer and found that the expected amplitudes are comparable with the observed amplitudes.

It is seen in Fig. 11.6 that width of peaks in the power spectrum of low-degree modes becomes broader with the increase of frequency σ. This tendency seems common in the higher range of l. The top panel of Fig. 42.1 shows the observed linewidth of modes with $l = 19 - 24$ and $l \simeq 60$ (Libbrecht, 1988b). The middle panel of Fig. 42.1 shows power per mode normalized to represent the mean square surface (radial) velocity per mode in $(\mathrm{cm\ s}^{-1})^2$. The bottom panel of Fig. 42.1 shows total energy per mode as a function of frequency derived from the observation and theoretical calculation of modes. Libbrecht (1988b, d) has discussed these data in relation to the possible excitation mechanisms. Theoretical growth rates are, however, not very accurate due to the uncertainty of convection-oscillation coupling, and the relation between the linear growth rate and the power of oscillations is not straightforward. More extensive theoretical investigations are highly desirable. Observations of the phase relationship between the velocity amplitude and the brightness amplitude of individual modes will provide helpful keys for estimating of the damping/excitation rate of modes and for understanding the excitation mechanism.

For g-mode oscillations, stability analysis shows that these modes are stable. Stochastic excitation mechanisms do not work to excite these

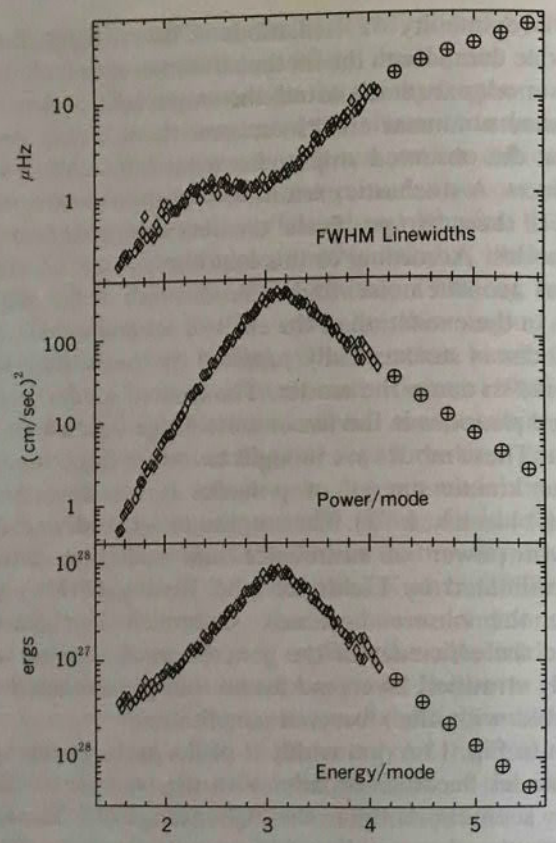

Fig. 42.1 FWHM linewidth (top), power per mode (middle), and total energy per mode (bottom) as a function of frequency, for modes with $l \sim 20$ analyzed by Libbrecht (1988b). The squares show fit from individual mode features with $l = 19 - 24$, and circles are the result of a more indirect high frequency analysis of $l \simeq 60$ modes.

modes, because the time scales of oscillations and of turbulence differ significantly. In order to explain reported observations of g-modes, nonlinear mode coupling has been discussed by Dziembowski (1982, 1983), and a possibility of excitation due to the magnetic torque has been discussed by Dziembowski, Paternó, and Ventura (1985).

43. Asteroseismology

The periods of the pulsations in classical variables have been used to get information about the structure of those stars. Although most of the classical pulsating variables present only a single mode (the radial

fundamental mode or the first overtone), the period has provided us a measure of the mean density of the star. Some of those stars, such as the double-mode Cepheids, are pulsating in two different modes, and then the stellar mass can be determined as one more item of information from the pulsations in addition to the mean density. Thus, the increase of pulsating modes in a star leads to the increase of the amount of information derived from the pulsation. The most successful case is the sun. Stimulated by the success of helioseismology, a similar attempt to probe the internal structure of stars in general is encouraged. In recent years, small amplitude pulsations have been discovered in many stars which were hitherto regarded as non-pulsating stars as reviewed in Chapter II. The most important characteristic of pulsations in these newly discovered variables is that their pulsations consist of many more eigenmodes than those in classical variables. This fact opens the possibility of a seismological approach to stars in general, and the research field probing the internal structure of stars in general is now called "asteroseismology." In this section, we evaluate the prospect and review the present status of asteroseismology. Some other useful reviews on the subject have been given by Christensen-Dalsgaard (1984c, 1986), Dziembowski (1984a), Shibahashi (1986), and Däppen, Dziembowski, and Sienkiewicz (1988b). Harvey (1988) reviewed techniques for observing stellar oscillations.

Though the success of helioseismology is quite encouraging, the seismological approach to stars in general is much more difficult than that to the sun. In most cases, the stellar image cannot be resolved into a two-dimensional disk image. Hence, the degree of the detectable oscillations is restricted to $0 \leq l \leq 4$. Otherwise the stellar surface is divided into many small regions oscillating in different phases, and the contribution of each region is canceled by others, so that the total amplitude of the variability of the star is too small to be detected. Some exceptions are rapidly rotating stars, in which rotationally broadened line profiles help the visibility of variation caused by intermediate degree modes up to $l \approx 10$ (see Section 7.3). As a consequence, the number of observed eigenmodes in an individual star is much less than in the solar case, and it is in many cases only a few. The degree l of a mode is not always uniquely determined since the stellar image cannot be resolved. The adjacent overtones are not always observed, and then it is difficult to determine the radial order n. Except for the sun and some binary stars, the radius and mass of a star are not determined precisely from other independent observations. If these quantities could be known, they would give strict constraints to the seismological approach. In practice, instead, these quantities also have to be

determined by using the oscillation data themselves. All of the facts described above make asteroseismology more difficult than helioseismology. Nevertheless, since asteroseismology is the unique method of probing observationally the interior of stars which can never be seen in principle, it is worth investigating. Indeed, solar-like oscillations have been reported in some stars, and a useful theoretical method of determining stellar mass and age has been proposed. The rapid oscillations in Ap stars are now regarded as a unique tool to investigate stellar internal magnetism. In this section, we discuss first the asteroseismology of sun-like oscillations, the rapidly oscillating Ap stars, and white dwarfs.

43.1 Sun-Like Oscillations

High order p-modes with low degrees such as $l = 0 - 4$ penetrate the stellar deep interior, and may be useful to the seismological approach. By assuming Goldreich and Keeley's (1977a, b) mechanism for the stochastic wave excitation by convective motion in late type stars, Christensen-Dalsgaard and Frandsen (1983b) estimated the amplitudes in brightness of high order p-modes with low degrees of those stars as $\Delta I/I \approx 10^{-5}$, which is much smaller than the photometric noise level for the ground-based observation ($\approx$ millimagnitude). Some aspiring attempts to detect such small amplitude oscillations have been made; two groups (Noyes, Baliunas, Belserene, Duncan, Horne, and Widrow, 1984; Gelly, Grec, and Fossat, 1986) have so far reported possible detection of them in stars α Cen (G2V) and α CMi (F5IV) and ε Eri (K2V), respectively, and Frandsen (1987) reported an upper limit on p-mode amplitudes in β Hyi (G2IV). According to the asymptotic theory of oscillations (Tassoul, 1980; see Section 16), the angular eigenfrequency σ_{nl} of the mode with the radial order n and the degree $l(n \gg l \approx 1)$ is given by (16.35), and the eigenfrequencies $\nu \equiv \sigma/2\pi$ of p-modes with even and odd l alternate, to first order, with equal spacing of $\nu_0/2$. Since the signal-to-noise ratio of these data is still marginal and the periodic oscillation is not conspicuous in the raw data, those two groups first calculated the power spectra of the data for variability and then searched for expected regular patterns in them. The Nice group (Gelly et al., 1986) reported in this way sun-like oscillations around $\nu \approx$ 3mHz with an equi-distance of 82.7μHz for α Cen and those around $\nu \approx$ 1.5mHz with an equi-distance of 43.7μHz for α CMi from their observation of radial velocity by means of their sodium cell spectrophotometer. Noyes et al. (1984) performed nightly monitoring of the intensities of the Ca H and K lines, and they also reported the sun-like oscillations in ε Eri around $\nu \approx 1.7$mHz with an equi-distance of 86μHz.

By using the frequency spacing thus obtained, we can impose some constraints on the physical parameters of those stars. The quantity ν_0 represents the inverse of the time required for the round trip of the sound wave between the surface and the center, and it is roughly proportional to $(M/R^3)^{1/2}$. Therefore, by assuming the mass of a star, we can estimate its radius from the observed quantity of spacing between eigenfrequencies of p-modes with low, even and odd degrees, ν_0. For α CMi, the radius thus obtained is $1.87R_\odot$ and it seems reasonable (Gelly et al., 1986). Since α Cen is a member of the closest multiple star system, its mass is well measured as $M = 1.09M_\odot$. Furthermore, the precise measurement of its temperature and of its distance leads to $R = 1.23 \pm 0.04R_\odot$. However, the radius inferred from the value of ν_0 is $R = 0.93R_\odot$ and hence there is an evident contradiction (Demarque, Guenter, and van Altena, 1986; Gelly et al., 1986).

According to the asymptotic theory (Tassoul, 1980), the departure from the true equi-distance of the power spectrum is given by

$$\sigma_{n,l} - \sigma_{n-1,l+2} \approx (4l+6) A \nu_0^2 / \sigma_{n,l} \equiv 2\pi (4l+6) D_0 , \qquad (43.1)$$

where

$$A \equiv \nu_0^{-1} \left[c(R)/R - \int_0^R \frac{dc}{dr} r^{-1} \, dr \right] . \qquad (43.2)$$

Since A is sensitive to conditions near the center of the star (Provost,

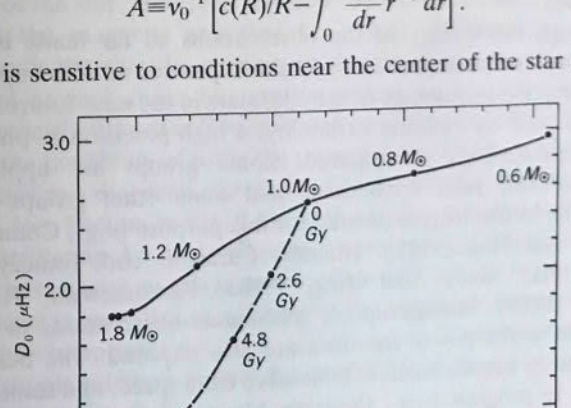

Fig. 43.1 The location of the ZAMS (solid line) and of a $1M_\odot$ evolution sequence (dashed line) in a (ν_0, D_0)-diagram, where $\nu_0 \equiv [2\int_0^R c^{-1} dr]^{-1}$ and $D_0 \equiv (\sigma_{n,l} - \sigma_{n-1,l+2})/[2\pi(4l+6)]$. In this diagram, we evaluate D_0 at $n = 22$ and $l = 1$. From Christensen-Dalsgaard (1984c).

1984), the departure from the equi-distance strongly depends on the evolutionary stage of the star. Hence, we can distinguish various models differing in mass and age on a two-dimensional (ν_0, D_0)-diagram (Christensen-Dalsgaard, 1984c, 1986, 1988; Ulrich, 1986a, 1988; Gough, 1987), if the chemical composition is given, as we can do on the HR diagram. Figure 43.1 shows the evolutionary track of a solar model on the (ν_0, D_0)-diagram. Plotting the observed values of ν_0 and D_0 on this diagram, we can determine the mass and age of a star. Precise measurements of eigenfrequencies of p-modes will become a powerful tool to determine these fundamental quantities of stars.

Guenter and Demarque (1986) compared the calculated oscillation spectrum and the location on the HR diagram of models of ε Eri with the observation by parameterizing the mass, the metallicity, and the mixing length. The best fit among their models has $M = 0.8M_\odot$, $Z = 0.02$, $\alpha = 1.00$, $R = 0.80R_\odot$, and an age of 11.5 Gyr. This model is so old that the high chromospheric activity (the observation was carried out by monitoring Ca H and K lines) and rapid rotation rate of the star seem to contradict their conclusion (Guenter, 1987). Soderblom and Däppen (1986) have proposed another possibility, that of a young stellar model. A precise measurement of D_0 will be useful to examine their conclusions.

Though the quality of the observations so far made is not yet satisfactory, the attempts described above provide us with hope that we can develop the seismology of sun-like stars in the near future. In order to detect their very minute variability, a high precision in photometry and/or spectroscopy is required. Some groups are applying the instruments for solar oscillations, and some other groups are now developing instruments dedicated for this purpose (e.g., Connes, 1985; Butcher and Hicks, 1986; Rhodes, Cacciani, and Tomczyk, 1986; Pietraszewski, Reay, and Ring, 1986a; Pietraszewski, Ring, and Forrest, 1986b). Uninterrupted, continuous observations to get high resolution in the power spectrum are also required. The best way to achieve these requirements is to observe from space, and some projects are now in progress (e.g., Praderie, Mangeney, Lemaire, Puget, and Bisnovatyi-Kogan, 1988; Soderblom, 1988). Though the range of l of detectable modes is limited to $0 \le l \le 4$, if many overtones differing in radial order are detected we can, in principle, infer the sound velocity distribution in the stellar interior as the inverse problem. The recipe is essentially the same as that outlined in Section 41 for the inverse problem of solar oscillations. Whether or not such an inverse approach is practically applicable depends on the quality of observations; at the present moment, it is quite uncertain.

43.2 Rapidly Oscillating Ap Stars

The rapidly oscillating Ap stars are another group of stars which reveal high-order p-mode oscillations with low degrees l. Therefore, discussions in the previous subsection are also valid for these stars. Another interesting and unique feature is that the oscillations in Ap stars seem significantly influenced by the stellar magnetism as well as the rotation. We mainly discuss this aspect in the following.

Let us consider a uniformly rotating, magnetic star, whose magnetic axis is inclined to the rotation axis by the angle β. We assume here that the effect of the magnetic field upon the oscillations dominates over that of the rotation. Then a form of normal modes labeled by the azimuthal order m ($m = -l, \ldots, l$) with respect to the magnetic axis is given by equation (19.84) (Kurtz and Shibahashi, 1986), and the observable luminosity variation due to a normal mode is given by equation (19.92). Equation (19.92) means that even if only a single mode is excited, $(2l+1)$-fold frequency components, $(\sigma^{(0)} + \sigma^{(1)mag}_{|m|} + m\Omega\cos\beta) - m'\Omega$ for $m' = -l, \ldots, l$, with spacing equal to the rotational frequency Ω of the star with respect to an inertial frame are observed as a result of the variation in the aspect angle of the eigenmode with the rotation of the star. Here, β is the angle between the rotation axis of the star and the magnetic axis (see Fig. 19.1). Furthermore, equation (19.92) indicates that the relative amplitudes of those components are not equal to each other but are dependent on the rotation and the magnetic field of the star (Dziembowski and Goode, 1985, 1986). This leads to the possibility of using the observed fine structure of oscillation frequencies as a diagnosis of rotation and the internal magnetic field of Ap stars (see Section 9; Fig. 9.4). In this sense, the observation of the rapidly oscillating Ap stars will open a new aspect of asteroseismology.

Let us consider an axisymmetric mode with respect to the magnetic axis of the star ($m = 0$). Let $A_l^{m'}$ denote the amplitude corresponding to a frequency component $\sigma = \sigma^{(0)} + \sigma^{(1)mag}_{m=0} - m'\Omega$. Then equation (19.92) leads to simple relations among the amplitudes of the $(2l+1)$-fold fine structure (see Fig. 9.4):

$$\frac{A_l^{m'} + A_l^{-m'}}{A_l^0} = \frac{2d^{(l)}_{0m'}(\beta)d^{(l)}_{m'0}(i)}{d^{(l)}_{00}(\beta)d^{(l)}_{00}(i)} \tag{43.3}$$

since

$$d^{(l)}_{ij}(\beta) = -d^{(l)}_{i-j}(\beta)\,, \tag{43.4}$$

and

$$\frac{A_l^{m'}-A_l^{-m'}}{A_l^{m'}+A_l^{-m'}}=\frac{m' C_{nl}\Omega}{\sigma_{|m|=0}^{(1)mag}-\sigma_{|m|=1}^{(1)mag}}, \tag{43.5}$$

where β and i denote the angle between the rotation axis and the magnetic axis and that between the rotation axis of the star and the line-of-sight, respectively. In equations (43.3) and (43.4), $d_{mm'}^{(l)}(\beta)$ and $d_{mm'}^{(l)}(i)$ are defined by equations (19.69) and (19.88), respectively, and they are constants depending on the mode considered and the geometrical configuration. Equation (43.3) means that the ratio of the summation of the amplitudes of $\pm m'$-components to the amplitude of the central component of the fine structure provides us information about the geometrical configuration. Equation (43.5) means that the relative difference of the amplitudes of $\pm m'$-components gives a ratio between the effects of the rotation and of the magnetic field upon the oscillation. It should be noted that in equation (43.5) the magnetic effect on the oscillation appears only in terms of $\sigma_{|m|=0}^{(1)mag}-\sigma_{|m|=1}^{(1)mag}$ since the eigenfunction with $m = 0$ is modified by the Coriolis force to be mixed only with $m = \pm 1$ components. It should also be noted here that the exact form of the magnetic perturbation to frequency $\sigma_{|m|}^{(1)mag}$ is not necessary in deriving the above formulae. Only axial symmetry is taken into account. For $l = 1$, equations (43.3) and (43.5) are reduced to

$$\frac{A_1^1+A_1^{-1}}{A_1^0}=\tan\beta\tan i \tag{43.6}$$

and

$$\frac{A_1^1-A_1^{-1}}{A_1^1+A_1^{-1}}=\frac{C_{n,1}\Omega}{\sigma_{|m|=0}^{(1)mag}-\sigma_{|m|=1}^{(1)mag}}. \tag{43.7}$$

Also for $l = 2$, those equations are reduced to

$$\frac{A_2^2+A_2^{-2}}{A_2^0}=\frac{3\sin^2\beta\sin^2 i}{(3\cos^2\beta-1)(3\cos^2 i-1)}, \tag{43.8}$$

$$\frac{A_2^2+A_2^{-2}}{A_2^2+A_2^{-2}}=\frac{2C_{n,2}\Omega}{\sigma_{|m|=0}^{(1)mag}-\sigma_{|m|=1}^{(1)mag}}, \tag{43.9}$$

$$\frac{A_2^1-A_2^{-1}}{A_2^0}=\frac{12\sin\beta\cos\beta\sin i\cos i}{(3\cos^2\beta-1)(3\cos^2 i-1)}, \tag{43.10}$$

and

$$\frac{A_2^1-A_2^{-1}}{A_2^1+A_2^{-1}}=\frac{C_{n,2}\Omega}{\sigma_{|m|=0}^{(1)mag}-\sigma_{|m|=1}^{(1)mag}}. \tag{43.11}$$

By using these formulae, if we obtain fine structures in the power

Table 43.1 Application of equations (43.6) and (43.7).

HD	$\tan\beta\tan i$	$\frac{C_{n,1}\Omega}{\sigma_0^{(1)mag}-\sigma_1^{(1)mag}}$	Π_{rot}	H_e	Reference
6532	2.14	0.295	$1^d.7858$		Kurtz and Kreidl (1985)
83368	9.65	0.10	2.85	−700~+700 G	Kurtz and Shibahashi (1986)

spectrum, we can compare the relative importance of the effects of the magnetic field and of the rotation on the oscillations and derive some constraints on the geometric configuration of the star. The latter can be verified by using the variation in the observed magnetic field, if we apply the oblique rotator model for the magnetic field. Table 43.1 lists the results of the application of equations (43.6) and (43.7) to some of the rapidly oscillating Ap stars listed in Table 9.1. The second and the third columns give $\tan\beta\tan i$ and $C_{n,l=1}\Omega/(\sigma_{|m|=0}^{(1)mag}-\sigma_{|m|=1}^{(1)mag})$ derived from those equations, respectively. The fourth and the fifth columns give the rotational periods and the surface magnetic field strength obtained from other independent observations. For HD 6532, the surface magnetic field has not yet been measured. Comparing the values of $C\Omega/(\sigma_{|m|=0}^{(1)mag}-\sigma_{|m|=1}^{(1)mag})$ and the rotation period of this star and of HD 83368, we expect that the surface magnetic field of HD 6532 is of the order of 300 G insofar as we suppose $\sigma_{|m|}^{(1)mag}\propto H_e^2$ (Kurtz and Shibahashi, 1986). The measurement of the surface magnetic field strength H_e of HD 6532 may allow examination of this prediction based on the asteroseismological approach to Ap stars.

So far we have not specified a form of $\sigma_{|m|}^{(1)mag}$. In the case of a dipole magnetic field, the denominator of the right-hand side of equation (43.5), $\sigma_{|m|=0}^{(1)mag}-\sigma_{|m|=1}^{(1)mag}$, is positive. Then, equation (43.5) predicts that the amplitude of the lower frequency-component in the fine structure is higher than that of the higher frequency-component (see Fig. 9.4). Table 43.1 shows that this is the case for HD 6532 and HD 83368. We can infer the internal magnetic field strength of Ap stars from equation (43.5). Although the directly observable magnetic field strength, H_e, gives us only the magnetic field strength at the stellar surface, the information of the magnetism yielded by the oscillation data provides us a field strength averaged in the stellar interior by means of the eigenfunctions. Such information will provide us useful concepts for the understanding of the physics of Ap stars.

43.3 White Dwarfs

Since the number of modes of an individual pulsating white dwarf is larger than those of other type pulsating stars except for the sun, asteroseismology of white dwarfs may be promising. The oscillations in white dwarfs are regarded as nonradial g-modes. According to the asymptotic theory for high order g-modes with low degrees l, there is a simple relation given by equation (11.8) among the periods, the degree l, and the radial order n (Tassoul, 1980; Section 16) as in the case of p-modes. Kawaler (1987a,b, 1988b) applied this relation to obtain some constraints on the physical quantities of some of pulsating white dwarfs.

Cooling rates of pre-white dwarfs are thought to be rapid enough to enable us to detect the resultant period change of pulsations (Winget, Hansen, and Van Horn, 1983). Hence, detection of such a period change will provide us a direct measurement of stellar evolution. The frequency of each eigenmode is very sensitive to the internal distribution of the Brunt-Väisälä frequency, which is sensitive to the internal temperature of the white dwarf as well as the stellar radius. At the pre-white dwarf stage, as the star becomes more compact, the period becomes shorter. At some later stage, the effect of the cooling of the internal temperature upon the frequency of g-mode oscillations may dominate that of the decrease of the stellar radius, and the period tends to increase. Kawaler, Hansen, and Winget (1985a) theoretically showed that the transition from negative to positive $d\Pi/dt$ occurs at nearly 1000 solar luminosity for a wide variety of the planetary nebula nuclei and pre-white dwarf models, and $d\Pi/dt$ is near zero only for a very short time. Since the cooling time scale of DO pre-white dwarfs is only of the order of 10^6 yr, while it is 10^{7-8} yr (10^9 yr) for DB (DA) white dwarfs, Winget et al. (1983) expected that the period change in oscillations of PG1159 variables was detectable within 2-3 years. In fact, such a measurement of period changes was later realized by Winget, Kepler, Robinson, Nather, and O'Donoghue (1985). The observed period change rates $\Pi/\dot{\Pi}$ are $=1.4 \times 10^6$ yr for PG1159-035 (Winget et al., 1985) and $|\Pi/\dot{\Pi}| > 6.9 \times 10^8$ yr for a ZZ Ceti star, G117-B15A (Kepler, Winget, Robinson, and Nather, 1988). Though these absolute values are in agreement with the expectation, the sign of $\dot{\Pi}$ for PG1159-035 ($\dot{\Pi} = -1.2 \times 10^{-11}$s s^{-1}) is contrary to the theoretical expectation of Kawaler et al. (1985a). Kawaler, Winget, and Hansen (1985b) claimed that this may indicate that some other important factors such as the rotation, the diffusion of chemical elements, and so on should be taken into account to estimate $\dot{\Pi}$. Measurement of period change will give us some clues to understand the evolutionary stage of pulsating hot pre-white dwarfs.

The eigenfrequencies of g-modes are mainly governed by the Brunt-Väisälä frequency distribution in the star. Therefore, we can, in principle, obtain some information about the Brunt-Väisälä frequency distribution in the star by means of a seismological approach. The Brunt-Väisälä frequency is related with the entropy gradient, which is itself dependent on the past nuclear reaction, cooling rate, degeneracy, diffusion of elements, and convection. None of these fundamental processes have been well understood. Therefore, the seismological study based on the inverse problem of white dwarf oscillations may provide a unique tool to investigate these elementary processes, and hence it is worth doing, though such an attempt using the available data at the moment seems somehow ambitious. The following is an inversion method developed by Shibahashi, Sekii, and Kawaler (1988), which is a variant of an inversion method described in Section 41.2 to probe the sound velocity distribution in the sun from the p-mode oscillations of the sun.

The wave equation governing the radial part of g-mode oscillation is, in some limiting cases, reduced to a form similar to the Schrödinger equation in quantum mechanics, which is written as

$$\frac{d^2\psi}{dr^2}+\frac{N^2}{r^2}\left[\frac{l(l+1)}{\sigma^2}-\Xi_l(r)\right]\psi=0\,. \tag{43.12}$$

Here, ψ denotes an eigenfunction, $l(l+1)/\sigma^2$ is regarded as the eigenvalue, and $\Xi_l(r)$ is the "gravity wave potential" which consists of a product of $l(l+1)$ and the inverse of Brunt-Väisälä frequency and the l-independent part $\Theta(r)$:

$$\Xi_l(r)\equiv\frac{l(l+1)}{N^2}+\Theta(r)\,. \tag{43.13}$$

The first term in the right-hand side of equation (43.13) dominates over $\Theta(r)$ in the inner part of a white dwarf, while $\Theta(r)$ becomes large in the outer part. Based on the WKBJ asymptotic method, the quantization rule leads to

$$(n+\epsilon)\pi=\int_{r_1}^{r_2}\left[\frac{l(l+1)}{\sigma^2}-\Xi_l(r)\right]^{1/2}\frac{N}{r}\,dr\,, \tag{43.14}$$

where n is the radial order of the mode and r_1 and r_2 are the turning points at which the integrand of the right-hand side of equation (43.14) vanishes. The quantization rule gives only a relation between discrete eigenvalues $l(l+1)/\sigma^2$ and the corresponding integers n. But hereafter we extend this relation to nonintegers n by interpolation and deal with

equation (43.14) as if it were a relation among continuous variables $l(l+1)/\sigma^2$, n, and l. If we can identify each of the observed modes, then we can regard equation (43.14) as an integral equation, in which $(n+\epsilon)\pi$ is the known function of $l(l+1)/\sigma^2$, the kernel is $[l(l+1)/\sigma^2-\Xi_l]^{1/2}$, and the unknown to be solved is N/r, since, for a fixed value of l, the left-hand side of equation (43.14) is a function of $l(l+1)/\sigma^2$.

The mathematical procedure to solve this integral equation is parallel to that to solve the integral equation for p-mode oscillations, equation (41.33). The solution gives the distance between two turning points measured with the gravity wave velocity:

$$s(\Xi_l,l)\equiv\int_{r_1}^{r_2}\frac{N}{r}\,dr$$

$$=2\int_{[l(l+1)/\sigma^2]_{min}}^{\Xi_l}\frac{\partial n}{\partial[l(l+1)/\sigma^2]}\,[\Xi_l-l(l+1)/\sigma^2]^{-1/2}\,d[l(l+1)/\sigma^2]\,. \tag{43.15}$$

Here, the lower limit of the integral region corresponds to the minimum of the gravity wave potential, and it is obtained by extrapolating eigenvalues to $n=0$. Once we get solutions (43.15) for some different degrees, we can obtain

$$d[1/N(r_1)]/d\ln r_1=(2l+1)/[2l(l+1)]\cdot(\partial s/\partial l)^{-1} \tag{43.16}$$

by differentiating solutions (43.15) with respect to l since the inner turning point of r_1 is approximately given by

$$N^2(r_1)=\sigma^2\,. \tag{43.17}$$

The right-hand side of equation (43.16) is evaluated at a given $l(l+1)/\sigma^2$; thus, by using equation (43.17), we should regard equation (43.16) as an equation to give $d[1/N(r_1)]/d\ln r_1$ as a function of $N(r_1)$. By using a reasonable range of l, we eventually obtain the Brunt-Väisälä frequency distribution in the white dwarf.

Figure 43.2 shows the result of the numerical simulation performed by Shibahashi et al. (1988). It shows the true Brunt-Väisälä frequency of the model (thin curve) as a function of $\int_0^r N/r\,dr$ (lower scale) and the Brunt-Väisälä frequency obtained as the solution of the inverse problem of 95 eigenmodes of g-modes with $l=1-10$ (thick curve), which are shown in the $(l,[l(l+1)/\sigma^2]^{1/2})$-diagram of Fig. 43.3. In solving the integral equation, Shibahashi et al. (1988) supposed that the modes were well identified and used wider ranges of l than the actually detectable modes in order to examine the validity of the inversion

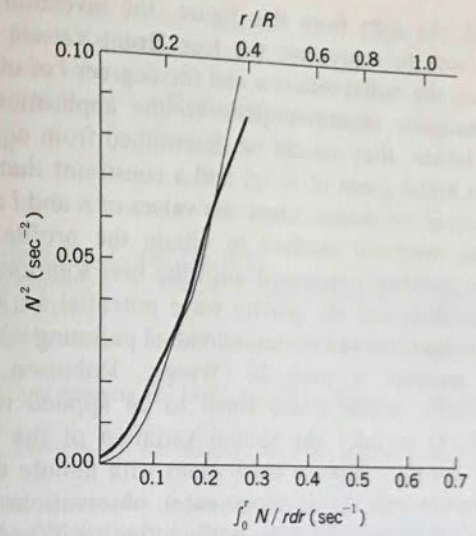

Fig. 43.2 The Brunt-Väisälä frequency distribution in the pre-white dwarf model of Shibahashi et al. (1988) ($M=0.60M_\odot$, $L=100L_\odot$) (thin curve) as a function of $\int_0^r N/r\,dr$ and the inverted result from the g-mode oscillations spectrum (thick curve). The upper scale of the abscissa indicates r/R as a reference.

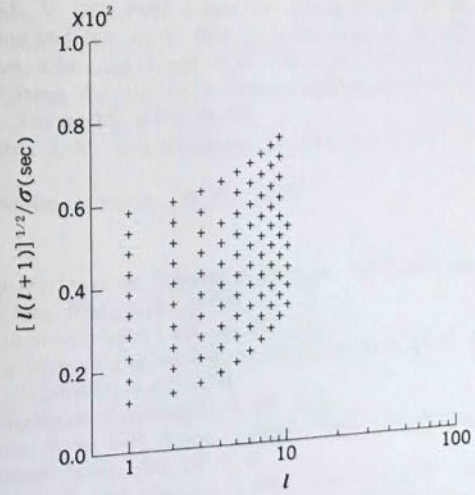

Fig. 43.3 The eigenmodes used in the numerical simulation for the inverse problem performed by Shibahashi et al. (1988). The ordinate and the abscissa indicate l and $[l(l+1)]^{1/2}/\sigma$, respectively.

method itself. As seen from this figure, the inversion method itself works quite well to reproduce the true Brunt-Väisälä frequency. In practical cases, the radial orders n and the degrees l of observed modes cannot be uniquely identified prior to the application of equation (43.14); or, rather, they should be determined from equation (43.14) itself with an initial guess of $N^2(r)$ and a constraint that they must be integers for observed modes. Once the values of n and l are fixed, then we apply the inversion method to obtain the profile of N^2. Such processes are iteratively repeated until the best solutions for both the mode identification and the gravity wave potential are obtained. The number of modes observed for an individual pulsating white dwarf is at the present moment at most 28 (Winget, Robinson, Nather, and Fontaine, 1982b), which is too small to be applied to the integral equation (43.14) to infer the spatial variation of the Brunt-Väisälä frequency in the star. If more oscillations with minute amplitudes are detected in future with the development in observations, the inference of N^2-profile following the recipe outlined here will become possible.

References

A

Abt, H. A. 1957, *Astrophys. J.*, **126**, 138. [§ 5].

Aizenman, M. L., Hansen, C. J., Cox, J. P., and Pesnell, W. D. 1984, *Astrophys. J. Letters*, **286**, L43. [§ 19].

Aizenman, M. L., Hansen, C. J., and Ross, R. R. 1975, *Astrophys. J.*, **201**, 387. [§ 27].

Aizenman, M. L., and Smeyers, P. 1977, *Astrophys. Space Sci.*, **48**, 123. [§§ 13, 14, 19].

Aizenman, M. L., Smeyers, P., and Weigert, A. 1977, *Astron. Astrophys.*, **58**, 41. [§§ 3, 15, 16].

Ando, H. 1976, *Publ. Astron. Soc. Japan*, **28**, 517. [§ 28].

Ando, H. 1981, *Monthly Notices Roy. Astron. Soc.*, **197**, 1139. [§§ 35, 36].

Ando, H. 1983, *Publ. Astron. Soc. Japan*, **35**, 343. [§ 36].

Ando, H. 1985, *Publ. Astron. Soc. Japan*, **37**, 47. [§§ 33, 36].

Ando, H. 1986, *Astron. Astrophys.*, **163**, 97. [§ 36].

Ando, H. 1989, *Publ. Astron. Soc. Japan*, in press. [§ 33].

Ando, H., and Osaki, Y. 1975, *Publ. Astron. Soc. Japan*, **27**, 581. [§§ 3, 11, 25, 28, 40, 42].

Ando, H., and Osaki, Y. 1977, *Publ. Astron. Soc. Japan*, **29**, 221. [§ 38].

Andrews, D. G., and McIntyre, M. E. 1978, *J. Atmos. Sciences*, **35**, 175. [§ 36].

Antia, H.M., Chitre, S.M., and Gough, D.O.1988, in *Advances in Helio- and Asteroseismology, IAU Symp. No. 123*, ed. J. Christensen-Dalsgaard and S. Frandsen (D. Reidel Publ. Co., Dordrecht), p.371. [§ 42].

Antia, H. M., Chitre, S. M., and Narasimha, D. 1982, *Solar Phys.*, **77**, 303. [§§ 30, 42].

Auré, J.-L. 1971, *Astron. Astrophys.*, **11**, 345. [§ 29].

B

Baade, D. 1981, in *Workshop on Pulsating B Stars*, ed. G.E.V.O.N. and C. Sterken, (Observatiore de Nice, Nice), p.267. [§ 36].

Baade, D. 1984, *Astron. Astrophys.*, **135**, 101. [§§ 7, 8].

Baade, D. 1986a, in *Seismology of the Sun and the Distant Stars*, ed. D. O. Gough (D. Reidel Publ. Co., Dordrecht), p.465. [§ 8].

Baade, D. 1986b, *Highlights of Astronomy*, **7**, 225. [§ 8].

Baade, D., and Weiss, W.W. 1987, *Astron. Astrophy. Suppl.*, **67**, 147. [§ 7].

Baade, W. 1926, *Astron. Nachr.*, **228**, 359. [§ 6].

Backus, G., and Gilbert, F. 1968, *Geophys. J. Roy. Astron. Soc.*, **16**, 169. [§ 41].

Backus, G., and Gilbert, F. 1970, *Phil. Trans. Roy. Soc. London, Ser. A*, **266**, 123. [§ 41].

Baglin, A. 1971, in *White Dwarfs, IAU Symp. No. 42*, ed. W. J. Luyten (D. Reidel Publ. Co., Dordrecht), p.136. [§ 29].

Note : Numbers in square brackets refer to the sections in which the reference is cited.

Bahcall, J. N., and Ulrich, R. K. 1988, *Rev. Mod. Phys.*, **60**, 297. [§ 40].
Baker, N. H. 1966, in *Stellar Evolution*, ed. R. F. Stein and A. G. W. Cameron (Plenum Press, New York), p.333. [§ 26].
Baker, N. H., and Gough, D. O. 1979, *Astrophys. J.*, **234**, 232. [§§ 21, 30].
Baker, N. H., and Kippenhahn, R. 1962, *Z. Astrophys.*, **54**, 114. [§ 25].
Baker, N. H., Moore, D. W., and Spiegel, E. A. 1971, *Q. J. Mech. Appl. Math.*, **24**, 391. [§ 18].
Balachandran, S., Robinson, E. L., and Kepler, S. O. 1983, *Publ. Astron. Soc. Pacific*, **95**, 653. [§ 10].
Balona, L. A. 1985, *Monthly Notices Roy. Astron. Soc.*, **214**, 559. [§ 8].
Balona, L. A. 1986a, *Monthly Notices Roy. Astron. Soc.*, **219**, 111. [§§ 7, 8].
Balona, L. A. 1986b, *Monthly Notices Roy. Astron. Soc.*, **220**, 647. [§§ 7, 8].
Balona, L. A. 1987, *Monthly Notices Roy. Astron. Soc.*, **224**, 41. [§§ 7, 8].
Balona, L. A., and Engelbrecht, C. A. 1983, *Monthly Notices Roy. Astron. Soc.*, **202**, 293. [§ 8].
Balona, L. A., and Engelbrecht, C. A. 1985a, *Monthly Notices Roy. Astron. Soc.*, **212**, 889. [§ 8].
Balona, L. A., and Engelbrecht, C. A. 1985b, *Monthly Notices Roy. Astron. Soc.*, **214**, 559. [§ 8].
Balona, L. A., and Engelbrecht, C. A. 1986, *Monthly Notices Roy. Astron. Soc.*, **219**, 131. [§ 8].
Balona, L. A., and Shobbrook, R. R. 1983, *Monthly Notices Roy. Astron. Soc.*, **205**, 309. [§ 8].
Balona, L. A., and Stobie, R. S. 1979a, *Monthly Notices Roy. Astron. Soc.*, **187**, 217. [§ 6].
Balona, L. A., and Stobie, R. S. 1979b, *Monthly Notices Roy. Astron. Soc.*, **189**, 659. [§ 6].
Balona, L. A., and Stobie, R. S. 1980, *Monthly Notices Roy. Astron. Soc.*, **190**, 931. [§ 6].
Belvedere, G., and Paternó, L. 1984, ed. *Oscillations as a Probe of the Sun's Interior*, published as *Mem. Soc. Astron. Ital.*, **55**. [§ 37].
Berthomieu, G., Cooper, A. J., Gough, D. O., Osaki, Y., Provost, J., and Rocca, A. 1980, in *Nonlinear and Nonradial Stellar Pulsation*, ed. H. A. Hill and W. A. Dziembowski (Springer-Verlag, Berlin), p.307. [§ 40].
Berthomieu, G., Gonczi, G., Graff, Ph., Provost, J., and Rocca, A., 1978, *Astron. Astrophys.*, **70**, 597. [§§ 3, 34].
Berthomieu, G., and Provost, J. 1983, *Astron. Astrophys.*, **122**, 199. [§ 19].
Berthomieu, G., Provost, J., and Schatzman, E. 1984, *Nature*, **308**, 354. [§ 40].
Biront, D., Goossens, M., Cousens, A., and Mestel, L. 1982, *Monthly Notices Roy. Astron. Soc.*, **201**, 619. [§ 29].
Bolton, C. T. 1982, in *Be stars, IAU Symp. No. 98*, ed. M. Jaschek and H.-G. Groth (D. Reidel Publ. Co., Dordrecht), p.181. [§ 36].
Bond, H. E., and Grauer, A. D. 1987, *Astrophys. J. Letters*, **321**, L123. [§ 10].
Bond, H. E., Grauer, A. D., Green, R. F., and Liebert, J. W. 1984, *Astrophys. J.*, **279**, 751. [§ 10].
Boury, A., Gabriel, M., Noels, A., Scuflaire, R., and Ledoux, P. 1975, *Astron. Astrophys.*, **41**, 279. [§ 27].
Boussinesq, J. 1903, *Théorie analytique de la chaleur*, Vol. 2 (Gauthier-Villars, Paris), p.172. [§ 29].
Brickhill, A. J. 1975, *Monthly Notices Roy. Astron. Soc.*, **170**, 405. [§ 10].

Brodsky, M. A., and Levshin, A. 1979, *Geophys. J. Roy. Astron. Soc.*, **58**, 631. [§ 41].
Brodsky, M. A., and Vorontsov, S. V. 1988, in *Advances in Helio- and Asteroseismology, IAU Symp. No. 123*, ed. J. Christensen-Dalsgaard and S. Frandsen (D. Reidel Publ. Co., Dordrecht), p.133. [§ 41].
Brookes, J. R., Isaak, G. R., and van der Raay, H. B. 1978, *Monthly Notices Roy. Astron. Soc.*, **185**, 1. [§§ 11, 39].
Brown, T. M. 1984, in *Solar Seismology from Space*, ed. R. K. Ulrich, J. Harvey, E. J. Rhodes, Jr., and J. Toomre (Jet Propulsion Laboratory, Pasadena), p.157. [§§ 11, 39].
Brown, T. M. 1985, *Nature*, **317**, 591. [§§ 3, 39].
Brown, T. M. 1986, in *Seismology of the Sun and the Distant Stars*, ed. D. O. Gough (D. Reidel Publ. Co., Dordrecht), p.199. [§ 39].
Brown, T. M. 1988, in *Advances in Helio- and Asteroseismology, IAU Symp. No. 123*, ed. J. Christensen-Dalsgaard and S. Frandsen (D. Reidel Publ. Co., Dordrecht), p.453. [§ 39].
Brown, T. M., Mihalas, B. W., and Rhodes, E. J., Jr. 1986, in *Physics of the Sun, Vol. I.*, ed. P. A. Sturrock, T. E. Holzer, D. M. Mihalas, and R. K. Ulrich (D. Reidel Publ. Co., Dordrecht), p.177. [§ 37].
Brown, T. M., and Morrow, C. A. 1987a, *Astrophys. J. Letters*, **314**, L21. [§ 39].
Brown, T. M., and Morrow, C. A. 1987b, in *The Internal Solar Angular Velocity*, ed. B. R. Durney and S. Sofia (D. Reidel Publ. Co., Dordrecht), p.7. [§ 39].
Brown, T. M., Stebbins, R. T., and Hill, H. A. 1978, *Astrophys. J.*, **223**, 324. [§ 11].
Butcher, H. R., and Hickes, T. R. 1986, in *Seismology of the Sun and the Distant Stars*, ed. D. O. Gough (D. Reidel Publ. Co., Dordrecht), p.347. [§ 43].

C

Cacciani, A., and Fofi, M. 1978, *Solar Phys.*, **59**, 179. [§§ 11, 39].
Cacciani, A., and Rhodes, E. J., Jr. 1984, in *Solar Seismology from Space*, ed. R. K. Ulrich, J. Harvey, E. J. Rhodes, Jr., and J. Toomre (Jet Propulsion Laboratory, Pasadena), 115. [§§ 11, 39].
Campbell, C. G., and Papaloizou, J. C. B. 1986, *Monthly Notices Roy. Astron. Soc.*, **220**, 577. [§ 29].
Carney, B. W., and Peterson, R. C. 1985, *Monthly Notices Roy. Astron. Soc.*, **212**, 33p. [§ 9].
Castor, J. I. 1971, *Astrophys. J.*, **166**, 109. [§§ 18, 24].
Chandrasekhar, S. 1964, *Astrophys. J.*, **139**, 664. [§ 14].
Chitre, S. M. 1988, in *Advances in Helio- and Asteroseismology, IAU Symp. No. 123*, ed. J. Christensen-Dalsgaard and S. Frandsen (D. Reidel Publ. Co., Dordrecht), p.345. [§ 42].
Chlebowsky, T. 1978, *Acta Astron.*, **28**, 441. [§ 34].
Christensen-Dalsgaard, J. 1982a, *Monthly Notices Roy. Astron. Soc.*, **199**, 735. [§ 40].
Christensen-Dalsgaard, J. 1982b, in *Pulsations in Classical and Cataclysmic Variable Stars*, ed. J. P. Cox and C. J. Hansen (Univ. of Colorado and National Bureau of Standards, Boulder), p.99. [§ 37].
Christensen-Dalsgaard, J. 1984a, in *Theoretical Problems in Stellar Stability and Oscillations*, ed. A. Noels and M. Gabriel (Université de Liège, Liège), p.155. [§ 37].
Christensen-Dalsgaard, J., 1984b, in *Solar Seismology from Space*, ed. R. K. Ulrich, J. Harvey, E. J. Rhodes, Jr., and J. Toomre (Jet Propulsion Laboratory, Pasadena), p.219. [§ 39].
Christensen-Dalsgaard, J. 1984c, in *Space Research Prospects in Stellar Activity and*

Variability, ed. A. Mangeney and F. Praderie (Observatoire de Paris, Meudon), p.11. [§ 43].
Christensen-Dalsgaard, J. 1986, in *Seismology of the Sun and the Distant Stars*, ed. D. O. Gough (D. Reidel Publ. Co., Dordrecht), p.23. [§ 43].
Christensen-Dalsgaard, J. 1988, in *Advances in Helio- and Asteroseismology, IAU Symp. No. 123*, ed. J. Christensen-Dalsgaard and S. Frandsen (D. Reidel Publ. Co., Dordrecht), p.295. [§ 43].
Christensen-Dalsgaard, J., Dilke, F. W. W., and Gough, D. O. 1974, *Monthly Notices Roy. Astron. Soc.*, **169**, 429. [§ 27].
Christensen-Dalsgaard, J., Duvall, T. L., Jr., Gough, D. O., Harvey, J. W., and Rhodes, E. J., Jr. 1985a, *Nature*, **315**, 378. [§ 41].
Christensen-Dalsgaard, J., and Frandsen, S. 1983a, *Solar Phys.*, **82**, 165. [§§ 21, 42].
Christensen-Dalsgaard, J., and Frandsen, S. 1983b, *Solar Phys.*, **82**, 469. [§ 43].
Christensen-Dalsgaard, J., and Frandsen, S. 1988, ed. *Advances in Helio- and Asteroseismology, IAU Symp. No. 123* (D. Reidel Publ. Co., Dordrecht). [§ 37].
Christensen-Dalsgaard, J., and Gough, D. O. 1984a, in *Solar Seismology from Space*, ed. R. K. Ulrich, J. Harvey, E. J. Rhodes, Jr., and J. Toomre (Jet Propulsion Laboratory, Pasadena), p.79. [§ 41].
Christensen-Dalsgaard, J., and Gough, D. O. 1984b, in *Solar Seismology from Space*, ed. R. K. Ulrich, J. Harvey, E. J. Rhodes, Jr., and J. Toomre (Jet Propulsion Laboratory, Pasadena), p.199. [§ 40].
Christensen-Dalsgaard, J., Gough, D. O., and Toomre, J. 1985b, *Science*, **229**, 923. [§ 37].
Christensen-Dalsgaard, J., Thompson, M., and Gough, D. O. 1988, in *Seismology of the Sun and Sun-like Stars*, ed. E. Rolfe (ESA SP-286, Paris), in press. [§ 41].
Christy, R. F. 1967, *Astron. J.*, **72**, 293. [§ 7].
Claverie, A., Isaak, G. R., McLeod, C. P., van der Raay, H. B., and Roca Cortés, T. 1979, *Nature*, **282**, 591. [§ 11].
Claverie, A., Isaak, G. R., McLeod, C. P., van der Raay, H. B., and Roca Cortés, T. 1981a, *Astron. Astrophys.*, **91**, L9. [§ 11].
Claverie, A., Isaak, G. R., McLeod, C. P., van der Raay, H. B., and Roca Cortés, T. 1981b, *Solar Phys.*, **74**, 51. [§ 11].
Claverie, A., Isaak, G. R., McLeod, C. P., van der Raay, H. B., Pallé, P. L., and Roca Cortés, T. 1984, *Mem. Soc. Astron. Ital.*, **55**, 63. [§ 11].
Clement, M. J. 1986, *Astrophys. J.*, **301**, 185. [§ 34].
Connes, P. 1986, *Astrophys. Space Sci.*, **110**, 211. [§ 43].
Cordova, F. A., and Mason, K. O. 1982, in *Pulsations in Classical and Cataclysmic Variable Stars*, ed. J. P. Cox and C. J. Hansen (Univ. of Colorado and National Bureau of Standards, Boulder), p.23. [§ 10].
Cowling, T. G. 1941, *Monthly Notices Roy. Astron. Soc.*, **101**, 367. [§§ 3, 12, 15, 17].
Cowling, T. G. 1957, *Magnetohydrodynamics* (Interscience Tract, New York). [§§ 26, 29].
Cowling, T. G., and Newing, R. A. 1949, *Astrophys. J.*, **109**, 149. [§ 19].
Cox, A. N. 1987, in *Stellar Pulsation*, ed. A. N. Cox, W. M. Sparks, and S. G. Starrfield (Springer-Verlag, Berlin), p.36. [§ 8].
Cox, A. N., and Cahn, J. H. 1988, *Astrophys. J.*, **326**, 804. [§ 27].
Cox, A. N., Starrfield, S. G., Kidman, R. B., and Pesnell, W. D. 1987, *Astrophys. J.*, **317**, 303. [§ 28].
Cox, J. P. 1955, *Astrophys. J.*, **122**, 286. [§§ 21, 27].
Cox, J. P. 1967, in *Aerodynamic Phenomena in Stellar Atmospheres, IAU Symp. No. 28*, ed. R. N. Thomas (Academic Press, New York), p.3. [§ 27].
Cox, J. P. 1974, *Rep. Prog. Phys.*, **37**, 563. [§§ 26, 27].
Cox, J. P. 1976, *Ann. Rev. Astron. Astrophys.*, **14**, 247. [§ 4].
Cox, J. P. 1980, *Theory of Stellar Pulsation* (Princeton Univ. Press, Princeton). [§§ 4, 14].
Cox, J. P. 1984, *Astrophys. J.*, **280**, 220. [§ 29].
Cox, J. P. 1985, in *Cepheids: Observation and Theory, IAU Colloq. No. 82*, ed. B. F. Madore (Cambridge Univ. Press, Cambridge), p.126. [§ 35].
Cox, J. P., Cox, A. N., Olsen, K. H., King, D. S., and Eilers, D. D. 1966, *Astrophys. J.*, **144**, 1038. [§ 26].
Cox, J. P., and Giuli, R. T. 1968, *Principles of Stellar Structure* (Gordon and Breach, New York). [§ 13].
Cuypers, J. 1980, *Astron. Astrophys.*, **89**, 207. [§ 19].

D

Däppen, W., Anderson, L., and Mihalas, D. 1987, *Astrophys. J.*, **319**, 195. [§ 40].
Däppen, W., Dziembowski, W. A., and Sienkiewicz, R. 1988b, in *Advances in Helio- and Asteroseismology, IAU Symp. No. 123*, ed. J. Christensen-Dalsgaard and S. Frandsen (D. Reidel Publ. Co., Dordrecht), p.233. [§ 43].
Däppen, W., Gilliland, R. L., and Christensen-Dalsgaard, J. 1986, *Nature*, **321**, 229. [§ 40].
Däppen, W., and Gough, D. O. 1984, in *Theoretical Problems in Stellar Stability and Oscillations*, ed. A. Noels and M. Gabriel (Université de Liège, Liège), p.264. [§ 41].
Däppen, W., and Gough, D. O. 1986, in *Seismology of the Sun and the Distant Stars*, ed. D. O. Gough (D. Reidel Publ. Co., Dordrecht), p.275. [§ 41].
Däppen, W., Mihalas, D., Hummer, D. G., and Mihalas, B. W. 1988a, *Astrophys. J.*, **332**, 261. [§ 40].
Davis, R., Jr. 1988, talk given at *Neutrino 88* held at Boston, June 1988. [§ 40].
DeGregoria, A. J. 1977, *Astrophys. J.*, **217**, 175. [§ 27].
Delache, P., and Scherrer, P. H. 1983, *Nature*, **306**, 651. [§ 11].
Demarque, P., Guenter, D. B., and van Altena, W. F. 1986, *Astrophys. J.*, **300**, 773. [§ 43].
Deming, D., Glenar, D. A., Käufl, H. U., Hill, A. A., and Espenak, F. 1986, *Nature*, **322**, 232. [§ 38].
Denis, I. A., and Denis, C. 1984, in *Theoretical Problems in Stellar Stability and Oscillations*, ed. A. Noels and M. Gabriel (Université de Liège, Liège), p.270. [§ 41].
Deubner, F.-L. 1975, *Astron. Astrophys.*, **44**, 371. [§§ 3, 11].
Deubner, F.-L. 1977, in *The Energy Balance and Hydrodynamics of the Solar Chromosphere and Corona*, ed. R.-M. Bonnet and Ph. Delache (G. de Bussac, Clermond-Ferrand), p.45. [§ 11].
Deubner, F.-L., and Gough, D. O. 1984, *Ann. Rev. Astron. Astrophys.*, **22**, 593. [§§ 37, 41].
Dilke, F. W. W., and Gough, D. O. 1972, *Nature*, **240**, 262. [§ 27].
Dolez, N., Gough, D. O., and Vauclair, S. 1988, in *Advances in Helio- and Asteroseismology, IAU Symp. No. 123*, ed J. Christensen-Dalsgaard and S. Frandsen (D. Reidel Pub. Co., Dordrecht), p.291. [§ 28].
Dolez, N., and Vauclair, G. 1981, *Astron. Astrophys.*, **102**, 375. [§§ 3, 28].
Drazin, P. G., and Reid, W. H. 1981, *Hydrodynamic Stability* (Cambridge Univ. Press,

Cambridge). [§ 29].
Durney, B. R. 1987, in *The Internal Solar Angular Velocity*, ed. B. R. Durney and S. Sofia (D. Reidel Publ. Co., Dordrecht), p.235. [§ 20].
Durney, R. B., Hill, F., and Goode, P. R. 1988, *Astrophys. J.*, **326**, 486. [§ 39].
Durney, B. R., and Sofia, S. 1987, ed. *The Internal Solar Angular Velocity* (D. Reidel Publ. Co., Dordrecht). [§ 37].
Duvall, T. L., Jr. 1982, *Nature*, **300**, 242. [§ 41].
Duvall, T. L., Jr., and Harvey, J. W. 1983, *Nature*, **302**, 24. [§ 11].
Duvall, T. L., Jr., and Harvey, J. W. 1984, *Nature*, **310**, 19. [§§ 11, 39, 41].
Duvall, T. L., Jr., Dziembowski, W. A., Goode, P. R., Gough, D. O., Harvey, J. W., and Leibacher, J. W. 1984, *Nature*, **310**, 22. [§ 41].
Duvall, T. L., Jr., Harvey, J. W., Libbrecht, K. G., Popp, B. D., and Pomerantz, M. A. 1988, *Astrophys. J.*, **324**, 1158. [§§ 11, 39, 41].
Duvall, T. L., Jr., Harvey, J. W., and Pomerantz, M. A. 1986, *Nature*, **321**, 500. [§ 39].
Dziembowski, W. 1971, *Acta Astron.*, **21**, 289. [§§ 15, 18, 24].
Dziembowski, W. 1977a, *Acta Astron.*, **27**, 95. [§§ 21, 22, 24, 28].
Dziembowski, W. 1977b, *Acta Astron.*, **27**, 203. [§ 6].
Dziembowski, W. 1982, *Acta Astron.*, **32**, 147. [§ 42].
Dziembowski, W. 1983, *Solar Phys.*, **82**, 259. [§ 42].
Dziembowski, W. 1984a, *Adv. Space Res.*, **4**, 143. [§ 43].
Dziembowski, W. 1984b, in *Theoretical Problems in Stellar Stability and Oscillations*, ed. A. Noels and M. Gabriel (Université de Liège, Liège), p.346. [§ 25].
Dziembowski, W., and Goode, P. R. 1984, *Mem. Soc. Astron. Ital.*, **55**, 185. [§ 19].
Dziembowski, W., and Goode, P. R. 1985, *Astrophys. J. Letters*, **296**, L27. [§§ 9, 19, 43].
Dziembowski, W., and Goode, P. R. 1986, in *Seismology of the Sun and Distant Stars*, ed. D. O. Gough (D. Reidel Publ. Co., Dordrecht), p.441. [§§ 9, 19, 43].
Dziembowski, W., and Koester, D. 1981, *Astron. Astrophys.*, **97**, 16. [§§ 3, 28].
Dziembowski, W. A., Paternó, L., and Ventura, R. 1985, *Astron. Astrophys.*, **151**, 47. [§ 42].
Dziembowski, W. A., Paternó, L., and Ventura, R. 1988, *Astron. Astrophys.*, **200**, 213. [§ 40].

E ~ F

Eckart, C. 1960, *Hydrodynamics of Oceans and Atmospheres* (Pergamon Press, London). [§§ 4, 11, 25, 34].
Eddington, A. S. 1926, *The Internal Constitution of the Stars* (Cambridge Univ. Press, Cambridge), p.198. [§§ 3, 25].
Edmonds, A. R. 1957, *Angular Momentum in Quantum Mechanics* (Princeton Univ. Press, Princeton). [§ 19].
Eggleton, P. P., Faulkner, J., and Flannery, B. P. 1973, *Astron. Astrophys.*, **23**, 325. [§ 40].
Faulkner, J., Gough, D. O., and Vahia, M. N. 1986, *Nature*, **321**, 226. [§ 40].
Fitch, W. S. 1973, *Astrophys. J. Letters*, **181**, L95. [§ 10].
Fontaine, G., Bergeron, P., Lacombe, P., Lamontagne, R., and Talon, A. 1985a, *Astron. J.*, **90**, 1094. [§ 10].
Fontaine, G., McGraw, J. T., Dearborn, D. S. P., Gustafson, J., and Lacombe, P. 1982, *Astrophys. J.*, **258**, 651. [§ 10].
Fontaine, G., and Wesemael, F. 1984, *Astron. J.*, **89**, 1728. [§ 10].

Fontaine, G., Wesemael, F., Bergeron, P., Lacombe, P., Lamontagne, R., and Saumon, D. 1985b, *Astrophys. J.*, **294**, 339. [§ 10].
Francis, S. H. 1973, *J. Geophys. Res.*, **78**, 2278. [§§ 15, 16].
Frandsen, S. 1987, *Astron. Astrophys.*, **181**, 289. [§ 43].
Frazier, E. N. 1968, *Z. Astrophys.*, **68**, 345. [§ 11].
Fricke, K. J. 1968, *Z. Astrophys.*, **68**, 317. [§ 29].
Fricke, K. J., and Kippenhahn, R. 1972, *Ann. Rev. Astron. Astrophys.*, **10**, 45. [§ 29].
Fröhlich, C., and Delache, P. 1984, *Mem. Soc. Astron. Ital.*, **55**, 99. [§ 11].

G

Gabriel, M. 1964, *Ann. Astrophys.*, **27**, 141. [§ 27].
Gabriel, M. 1969, *Astron. Astrophys.*, **1**, 321. [§ 29].
Gabriel, M. 1988, in *Advances in Helio- and Asteroseismology, IAU Symp. No. 123*, ed. J. Christensen-Dalsgaard and S. Frandsen (D. Reidel Publ. Co., Dordrecht), p.375. [§§ 30, 42].
Gabriel, M., and Noels, A. 1976a, *Astron. Astrophys.*, **46**, 313. [§ 29].
Gabriel, M., and Noels, A. 1976b, *Astron. Astrophys.*, **53**, 149. [§ 29].
Gabriel, M., and Noels, A. 1977, *Astron. Astrophys.*, **54**, 631. [§ 29].
Gabriel, M., Noels, A., Scuflaire, R., and Mathys, G. 1985, *Astron. Astrophys.*, **143**, 206. [§ 9].
Gabriel, M., and Scuflaire, R. 1979, *Acta Astron.*, **29**, 135. [§ 6].
Gabriel, M., Scuflaire, R., Noels, A., and Boury, A. 1975, *Astron. Astrophys.*, **40**, 33. [§§ 21, 27, 30].
Gelly, B., Fossat, E., and Grec, G. 1988, *Astron. Astrophys.*, **200**, L29. [§ 11]
Gelly, B., Fossat, E., Grec, G., and Schmider, F.-X. 1988, *Astron. Astrophys.*, **200**, 207. [§ 11].
Gelly, B., Grec, G., and Fossat, E. 1986, *Astron. Astrophys.*, **164**, 383. [§ 43].
Gies, D. R., and Kullavanijaya, A. 1988, *Astrophys. J.*, **326**, 813. [§§ 8, 35].
Gilliland, R. L., and Däppen, W. 1988, *Astrophys. J.*, **324**, 1153. [§ 40].
Gilliland, R. L., Faulkner, J., Press, W. H., and Spergel, D. N. 1986, *Astrophys. J.*, **306**, 703. [§ 40].
Gingerich, O., Noyes, R. W., Kalkofen, W., and Cuny, Y. 1971, *Solar Phys.*, **18**, 347. [§ 15].
Goldreich, P., and Keeley, D. A. 1977a, *Astrophys. J.*, **211**, 934. [§ 42].
Goldreich, P., and Keeley, D. A. 1977b, *Astrophys. J.*, **212**, 243. [§§ 42, 43].
Goldreich, P., and Kumar, P. 1988, *Astrophys. J.*, **326**, 462. [§ 42].
Goldreich, P., and Schubert, G. 1967, *Astrophys. J.*, **150**, 571. [§ 29].
Gonczi, G. 1982, *Astron. Astrophys.*, **110**, 1. [§ 21, 30].
Gonczi, G., and Osaki, Y. 1980, *Astron. Astrophys.*, **84**, 304. [§§ 21, 30].
Gough, D. O. 1976, *Astrophys. J.*, **214**, 196. [§ 21, 30].
Gough, D. O. 1980, in *Nonradial and Nonlinear Stellar Pulsation*, ed. H. A. Hill and W. A. Dziembowski (Springer-Verlag, Berlin), p. 273. [§ 38].
Gough, D. O. 1982, in *Pulsations in Classical and Cataclysmic Variable Stars*, ed. J. P. Cox and C. J. Hansen (Univ. of Colorado and National Bureau of Standards, Boulder), p.117. [§§ 37, 41].
Gough, D. O. 1983, ed. *Problems of Solar and Stellar Oscillations, IAU Colloq. No. 66*, published as *Solar Phys.*, **82**. [§ 37].
Gough, D. O. 1984a, *Phil. Trans. Roy. Soc. London, Ser. A*, **313**, 27. [§§ 3, 41].
Gough, D. O. 1984b, *Mem. Soc. Astron. Ital.*, **55**, 13. [§ 41].
Gough, D. O. 1984c, in *Solar Seismology from Space*, ed. R. K. Ulrich, J. Harvey, E.

J. Rhodes, Jr., and J. Toomre (Jet Propulsion Laboratory, Pasadena), p.49. [§ 41].
Gough, D. O. 1985a, *Solar Phys.*, **100**, 65. [§41].
Gough, D. O. 1985b, *Highlights of Astronomy*, **7**, 283. [§ 37].
Gough, D. O. 1986a, ed. *Seismology of the Sun and the Distant Stars* (D. Reidel Publ. Co., Dordrecht). [§ 37].
Gough, D. O. 1986b, in *Seismology of the Sun and the Distant Stars*, ed. D. O. Gough (D. Reidel Publ. Co., Dordrecht), p.125. [§§ 37, 41].
Gough, D. O. 1986c, in *Hydrodynamic and Magnetohydrodynamic Problems in the Sun and Stars*, ed. Y. Osaki (Univ. of Tokyo, Tokyo), p.117. [§ 16].
Gough, D. O. 1987, *Nature*, **326**, 257. [§ 43].
Gough, D. O., and Taylor, P. P. 1984, *Mem. Soc. Astron. Ital.*, **55**, 215. [§ 19].
Grauer, A. D., and Bond, H. E. 1984, *Astrophys. J.*, **277**, 211. [§ 10].
Grauer, A. D., Bond, H. E., Green, R. F., and Liebert, J. 1988, *Astron. J.*, **95**, 879. [§ 10].
Grec, G., Fossat, E., and Pomerantz, M. A. 1980, *Nature*, **288**, 541. [§ 11].
Grec, G., Fossat, E., and Pomerantz, M. A. 1983, *Solar Phys.*, **82**, 55. [§§ 11, 41].
Greenspan, H. P. 1969, *The Theory of Rotating Fluids* (Cambridge Univ. Press, Cambridge). [§§ 19, 31, 33].
Greenstein, J. L. 1982, *Astrophys. J.*, **258**, 661. [§ 10].
Greenstein, J. L. 1984, *Astrophys. J.*, **276**, 602. [§ 10].
Guenter, D. B. 1987, *Astrophys. J.*, **312**, 211. [§ 43].
Guenter, D. B., and Demarque, P. 1986, *Astrophys. J.*, **301**, 207. [§ 43].

H ~ I

Hansen, C. J. 1978, *Ann. Rev. Astron. Astrophys.*, **16**, 15. [§ 22].
Hansen, C. J. 1980, in *Nonradial and Nonlinear Stellar Pulsation*, ed. H. A. Hill and W. A. Dziembowski (Springer-Verlag, Berlin), p.445. [§ 15].
Hansen, C. J., Aizenman, M. L., and Ross, R. R. 1976, *Astrophys. J.*, **207**, 736. [§ 15].
Hansen, C. J., Cox, J. P., and Van Horn, H. M. 1977, *Astrophys. J.*, **217**, 151. [§§ 19, 34].
Hansen, C. J., and Van Horn, H. M. 1979, *Astrophys. J.*, **233**, 253. [§ 15].
Harvey, J. W. 1988, in *Advances in Helio- and Asteroseismology, IAU Symp. No. 123*, ed. J. Christensen-Dalsgaard and S. Frandsen (D. Reidel Publ. Co., Dordrecht), p.497. [§ 43].
Harvey, J. W., and Duvall, T. L., Jr. 1984, in *Solar Seismology from Space*, ed. R. K. Ulrich, J. Harvey, E. J. Rhodes, Jr., and J. Toomre (Jet Propulsion Laboratory, Pasadena), p.165. [§§ 40, 41].
Henning, H. M. and Scherrer, P. H. 1986, in *Seismology of the Sun and the Distant Stars*, ed. D. O. Gough (D. Reidel Publ. Co., Dordrecht), p.55. [§ 41].
Henning, H. M., and Scherrer, P. H. 1988, in *Advances in Helio- and Asteroseismology, IAU Symp. No. 123*, ed. J. Christensen-Dalsgaard and S. Frandsen (D. Reidel Publ. Co., Dordrecht), p.29. [§ 11].
Henyey, L. G., Forbes, J. E., and Gould, N. L. 1964, *Astrophys. J.*, **139**, 306. [§ 18].
Hermans, D., Goossens, M., Kerner, W., and Lerbinger, K. 1988, in *Advances in Helio- and Asteroseismology, IAU Symp. No. 123*, ed J. Christensen-Dalsgaard and S. Frandsen (D. Reidel Publ. Co., Dordrecht), p.395. [§ 29].
Hill, F., Gough, D. O., and Toomre, J. 1984a, *Mem. Soc. Astron. Ital.*, **55**, 153. [§ 41].
Hill, F., Gough, D. O., and Toomre, J. 1984b, in *Solar Seismology from Space*, ed. R. K. Ulrich, J. W. Harvey, E. J. Rhodes, Jr., and J. Toomre (Jet Propulsion Laboratory, Pasadena), p.95. [§ 41].
Hill, H. 1985, *Astrophys. J.*, **290**, 765. [§ 11].
Hill, H. A., and Dziembowski, W. A. 1980, ed. *Nonradial and Nonlinear Stellar Pulsation* (Springer-Verlag, Berlin). [§ 37].
Hill, H., Tash, J., and Padin, C. 1986, *Astrophys. J.*, **304**, 560. [§ 11].
Hōshi, R. 1968, *Prog. Theor. Phys., Kyoto*, **39**, 957. [§ 29].
Hummer, D. G., and Mihalas, D. 1988, *Astrophys. J.*, **331**, 794. [§40].
Iben, I., Jr. 1982, *Astrophys. J.*, **260**, 821. [§ 15].
Iben, I., Jr. 1984, *Astrophys. J.*, **277**, 333. [§ 15].
Isaak, G. R. 1986, in *Seismology of the Sun and the Distant Stars*, ed. D. O. Gough (D. Reidel Publ. Co., Dordrecht), 223. [§ 11].
Isaak, G. R., Jefferies, S. M., McLeod, C. P., New, R., van der Raay, H. B., Pallé, P. L., Régulo, C., and Roca Cortés, T. 1988, in *Advances in Helio- and Asteroseismology, IAU Symp. No. 123*, ed. J. Christensen-Dalsgaard and S. Frandsen (D. Reidel Publ. Co., Dordrecht), p.201. [§ 11].
Isaak, G. R., van der Raay, H. B., Pallé, P. L., Roca Cortés, and Delache, P. 1984, *Mem. Soc. Astron. Ital.*, **55**, 91. [§ 11].
Ishibashi, S. 1987, *Publ. Astron. Soc. Japan*, **39**, 69. [§ 36].
Ishibashi, S., and Ando, H. 1985, *Publ. Astron. Soc. Japan*, **37**, 293. [§ 33].
Ishibashi, S., and Ando, H. 1986, *Publ. Astron. Soc. Japan*, **38**, 295. [§ 33].

J ~ K

Jakate, S. 1979, *Astron. J.*, **84**, 1042. [§ 8].
Jarzebowski, T., Jerzykiewicz, M., LeContel, J.-M., and Musielok, B. 1979, *Acta Astron.*, **29**, 517. [§ 8].
Jeffery, C. S., Skillen, I., Hill, P. W., Kilkenney, D., Malaney, R. A., and Morrison, K. 1985, *Monthly Notices Roy. Astron. Soc.*, **217**, 701. [§ 5].
Jeffrey, W. 1988, *Astrophys. J.*, **327**, 987. [§ 41].
Jimenez, A., Pallé, P. L., Roca Cortés, T., Domingo, V., and Korzennik, S. 1987, *Astron. Astrophys.*, **172**, 323. [§ 39].
Jones, W. L. 1976, in *Handbuch der Physik, Bd. 49, Teil V*, ed. S. Flügge (Springer-Verlag, Berlin), p.177. [§§ 15, 16].
Kaisig, M., Knölker, M., and Stix, M. 1984, in *Theoretical Problems in Stellar Stability and Oscillations*, ed. A. Noels and M. Gabriel (Université de Liège, Liège), p.239. [§ 40].
Kambe, E., and Osaki, Y. 1988, *Publ. Astron. Soc. Japan*, **40**, 313. [§§ 7, 8].
Kato, S. 1966, *Publ. Astron. Soc. Japan*, **18**, 374. [§§ 26, 29].
Kawaler, S. 1987a, in *Stellar Pulsation*, ed. A. N. Cox, W. M. Sparks, and S. G. Starrfield (Springer-Verlag, Berlin), p.367. [§ 43].
Kawaler, S. D. 1987b, in *The Second Conference on Faint Blue Stars, IAU Colloq. No. 95*, ed. A. G. D. Philip, D. Latham, and J. Liebert (L. Davis Press, Schenectady), p.297. [§ 43].
Kawaler, S. D. 1988a, *Astrophys. J.*, **334**, 220. [§§ 21, 27].
Kawaler, S. D. 1988b, in *Advances in Helio- and Asteroseismology, IAU Symp. No. 123*, ed. J. Christensen-Dalsgaard and S. Frandsen (D. Reidel Publ. Co., Dordrecht), p. 329. [§ 43].
Kawaler, S. D., Hansen, C. J., and Winget, D. E. 1985a, *Astrophys. J.*, **295**, 547. [§§ 10, 15, 27, 43].
Kawaler, S. D., Winget, D. E., and Hansen, C. J. 1985b, *Astrophys. J.*, **298**, 752.

[§ 43].
Kawaler, S. D., Winget, D. E., Hansen, C. J., and Iben, I., Jr. 1986, *Astrophys. J. Letters*, **306**, L41. [§ 27].
Kepler, S. O. 1984a, *Astrophys. J.*, **278**, 754. [§ 10].
Kepler, S. O. 1984b, *Astrophys. J.*, **286**, 314. [§ 10].
Kepler, S. O., Robinson, E. L., and Nather, R. E. 1983, *Astrophys. J.*, **271**, 744. [§ 10].
Kepler, S. O., Robinson, E. L., Nather, R. E., and McGraw, J. T. 1982, *Astrophys. J.*, **254**, 676. [§ 10].
Kepler, S. O., Winget, D. E., Robinson, E. L., and Nather, R. E. 1988, in *Advances in Helio- and Asteroseismology, IAU Symp. No. 123*, ed. J. Christensen-Dalsgaard and S. Frandsen (D. Reidel Publ. Co., Dordrecht), p.325. [§§ 10, 43].
King, D. S., and Cox, J. P. 1968, *Publ. Astron. Soc. Pacific*, **80**, 365. [§ 27].
Kippenhahn, R. 1967, *Z. Astrophys.*, **67**, 271. [§ 29].
Kippenhahn, R., Weigert, A., and Hoffmeister, E. 1967, in *Methods in Computational Physics*, ed. B. Alder, S. Fernbach, and M. Rotenberg (Academic Press, New York), p.129. [§ 18].
Knobloch, E., and Spruit, H. C. 1983, *Astron. Astrophys.*, **125**, 59. [§ 29].
Koester, D., Vauclair, G., Dolez, N., Oke, J. B., Greenstein, J. L., and Weidemann, V. 1985, *Astron. Astrophys.*, **149**, 423. [§ 10].
Korzennik, S. G., Cacciani, A., Rhodes, E. J., Jr., Tomczyk, S., and Ulrich, R. K. 1988, in *Seismology of the Sun and Sun-like Stars*, ed. E. Rolfe (ESA SP-286, Paris), in press. [§§ 39, 41].
Korzennik, S. G. and Ulrich, R. K. 1989, *Astrophys. J.*, in press. [§§ 40, 41].
Kosovichev, A. G., and Gough, D. O. 1988, in *Seismology of the Sun and Sun-like Stars*, ed. E. Rolfe (ESA SP-286, Paris), in press. [§ 41].
Kreidl, T. J. 1985, *Inf. Bull. Var. Stars No. 2739*. [§ 9].
Kreidl, T. J., and Kurtz, D. W. 1986, *Monthly Notices Roy. Astron. Soc.*, **220**, 313. [§ 9].
Kubiak, M. 1978, *Acta Astron.*, **28**, 153. [§ 7].
Kuhn, J. R. 1988, *Astrophys. J., Letters*, **331**, L131. [§ 39].
Kumar, P., Franklin, J., and Goldreich, P. 1988, *Astrophys. J.*, **328**, 879. [§ 42].
Kumar, P., and Goldreich, P. 1989, *Astrophys. J.*, in press. [§ 42].
Kurtz, D. W. 1978, *Inf. Bull. Var. Stars, No. 1436*. [§ 9].
Kurtz, D. W. 1980, *Monthly Notices Roy. Astron. Soc.*, **191**, 115. [§ 9].
Kurtz, D. W. 1981, *Monthly Notices Roy. Astron. Soc.*, **196**, 61. [§ 9].
Kurtz, D. W. 1982, *Monthly Notices Roy. Astron. Soc.*, **200**, 807. [§§ 6, 9].
Kurtz, D. W. 1983a, *Monthly Notices Roy. Astron. Soc.*, **202**, 1. [§ 9].
Kurtz, D. W. 1983b, *Monthly Notices Roy. Astron. Soc.*, **205**, 3. [§ 9].
Kurtz, D. W. 1984, *Monthly Notices Roy. Astron. Soc.*, **209**, 841. [§ 9].
Kurtz, D. W. 1986a, in *Seismology of the Sun and the Distant Stars*, ed. D. O. Gough (D. Reidel Publ. Co., Dordrecht), p. 417. [§ 9].
Kurtz, D. W. 1986b, *Highlights of Astronomy*, **7**, 237. [§ 9].
Kurtz, D. W. 1988, in *Multimode Stellar Pulsations*, ed. G. Kovács, L. Szabados, and B. Szeidl (Konkoly Observatory, Budapest), p.107. [§ 9].
Kurtz, D. W., and Balona, L. A. 1984, *Monthly Notices Roy. Astron. Soc.*, **210**, 779. [§ 9].
Kurtz, D. W., and Kreidl, T. J. 1985, *Monthly Notices Roy. Astron. Soc.*, **216**, 987. [§§ 9, 43].
Kurtz, D. W., and Martinez, P. 1987, *Monthly Notices Roy. Astron. Soc.*, **226**, 187.

[§ 9].
Kurtz, D. W., Schneider, H., and Weiss, W. W. 1985, *Monthly Notices Roy. Astron. Soc.*, **215**, 77. [§ 9].
Kurtz, D. W., and Seeman, J. 1983, *Monthly Notices Roy. Astron. Soc.*, **205**, 11. [§ 9].
Kurtz, D.W., and Shibahashi, H. 1986, *Monthly Notices Roy. Astron. Soc.*, **223**, 557. [§§ 9, 19, 43].
Kurtz, D. W., and Wegner, G. 1979, *Astrophys. J.*, **232**, 510. [§ 9].

L

Lamb, H. 1932, *Hydrodynamics* (Cambridge Univ. Press, Cambridge). [§ 11].
Landolt, A. U. 1968, *Astrophys. J.*, **153**, 151. [§ 10].
Langer, N., El Eid, M. F., and Fricke, K. J. 1985, *Astron. Astrophys.*, **145**, 179. [§ 29].
Langer, R. E. 1959, *Trans. Am. Math. Soc.*, **90**, 113. [§ 16].
Lasker, B. M., and Hesser, J. E. 1971, *Astrophys. J. Letters*, **163**, L89. [§ 10].
Lebreton, Y., Berthomieu, G., and Provost, J. 1988, in *Advances in Helio- and Asteroseismology, IAU Symp. No. 123*, ed. J. Christensen-Dalsgaard and S. Frandsen (D. Reidel Publ. Co., Dordrecht), p.95. [§ 11].
Lebreton, Y., Berthomieu, G., Provost, J., and Schatzman, E. 1988, *Astron. Astrophys.*, **200**, L5. [§ 40]
LeContel, J.-M., Ducatel, D., Sareyan, J.-P., Morel, P. J., Chapellier, E., and Endiqnoux, A. 1987, in *Stellar Pulsation*, ed. A. N. Cox, W. M. Sparks, and S. G. Starrfield (Springer-Verlag, Berlin), p.67. [§ 8].
LeContel, J.-M., Sareyan, J.-P., and Valtier, J.-C. 1981, in *Workshop on Pulsating B stars*, ed. G.E.V.O.N and C. Sterken (Observatoire de Nice, Nice), p.45. [§ 8].
Ledoux, P. 1941, *Astrophys. J.*, **94**, 537. [§ 27].
Ledoux, P. 1947, *Astrophys. J.*, **105**, 305. [§ 29].
Ledoux, P. 1951, *Astrophys. J.*, **114**, 373. [§§ 3, 7, 19].
Ledoux, P. 1974, in *Stellar Instability and Evolution, IAU Symp. No. 59*, ed. P. Ledoux, A. Noels, and A. W. Rodgers (D. Reidel Publ. Co., Dordrecht), p.135. [§§ 4, 29].
Ledoux, P. 1978, in *Theoretical Principles in Astrophysics and Relativity*, ed. N. R. Lebovitz, W. H. Reid, and P. O. Vandervoort (Univ. of Chicago Press, Chicago), p.15. [§ 27].
Ledoux, P., Noels, A., and Boury, A. 1982, *Astron. Astrophys.*, **108**, 49. [§ 27].
Ledoux, P., and Walraven, Th. 1958, in *Handbuch der Physik, Bd. 51*, ed. S. Flügge (Springer-Verlag, Berlin), p.353. [§§ 3, 4, 13, 14].
Lee, U. 1985a, *Publ. Astron. Soc. Japan*, **37**, 261. [§ 22].
Lee, U. 1985b, *Publ. Astron. Soc. Japan*, **37**, 279. [§ 28].
Lee, U. 1988, *Monthly Notices Roy. Astron. Soc.*, **232**, 711. [§ 35].
Lee, U., and Osaki, Y. 1982, *Publ. Astron. Soc. Japan*, **34**, 39. [§ 28].
Lee, U., and Saio, H. 1986, *Monthly Notices Roy. Astron. Soc.*, **221**, 365. [§§ 3, 35].
Lee, U., and Saio, H. 1987a, *Monthly Notices Roy. Astron. Soc.*, **224**, 513. [§§ 3, 34].
Lee, U., and Saio, H. 1987b, *Monthly Notices Roy. Astron. Soc.*, **225**, 643. [§ 35].
Lee, U., and Saio, H. 1989a, *Monthly Notices Roy. Astron. Soc.*, in press. [§ 34].
Lee, U., and Saio, H. 1989b, *Astrophys. J.*, submitted. [§ 34].
Lee, U., and Shibahashi, H. 1986, *Publ. Astron. Soc. Japan*, **38**, 787. [§ 41].
Leibacher, J. W. 1984, in *Theoretical Problems in Stellar Stability and Oscillations*, ed. A. Noels and M. Gabriel (Université de Liège, Liège), p.298. [§ 41].
Leibacher, J. W., Noyes, R. W., Toomre, J., and Ulrich, R. K. 1985, *Scientific Amer-*

ican, 34. [§ 37].
Leibacher, J. W., and Stein, R. F. 1981, in *The Sun as a Star*, ed. S. D. Jordan (NASA SP-450), p.263. [§ 37].
Leighton, R. B., Noyes, R. W., and Simon, G. W. 1962, *Astrophys. J.*, **135**, 474. [§§ 3, 11].
Lesh, J. R., and Aizenman, M. L. 1973, *Astron. Astrophys.*, **22**, 229. [§ 8].
Libbrecht, K. G. 1986, *Nature*, **319**, 753. [§ 39].
Libbrecht, K. G. 1988a, *Astrophys. J. Letters*, **330**, L51. [§ 9].
Libbrecht, K. G. 1988b, *Astrophys. J.*, **334**, 510. [§ 42].
Libbrecht, K. G. 1988c, *Space Sci. Rev.*, **47**, 275. [§ 37].
Libbrecht, K. G. 1988d, in *Seismology of the Sun and Sun-like Stars*, ed. E. Rolfe (ESA SP-286, Paris), in press. [§§ 39, 41, 42].
Libbrecht, K. G. 1989, *Astrophys. J.*, **336**, 1092. [§§ 3, 39].
Libbrecht, K. G., and Kaufman, J. M. 1988, *Astrophys. J.*, **324**, 1172. [§ 41].
Libbrecht, K. G., Popp, B. D., Kaufman, J. M., and Penn, M. J. 1986, *Nature*, **323**, 235. [§§ 11, 39].
Libbrecht, K. G., and Zirin, H. 1986, *Astrophys. J.*, **308**, 413. [§§ 11, 39, 41].
Liebert, J., Wesemael, F., Hansen, C. J., Fontaine, G., Shipman, H. L., Sion, E. M., Winget, D. E., and Green, R. F. 1986, *Astrophys. J.*, **309**, 241. [§ 10].
Lomb, N. R. 1978, *Monthly Notices Roy. Astron. Soc.*, **185**, 325. [§ 8].
Longuet-Higgins, M. S. 1964, *Proc. Roy. Soc. London, Ser. A*, **279**, 446. [§ 19].
Lord Kelvin 1863 → Thomson, W. [§ 3].
Lucy, L. B. 1976, *Astrophys. J.*, **206**, 499. [§ 5].
Lynas-Gray, A. E., Kilkenny, K., Skillen, I., and Jeffery, C. S., 1987, *Monthly Notices Roy. Astron. Soc.*, **227**, 1073. [§ 5].
Lynden-Bell, D., and Ostriker, J. P. 1967, *Monthly Notices Roy. Astron. Soc.*, **136**, 293. [§§ 14, 19].
Lynds, C. R., Worden, S. P., and Harvey, J. W. 1976, *Astrophys. J.*, **207**, 174. [§ 6].

M ~ N

Maeder, A. 1985, *Astron. Astrophys.*, **147**, 300. [§ 27].
Martens, L., and Smeyers, P. 1986, *Astron. Astrophys.*, **155**, 211. [§ 34].
Matthews, J. M. 1988, *Monthly Notices Roy. Astron. Soc.*, **235**, 7p. [§ 28].
Matthews, J. M., Kurtz, D. W., and Wehlau, W. H. 1988a, *Astrophys. J.*, **300**, 348. [§ 9].
Matthews, J. M., Kurtz, D. W., and Wehlau, W. H. 1988c, in *Advances in Helio- and Asteroseismology, IAU Symp. No. 123*, ed. J. Christensen-Dalsgaard and S. Frandsen (D. Reidel Publ. Co., Dordrecht), p.261. [§ 9].
Matthews, J. M., Wehlau, W. H., Walker, G. A. H., and Yang, S. 1988b, *Astrophys. J.*, **324**, 1099. [§ 9].
McGraw, J. T. 1977, *Astrophys. J. Letters*, **214**, L123. [§ 10].
McGraw, J. T., Fontaine, G., Dearborn, D. S. P., Gustafson, J., Lacombe, P., and Starrfield, S. G. 1981, *Astrophys. J.*, **250**, 349. [§ 10].
McGraw, J. T., and Robinson, E. L. 1975, *Astrophys. J. Letters*, **200**, L89. [§ 10].
McGraw, J. T., and Robinson, E. L. 1976, *Astrophys. J. Letters*, **205**, L155. [§ 10].
McGraw, J. T., Starrfield, S. G., Liebert, J., and Green, R. F. 1979, in *White Dwarfs and Variable Degenerate Stars, IAU Colloq. No. 53*, ed. H. M. Van Horn and V. Weidemann (Univ. of Rochester, Rochester), p.377. [§ 10].
McIntyre, M. E. 1980, *Pure Appl. Geophys.*, **118**, 152. [§ 36].
McNamara, B. J. 1985, *Astrophys. J.*, **289**, 213. [§ 8].

McNamara, B. J. 1987, in *Stellar Pulsation*, ed. A. N. Cox, W. M. Sparks, and S. G. Starrfield (Springer-Verlag, Berlin), p.92. [§ 8].
McNamara, D. H., and Hansen, K. 1961, *Astrophys. J.*, **134**, 207. [§ 8].
Mihalas, D., Däppen, W., and Hummer, D.G. 1988, *Astrophys. J.*, **331**, 815. [§ 40]
Musman, S., and Rust, D. M. 1970, *Solar Phys.*, **13**, 261. [§ 11].
Nakano, T. 1972, *Ann. Phys.*, **73**, 326. [§ 20].
Nather, R. E., and Robinson, E. L. 1974, *Astrophys. J.*, **190**, 637. [§ 6].
Nishikawa, J., Hamana, S., Mizugaki, K., and Hirayama, T. 1986, *Publ. Astron. Soc. Japan*, **38**, 277. [§ 11].
Noels, A., Boury, A., Gabriel, M., and Scuflaire, R. 1976, *Astron. Astrophys.*, **49**, 103. [§ 27].
Noels, A., Boury, A., Scuflaire, R., and Gabriel, M. 1974, *Astron. Astrophys.*, **31**, 185. [§ 27].
Noels, A., Scuflaire, R., and Gabriel, M. 1984, *Astron. Astrophys.*, **130**, 389. [§ 40].
Noyes, R. W., Baliunas, S. L., Belserene, E., Duncan, D. K., Horne, J., and Widrow, L. 1984, *Astrophys. J. Letters*, **285**, L23. [§ 43].
Noyes, R. W., and Rhodes, E. J., Jr. 1984, ed. *Probing the Depths of a Star: The Study of Solar Oscillations from Space* (Jet Propulsion Laboratory, Pasadena). [§ 39].

O ~ P

Oberbeck, A. 1879, *Ann. Phy. Chem.*, **7**, 271. [§ 29].
O'Donoghue, D. 1986, in *Seismology of the Sun and the Distant Stars*, ed. D. O. Gough (D. Reidel Publ. Co., Dordrecht), p.467. [§ 10].
O'Donoghue, D., and Warner, B. 1987, *Monthly Notices Roy. Astron. Soc.*, **228**, 949. [§ 10].
Ogura, Y., and Phillips, N. A. 1962, *J. Atmos. Sci.*, **19**, 173. [§ 20].
Olver, F. W. J. 1954, *Phil. Trans. Roy. Soc. London, Ser. A*, **247**, 307. [§ 16].
Osaki, Y. 1966, *Publ. Astron. Soc. Japan*, **18**, 384. [§ 27].
Osaki, Y. 1971, *Publ. Astron. Soc. Japan*, **23**, 485. [§§ 3, 7].
Osaki, Y. 1974, *Astrophys. J.*, **189**, 469. [§§ 3, 35].
Osaki, Y. 1975, *Publ. Astron. Soc. Japan*, **27**, 237. [§§ 3, 15, 17].
Osaki, Y. 1976, *Publ. Astron. Soc. Japan*, **28**, 105. [§§ 17, 26].
Osaki, Y. 1977, *Publ. Astron. Soc. Japan*, **29**, 235. [§§ 16, 21, 25, 28].
Osaki, Y. 1982, in *Pulsations in Classical and Cataclysmic Variable Stars*, ed. J. P. Cox and C. J. Hansen (Univ. of Colorado and National Bureau of Standards, Boulder), p. 303. [§ 35].
Osaki, Y. 1986a, *Publ. Astron. Soc. Pacific*, **98**, 32. [§ 36].
Osaki, Y. 1986b, in *Seismology of the Sun and the Distant Stars*, ed. D. O. Gough (D. Reidel Publ. Co., Dordrecht), p.453. [§§ 7, 8].
Osaki, Y., and Hansen, C. J. 1973, *Astrophys. J.*, **185**, 277. [§§ 10, 15, 18].
Owen, J. W. 1957, *Monthly Notices Roy. Astron. Soc.*, **117**, 384. [§ 17].
Page, C. G. 1972, *Monthly Notices Roy. Astron. Soc.*, **159**, 25p. [§ 10].
Pallé, P. L., Perez, J. C., Régulo, C., Roca Cortés, T., Isaak, G. R., McLeod, C. P., and van der Raay, H. B. 1986a, *Astron. Astrophys.*, **169**, 313. [§§ 11, 41].
Pallé, P. L., Perez, J. C., Régulo, C., Roca Cortés, T., Isaak, G. R., McLeod, C. P., and van der Raay, H. B. 1986b, *Astron. Astrophys.*, **170**, 114. [§ 41].
Papaloizou, J., and Pringle, J. E. 1978, *Monthly Notices Roy. Astron. Soc.*, **182**, 423. [§§ 7, 19, 35].
Pedlosky, J. 1979, *Geophysical Fluid Dynamics* (Springer-Verlag, Berlin). [§§ 31, 33].
Pekeris, C. L. 1938, *Astrophys. J.*, **88**, 189. [§ 3].

Penrod, G. D. 1987, in *Physics of Be stars, IAU Colloq. No. 92,* ed. A. Slettebak and T. P. Snow (Cambridge Univ. Press, Cambridge), p.463. [§ 8].
Percy, J. R. 1986, *Highlights of Astronomy,* **7**, 265. [§ 8].
Pesnell, W. D. 1984, *Astrophys. J.*, **285**, 778. [§§ 15, 21].
Petterson, J. A. 1980, *Astrophys. J.*, **241**, 247. [§§ 6, 10].
Phillips, D. L. 1962, *J. Ass. Comput. Mach.*, **9**, 84. [§ 41].
Pietraszewski, K. A. R. B., Reay, N. K., and Ring, J. 1986a, in *Seismology of the Sun and the Distant Stars,* ed. D. O. Gough (D. Reidel Publ. Co., Dordrecht), p.377. [§ 43].
Pietraszewski, K. A. R. B., Ring, J., and Forrest, A. K. 1986b, in *Seismology of the Sun and the Distant Stars,* ed. D. O. Gough (D. Reidel Publ. Co., Dordrecht), p.391. [§ 43].
Praderie, F., Mangeney, A., Lemaire, Ph., Puget, P., and Bisnovatyi-Kogan, G. S. 1988, in *Advances in Helio- and Asteroseismology, IAU Symp. No.123,* ed. J. Christensen-Dalsgaard and S. Frandsen (D. Reidel Publ. Co., Dordrecht), p.549. [§ 43].
Provost, J. 1984, in *Observational Tests of Stellar Evolution Theory, IAU Symp. No. 105,* ed. A. Maeder and A. Renzini (D. Reidel Publ. Co., Dordrecht), p.47. [§ 43].
Provost, J., Berthomieu, G., and Rocca, A. 1981, *Astron. Astrophys.*, **94**, 126. [§§ 19, 34].

R

Rao, C. R., and Mitra, S. K. 1971, *Generalized Inverse Matrices and Its Applications* (Wiley and Sons, New York). [§ 41].
Reeves, H. 1965, in *Stellar Structure,* ed. L. H. Aller and D. B. McLaughlin (Univ. of Chicago Press, Chicago), p.113. [§ 27].
Rhodes, E. J., Jr., Cacciani, A., Blamont, J., Tomczyk, S., Ulrich, R. K., and Howard, R. F. 1984, in *Solar Seismology from Space* ed. R. K. Ulrich, J. Harvey, E. J. Rhodes, Jr., and Toomre, J. (Jet Propulsion Laboratory, Pasadena), p. 125. [§ 11].
Rhodes, E. J., Jr., Cacciani, A., and Tomczyk, S. 1986, in *Seismology of the Sun and the Distant Stars,* ed. D. O. Gough (D. Reidel Publ. Co., Dordrecht), p.359. [§ 43].
Rhodes, E. J., Jr., Cacciani, A., Woodard, M., Tomczyk, S., Korzennik, S., and Ulrich, R. K. 1987, in *The Internal Solar Angular Velocity,* ed. B. R. Durney and S. Sofia (D. Reidel Publ. Co., Dordrecht), p.75. [§ 39].
Rhodes, E. J., Jr., Ulrich, R. K., and Simon, G. W. 1977, *Astrophys. J.*, **218**, 901, [§ 11].
Rhodes, E. J., Jr., Woodard, M. F., Cacciani, A., Tomczyk, S., Korzennik, S. G., and Ulrich, R. K. 1988, *Astrophys. J.*, **326**, 479. [§ 11]
Richstone, D. O. 1974, *Astrophys. J.*, **188**, 327. [§ 29].
Ritter, A. 1879, *Wiedemanns Ann.*, **8**, 179. [§ 3].
Robe, H. 1968, *Ann. Astrophys.*, **31**, 475. [§ 17].
Robinson, E. L., Kepler, S. O., and Nather, R. E. 1982, *Astrophys. J.*, **259**, 219. [§ 10].
Robinson, E. L., and McGraw, J. T. 1976, *Astrophys. J. Letters,* **207**, L37. [§ 10].
Robinson, E. L., Nather, R. E., and McGraw, J. T. 1976, *Astrophys. J.*, **210**, 211. [§ 10].
Robinson, E. L., Stover, R. J., Nather, R. E., and McGraw, J. T. 1978, *Astrophys. J.*, **220**, 614. [§ 10].
Rolfe, E. 1988, ed. *Seismology of the Sun and Sun-like Stars* (ESA SP-286, Paris), in press. [§ 37].
Rosenbluth, M. N., and Bahcall, J. N. 1973, *Astrophys. J.*, **184**, 9. [§ 29].
Rosendhal, J. D. 1970, *Astrophys. J.*, **159**, 107. [§ 5].
Rossby, C. G. 1939, *J. Marine Res.*, **2**, 38. [§ 33].
Rosseland, S. 1949, *The Pulsation Theory of Variable Stars* (Clarendon Press, Oxford). [§ 3].
Roth, M. L., and Weigert, A. 1979, *Astron. Astrophys.*, **80**, 48. [§ 17].
Rust, D. M., Appourchaux, T., and Hill, F. 1988, in *Advances in Helio- and Asteroseismology, IAU Symp. No. 123,* ed. J. Christensen-Dalsgaard and S. Frandsen (D. Reidel Publ. Co., Dordrecht), p.475. [§§ 11, 39].

S

Saio, H. 1980, *Astrophys. J.*, **240**, 685. [§§ 21, 27].
Saio, H. 1981, *Astrophys. J.*, **244**, 299. [§ 34].
Saio, H. 1982, *Astrophys. J.*, **256**, 717. [§§ 19, 34].
Saio, H., and Cox, J. P. 1980, *Astrophys. J.*, **236**, 549. [§§ 3, 22, 28].
Saio, H., Wheeler, C. J., and Cox, J. P. 1984, *Astrophys. J.*, **281**, 318. [§ 23].
Sakashita, S., and Hayashi, C. 1959, *Prog. Theor. Phys., Kyoto,* **22**, 830. [§ 29].
Scherrer, P. H. 1982, in *Pulsations in Classical and Cataclysmic Variable Stars* ed. J. P. Cox and C. J. Hansen (Univ. of Colorado and National Bureau of Standards, Boulder), p.83. [§ 37].
Scherrer, P. H., and Wilcox, J. M. 1983, *Solar Phys.*, **82**, 37. [§ 11].
Scherrer, P. H., Wilcox, J. M., Christensen-Dalsgaard, J., and Gough, D. O. 1982, *Nature,* **297**, 312. [§ 11].
Scherrer, P. H., Wilcox, J. M., Kotov, V. A., Severny, A. B., and Tsap, T. T. 1979, *Nature,* **277**, 635. [§ 11].
Scherrer, P. H., Wilcox, J. M., Kotov, V. A., Severny, A. B., and Tsap, T. T. 1980, *Astrophys. J. Letters,* **237**, L97. [§ 11].
Schiff, L. 1955, *Quantum Mechanics,* 2nd ed. (McGraw-Hill, New York). [§ 14].
Schmalberger, D. C. 1960, *Astrophys. J.*, **132**, 591. [§ 8].
Schwarzschild, M. 1975, *Astrophys. J.*, **195**, 137. [§ 6].
Schwarzschild, M., and Härm, R. 1958, *Astrophys. J.*, **128**, 348. [§ 29].
Schwarzschild, M., and Härm, R. 1965, *Astrophys. J.*, **142**, 855. [§ 29].
Scuflaire, R. 1974, *Astron. Astrophys.*, **36**, 107. [§§ 3, 4, 17].
Scuflaire, R., and Noels, A. 1986, *Astron. Astrophys.*, **169**, 185. [§ 27].
Scuflaire, R., Noels, A., Gabriel, M., and Boury, A. 1976, *Astrophys. Space Sci.*, **39**, 463. [§ 29].
Sekii, T., and Shibahashi, H. 1987, in *Stellar Pulation,* ed. A. N. Cox, W. M. Sparks, and S. G. Starrfield (Springer-Verlag, Berlin), p.322. [§ 41].
Sekii, T., and Shibahashi, H. 1988, in *Seismology of the Sun and Sun-like Stars,* ed. E. Rolfe (ESA SP-286, Paris), in press. [§ 41].
Sekii, T., and Shibahashi, H. 1989, *Publ. Astron. Soc. Japan,* in press. [§ 41].
Severny, A. B., Kotov, V. A., and Tsap, T. T. 1976, *Nature,* **259**, 87. [§ 11].
Severny, A. B., Kotov, V. A., and Tsap, T. T. 1980, *Astron. Astrophys.*, **88**, 317. [§ 11].
Severny, A. B., Kotov, V. A., and Tsap, T. T. 1983, *Nature,* **307**, 247. [§ 11].
Shakura, N. I., and Sunyaev, R. A. 1973, *Astron. Astrophys.*, **24**, 337. [§ 20].
Shibahashi, H. 1979, *Publ. Astron. Soc. Japan,* **31**, 87. [§§ 3, 16].
Shibahashi, H. 1980, *Publ. Astron. Soc. Japan,* **32**, 341. [§ 29].
Shibahashi, H. 1983, *Astrophys. J. Letters,* **275**, L5. [§§ 26, 29].

Shibahashi, H. 1984, *Mem. Soc. Astron. Ital.*, **55**, 181. [§ 9].
Shibahashi, H. 1986, in *Hydrodynamic and Magnetohydrodynamic Problems in the Sun and Stars*, ed. Y. Osaki (Univ. of Tokyo, Tokyo), p.195. [§§ 19, 43].
Shibahashi, H. 1987, in *Stellar Pulsation*, ed. A. N. Cox, W. M. Sparks, and S. G. Starrfield (Springer-Verlag, Berlin), p.112. [§ 9].
Shibahashi, H. 1988, in *Advances in Helio- and Asteroseismology, IAU Symp. No. 123*, ed. J. Christensen-Dalsgaard and S. Frandsen (D. Reidel Publ. Co., Dordrecht), p.133. [§§ 3, 41].
Shibahashi, H., Noels, A., and Gabriel, M. 1983, *Astron. Astrophys.*, **123**, 283. [§§ 11, 40, 41].
Shibahashi, H., and Osaki, Y. 1976a, *Publ. Astron. Soc. Japan*, **28**, 199. [§§ 3, 16, 17, 29].
Shibahashi, H., and Osaki, Y. 1976b, *Publ. Astron. Soc. Japan*, **28**, 533. [§§ 15, 16, 27].
Shibahashi, H., and Osaki, Y. 1981a, *Publ. Astron. Soc. Japan*, **33**, 427. [§§ 21, 23, 24, 25, 28].
Shibahashi, H., and Osaki, Y. 1981b, *Publ. Astron. Soc. Japan*, **33**, 713. [§ 11].
Shibahashi, H., Osaki, Y., and Unno, W. 1975, *Publ. Astron. Soc. Japan*, **27**, 401. [§ 15, 27].
Shibahashi, H., and Saio, H. 1985, *Publ. Astron. Soc. Japan*, **37**, 245. [§ 9].
Shibahashi, H., and Sekii, T. 1988, in *Seismology of the Sun and Sun-like Stars*, ed. E. Rolfe (ESA SP-286, Paris), in press. [§ 41].
Shibahashi, H., Sekii, T., and Kawaler, S. 1988, in *Atmospheric Diagnostics of Stellar Evolution: Chemical Peculiarity, Mass Loss, and Explosion, IAU Colloq. No. 108*, ed. K. Nomoto (Springer-Verlag, Berlin), p.86. [§ 43].
Shobbrook, R. R. 1972, *Monthly Notices Roy. Astron. Soc.*, **157**, 5p. [§ 8].
Shobbrook, R. R. 1979, *Monthly Notices Roy. Astron. Soc.*, **189**, 571. [§ 8].
Shobbrook, R. R., Herbison-Evans, D., Johnston, I. D., and Lomb, N. R. 1969, *Monthly Notices Roy. Astron. Soc.*, **145**, 131. [§ 8].
Shobbrook, R. R., and Lomb, N. R. 1972, *Monthly Notices Roy. Astron. Soc.*, **156**, 181. [§ 8].
Shobbrook, R. R., and Stobie, R. S. 1974, *Monthly Notices Roy. Astron. Soc.*, **169**, 643. [§ 5].
Sienkiewicz, R. 1980, *Astron. Astrophys.*, **85**, 295. [§ 27].
Smeyers, M., Briers, R., Tassoul, M., Degryes, K., Polfliet, R., and Van Hoolst, T. 1988, in *Seismology of the Sun and Sun-like Stars*, ed. E. Rolfe (ESA SP-286, Paris), in press. [§ 16].
Smeyers, P., Craeynest, D., and Martens, L. 1981, *Astrophys. Space Sci.*, **78**, 483. [§ 19].
Smeyers, P., and Martens, L. 1983, *Astron. Astrophys.*, **125**, 193. [§ 34].
Smeyers, P., and Tassoul, M. 1988, *Astrophys. J. Suppl.*, **65**, 429. [§ 16].
Smith, M. A. 1977, *Astrophys. J.*, **215**, 574. [§§ 7, 8].
Smith, M. A. 1980a, *Astrophys. J.*, **240**, 149. [§§ 3, 8].
Smith, M. A. 1980b, in *Nonradial and Nonlinear Stellar Pulsation*, ed. H. A. Hill and W. A. Dziembowski (Springer-Verlag, Berlin), p.60. [§§ 3, 8].
Smith, M. A. 1980c, *Highlights of Astronomy*, **5**, 457. [§ 8].
Smith, M. A. 1981, *Astrophys. J.*, **240**, 149. [§ 8].
Smith, M. A. 1985, *Astrophys. J.*, **297**, 206. [§§ 7, 8].
Smith, M. A. 1986, in *Hydrodynamic and Magnetohydrodynamic Problems in the Sun and Stars*, ed. Y. Osaki (Univ. of Tokyo, Tokyo), p.145. [§ 8].

Smith, M. A., and Karp, A. H. 1976, in *Proc. Solar and Stellar Pulsation Conf.*, ed. A. N. Cox and R. G. Deupree (Los Alamos Publ.), p.289. [§ 8].
Soderblom, D. R. 1988, in *Advances in Helio- and Asteroseismology, IAU Symp. No. 123*, ed. J. Christensen-Dalsgaard and S. Frandsen (D. Reidel Publ. Co., Dordrecht), p.555. [§ 43].
Soderblom, D. R. and Däppen, W. 1988, in *Advances in Helio- and Asteroseismology, IAU Symp. No. 123*, ed. J. Christensen-Dalsgaard and S. Frandsen (D. Reidel Publ. Co., Dordrecht), p.281. [§ 43].
Spergel, D. N., and Press, W. H. 1985, *Astrophys. J.*, **294**, 663. [§ 40].
Spiegel, E. A., and Veronis, G. 1960, *Astrophys. J.*, **131**, 442. [§§ 20, 29].
Stamford, P. A., and Watson, R. D. 1976, *Proc. Astron. Soc. Australia*, **3**, 75. [§ 7].
Stamford, P. A., and Watson, R. D. 1977, *Monthly Notices Roy. Astron. Soc.*, **180**, 551. [§ 7].
Stamford, P. A., and Watson.R. D. 1981, *Astrophys. Space Sci.*, **77**, 131. [§ 6].
Starrfield, S. G., Cox, A. N., Hodson, S. W., and Pesnell, W. D. 1983, *Astorphys. J. Letters*, **268**, L27. [§ 28].
Starrfield, S. G., Cox, A. N., Kidman, R. B., and Pesnell, W. D. 1984, *Astrophys. J.*, **281**, 800. [§§ 10, 28].
Starrfield, S. G., Cox, A. N., Kidman, R. B., and Pesnell, W. D. 1985, *Astrophys. J. Letters*, **293**, L23. [§ 28].
Stein, R. F., and Leibacher, J. 1974, *Ann. Rev. Astron. Astrophys.*, **12**, 407. [§§ 3,11].
Stellingwerf, R. F. 1978, *Astron. J.*, **83**, 1184. [§ 28].
Stellingwerf, R. F. 1979, *Astrophys. J.*, **227**, 935. [§ 28].
Stellingwerf, R. F. 1984, *Astrophys. J.*, **284**, 712. [§ 21].
Stevenson, D. J. 1979, *Monthly Notices Roy. Astron. Soc.*, **187**, 129. [§ 29].
Stover, R. J., Hesser, J. E., Lasker, B. M., Nather, R. E., and Robinson, E. L. 1980, *Astrophys. J.*, **240**, 865. [§ 10].
Struve, O. 1955, *Sky and Telescope*, **14**, 461. [§ 8].
Sugimoto, D. 1970, *Astrophys. J.*, **159**, 619. [§ 24].

T ~ U

Tassoul, J.-L. 1978, *Theory of Rotating Stars* (Princeton Univ. Press, Princeton). [§ 31].
Tassoul, M. 1980, *Astrophys. J. Suppl.*, **43**, 469. [§§ 3, 9, 11, 16, 43].
Thompson, I. B. 1983, *Monthly Notices Roy. Astron. Soc.*, **205**, 43p. [§ 9].
Thomson, W. 1863, *Phil. Trans. Roy. Soc. London*, **153**, 612. [§ 3].
Totsuka, Y. 1988 in *Proc. XXIV International Conference on High-Energy Physics* held at München, August 1988. [§ 40].
Turck-Chièze, S., Cahen, S., Cassé, M, and Doom, C. 1988, *Astrophys. J.*, **335**, 415. [§ 40].
Ulrich, R. K. 1970, *Astrophys. J.*, **162**, 993. [§ 11].
Ulrich, R. K. 1982, *Astrophys. J.*, **258**, 404. [§ 40].
Ulrich, R. K. 1986a, *Astrophys. J. Letters*, **306**, L37. [§ 43].
Ulrich, R. K. 1986b, in *Seismology of the Sun and the Distant Stars*, ed. D. O. Gough (D. Reidel Publ. Co., Dordrecht), p.187. [§ 40].
Ulrich, R. K. 1988, in *Advances in Helio- and Asteroseismology, IAU Symp. No. 123*, ed. J. Christensen-Dalsgaard and S. Frandsen (D. Reidel Publ. Co., Dordrecht), p.299. [§ 43].
Ulrich, R. K., Harvey, J., Rhodes, E. J., Jr., and Toomre, J. 1984, ed. *Solar Seismology from Space* (Jet Propulsion Laboratory, Pasadena). [§ 37].

Ulrich, R. K., and Rhodes, E. J., Jr. 1977, *Astrophys. J.*, **218**, 521. [§§ 15, 38, 40, 42].
Ulrich, R. K., and Rhodes, E. J., Jr. 1983, *Astrophys. J.*, **265**, 551. [§§ 11, 40].
Ulrich, R. K., and Rhodes, E. J., Jr. 1984, in *Theoretical Problems in Stellar Stability and Oscillations*, ed. A. Noels and M. Gabriel (Universitè de Liége, Liége), p.250. [§ 40].
Underhill, A. B. 1966, *Early Type Stars* (D. Reidel Publ. Co., Dordrecht), p.246. [§ 8].
Underhill, A. B. 1982, in *B Stars With and Without Emission Lines*, ed. A. B. Underhill and V. Doazan (NASA SP-456), p.3. [§ 8].
Unno, W. 1967, *Publ. Astron. Soc. Japan*, **19**, 140. [§§ 21, 27, 30].
Unno, W. 1969, *Publ. Astron. Soc. Japan*, **21**, 240. [§ 30].
Unno, W. 1970, *Publ. Astron. Soc. Japan*, **22**, 299. [§ 29].
Unno, W. 1975a, *Publ. Astron. Soc. Japan*, **27**, 81. [§§ 3, 27].
Unno, W. 1975b, *Publ. Astron. Soc. Japan*, **27**, 605. [§§ 25, 29].
Unno, W. 1977, in *Problems of Stellar Convection, IAU Colloq. No. 38*, ed. E. A. Spiegel and J.-P. Zahn (Springer-Verlag, Berlin), p.315. [§§ 21, 30].
Unno, W. 1987, in *The Internal Solar Angular Velocity*, ed. B. R. Durney and S. Sofia (D. Reidel Publ. Co., Dordrecht), p.343. [§ 20].
Unno, W., Kondo, M., and Xiong, D. 1985, *Publ. Astron. Soc. Japan*, **37**, 235. [§ 20].
Unno, W., and Saio, H. 1987, in *The Internal Solar Angular Velocity*, ed. B. R. Durney and S. Sofia (D. Reidel Publ. Co., Dordrecht), p.97. [§ 34].

V ~ Z

Vandakurov, Y. V. 1976, *Astron. Zh.*, **44**, 786. [§ 16].
Vauclair, G., Chevreton, M., and Dolez, N. 1987, *Astron. Astrophys.*, **175**, L13. [§ 10].
Vauclair, G., Dolez, N., and Chevreton, M. 1981, *Astron. Astrophys.*, **103**, L17. [§ 10].
Veronis, G. 1965, *J. Marine Res.*, **23**, 1. [§ 29].
Vitense, E. 1953, *Z. Astrophys.*, **32**, 135. [§ 20].
Vogt, S. S. and Penrod, G. D. 1983, *Astrophys. J.*, **275**, 661. [§§ 7, 8, 36].
Vorontsov, S. V. 1988, in *Seismology of the Sun and Sun-like Stars*, ed. E. Rolfe (ESA SP-286, Paris), in press. [§ 41].
Waelkens, C. L. 1987, in *Stellar Pulsation*, ed. A. N. Cox, W. M. Sparks, and S. G. Starrfield (Springer-Verlag, Berlin), p.75. [§ 8].
Waelkens, C. L., and Rufener, F. 1985, *Astron. Astrophys.*, **152**, 6. [§ 8].
Walker, G. A. H., Moyes, K., Yang, S., and Fahlman, G. G. 1981, in *Workshop on Pulsating B Stars*, ed. G.E.V.O.N and C. Sterken (Observatoire de Nice, Nice), p.141. [§ 8].
Walker, G. A. H., Yang, S., and Fahlman, G. G. 1979, *Astrophys. J.*, **233**, 199. [§§ 8, 36].
Walker, G. A. H., Yang, S, and Fahlman, G. G. 1987, *Astrophys. J. Letters*, **320**, L139. [§ 5].
Walker, M. F. 1954a, *Astrophys. J.*, **119**, 631. [§ 6].
Walker, M. F. 1954b, *Astrophys. J.*, **120**, 58. [§ 6].
Warner, B. 1986, *Astrophys. Space Sci.*, **118**, 271. [§ 10].
Warner, B., and Nather, R. E. 1972, *Monthly Notices Roy. Astron. Soc.*, **156**, 1. [§ 10].
Warner, B., Peters, W. L., Hubbard, W. B., and Nather, R. E. 1972, *Monthly Notices Roy. Astron. Soc.*, **159**, 321. [§ 6].

Warner, B., and Robinson, E. L. 1972, *Nature, Phys. Sci.*, **239**, 2. [§ 10].
Weigert, A. 1966, *Z. Astrophys.*, **64**, 395. [§ 29].
Weiss, W. W. 1986, in *Upper Main Sequence Stars with Anomalous Abundances, IAU. Colloq. No. 90*, ed. C. R. Cowley, M. M. Dworetsky, and C. Megessier (D. Reidel Publ. Co., Dordrecht), p.219. [§ 9].
Wesselink, A. J. 1946, *Bull. Astron. Insts. Neth.*, **10**, 91. [§ 6].
Wesselink, A. J. 1947, *Bull. Astron. Insts. Neth.*, **10**, 256. [§ 6].
Wesemael, F., Green, R. F., and Liebert, J. 1985, *Astrophys. J. Suppl.*, **58**, 379. [§ 10].
Whitaker, W. A. 1963, *Astrophys. J.*, **137**, 914. [§ 11].
Whittaker, E. T., and Watson, G. N. 1965, *A Course of Modern Analysis* (Cambridge Univ. Press, Cambridge). [§ 13].
Winget, D. E., and Fontaine, G. 1982, in *Pulsations in Classical and Cataclysmic Variable Stars*, ed. J. P. Cox and C. J. Hansen (Univ. of Colorado and National Bureau of Standards, Boulder), p.46. [§ 10].
Winget, D. E., Hansen, C. J., and Van Horn, H. M. 1983b, *Nature*, **303**, 781. [§ 43].
Winget, D. E., Kepler, S. O., Robinson, E. L., Nather, R. E., and O'Donoghue, D. 1985, *Astrophys. J.*, **292**, 606. [§§ 10, 15, 43].
Winget, D. E., Nather, R. E., and Hill, J. A. 1987, *Astrophys. J.*, **316**, 305. [§ 10].
Winget, D. E., Robinson, E. L., Nather, R. E., and Balachandran, S. 1984, *Astrophys. J. Letters*, **279**, L15. [§ 10].
Winget, D. E., Robinson, E. L., Nather, R. E., and Fontaine, G. 1982b, *Astrophys. J. Letters*, **262**, L11. [§ 10].
Winget, D. E., Van Horn, H. M., and Hansen, C. J. 1981, *Astrophys. J. Letters*, **245**, L33. [§§ 10, 15].
Winget, D. E., Van Horn, H. M., Tassoul, M., Hansen, C. J., and Fontaine, G. 1983a, *Astrophys. J. Letters*, **268**, L33. [§ 28].
Winget, D. E., Van Horn, H. M., Tassoul, M., Hansen, C. J., Fontaine, G., and Carroll, B. W. 1982a, *Astrophys. J. Letters*, **252**, L65. [§§ 3, 10, 28].
Wolff, C. L. 1979, *Astrophys. J.*, **227**, 943. [§ 3].
Wood, M. A., Winget, D. E., Nather, R. E., Hessman, F. V., Liebert, J., Kurtz, D. W., Wesemael, F., and Wegner, G. 1987, *Astrophys. J.*, **313**, 757. [§ 10].
Woodard, M., and Hudson, H. S. 1983a, *Nature*, **305**, 589. [§ 11].
Woodard, M., and Hudson, H. S. 1983b, *Solar Phys.*, **82**, 67. [§ 11].
Woodard, M. A., and Noyes, R. W. 1985, *Nature*, **318**, 449. [§ 11].
Xiong, D. R. 1978, *Chinese Astron.*, **2**, 118. [§§ 20, 21, 30].
Xiong, D. R. 1984, *Astron. Astrophys.*, **150**, 133. [§ 29].
Zhevakin, S.A. 1953, *Russian Astron. J.*, **30**, 161. [§§ 12, 28].

List of Symbols

$\boldsymbol{A}$	vector form of Schwarzschild discriminant in Sect. 33
$\boldsymbol{A}$	matrix composed of A_{ij} in Sect. 41
A	Schwarzschild discriminant; $(=\frac{d\ln\rho}{dr}-\frac{1}{\Gamma_1}\frac{d\ln p}{dr})$
A	velocity amplitude in the radial direction in Sect. 7
A	quantity defined by equation (43.2) in Sect. 43
A^*	nondimensional quantity defined by equation (18.21); $(=-rA)$
A^n_{ij}	quantity defined by equation (18.74) in Sect. 18.2
A_{ij}	quantity defined by equation (41.5) in Sect. 41
$A_l^{m'}$	amplitude corresponding to a frequency component $\sigma=\sigma^{(0)}+\sigma^{(1)mag}_{m=0}-m'\Omega$ in Sect. 43
a	radiation density constant
a	$=c(r)/r$ in Sect. 41
a_i $(i=0, 1, 2, 3)$	coefficients of equation (29.20) in Sect. 29
a_i	expansion coeffeicients of m-splitting of frequency defined by equation (36.16) in Sect. 36
a_{ij}	constant coefficient matrix defined by equation (18.24) in Sect. 18.2
$\boldsymbol{B}$	linear operator with respect to $\boldsymbol{\xi}$ defined by equation (19.13)
$\boldsymbol{B}_{m''m}$	matrix defined by equation (19.28)
$\boldsymbol{B}$	magnetic field
$\boldsymbol{B}$	unitary matrix diagonalizing matrix $\boldsymbol{W}$ in Sect. 34
B	strength of magnetic field
B^n_{ij}	quantity defined by equation (18.75) in Sect. 18.2
B_0	angle between the solar equator and the line-of-sight in Sect. 39
B_1, B_1'	quantities defined by equation (30.21)
B_2, B_2'	quantities defined by equation (30.22)
B_3, B_3'	quantities defined by equation (30.23)
b_{ij}	constant coefficient matrix defined by equation (18.33)
$b_{\rm I}$, $b_{\rm II}$, $b_{\rm III}$	branching factor in pp-chain
b_1	quantity defined by equation (29.15) in Sect. 29
$\boldsymbol{C}$	bi-diagonal matrix defined by equation (34.22) in Sect. 34
C (subscript)	convective quantities of state, e.g., ρ_C, T_C etc.
C_{jk}	nuclear reaction rate of the j- and k-nuclei in Sect. 27
C_{nl}	constant coefficient deciding rotational splitting of frequency [see equation (19.46)]
$\boldsymbol{c}$	constant column vector defined by equation (18.107) in Sect. 18.2
c	sound speed; $(=\sqrt{\Gamma_1 p/\rho})$
c	light speed
c_*	quantities at the stellar center; e.g., T_c
c (subscript)	specific heat at constant pressure; $[=(\partial S/\partial \ln T)_p]$
c_p	quantity defined by equation (20.47) in Sect. 20
c_p^*	specific heat at constant volume; $[=(\partial S/\partial \ln T)_\rho]$
c_v	quantity defined by equation (18.19); $[=(r/R)^3/(M_r/M)]$
c_1	

c_2 quantity defined by equation (24.13)
c_3 quantity defined by equation (24.14); $(=4\pi r^3\rho\varepsilon_N/L_R)$
c_4 quantity defined by equation (24.15); $[=4\pi r^3\rho c_p T\,(GM/R^3)^{1/2}/L_R]$
$\boldsymbol{D}$ diagonal matrix defined by equation (34.34) in Sect. 34
D discriminant in Sect. 18 and 24
$D_i\ (i=1,\ldots,4)$ quantities defined by equation (22.6)−(22.10) in Sect. 22
D_0 quantity defined by equation (43.1) in Sect. 43
D/Dt time derivative following the unperturbed rotation; $(=\partial/\partial t+\Omega\partial/\partial\phi)$
d/dt Lagrangian time derivative $(=\partial/\partial t+\boldsymbol{v}\cdot\nabla)$ in Sect. 33
$\boldsymbol{d}$ matrix consisting of $d^{(l)}_{mm'}$
d_t operator defined by equation (20.52) in Sect. 20
d^n_t quantity defined by equation (18.77) in Sect.18
$d^{(l)}_{mm'}$ quantity defined by equation (19.69) in Sect. 19 and 43
E total energy of a star; $[=\int_0^M(\frac{1}{2}\boldsymbol{v}^2+\frac{1}{2}\Phi+U)dM_r]$
E_W global wave energy of a star defined by equation (25.15); $[=\int_0^M(e_W+\frac{1}{2}\frac{\rho'}{\rho}\Phi')dM_r]$
E (subscript) quantities in equilibrium
$\boldsymbol{e}_i$ unit vector; e.g., $\boldsymbol{e}_r$, $\boldsymbol{e}_\theta$, $\boldsymbol{e}_\phi$
e_K kinetic energy density of oscillation $(=\sigma^2\rho|\boldsymbol{\xi}|^2)$ in Sect. 18
e_W wave energy defined by equation (25.12)
$\boldsymbol{F}$ total flux; $(=\boldsymbol{F}_C+\boldsymbol{F}_R)$
$\boldsymbol{F}_C$ convective flux
$\boldsymbol{F}_K$ turbulent conductive flux in Sect. 20 and 30
$\boldsymbol{F}_R$ radiative flux
$\boldsymbol{F}_W$ wave energy flux $(=p'\boldsymbol{v}+\rho\boldsymbol{v}\Phi')$ in Sect. 25
$\boldsymbol{F}_{R,C}$ radiative flux from a convective element defined by equation (20.43) in Sect. 20
$\boldsymbol{F}_{K,C}$ conductive flux of convection energy defined by equation (20.44) in Sect. 20
F function representing Duvall's relation given by equation (41.35) in Sect. 41
F_h flux in the horizontal direction
F_r flux in the radial direction
F^n_{ij} quantity defined by equation (18.68) in Sect. 18.2
$\boldsymbol{f}$ external forces
f nonradial f-mode
$f(x)$ function defined by equation (16.13) in Sect. 16
f_E Eddington factor [see equation (21.26)]
$f_i(y^n_j;\lambda_k)$ symbolical form of the differential equations (18.14)–(18.17)
f^n_{ij} abbereviation of $f_i(y^n_j;\lambda_k)$
f_{ij} energy fraction generated by ij-reaction defined by equation (27.18)
G gravitational constant
G-mode g-mode trapped effectively in μ-gradient zone
G^n_{kj} quantities defined by equations (18.68) and (18.70) in Sect. 18.2
g gravitational acceleration
g-mode g-mode trapped effectively in envelope in Sect. 17
g_n n-th overtone of nonradial g-mode belonging to spherical harmonics $Y^m_l(\theta,\phi)$

g^l_k, g^N_k symbolical forms of boundary conditions in Sect. 18
g_N quantity defined by equation (29.14); $[=\varepsilon_N\varepsilon_T/(c_pT)]$
$\boldsymbol{H}$ column vector composed of H_l in Sect. 34
H_e observed magnetic field strength of a star in Sect. 9 and 43
H_l spheroidal component of relative horizontal displacement vector $\boldsymbol{\xi}_\perp/r$ defined by equation (34.1) in Sect. 34
H_p pressure scale height; $[=-dr/d\ln p=p/(\rho g)]$
h enthalpy
$\bar{h}$ specific angular momentum in Sect. 36
$h(r)$ function defined by equation (15.7)
Im imaginary part
I the order of differential equation in Sect. 18.2
$\bar{I}$ component of ΔI proportional to $Y^m_l(\theta,\phi)$ defined by equation (39.13)
$\hat{I}$ Fourier component of $\bar{I}$ with respect to time defined by equation (39.14)
I_{nl} quantity defined by equation (19.23)
ΔI brightness variation
i inclination of the stellar equator to the celestial plane
i $=\sqrt{-1}$
J mean intensity [see equation (21.26)]
J^m_l quantity defined by equation (34.5) in Sect. 34
$\boldsymbol{K}$ bi-diagonal matrix defined by equation (34.22) in Sect. 34
$\boldsymbol{K}$ kernel matrix in Sect. 41
K half of full amplitude in radial velocity curve
K radiative conductivity; $[=4ac_*T^3/(3\kappa\rho)]$
K number of eigenvalues in Sect. 18.2
K_{nlm} kernel of integral equation in Sect. 41
$\boldsymbol{k}$ wave-number vector
k Boltzman constant
k ratio of the velocity amplitude of a spheroidal mode in the horizontal direction to that in the radial direction in Sect. 7
k_h horizontal wave number
k_r radial wave number
$\mathcal{L}$, $\mathcal{L}_{ad}$ linear operators with respect to ξ_r in Sect. 4
$\boldsymbol{\mathcal{L}}$ linear operator with respect to $\boldsymbol{\xi}$ defined by equation (14.45)
$\boldsymbol{L}$, $\bar{\boldsymbol{L}}$ diagonal matrices defined by equation (34.22)
L stellar luminosity
L number of boundary condition including normalization condition in Sect. 18.2
L_I number of inner boundary conditions in Sect. 18.2
L_C convective luminosity
L_R radiative luminosity
L_l Lamb frequency; $\{=\frac{[l(l+1)]^{1/2}c_s}{r}\}$
L_r luminosity at radius r
L^n_i quantities defined by equation (18.69) in Sect. 18.2
$L_\odot$ solar luminosity; $(=3.827\ \mathrm{erg\ s^{-1}})$
L^2 $l(l+1)$ in Sect. 41
l degree of spherical surface harmonic $Y^m_l(\theta,\phi)$
l_R quantity defined by equation (29.14); $[=Kk^2/(c_p\rho)]$

λ_j $=|m|+2(j-1)$ for even modes; $=|m|+2j-1$ for odd modes in Sect. 33

l_c mixing length

$\boldsymbol{M}$ linear operator with respect to $\boldsymbol{\xi}$ defined by equation (19.11)

$\boldsymbol{M}_{m'm}$ matrix defined by equation (19.27)

$M, \bar{M}$ bi-diagonal matrices defined by equation (34.22)

M stellar mass

M macroturbulence velocity in Sect. 7.6

M_C mass of the convective zone

M_r mass inside thte radius r

M_R^m quantities defined by equation (18.76) in Sect. 18.2

M_{bol} bolometric magnitude

$M_\odot$ solar mass; $(=1.989\times10^{33}$ g)

m azimuthal order of spherical surface harmonic $Y_l^m(\theta, \phi)$

m_u mass of the atomic mass unit

Δm_r light amplitude in magnitude

N Brunt-Väisälä frequency; $\{=[-g(\frac{d\ln\rho}{dr}-\frac{1}{\Gamma_1}\frac{d\ln p}{dr})]^{1/2}\}$

N_j number density of nuclei with atomic weight j in Sect. 27

N_g number of g-type nodes (*cf.* Sect. 17)

N_p number of p-type nodes (*cf.* Sect. 17)

N_l^m normalization constant of spherical harmonics

n radial order of mode [ordinal number of modes; $(=N_p-N_g)$]

n_G number of nodes in μ-gradient zone in Sect. 17

n_g number of nodes in envelope gravity-wave zone in Sect. 17

n_p number of nodes in envelope acoustic-wave zone in Sect. 17

$\boldsymbol{O}_{m'm}$ matrix defined by equation (19.26)

$\mathcal{P}_r$ Reynolds stress in Sect. 20 and 30

$\boldsymbol{P}_n$ matrix defined by equations (18.79), (18.87), and (18.97) in Sect. 18.2

P function defined by equation (16.3) in Sect. 16

P_{3r} function defined by equation (22.20) in Sect. 22

$P_l^m(\mu)$ Ferrers' associated Legendre polynomials

p pressure

p_t turtulent pressure

p_{gas} gaseous pressure

p_{rad} radiation pressure

p-mode p-mode trapped effectively in the envelope in Sect. 17

p_n n-th overtone of nonradial p-mode belonging to spherical harmonics $Y_l^m(\theta, \phi)$

$\boldsymbol{Q}_n$ matrix defined by equations (18.80), (18.88), and (18.98) in Sect. 18.2

Q pulsation constant (Q-value); $[=\Pi(\bar{\rho}/\bar{\rho}_\odot)^{1/2}]$

Q function defined by equation (16.4) in Sect. 16

Q_{3r} function defined by equation (22.21) in Sect. 22

Q_{jk} energy generated by nuclear reaction of j-and k-nuclei in Sect. 27

Q_l^m amplitude of toroidal mode

$Q_l^m(\mu)$ Ferrers' associated Legendre polynomials

$\boldsymbol{q}_n$ matrix defined by equations (18.81), (18.89), and (18.99) in Sect. 18.2

q mass fraction; $(=M_r/M)$

$\mathcal{R}$ gas constant

$\boldsymbol{R}_n$ matrix defined by equations (18.83), (18.91), and (18.94) in Sect. 18.2

R stellar radius

$R(r)$ distance from the origin of the phase diagram in Sect. 16

R_i Richardson number in Sect. 35

$R_\odot$ solar radius; $(=6.960\times10^{10}$ cm)

Re real part

$\boldsymbol{r}$ position vector

$\boldsymbol{r}_n$ matrix defined by equations (18.84), (18.92), and (18.95) in Sect. 18.2

r radial coordinate

r_t penetration depth r at the turning point defined by equation (38.3) in Chapter VII

$\mathcal{S}_t$ stress tensor

$\boldsymbol{S}_n$ matrix defined by equations (18.86) and (18.96)

S entropy

S_l velocity amplitude of spheroidal component in Sect. 7

s temporal dependence of perturbations; $f' \propto \exp(st)$ in Sect. 29

s acoustic length defined by equation (41.40) in Sect. 41

$\boldsymbol{T}$ column vector composed of T_l in Sect. 34

T temperature

T_l velocity amplitude of toroidal component in Sect. 7

T_l toroidal component of relative displacement vector $\boldsymbol{\xi}_T r$ defined by equation (34.1)

T_{eff} effective temperature

t time

$\boldsymbol{U}$ orthogonal matrix diagonalizing the matrices $\boldsymbol{A}$ or $\boldsymbol{K}$ in Sect. 41

U specific internal energy

U homology invariant; $(=\frac{d\ln M_r}{d\ln r}=\frac{4\pi r^3\rho}{M_r})$

$\boldsymbol{u}$ velocity including turbulent convective velocity fields

$\boldsymbol{u}$ vector composed of unknown $u(r_j)$ in Sect. 41

u unknown function to be solved in integral equation in Sect. 41

$\boldsymbol{V}$ convective velocity; $(=\boldsymbol{V}_l+\boldsymbol{V}_t)$

$\boldsymbol{V}$ unitary matrix diagonalizing the matrix $\boldsymbol{K}$ in Sect. 41

$\boldsymbol{V}_l$ laminar convective velocity

$\boldsymbol{V}_p$ poloidal component (r- and θ-components) of velocity in Sect. 36

$\boldsymbol{V}_t$ turbulent convective velocity

$\boldsymbol{V}_{sph}$ pulsation velocity due to spheroidal mode [see equation (7.1)]

$\boldsymbol{V}_{tor}$ pulsation velocity due to toroidal mode [see equation (7.2)]

V homology invariant; $(=-\frac{d\ln\rho}{d\ln r}=\frac{GM_r\rho}{rp})$

V_e equatorial rotational velocity

V_g quantity defined by equation (18.18); $(=-\Gamma_1^{-1}\frac{d\ln p}{d\ln r})$

$<V>$ representative velocity of convection in Sect. 30

$\boldsymbol{v}$ velocity fields other than convection

$\boldsymbol{v}_g$ group velocity

$\boldsymbol{v}_{ph}$ phase velocity

$\boldsymbol{v}_p'$ poloidal component of linear perturbation of velocity in Sect. 36

v variable defined by equation (16.9) in Sect. 16

$\tilde{v}$ component of $v_{2l,mr}$ proportional to $Y_l^m(\theta, \phi)$ defined by equation

	(39.10)
$\hat{v}$	Fourier component of $\bar{v}$ with respect to time defined by equation (39.11)
v_D	observed Doppler velocity in Sect. 39
$v_{D,osc}$	oscillatory velocity field observed on the solar disk in Sect. 39
v_T	$=[\partial \ln(1/\rho)/\partial \ln T]_p$
v_T^*	quantity defined by equation (20.54) in Sect. 20
$\boldsymbol{W}$	symmetric tridiagonal matrix defined by equation (34.28)
W	variable defined by equation (16.15) in Sect. 16
W	work integral; $(=W_N+W_N+W_C)$
W_C	work due to the variation of convective energy flux defined by equation (26.4)
W_F	work due to the variation of radiative energy flux defined by equation (26.3)
W_N	work due to nuclear energy generation defined by equation (26.2)
W_{leak}	kinetic energy leaked by running waves in Sect. 27
W_{mech}	mechanical work defined by equation (30.1); $(=W_{pr}+W_{str})$
W_{pr}	a part of mechanical work due to turbulent pressure defined by equation (30.4)
W_{str}	a part of mechanical work due to turbulent viscous stress term defined by equation (30.5)
W_{th}	thermal work
ΔW	derivative of the work integral $(=dW/dM_r)$ in Sect. 27
$\boldsymbol{w}$	matrix defined by equation (18.103) in Sect. 18.2
$\boldsymbol{w}$	vector composed of w_i in Sect. 41
w	variable defined by equation (16.10) in Sect. 16
w_i	observationally known data in Sect. 41
X	hydrogen abundance
X	quantity defined by equation (20.48) in Sects. 20 and 30
X_i	mass fraction of an element i
X_3	mass fraction of ^{3}He
x	nondimensional radius fraction; $(=r/R)$
x	one of the two-dimensional coordinates on the solar disk in Sect. 39
$\boldsymbol{Y}_i\ (i=1, 2)$	column vector composed of y_i^l in Sect. 34
Y	helium abundance
Y	quantity defined by equation (20.49) in Sects. 20 and 30
$Y_l^m(\theta, \phi)$	spherical surface harmonics defined by equation (13.58)
$\cdot Y_l^m(\theta, \phi)$	function defined by equation (34.37)
y	one of the two-dimensional coordinates on the solar disk in Sect. 39
$y_i\ (i=1,2,3,4,5,6)$	nondimensional variables defined by equations (18.1)–(18.4) for $i=1$, 2, 3, and 4 and by equations (24.5) and (24.6) for $i=5$ and 6
$y_i^l\ (i=1,2,3)$	nondimensional variables defined by equation (34.6) wih superscript representing terms proportional to $Y_l^m(\theta, \phi)$ in Sect. 34
y_i^n	i-th nondimensional variable $y_i(x)$ at $x=x_n$ in Sect. 18 and 24
$\boldsymbol{Z}$	matrix defined by equation (18.105) in Sect. 18.2
$\boldsymbol{Z}_i\ (i=1,2)$	column vector defined by equation (34.33) in Sect. 34
Z	mass fraction of heavy elements
Z	quantity defined by equation (20.50) in Sects. 20 and 30

z	height
$\boldsymbol{\alpha}$	matrix consisting of eigenvectors in Sect. 19
α	ratio of the mixing length to the pressure scale height; $(=l_t/H)$
α	relative amplitude of oscillation $\lvert\nabla\cdot\boldsymbol{\xi}\rvert$ or $\lvert\delta\rho/\rho\rvert$ in Sect. 30
α_0	quantity defined by equation (26.10)
α_1	quantity defined by equation (26.12)
α_m	expansion coefficient of $\boldsymbol{\xi}^{(0)}$ in a rotating star defined by equation (19.19)
β	ratio of the gas pressure to the total pressure
β	angle of the rotation axis to the magnetic axis of a star
β_{nlm}	expansion coefficients of $\boldsymbol{\xi}^{(1)}$ in a rotating star defined by equations (19.20) and (19.31)
Γ_1	adiabatic exponent; $[=(\frac{\partial \ln p}{\partial \ln \rho})_S]$
Γ_2	adiabatic exponent; $[=1/\{1-(\partial \ln T/\partial \ln p)_S\}]$
Γ_3	adiabatic exponent; $[=(\frac{\partial \ln T}{\partial \ln \rho})_S+1]$
γ	ratio of the specific heats; $[=c_p/c_v]$
γ_g	ratio of the specific heats for the ideal gas
γ	quantity defined by equation (18.35) in Sect. 18
γ_{lm}	expansion coefficients of $\boldsymbol{\xi}^{(0)}$ in a rotating star defined by equations (19.20) and (19.32)
Δ	quantity defined by equation (17.6)
δ	Lagrangian perturbation, e.g., δT, δp, etc.
$\delta_{ll'}$	Kronecker's delta
δ_1, δ_2	quantities defined by equation (20.28)
$\delta_n^{(l)}$	argument of complex variable $\xi_{r,nl}$ in Sect. 4
ε_N	rate of nuclear energy generation
ε_S	entropy dependence of nuclear energy generation rate; $[=c_p(\frac{\partial \ln \varepsilon_N}{\partial S})_p]$
ε_T	temperature dependence of nuclear energy generation rate; $[=(\frac{\partial \ln \varepsilon_N}{\partial \ln T})_\rho]$
ε_V	rate of viscous dissipation
ε_{ad}	pressure dependence of nuclear energy generation rate; $[=(\frac{\partial \ln \varepsilon_N}{\partial \ln p})_S]$
ε_ρ	density dependence of nuclear energy generation rate; $[=(\frac{\partial \ln \varepsilon_N}{\partial \ln \rho})_T]$
ϵ	small quantity
ϵ	phase correction term in the quantization rule defined by equation (41.33) in Sect. 41
ζ	variable defined by equation (16.14) in Sect. 16
ζ	radial component of vorticity $\boldsymbol{\omega}$ in Sect. 33
$\boldsymbol{\eta}_m$	toroidal modes defined by equation (19.21)
η	growth rate; $(=-\sigma_I/\sigma_R)$
η	quantity defined by equation (34.15) in Sect. 34
$\tilde{\eta}$	canonical variable; $[=\frac{p'}{\rho}\exp(-\int_0^r \frac{N^2}{g}dr)]$ in Sect. 15
$\tilde{\eta}_N$	canonical variable defined in Sect. 22
Θ	l-independent part of gravity wave potential defined by equation (43.13) in Sect. 43
θ	polar angle in polar coordinates (r, θ, ϕ)
θ_B	polar angle measured with respect to the magnetic axis of a star in the co-rotating frame in Sect. 19.5
θ_I	polar angle measured with respect to the rotation axis of a star in an inertial frame in Sect. 19.5

θ_L polar angle measured with respect to the line-of-sight in an inertial frame in Sect. 19.5

θ_R polar angle measured with respect to the rotation axis of a star in the co-rotating frame in Sect. 19.5

θ_i average weight in difference scheme in Sect. 18 and 24

κ inverse of penetration depth of the evanescent wave; $[\kappa^2 = -k_r^2]$

κ opacity

κ_S entropy dependence of opacity with constant pressure; $[= c_p(\frac{\partial \ln \kappa}{\partial S})_p]$

κ_T temperature dependence of opacity with constant density; $[= (\frac{\partial \ln \kappa}{\partial \ln T})_\rho]$

κ_{ad} pressure dependence of opacity with constant entropy; $[= (\frac{\partial \ln \kappa}{\partial \ln p})_S]$

κ_ρ density dependence of opacity with constant temperature; $[= (\frac{\partial \ln \kappa}{\partial \ln \rho})_T]$

κ_t eddy conductivity

$\boldsymbol{\Lambda}$ diagonal matrix consisting of the characteristic values of the matrix $\boldsymbol{O}$

$\boldsymbol{\Lambda}$ diagonal matrix defined by equation (34.21) in Sect. 34

Λ^n_{lk} quantity defined by equation (18.70)

λ wavelength of spectral line

λ_K eigenvalue in Sect. 18.2

λ_h horizontal wavelength

λ_i roots of characteristic equation in Sect. 18.1

λ_i characteristic values of matrix $\boldsymbol{\Lambda}$ in Sect. 41

$\lambda_j^{(m)}$ j-th eigenvalue of the diagonal matrix $\boldsymbol{D}$ in Sect. 34

$\lambda(r)$ phase angle of the phase diagram in Sect. 16

$\Delta\lambda$ wavelength measured from the line center in Sect. 7

$\Delta\lambda_R$ rotational width of spectral line in Sect. 7

μ mean molecular weight

μ $= \cos\theta$ in Sect. 13

μ ordering number defined by equation (34.38) in Sect. 34

μ_t turbulent viscosity

ν frequency; $(= \sigma/2\pi = 1/\Pi)$

ν_0 characteristic frequency defined by equation (9.2)

ν_0 frequency of the main pulsation in Sect. 10

ν_{ij} temperature dependence of nuclear reaction rate of i- and j-nuclei [see equation (27.18)]

Ξ_l radial component of the relative displacement vector $\boldsymbol{\xi}/r$ in Sect. 34

Ξ_l gravity wave potential in Sect. 43

$\boldsymbol{\xi}$ displacement vector

ξ_h radial part of the displacement in the horizontal direction

ξ_r radial part of the displacement in the radial direction

ξ (k', l', m')-mode in Sect. 14

ξ canonical variable; $[= r^2\xi_r \exp(-\int_0^r \frac{g}{c^2} dr)]$ in Sect. 15

ξ_N canonical variable defined in Sect. 22

$\boldsymbol{\Pi}$ matrix defined by equation (18.102)

Π period of oscillation

Π_0 characteristic period of oscillation defined by equation (11.9)

π number π

ϖ radial coordinate in cylindrical coordinates (ϖ, θ, z) in Sect. 36

ρ density

$\bar{\rho}$ stellar mean density

ρ_p $= (\frac{\partial \ln \rho}{\partial \ln p})_{T,X_i}$

$\boldsymbol{\Sigma}$ matrix defined by equation (18.101) in Sect. 18.2 and by equation (41.7) in Sect. 41

σ angular frequency of oscillation; e.g., $f' \propto \exp(i\sigma t)$

σ_A Alfven angular frequency defined by equation (29.15)

σ_I imaginary part of angular frequency

σ_R real part of angular frequency

σ_c angular frequency of oscillation in the co-rotating frame of the star

σ_{ac} acoustic cut-off angular frequency in a plane isothermal atmosphere; $[= c/(2H_p)]$

σ_{ad} angular eigenfrequency of adiabatic oscillation in Sect. 25

σ_{ij} $= \mathscr{E}_t/\mu_t$

σ_{rad} Stefan-Boltzman constant

$\sigma_m^{(1)rot}$ perturbation in angular frequency of the mode with azimuthal order m due to rotation

$\sigma_m^{(1)mag}$ perturbation in angular frequency of the mode with azimuthal order m due to magnetic fields

σ_0 angular frequency of oscillation in the absence of rotation

τ quantity defined by equation (36.16) in Sect. 36

τ acoustic radius defind by equation (41.32) in Sect. 41

τ_C representative time scale of convection

τ_{HK} Helmholtz-Kelvin time scale defined by equation (12.2)

τ_{NA} quantity defined by equation (36.19) in Sect. 36

τ_{damp} damping time

τ_{dyn} dynamical time scale given by equation (12.3) or (22.2)

τ_{ff} free-fall time scale defined by equation (12.1)

τ_{osc} oscillation time scale

τ_{th} thermal time scale given by equation (12.3) or (22.2)

τ_{tr} travel time in Sect. 15

τ_{tr} quantity defined by equation (36.18) in Sect. 36

τ_0 acoustic radius at which the acoustic potential is the minimum in Sect. 41

τ_1, τ_2 acoustic radii at the inner and outer turning points in Sect. 41

Φ gravitational potential

Φ_l acoustic potential defined by equation (41.29) in Sect. 41

ϕ azimuth angle in polar coordinates (r, θ, ϕ)

ϕ_B azimuth angle measured with respect to the magnetic axis of a star in the co-rotating frame in Sect. 19.5

ϕ_I azimuth angle measured with respect to the rotation axis of a star in an inertial frame in Sect. 19.5

ϕ_L azimuth angle measured with respect to the line-of-sight in an inertial frame in Sect. 19.5

ϕ_R azimuth angle measured with respect to the rotation axis of a star in the co-rotating frame in Sect. 19.5

ϕ_p phase of nonradial oscillation

χ quantity defined by equation (41.65) in Sect. 41

χ_ρ $= (\frac{\partial \ln \rho}{\partial \ln p})_T$

χ_T $= (\frac{\partial \ln \rho}{\partial \ln T})_p$

Ψ l-independent part of acoustic potential Φ_l in Sect. 41

Ψ_i	function defined by equation (41.9) in Sect. 41
ψ	stream function in Sect. 33
$\boldsymbol{\xi}$	eigenfunction such as $\rho^{1/2}c^2\nabla\cdot\boldsymbol{\xi}$ in Sect. 41 and 43.3
$\boldsymbol{\varpi}$	angular velocity vector of stellar rotation
$\boldsymbol{\Omega}$	angular velocity vector of a rotating frame in Sect. 19
$\boldsymbol{\Omega}_0$	angular frequency of stellar rotation
Ω	dimensionless angular frequency of stellar rotation; $[=\Omega/(GM/R^3)^{1/2}]$ in Sect. 34
$\hat{\Omega}$	angular frequency of a rotating frame
Ω_0	vorticity
$\boldsymbol{\omega}$	dimensionless frequency; $[=\sigma/(GM/R^3)^{1/2}]$
ω	real part of ω
ω_R	imaginary part of ω
ω_I	dimensionless angular frequency in the frame rotating with Ω; $[=\omega+m\hat{\Omega}]$
ω_c	dimensionless critical cut-off angular frequencies in Sect. 18
ω_{c1}, ω_{c2}	nondimensional angular frequency of r-mode in the limit of $\Omega\to 0$ in Sect. 34
ω_0	temperature gradient; $(=d\ln T/d\ln p)$
∇	adiabatic temperature gradient; $[=(\partial\ln T/\partial\ln p)_S]$
∇_{ad}	radiative temperature gradient
∇_{rad}	gradient of mean molecular weight; $(=d\ln\mu/d\ln p)$
∇_μ	poloidal component of the differential operator ∇ defined by equation (36.9) in Sect. 36
∇_l	Eulerian perturbation; e.g., p', T', etc.
$'$	Lagrangian perturbation; e.g., δp, δT, etc.
δ	nonlinear contribution to fine average from small-scale turbulence
$<>$	local spatial average in Sect. 20
$-$(overbar)	trial value in Sect. 18.2
$-$(overbar)	zonal (azimuthal) average in Sect. 36
$-$(overbar)	time average with a long time span in Sect. 39
$-$(overbar)	convective quantities of state; e.g., ρ_C, T_C, etc.
suffix C	quantities at the stellar center; e.g., T_c, ρ_c, etc.
suffix c	specification of the mode with radial order n, spherical degree l, and azimuthal order m
suffix nlm	quantities associated with the sun; e.g., $M_\odot$
suffix $\odot$	horizontal component; e.g., $\boldsymbol{\xi}_\perp$, $\nabla_\perp$, etc.
suffix $\perp$	equilibrium quantities
suffix 0	real part
suffix R	imaginary part
suffix I	zero-order term in perturbation analysis
superscript (0)	first-order term in perturbation analysis
superscript (1)	spheroidal mode in Sect. 18
superscript (sph)	transposed matrix; e.g., $^t\mathbf{K}$
superscript t	Moore-Penrose generalized matrix; e.g., $\mathbf{K}^+$
superscript +	sign of x; $(=|x|/x)$
sgn(x)	

Subject Index